



Nozzle Design for Improved Useful Fluid Flow in Grinding

Vadim Alexis Baines-Jones

A thesis submitted in partial fulfilment of the requirements of Liverpool
John Moores University for the award of Doctor of Philosophy

January 2010

© V A Baines-Jones, 2010



Nozzle Design for Improved Useful Fluid Flow in Grinding

Vadim Alexis Baines-Jones

A thesis submitted in partial fulfilment of the requirements of Liverpool
John Moores University for the award of Doctor of Philosophy

January 2010

© V A Baines-Jones, 2010

Abstract

This thesis examines the way in which basic mathematical and computational modelling can be used to advance the understanding of fluid flow mechanisms in coolant nozzles used specifically in the grinding environment. It shows how experimental results from a variety of nozzles can be used to confirm and adapt computational simulations to predict nozzle flows accurately.

Analytical modelling of coolant nozzles is at best fragmentary in the open literature. For robust nozzle modelling, not only the internal fluid mechanics need to be considered, but the geometry of the nozzle as well as the influence of the forces acting on the jet by the air velocity and surface tension at the nozzle exit. With ardent research into coolant application in grinding, and the use of higher jet velocity nozzles, the influence of higher velocities on the jet and hence on nozzle performances must be considered. A modelling framework, using computational fluid dynamics (CFD) is developed which allows the construction of complex, multi variable models (as well as multiphase models – i.e. more than one fluid) from descriptions of the nozzle geometry. By taking advantage of the geometry of the nozzle, i.e. its symmetry, these descriptions can be simplified and the number of free parameters (and ultimately elements needed to accurately describe the situation) in the models reduced.

Experimental investigations are carried out in the flow field of turbulent free jets issuing from a range of coolant nozzles using a static Pitot tube system. The studies include documentation of the flow field, validation CFD results for higher velocity measurements, and examination of the coherence length/ jet break-up phenomenon from the nozzle exit-flow analysis.

The fluid velocity measurements from the Pitot tube system show good agreement with that of the CFD simulations in the near field of nozzle. The peak velocity break-up of the jets in different nozzles are found to be significantly different in both shape and magnitude. It is observed that the Rouse-nozzle jet has a smaller mean decay than the standard orifice type jet. A sensitivity analysis is carried out in the nozzle flow to resolve the discrepancies in lower peak velocity break-up in the earlier CFD simulations observed in the regions of large flow velocity gradient. The effect of grid (mesh) size,

mesh resolution, and free surface flow estimation in the calculation of turbulence and ultimately the jet break-up length is studied in this part.

Advantages and drawbacks of the developed CFD model are presented and discussed. Further application of the model is possible in all types of nozzle simulations such as spraying and abrasive water-jet cutting, as well as other metal working procedures. Here also, performance coefficients can be given empirically and improve the robustness of nozzle performance simulations. This work is relevant to many sectors in the manufacturing industry as well as the high-precision industrial arenas. The most notable result achieved from the present work is the nozzle loss and jet-length simulation system that promises an economical solution for reducing environmental impact (through use of less coolant aimed more efficiently) as well as improving production efficiency by ensuring good fluid coverage at the grinding contact. This requires further work to develop the model.

Acknowledgements

Thanks are given to the research manager, Dr. M.N. Morgan, for his direction and providing me with the chance for this research work.

I would like to thank my supervisors; Dr André Batako for his guidance and help throughout the course of this project, as well as the amount of time and effort invested in me giving me the confidence to complete this work; Dr David Allanson for his invaluable insights into fluid dynamics and Tribology, and Professor Brian Rowe for allowing me to probe his vast knowledge of fluid delivery and everything grinding.

Thanks are due to Mr. T. Scargill of the Advanced Manufacturing Technology Research Laboratory (AMTReL) workshops for all of his practical assistance during the experimental work. In addition, I would like to thank everyone at AMTReL for all their assistance in manufacture and for keeping me going through the hard times.

I thank the support of the University, the Engineering Department, as well as the funding provided by national research agencies (EPSRC) and industrial sponsors on the project, with special thanks to Ed Brown and Cinetic Landis Ltd for supporting me at a time when funding was due to end.

My sincere thanks go to my brother for his patience throughout an editing and cross-reviewing process (which constitutes a rather difficult balancing act). Thanks to my parents for putting up with a string of trips around the country, lost weekends, and odd working hours, and for all their support during my studies, and finally, to my fiancée, for her continued encouragement, support and dedication in getting me over the final hurdle.

Contents

ABSTRACT	II	
ACKNOWLEDGEMENTS	IV	
TABLE OF FIGURES	IX	
LIST OF TABLES	XV	
NOMENCLATURE	XVI	
CHAPTER 1	INTRODUCTION	1
1.1	BACKGROUND	1
1.2	AIM	4
1.3	RESEARCH OBJECTIVES	4
1.4	CONTRIBUTIONS TO KNOWLEDGE	5
1.5	THESIS SCOPE	5
1.5.1	<i>Research Methodology</i>	6
CHAPTER 2	REVIEW OF PREVIOUS WORK	8
2.1	MACHINING	8
2.2	THE GRINDING PROCESS	8
2.2.1	<i>Grinding mechanisms</i>	9
2.2.2	<i>Types of grinding</i>	10
2.2.3	<i>Advances in grinding</i>	13
2.2.4	<i>Grinding coolant</i>	15
2.2.5	<i>Thermal Economy during the grinding process</i>	19
2.2.6	<i>Health concerns with cutting fluids</i>	22
CHAPTER 3	EFFECTIVE COOLANT APPLICATION	26
3.1	GRINDING FLUID NOZZLES	26
3.1.1	<i>Nozzles for High Speed Grinding</i>	27
3.1.2	<i>Coherent Jet Nozzle</i>	31
3.1.3	<i>The Grinding Contact</i>	35
3.1.4	<i>Shoe nozzles</i>	36
3.1.5	<i>Position of Grinding Fluid Nozzles</i>	37
3.1.6	<i>Coolant flow rate</i>	39
3.1.7	<i>Useful Flow</i>	41
3.1.8	<i>Collection of useful flow</i>	42
3.1.9	<i>Air Barrier</i>	43
3.2	SUMMARY	45
CHAPTER 4	REVIEW OF CFD TECHNIQUES	46
4.1	CFD METHODS AND REASONING	46

4.2	THE FVM AND MESH DISCRETISATION	47
4.3	FLUID MECHANICS USING CFD	50
4.3.1	<i>Internal Pipe flow</i>	50
4.4	SUMMARY	53
CHAPTER 5	CFD STUDIES OF NOZZLE INTERNAL AND EXIT FLOWS	54
5.1	INTRODUCTION	54
5.2	SIMULATION SETUP	54
5.3	THREE-DIMENSIONAL SIMULATION SETUP	55
5.3.1	<i>Upwind</i>	66
5.3.2	<i>Residual Type and Target</i>	68
5.3.3	<i>Mesh Resolution near the Wall using Yplus (y+)</i>	71
5.3.4	<i>Results</i>	72
5.4	INTERNAL FLOW ANALYSIS OF A SUDDEN CONTRACTION – ORIFICE NOZZLE	78
5.4.1	<i>Results</i>	78
5.5	INTERNAL FLOW ANALYSIS OF THE ROUSE SHAPED CONTRACTION	82
5.5.1	<i>Results</i>	82
5.6	INTERNAL FLOW ANALYSIS OF CONVENTIONAL GRINDING NOZZLES	86
5.6.1	<i>Triangular wedge nozzle</i>	88
5.6.2	<i>Rectangular slot nozzle</i>	90
5.6.3	<i>Cylindrical orifice nozzle</i>	91
5.6.4	<i>Discussion</i>	92
CHAPTER 6	THEORETICAL MODELLING OF JET COHERENCY	94
6.1	INTRODUCTION	94
6.2	COHERENCE LENGTH FROM FLUID JET BREAK UP	94
6.2.1	<i>The turbulent jet</i>	97
6.2.2	<i>Effect of internal nozzle body shape on jet coherency</i>	99
6.3	COMPUTATIONAL MODELLING OF MULTIPHASE FLUID FLOWS	104
6.4	COMPARISON OF AVAILABLE CFD TOOLS	104
6.4.1	<i>PHOENICS</i>	104
6.4.2	<i>FLUENT</i>	105
6.4.3	<i>CFX 10</i>	105
6.5	THREE DIMENSIONAL EXIT FLOW ANALYSIS SETUP	107
6.5.1	<i>Geometry creation</i>	107
6.5.2	<i>Meshing</i>	108
6.5.3	<i>Pre-processing</i>	110
6.5.4	<i>Post-processing</i>	112
6.6	THREE DIMENSIONAL NOZZLE-EXIT-FLOW ANALYSES	113
6.7	MODELLING OF MULTIPHASE FLOW	113
6.8	TURBULENCE MODELS	114

6.8.1	<i>Shear stress transport model</i>	114
6.8.2	<i>ANSYS CFX software's near-wall treatment</i>	114
6.9	RESULTS	115
6.10	SLOT NOZZLE INVESTIGATION	127
6.11	SUMMARY	131
CHAPTER 7	CONSTRUCTION AND DESIGN	133
7.1	NOZZLE DESIGN AND CONSTRUCTION	133
7.2	NOZZLE EXIT SHAPE	136
7.3	FLOW CONDITIONERS	136
7.4	FLUID PRESSURE MEASUREMENTS	139
7.4.1	<i>Measurement technique</i>	142
7.5	NOZZLE INSPECTION TEST RIG	142
7.6	PITOT SYSTEM TO DETERMINE JET COHERENCY	142
7.7	FLUID DELIVERY SYSTEM	146
7.8	NOZZLE POSITIONING SYSTEM	147
7.9	FLUID COLLECTION	149
CHAPTER 8	EXPERIMENTAL PROCEDURE AND RESULTS	151
8.1	FLOW CONDITIONER TESTS	151
8.1.1	<i>Flow conditioner design</i>	153
8.1.2	<i>Flow conditioner results</i>	155
8.2	NOZZLE COHERENCE LENGTH TESTS	157
8.2.1	<i>Nozzle coherence length determination</i>	158
8.3	COLLECTION TESTS FOR NOZZLE POSITION	169
8.4	VERIFICATION AND VALIDATION OF THE SIMULATIONS	173
8.4.1	<i>Verification</i>	174
8.4.2	<i>Validation</i>	177
8.5	FURTHER NOZZLE COMPARISON AND VERIFICATION WORK	185
8.6	RESULTS	186
CHAPTER 9	DISCUSSION	192
9.1	DEVELOPMENT OF THE SIMULATION	192
9.1.1	<i>Limitations of the simulation</i>	194
9.1.2	<i>Experimental methods</i>	195
9.2	SUMMARY	199
CHAPTER 10	CONCLUSIONS AND RECOMMENDATIONS FOR FUTURE WORK	200
10.1	CONCLUSIONS	200
	RECOMMENDATIONS FOR FUTURE WORK	202
REFERENCES		203

Appendix A	→	Working Drawings	A1
Appendix B	→	Photographs	B1
Appendix C	→	Positioning Case Study	C1
Appendix D	→	Multiphase System Theory	D1
Appendix E	→	Additional Results	E1
Appendix F	→	Hysol X Data Sheet	F1
Appendix G	→	Publications	G1

Table of Figures

Figure 2-1 Chip formation from the workpiece	9
Figure 2-2 Ploughing in the grinding contact (Monici 2005)	10
Figure 2-3 Centred cylindrical grinding (Cinetic Landis Ltd 2007)	11
Figure 2-4 Schematic of cylindrical grinding	11
Figure 2-5 Typical surface grinding process.....	12
Figure 2-6 Illustration of volumetric material removal during surface grinding.....	13
Figure 2-7 Device used to reduce the air barrier surrounding the grinding wheel (Campbell 1997)	15
Figure 2-8 Functions and aims of coolant.....	16
Figure 2-9 Total energy dissipation during a typical disc and cup grind, adapted from Ott, (2001).....	19
Figure 2-10 Heat Distribution during a typical cup grind (incorrect fluid application) .	20
Figure 2-11 Heat Distribution during a cup grind (correct fluid application)	21
Figure 2-12 Heat distribution during grinding with wheels @ ($v_s > 100$ m/s)	21
Figure 3-1 Click and fit nozzles.....	26
Figure 3-2 High-speed jet nozzle design.....	27
Figure 3-3 Graphical representation of the Reynolds number (Spirax 2007).....	29
Figure 3-4 Typical orifice nozzle.....	29
Figure 3-5 Typical slot-nozzle exit chamber	30
Figure 3-6 Possible zones of eddy formation in a conventional converging nozzle.....	33
Figure 3-7 Fire hose design proposed by Rouse et al (1952).....	34
Figure 3-8 Different ways of creating a real and false grinding nip within the grinding zone	35
Figure 3-9 Typical coolant shoe nozzle	36
Figure 3-10 Tangential fluid supply.....	38
Figure 3-11 Direct fluid supply to the wheel	39
Figure 3-12 Effect of coolant flow rate and nozzle cross-section on.....	41
Figure 3-13 Coolant supply and the air barrier in grinding (Inasaki 1998)	44
Figure 3-14 Cutting fluid backing up due to boundary layer effects.....	45
Figure 3-15 Summary of fluid application techniques (Brinksmeier et al 1999)	45
Figure 4-1 Flow schematic to determine pressure loss and extent of flow separation (ESDU 2007)	52
Figure 4-2 Typical ANSYS CFX results vs. experimental data (ESDU 2007)	52

Figure 4-3 CFX Prediction Results vs. Bullen's experimental data (ESDU 2007).....	52
Figure 5-1 Geometry Creation in Design Modeller™	56
Figure 5-2 Geometry after the revolve operation.....	56
Figure 5-3 A 4 point convergence curve.....	57
Figure 5-4 ICEM CFD image with regions selected.....	58
Figure 5-5 ICEM Meshing Controls	58
Figure 5-6 Initial tetrahedral mesh with quality statistics.....	60
Figure 5-7 Smoothed mesh with quality statistics	60
Figure 5-8 Aspect ratio of tetrahedral and triangular elements	61
Figure 5-9 Mesh improvement using prismatic elements.....	61
Figure 5-10 Hybrid Mesh with Prismatic elements at the walls.....	62
Figure 5-11 Physics definition for the internal pipe example.....	63
Figure 5-12 Flow conditions for boundary 1	64
Figure 5-13 Flow conditions for boundary 2	64
Figure 5-14 Flow conditions for boundary 3	65
Figure 5-15 Solver control criteria.....	65
Figure 5-16 Defining the solver run and allocating computer usage.....	67
Figure 5-17 RMS residuals	69
Figure 5-18 MAX residuals	70
Figure 5-19 RMS residuals using upwind	70
Figure 5-20 Max residuals using upwind.....	71
Figure 5-21 Three-dimensional velocity vector plot for the pipe (projected onto z).....	73
Figure 5-22 Velocity slice through the pipe.....	73
Figure 5-23 Pressure contour on a slice through the centre of the pipe.....	73
Figure 5-24 Line location for results analysis on the sloped nozzle.....	74
Figure 5-25 Velocity for the entire length of the pipe	75
Figure 5-26 Velocity profile spanning the regions of eddy formation	75
Figure 5-27 Eddy viscosity along the pipe.....	76
Figure 5-28 Line immediately following the change in cross-section.....	76
Figure 5-29 Velocity Profile immediately following the change in section	77
Figure 5-30 Velocity Gradient in the U (x) direction	78
Figure 5-31 Close up of the velocity gradient at the point of contraction	78
Figure 5-32 Line location for results analysis on the orifice nozzle.....	79
Figure 5-33 Residuals for an Upwind convergence at 1e-06.....	79

Figure 5-34 Total Velocity vector plot → Close up of recirculation in corners of orifice nozzle.....	80
Figure 5-35 Velocity on a slice plane through the centre of the flow showing areas of recirculation	80
Figure 5-36 Velocity profile along the centre of the nozzle	81
Figure 5-37 Velocity profile immediately after the change in section	81
Figure 5-38 Line location for results analysis on the Rouse based nozzle design.....	83
Figure 5-39 Velocity slice through the centre of the nozzle	83
Figure 5-40 Eddy Viscosity at the walls of the Rouse based nozzle	83
Figure 5-41 Close up of the total pressure distribution around the change in section....	84
Figure 5-42 Velocity profile along line 3 of the Rouse nozzle.....	85
Figure 5-43 Velocity profile across the nozzle immediately after the change in section	85
Figure 5-44 Velocity along the central axis.....	86
Figure 5-45 TKE distribution in the nozzle	89
Figure 5-46 Eddy viscosity distribution in the nozzle with 23° gradual contraction.....	89
Figure 5-47 Total velocity distribution.....	89
Figure 5-48 Velocity in the vertical direction in the nozzle with 23° gradual contraction	89
Figure 5-49 Velocity vector plot in the nozzle with 23° gradual contraction.....	90
Figure 5-50 Streamlines of velocity distribution in the nozzle with 23° gradual contraction.....	90
Figure 5-51 Velocity in the vertical direction in the long slot nozzle.....	91
Figure 5-52 Streamlines in the long slot nozzle.....	91
Figure 5-53 Streamline in the orifice nozzle.....	92
Figure 5-54 Velocity in the Y direction for the orifice nozzle.....	92
Figure 6-1 Schematic for the definition of coherence length (adapted from Cui 1995).	95
Figure 6-2 General shape of a liquid jet break up curve (adapted from Cui 1995)	95
Figure 6-3 Effect of transition to turbulence on break up curve (Grant and Middleman 1966)	97
Figure 6-4 Correlation of turbulent breakup data (Grant and Middleman 1966)	98
Figure 6-5 Nozzle factors effecting jet break up length.....	99
Figure 6-6 Orifice nozzle design (internal area of fluid shown).....	99
Figure 6-7 Nozzle design based on Webster (1995a) (internal area of fluid shown) ...	100
Figure 6-8 Straight sided nozzle design (internal area of fluid shown).....	100

Figure 6-9 Fluid velocity versus coherence length using the Grant and Middleman equations	103
Figure 6-10 Geometry for the Rouse based nozzle body.....	107
Figure 6-11 Three dimensional geometry of the nozzle flow region.....	107
Figure 6-12 Nozzle with the user specified enclosure	108
Figure 6-13 2D regions from ICEM	108
Figure 6-14 Mesh statistics after both tetrahedral and prismatic meshing	109
Figure 6-15 Completed volume mesh from ICEM	110
Figure 6-16 Quality of the mesh after 5 smoothing iterations	110
Figure 6-18 Physics for the fluid pairs.....	111
Figure 6-19 Fluid models for use in the simulation.....	111
Figure 6-20 Solver criteria for the solution.....	112
Figure 6-21 Completed simulation tree from CFX-Pre	112
Figure 6-22 Flow chart for simulation setup.....	113
Figure 6-23 k-e model prediction of diffuser flows (ANSYS User Guide 2005).....	115
Figure 6-24 SST model prediction of diffuser flows (ANSYS User Guide 2005).....	115
Figure 6-25 Model with adaptive meshing and boundary conditions.....	116
Figure 6-26 Vector plot for the slant nozzle at 10 l/min.....	118
Figure 6-27 Superficial vector plot for the slant nozzle at 10 l/min (water).....	118
Figure 6-28 Superficial vector plot for the slant nozzle at 10 l/min (air)	119
Figure 6-29 Areas of mesh refinement in the slant nozzle	119
Figure 6-30 Water velocity in the vertical direction (y direction)	120
Figure 6-31 Isosurface for velocity at 4m/s	121
Figure 6-32 Isosurface for velocity at 5m/s	122
Figure 6-33 Isosurface for velocity at 6m/s	122
Figure 6-34 Vector plot for the slant nozzle at 20 l/min.....	123
Figure 6-35 Superficial velocity vector plot for the slant nozzle at 20 l/min (water)...	124
Figure 6-36 Superficial vector plot for the slant nozzle at 20 l/min (air)	124
Figure 6-37 Areas of refinement for the slant nozzle jet	125
Figure 6-38 Water velocity in the vertical direction (y direction) for the slant nozzle at 20 l/min	126
Figure 6-39 Isosurface for velocity at 7m/s	126
Figure 6-40 Isosurface for velocity at 10m/s	127
Figure 6-41 Water Velocity on a central slice plane.....	128

Figure 6-41 Total pressure on a centralised slice plane	129
Figure 6-42 Velocity profile at the nozzle exit	129
Figure 6-43 Velocity profile relaxation for C_L	130
Figure 6-44 Velocity profiles for the slot nozzle	131
Figure 7-1 Sketch of a conventional high-speed slotted jet nozzle.....	135
Figure 7-2 Sketch of the new rectangular nozzle proposed in Cui (1995) p.38	135
Figure 7-3 Mitsubishi flow conditioner	137
Figure 7-4 Grid based flow conditioner (Grid size varies dependant on research)	137
Figure 7-5 Uniform velocity flow conditioner.....	138
Figure 7-6 Velocity profile after the flow conditioner (Cui 1995)	138
Figure 7-7 Pressure measurements in a dynamic fluid system	140
Figure 7-8 Pressure transducer with unamplified output.....	141
Figure 7-9 Modification of the Jacobson surface grinder for experimental nozzle tests	143
Figure 7-10 Sketch of the jet coherency measurement system.....	144
Figure 7-11 Measurement of the jet width.....	144
Figure 7-12 Pitot tube motion through the fluid stream.....	145
Figure 7-13 Nozzle positioning system	148
Figure 7-14 Fluid collection method.....	150
Figure 8-1 Calibration of the pressure transducer.....	152
Figure 8-2 Pressure sensor calibration for the nozzle coherence length tests.....	153
Figure 8-3 Types of flow conditioners used for jet width testing.....	154
Figure 8-4 Velocity profiles for the stream with no conditioning (conditioner 1- measured values).....	155
Figure 8-5 Surface image for the stream with no conditioning (conditioner 1- measured values).....	156
Figure 8-6 Coherence length and jet width for nozzle 5 with flow conditioner 4- measured values	157
Figure 8-7 Jet width vs. peak velocity width measurements	159
Figure 8-8 Velocity profiles for nozzle 1 - measured values.....	160
Figure 8-9 Velocity surface graph for nozzle 1- measured values	161
Figure 8-10 Coherence length and jet width for nozzle 1- measured values.....	161
Figure 8-11 Velocity profiles for nozzle 2- measured values.....	162
Figure 8-12 Velocity surface graph for nozzle 2- measured values	162

Figure 8-13 Coherence length and jet width for nozzle 2- measured values.....	162
Figure 8-14 Lechler solid jet nozzle	166
Figure 8-15 “figure-8” flow conditioner.....	166
Figure 8-16 Coherence length of each of the nozzles examined experimentally	167
Figure 8-17 Example of coverage using different nozzle to wheel/workpiece contact zone distances	168
Figure 8-18 Nozzle distance experimental arrangement.....	171
Figure 8-19 Effect of nozzle distance from the grinding contact on collected fluid	171
Figure 8-20 Nozzle movement distance experimental arrangement.....	172
Figure 8-21 Effect of differing nozzle position on collected flow.....	172
Figure 8-22 Mesh Refinement study for the improved model.....	177
Figure 8-23 Adaptive mesh refinement in the slant nozzle with 2.5mm diameter orifice	177
Figure 8-24 Experimental results for Rouse nozzle 9mm @ 20 l/min	179
Figure 8-25 Simulation results for Rouse nozzle 9mm @ 20 l/min	180
Figure 8-26 Comparison of centre line velocities (2.5 Slant @ 20 l/min).....	181
Figure 8-27 Transverse velocity profile at nozzle orifice.....	182
Figure 8-28 Transverse velocity profile at 100mm from nozzle orifice.....	183
Figure 8-29 Transverse velocity profile at 450mm from nozzle orifice.....	183
Figure 8-30 Transverse velocity profile at 650mm from nozzle orifice.....	184
Figure 8-31 Velocity contour plot for the 2.5mm Ø slot nozzle through the centre of the jet.....	184
Figure 8-32 Illustration of the paths for centreline and streamline velocity predictions	186
Figure 8-33 Water Superficial velocity for the orifice nozzle	187
Figure 8-34 Centreline and streamline velocities for the orifice nozzle.....	188
Figure 8-35 Water Superficial velocity for the Rouse based nozzle.....	188
Figure 8-36 Close up of the central core of the Rouse based nozzle	189
Figure 8-37 Centreline and streamline velocities for the orifice nozzle	189
Figure 8-38 Velocity decay for the orifice nozzle	190
Figure 8-39 Velocity decay for the Rouse based nozzle.....	191
Figure 9-1 Experimental and predicted values of coherence length.....	197

List of Tables

Table 2-1 Grinding fluid characteristics (1, worst; 4, best) (Webster 1995c)	17
Table 2-2 Fluid selection table.....	18
Table 2-3 Average composition of grinding swarf (Chang et al 2006)	22
Table 2-4 Overview of different grinding regimes	25
Table 6-1 Mesh criteria for the Rouse based nozzle.....	109
Table 6-2 Initial Pre-Process settings.....	111
Table 6-3 Boundary conditions for Rouse based nozzle with free surface flow	113
Table 7-1 Relationship between (D_n), (D_j) and (C_d) for Rouse based nozzles	134
Table 8-1 Distribution of each hole on the disk.....	154
Table 8-2 Eight nozzles investigated in the experimentation	160
Table 9-1 Different nozzle types examined	196
Table 9-2 Nozzle loss factors for coherence length.....	198

Nomenclature

Symbol	Meaning
a	Applied depth of cut, acceleration, area
a_e	True depth of cut
a_{sw}	Wheel wear,
a_t	Thermal expansion
A	Cross-Sectional Area, constant
b	Width
b_d	Effective width of dressing tool
b_s	Wheel width
b_w	Workpiece width
C_d	Orifice discharge coefficient
C_a	Contraction coefficient
C_L	Coherence length
C_r	Contraction ratio
C_v	Velocity coefficient
d_e	Equivalent wheel diameter
d_h	Hole diameter
d_i	Internal hole diameter
d_j	Jet diameter
d_n, D_n	Nozzle diameter
d_p	Pipe diameter
d_s	Wheel diameter
d_w	Workpiece diameter
D	Diameter of nozzle feed pipe
E	Young's modulus
E_Q	Error in the target quantity
F_n	Normal grinding force
F_s	Safety factor
F_t	Tangential grinding force
L_f	Losses in flow
h	Height
h_{air}	Air boundary layer thickness
h_g	Depth of wheel surface grains
h_{eq}	Equivalent chip thickness
h_m	Maximum removal height
h_{slot}	Height of slot
h_0	Removal height at chip formation
H	Jet thickness
N_f	Nozzle loss factors
N_t	Nozzle gap thickness
k	Stiffness
L	Length

l_n	Nozzle length
l_p	Pipe length
m	Mass
p	Order of numerical scale
p_a	Absolute atmospheric pressure
p_s	Pressure on wheel surface
p_n	Pressure at nozzle inlet
\tilde{p}	Truncation decay rate
P	Grinding power
P_f	Spindle power due to fluid
P_j	Nozzle jet power
P_p	Pump Pressure
Q	Target quantity
\dot{Q}	Useful flowrate
Q_f	Flowrate
Q_w	Volumetric removal rate
Q'_w	Specific volumetric removal rate
r	Mesh refinement ratio
r_j	Jet Radius
r_s	Wheel radius
r_n	Radius of the pipe at nozzle inlet
R	Gas constant
T_f	Turning torque on the spindle due to the fluid
U, u	component of velocity in a particular Cartesian direction
V	velocity magnitude
v_f	Infeed rate
v_a	Air velocity
v_j	Jet velocity
v_n	Fluid velocity at nozzle outlet
v_s	Wheel surface speed
v_w	Workpiece surface speed
w_{slot}	Slot width

Greek symbols

θ	Angle
Δ	Change in
η	Coefficient of dynamic viscosity
ν	Coefficient of kinematic viscosity, Poisson's ratio
μ	Friction coefficient, grinding force ratio
ρ	Mass density/ Fluid density
ζ	Vorticity, damping ratio
Φ	Wheel porosity

Φ_s	Wheel surface porosity
ω	Angular velocity, Angular frequency
α	Angular acceleration, constant
β	Angle, constant
δ	Deflection
ε	Energy defect ratio
σ	Surface tension of water/air boundary
ζ	Disturbance
φ	Unknown flow variables
Constants	
Ma	Mach number
Re	Reynolds number
We	Weber number
Acronyms / Initialisms	
AMTReL	Advanced Manufacturing and Research Laboratory
ANSYS	Analysis System (Commercial name)
BSP	British Standard Pipe
CBN	Cubic Boron Nitride
CC	Cell-Centred
CFD	Computational Fluid Dynamics
CSV	Comma Separated Value
FDM	Finite Difference Method
FEM	Finite Element Method
FVM	Finite Volume Method
GCI	Grid Convergence Indicator
GERI	General Engineering Research Institute
HEDG	High Efficiency Deep Grinding
HRC	Rockwell Hardness (using a Brale indenter)
LDA	Laser Doppler Anemometry
MKE	Mean Kinetic Energy
PCD	Pitch circle Diameter
PDE	Partial Differential Equation
PIV	Particle Image Velocimetry
TKE	Turbulent Kinetic Energy
Superscripts	
n	Timestep index
T	Vector transpose
($\bar{\quad}$)	Time-average of a property
($\overline{\quad}$)	Time average of a property weighted with σ
	Instantaneous fluctuation from time-average

Chapter 1 Introduction

1.1 Background

The grinding process is under continuous improvement. Advances are occurring in all areas of process technology. In the area of abrasive technologies for example, special micro-fracturing abrasive grits, grown from seeds, permit machining of new and difficult to machine materials at improved material removal rates, at lower grinding temperatures and with improved quality. Developments in machine tool, machine element and wheel technologies have led to the development of the high-speed grinding process, where wheel velocities in excess of 250 m/s are being achieved using synthesised abrasives such as Cubic Boron Nitride (CBN) in special bonding materials. The present area receiving much attention is high efficiency deep grinding (HEDG). HEDG is defined as grinding with deep cuts at high work and wheel speeds and with a high efficiency (Rowe et al 2003).

Due to these advances, adequate application of grinding fluid is highlighted as one of the more important areas of research (Malkin 2008). However, improvement to the design of fluid-delivery systems is constrained by limited understanding of nozzle flows, nozzle positioning, and system requirements for optimal fluid delivery. The process requires high power; this is not beneficial to industry as a whole. To reduce the amount of power needed, effective coolant delivery is necessary (Malkin 2008).

One of the most vital issues within modern grinding processes is deciding upon the correct cutting fluid. Additionally, this correctly selected coolant must be applied efficiently and effectively to obtain the required results. Large engineering firms often pay significant amounts of money for the use of a grinding fluid that has the specific properties they require, but never achieve the optimum output because they are simply supplying the fluid incorrectly.

Although today's cutting fluids are very different from those used many years back, when cutting fluids were considerably more dangerous to human health, some manufacturing questions exist to which the answers are not always apparent. The main functions of coolants are lubrication, bulk and localised cooling, flushing or swarf removal, wheel cleaning and the reduction of workpiece corrosion (Brinksmeier et al

1999). These lead to further purposes more reflective of the needs of industry rather than from a purely mechanical background, namely:

- reduced cycle time (increased process speed);
- improved workpiece quality (e.g.: surface finish, tolerances and so forth);
- reduction in the machine running costs;
- protection of the machine tooling.

As higher removal rates, longer wheel life, and higher quality parts become a necessity, fluid application in the grinding process is increasingly important. Webster (1995a) highlighted the importance of the correct application of grinding coolant when he made the comparison between the coolant selection part of the process and that of wheel selection.

With modern manufacturers requiring high process speeds and reduced production costs and times, the correct method of coolant application, is as vital as selecting the correct wheel to meet the demands of the process. Guo & Malkin (1992) discussed the possibility of using the grinding wheel and its momentum as a pumping mechanism to force as much of the grinding coolant into the grinding contact as possible. Webster (1995a) pointed out that if the wheel is not used in this way, then high contact arc temperatures will exist and will carry on through the grinding zone until bulk cooling takes place after the wheel has passed. This in turn reduces the coolant's ability to keep the grinding contact lubricated and cool, leading to higher grinding forces and an increased risk of thermal damage. It is not the only problem, however, that this cooling of the workpiece after the wheel has passed, can cause. The bulk cooling can create unwanted stresses in the workpiece surface as well as causing the wheel bond and abrasives to overheat ultimately leading to cracking and burning of the parts surface. Control of the maximum grinding temperature is crucial for achieving favourable grinding residual stresses.

At the start of a process, fluid selection is critical (Webster 1999). A suitable fluid for the lubricity and the heat transfer properties required is of paramount importance. The next task faced in the process is how to get the selected fluid into the grinding zone where it is most effective. The difficulty faced in achieving fluid penetration into the grinding zone is the air barrier that circulates with the wheel running at high speeds. The consensus view on achieving this is to match the coolant jet speed to the wheel

peripheral speed. Because of these high nozzle velocities, and with pre-nozzle problems associated with losses in bends and contractions, the jet often breaks up at very short distances (Webster 1999).

Webster's (1995a) round coherent jet nozzle, based on the fire hose nozzles by Rouse et al (1952), is one solution to this jet break up, however knowledge on the nozzle and any possible improvements is limited. The main problem with this solution is cost limitations of the pumping system. In high-speed grinding, above 100m/s at the wheel periphery, the pump pressure requirements can easily surpass 4MPa (Webster 1999). Klocke et al, (2000) proposed the use of shoe nozzles to remove this requirement. Shoe nozzles fit closely around the wheel periphery with fluid supplied to them at very low pressures. The grinding wheel then accelerates the fluid up to its own speed hence matching the periphery speed and accelerating the fluid into the grinding contact. A problem with matching the speed, however, is the power requirement on the main spindle to accelerate the fluid.

It is evident therefore that grinding fluid plays an important role in achieving high removal rates and good work piece quality and it is vital that the fluid is applied correctly and in the right amount. Because of incorrect fluid application, fluid burn-out is still common, grinding quality suffers considerably and substantial amounts of energy is usually wasted in larger production grinding systems (Webster 1995). This is largely because only a small amount of supplied flow ever actually reaches the grinding contact thus turning it into 'useful flow'.

The purchase, management and disposal of metalworking fluids make up an estimated 16 per cent of manufacturing costs in the UK engineering industry (GG199 1999). However, many workshops are not getting the best out of their metalworking fluids and could reduce their operating costs significantly by implementing and improving fluid management and control practices. For companies with poor fluid management procedures, savings of 40 – 60 per cent may be possible by implementing proven waste minimisation techniques (GG199 1999). Industry estimates that metalworking fluids contribute as much as 10 per cent to the cost of a finished part. It includes the initial cost, housekeeping, and cleaning and disposal (GG199 1999). The goals of metalworking fluids management are to reduce costs by increasing the life of the

metalworking fluids and decreasing the amount of disposal. A recent survey conducted from metalworking companies for the UK government found that the average cost of cutting fluid concentrate was £2.32 per litre (GG199 1999). This equates to an average cost of £460 per cubic meter of swarf generated for the lowest users and over £2300 per cubic meter for the highest users surveyed. Stricter legislative controls on the disposal of used metalworking fluids means that the overall costs for consumption of metalworking fluids is also on the rise, again highlighting the need for a better and more optimised fluid management and consumption program.

The focus of the work described in this thesis was to investigate nozzle flows in a range of nozzle geometries. The important effects, that correct nozzle positioning has on overall system performance, was one of the main criteria investigated. The jet coherency length was also studied, as this is critical to achievement of adequate cooling in the grinding contact. The work aimed to result in an enhanced understanding of the requirements for effective coolant application in grinding based on overall system design. Collaborating industrial partners appraised the work completed in a manufacturing environment.

1.2 Aim

The main aim of this research was to design, evaluate and implement application specific nozzle solutions for achievement of useful flow in the grinding environment.

1.3 Research objectives

The completion of the aim was through a number of tasks namely:

- I. A review of existing techniques in the field of grinding. In cylindrical grinding, centreless grinding, surface and creep feed grinding, different nozzles and methods of application are in use. It is critical to familiarise and understand the basics of operation of these grinding techniques and the interaction between the fluids, wheel and the workpiece.
- II. A review of previous work concerning the effects of nozzle design, fluid type and fluid pressure in the grinding process.
- III. A determination of the main parameters affecting nozzle design for optimal coolant delivery (useful flowrate \dot{Q}).

- IV. The development of a theoretical model using CFD to model fluid flows through differing nozzles.
- V. The development of an experimental rig to analyse the effect of changing nozzle parameters and pre-flow conditioners, on the amount of fluid passing through the grinding contact.
- VI. Undertake experimentation to validate the theory for a range of grinding parameters investigated including:
 - a. fluid type;
 - b. nozzle position;
 - c. entry length, corner geometry and edge conditions for the nozzle.
- VII. Investigation of criteria important to the jet coherence of the nozzle both analytically and experimentally.

The outcome of this research aimed for a novel approach to grinding fluid application, which removes the detrimental effects caused by excessive heat transfer (into the workpiece) within the grinding operation.

1.4 Contributions to knowledge

- A working model to predict the fluid path exiting a nozzle orifice has been established and validated experimentally;
- An experimental arrangement to measure jet thickness and jet break-up has been designed and tested;
- The jet break-up length for several coolant nozzles has been established;
- The effect of pre-conditioning on jet break-up has been assessed experimentally;
- Simulation of interior nozzle flows has been attempted, impacting on design, understanding of interior flow phenomenon and efficiency.

1.5 Thesis scope

In this thesis, a method for the prediction of coherence length of coolant nozzles is proposed. The approach is based on the construction of a computational fluid dynamics (CFD) simulation, using ANSYS CFX, supported with theoretical analyses. The thesis concentrates on both internal and external flow prediction to offer advice for improved coolant nozzle design. The scope of research includes:

- The design of the simulation and the CFD: the physical setup and meshing approach are proposed, and the structure of the simulation, and its solver criteria and reliability and accuracy, are defined;
- The formalisation of the notion of ‘coherence length’: a taxonomy of coherence length and jet breakup is developed, including definitions and relations of several kinds of coolant nozzles. Rules to apply grinding coolant correctly in grinding are then developed aiming at extracting clarification from literature and then studies into collected flow;
- Experimentation: a system is developed to demonstrate the success of the proposed approach. Another purpose of the developed machine tool is to validate the results and visual examine fluid jet behaviour. A number of nozzles are used for experiments with a nozzle positioning and fluid collection system.

The original contribution of the thesis lies in three aspects:

1. Coherence length prediction;
2. Nozzle positioning guidance and rules;
3. Nozzle development through internal simulation.

The literature survey in Chapters 2 and 3 shows that prior to this work there was not any approach or tool dealing with the simulation of external flows for grinding fluid nozzles.

1.5.1 Research Methodology

Chapter 2 provides an overview of grinding, grinding coolant, and in particular, their connection and impact on the overall process.

Chapter 3 investigates the existing related work on effective coolant application, namely nozzle design and application techniques.

Chapter 4 presents a review of the relevant CFD techniques.

Chapter 5 explores the proposed CFD language in detail, including both internal and external analysis of each nozzle investigated.

Chapter 6 presents theory defining the factors affecting coherency of a fluid stream as well as the basis of fluid mechanics relating to the objectives of this project.

Chapter 7 introduces the equipment and sensors used in the experimental study that was predominantly based on a purpose modified surface grinding machine.

Chapter 8 presents the results of the experimental tests. Optimal fluid flow testing of the system is identified with reference to previous experimental work carried out on finding the coherency of differing nozzle and system designs. Key milestones for the final design, integration, installation, and testing of the fluid system on the modified Jacobson surface grinder are identified with reference to the previous experimental work carried out.

Chapter 9 discusses the proposed approach and the supporting simulation according to a set of criteria.

In Chapter 10, conclusions are drawn based on the discussion, and prospective further work is discussed.

Chapter 2 Review of Previous Work

2.1 Machining

It is important to view machining as a system consisting of the workpiece, the tool and the machine. Traditional machining includes turning, milling, drilling, and grinding; the latter of which is the subject of this work.

2.2 The grinding process

Grinding is the common name for machining processes that utilise hard abrasive particles as the cutting medium. Grinding is a major manufacturing process that accounts for about 20-25 per cent of the total expenditure on machining operations in industrialised countries (Malkin 2008).

In grinding, an abrasive material rubs against the metal part and removes tiny pieces of material. Grinding is often a finishing process used to improve surface finish, abrade hard materials, and tighten the tolerance on flat and cylindrical surfaces by removing a small amount of material. The abrasive material is typically on the surface of a wheel or belt and abrades material in a way similar to sanding. On a microscopic scale, the chip formation in grinding is the same as that found in other machining processes.

The abrasive action of grinding generates heat. Therefore, flooding of the cutting area with grinding coolant is necessary to minimise distortion of, and the risk of thermal damage to, the part.

Reasons for grinding are:

1. the material is too hard for machining economically using other processes. (The material may have been hardened in order to produce a low-wear finish, such as that in a bearing raceway);
2. when it is preferable, abrasive processes can achieve the tolerances required. Grinding can produce flatness tolerances of less than ± 0.0015 mm on a 200 x 200 mm steel surface with adequate supports (Badger 2004);
3. the part needs a high surface quality or surface finish.

There are few grinding limitations on material type e.g. aluminium, steel, ceramics or glass. Grits that can wear away at diamond are usually composed of diamond themselves (Badger 2004). Grinding forms the basis of manufacturing of countless types of products.

2.2.1 Grinding mechanisms

Three main mechanisms involved in grinding are sliding, ploughing, and chip formation. Energy is expended without material removal during sliding and ploughing (see Figure 2-2). Chip formation starts when the grinding wheel grains reach a depth of cut. The depth of cut is affected by the sharpness of the cutting edge, its orientation, its rake angle, the coefficient of friction and the applied force. After chip formation begins, (illustrated in Figure 2-1), ploughing may persist (Malkin 2008).

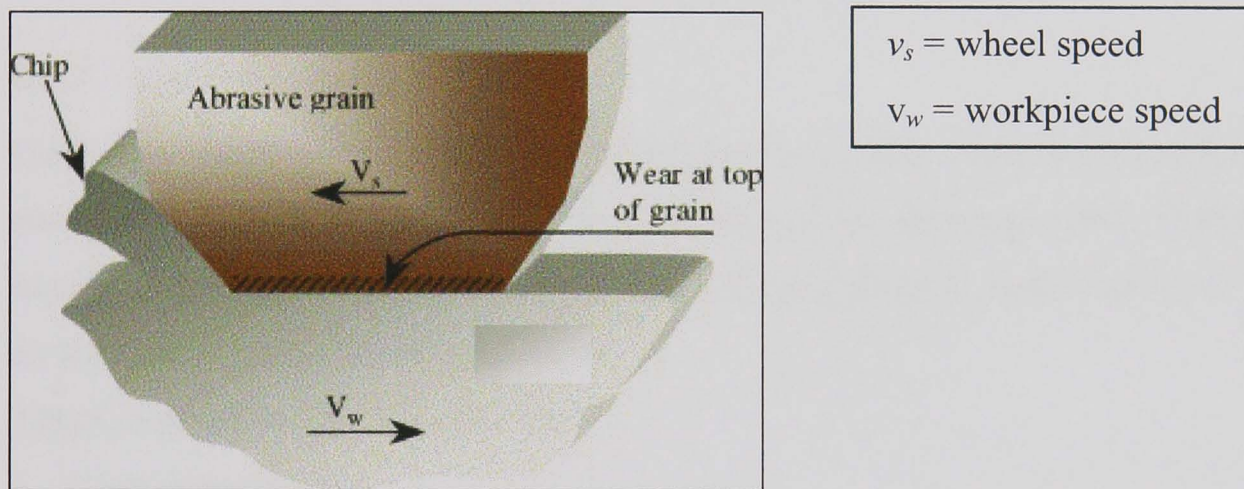
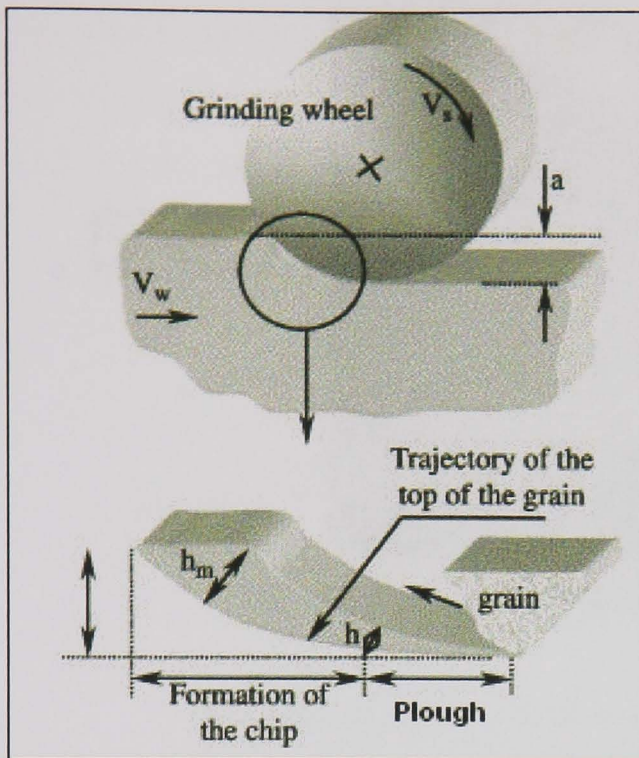


Figure 2-1 Chip formation from the workpiece

Ploughing is associated with the side flow of material from the cutting path to form ridges. It can include plastic deformation of the material passing under the cutting edge (Abebe 1981). Ploughing deformation occurs as the abrasive grain initially cuts into the workpiece. As the cutting point on the grain passes through the grinding zone, its depth of cut increases from zero to a maximum value h_m at the end of the cut. Initially (in up grinding) the grit makes elastic contact (sliding) followed by plastic deformation (ploughing) of the workpiece (Malkin 2008). Figure 2-2 shows the region in which ploughing occurs, just before the formation of chips.



a = depth of cut;
 h_m = maximum removal height;
 h_o = removal height at chip formation.

Figure 2-2 Ploughing in the grinding contact (Monici 2005)

2.2.2 Types of grinding

Over time, many different types of grinding machines have evolved but they all remove material in essentially the same way by the use of the grinding wheel. Differences in machines typically involve the way the part being ground is supported which depends on the type of surface to be generated.

Types of grinding processes include.

- Centreless grinding.
 - Through-feed grinding.
 - Plunge or form grinding.
- Cylindrical grinding.
 - External (Outside diameter grinding).
 - Internal (Inside diameter grinding).
- Surface grinding.

This work is concerned principally with the plane surface grinding operations.

2.2.2.1 Cylindrical grinding

Grinding for surfaces of rotation (axially symmetric surfaces) can be either centred or centreless. Centred grinding involves fixing the part on a spindle axis whilst being ground, as illustrated in Figure 2-3 and described schematically in Figure 2-4.

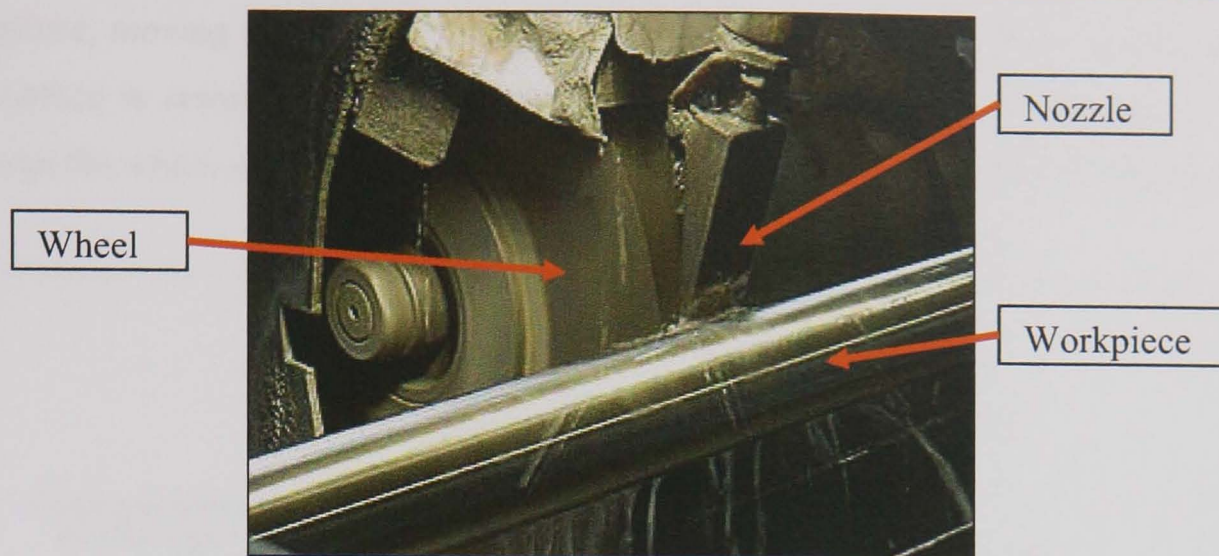


Figure 2-3 Centred cylindrical grinding (Cinetic Landis Ltd 2007)

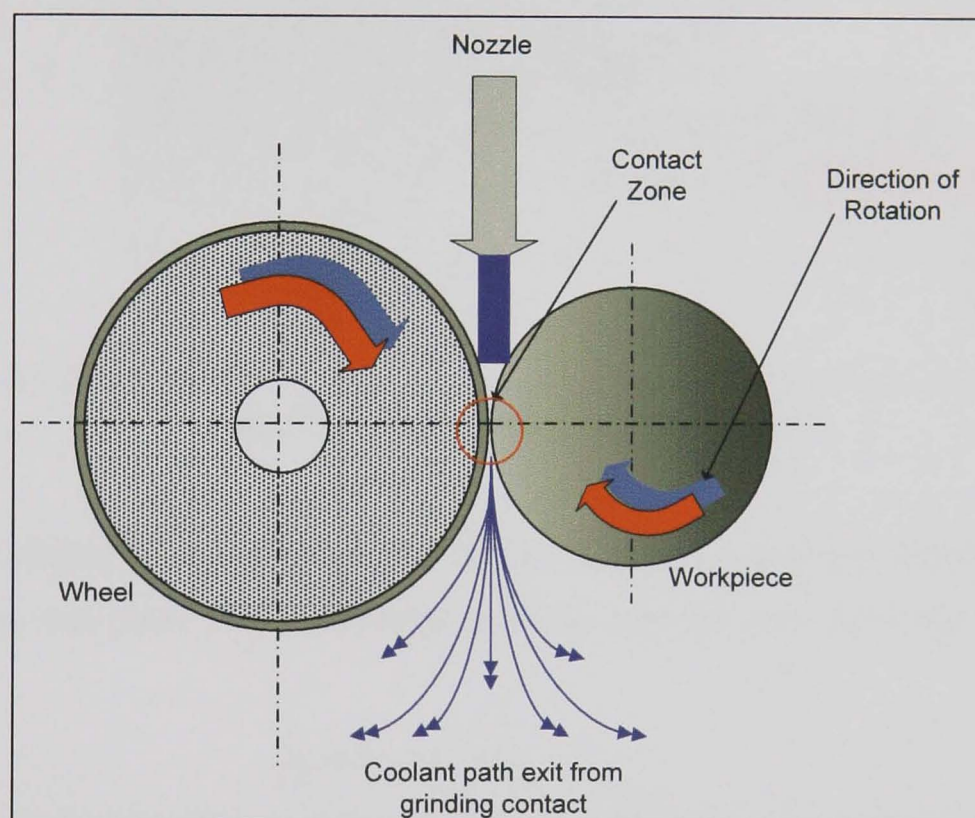


Figure 2-4 Schematic of cylindrical grinding

A point to note in the schematic above is the rotation of the workpiece and the grinding wheel. With external cylindrical grinding, the workpiece and the grinding wheel rotate in like directions. This is so that the surface of the grinding wheel and the surface of the workpiece are moving in opposite directions at the point of contact. This aids material removal in the process and increases productivity.

2.2.2.2 *Surface grinding*

Surface grinding is a process that moves a grinding wheel relative to a surface in a plane. When the edge of the grinding wheel, moving at a wheel speed v_s , meets the

workpiece, moving at a speed of v_w , an amount of material, a_e , is removed such that a flat surface is created (Figure 2-5). A fluid jet presented to the grinding nip, or area between the wheel and workpiece forming a pool of coolant, is supplied at a speed of v_j .

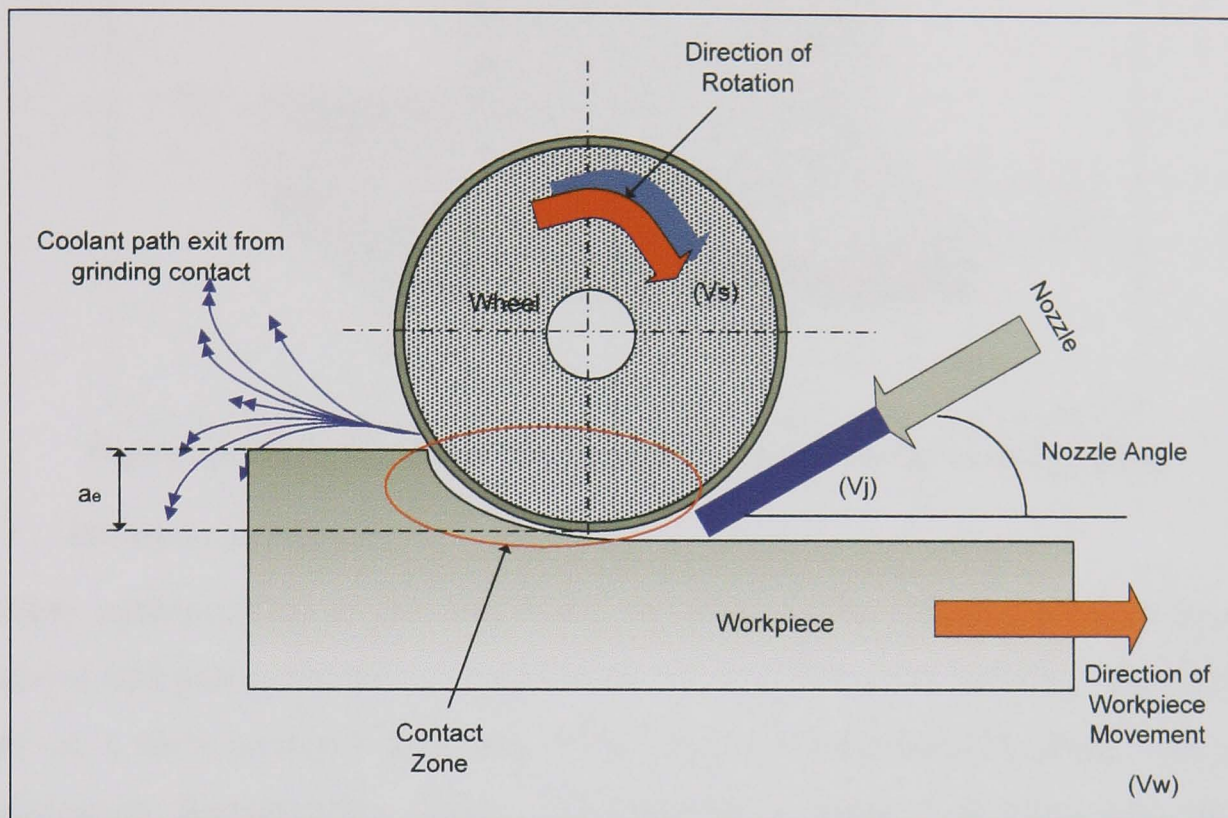


Figure 2-5 Typical surface grinding process

Figure 2-6 illustrates in surface grinding the volume of material removed from the workpiece in one pass. The volumetric material removal rate from the workpiece is, therefore:

$$Q_w = b_w \times a_e \times v_w \quad [2.1]$$

where b_w is the width of the workpiece (or the width of cut if the workpiece is larger than the wheel).

In surface grinding, the wheel is fed down a set distance, a , known as the depth of cut. The real depth of cut varies from this value however, as machine tool deflection and other complexities such as wheel modulus and workpiece hardness affect the desired result. The real or 'effective' depth of cut, a_e , is the actual depth of material removed from the workpiece; the amount of material removed minus the effect from deflections, wheel wear and thermal expansion. In general:

$$a_e = a - \delta - a_{sw} + a_t \quad [2.2]$$

where a_{sw} is the wheel wear, a_t is the thermal expansion and δ is the deflection.

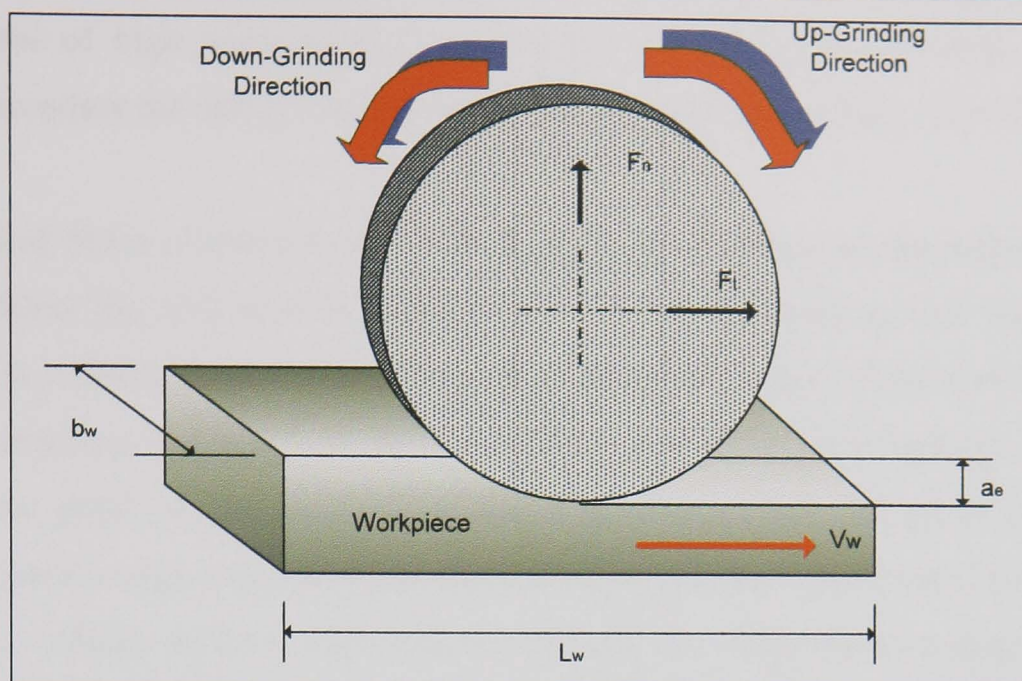


Figure 2-6 Illustration of volumetric material removal during surface grinding

2.2.3 Advances in grinding

A better understanding of the mechanics involved in the grinding process (thermal, structural and procedural for example) have allowed for much speedier modifications based on a more scientific approach. This increased understanding along with recent technological developments means that grinding is being used more and more in industrial processes. A single creep-feed grinding operation now replaces separate milling and finish grinding operations saving time and money (Monici 2005). These new developments make high production rates, without damage to the workpiece caused by excessive temperatures, possible. High efficiency deep grinding (HEDG) requires high power and effective coolant delivery. A further key feature of HEDG is that (theoretically) grinding temperatures are relatively low despite the high material removal rates. A new research machine tool was developed to undertake HEDG in the Advanced Manufacturing Technology Research Laboratory (AMTReL). Key elements of the machine were high power, a linear drive to facilitate high work speed and a hydrostatic bearing arrangement for high wheel speed and high stiffness.

Regimes of deep grinding range from creep feed grinding conducted at low workspeeds to HEDG at fast workspeeds (Rowe et al 2003). An explanation is proposed in this work for why it is possible to work efficiently at these two extremes of removal rate without experiencing the severe problems experienced in the intermediate range. It is proposed that the angle of inclination of the contact plane is an important parameter for the

achievement of high workspeeds. It is argued that workpiece melting provides an ultimate boundary for energy dissipation within the workpiece (Rowe et al 2003).

Outwater and Shaw (1952) assumed that the energy of grinding is dissipated at the shear plane between the chip and the workpiece. The heat transfer to the workpiece was modelled as a sliding heat source at the shear plane so that part of the heat is conducted into the workpiece and part into the chip. Sliding also takes place between the chip and the abrasive grain so that part of the heat is conducted into the grain. Hahn (1962) reasoned from energy considerations that the principal heat generation is at the grain-workpiece rubbing surface. This follows because the shear-plane energy assumption cannot account for the much larger energy experienced in practice, where both shear plane and wear flat energies are important. However, there is a limit to the shear-zone energy that can be carried away by the chips, as Malkin (1971) pointed out. This limit is the melting energy and for ferrous materials is approximately 6 J/mm^3 . The total grinding energy is converted into heat. In most grinding processes, it is safe to assume that the total grinding energy is much greater than the melting energy, as demonstrated by Malkin (1971). It is now shown that this assumption is not safe for high efficiency deep grinding where the total energy may be of the same order and only slightly greater than the melting energy (Rowe et al 2003).

In a high efficiency deep grinding model proposed by Rowe et al (2003), it is impossible to prevent the maximum temperature in the grinding contact approaching the melting temperature of the workpiece material with the inevitable consequence of material softening during the removal process. Even though the contact time between the wheel and the workpiece is relatively short, the contact time is much longer than the contact time between an abrasive grain and the workpiece. It is evident that the material temperature on the contact surface heated locally will be removed with much lower stresses than would normally be the case. In effect, HEDG is a heat assisted removal process. In consequence of the high work speeds and large angle of inclination in HEDG, the finished workpiece surface sees only a small proportion of the heat dissipated in the contact region. The chips remove most of the remaining heat. It is argued whether any of the heat is removed by traditional cooling. It therefore appears that the heat dissipated in the finished workpiece in this example should be low enough to prevent thermal damage (Rowe et al 2003).

2.2.4 Grinding coolant

In a large number of cases, coolant is applied incorrectly. Often a great amount of coolant is used when improved results would be achieved by directing smaller amounts of coolant accurately (Webster et al 1995a). Applying coolant properly and consistently is critical to grinding operations. Some of the benefits of applying coolant properly are reducing and preventing the number of rejected workpieces by reducing thermal softening, burning and hardening as well as reducing cycle time and tool wear. Improvements are seen in dimensional accuracy, throughput, and part-to-part and setup-to-setup consistency. All these mean significant cost reduction (Monici et al 2005).

Figure 2-7, shows an example of one way of improving the application of a cutting fluid in grinding utilising a device used for stripping the wheel of the air barrier. Campbell (1997) (Figure 2-7), proposed this solution using a steel device to minimise the effect of the air barrier that circulates round the grinding wheel. This used a metal plate or deflector positioned very close to the wheel surface ($30\ \mu\text{m}$), and allowed an increase of 500 rpm in the actual wheel speed using exactly the same coolant pressure measured within the grinding zone.

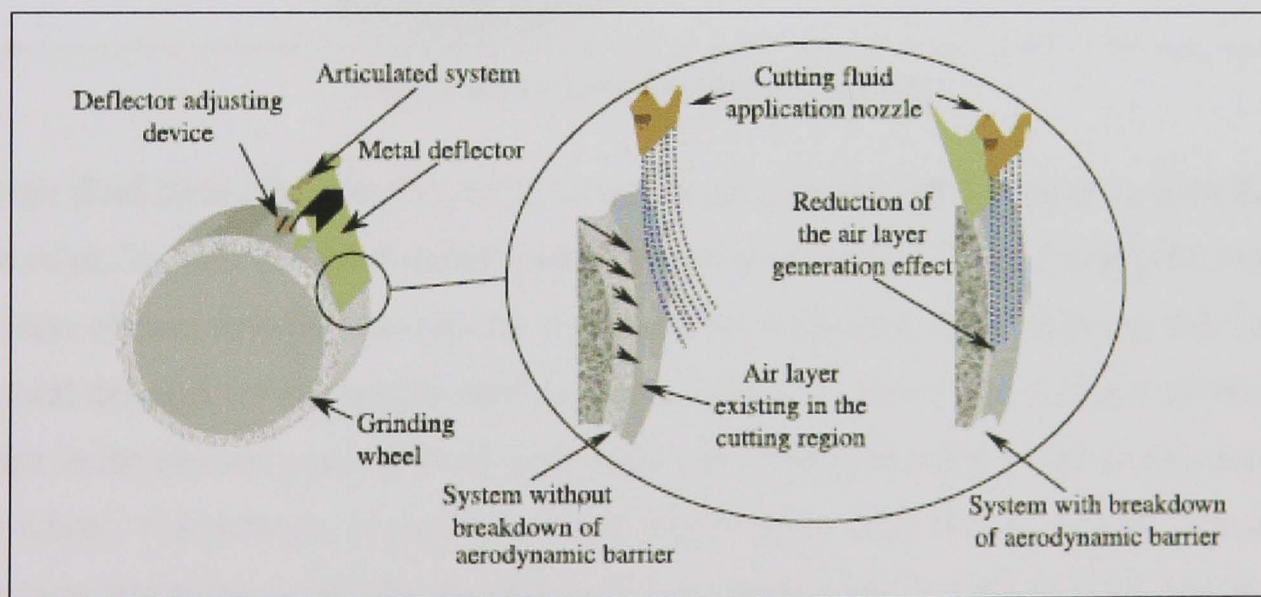


Figure 2-7 Device used to reduce the air barrier surrounding the grinding wheel (Campbell 1997)

According to Runge and Duarte (1990) and Motta and Machado (1995), coolant can perform not only one, but several functions within the grinding operation. Cutting fluid is applied to the grinding zone to limit the heat generated by the grinding operation. The lubrication properties of the cutting fluid prevent the generation of some of this heat by reducing the amount of friction in the grinding zone. The cutting fluid also reduces the

amount of heat in the grinding zone by conduction thus removing some of the heat generated into the fluid rather than into the workpiece reducing the risk of thermal damage. Malkin (1989, p.74) concluded, "The colder the fluid, the more effective the heat transfer." The final purpose of the cutting fluid is to flush away chips generated from the grinding process. Without this necessary chip removal action of the cutting fluid, the grinding chips or swarf may clog the wheel causing wheel loading or it may scratch a fine surface. The forces and energy input (limited however by wheel power) would greatly increase, as would the heat input to the workpiece causing increased risk of thermal damage (Ge et al 2003). Figure 2-8 shows the functions of coolants with the aims projected from these functions.

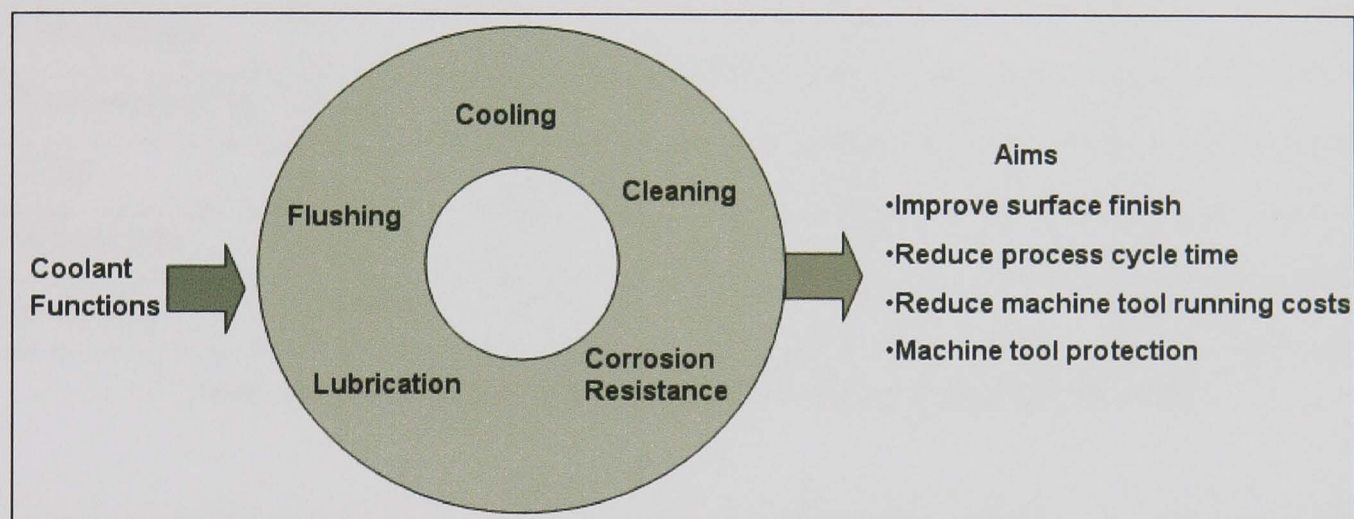


Figure 2-8 Functions and aims of coolant

As the fluid enters the grinding zone, it turns from a liquid into a vapour. It does this in two steps. Initially the fluid enters a state known as nucleate boiling. During this period, the rate of heat transfer between the fluid and the workpiece rises, reducing the risk of thermal damage. As the temperature increases further, however, the fluid enters the next phase in the process and a film of fluid vapour is developed between the workpiece and the wheel. This process is known as fluid film boiling. This vapour or film acts as an insulator and reduces the heat transfer from workpiece to fluid. This inhibits the process and as a result, the workpiece may become permanently damaged at a molecular level through exposure to intense temperatures i.e. thermal damage (Malkin 2008). Therefore, it can be concluded that for the coolant to remain effective within the process, the temperature at which the workpiece is, does not exceed that of the fluid's film boiling temperature. The heat flux that causes the fluid to reach the film boiling temperature is described as the critical burnout limit (Webster 1995c).

Blenkowski (1993) showed that there are four common types of cutting fluids, classified according to their composition: synthetics, semi-synthetics, soluble oil and straight (or neat) oil. Each fluid has its own distinct properties with the main differing characteristic being the type of oil that its base is, namely synthetic oil or a mineral oil. Mineral oils are naphthenic and paraffinic hydrocarbons that are refined from crude oil. Table 2-1 highlights and ranks the properties of these four major kinds of grinding fluids.

	Synthetics	Semi-synthetics	Soluble Oil	Neat oil
Heat removal	4	3	2	1
Lubricity	1	2	3	4
Maintenance	3	2	1	4
Filterability	4	3	2	1
Environmental	4	3	2	1
Cost	4	3	2	1
Wheel life	1	2	3	4
G-Ratios	2.5-7.5	2.5-6.5	4-12	60-120

Table 2-1 Grinding fluid characteristics (1, worst; 4, best) (Webster 1995c)

The four different cutting fluid types listed in Table 2-1 each have their own clear advantages and disadvantages. In an ideal world, a machine operator would have the good points from each of the cutting fluids with none of the bad points to create a ‘super’ fluid. This may contain the maintenance, lubricity and increased wheel life properties of neat oils with the heat removal, filterability, cost and environmental properties of synthetics. Cutting fluid manufacturers are trying to combat these problems with high-level coolants containing a concentrated base that is then mixed with water to form an emulsion (synthetic). Much research effort has looked at the different additives that can be mixed with oil to improve some of its negative characteristics with interesting results. Klocke (2000) showed that if the oil additive concentration increases the process forces, the grinding energy and temperatures decrease while the wheel life increases. This is shown in Table 2-1 with the relevant G-ratios (rate of wheel wear; obtained by dividing the volume of material removed in a particular operation by the volume of the wheel worn away) given for the four different fluid types.

Research from Minke (1999) compared, for different grinding situations, oil and water based cutting fluids suggesting that if surface integrity were most important, then the ranking sequence for cutting fluids from top to bottom would be ester oil, oil-based coolant then water-based emulsions. Minke also showed that the water-based emulsions increased the overall grinding energy leading to an incapability of the grinding fluid to control the temperature and heat transfer to the workpiece resulting in thermal damage. It is also worth noting that when choosing a cutting fluid, certain other advantages and disadvantages (Table 2-2) need identifying, not just the criteria in Table 2-1. This emphasises the previous point.

Traditionally, cutting fluids have been seen as a solution rather than a problem in metal cutting. They prevent overheating of the workpiece, increase tool life, improve surface finish, help to remove swarf from the cutting area, reduce cutting forces, enhance size control and afford some corrosion resistance to work and machine tool (Trent 2000). This set of attributes represents a significant benefit to the manufacturing process and, until recently with new government and European policies, any problems associated with the use of cutting fluids have been accepted as the price of increased productivity.

	Advantages	Disadvantages
Synthetics	High heat transfer. Low impact on environment.	Causes shortening of the wheel life and corrosion to workpieces in prolonged contact.
Semi-synthetics	Good lubrication qualities for medium-heavy duty grinding operations.	Require good quality water supply but tend to foam easily.
Soluble Oils	Provides enhanced corrosion resistance. Better crack penetration ability.	Poor emulsion stability/ prone to separation.
Neat Oils	Good lubricity prolongs wheel life. Higher viscosity oils adhere more strongly, less misting.	Harmful effects on the environment. High costs for maintenance and disposal.

Table 2-2 Fluid selection table

2.2.5 Thermal Economy during the grinding process

During the grinding process, the grinding energy is transformed from kinetic energy into heat, by means of friction between the wheel, or more specifically the abrasive grain, and the workpiece, and crushing and deformation of the workpiece whilst in contact, as well as that generated in the bond material. In a typical conventional grinding process using circular discs and cup wheels, this can be up to 90-92 per cent of the total grinding energy (Ott 2001). The remaining 8 per cent or so of the total energy supplied is converted by the shearing action of material from the workpiece, and that of chip deformation.

Looking back at Figure 2-1, friction occurs principally between the chip and the grain's cutting edge, with a smaller amount at the clearance angle. The reason why a great amount of heat is generated at this point is that often the grain's cutting edge is shaped incorrectly for cutting of the workpiece and ultimately chip formation, due to the size and random shape of the individual grain. It is impossible to say what percentages of the grains actually successfully remove material from the workpiece, but a large proportion of the grains often merely plough the surface of the workpiece (Figure 2-2). The amount of friction generated within the grinding process (Figure 2-9) principally depends on the conditions of the grinding process, and this is largely determined from the total grinding energies supplied. Ott (2001 p.6) also states, "This can be largely reduced by using a good lubricating cooling agent."

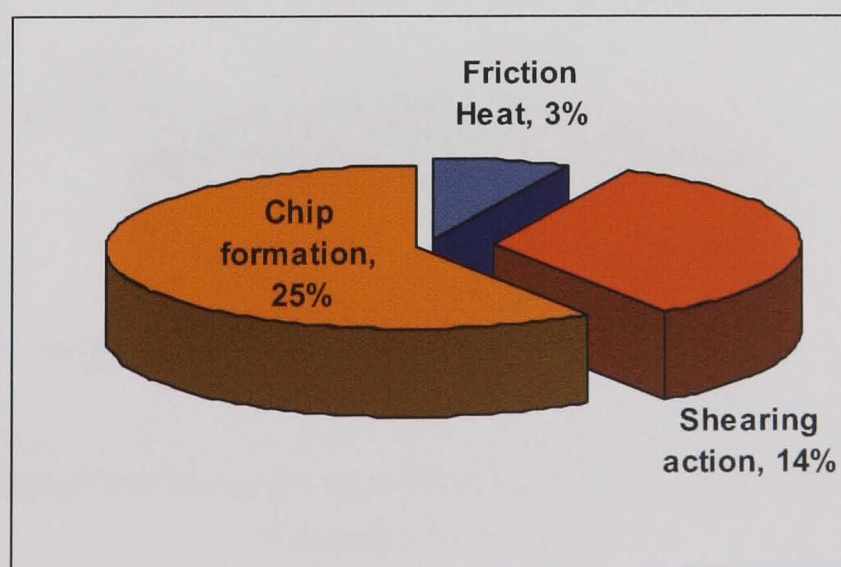


Figure 2-9 Total energy dissipation during a typical disc and cup grind, adapted from Ott, (2001)

Moving this forward, a clear action is required to remove this heat from the process so that the risk of thermal damage or burning of the workpiece is reduced. If 100 per cent of the heat generated were transferred to either the chips or the coolant, then the process would be ideally efficient and could be run at higher speeds, with higher depths of cut, drastically reducing cycle times. This however is not the case, and in typically poor conventional grinding situations with incorrect or insufficient grinding coolant, up to 43 per cent of the heat is transmitted to the workpiece with only a combined total of 46 per cent removed by the coolant and chips (Ott 2001) (Figure 2-10). The wheel also removes some of the heat from the grinding contact. This is a conservative figure however, Rowe (2008) stated that much larger proportions of heat can be conducted into the workpiece using conventional abrasives, almost 60-70 per cent.

In a generic example given by Ott (2001), if the grinding conditions are well adjusted, including correct coolant supply through improved application and coolant quality, then up to 79 per cent of the heat generated is removed by the coolant and chips in combination, with a mere 14 per cent transmitted to the workpiece; the rest removed by the air and wheel. This highlights (Figure 2-11) clearly the importance of correct coolant positioning, when approximately two thirds of the heat transmitted in poor cooling conditions, is removed from the workpiece by improving the coolant application.

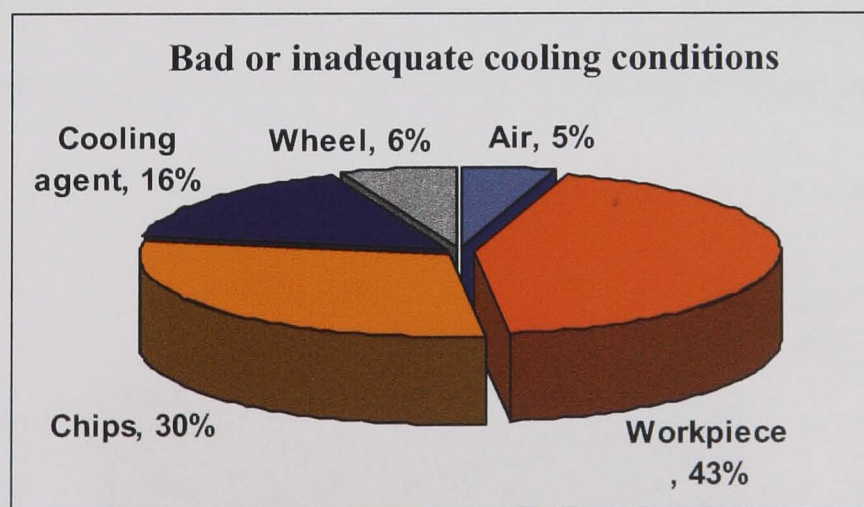


Figure 2-10 Heat Distribution during a typical cup grind (incorrect fluid application)

Adapted from Ott, (2001)

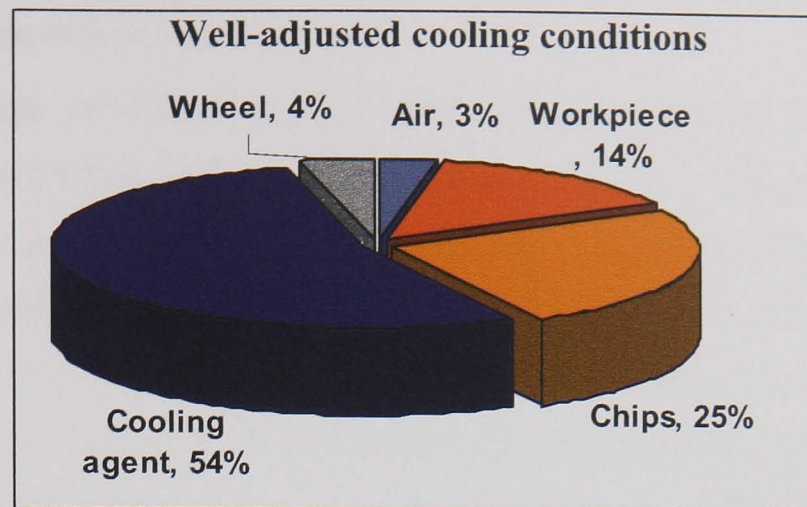


Figure 2-11 Heat Distribution during a cup grind (correct fluid application)

Adapted from Ott, (2001)

With advances in technology and speeds due to improved machine rigidity, during high speed grinding where the wheel is running at speeds in excess of 100 m/s, Ott (2001) states that only 14 per cent of the heat generated by the process is transferred to the workpiece. The chips remove up to 60 per cent, with the cooling agent taking a further 26 per cent of the heat (Figure 2-12). Ott (2001, p.8) puts a disclaimer on this statement however saying, "Optimised cooling conditions are an absolute necessity here." It is worth noting however that these results are not generic, these are exceptional. In shallow cut operations, it is usual that 70 – 80 per cent of the heat enters the workpiece. Only small amounts enter the wheel, leave with the chips or go with the fluid. A common example of this would be 5 per cent to the wheel, 10 per cent to the chips and 15 per cent to the fluid. In creep feed, 90 per cent can be removed by the fluid, a small proportion by the wheel and another small amount to the grinding chips. This suggests that the operation used by Ott (2001) is a high wheel-speed creep operation (Morgan 2007).

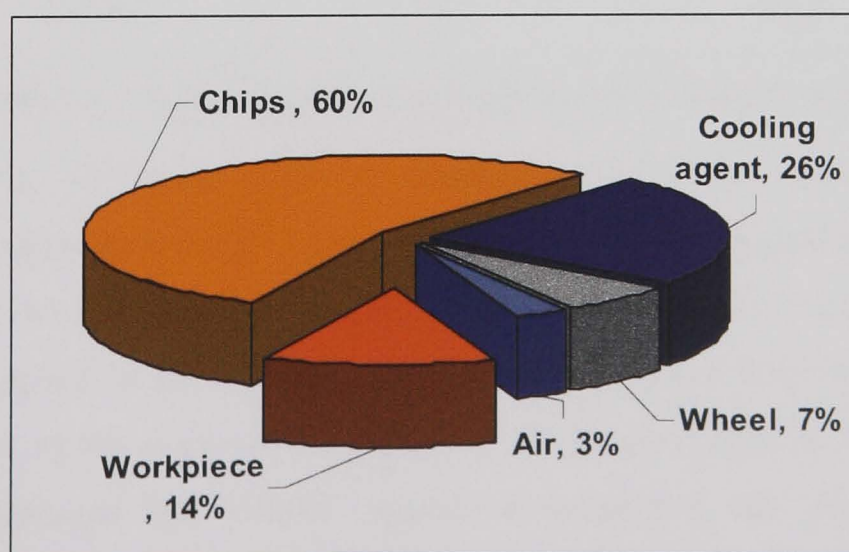


Figure 2-12 Heat distribution during grinding with wheels @ ($v_s > 100$ m/s)

Adapted from Ott, (2001)

2.2.6 Health concerns with cutting fluids

Most cutting fluids provide a breeding ground for bacteria that is hazardous to the machine operator (Sluhan 1994, Hoff 2002). Cutting fluids are also known to cause skin disorders such as dermatitis. Moreover, there is the potentially fatal effect of leached heavy metals in the fluid affecting the human respiratory and dietary system (Sluhan 1994). Once the fluid has been used, it contains small amounts of wheel debris and workpiece material. Dahmen et al (1997) developed a process using supercritical carbon dioxide to separate the debris and it was originally implemented for glass grinding with high oil and lead content. The researchers have since modified the system to accommodate metal grinding. In the early 1990s, Germany estimated that 130,000–250,000 tons of cutting fluid per year was used.

After a certain amount of time, all this fluid needs disposing and replacing in order to maintain a consistent production level. From Table 2-3, one can understand why there is a need to dispose of cutting fluids in the most ecologically friendly manner. The proper disposal of the oil, alloys and iron is the most critical because they pose the greatest environmental hazard (HSE 2003).

Material	Weight Percentage (%)
Iron	50–80
Wheel material (SiC, CBN, Al ₂ O ₃)	4–20
Oil	0.5–40
Water	0–30
Alloys	0–15

Table 2-3 Average composition of grinding swarf (Chang et al 2006)

The combination of rising costs of disposal through the introduction of new environmental legislation (HSE 2002) and the uncertainty regarding health risks to machine operatives has led to an increase in research to reduce costs by recycling or reducing consumption of these fluids, or eliminating the fluid from the cutting process. As an indication of the scale of consumption of cutting fluids, in Germany alone in 1994 it was estimated that 350,000 tonnes of emulsified oils were processed and subsequently disposed of. According to the German automotive industry, 7-17 per cent of the manufacturing cost of components is attributable to cutting fluids when

associated costs of monitoring, maintenance, health precautions and absenteeism are also taken into account (Klocke and Eisenblätter 1997). Comparatively, in the same report, tool costs are quoted as being 2-4 per cent. Whilst it may be difficult to determine precise costs associated with the use of cutting fluids, there is clearly considerable potential for savings.

With a global market of over 600 million gallons (2271 million litres) prior to dilution (Glenn 1998), the environmental and cost issues concerned with the use, recovery, and cleaning of cutting fluids cannot be ignored. With the recently devised and introduced ISO14000 environmental series legislation, companies are seeking to reduce their consumption of metalworking fluids and to adopt cost effective methods of recycling these fluids or, preferably, remove them from the processes completely.

ISO 14000, first published in 1996, specifies the actual requirements for an environmental management system. It applies to those environmental aspects which the organisation has control and over which it can be expected to have an influence. Environmental and health considerations weigh against the disposal of cutting fluid as effluent. It is now generally accepted that where cutting fluids must be used, either recycling or life extension should be implemented.

Project management procedures now encompass environmental issues. Environmental concerns relating to both the general environment through river and sewer discharges, and to cost reductions and safe working environments for operatives, need addressing. For example, the accumulation of dissolved nitrogen compounds, commonly used as emulsifiers in cutting fluids, cause eutrophication (water pollution caused by excessive plant nutrients) of water in lakes and streams, whilst forming nitrogen oxides when incinerated. Incineration difficulties are also associated with chlorine derivatives; these generally form quantities of toxic dioxins when burnt (Akagawa 1997).

Foaming and scumming are two further difficulties associated with coolant application in grinding. There are different reasons for foam, which include:

- Mechanically created foam - where the coolant doesn't have enough time to rest and allow entrapped air to escape;

- Chemically produced foam - some coolants are soap derivate (anionic) emulsifier systems that have high foam tendency; chemical contaminates - hydraulic oils are not compatible with coolants as their additives contain sulphur, zinc and polymerised vegetable esters that can lead to emulsification resulting in foam.

In addition, too high or low concentration of coolant will greatly increase the likelihood of uncontrollable foam. Scumming (used usually with reference to foaming) is the particular type of foaming associated with the coolant reacting with 'hard water'. The chemical reacts with the lime in the water to produce a 'scum'. According to Ott (2001), it only takes around 30 seconds a week to eliminate foaming and scumming in machine tool coolant. Ott (2001) says "that by dedicating just half a minute each week to checking concentrate levels using a refractometer, foaming and scumming become problems of the past." Fluid manufacturers determine the concentration at which the fluid should be used so that optimum performance can be achieved. Ott (2001) says that synthetic, semi-synthetic and mineral oil-based fluids that are mixed with water need to be maintained at the correct concentration level and monitored weekly. Ott (2001) devotes substantial sums researching and processing fluids in order that the potential problems are eliminated at source.

Selection of the fluid depends on some key factors. The questions to be answered are:

- Is the fluid appropriate for the job?
- Is it suitable for the specific machine?
- What effect does it have on long-term machine performance?
- What is the lifetime cost of the fluid?
- Are there hidden costs (difficulties in use, disposal costs, and health and safety implications)?

From discussion with the industrial partners on the project, many say that to avoid foaming and scumming problems, thermal damage and increased power consumption, the efficient delivery of fluid is vital to the production process, and should take into account both pressure and water condition. Most cutting fluid manufacturers explain the reasons their fluids are effective and better in most cases, than previously used, as long as they are being used effectively, however none of these manufacturers propose ways to deliver their coolant effectively.

Table 2-4 shows a comparison of the current grinding processes used at automotive manufacturers around the world. They are a combination of technologies that produce the parts efficiently. For an overview of the differing industrial grinding process currently employed, Abtec (2010) have an overview on the product list.

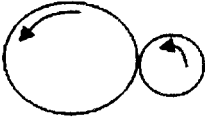
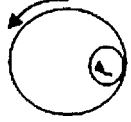
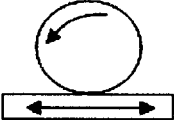
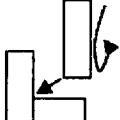
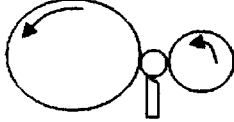
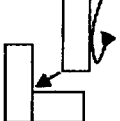
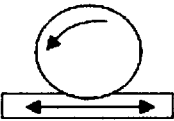
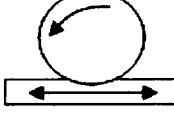
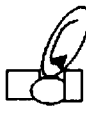
Schematic	Name	Material removal rate (mm ³ /mm.s)	Wheel Speeds (m/s)	Automotive uses	Coolant Application
	External Cylindrical	10-100	40-150	Crank / Cam	Jet / shoe
	Internal Cylindrical	10-60	40-70	Bore grinding	Internal / flood / jet
	Surface	18384	35-120	Cam face plates / general	Flood / jet
	Vector Plunge	30	70-125	Big crankshaft grinding	Jet
	Centreless	10-60	20-100	Multi-wheel camshaft grinding	Shoe / flood
	Face and Shoulder	25	30-80	Thrust wall and flange end	Shoe / flood
	HEDG	100-1000	100-300	Rough grinding of cast shafts (webs etc)	Jet
	VIPER	<300	100-200	Rough grinding of cast shafts (webs etc)	Jet
	Form / Profile Grinding	10-45	30-80	Crank/Cam shaft radii and undercuts	Jet / Flood

Table 2-4 Overview of different grinding regimes

Chapter 3 Effective Coolant Application

Cutting fluid can be applied through manual, flood or mist application. In flood cooling, fluid is directed under pressure to the work area. Fluids can be sprayed onto the work area as a mist. The pressure and direction of the mist stream are also crucial to the success of the application. Coolants are typically stored and distributed by a pump and tank system in each machine or from the use of a central system.

3.1 Grinding fluid nozzles

Nozzles made up of short interlocking plastic tubes (Figure 3-1) may be adequate for general toolroom application. For high volume production, however, these interlocking tubes are inadequate as they create turbulence, spray in many directions, and cannot be held in the correct position for very long, preventing uniform velocity fluid delivery.

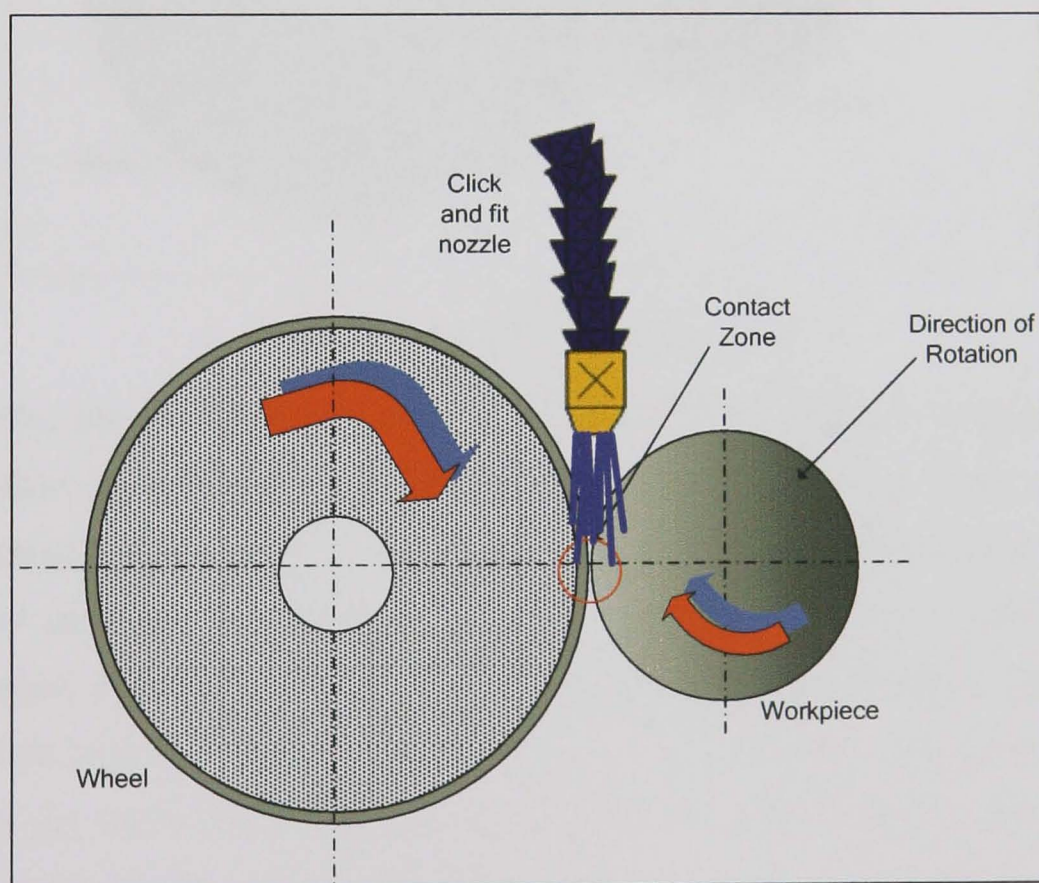


Figure 3-1 Click and fit nozzles

More suitably designed nozzles have a long straight section of at least 50 mm length, as illustrated in (Figure 3-2). The nozzle must have very sharp edges at the point of exit and must be free of 'nicks' and other damage to reduce nozzle losses and minimise turbulence. In the illustration, the nozzle is inclined at an angle of about 20° and this is a

typical set-up for cylindrical grinding of steels (Trmal & Kaliszer 1976). Jet nozzles supply coolant at high jet-speeds to break through the layer of air that builds up around the grinding wheel. This is why the fluid entrains and 'sticks' to the wheel's surface, as opposed to click nozzles that operate only at relatively low pressures.

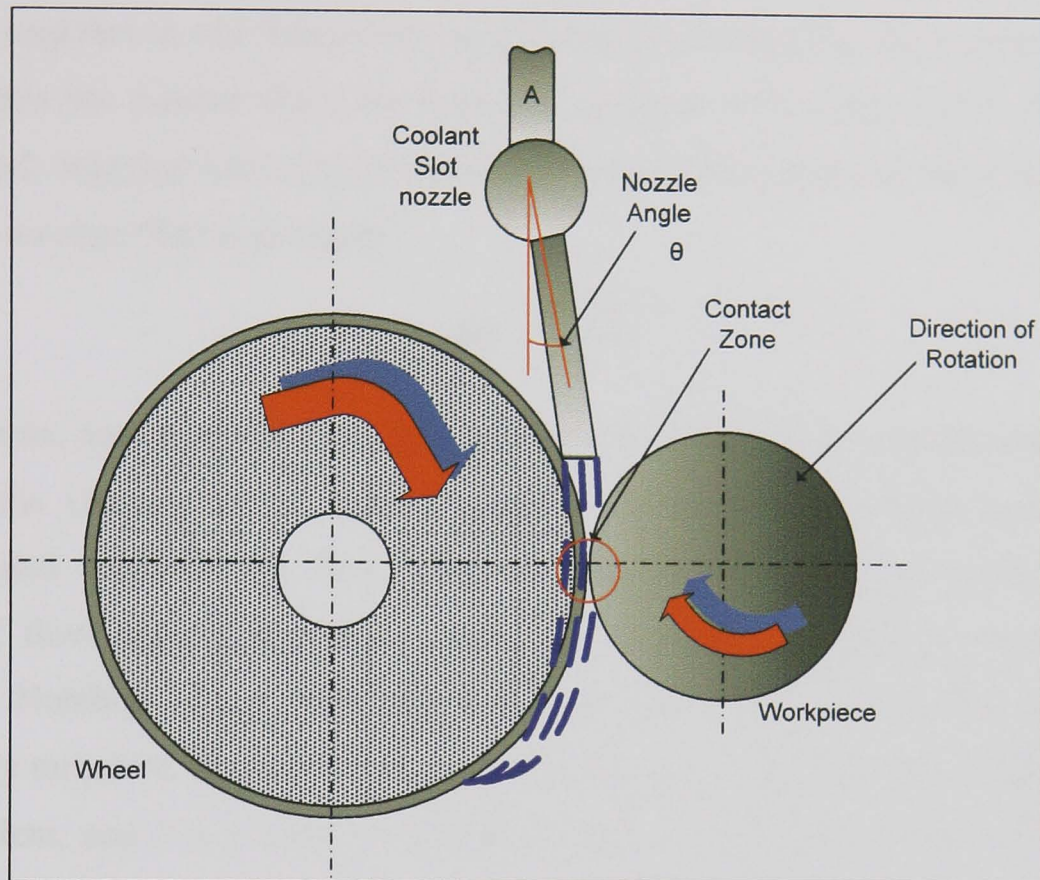


Figure 3-2 High-speed jet nozzle design

Alternatively, the shoe nozzle design ensures equal fluid velocity delivery at lower pressures than the jet nozzle in Figure 3-2. The shoe is a chamber fitting tight to the grinding wheel, leaving a gap of only 0.5mm, which is flooded with copious amounts of fluid at low pressure. The grinding wheel picks up the fluid and accelerates it to the grinding wheel's peripheral speed, in that way attaining equal grinding fluid velocity delivery. One other key factor of the shoe nozzle design is that it acts as an air scraper that directs the layer of turbulent air, following the wheels periphery, away from the grinding wheel (Gviniashvili 2003). The nozzles in Figure 3-1 and Figure 3-2 are designed mainly for cylindrical and surface grinding operations.

3.1.1 Nozzles for High Speed Grinding

The purpose of a nozzle is to direct cutting fluid to a position to achieve maximum fluid flow in the grinding contact area. The nozzle also fulfils the purpose of increasing the fluid velocity by contracting the cross-sectional area of the jet stream. A well-designed

turbulent flow nozzle converts more of the pressure energy in the flow into kinetic energy than does a laminar flow nozzle (Rowe et al 2004). A laminar flow nozzle however has the benefit that the jet stream maintains its coherency for a greater length meaning that turbulent flow nozzles must be positioned as close to the grinding contact as possible. There are many factors that have an effect on fluid flow in pipes. They are all drawn together in one dimensionless quantity to express the characteristics of flow, i.e. the Reynolds number (Re). For Reynolds numbers of less than 2,000, laminar flow is produced; implying lower jet velocities compared with peripheral wheel velocity. The Reynolds number (Re) is given by:

$$\text{Re} = \frac{\rho v_j d_j}{\eta} \quad [3.1]$$

where ρ is the density of the fluid, v_j is the velocity of the jet, d_j is the diameter of the jet and η is the viscosity of the fluid. Typically, viscous stresses within a fluid tend to stabilize and organize the flow, whereas excessive fluid inertia tends to disrupt organized flow leading to chaotic turbulent behavior. Fluid flows are laminar for Reynolds Numbers up to 2000. Beyond a Reynolds Number of 4000, the flow is completely turbulent. Between 2000 and 4000, the flow is in transition between laminar and turbulent, and it is possible to find sub-regions of both flow types within a given flow field.

For a particular fluid, if the velocity is low, the resultant Reynolds number is low. If another fluid with a similar density, but with a higher dynamic viscosity is transported through the same pipe at the same velocity, the Reynolds number is reduced. For a given system where the pipe size, the dynamic viscosity (and by implication, temperature) remain constant, the Reynolds number is directly proportional to velocity.

Figure 3-3 is a graphical representation of the different Reynolds flows.

The turbulent nozzle is an orifice of short length to diameter ratio, preferably < 0.25 (Figure 3-4). The ideal design for a turbulent nozzle is a smooth convergent nozzle with a smooth orifice. Another design uses a concave convergent section with a convex convergent exit. The smooth chamfer or smooth flat face avoids jet stream interference (Rowe et al 2004).

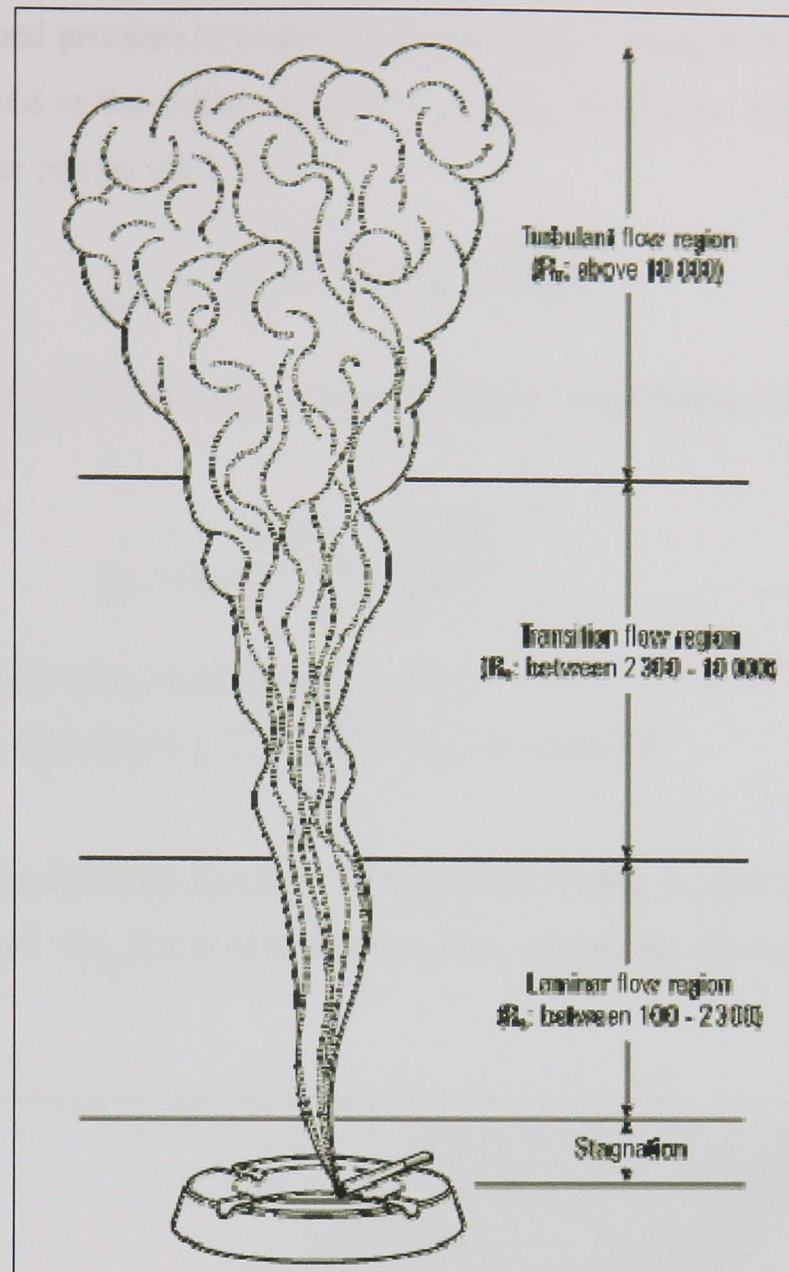


Figure 3-3 Graphical representation of the Reynolds number (Spirax 2007)

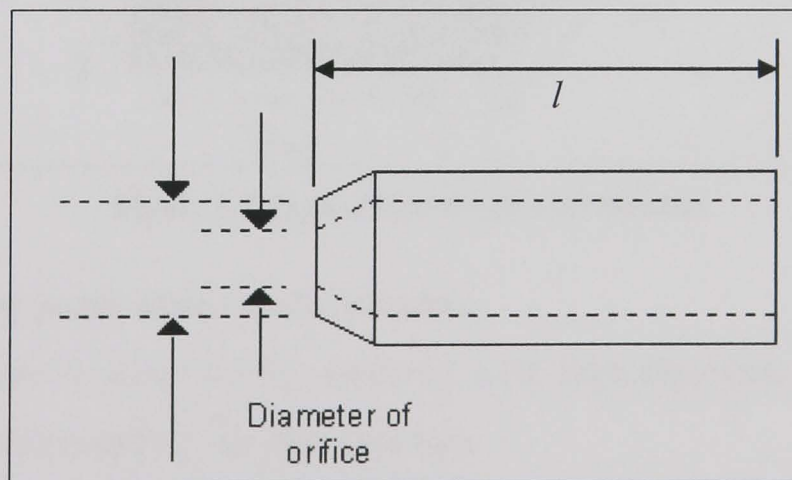


Figure 3-4 Typical orifice nozzle

Design equations proposed for this type of nozzle (Figure 3-4) design are:

$$P_p = \frac{l \times V_{Orifice}^2}{2C_v^2} \quad [3.2]$$

where: P_p = pumped pressure available at nozzle inlet, l = length of the nozzle, $V_{orifice}$ is the velocity of fluid at the orifice, and C_v = velocity coefficient (typically $0.95 < C_v < 0.98$). The flowrate can be given as:

$$Q_f = C_a \frac{\pi \times d_{orifice}^2 \times V_{orifice}}{4} \quad [3.3]$$

where: C_a = contraction coefficient (typically 0.63). Furthermore, the flowrate expands to:

$$Q_f = C_d \frac{\pi d_{orifice}^2}{4} \sqrt{2 \frac{P_p}{l}} \quad [3.4]$$

with: C_d = orifice discharge coefficient = $C_a \times C_v$.

C_d varies with Re, typically $0.3 < C_d < 0.56$ for $10^2 < Re < 10^6$.

For wider grinding contacts than the orifice nozzle is able to deal with, the slot nozzle (Figure 3-5) is used. The slot nozzle allows a flat, smooth jet of coolant to flow into the grinding contact.

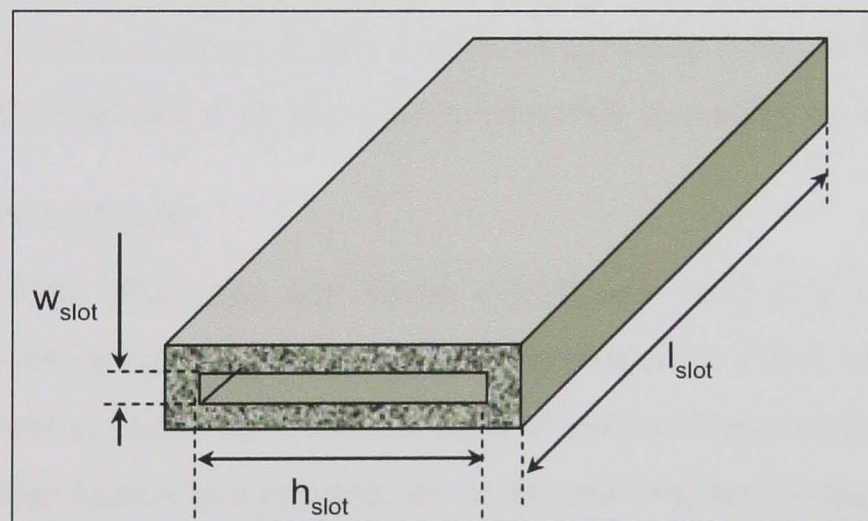


Figure 3-5 Typical slot-nozzle exit chamber

There are three key points found in slot nozzles:

- laminar flow is more readily achieved with high flowrates due to narrow slot thickness and length of pre-slot chamber;
- easy to design for laminar or turbulent flows;
- a large chamber between the supply pipe and the slot allows the flow to find a smooth path.

Design equations proposed for this type of nozzle design (Rowe et al 2004) are:

$$\text{Re} = \frac{\rho h_{\text{slot}} v_j}{\eta} \quad [3.5]$$

and

$$P_p = \frac{12\eta l_{\text{slot}} v_j}{h_{\text{slot}}^2} + \rho v_j^2 \quad [3.6]$$

where: P_p = pumped pressure available at nozzle inlet. The flowrate is given by:

$$Q_f = v_j h_{\text{slot}} w_{\text{slot}} \quad [3.7]$$

Research by Rowe (2001) identified three important design considerations for the achievement of optimal fluid flow using slot nozzles:

- width of slot should be at least 20 times the height of the slot for laminar flow;
- length of slot should be as short as possible for turbulent flow;
- smooth concave converging section, as in orifice case, gives turbulent flow.

Webster, Cui and Mindek (1995b) carried out research into the effects of a coherent jet as opposed to a jet of cutting fluid dispersed upon exit from the nozzle. This research showed that by using a measurement system of grinding temperature detection, the temperature was minimised with the coherent jet nozzle in contrast to the dispersed jet.

3.1.2 Coherent Jet Nozzle

Rouse et al (1952), McCarthy and Molly (1974) and Hoyt and Taylor (1974) all investigated nozzle design within their specific applications. These researchers looked at finding the most suitable way of producing a jet that maintains its shape over a given distance, otherwise known as a coherent jet. In the grinding environment however, until the work of Webster, Cui and Mindek (1995b) little effort was focused on coherent jets. With the focus of the coolant being reduction of temperature in the grinding contact, by supplying the maximum amount of fluid into that area, it appears reasonable to assume that supply using a coherent jet will be less difficult than supply with a non-coherent jet from a conventional nozzle. One major advantage of a coherent jet is that firing it from a distance allows for placement of the nozzle at a larger distance from the grinding zone reducing the amount of equipment close to complex workpieces.

Webster's design of the coherent jet nozzle came about from the need of a water based coolant application system for use in creep feed grinding where removal of the process heat is extremely important. Application of water-based fluids at high velocity is much more difficult because it has a lower viscosity giving a larger Reynolds number, thus creating a dispersed jet. This requires the operator to position the nozzle as close to the workpiece as possible, but creates problems with larger workpieces, and often-excessive amounts of coolant are required. This in turn leads to an increase in power consumption and increased refrigeration and storage capacities. Another problem is the air-barrier, most commonly overcome by matching the wheel speed and the coolant jet speed. Poor nozzle design and plumbing problems lead to a dispersed jet. Changes in pipe diameter, elbows and edges also cause turbulence preventing the conditioning to a coherent jet. A shoe type nozzle is good at overcoming these problems with the large contact area. It creates difficulties, as a small gap is required between the shoe and the wheel, to aid in fluid penetration. Shoe nozzles are also considered too bulky for general purpose grinding (Webster et al 1995b).

Rouse, Howe and Metzler (1952), presented a round nozzle for fire hose applications. Effort when using this however must be made to reduce the dispersed or misdirected flow. Also, eddies and losses in the nozzle and hose cause an unwanted turbulence within the flow giving greater rise to the possibility of a dispersed jet. Owczarek and Rockwell, (1972) investigated planar nozzles (two-dimensional flat sided nozzles). Nozzles with convex inner wall profiles exhibit corner secondary flows with high-pressure loss. With rectangular nozzles, the transition from circular to rectangular causes secondary flows (Webster et al 1995). Many problems exist within current nozzle designs, elbows, double elbows and welded flanges. The use of a honeycomb (similar to a flow conditioner – a device to alter fluid-flow profile properties) may be viable to reduce the turbulence in the flow. The vena contracta makes a nozzle exit jet smaller than the actual pipe diameter. The vena contracta effect occurs when a fluid flows through any opening. What happens, briefly, is that the flowing fluid 'sticks' to the edges of the opening, thus effectively reducing the size of the opening. In a typical orifice, this effect can reduce the capacity of the outlet to 60 - 80 per cent of its physical size. The vena contracta exists as the recirculating flow behind the wall causes a pressure to force the fluid into the centre creating the phenomena.

Figure 3-6 shows the eddy formation and secondary flow causing jets to disperse as predicted by Cui (1995). When analysing the “edge” of a fluid stream, it is common to assume that the part of the fluid that is in contact with the walls (change in section) must be at rest. However, this is not the case due to the “limiting layer”, according to which, immediately next to the wall, there is a thin layer of fluid with a velocity parallel to the surface of the object that crests rapidly, from zero at the surface itself to the velocity of the main body of fluid away from the walls. This limiting layer is very thin upstream, but broadens downstream, i.e. at the change in section.

Inside this layer, the fluid begins to move backwards and in circles, until eddies form when the Reynolds number reaches a certain level. As the fluid velocity grows, increasing the Reynolds number the limit layer widens forming larger eddies. These eddies cause the jet to break up and form secondary, chaotic flows that vary in time.

Figure 3-6 shows the theory of a vena contracta forming as the fluid flows from a large region into a smaller region. Common fluid dynamics theory predicts this formation, but later this work looks at this theory using CFX to investigate further the flow in these regions. The reason CFX is used to predict the vena contracta is because the quantitative assessment of the width of the vena contracta is inherently difficult due to the many factors (e.g. surface finish, initial width, fluid type) influencing this width. For this reason, a quantitative assessment of the vena contracta is not presented herein.

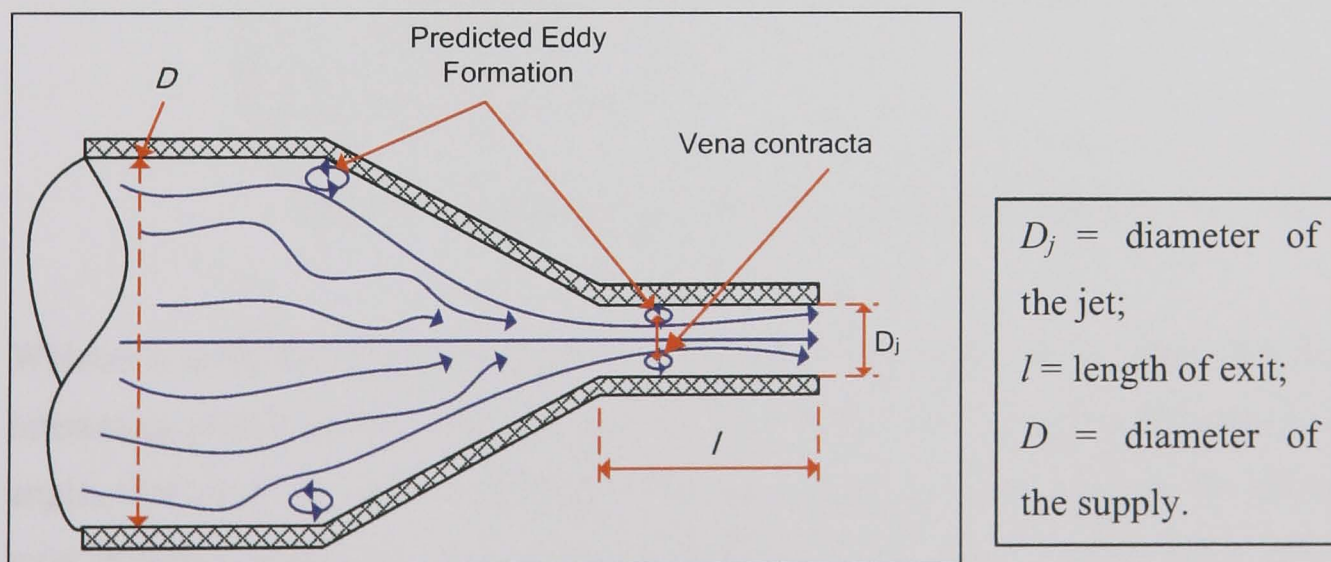


Figure 3-6 Possible zones of eddy formation in a conventional converging nozzle
(adapted from McCarthy and Molloy 1973)

Webster et al (1995b) proposed a new design of coolant nozzle based on the fire hose design by Rouse et al (1952) (Figure 3-7) to try to combat these design problems.

A large amount of the experimental work carried out was concerned with producing the ideal coherent jet for the application of fluid flow into the grinding contact.

Webster found critical factors for jet coherency to be as follows:

- the contraction ratio of the pipe inlet diameter to nozzle exit diameter;
- the finish of the internal surface of the nozzle;
- the nozzle exit sharpness.

However, these effects were not quantified. They were vital in turbulent flow as laminar flow is not possible at Reynolds numbers greater than 2300, typical of this type of nozzle application.

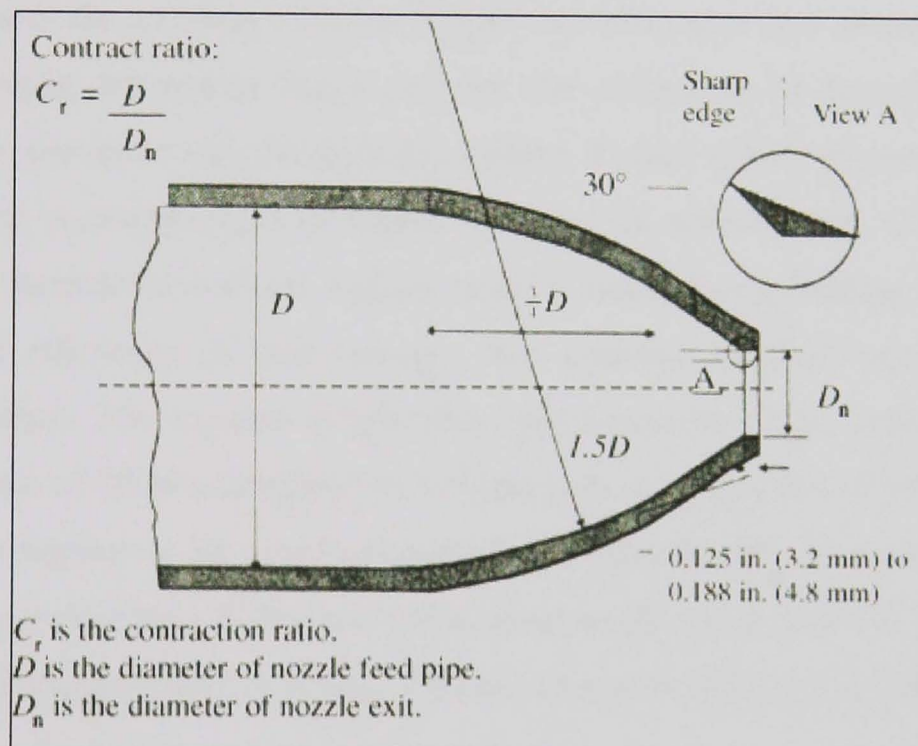


Figure 3-7 Fire hose design proposed by Rouse et al (1952)

Webster's work also looked at other important factors in coolant application, and found interesting results on the different types of nozzles, as well as positioning and nozzle angle, that could be used in differing grinding operations. In contrast to the grinding tests Webster carried out with actual production nozzles, better results were obtained when using the circular nozzles he developed during grinding of a particular workpiece. Tests also carried out showed that the nozzle angle was not critical as long as the jet stream remained above the workpiece. They showed that the cooling effectiveness is somewhat insensitive to the nozzle angle as long as the coolant is directed correctly into

the grinding contact. Most importantly, Webster's results show that the developed coherent circular nozzle is significantly better than the other nozzles tested, especially at long distances from the grinding zone. In fact, the nozzle designed was tested at a distance of 305 cm with virtually no change in the cooling performance. It is believed that this improved cooling performance is due to the increased jet coherency of the circular nozzle flow relative to other nozzles (Webster et al 1995).

3.1.3 The Grinding Contact

All nozzle designs attempt to place large fluxes of coolant into the grinding contact by different means. Jet nozzles try to target the grinding contact directly. As the grinding wheel begins to engage with the workpiece in up-cut grinding or disengages in down-cut grinding, there is a region in which there is no nip to constrain the fluid and direct this coolant into the grinding contact. Figure 3-8 illustrates this situation. The nip is vital in providing the wedge shape area for the coolant to be forced down through hydrodynamic pressures into the grinding contact. Powell (1979) showed that heat flux before burning occurred could be higher by using an artificial nip. Critical heat flux describes the thermal limit where a phase change occurs during heating which suddenly decreases the efficiency of heat transfer, thus causing localised overheating of the workpiece surface. The increase in heat flux varied between 12 per cent when using jet speeds in excess of 20 m/s compared to a 50 per cent at a jet speed of 9 m/s. The critical heat flux was highest at jet speeds exceeding 20 m/s and, for the particular example, critical values greater than 30 W/mm^2 were achieved (Rowe et al 2004). When fluid has reached the grinding contact, it is assumed that it remains there and is the effective flow.

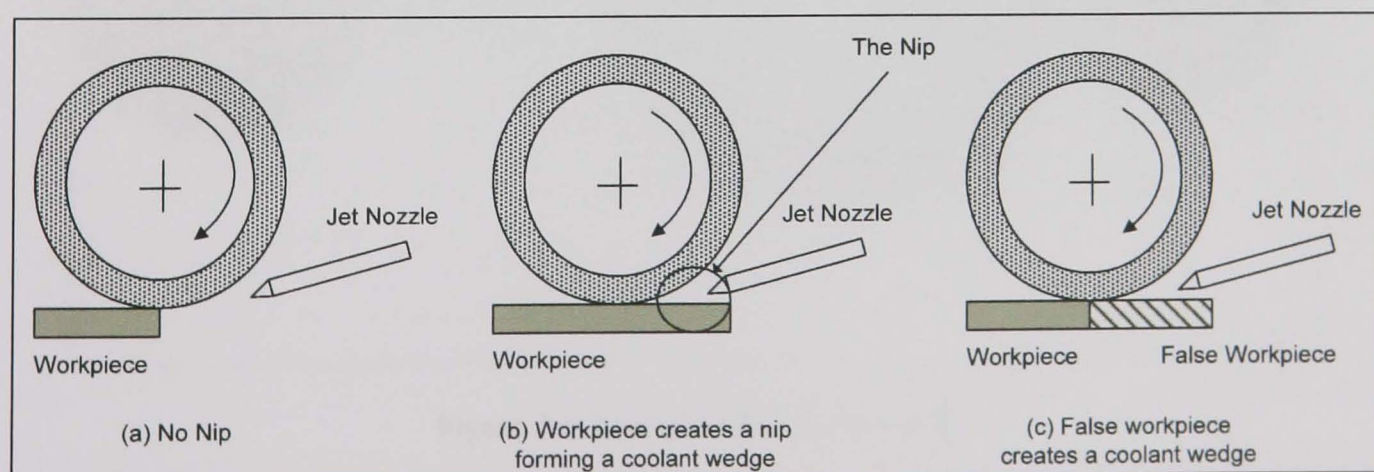


Figure 3-8 Different ways of creating a real and false grinding nip within the grinding zone

Another way of supplying coolant to the grinding contact without the need for a coherent jet is with the use of a shoe nozzle. Powell (1979) carried out work on this type of nozzle extensively.

3.1.4 Shoe nozzles

The grinding wheel picks up the grinding fluid and accelerates it to its surface speed, thereby achieving equal velocity delivery. Additionally, the shoe nozzle acts as an air scraper that directs the layer of turbulent air away from the grinding wheel. Figure 3-9 shows a typical example of a shoe nozzle, including how it is positioned on the wheel. Powell (1979) assumed that an adequate supply of coolant is that which penetrates the wheel deep enough so that, even with fluid loss from centrifugal forces, there remains a thin film of coolant within the grinding zone. He also states, there must be some critical depth at which no further penetration of the coolant will increase the performance. He declares that the shoe must be positioned as close to the workpiece, and the wheel, as possible in order to reduce leakage in the system. To achieve this minimum gap, Powell (1979) used a fibreglass shoe and ground it after each dressing of the wheel; this proved successful.

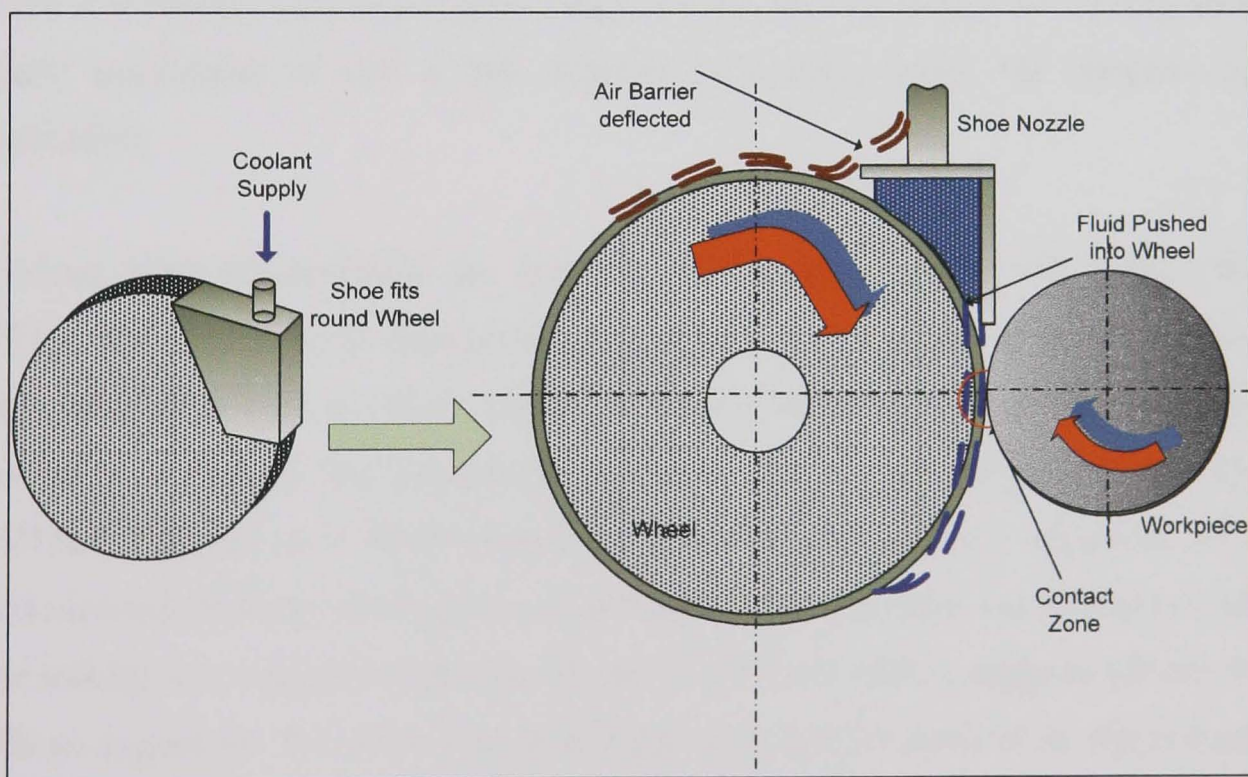


Figure 3-9 Typical coolant shoe nozzle

The pressure in the nozzle is the important factor when measuring penetration as flow transducers will not detect losses in flowrate if leakage increases or decreases. Powell

(1979) carried out a two dimensional analysis of the flow into a porous grinding wheel with the following assumptions:

- the depth of penetration is small relative to the radius of the wheel;
- the applied pressure is constant over the shoe exit;
- no flow is lost from the sides of the wheel;
- the fluid is accelerated up to the tangential velocity instantaneously.

From this, Powell (1979) calculated the depth of penetration of the fluid, the leakage of fluid and the total power of the system. In one of Powell's (1979) calculations, the power consumed by the shoe nozzle was 60-80 per cent of the total spindle power. This highlights one of the major problems faced when using shoe nozzles. Another area is the effective positioning of the shoe nozzle. As the wheel wears the nozzle moves further from the wheel periphery reducing its effectiveness by increasing the side leakage and reducing the fluids penetration into the grinding wheel pores.

3.1.5 Position of Grinding Fluid Nozzles

Correct positioning improves the delivery of the grinding fluid into the grinding contact zone by ensuring that the grinding wheel can pick up the fluid and draw it into the area where it is needed. This is the second area of focus for this work with it being noted that nozzle positioning is also a key element to system design for effective coolant application.

Previous work demonstrated the importance of nozzle position and shape (Webster 1995c). Delivery of fluid approximately tangential to the grinding wheel is a common approach (Akiyama et al 1984). Tangential supply of cutting fluid involves directing the coolant in a straight line towards the grinding contact zone (Figure 3-10). Work at AMTReL (Ebbrell et al 2000) found that delivery of fluid via a tangential jet led to increased side leakage. Raising the nozzle slightly (12 mm from the horizontal) reduced side leakage to a negligible quantity. However, Furutani (2002) suggests greater misting with an angled jet. It is clear that both angle and position need to be under control to overcome these problems. Trmal and Kaliszer (1976), Akiyama et al (1984), and Campbell (1995) suggest however that the coolant be directed at the periphery of the wheel to allow maximum penetration of the coolant into the grinding contact. Regrettably, different investigations have offered conflicting optimum angles at which to position the nozzle. This disparity may be due to variability of the viscosity of the

cutting fluid and its velocity at nozzle exit as well as the porosity of the wheel (Campbell 1995).

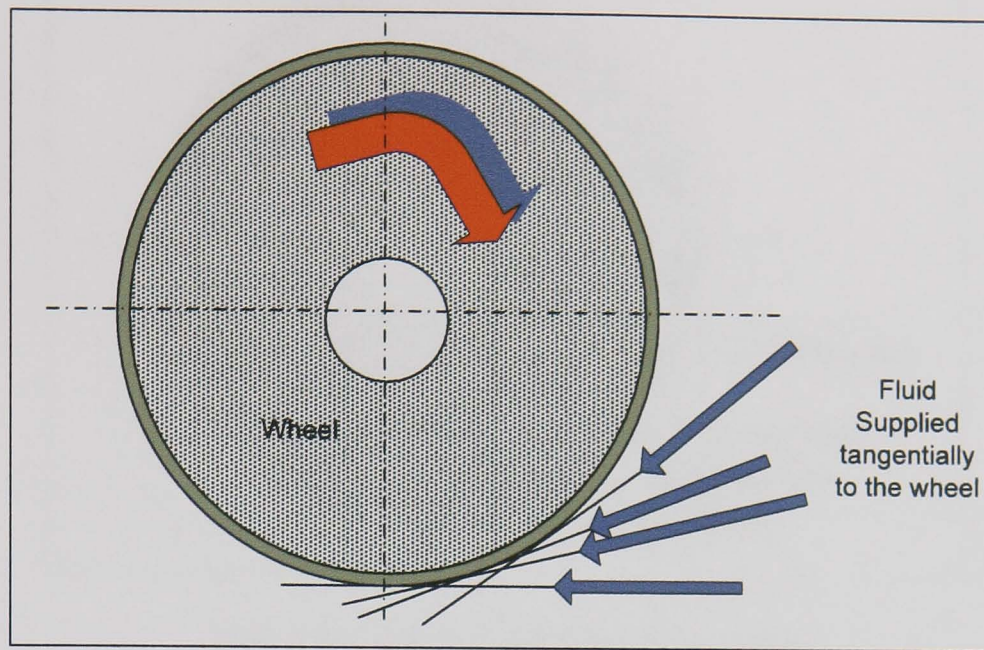


Figure 3-10 Tangential fluid supply

Campbell (1995) found, for example, that with a high nozzle velocity and a small angle, combined with a nozzle position relatively high above the workpiece, the coolant would deflect off the grinding wheel and away from the grinding contact area. Campbell (1995) concluded that it is not enough alone to have a highly coherent jet, well designed (allowing for good edge conditions, symmetry, entry length, smooth geometry etc.) that matches the jet speed to the wheel speed as described by Webster et al (1995b). The fluid stream needs pointing at the correct angle where it achieves the best grinding performance through lubrication, cooling and cleaning. Campbell (1995) ran an experiment to determine the correct nozzle angle using a straight oil coolant and a rectangular cross-section coolant nozzle. In discrete increments of five degrees, Campbell varied the primary nozzle angle between 5° and 30° . Measuring the hydrodynamic pressures (in the grinding contact with the use of a pressure sensor), he found that the best nozzle angle, under these conditions, in terms of coolant flow into the grinding zone, was 5° from the horizontal. However, later tests conducted with a water-soluble coolant, indicated that the optimal nozzle angle differed from that with the straight oil. This is an area highlighted for investigation within this work. Another possible approach is fluid supply directly into the grinding wheel surface. This is shown schematically in Figure 3-11. This is highlighted as an area requiring some research effort as the current literature is conflicting on the benefits of direct coolant application into the wheel surface.

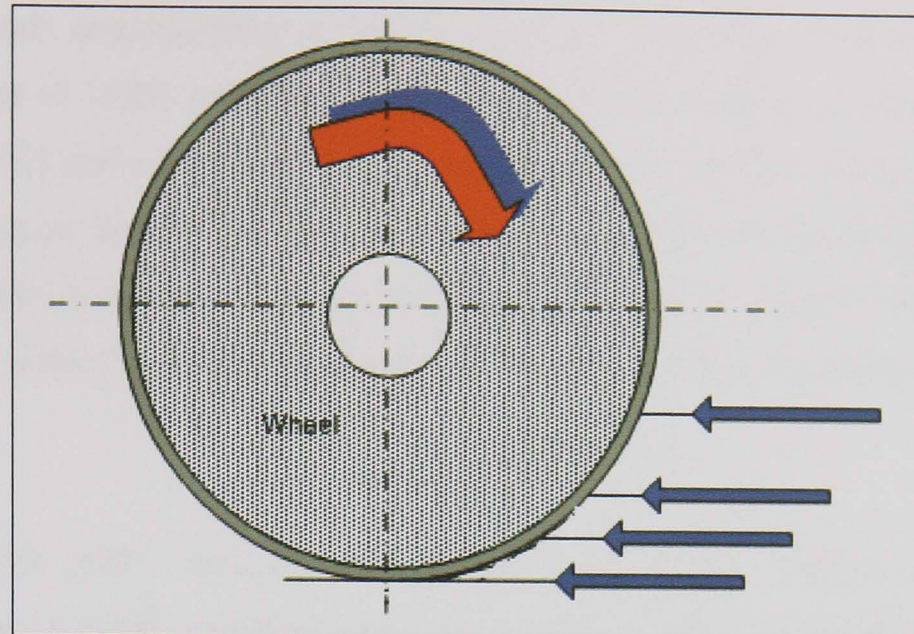


Figure 3-11 Direct fluid supply to the wheel

A possible further way to optimise the coolant delivery system is through the adjustment of nozzle geometry to the grinding wheel profile. Noichl (1992 cited in Brinksmeier et al 1999) showed that a modification of nozzle geometry to the grinding wheel, with an opening cross-section dimensioned according to flow rate, could lead to a significant increase of the material removal rate. The modification of nozzle geometry, for instance a continuous adjustment of the nozzle geometry to the decreasing grinding wheel diameter is also the subject of several patents and papers open to public inspection. König et al (1986 cited in Brinksmeier et al 1999) showed in experiments for dressing, that the use of a ring nozzle, enclosing a non-rotating dresser, instead of a conventional free jet nozzle, leads to a significant decrease of dresser wear.

3.1.6 Coolant flow rate

N.N, 1987 and Ott, 1991 (cited in Brinksmeier et al 1999) gave advice on the correct coolant flow rate and the geometry and dimensions for flood cooling, for the achievement of best possible cooling within the grinding contact. For effective cooling, many industries (and researchers alike) use an excessive amount of coolant; especially when using jet nozzles, with the theory that 'more is better'. Engineer et al (1992) and Okuyama et al (1993 cited in Brinksmeier et al 1999) reported on the effect of coolant supply depending on different parameters, such as nozzle output flowrate. Okuyama et al (1993 cited in Brinksmeier et al 1999) measured the heat transfer coefficient close to the contact zone to report on the influence of different parameter variations. Due to a geometrical limitation of the flow rate through the grinding arc, Okuyama showed

increasing coolant jet velocity could lead to a digressive incline of the heat transfer coefficient and consequently, a lower cooling efficiency. Vits (1985 cited in Brinksmeier et al 1999) confirmed that the contact zone limits the coolant flow rate. Engineer (1992) analysed the effects of workspeed, of supplied coolant flow rate and nozzle position on the amount of coolant able to pass through the grinding contact. He found that above a certain flow rate, saturation takes place; excess coolant is rejected resulting in a reduction of the proportion of coolant delivered usefully to the grinding contact.

Works by Vits (1985 cited in Brinksmeier et al 1999), Treffert (1995 cited in Brinksmeier et al 1999), and Kovacevic and Mohan (1995) indicate that an increase of coolant flow rate with all other process parameters remaining constant, in flooding, gives improved workpiece surface quality.

The effect of increasing coolant flowrate on residual stress in the workpiece had limited experimental research until the work of Vansevenant (1987) and Treffert (1987). Both noted that at low coolant flow rates (0.1 to 0.8 l per (min × mm)), residual stresses at the workpiece surface decrease with increasing flowrate. Czenkusch (1999 cited in Brinksmeier et al 1999) investigated the effect of coolant flowrate and nozzle cross-section on residual stresses (Figure 3-12).

Even though nozzles with smaller cross-sections give rise to lower flowrates, they also achieve lower residual tensile stresses due to the higher jet velocity achievable. This is because higher coolant velocity jets force more coolant into the pores of the grinding wheel leading to more fluid being carried through the grinding contact by the wheel (Brinksmeier 1999). This however is only true up to a point. When maximum penetration is achieved (maximum useful flow through the contact from penetration into the pores) increasing the coolant velocity simply wastes pumping power and coolant. The reason that the stresses are lowered is due to the contact mechanics between the wheel and the workpiece; more fluid in the contact reduces the amount of sliding due to correct lubrication, reducing the overall forces in the grinding contact, reducing the temperature in the contact, and hence stresses are reduced.

Brucher (1996 cited in Brinksmeier et al 1999) and Klocke et al, (2000) investigated the hydrodynamic effects in the contact zone. They found that force, perpendicular to the

contact zone, usually increases with increasing coolant flow rates at constant nozzle geometry. Minke (1993) considered tangential force and therefore spindle power, and found an increase in this force relating to higher flow rates. Increased spindle power at higher flow rates is due to the increase in power needed by the grinding wheel to accelerate the coolant up to speed to force it through the grinding contact. This power is classified as no-load power, termed lost power, and can amount to 80 per cent of the total power (Minke et al 1993, König 1997 cited in Brinksmeier et al 1999). This leads onto an important part of this work, with the knowledge that more is not always better, and supplying the correct or most useful amount of coolant is deemed the correct solution.

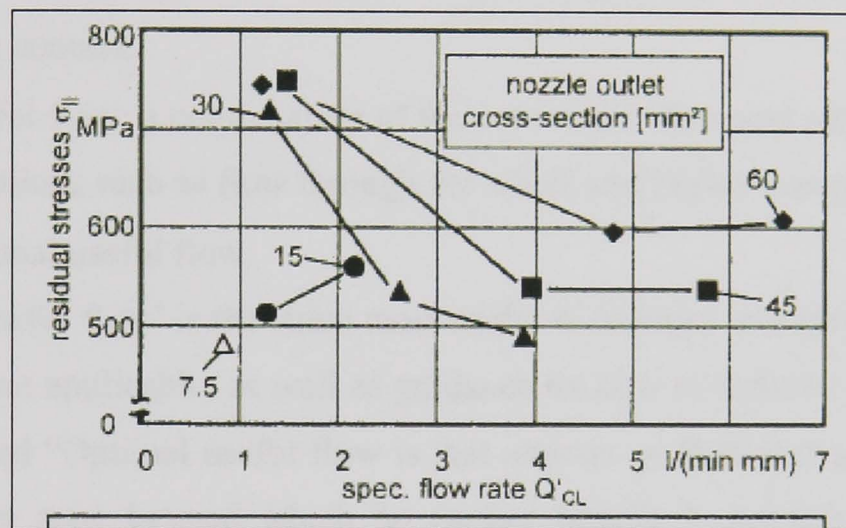


Figure 3-12 Effect of coolant flow rate and nozzle cross-section on residual stresses Czenkusch (1999 cited in Brinksmeier et al 1999)

3.1.7 Useful Flow

Many authors justify the need for a parameter such as ‘useful flow’. Brinksmeier (1999, p.597) stated, “Further investigations in the fields of fluid dynamics processes in supply nozzles and in the grinding zone are the key to optimisation of cooling and lubrication during grinding.” From this work, many authors now adopt the term ‘useful flow’. Engineer (1992), Chang (1994), Cui (1995), Rowe (2004) and Gviniashvili (2005) looked further into this term and all came up with their own definition of useful flow. Work by Jackson et al (2006) focused on this useful flow term, and is the basis of one of the measurables for this work; improving the application system.

Jackson et al (2006) base the definition of useful flowrate solely on the volume of flow passing through the grinding contact zone. This term uses the amount of fluid delivered

by the coolant nozzle, but encompasses the bulk porosity of the wheel, the wheel speed, nozzle position and the jet velocity. Their work took this definition further, focusing on a term they described as ‘optimal useful flow’. They stated that three major benefits would result from the understanding and completion of work to determine the optimal useful flowrate, namely:

- reducing the overall cost of the process in a manufacturing environment;
- reducing the environmental impact of the fluid;
- improving the overall process performance.

They split the definition of flows into three sections.

- The convenient flow: the amount of fluid physically able to pass through the grinding contact;
- The useful flow: a combination of the convenient flow and additional fluid flow modifications such as flow through the wheel and higher contact zone pressure;
- The optimal useful flow.

This ‘optimal useful flow’ is the value most useful to industry and gives users a specific minimum amount applicable, as well as guidance on how to achieve this. Jackson et al (2006, p.4) stated “Optimal useful flow is that amount of fluid that passes through the grinding contact zone beyond which no further benefit to lubrication or cooling is achieved”. This however, has to take into account the effect on material removal rate that is of great commercial importance. In this work, the optimal useful fluid flow is described as that amount of fluid passing through the grinding contact at which no further increase in supply affects the amount of collected flow at the rear of the grinding contact.

3.1.8 Collection of useful flow

Engineer (1992) showed the accepted mechanical method for collection of useful flow including the key principles: side scrapers, post contact zone scrape, collection, and channelling and containment systems. Chang (1994) showed that fluid after contact with the workpiece, and hence classified as useful flow, is ejected from the wheel up to 90° after the grinding contact. An important criterion to note is that after collection, weighing the fluid, as opposed to measurement through volume of fluid, minimises any errors caused by foaming and scumming. Foaming is a mass of bubbles of air in a matrix of coolant film, especially an accumulation of fine, frothy bubbles formed in or on the surface of the coolant. Scum is a film layer of extraneous or impure matter that

forms on or rises to the surface of the coolant. This work uses a collection method to analyse the amount of useful fluid flow penetrating the grinding contact with a selection of nozzles (described later).

3.1.9 Air Barrier

Bucher (1996) advises the use of ‘scrapers’ to ensure better wetting. The use of scrapers reduces the build up of airflow at the wheel circumference, effectively reducing the ‘air barrier’ (Radhakrishnan 1977). Ebbrell et al (1999), using finite element methods, simulated the airflow near the grinding wheel. They undertook experimental investigations of the air barrier looking at the coolant flow shortly before entering the contact zone using Laser-Doppler-Anemometer (LDA) techniques to investigate further the effects of the air barrier. The effect of this air barrier on coolant penetration into the grinding contact is however, unclear. According to Vits (1985 cited in Brinksmeier et al 1999), Tawakoli (1990) and Heuer (1992 cited in Brinksmeier et al 1999), the air barrier plays only a minor role. In stark contrast to this, Trmal (1976 cited in Brinksmeier et al 1999), Radhakrishnan (1977), Okuyama (1993) and Inasaki (1998) state that its influence is extremely important, especially in a high-speed grinding processes.

Work by Inasaki (1998) shows that the air barrier is generated through two major airflows around the wheel surface:

- air flow in the circumferential direction (dragged through with surface roughness);
- air spouting normal to the wheel surface.

Figure 3-13 shows how Inasaki (1998) predicts this air spouting induced by a centrifugal force of wheel rotation. These two airflows are merged into an air barrier along the ground groove thus hindering effective coolant entry (Inasaki 1998). However, Rowe (2008) states that spouting normal to the wheel surface is unlikely. It has never been observed because flow out of the wheel always emerges tangentially and all observations confirm this. The influence of the air barrier, pictured in Ebbrell’s photo Figure 3-14, clearly affects the fluid flow. Figure 3-14 shows the coolant ‘damming’ in front of the contact zone meaning no coolant, due to this air barrier, can penetrate and effectively cool the workpiece. This highlights the difficulty in understanding of the air barrier. Wu (2007) investigated the air barrier further.

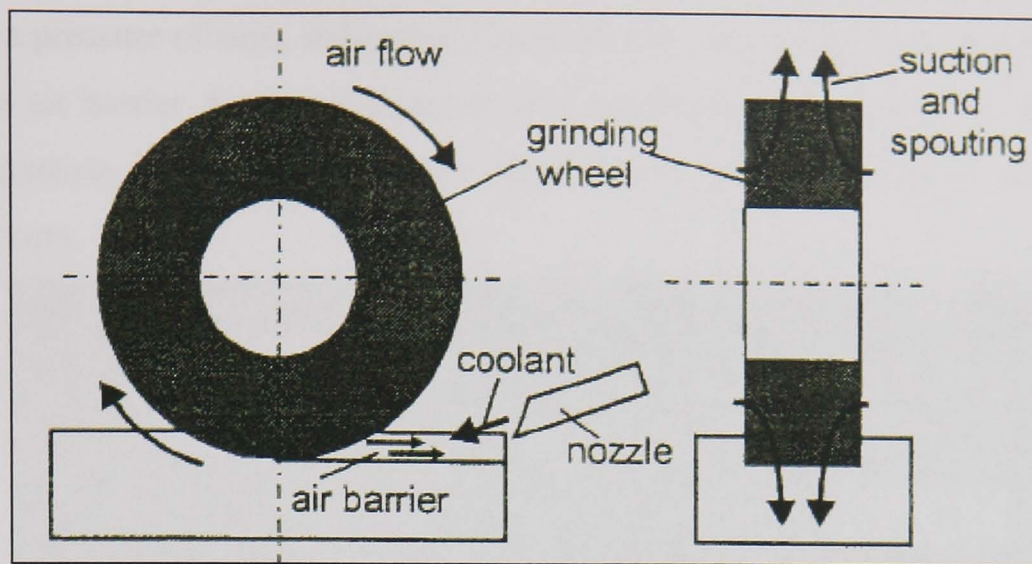


Figure 3-13 Coolant supply and the air barrier in grinding (Inasaki 1998)

If coolant is to penetrate the air barrier to remove the heat in the contact zone, then the fluid momentum of the supplied coolant must exceed the momentum of the air barrier (Trmal and Kaliszer 1976). Inasaki (1998) calculated this critical limit for coolant penetration. Using high velocity jets however, causes problems associated not only with cost but also with health and safety. High-speed jets cause severe misting; meaning researchers currently try to find a way of penetrating the air barrier when increased jet velocity is not an option. The most common solution to the problem traditionally is the use of a scraper [Trmal and Kaliszer, (1976), Inasaki (1998), Okuyarma et al (1993)]. However, to use this device properly, as the wheel wears, the scraper needs readjusting to continue its work of breaking down the air barrier. It is therefore difficult to use this type of device in many industrial applications. Ott (1991 cited in Brinksmeier et al 1999) tried to get around this problem by using a two-component nozzle, in which a second cooling lubricant jet, perpendicular to the grinding wheel, diverts the air barrier. Elimination or reduction of the air barrier is the subject of a large number of patents and papers open to public inspection. The patented appliances extend from scraper systems attached to the grinding wheel to air-barrier suction systems (Brinksmeier 1999).

The work by Trmal and Kaliszer (1976) showed the benefits of using scraper plates. They used a Pitot tube to measure the velocity of the boundary layer. In their work, they found a decrease in air velocity occurred when the scraper moved closer towards the wheel periphery. Campbell (1995) supported this work when investigating the hydrodynamic pressure at the wheel/workpiece interface caused by the passage of cutting fluid beneath the wheel. Campbell found a critical wheel speed at which he

measured a pressure of zero, indicating that no coolant passed through the grinding zone due to this air barrier. He found however that introducing a scraper plate allowed a 20 per cent increase in the grinding wheel speed before the hydrodynamic pressure again measured zero.

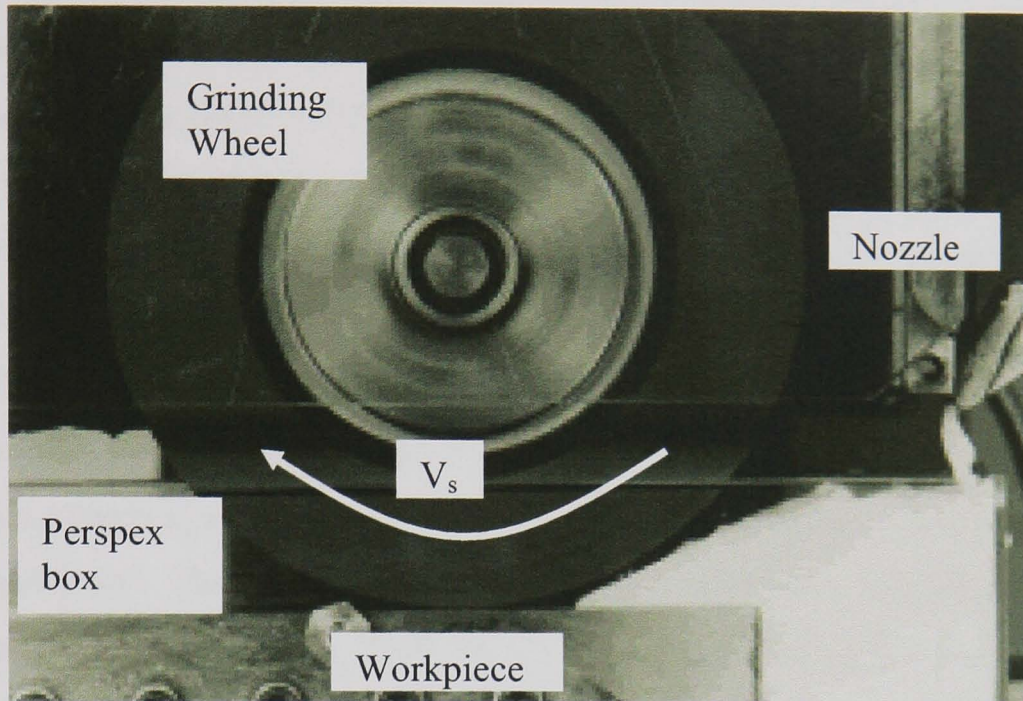


Figure 3-14 Cutting fluid backing up due to boundary layer effects

(The wheel periphery, rotating at 33.5 m/s, is 0.08 mm above the workpiece surface,) Ebbrell (1999)

3.2 Summary

As a summary to the nozzle work in this chapter, Figure 3-15 taken from Brinksmeier et al 1999, compares the current trends in fluid application in the grinding contact.

$Q_{CL} =$ flowrate		conventional flooding nozzles	
		a: flexible segmented hose b: tube	$Q_{CL} \uparrow \uparrow$
		c: free jet nozzle	
		shoe nozzle	$Q_{CL} \uparrow$
		spot jet nozzle	$Q_{CL} \uparrow$ or $Q_{CL} \downarrow$
		spray nozzle	$Q_{CL} \downarrow \downarrow$
		internal supply	$Q_{CL} \uparrow$ or $Q_{CL} \downarrow$
$\uparrow \uparrow$ very high, \uparrow high, \downarrow low, $\downarrow \downarrow$ very low			

Figure 3-15 Summary of fluid application techniques (Brinksmeier et al 1999)

Chapter 4 Review of CFD techniques

4.1 CFD methods and reasoning

Current FE (Finite element) software is based on two principal numerical methods:

- Finite Element Method (FEM code);
- Finite Volume Method (FVM code).

Both methods involve dividing the flow domain into a large number of finite elements or in the case of FVM, small control volumes and then solving the governing equations of fluid flow i.e. the three-dimensional Navier-Stokes equations. Systems of algebraic equations are solved by an iterative method in the process. The numerical methods differ in their definition and derivation of these algebraic equations. FEM uses simple piecewise functions (e.g. linear or quadratic) to describe the local variations of unknown flow variables ‘ ϕ ’. The Navier-Stokes equations are precisely satisfied by the exact solution of these variables ‘ ϕ ’. If the piecewise approximating functions for ‘ ϕ ’ are substituted into the equation it will not hold exactly and a residual is defined to measure the errors (Huebner 2001). The residuals are minimised next by multiplying them by a set of weighting functions and integrating. As a result, a set of algebraic equations for the unknown coefficients of the approximating functions is obtained (Bathe 1996). After this, the equations are solved to give the results. The relationship between FEM and FVM in triangular 2D meshes was first established in Idelsohn and Onate (1994).

For FVM, a formal integration of Navier-Stokes equations over all the control volumes of the solution domain is carried out. A variety of finite-difference-type approximations for the terms in the integrated equation representing flow processes such as convection, diffusion and sources are then applied. This converts the integral equations into a system of algebraic equations (Versteeg and Malalasekera 1995). One other method of solving the complex partial differential equations is the finite difference method (FDM). This method uses an approximation of the differential operator and gives an estimate of the resultant equation. For example, consider the ordinary differential equation:

$$u'(x) = 3u(x) + 2 \quad [4.1]$$

The Euler method for solving this equation uses the finite difference

$$\frac{u(x+h) - u(x)}{h} \approx u'(x) \quad [4.2]$$

to approximate the differential equation by

$$u(x + h) = u(x) + h(3u(x) + 2) \quad [4.3]$$

Equation [4.3] is known as a finite-difference equation. Solving this equation gives an approximate solution to the partial differential equation (PDE). The error between the approximate and the true solution is determined by the error that is made by going from a differential operator to a difference operator. This error is called the discretisation error. It is therefore an alternative way for solving PDEs but gives only an approximation of the equation. The main difference between FEM and FDM is that where FDM gives only an approximation to the differential equation, FEM gives an approximation to the actual solution of the differential equation. FEM has a superior ability to handle large and complex geometries, as well as the boundaries associated with such geometries, frequently required by those users looking for a software solution to analyse their problem often created from compiled three-dimensional CAD packages. FEM solvers and software packages handle complex geometries in a relatively simple manner. FDM packages allow only for modelling of the most basic 'block' geometries; however, they do this easily in comparison to FEM solvers. Although both FEM and FDM are approximations, those approximations used in FEM solutions are of higher accuracy.

Due to its nature, CFD problems generally need a large number of cells or grid points; often running into the millions for more complex and larger solutions. For this reason, FEM is often reserved for structural analysis involving stresses and deformations in solid bodies, where small but complex geometries are commonplace. CFD solvers use the FVM due to its ability to cope with large grids such as those present in external flow problems like the flow of air over an aeroplane wing or the flow of water over land.

4.2 The FVM and mesh discretisation

CFD modelling of fluid flow within a grinding process requires a complex mesh that accurately defines the actual geometry of the areas required for the fluid domains to represent. As nozzles are highly complex in geometrical terms in comparison to the modelling of flow merely through a pipe, fitting a commensurately complex mesh to the

geometry is essential. This is one of the most time consuming parts of the modelling process and requires a large amount of physical user time (in understanding the physics of the process) to represent the geometry with an accurate mesh. Representing the physical domain accurately often requires a mesh containing deformed regions. A large research effort by Chand (2005), Bijl et al (2005), and others, focused on developing mesh generation algorithms to improve the quality and reduce the non-orthogonality of these meshes. However, in multi-physics problems, even when starting with a high quality mesh, it may degrade during the solution process. In this case, with multi-physics or multiple flow environments, the solution needs adaptation to take into account any deformation occurring during the solution process.

The finite element method described by Zienkiewicz and Morgan (1983) and the finite volume method explained in Barth, (1992) are the grounding for the two most popular mesh discretisation methods. For modelling of fluid flows and accurately meshing geometrical constraints put on by fluid flow physical problems, the FVM is the method of choice due to its ability to handle the size and complexity constraints of such physical models. The FVM uses a number of methods to define the unknowns. Two typical methods are the vertex-centred method unknowns being defined at the mesh nodes, or cell-centred (CC) natural unknowns defined at the element centroid. Most commercially available packages use the CC method due to its ability to solve orthogonal meshes efficiently using simple approximations to discretise the terms in the transport equation. Most CFD codes such as those implemented into CFX, FLUENT (now both part of the larger ANSYS group and grouped for cross processing, available at www.ansys.com) and PHYSICA (available at www.multi-physics.com) use the CC method due to its low demands on computational power and the increase in simulation rates. With the complexity of flow geometries however, this method is often inefficient. Intensive research on alternative discretisation methods emerged because of this. Barth, (1992); Lyra et al, (1994); Crumpton and Giles, (1995); Sorensen et al (1999) used edge-based schemes, Coirier, (1994); Mavriplis, (1995); Haselbacher and Blasek, (2000) used cell based gradient reconstruction. Jameson et al (1986) used cell vertex techniques and Chakrabartty, (1990) employed a vertex-centred scheme for flow past complex geometries.

Other errors occur whilst solving the equations in the faces of volume method solutions. Reassurance of the workings of CFD packages requires a background understanding of the methods used to resolve these errors and the way in which meshes are discretised. This requires interpolation of the mesh to improve the derivatives at the cell faces (Moulinec and Wesseling 2000). Barth and Jespersen (1989) and Weiss et al (1999) proposed different interpolation schemes based on Taylor series expansions. Lehnhauser and Schafe (2002) reported significantly improved accuracy with a multi-dimensional Taylor series expansion scheme.

Increased expense comes with complication of the FVM when adding pressure correction schemes in the solution of the incompressible Navier-Stokes equations. Due to this expense and the complexities and difficulties it induces, it is often commonplace to omit these from the set up of CFD physical situations (Demirdzic 1982, Braaten and Shyy 1986). This however induces stability problems into the solution and often leads to a non-convergent solution particularly with badly formed or highly complex distorted meshes. With highly complex geometries, it is often impossible to mesh the entire domain accurately. Computational power limits the amount of refinement possible, and with memory limitations, the sheer number of elements or volumes permissible is reduced. Many authors have sought to rectify this (Peric 1990, Cho and Chung 1994, Lehnhauser and Schafe 2003, Zhu et al 2004).

Prakash and Patankar (1985) developed an alternative method to those prescribed in most FVM solutions. Their work including combining the FVM with the FEM. Baliga (1996) describes their work in more detail and Reyes et al, (2001) shows its successful implementation with reference to complex flow problems with obscure geometries such as those described in this work. This method is a vertex-based (VB) FVM (Taylor et al 2003). This is a more costly method than that using the CC method, requiring a much larger computational power demand with storage of the topographical information.

Dervieux (1985) developed the first mixed method of solving the problems described. His work describes the first principles of mixing the two to form the now well known and implemented FVM_FEM, employed by many in the simulation of turbulent flow, including three-dimensional turbulent compressible flow (Hallo et al 1997) and large eddy simulations (Koobus and Farhat 2004). Durlofsky (1993) combined finite volume-finite elements in the solution of multiphase flow in porous media.

All the above authors investigated deeply mathematical and numerical solutions to problems to try to solve a specific problem within the simulation environment. Most of the work focused on the importance of correct meshing by advising the development of separate meshes using numerical solutions where simplification of geometries is impractical. With the intensive research into the numerical methods and the effort to prove the validity of each method to a given physical simulation, the actual results of the simulations were of little importance to the work, other than proving the correctness of the solutions. This work relies mainly on the proofs provided by those mentioned in this section.

4.3 Fluid Mechanics using CFD

The numerical methods behind the principles used in all FE, FD, and FV methods above, form the foundations for most CFD simulations of fluid flow problems with numerical verification backing up theories to simulation procedures. This section aims to inform on the actual simulation of fluid flow problems and the previous work done in these areas. With relatively little work on simulation of internal flows in grinding nozzles and the flow of fluid in a grinding environment, this section highlights areas of interest relating to losses to the approach of fluid application in the grinding environment as well as other simulations of fluid flow in general.

Much of the work, in this field, at present is user defined and based on user specific meshing and code generation. This work aims at using a commercially available package to simulate various internal flows within a grinding environment, including investigations of flow patterns on exit from the nozzles. Most of the work involves turbulent flows due to the need for high pressures and flowrates in coolant nozzles to satisfy the criteria proposed by Webster (2000).

4.3.1 Internal Pipe flow

Fluid mechanics is a very large area of science and many theoretical models and numerical solutions for flow problems exist, but with the advent of new computational techniques, comparison of CFD predictions and previously accepted numerical solutions now come to the forefront. Ludicello (ESDU 2007) recently carried out a comparison between CFX results and those gained numerically in ESDU (2005) for pressure loss in pipes with sudden contractions (Figure 4-1). Pipes with sudden

contractions exist in many engineering applications, most pipefittings, and most application systems that lead up to the coolant nozzles in grinding. To analyse accurately and design these supply systems, the amount of pressure loss and flow separation must be determined to avoid unnecessary pre-nozzle pressure losses. There is little reliable experimental data on pressure loss in sudden contractions ESDU (2007). To validate existing experimental data ESDU (2007) used ANSYS CFX. The solver proved very robust, with the solution converging to a high accuracy with only a small number of iterations on meshes that were not completely orthogonal or high quality. ESDU (2007) used a rigorous procedure to reduce the sensitivity of the comparison to mesh size and distribution, residual levels, turbulence modelling and near-wall treatment, flow boundary profiles and location. Three turbulence models were tested:

- the k- ϵ model with scalable near-wall treatment;
- the k- ω model;
- the shear stress transport (SST) model with automatic near-wall treatment.

The results from the work done by ESDU (2007) show a good correlation between the experimental values and the work done using ANSYS CFX (Figure 4-2).

Ludicello from ESDU (2007, p31) comments that :

The ANSYS CFX results have helped us understand why the previous ESDU correlation for the pressure loss coefficient in turbulent flow was significantly higher than the ANSYS CFX predicted values.

The reasoning behind this came from errors within ESDUs' experimental data. The original correlation and other commonly used correlations based on experimental data by Benedict (1984) are biased on the high side. The information in Benedict (1984) is reputed to be very reliable however; the downstream measurement location of the static pressure is reported as being at the flow reattachment point and assumes fully developed flow. CFD calculations and measurements set the fully developed point at least 20 diameter lengths downstream of the contraction plane. It reattaches at about one diameter length. Consequently, ANSYS CFX predictions are lower than Benedict's data in the fully developed region but in close agreement at the flow reattachment point ESDU (2007).

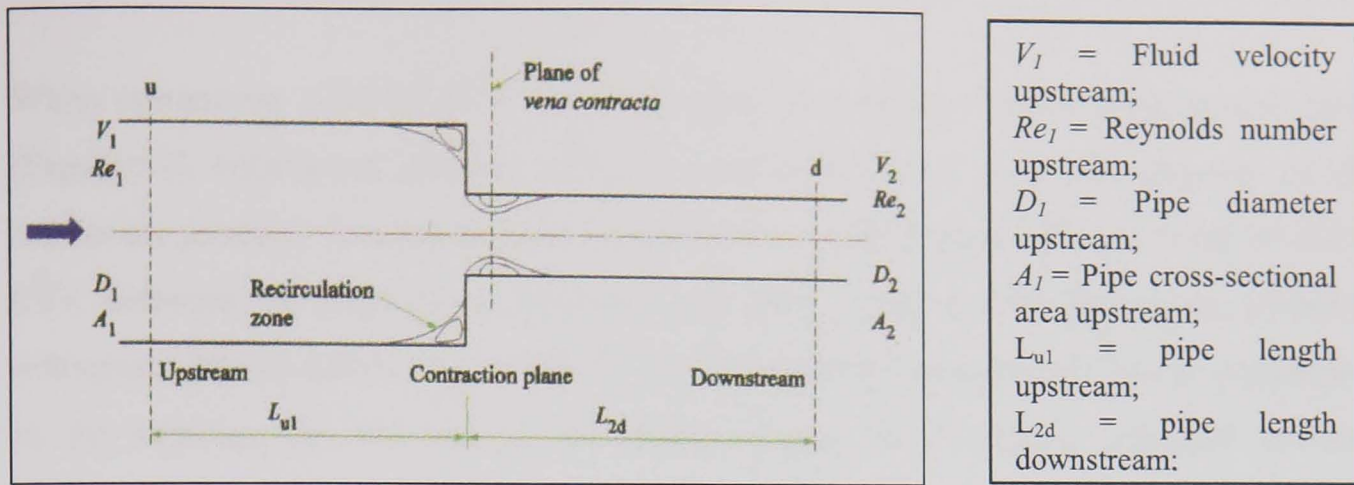


Figure 4-1 Flow schematic to determine pressure loss and extent of flow separation (ESDU 2007)

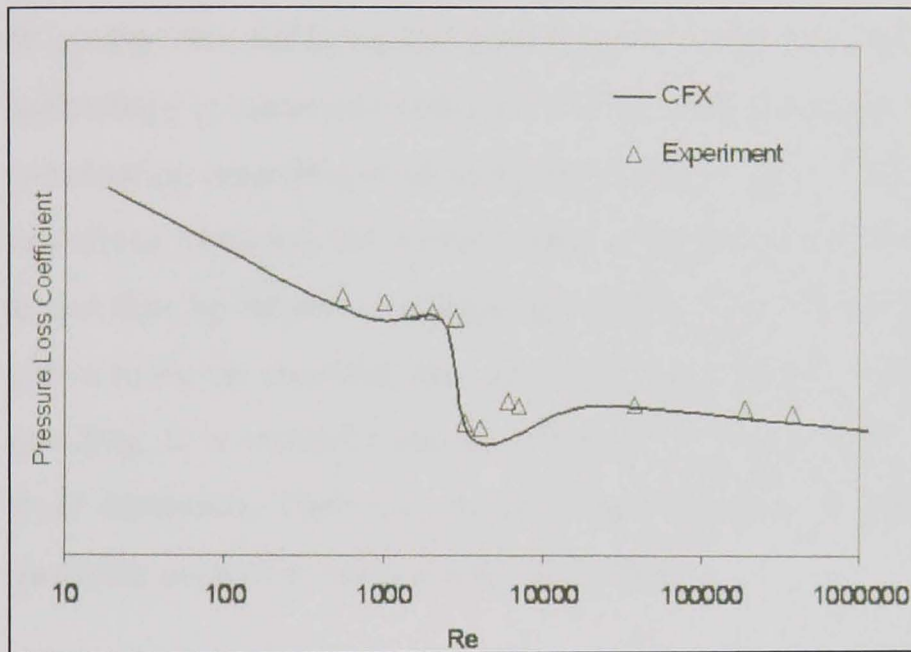


Figure 4-2 Typical ANSYS CFX results vs. experimental data (ESDU 2007)

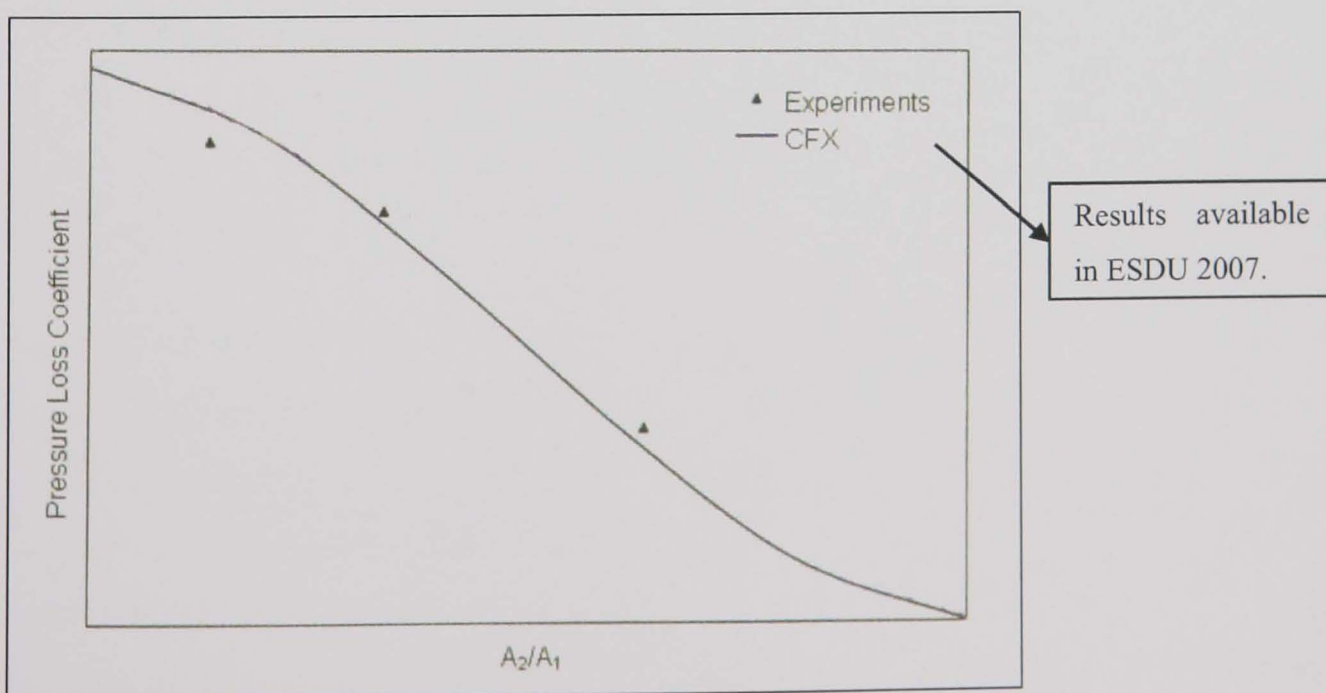


Figure 4-3 CFX Prediction Results vs. Bullen's experimental data (ESDU 2007)

When comparing ANSYS CFX data with that of Bullen's (1987) experimental data, (Figure 4-3, considered reliable, although some small errors exist) the majority of the results on pressure loss predictions correlate well. The results obtained with ANSYS CFX software, in some cases, proved to be more reliable than previously accepted references (EDSU 2007). The ANSYS CFX prediction accuracy gives great confidence in the software for the use of modelling internal flows within turbulent internal environments.

4.4 Summary

In reality, the mathematical prediction of fluid flow without the use of a simulation technology is inherently difficult. CFX, on the other hand, is shown to provide detailed information regarding fluid movement inside a pipe. It not only provides fluid pressures at various locations but it also predicted the movement of fluid throughout the domain. It can thus be helpful in analysing problems involving turbulent fluid flow. It can thus prove to be an essential tool for systematic design of coolant application systems for grinding. It is evident from the literature that CFD analysis offers detailed insight into fluid dynamics. Their use should be encouraged, as huge computation power is now available even to a single stand-alone user.

Chapter 5 CFD studies of nozzle internal and exit flows

5.1 Introduction

Although ANSYS CFX itself is a software tool, this work uses it to develop a model of cutting-fluid flow in nozzles. The simulation results presented here have been obtained using CFX as the code itself has been investigated and proved reliable by other researchers in CFD. It is proposed to model situations saving prototyping costs. It is observed that industries, such as aerospace and automotive, use modelling and simulation extensively for product development. It is not meant to replace existing theory, but simply use it to model and to reproduce actual nozzle situations in order to have a better understanding of nozzle flows, as well as help improve process performance.

This section of work uses ANSYS CFX to model the internal flow profiles for a range of nozzles and fluid flow situations with a range of entry conditions. This work includes the analysis of internal flows of the nozzle proposed by Webster et al (1995a) and work by Cui (1995) investigated using CFX. Further to this, the nozzles proposed by Gviniashvili (2003) are re-analysed in terms of internal performance of the nozzles. Each nozzle includes a length of pipe before the inlet to develop the flow before entry to the region of interest.

5.2 Simulation setup

For the early simulations, FLOTRAN enabled basic fluid visualisation inside conventional nozzles using CFD solutions. The robustness of these results as well as the software's capabilities comes into question. Due to this lack of ability and underperforming model in regions at the nozzle exit, ANSYS CFX, along with the ANSYS Workbench environment, was adopted.

There are two major benefits for using this new analysis software. One benefit of CFX is the understanding of fluid flow phenomena bundled into examples with the software, the other being its ability to handle most three dimensional flow problems, including multiphase flows described later, with a good level of confidence. In particular, the visualisation capability greatly enhances intuition of flow behaviour. CFX makes addressing a new class of problems possible, no longer limited by the narrow range of classical flow solutions, in particular turbulent two-phase flows.

The decision to use CFX in this work was made after a careful consideration of all the leading CFD packages. It was concluded that the ongoing integration of CFX with the popular ANSYS software suite, the robust solver provided by CFX, and the CAD capabilities of ANSYS Workbench gave CFX a clear advantage over competing software alternatives. The success of CFX and its wide use is apparent from a number of researchers focusing their work using this package. The Supercomputing Institute for Digital Simulation & Advanced Computation at the University of Minnesota recently acquired the CFX program and a number of graduate students are currently using the software for their doctoral research.

The package exhibits its best attributes for this work when looking at the disturbances after exit from the nozzle, and investigating the coherence length. The 3-D CFX software will provide for modelling of flows exiting to a local free environment i.e. the chamber constraint will not apply.

5.3 Three-dimensional Simulation Setup

CFD simulation with CFX technology is available in the ANSYS Workbench interface. Geometry creation, meshing, physics definition, solution, and post-processing for CFD come contained in a single simulation environment. This means that a simulation created from the very first steps, the geometry, is run through the entire process in the same environment, removing any errors through cross-package processing. The following is an example of an internal flow, set up for comparison with the predicted work by McCarthy and Molloy (1973) for nozzle design.

A. Geometry creation

As the geometry portal for all ANSYS products, the Design Modeller™ software provides a single geometry source for a complete range of engineering simulation tools. The Design Modeller™ software creates the detailed geometry required for engineering simulation, minimising geometry rework and simplifying analyses. To create the geometry for this analysis a basic sketch of a section of the pipe is created and then revolved around the axis: Figure 5-1.

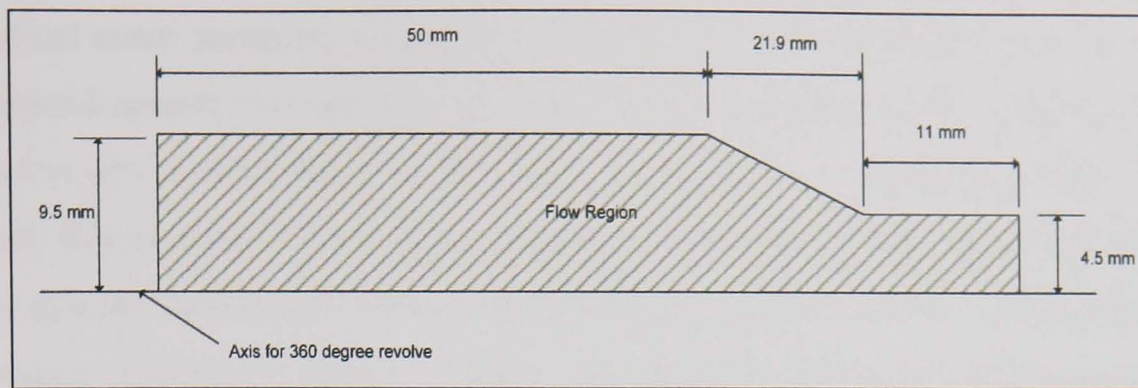


Figure 5-1 Geometry Creation in Design Modeller™

After the revolution, the section becomes a three-dimensional solid of the flow region. Note that the actual region of flow is created and not the pipe geometry (Figure 5-2). To move from a created pipe to the flow region using existing geometry the fill command is used.



Figure 5-2 Geometry after the revolve operation

B. Meshing

To provide accurate CFD results requires superior meshing technology. ANSYS, Inc. provides two choices for CFD meshing requirements within the ANSYS Workbench solution: the ANSYS CFX-Mesh and ICEM CFD products. For this work to provide a high quality mesh, meshing tools were investigated. ICEM CFD, provides the best solution for a high-quality mesh and was therefore used. This meshing tool generates a tetrahedral mesh directly from the CAD geometry. The tetra meshing uses an octree-based meshing algorithm to fill the volume with tetrahedral cells and to generate a surface mesh over the object surfaces. The nodes and the edges of the tetrahedral mesh are matched to the prescribed points and curves of the geometry.

Mesh convergence studies permit some reliability in the results generated from simulations. It is critical that a mesh convergence study is carried out especially in high accuracy work. The formal method of establishing mesh convergence requires a curve

of a critical result parameter (typically the velocity in pipe flows) in a specific location, to be plotted against some measure of mesh density. At least three convergence runs are required to plot a curve that indicates when convergence is achieved, or how far away the most refined mesh is from full convergence. However, if two runs of different mesh density give the same result, convergence is already achieved and no convergence curve is necessary. Figure 5-3 shows a 4-point convergence study used in this example with velocity at the outlet selected as the location. After four refinements, it is clear from the graph that no further refinement is necessary for the preliminary studies.

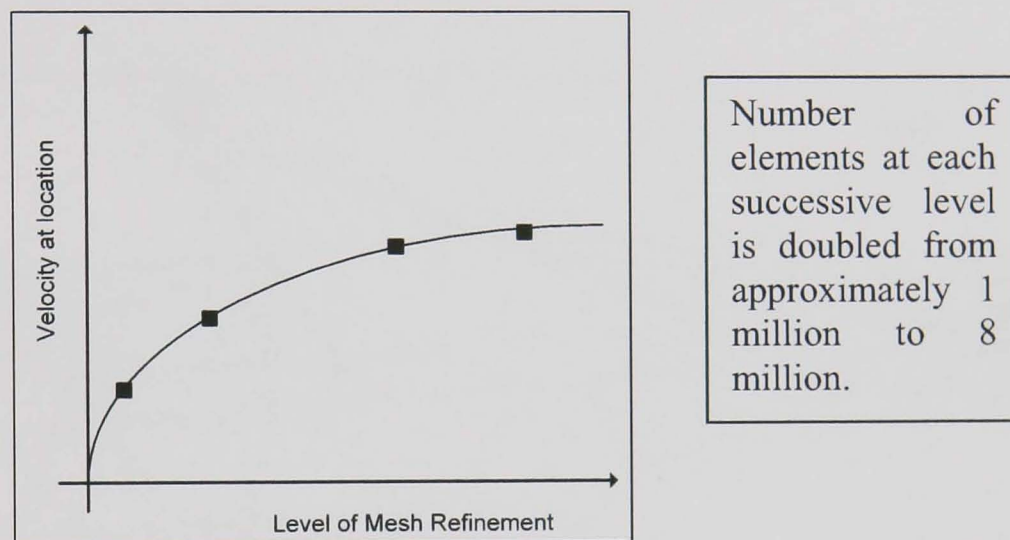


Figure 5-3 A 4 point convergence curve

In theory, for each successive level of mesh refinement in the convergence study, all elements in the model should split in all directions. To test convergence of a model by refining the mesh only in the regions of interest, and retain the unrefined (and probably unconverged) mesh elsewhere is an accepted method for the study due to areas of interest. There will exist transition regions, from coarse to fine meshes. These must be suitably distant from the region of interest (at least 3 elements away for linear elements).

Using larger elements away from regions of interest in a model is common practice but a more subtle point is, providing they do not misrepresent the geometry and suitable mesh transitions can be carried out, these elements can be considerably larger than those in regions of interest without jeopardising accuracy. Contrast this as a meshing strategy against that of filling an entire model with small, high quality elements, to improve overall accuracy. This latter approach is inefficient and requires a high computational

drain (the amount of effort placed on the CPU of a computer). This method is unnecessary for modelling internal flows in the simulations discussed in this work.

Areas requiring the implementation of a boundary condition, when modelling in ICEM CFD, are given a name for bounding in the pre-processing stage. These include inlets, outlets, solid objects in the flow, walls, and other such features. Figure 5-4 shows the zones used for this work. There are a number of options for meshing the domain in ICEM. After creation of the domain, global and local element size setting creates the basis for the volume mesh. The controls used are as in Figure 5-5.

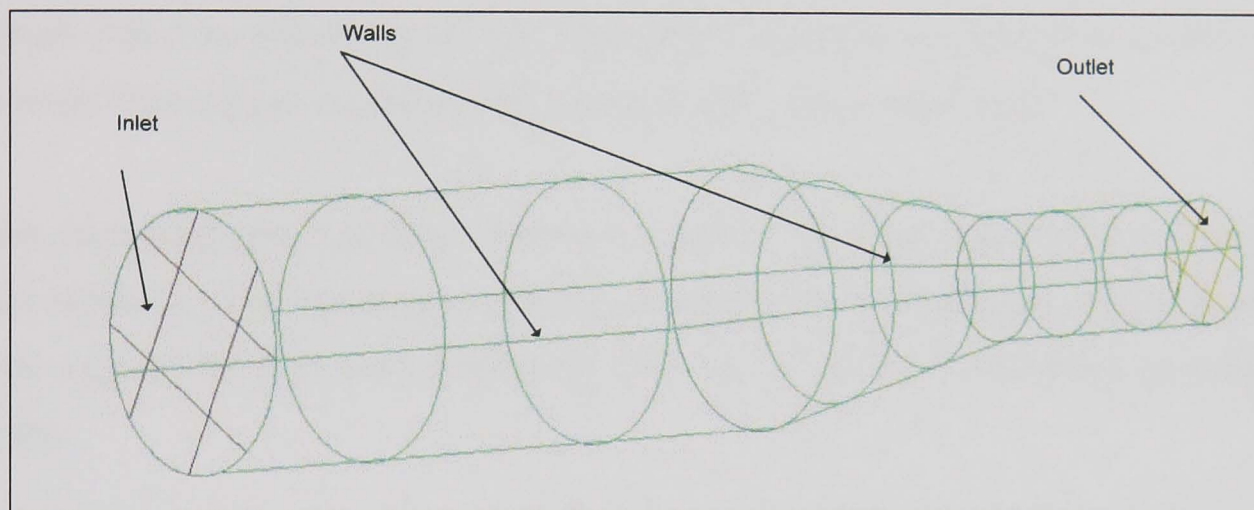


Figure 5-4 ICEM CFD image with regions selected

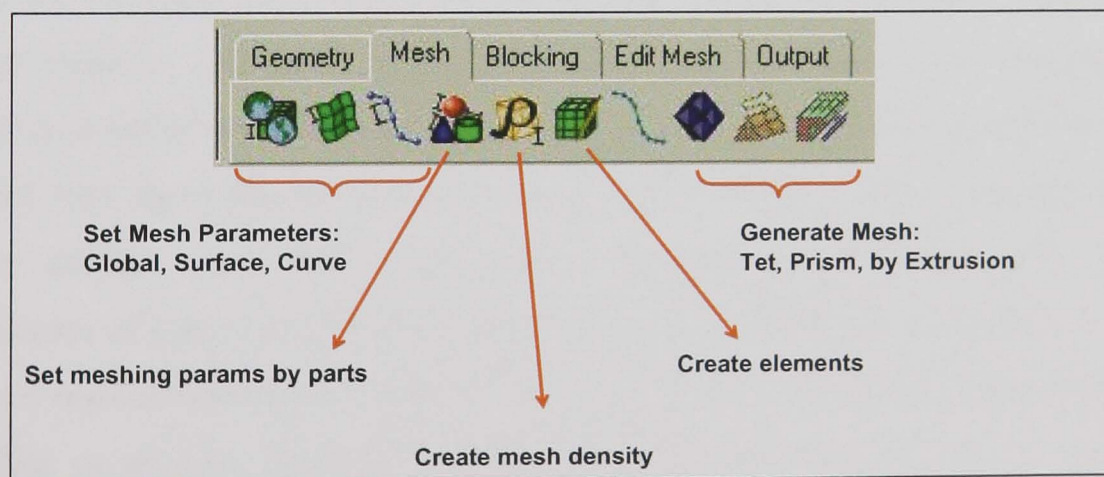


Figure 5-5 ICEM Meshing Controls

Working from left to right through the process creates the required mesh. The global mesh size in this work is set to 0.2mm with a maximum element size of five. This means the maximum element in the domain will be 0.2×5 or 1mm. This is on the final refined mesh.

Once the global conditions are set, any points of detailed interest required are modified locally. In this example, no further modification is required, so the tetrahedral mesh is produced accepting the default settings. Figure 5-6 shows this created tetrahedral mesh and mesh statistics before smoothing. It is clear that the grid is not satisfactory at present so a smoothing process is required. In smoothing the mesh, the tetrahedral smoother calculates individual cell quality based on the relative aspect ratio of each cell and the ratio between the volume of the cell and that of the largest tetrahedron that could fit inside the sphere that circumscribes the actual cell. Referring then to the user specified cell quality lower bound, the smoother modifies all cells below this quality criterion, nodes are moved and merged, edges are swapped, and in some cases, cells are deleted. After the smoothing process, Figure 5-7, the mesh statistics were plotted with the mesh visualisation to analyse any elements with a poor aspect ratio.

Mesh smoothing relocates mesh vertices to improve the mesh quality without changing mesh topology. It is necessary in this case to smooth the mesh as poor quality elements at the edges of the flow can significantly affect the velocities in these areas skewing the results.

To locate problems with the mesh that will usually lead to failure when translating or running the solution, error checking is essential. The problems rarely result from the meshing module. The most usual cause is manual editing of the elements. Many different types of error checking exist and running the required checkers takes little time but saves time in validating solved problems with bad residuals. To judge the mesh, different criteria exist. Both the quality control and the aspect ratio allow for identification of any problem areas within the mesh. Referring to Figure 5-7, a quality of 1.0 is a regular tetrahedral or equilateral triangle; when the quality approaches 0.0 the tetrahedral or triangle becomes progressively distorted. For TETRA_4 (tetrahedral) elements, ANSYS ICEM CFD calculates the ratio between the radii of an inscribed sphere to a circumscribed sphere for each element (Figure 5-8).

$$\text{Quality} = \frac{R_{inside} / R_{outside}}{(R_{Inside} / R_{outside})_{Ideal}}$$

where an aspect ratio of one is perfectly regular (with no change between sizes), and an aspect ratio of zero indicates that the element has zero volume. An isosceles triangle however, would have a smaller R_i/R_o due to the circles required to envelop these triangles.

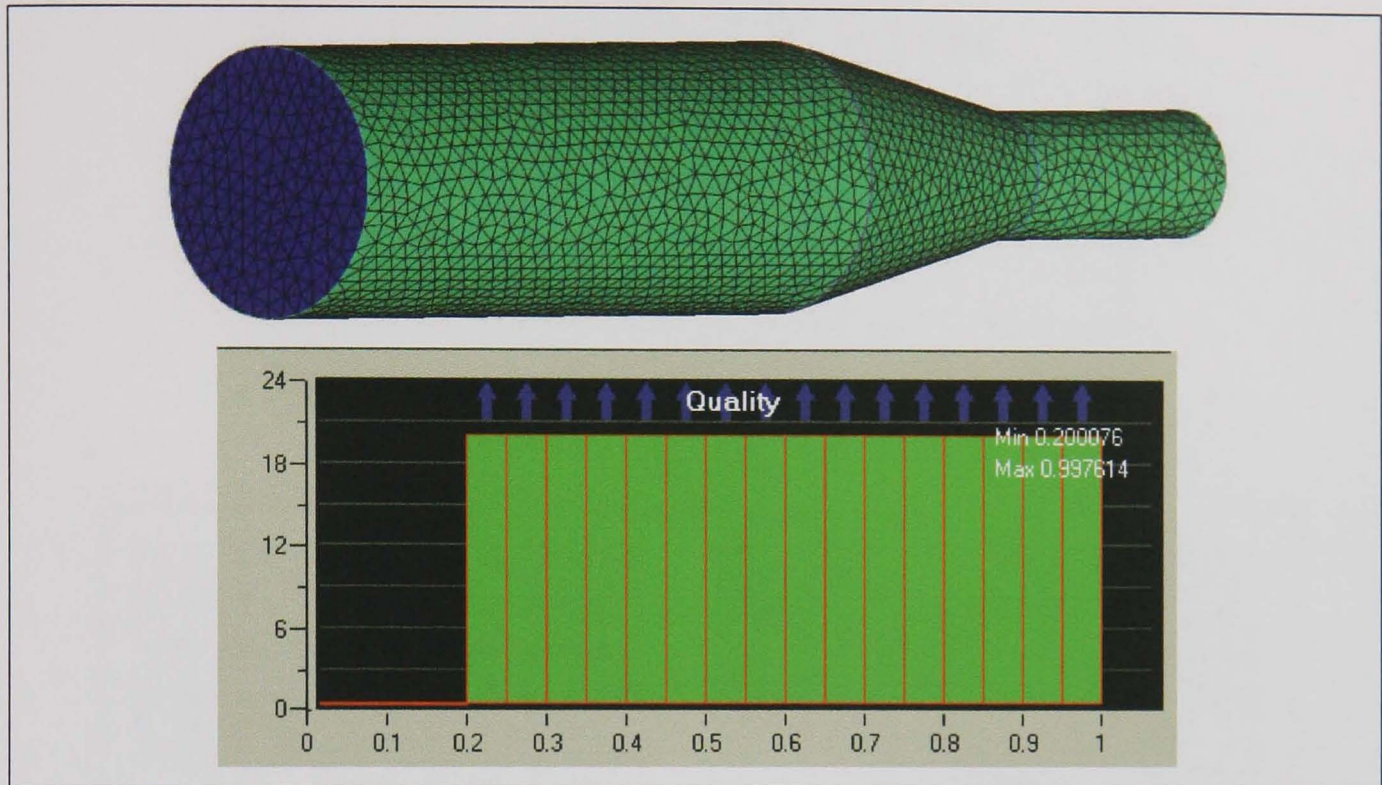


Figure 5-6 Initial tetrahedral mesh with quality statistics

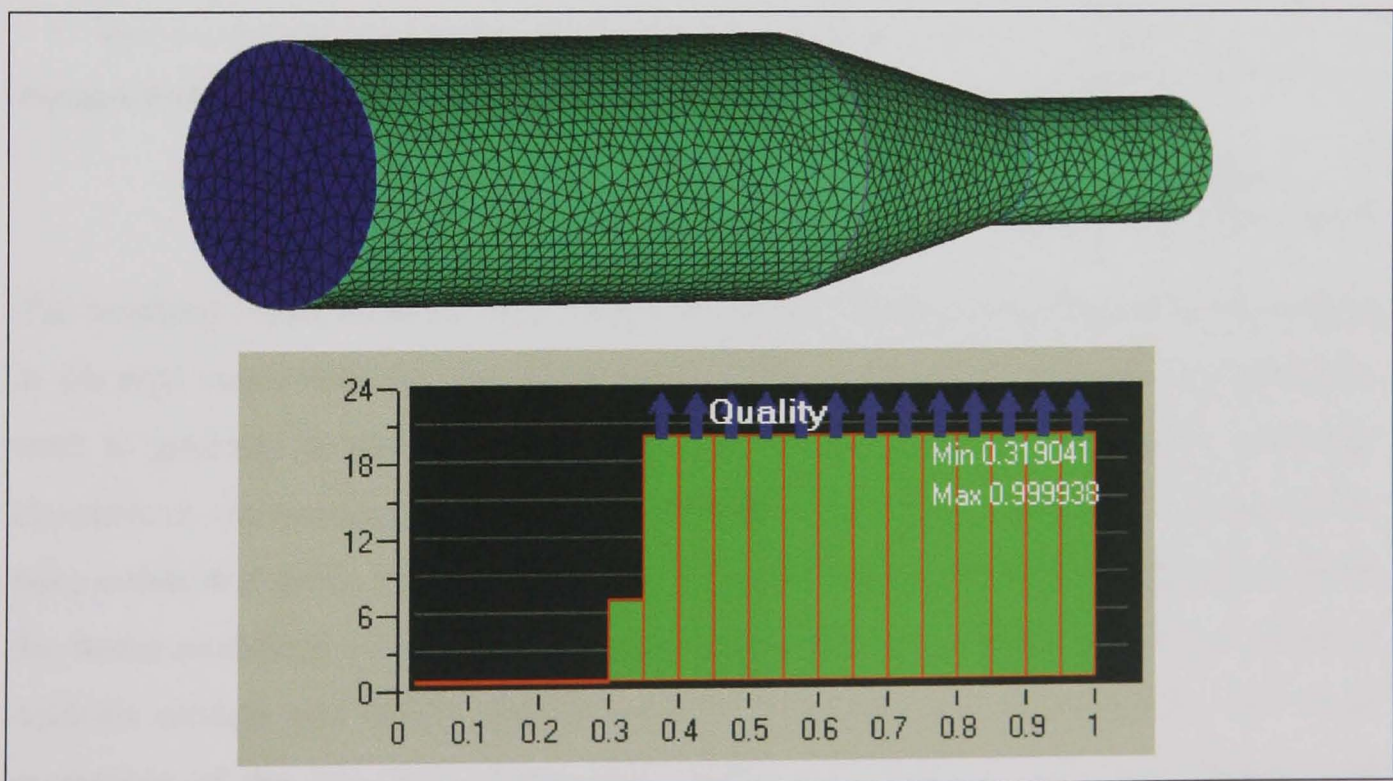


Figure 5-7 Smoothed mesh with quality statistics

Mesh smoothing has occurred throughout the meshed domain. Individual smoothing is difficult to see at this level hence the mesh smoothing statistics.

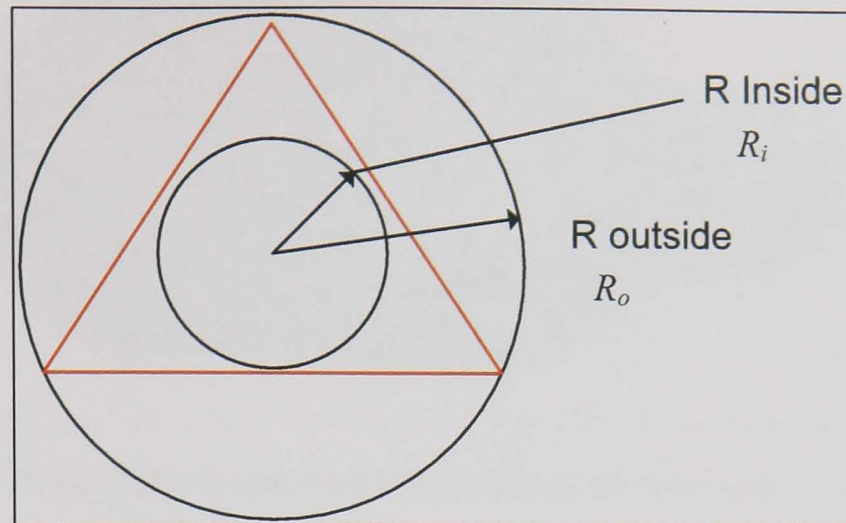


Figure 5-8 Aspect ratio of tetrahedral and triangular elements

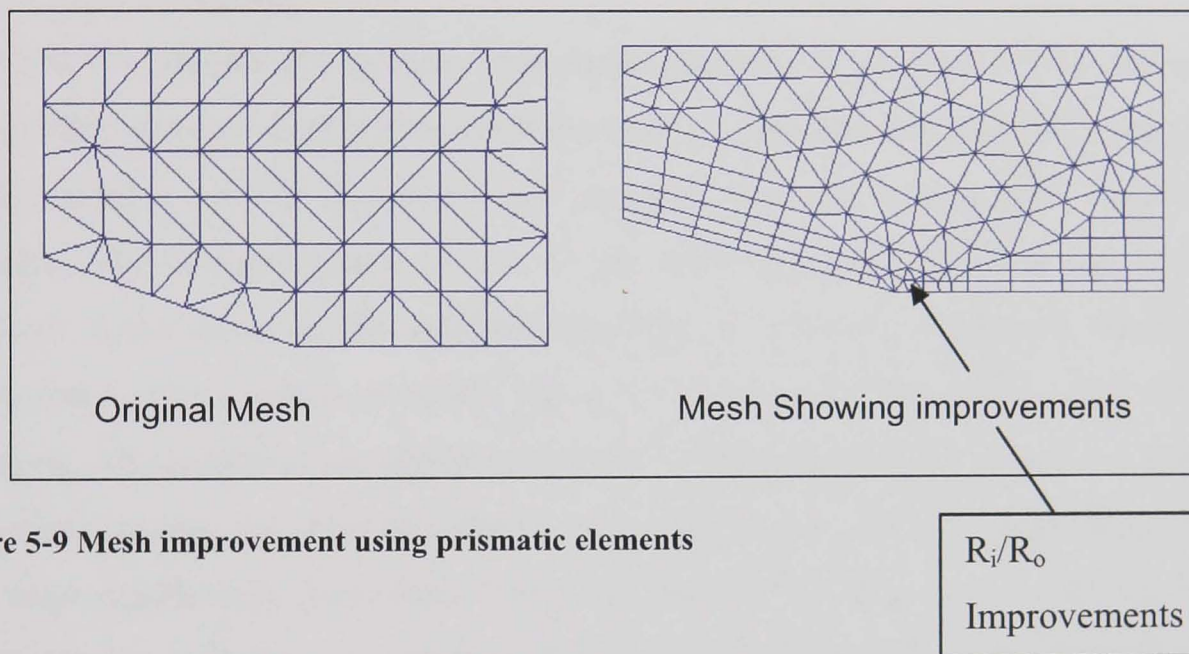


Figure 5-9 Mesh improvement using prismatic elements

The resulting mesh, after all smoothing and quality checks, needs further improvement at the pipe edges with the use of prismatic elements. Prismatic elements are primarily used to generate hybrid tetrahedral grids consisting of layers of triangular prismatic elements on the boundary surfaces and tetrahedral elements in the interior. Compared to pure tetrahedral grids, hybrid tetrahedral grids with near-surface prismatic layers allow for better modelling of the close-to-wall physics of the flow field, resulting in smaller analysis models and better analysis results. The prismatic elements allow for close inspection of the expected recirculation near to the walls (Figure 5-9). Figure 5-10 shows the hybrid tetrahedral mesh with near-surface prismatic layers for this work.

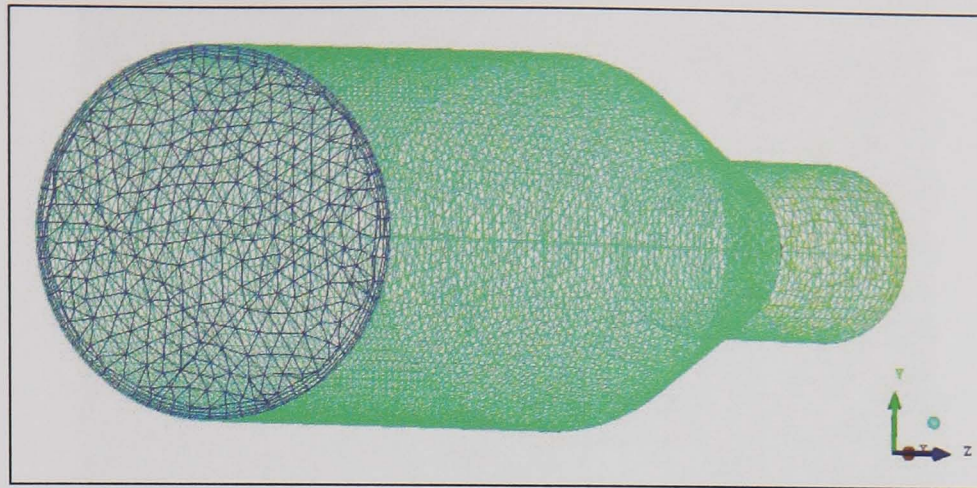


Figure 5-10 Hybrid Mesh with Prismatic elements at the walls

C. Pre-Processing

The CFX-Pre module is a modern, consistent and intuitive interface for the definition of the complex physics required for CFD analysis. In addition, this tool reads one or more meshes from a variety of sources and provides the user with options for assigning domains. The pre-processing is one of the most important parts of the simulation structure. Clear detail on the required boundary conditions and domain locations and interactions, allows others to model the same situation for verification and testing. In this work, all conditions are tabulated for ease of subsequent confirmation - It should be noted that running the same simulation on a different architecture might lead to results that vary significantly from those presented within this work. This is due to difficult floating point rounding (a common problem within computing) and therefore, each simulation should be run with 'double precision' to achieve the closest match to the work presented herein. There are many options in CFX-Pre. All magnitudes of physics and processes need understanding such as the correct choice of models for use within the simulation, the parameters to use, what equation class or group, for example. Once this is understood, modelling of internal flows is achieved by using the quick setup in CFX-Pre. Figure 5-11 - Figure 5-14 show the steps taken for the setup of this first internal flow analysis. The first thing to define is whether the simulation is steady state or transient. This informs the solver as to whether the solution will be run for a period, or as an on going problem to fully develop the fluid. Most of the work in this thesis is concerned with steady state problems as transient problems increase the inaccuracy and complexity of the results.

The image shows a 'Physics Definition' dialog box with the following settings:

- Domain Name:** Default Domain
- Mesh File:** jects\Internal\Int_str8t2.gtm
- Mesh Volumes:** Assembly
- Fluid:** Water
- Simulation Type:** Steady State
- Model Data:**
 - Reference Pressure: 1 [atm]
 - Heat Transfer: None
 - Turbulence: SST
- Solver Parameters:**
 - Advection Scheme: High Resolution
 - Convergence Control: Auto Timescale
 - Time Scale Option: Conservative

Figure 5-11 Physics definition for the internal pipe example

The properties of the cooling fluid with only 10 per cent HysolX are close enough to that of water in terms of flow and therefore water is assumed as the fluid in the simulation. The simulation is a steady state simulation and will therefore run continuously. The reference pressure is set to atmospheric, so all other pressures are in reference to this. No heat-transfer analysis is set as this is of no interest in this work for analysing internal flows of a single fluid at ambient temperature. The SST (shear stress transport) model allows for best calculation of near wall turbulence in CFD simulations; the convergence criteria are set to converge normally. This forms the first part of the pre-processor work.

The next step is to define the boundary conditions for the cross-section. The procedures for defining boundary conditions are not dependent on how the cross-section was drawn for the particular nozzle, and hence are constant throughout. The boundary conditions in this work relate to Figure 5-4 in that the regions created earlier are then used to describe these boundary areas.

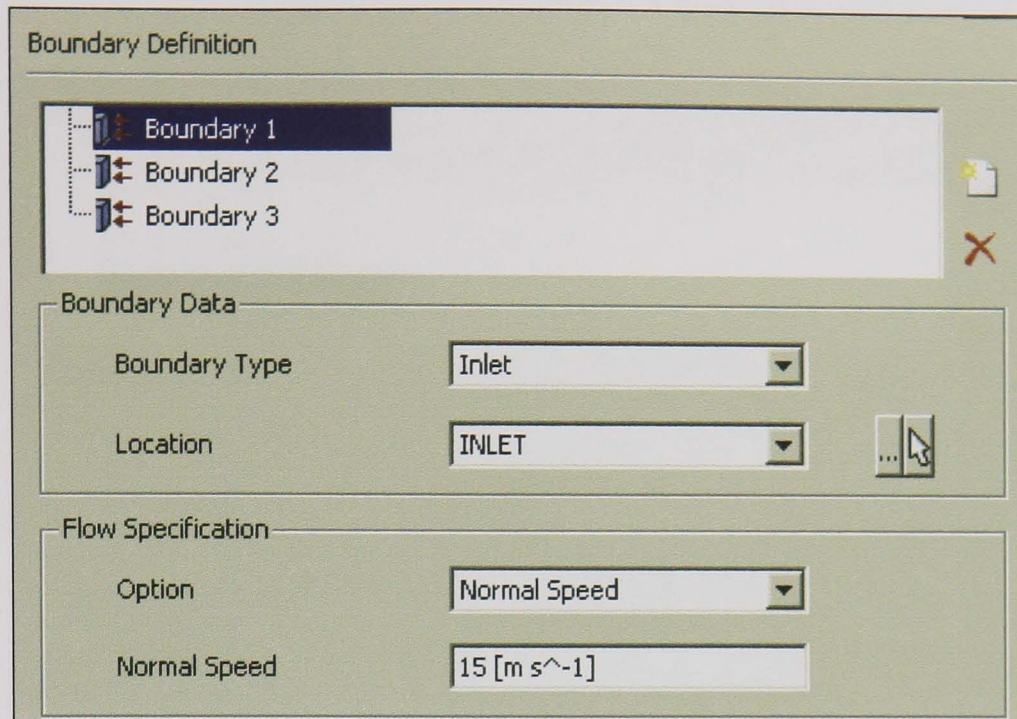


Figure 5-12 Flow conditions for boundary 1

With the inlet extended to allow the flow to develop a turbulent velocity profile, the inlet boundary condition is set to the required delivery speed. Later in this work, this is set to the actual flowrate applied to the pipe system allowing CFX to form its own supply-velocity calculation from the concentration of water and air at a given point.

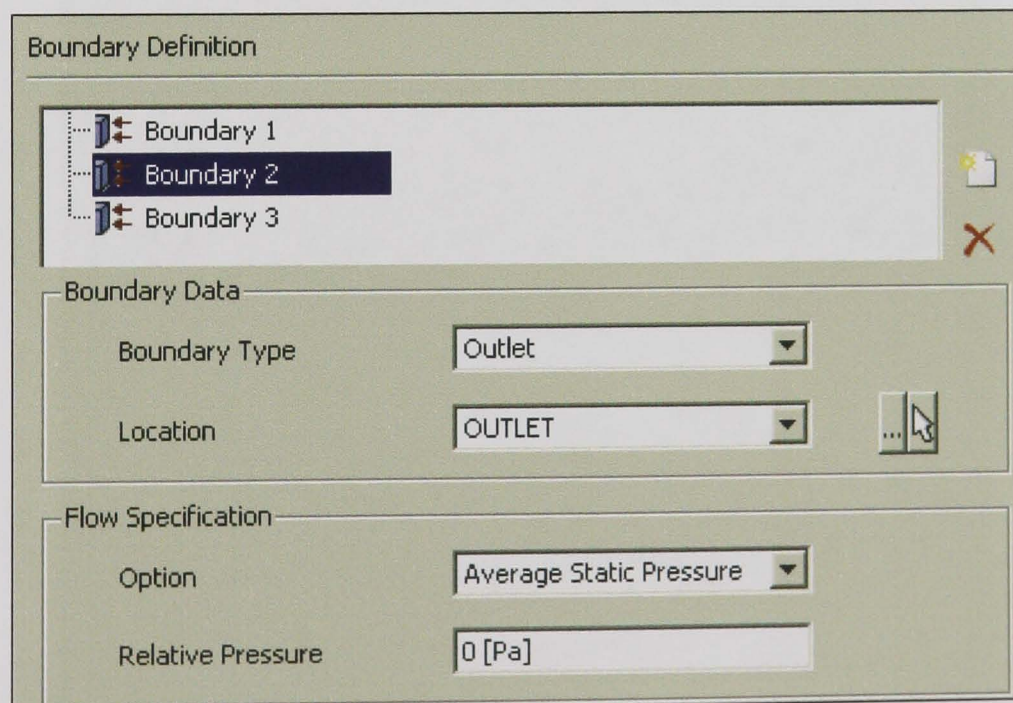


Figure 5-13 Flow conditions for boundary 2

The standard procedure to apply an outlet, is to set the relative pressure at that outlet to atmospheric. This is an average static pressure across the outlet region.

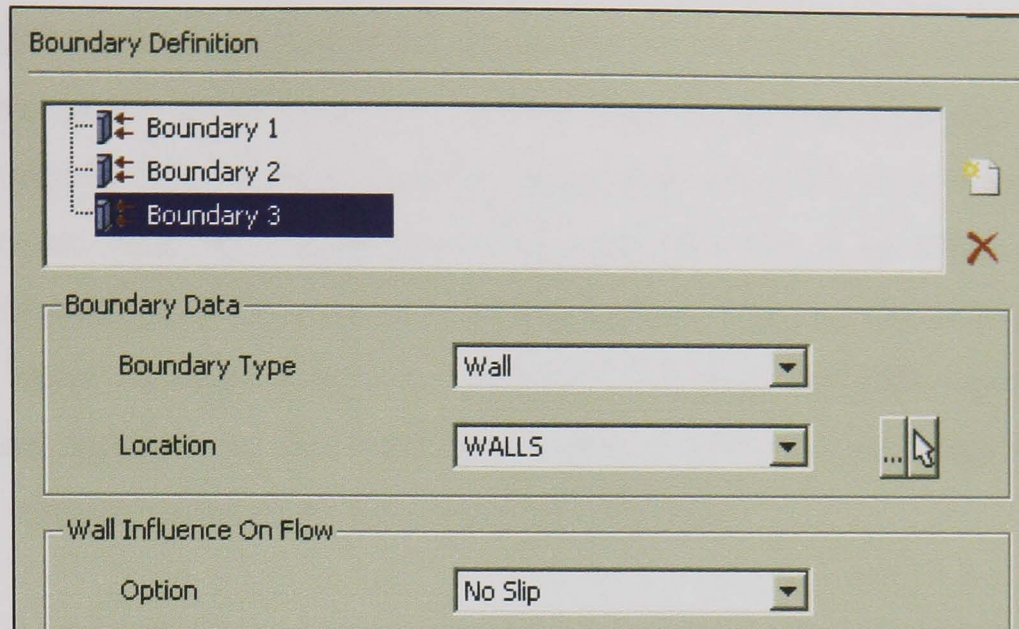


Figure 5-14 Flow conditions for boundary 3

Although CFX-Pre assumes all boundaries not explicitly set to be walls, it is important to check at this stage the remaining boundaries and set them to walls for confidence. Setting of the solver controls finishes the pre-processing (Figure 5-15).

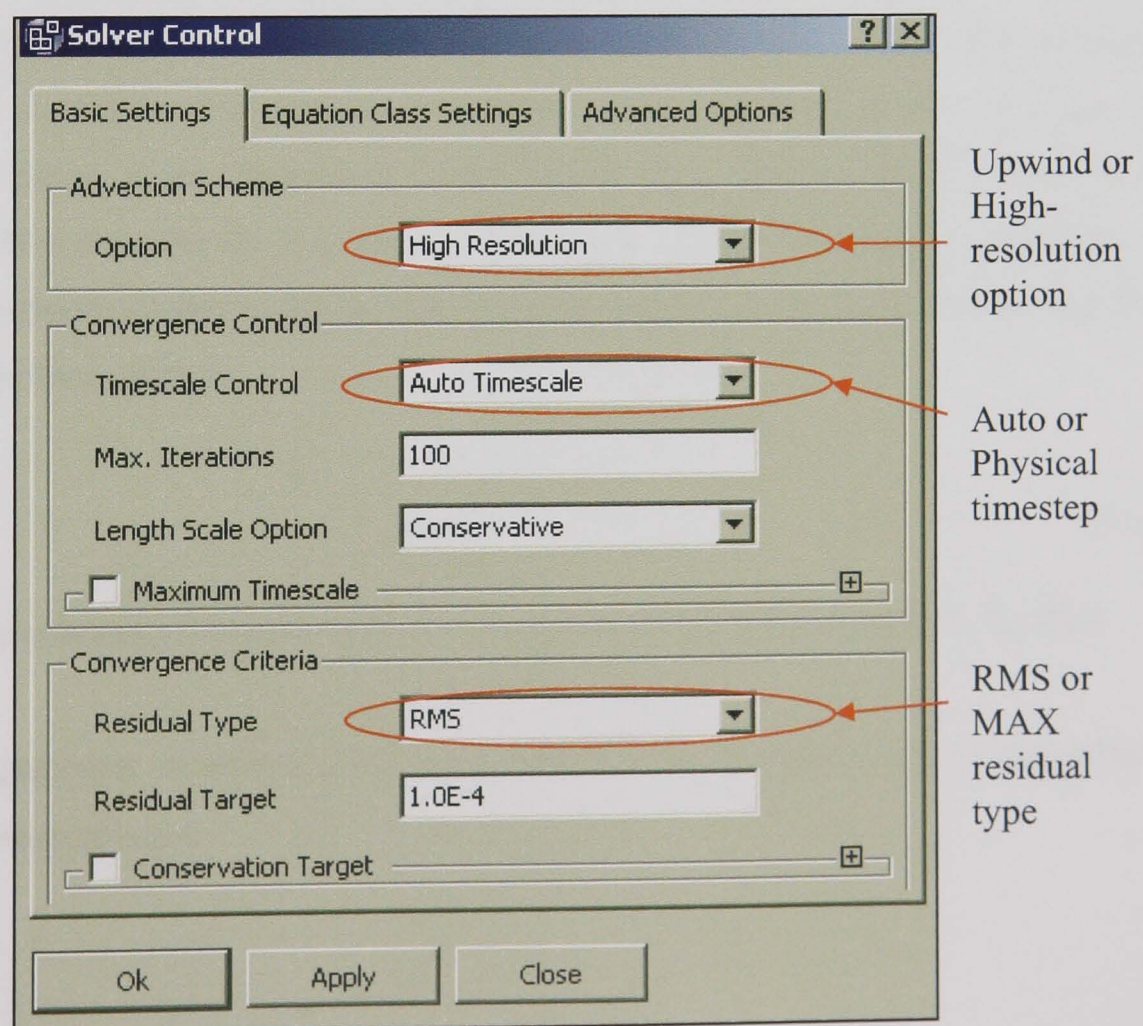


Figure 5-15 Solver control criteria

5.3.1 Upwind

This is equivalent to a specified blend-factor of zero. This setting gives the most robust performance of the CFX-Solver but suffers from Numerical Diffusion. Using this advection scheme is not recommended to obtain final results (except for the turbulence equations). All turbulence equations always use the first order upwind advection scheme, irrespective of the advection scheme setting. This can be overridden on the Equation Class Settings panel in CFX-Pre for more complex geometries and experimental research on the blend factor setup. For this work however, the high advection scheme is selected with the automatic timestep.

Auto Timestep - This option uses an internally calculated physical timestep size based on the specified boundary conditions, initial guesses and the geometry of the domain. This is the default setting for timestep control. The calculated timestep can be a conservative estimate to ensure convergence; faster convergence is achieved by setting a suitable physical timestep.

Physical Timestep - This option allows a fixed timestep size to be used for the selected equations over the entire flow domain. For advection-dominated flows, the physical timestep size should be some fraction of a length scale divided by a velocity scale. A good approximation is the ‘Dynamical Time’ for the flow. This is the time taken for a point in the flow to make its way through the fluid domain. For many simulations, a reasonable estimate is easy to make based on the length of the fluid domain and the mean velocity, for example:

$$\Delta t = \frac{L}{2U} \quad [5.1]$$

Where t is the timestep, L is the length of the pipe and U is mean velocity of the flow.

Now that all geometry, meshing and physics definition is completed, a run is defined to set the simulation process.

D. Solving

The heart of advanced CFD within the ANSYS Workbench interface is the CFX coupled algebraic multigrid solver. Simply put, it achieves reliable and fast convergence by solving the equations well. The solver is fully scalable; achieving linear increase in CPU time with problem size is easy to set up in both serial and parallel run-modes and is representative of true physics (ANSYS user Guide 2008). The Solver Manager provides feedback on convergence progress, allows dynamic display of many criteria and, when necessary, parameters can be adjusted without stopping the solver so convergence can be accelerated. The ANSYS CFX solver runs in the high accuracy mode by default, achieving accurate flow predictions robustly and reliably.

Figure 5-16 shows the defined run with solver criteria accepted. The simulation runs in serial mode and is a full simulation.

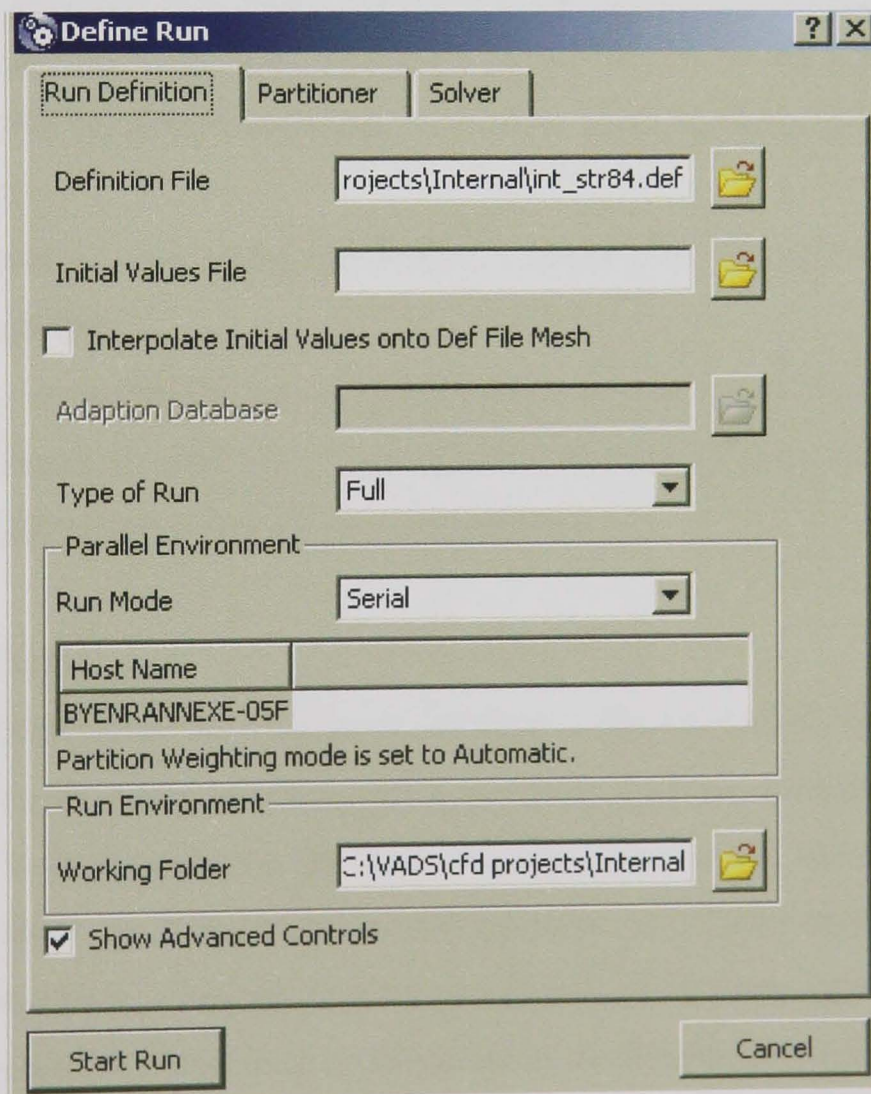


Figure 5-16 Defining the solver run and allocating computer usage

5.3.2 Residual Type and Target

Both the use of MAX (maximum) and RMS (root mean square) normalised values of the equation residuals allow for convergence checking. The CFX-Solver terminates the run when the equation residuals calculated using the method specified are below the 'Residual Target' value. Note that the residual level for turbulence transport equations (for k , ϵ , and the Reynolds stress components) does not form part of the convergence criteria.

MAX Residual Level

- $5e-3$ is very poor, global balances will be poor and quantitative data is largely unreliable. This is good enough for getting an estimate of flow phenomena.
- $5e-4$ is loose convergence, but good enough for many engineering applications.
- $1e-4$ is good convergence, often sufficient for most engineering applications.
- $5e-5$ is tight convergence. If geometry and boundary conditions are not well defined, then this may be more than necessary (since errors in the geometry/boundary conditions will be greater than this). It is often not possible to achieve this level of convergence.
- $1e-5$ or lower is very tight convergence, sometimes required for geometrically sensitive problems.
- $1e-6$ to $1e-7$ is machine round off. This level of convergence is not possible without double precision, in most cases. Convergence this tight is only of academic interest and is used for accurate predictions in this work.

RMS Residual Level

Typically, RMS residuals are a factor of 10 smaller than the MAX residual, and so the above guidelines for MAX residuals apply to RMS residuals, with the targets reduced appropriately. It is possible for the RMS residuals to become lower than the MAX residuals by a factor of 100 or more. In this situation, it is highly likely that the region of high MAX residuals is isolated to a very small area of the flow, typically where some unstable flow situation exists (e.g. a separation or re-attachment point, etc.). It may be the case that this small area of unstable flow / lack of tight convergence of the MAX residuals does not affect the overall prediction. Verification of important target criteria informs whether the tight RMS convergence and a spatially local lack of MAX residual

convergence is acceptable. If time is not an issue and the convergence rate is good, the accepted method is to converge to a small a target as possible. The level of convergence required is highly dependent on the specifics of the flow simulation and the type of ‘important numbers’ that are extracted from the simulation. It is highly recommended that numerical experiments within a class of simulation types be performed, to see how these important numbers change with different levels of convergence. This is the best way to determine how tightly to converge simulations for a given class of flow simulations. Figure 5-17 to Figure 5-20 show the developed residuals for this first example with differing target criteria.

Although the solution may converge normally each time the simulation is run, it is important to check the reliability and accuracy of the model after convergence. The most commonly used method analyses y^+ values. This variable analyses the near wall accuracy of the simulation.

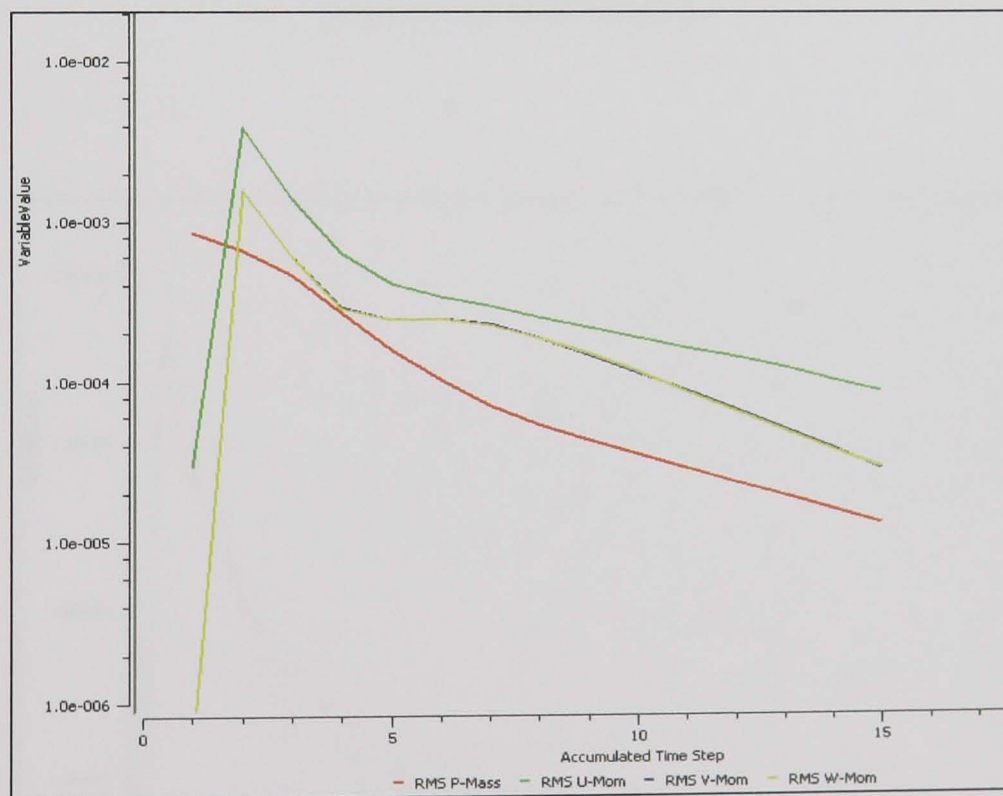


Figure 5-17 RMS residuals

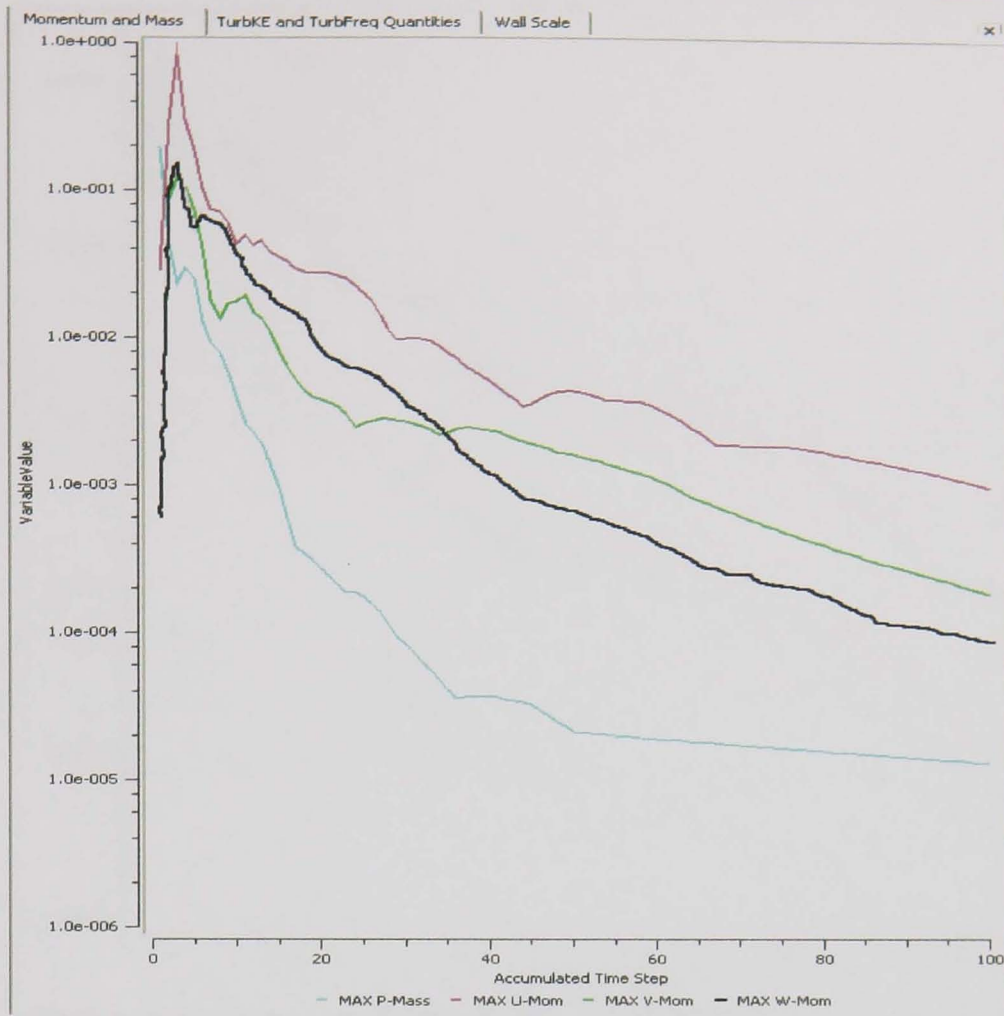


Figure 5-18 MAX residuals

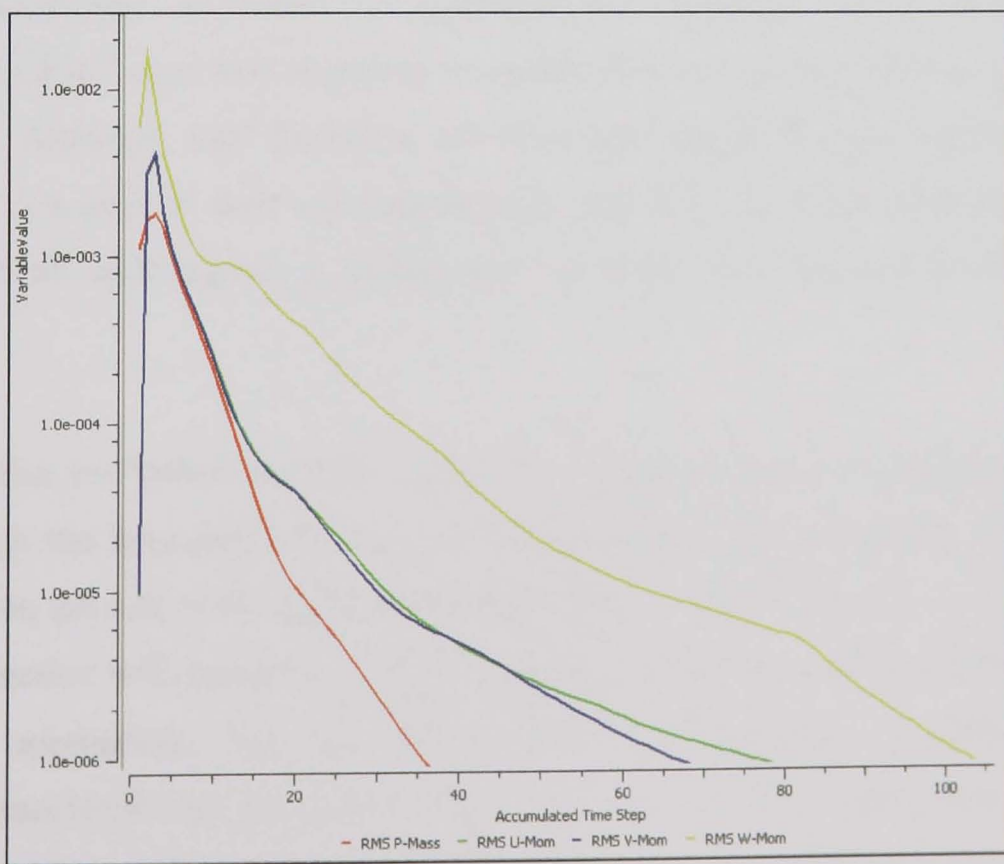


Figure 5-19 RMS residuals using upwind

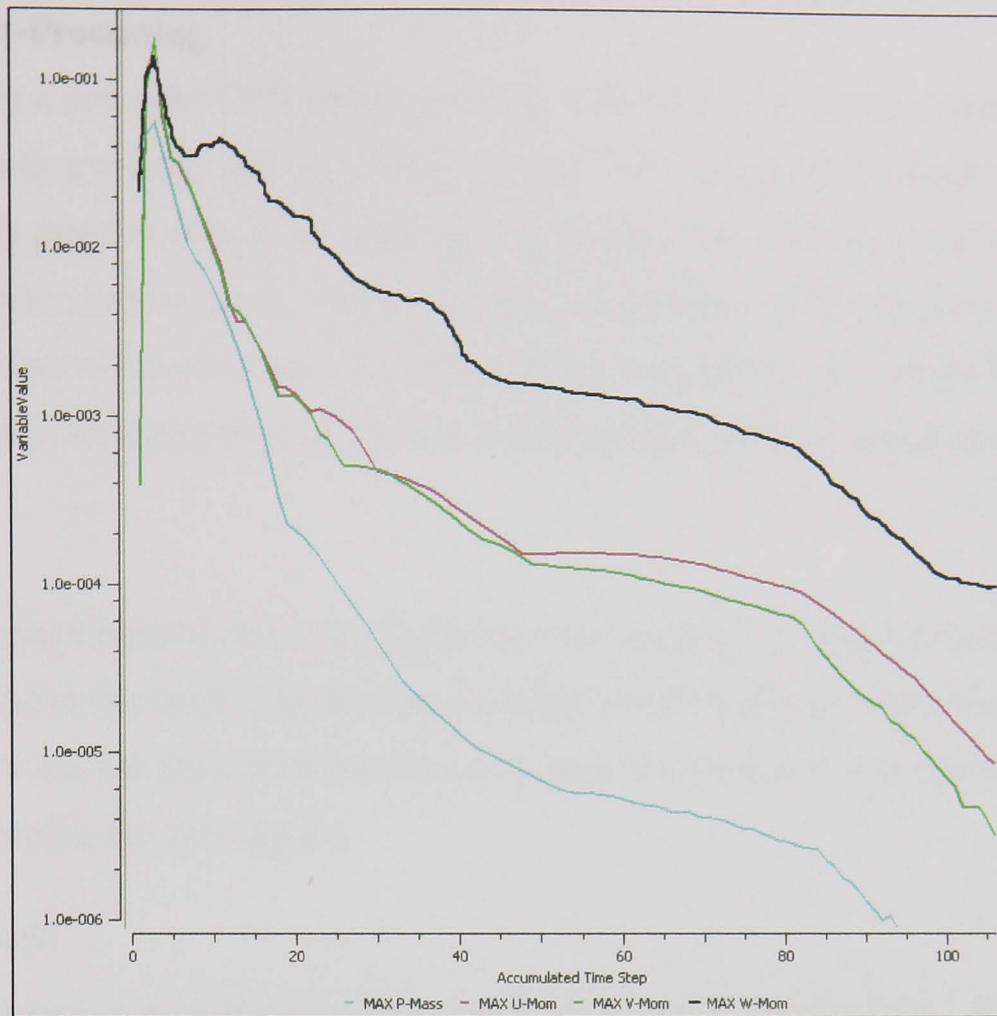


Figure 5-20 Max residuals using upwind

5.3.3 Mesh Resolution near the Wall using Yplus (y^+)

Unless specifically interested in resolving the boundary layer profile through simulation, CFX-5 uses wall functions to model the near wall region in a turbulent flow simulation. Although wall functions are extremely useful in reducing computational load, there is a limit to their valid application, and care should be taken to ensure that their use in all wall regions is appropriate, or if not, that the user is aware of their limitations.

The parameter y^+ (Yplus) is a non-dimensional variable based on the distance from the wall through the boundary layer to the first node away from the wall. It is therefore dependent on the size of the mesh in the wall region. If the value of y^+ is too large, then the wall function will impose wall type conditions further from the wall than normally physically appropriate. The use of 'Scalable Wall Function' in CFX-5 removed problems associated with the lower valid limit for y^+ . CFX-Post allows for examination of the value of y^+ at the wall to see where the mesh needs refining (or coarsening) to reduce (or increase) the value of y^+ in that region.

E. Post-Processing

CFX-Post is a powerful CFD post-processing tool. It uses an intuitive user interface to represent both graphical and quantitative results. The visualisation capabilities of CFX-Post quickly provide insight into flow field behaviour with features such as isosurfaces, slices, vectors, surface plots, animations and streamlines. The quantitative capability allows the user to extract values of interest that can be used to increase performance and obtain a better understanding of the real world problem that the simulation attempts to model.

There is a magnitude of plots and graphs for each simulation, but only those of interest are presented in this work. The post-processing for this problem involves the creation of a y^+ plot to analyse the simulation accuracy, then the graphical representation of areas of interest within the flow region.

5.3.4 Results

Figure 5-21 shows the velocity profile captured for the fluid simulation problem in the pipe. It shows the velocity vector plot for the total velocity (fluid speed in x, y, and z combined) in the pipe. In Figure 5-22 the fluid exhibits reverse flow in the area of contraction from the supply pipe to the converging section even with a large turbulent flow. As it exits the converging section and flows to the narrower chamber the velocity of the fluid increases significantly because of the smaller cross-section. However, before uniform velocity is reached at some distance within the narrow chamber there is a flow region of varying velocity at the interface of the two varying volumes. This is due to the change in section and the appearance of a vena contracta. This agrees with the work proposed by McCarthy and Molloy (1973), later investigated by Cui (1995).

Results for internal nozzle flows ran for a maximum of 200 iterations. Many converged before this point dependant on geometrical difficulty and domain preferences such as pressures and fluid velocities.

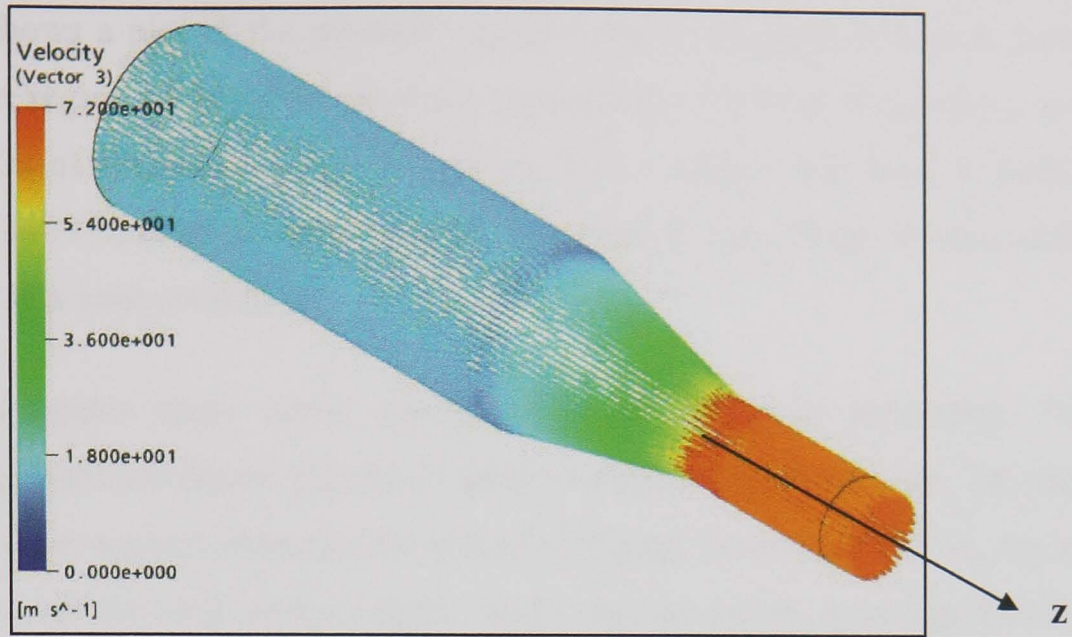


Figure 5-21 Three-dimensional velocity vector plot for the pipe (projected onto z)

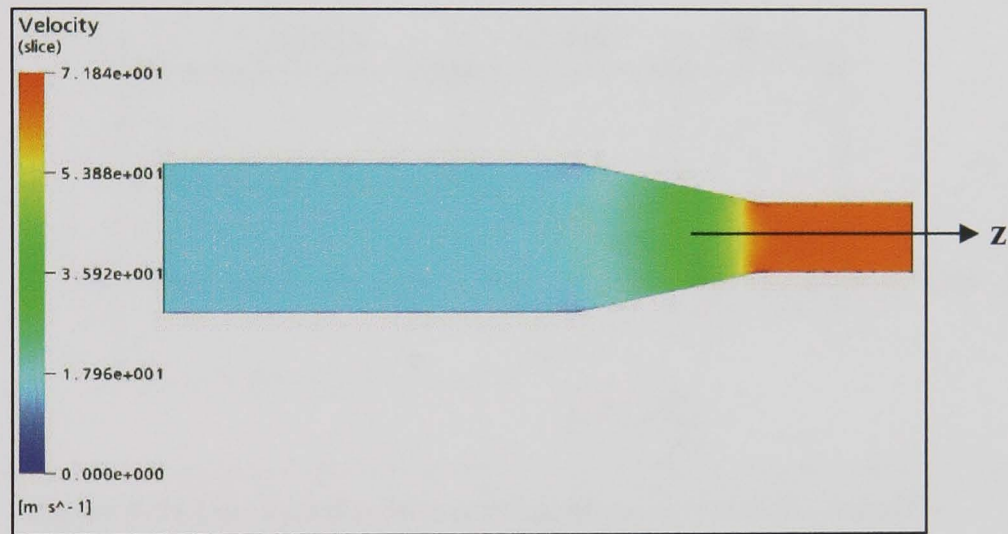


Figure 5-22 Velocity slice through the pipe

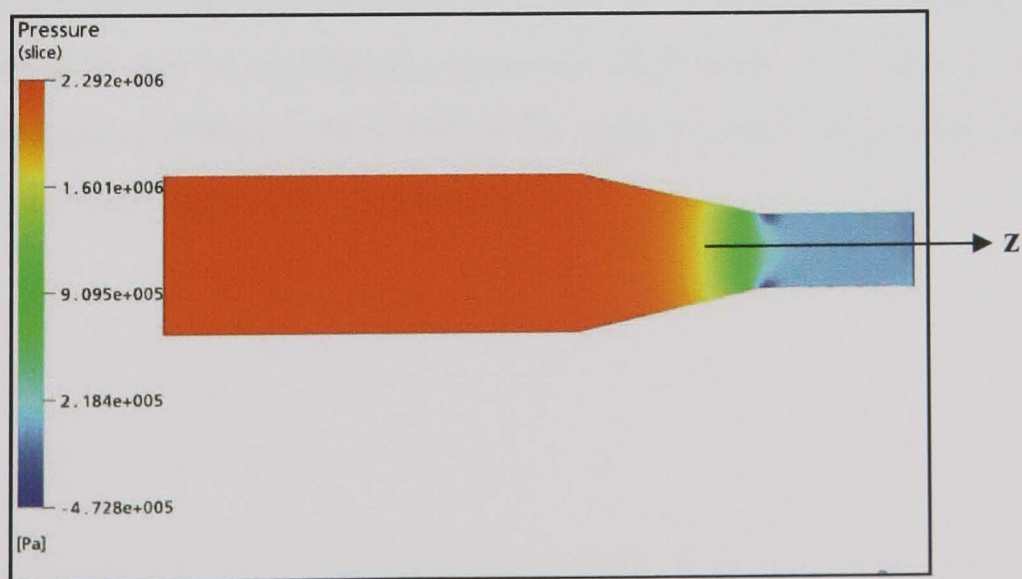


Figure 5-23 Pressure contour on a slice through the centre of the pipe

Figure 5-23 shows a plot of the pressure changes within the pipe. It's clear from this that there is a region of negative pressure immediately after the converging section, indicating areas of stagnation and recirculation. This confirms the work of McCarthy and Molloy, (1973) indicating areas of eddy formation at the change in section due to the formation of a vena contracta.

The previous figures show visual qualitative results from the simulation. To aid understanding, graphical data is plotted on areas of interest within the pipe. The areas of interest are a cross-section immediately after the change in section (line 1), the centre line (for plots over the total nozzle length: line2), and the region spanning the changes in section (Line 3). Figure 5-24 illustrates the locations of these three lines.

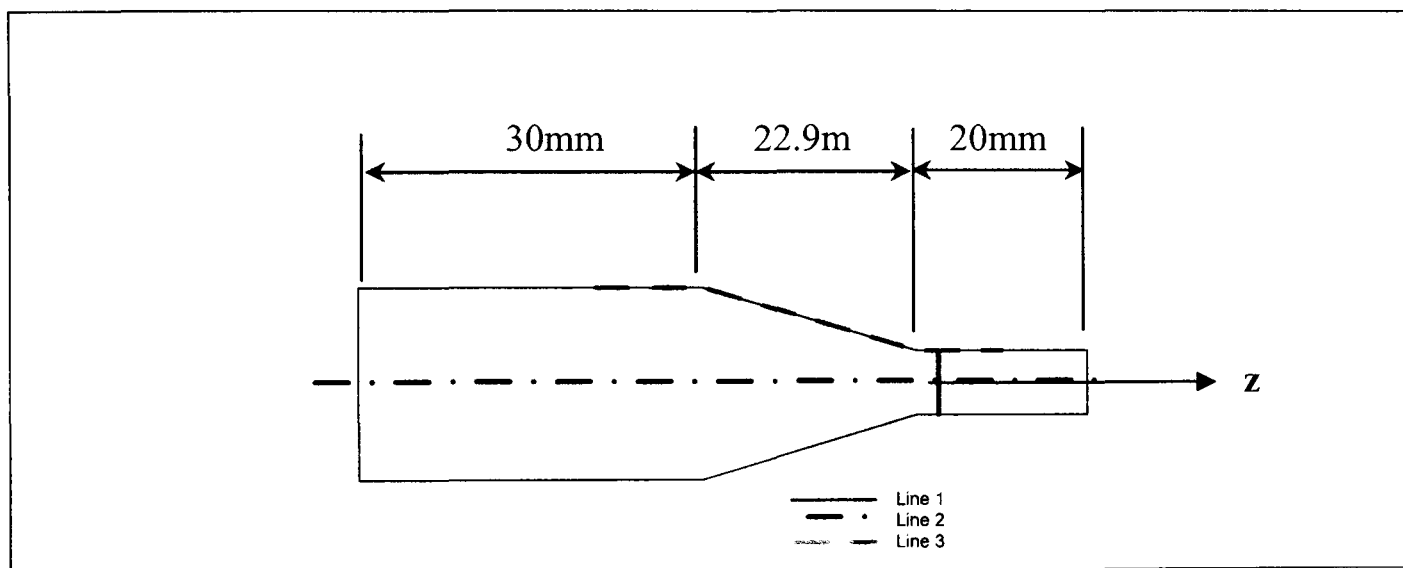


Figure 5-24 Line location for results analysis on the sloped nozzle

Figure 5-25 shows the change in fluid velocity over the entire length of the pipe. The velocity starts at 15m/s (the input velocity) and rises to a maximum of 68m/s at the pipe exit. This increase is due to the changes in section in the pipe. It is clear from Figure 5-25 that some kind of change occurs around the areas of contraction (both 30mm and 52.9mm from the inlet: Figure A8 – Appendix A).

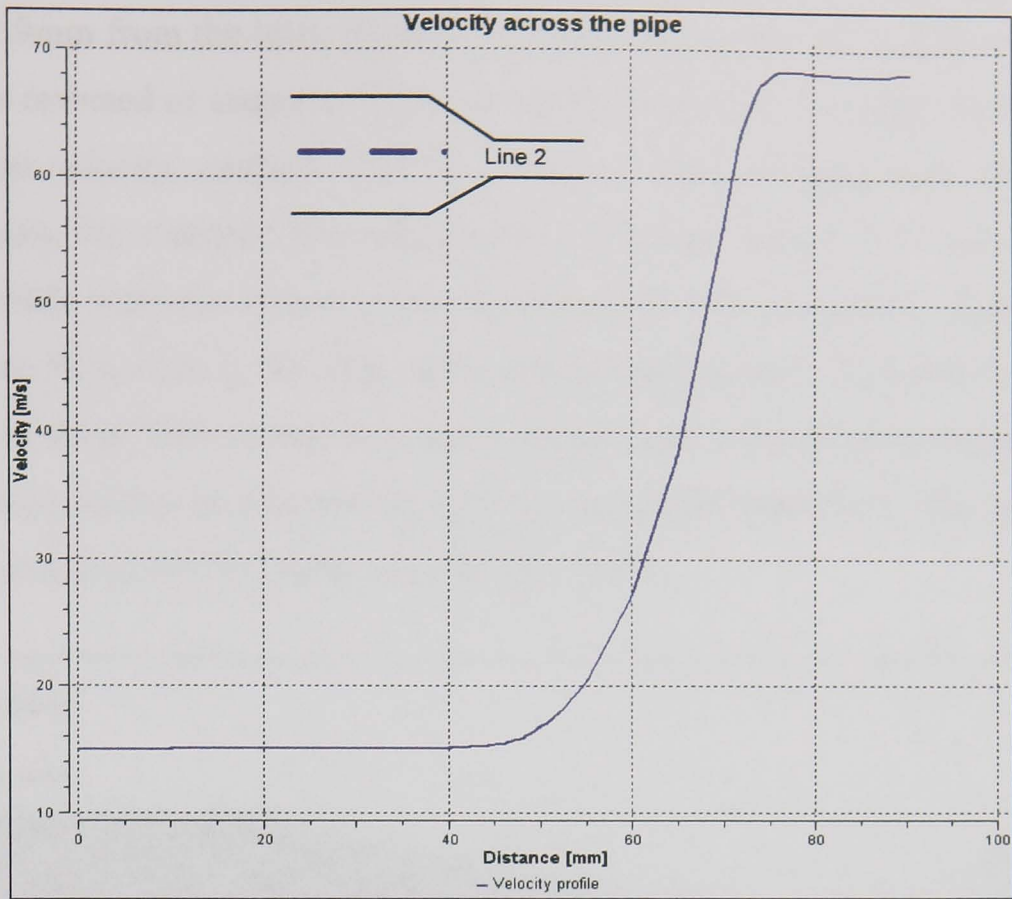


Figure 5-25 Velocity for the entire length of the pipe

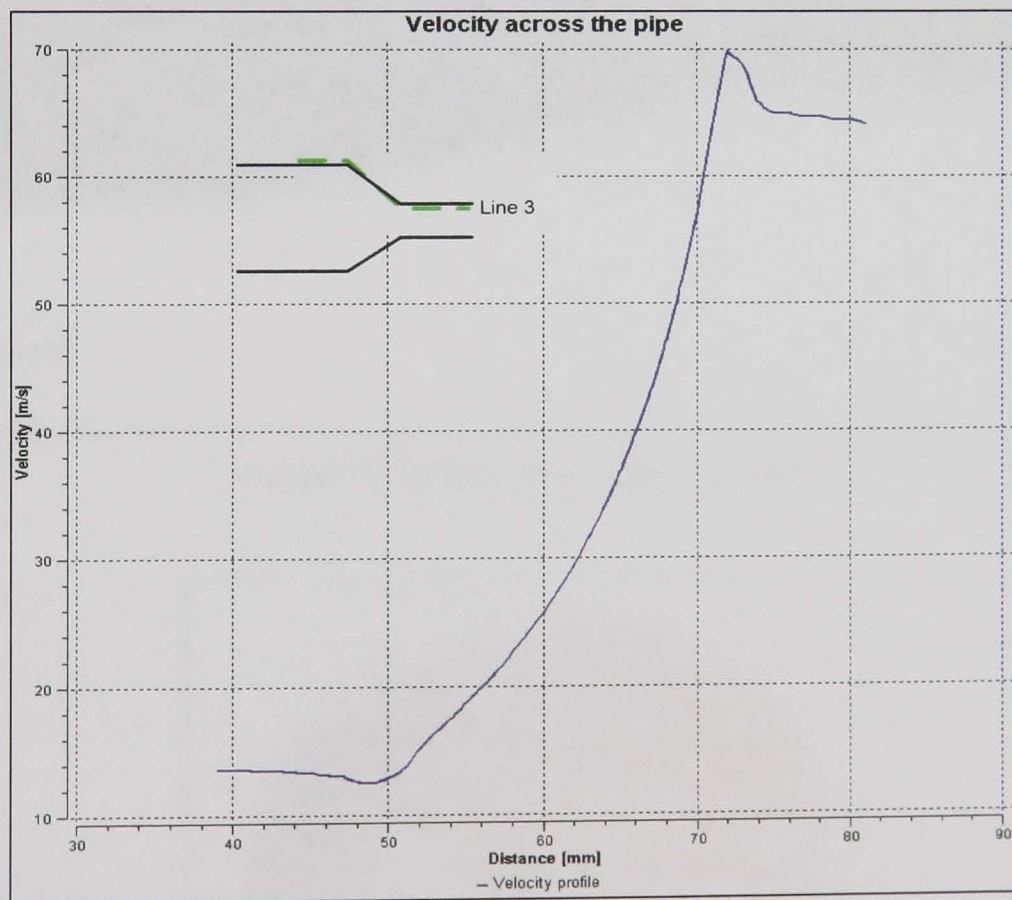


Figure 5-26 Velocity profile spanning the regions of eddy formation

Figure 5-26 shows the velocity profile along the change in section line. On close examination, it is clear that there exist areas of lower velocity just before the first change in section (50mm from the inlet: Figure A2), and just after the second change in

section (71.9mm from the inlet: Figure A2). This follows the theory that in these areas there exists reversed or stagnated flow due to the formation of eddies. This plot shows that the total velocity, coupled with the velocity in the remaining axes, as opposed to that following the standard flow direction, is lowered. Figure 5-27 shows the eddy viscosity. Eddy viscosity characterises the transport and dissipation of energy in the smaller-scale flow close to the edge of the nozzle ignoring the small-scale vortices. The formation of these eddies from this plot indicates the reversal areas starting from the first change in section and increasing until the end of the pipe flow. This again follows the theory proposed by McCarthy and Molloy (1973).

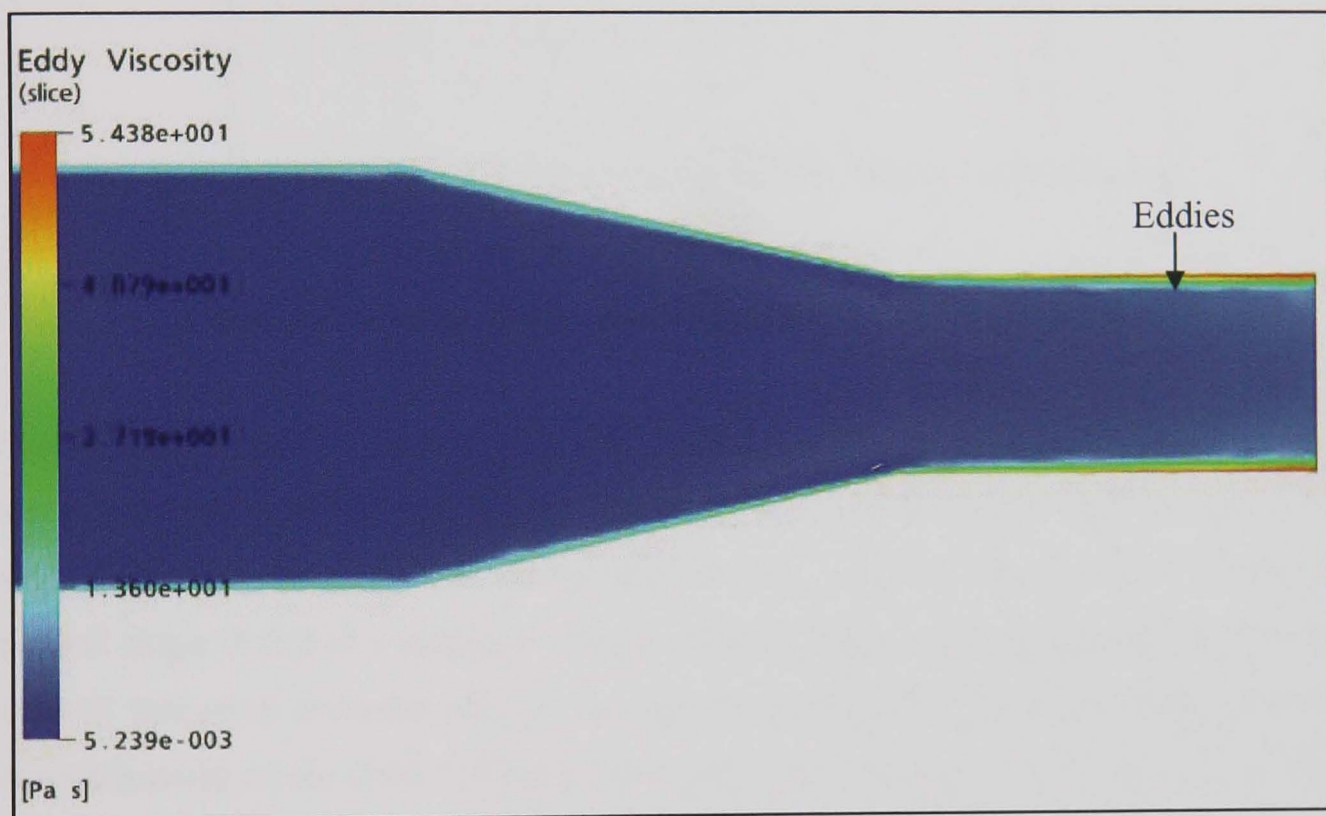


Figure 5-27 Eddy viscosity along the pipe

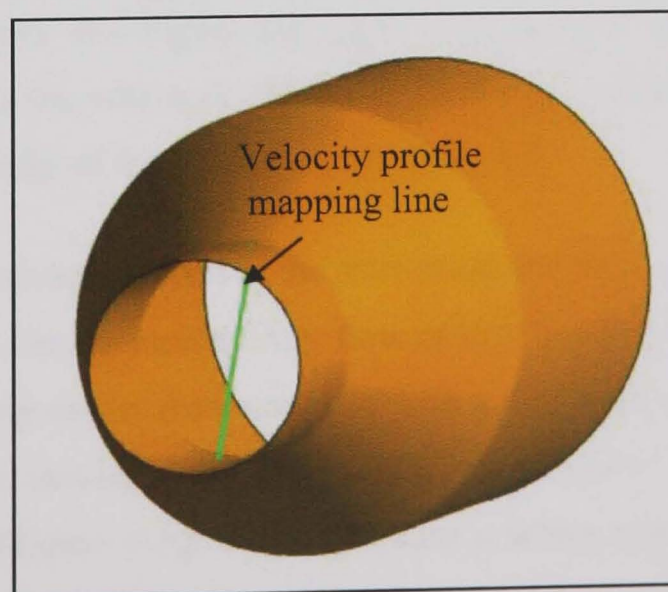


Figure 5-28 Line immediately following the change in cross-section

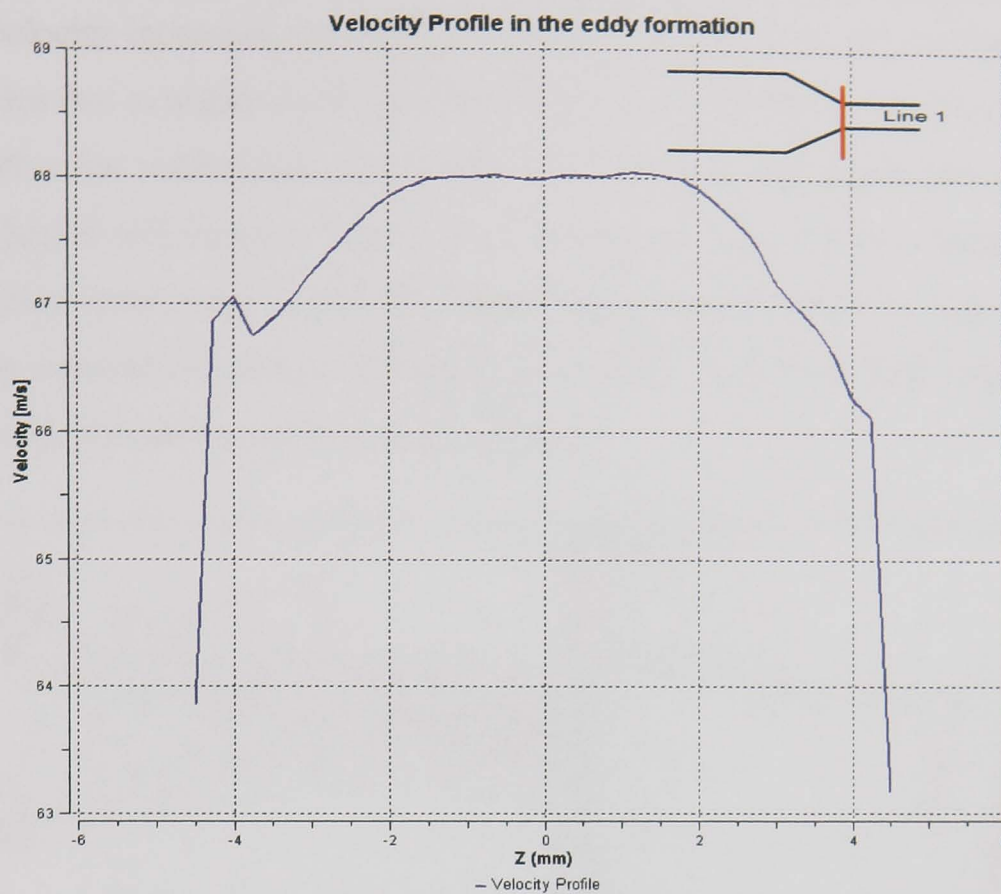


Figure 5-29 Velocity Profile immediately following the change in section

Figure 5-28 shows the position of a line created to map the velocity profile in a region immediately after the change in pipe diameter. Figure 5-29 shows this velocity profile created which is the magnitude of the total velocity. Looking at the velocity profile, the general shape is that of a turbulent velocity profile. There is however, a region of lower velocity just away from the edge of the pipe. This indicates a region of eddy formation or recirculation of the fluid, lowering the overall fluid velocity at this point. To analyse this phenomena further, two further vector profile plots shown in Figure 5-30 and Figure 5-31 were created. Figure 5-30 shows the velocity component in the U direction (x). It is observed from this figure that there exist areas of recirculation due to the formation of eddies in the near-wall regions at the change of section. The length of the arrow shows the intensity of the velocity in this direction.

In Figure 5-30, the velocity reverses at the start of the sloping contraction and continues up to the point of the vena contracta. Any flow in this direction removes fluid structure and causes jet break up earlier than would be with a flow with all of its components in the same direction, or laminar flow. The point of maximum U directional flow within the small exit region (Figure 5-30) shows the point at which most of the eddy formation occurs. On further investigations concerning flow near this point, it was noted that the

more the velocity increases, the further this distance lies from the contraction region. This indicates that at higher fluid velocities, the length after the contraction point should be longer than the reformation length otherwise jet break-up length (see chapter 6) at exit of the nozzle will increase. Figure 5-31 shows a close up of the velocity gradient in the U direction at the areas of interest following the contraction. It is seen that the flow turns at this point and increases significantly in the U direction, pushing back on itself indicating eddy formation and recirculating flow.

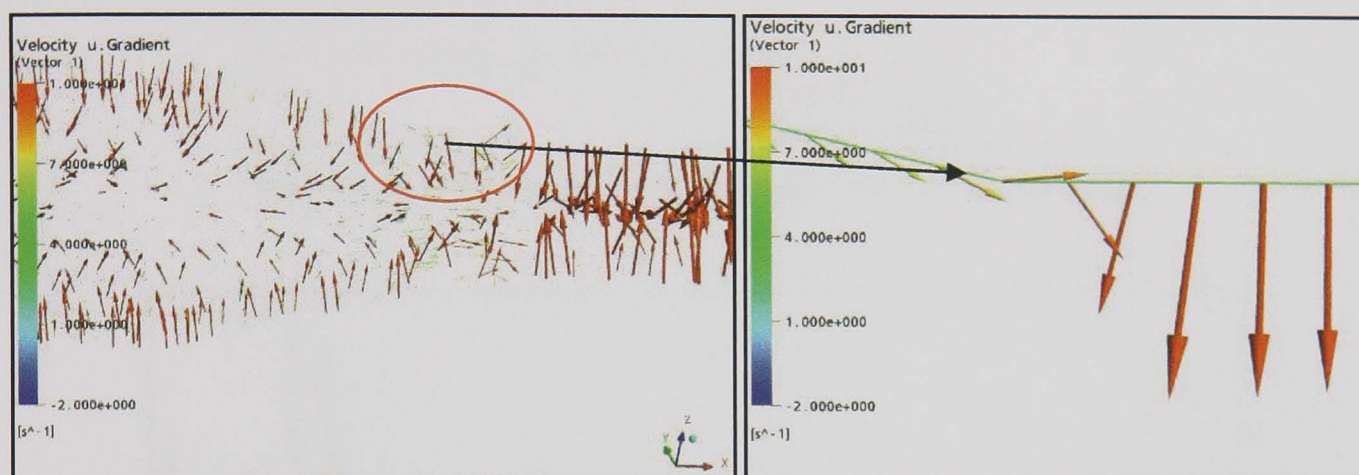


Figure 5-30 Velocity Gradient in the U (x) direction

Figure 5-31 Close up of the velocity gradient at the point of contraction

5.4 Internal flow analysis of a sudden contraction – orifice nozzle

Referring back to the work in chapter 3, the next nozzle under analysis is that of one with a sudden contraction such as an orifice nozzle. Geometry and setup information followed the same state as the previous example.

5.4.1 Results

This section contains the results for the simulation of the orifice nozzle. Other results are available by rerunning the simulation with the given data. Plots of velocity profiles and plots showing the eddy formation are presented. A plot of y^+ for each simulation exists to check for accuracy of the near wall treatment. The parameter y^+ (Yplus) is a non-dimensional variable based on the distance from the wall through the boundary layer to the first node away from the wall. It is therefore dependent on the size of the mesh in the wall region. If the value of y^+ is too large, then the wall function will impose wall type conditions further from the wall than normally physically appropriate. y^+ was used, therefore, as a check that the mesh structure at the nozzle walls (areas of high interest) was suitable. The graphs shown contain data from a line at the suspected eddy formation area, a line through the centre of the nozzle, and a line at the edge

following the change in section (see Figure 5-32). Figure 5-33 shows the residuals for the orifice simulation. Convergence took place at one hundred iterations with an upwind and $1e^{-06}$ residual target. Once again, the residuals appear smooth and converge well giving confidence in the results.

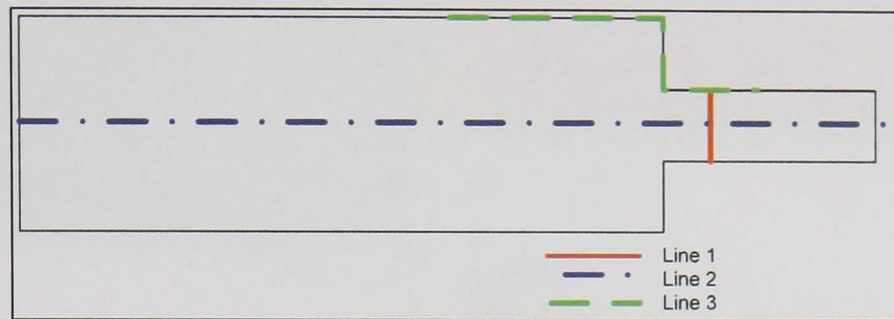


Figure 5-32 Line location for results analysis on the orifice nozzle

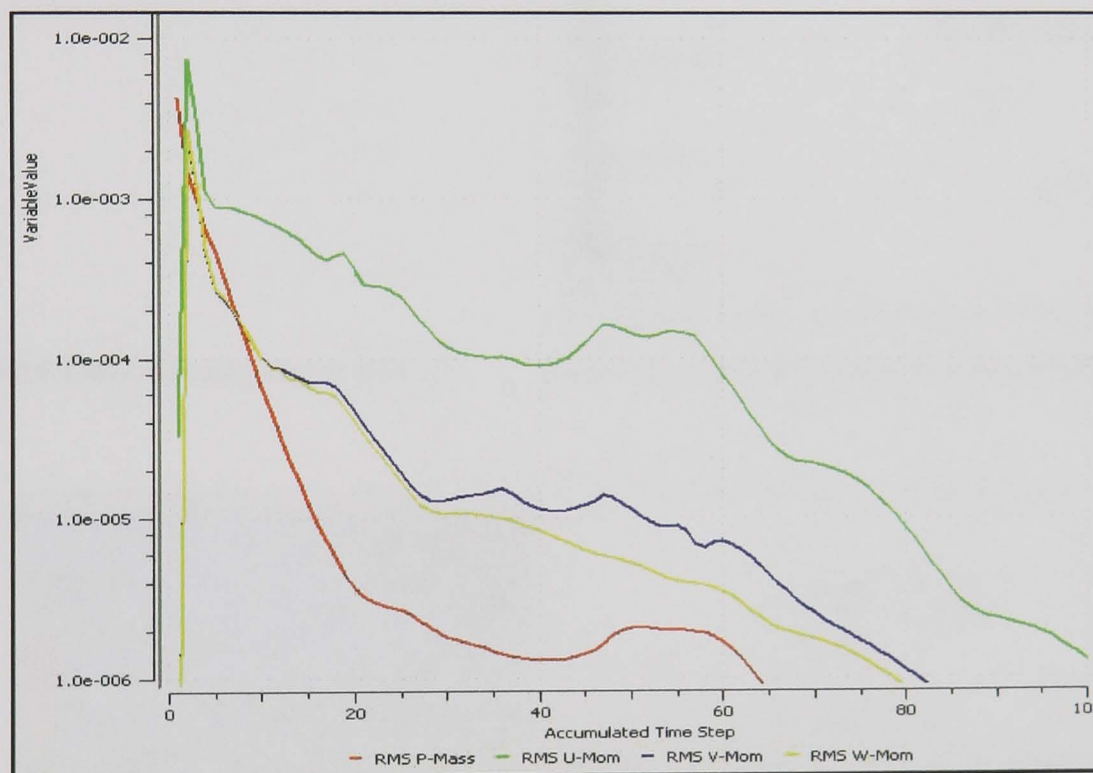


Figure 5-33 Residuals for an Upwind convergence at $1e^{-06}$

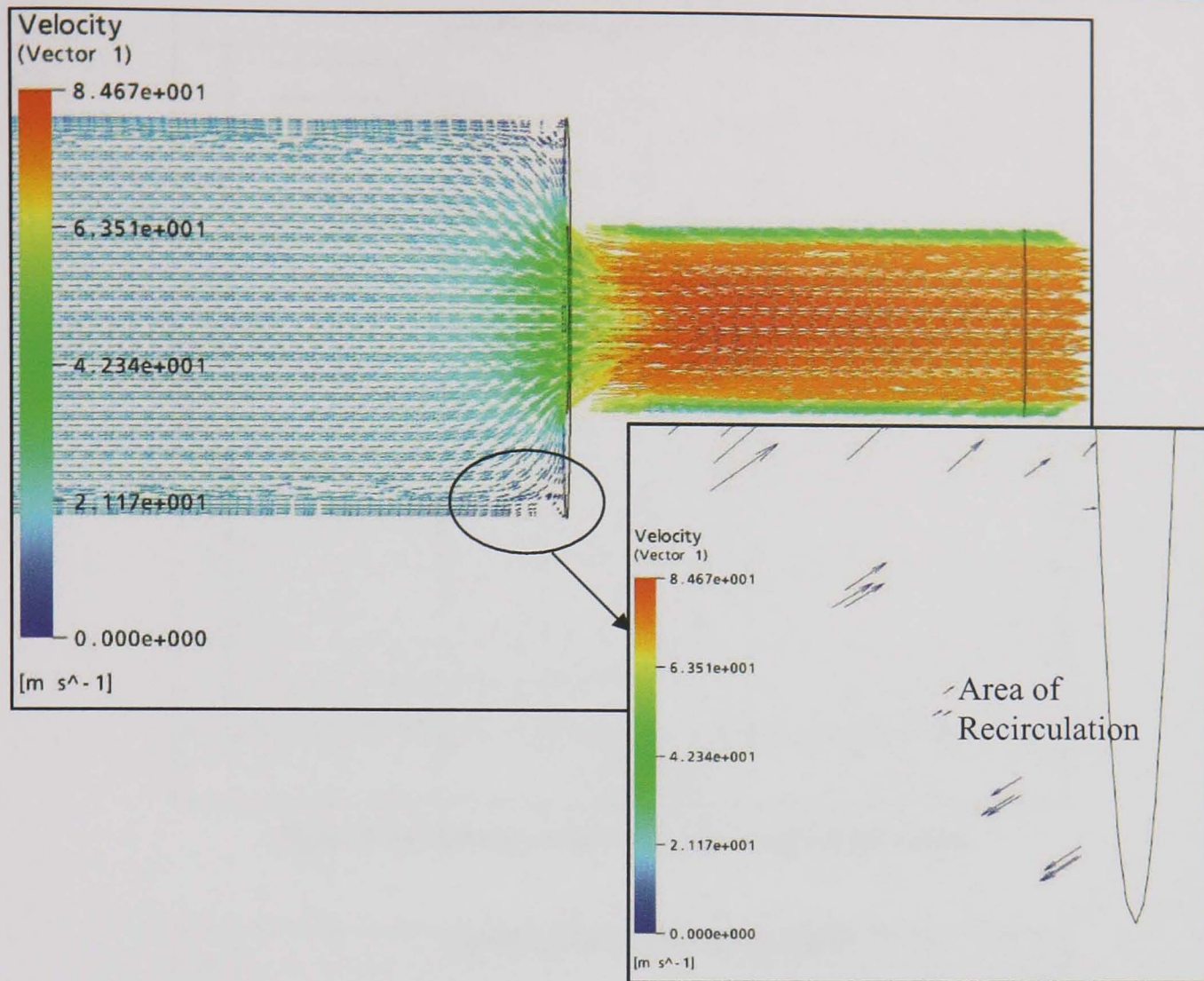


Figure 5-34 Total Velocity vector plot → Close up of recirculation in corners of orifice nozzle

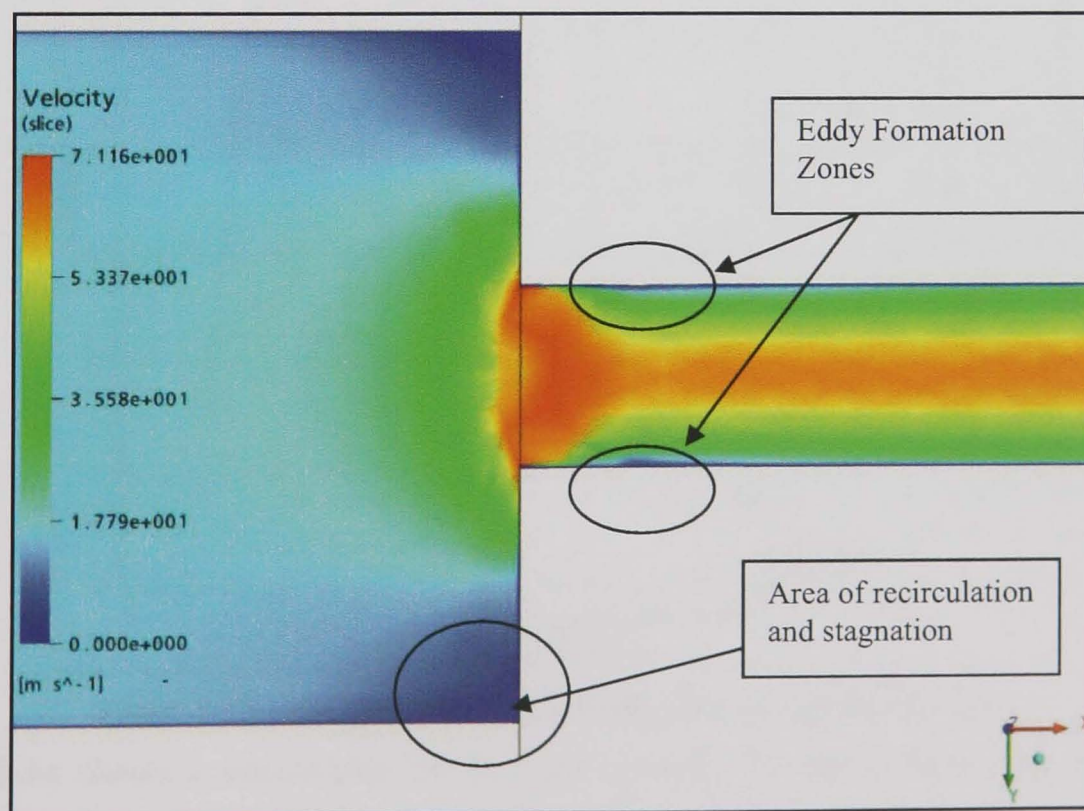


Figure 5-35 Velocity on a slice plane through the centre of the flow showing areas of recirculation

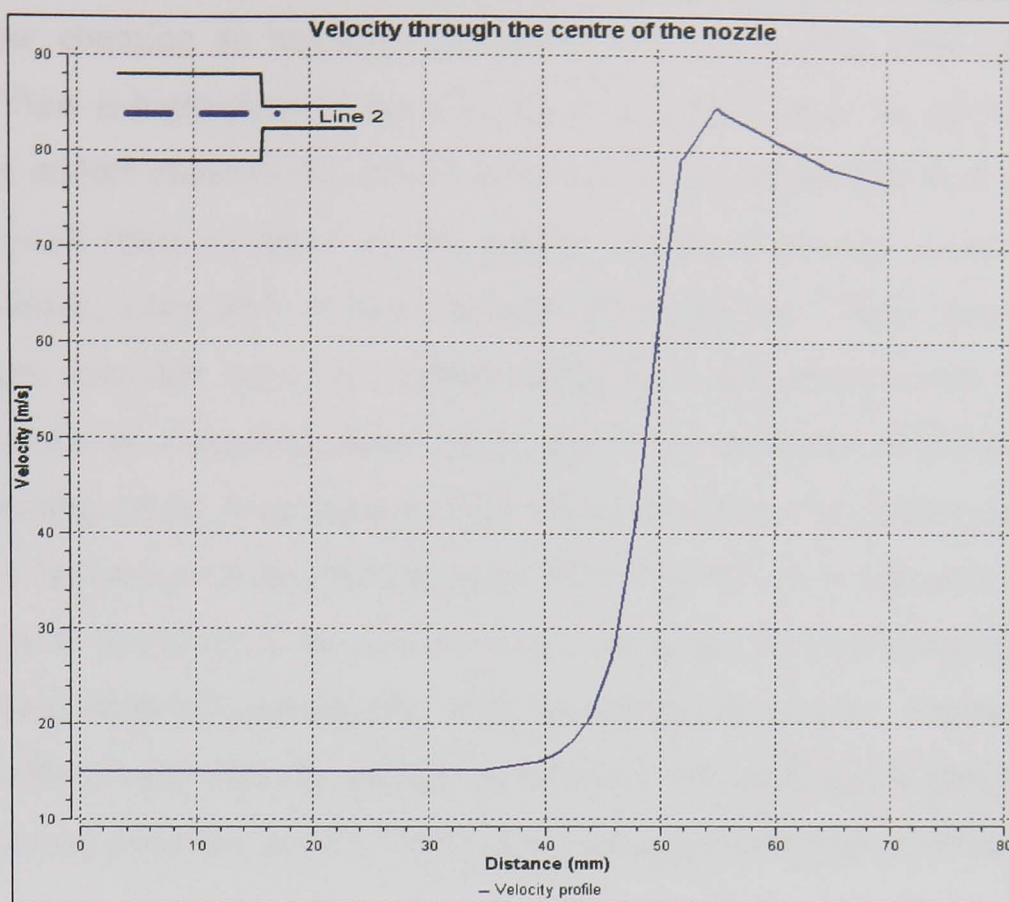


Figure 5-36 Velocity profile along the centre of the nozzle

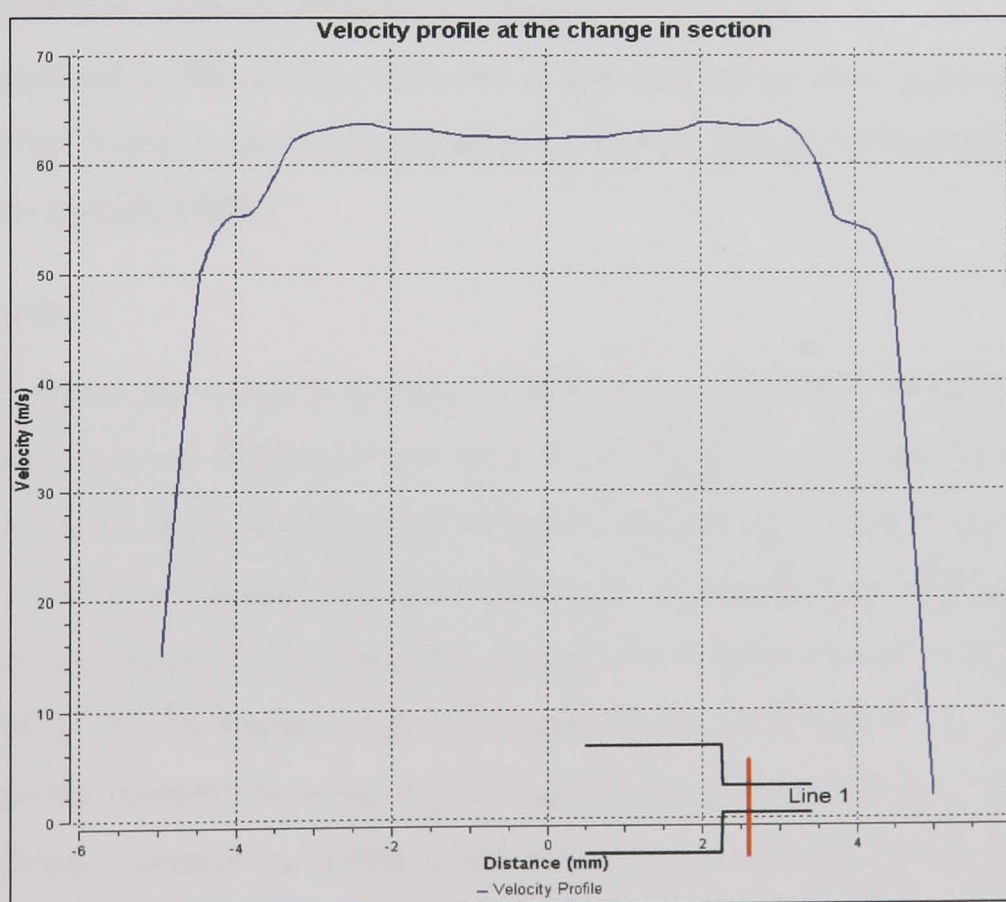


Figure 5-37 Velocity profile immediately after the change in section

Figure 5-34 shows a vector plot of the total velocity for the orifice type nozzle. The general trend of the vectors is that the main flow is in the expected X direction. It is seen however that in the corners of the large chamber, just before the entrance to the smaller chamber, there are areas of lower total velocity. This lowering is due to the

reverse flow counting as negative velocities and lowering the total velocity. This reversal of flow is highlighted in the close up of this wall region. Figure 5-35 is a slice through the middle plane of the nozzle with velocity rendered from blue to red on an increasing scale (dark to light). At the sudden change in section, areas of low total velocity indicate losses due to flow reversal and stagnation. There have been many investigations into the losses in sudden expansions and contractions. The method presented herein of visualising these losses allows for prediction of the areas of these losses permitting future development of the nozzle from this. For further information on specific loss factors, see Perry and Chilton (1973). Figure 5-36 is a graph of the velocity from the inlet to the outlet of the orifice nozzle. The graph shows a sharp rise in velocity with a sudden drop off immediately after the change in section. Figure 5-37 is the velocity profile shortly after the change in section. It can be observed that some regions of lower velocity exist due to eddy formation following the change in section.

5.5 Internal flow analysis of the Rouse shaped contraction

A nozzle analysed in this section, but with a radiused contraction, is based on the fire hose design by Rouse et al (1952). Geometry, meshing and pre-processing information followed that already shown.

5.5.1 Results

Figure 5-39 shows the velocity contour plotted onto a slice plane running through the centre of the nozzle as illustrated in Figure 5-38. There is a smooth transition in this nozzle between the large chamber and the small chamber. With the Rouse contraction, the velocity increases steadily with no clear signs of stagnation or recirculation in the transitional area. Figure 5-40 represents the eddy formations using an output function 'eddy viscosity'. In the Rouse nozzle, the eddy formation is minimal within the large chamber and the transitional areas, confirming the improvement to stabilising the flow using this Rouse contraction. There exists however, some eddy formation within the small exit chamber. This is caused by the sudden change in section at the previous point, indicating that the jet will break up at some point, but in contrast to the previous orifice nozzle example, the fluid stability is significantly higher with the Rouse nozzle.

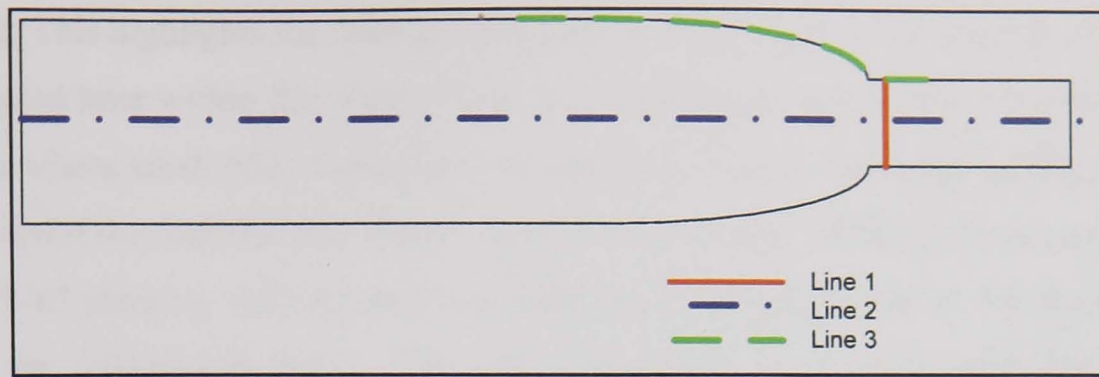


Figure 5-38 Line location for results analysis on the Rouse based nozzle design

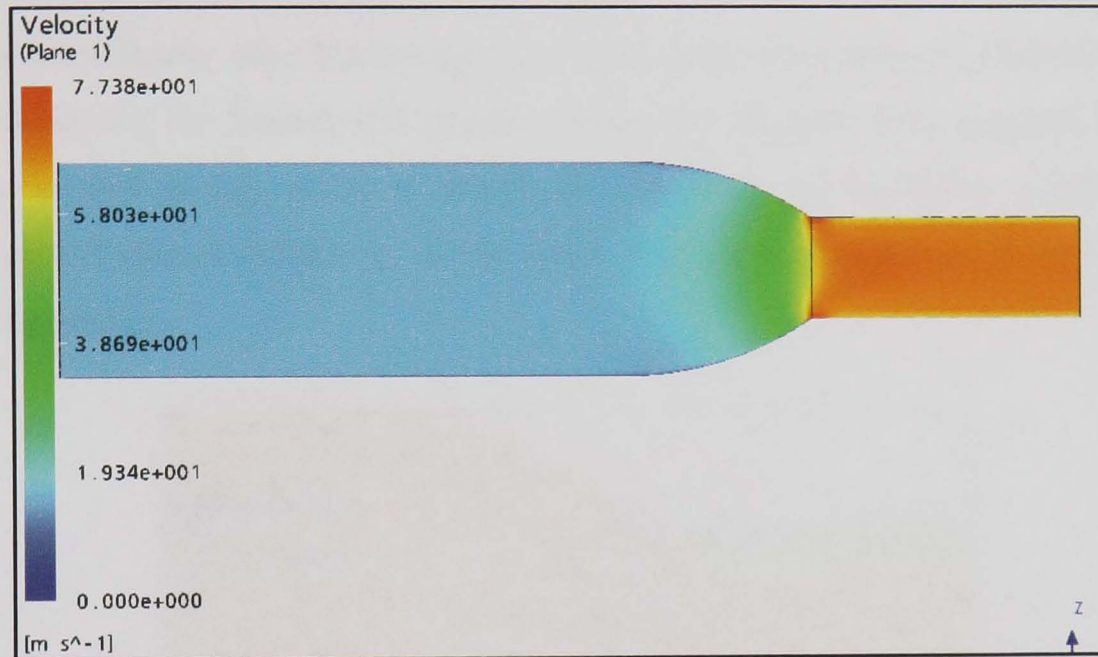


Figure 5-39 Velocity slice through the centre of the nozzle

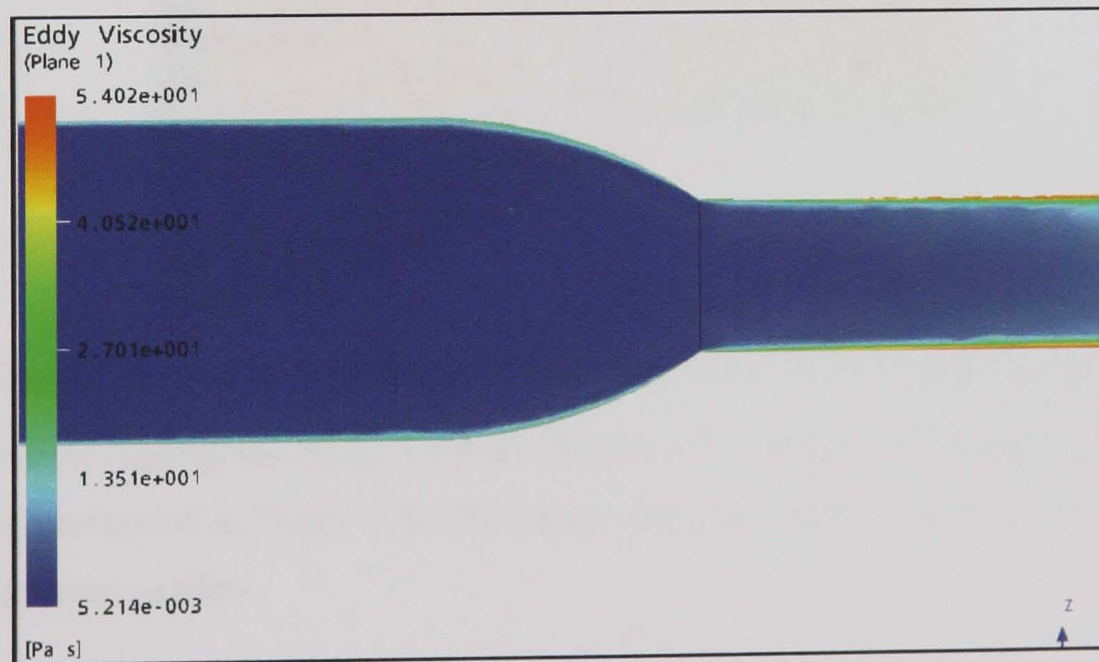


Figure 5-40 Eddy Viscosity at the walls of the Rouse based nozzle

Figure 5-41 represents the total pressure distribution within the Rouse nozzle. The pressure remains constant in the large chamber and through the curved transitional region until a small build up occurs around the exit of the large chamber into the small

chamber. This highlights the need for sharp exits to minimise this increased effect and is investigated later within this work. There exists a pressure drop at the sides of the small chamber where small eddy formations are apparent. This is due to the sudden change in section and it is noted that this 'layer' is much smaller than in the previous two cases.

Figure 5-42 shows a velocity plot just away from the edge wall in the Rouse nozzle around the transitional region. The velocity appears to increase smoothly until the change from the large chamber to the small chamber. This implies that the transition is smooth with no recirculating flow present. Figure 5-43 represents the velocity profile of the fluid immediately after the change in section. This curve appears smoother than the ones obtained for the sudden and angular contraction nozzles. This suggests that if the jet were to exit at this point, it would have a larger jet break-up length. This is investigated further in chapter 6. is the graph of velocity distribution along the central axis of the nozzle.

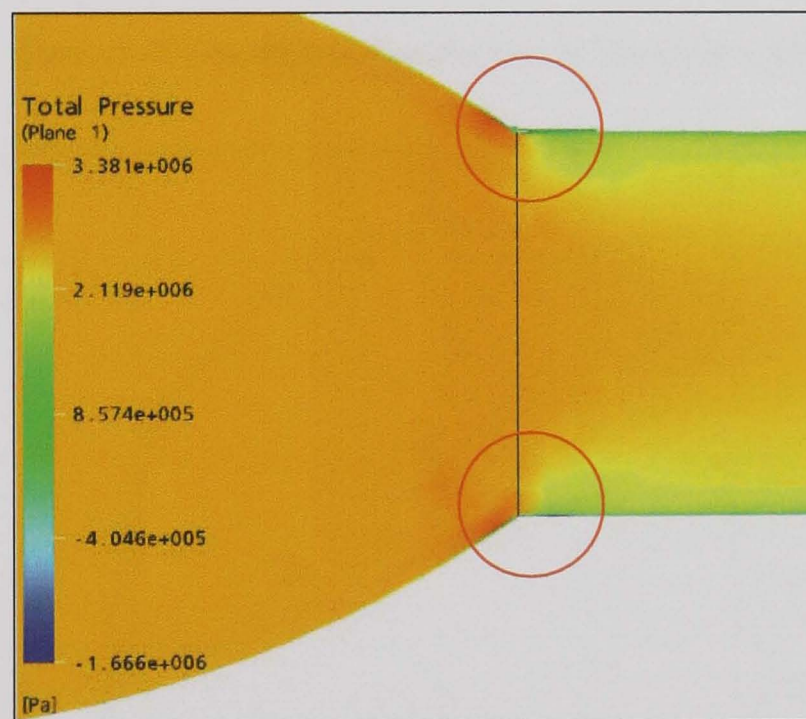


Figure 5-41 Close up of the total pressure distribution around the change in section

The two areas highlighted by the circles in Figure 5-41 confirm the presence of the vena contracta mentioned in Figure 3-6. They show areas of a drop in pressure just after the change in cross section.

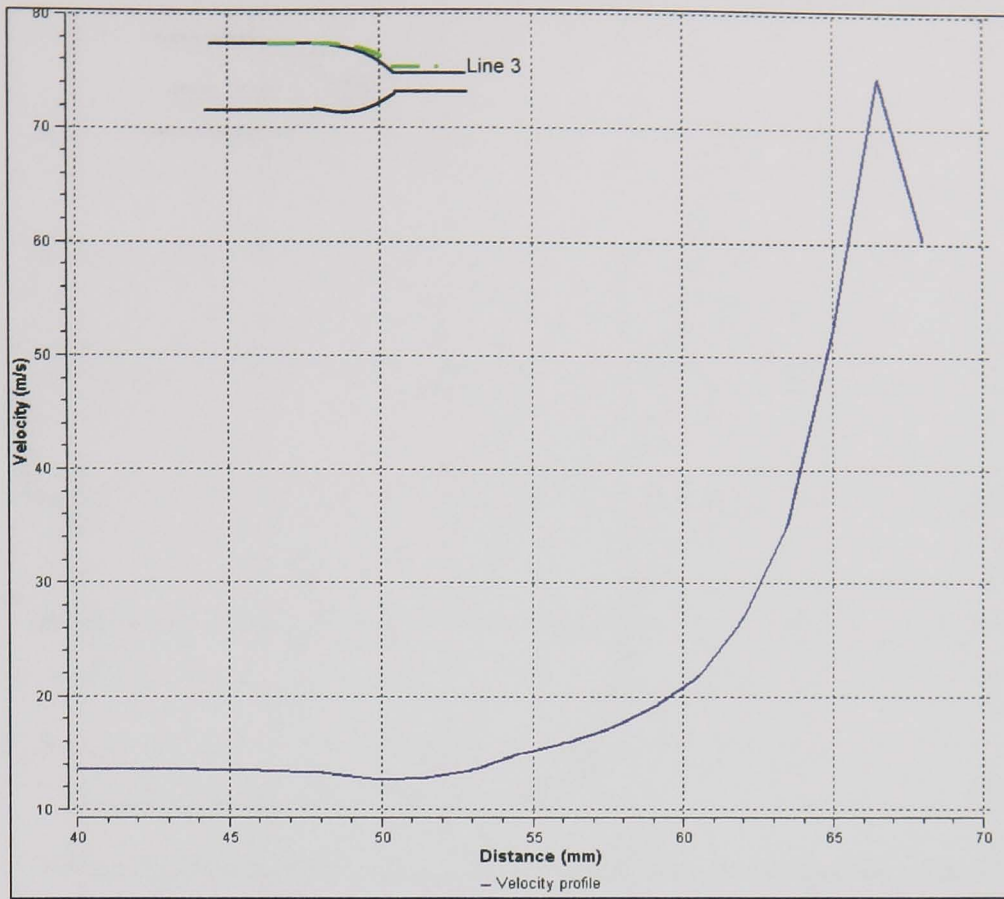


Figure 5-42 Velocity profile along line 3 of the Rouse nozzle

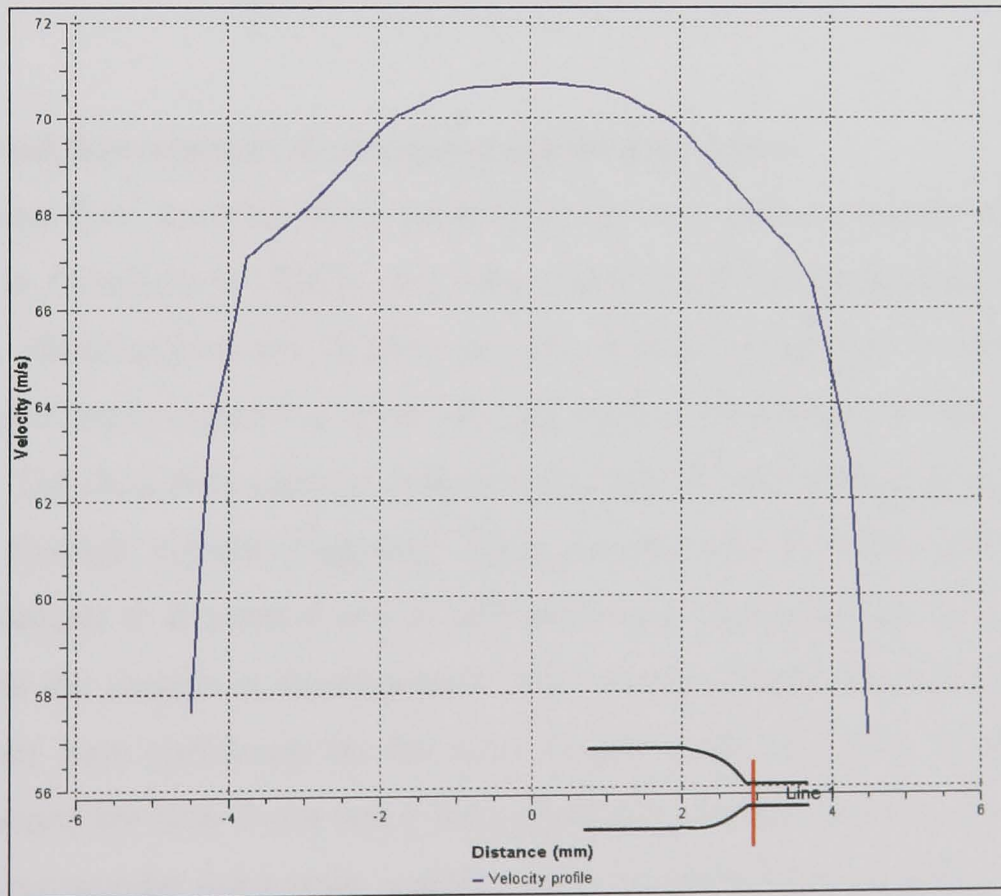


Figure 5-43 Velocity profile across the nozzle immediately after the change in section

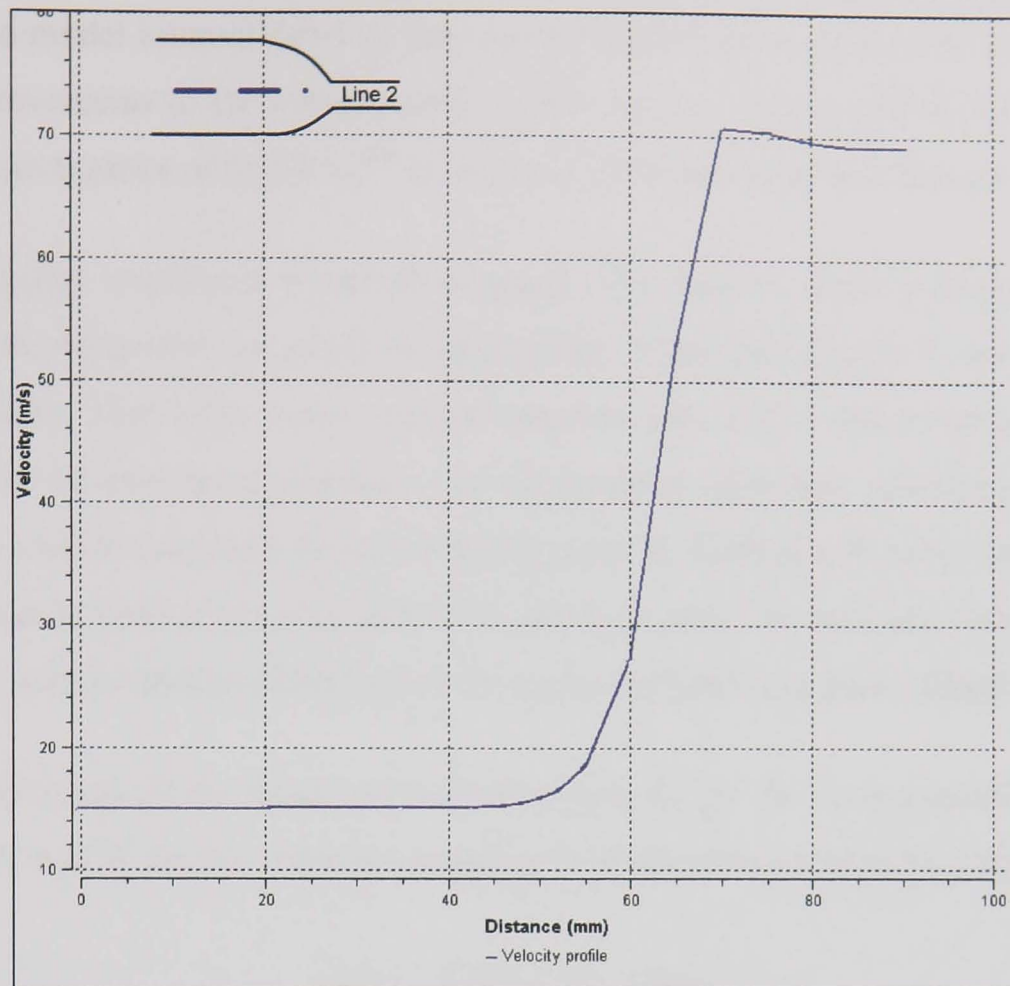


Figure 5-44 Velocity along the central axis

5.6 Internal flow analysis of conventional grinding nozzles

Internal fluid flow analyses were performed for conventional nozzle designs types suggested in Gviniashvili (2003) and other types involving modifications within the laboratory. Modifications are defined as any significant changes in nozzle internal geometry and improvement to areas of high nozzle losses due to recirculation and stagnation. The fluid flow analysis determined critical factors such as pressure losses of stagnation through velocity mapping. These results form the basis of internal fluid structure analysis to determine nozzle efficiency and lead to design change, which in turn induces the change in fluid pressure and velocity distribution inside the nozzles. The analyses were performed for the most severe nozzle operating conditions. Tests were performed for both water and a semi-synthetic grinding coolant. The wedge type nozzle, the rectangular slot nozzle, and the orifice nozzle were investigated.

Conventional coolant delivery nozzles often consist of a circular inlet diameter that then flows into a large chamber. This chamber then contracts in some way, be it a gradual contraction, rapid contraction, or using a curvature wall. Theory suggests that these contractions will create problems of losses within the nozzles. To investigate this, CFX

was used to model internal flows of the conventional nozzles. Designs were modified to see if improvements to the conventional coolant nozzles were possible. All simulations ran until convergence of MAX 10^{-04} (maximum residual size) was achieved.

Inlet and outlet conditions remained constant. The delivery fluid velocity was 5 m/s with both the water and the emulsion (water with 10 per cent Hysol X, see Appendix F for data sheet). The outlet was a constant pressure exit with a relative pressure of zero compared to the external atmosphere. One of the more important variables used to study turbulence and its evolution in the boundary layer is Turbulent Kinetic Energy (TKE). The flow can be partitioned into mean and turbulent parts; the total kinetic energy of the flow is the sum of the kinetic energy of the mean and turbulent flows (Baldocchi 2005).

The kinetic energy of the mean and turbulent parts of the flow is expressed as (per unit mass - U, V and W are the velocity components of the flow in respective directions):

$$\begin{aligned} \text{MKE} &= \frac{1}{2} \left(\overline{U}^2 + \overline{V}^2 + \overline{W}^2 \right) \\ \text{TKE} = e &= \frac{1}{2} \left(u'^2 + v'^2 + w'^2 \right) \end{aligned} \quad [5.2]$$

where MKE is the kinetic energy of the mean flow per unit mass, e is the kinetic energy of the turbulent flow per unit mass, and \overline{U} is the time averaged velocity in the U direction. Instantaneous values of TKE can vary dramatically. The mean TKE value is more representative of the overall flow

$$\text{TKE} = \overline{e} = \frac{1}{2} \left(\overline{u'^2} + \overline{v'^2} + \overline{w'^2} \right) \quad [5.3]$$

where u' is the instantaneous time averaged velocity.

TKE in fluid flows is produced by mechanically generated eddies. Layers of the fluid becoming increasingly stable suppress the TKE. The two important criteria are:

- if the production terms are larger than the loss terms, TKE will increase and the boundary layer becomes more turbulent;
- if the loss terms are larger than the productions terms, TKE will decrease and the boundary layer becomes less turbulent (CFX, 2003).

5.6.1 *Triangular wedge nozzle*

Figure 5-45 shows the turbulent kinetic energy distribution for a typical triangular shaped nozzle with a 23° contraction. The exact dimensions for the nozzle are given in Appendix A. A standard (expected) boundary at the surfaces exists, but a section immediately following the entrance to the nozzle chamber, indicates losses and an increase in the turbulent effects at this region.

The transfer of momentum caused by turbulent eddies is modelled with an effective eddy viscosity. This shows areas of high relative turbulent viscosity. Figure 5-46 shows this value with high areas noted on the down slope of the nozzle and at the bottom surface towards the back edge of the nozzle. This indicates areas of velocity loss in the main fluid direction.

Figure 5-47 shows the total velocity drawn on a contour through the centre of the nozzle. Regions of low total velocity are observed at the entry region to the nozzle chamber itself, and at the walls of the nozzle. The lower regions at the walls are due to the drag and would be observed in all nozzles. This is not exhibited in the supply pipes as the “free slip” condition is used to standardise all inputs. The condition at the walls is “no slip”, i.e. the fluid “sticks” to the walls. The lower regions further away from the walls however indicate flow losses within the nozzle. Due to conservation of mass, the same amount of flow leaves the nozzle as that which enters the nozzle, however, this plot highlights the velocity (not the flowrate) showing that as the fluid slows slightly (same flowrate but larger area) upon entry to the nozzle chamber, the flow does not separate and distribute evenly, but some recirculates and some stagnates.

Figure 5-48 shows this further by investigating only those velocities in the vertical direction. Any velocity in this direction above the mean velocity indicates areas of loss. These velocities show areas of recirculation and stagnation, values having negative effects on the efficiency of the nozzle. Figure 5-49 is a total velocity vector plot. The arrows show the direction of the flow with the size and colour showing the intensity or magnitude of this velocity. Although the arrows showing reverse flow are relatively small in comparison to the main fluid direction, they show recirculation present within the flow and highlight areas of the nozzle that if removed or improved, would increase overall nozzle efficiency.

Figure 5-50 is the plot of paramount importance to this work. This represents the actual flow path taken by particles of fluid present within the flow. Each particle is injected into the flow at the inlet with its path traced through the fluid flow. So not to affect the momentum of the fluid, the particle is massless. This type of plot (Figure 5-50) and the velocity in the vertical direction (Figure 5-49) are significant to investigating nozzle losses as it highlights the regions in which flow is not strictly following the expected, or desired, flow path. Investigations on other conventional nozzle were conducted. For comparison and design improvement in this work, only these two plots feature in this, the main body of work.

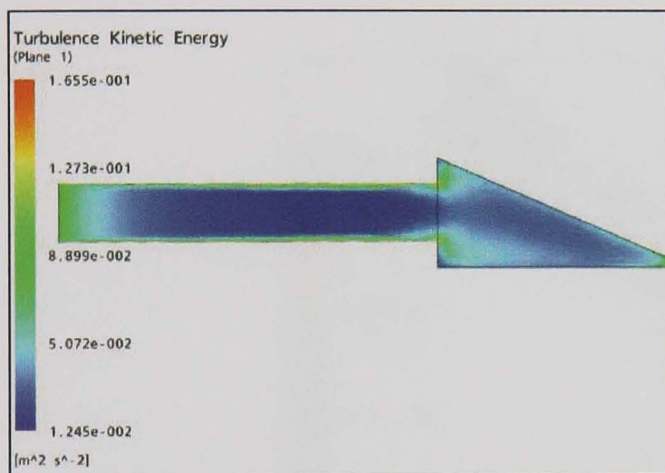


Figure 5-45 TKE distribution in the nozzle with 23° gradual contraction

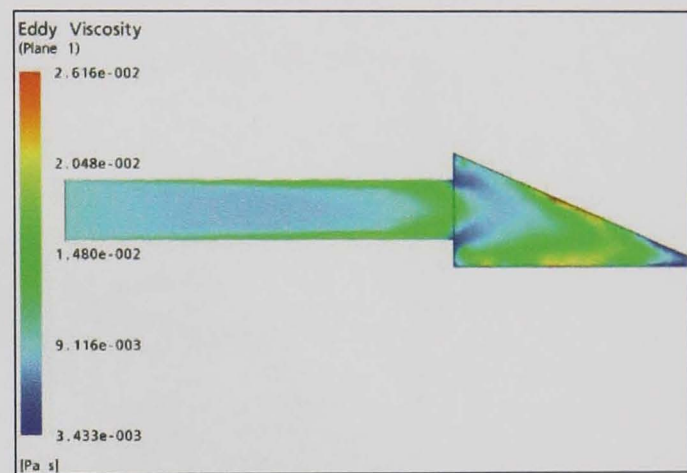


Figure 5-46 Eddy viscosity distribution in the nozzle with 23° gradual contraction

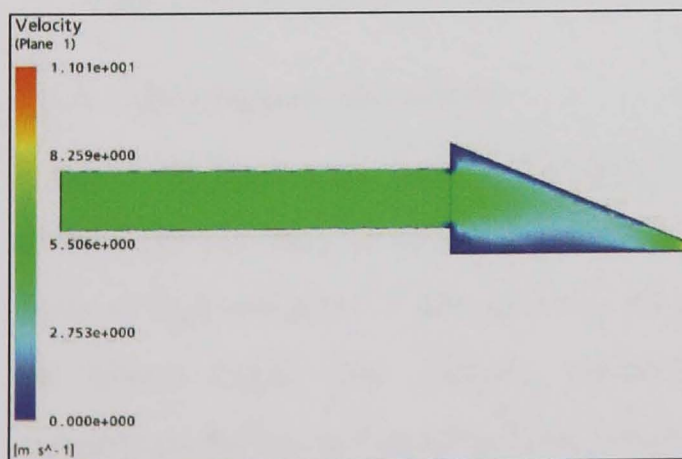


Figure 5-47 Total velocity distribution in the nozzle with 23° gradual contraction

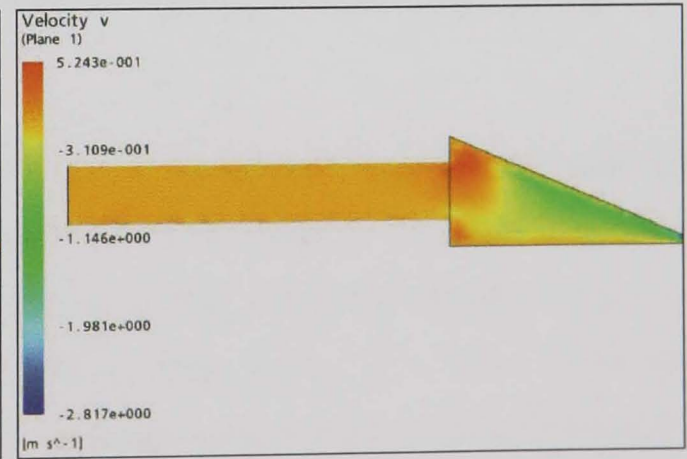
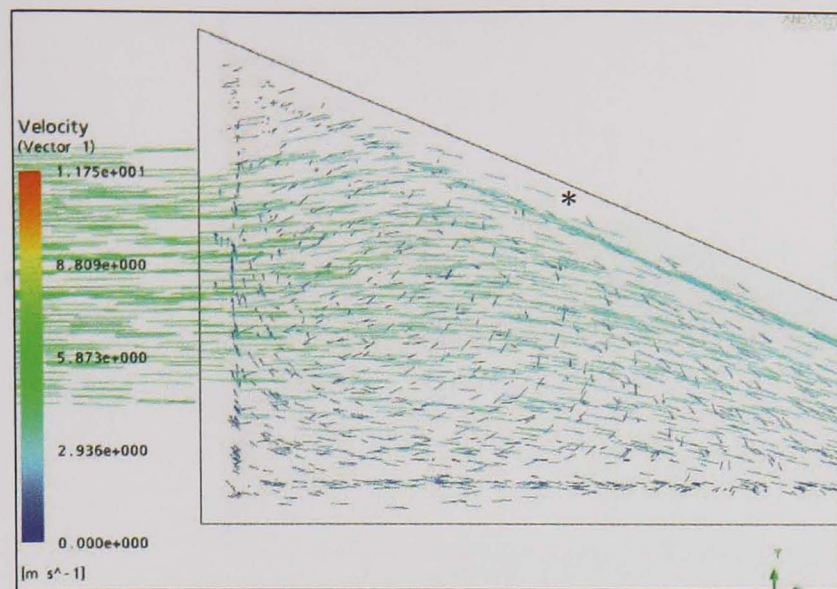


Figure 5-48 Velocity in the vertical direction in the nozzle with 23° gradual contraction



* Gap is due to the mesh.
The vectors (fluid velocity arrows) start at the centre of the first element from the wall.

Figure 5-49 Velocity vector plot in the nozzle with 23° gradual contraction

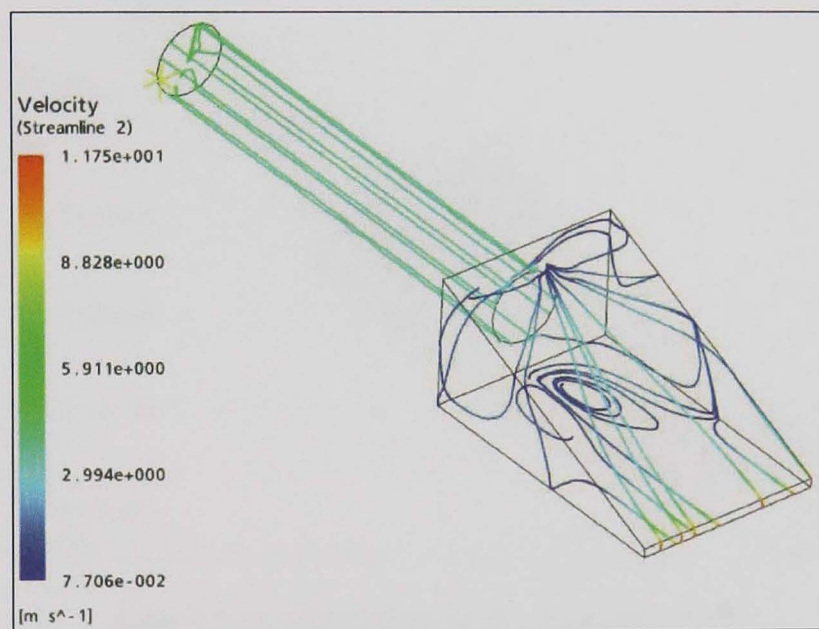


Figure 5-50 Streamlines of velocity distribution in the nozzle with 23° gradual contraction

5.6.2 Rectangular slot nozzle

Figure 5-51 shows the velocity intensity in the vertical direction for the conventional rectangular slot nozzle with a 1mm outlet gap and 8mm diameter inlet pipe. There are areas of high velocity in this direction at entry to the slot nozzle and negative values at the nozzle slope. This indicates reverse flow in these areas. It is clear from the streamlines shown in Figure 5-52 that there exist large areas of losses within this nozzle. Large amounts of recirculation are present at the rear of the nozzle chamber. The many particles' paths move not straight to the nozzle exit (an ideal path) but flow from the centre to the sides, then reverse to the rear, and then collide with the main nozzle flow, causing nozzle losses.

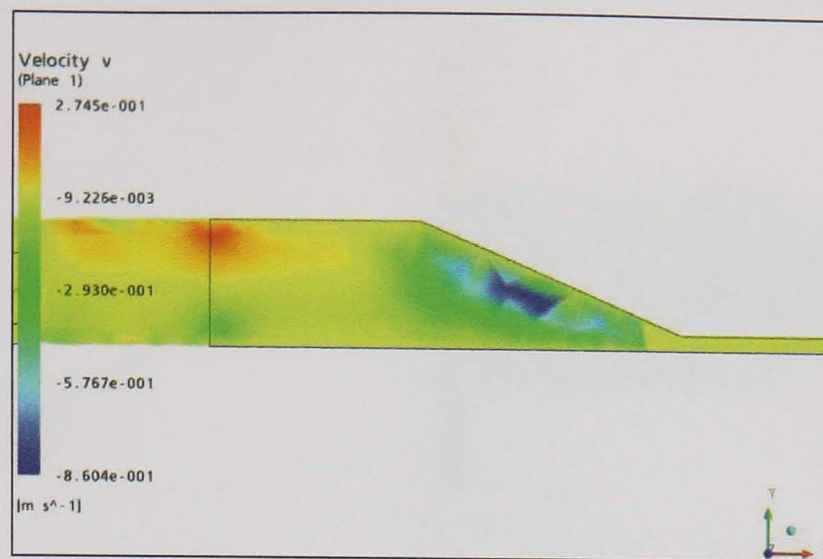


Figure 5-51 Velocity in the vertical direction in the long slot nozzle

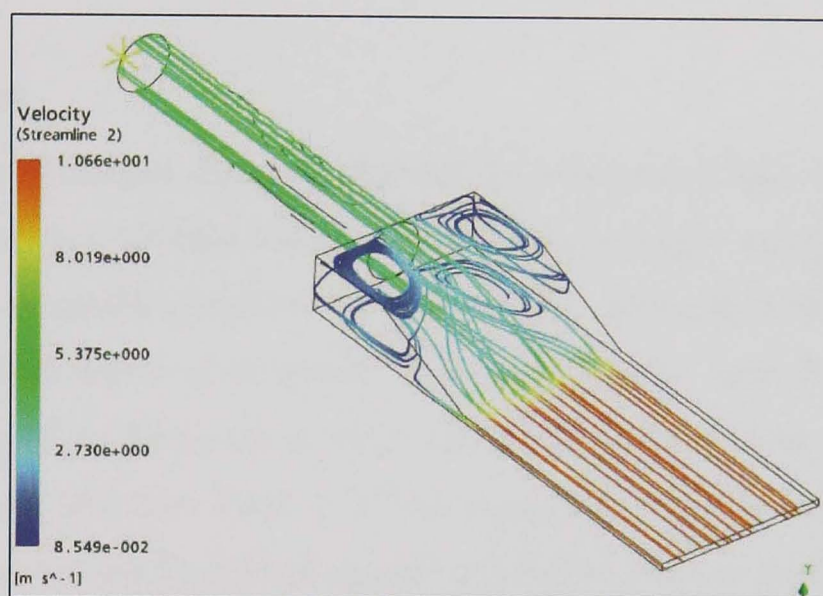


Figure 5-52 Streamlines in the long slot nozzle

5.6.3 Cylindrical orifice nozzle

Figure 5-53 shows the path of a massless particle close to the wall of the orifice. The main problem previously identified with the orifice nozzle is the change in section. At the sudden contraction, after rebounding off the wall at the change in section, the particle collides with the high velocities of the central flow. The particle cannot continue on its path to the outlet, and therefore all the energy is lost in this area. Figure 5-54 shows the velocity intensity in the vertical direction for the orifice nozzle with an 8mm inlet pipe and 7mm outlet pipe. Although the change in section is relatively small, there still exist areas of low velocity in the Y direction. These points indicate flow orthogonal to the required path. This represents significant losses for the fluid and removal of this phenomenon is recommended.

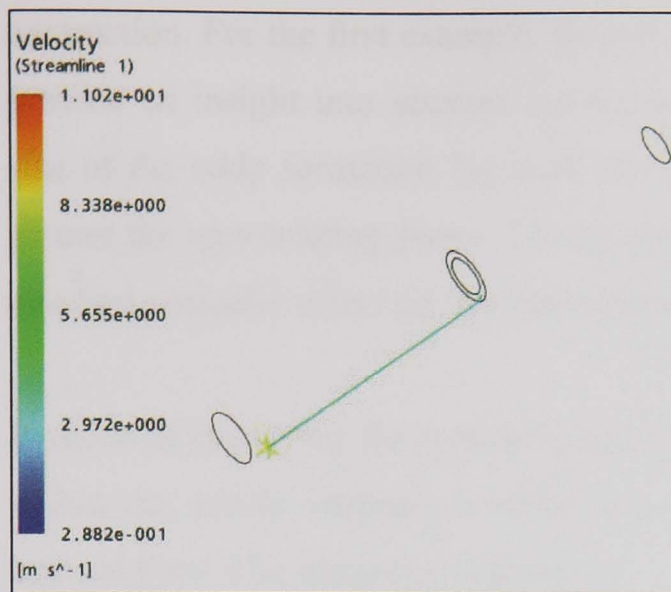


Figure 5-53 Streamline in the orifice nozzle

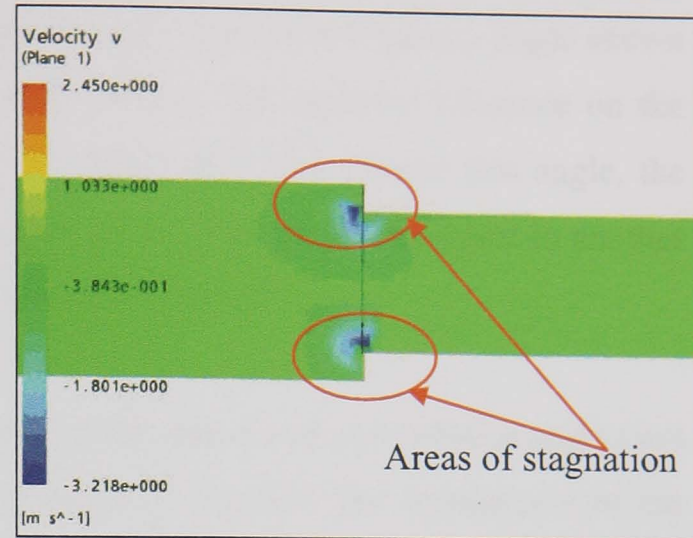


Figure 5-54 Velocity in the Y direction for the orifice nozzle

5.6.4 Discussion

The main flow in the nozzle chambers flowing from the inlet is fully developed in the x-y plane expressed by a standard turbulent flow velocity profile except for the region of contraction into the nozzle exit duct. As the main flow approaches the change in section region, the cross-section is continuously decreasing and the main flow is accelerated. The discontinuity of the geometry at the transition of the downwards oriented flow into the constant nozzle exit flow leads to a flow separation. Flow separation occurs when the boundary layer travels far enough against an adverse pressure gradient that the speed of the boundary layer falls almost to zero. The fluid flow becomes detached from the surface of the nozzle, and instead takes the forms of eddies and vortices. This flow separation is expressed by the formation of a recirculation zone at the proximal region of the nozzle exit chamber. Adjacent to the recirculation zone close to the centre line of the nozzle, a jet is formed with velocities about two times that of the mean velocity. In the lower and upper parts of the main nozzle chambers, a second recirculation domain establishes itself with extremely low velocities. Those small velocities are due to the fluid backing up against the walls and recirculating. As the jet exits the nozzle, the jet will start to break up. The distance at which this occurs is the subject for the work in the next chapter.

Velocity profile charts have been produced which show how the flow behaves both in the centre of the flow and at the wall of the pipe or nozzle. A number of inputs were tested including the flowrates, fluid velocities, fluid type and sharpness of the

contraction. For the first example, the results for water and the contraction angle shown provide an insight into internal nozzle fluid behaviour. The greatest influence on the size of the eddy formation lay with the contraction angle. The steeper this angle, the greater the recirculating flows. The smoothness of transition from one point to another also had a smaller effect on the size of the recirculating flow.

In terms of improving the nozzle design to reduce the amount of recirculation and losses within the nozzle, aspects of design were changed to monitor the smoothness of the internal flow. The important factors are:

- recirculation within the flow region;
- pressure losses due to the influence of the change in section;
- nozzle velocity profile at the exit.

These factors all cause the nozzle to under-perform. To remove some of these factors it is critical that a smooth change in section is implemented, such as that proposed by Rouse et al (1952) and later by Webster et al (1995a).

Chapter 6 Theoretical Modelling of Jet Coherency

6.1 Introduction

This chapter includes the theoretical work relating to fluid delivery in grinding. The primary focus of this work is the fundamentals of fluid behaviour before entry to the grinding contact as well as how to get the maximum amount of fluid into this contact. Jackson (2008) looks at the action of the fluid as it passes through the grinding contact and proposes a model for 'convenient useful flow', describing also the benefit this brings, and the advantages and requirements for industry. The work in this thesis investigates system design, requirements, and analysis of delivery design to supply this flow. For this reason, the measurable for theoretical, experimental and simulation work lies with collected flow. This allows for the comparison between delivery systems. As previously stated, in chapter 3, it is apparent that to deliver the maximum amount of fluid into the grinding contact, then a liquid jet focused at the entry region appears the most viable method. Due to process constraints, it is not always possible to position the nozzle very close to the entry region so a coherent jet is required.

6.2 Coherence length from fluid jet break up

Grant and Middleman (1966), Hoyt and Taylor (1977), Leib and Goldstein (1986) and Lin and Lian (1990) investigated the flow of a jet issuing from differing nozzles or hoses in differing industrial applications. The major research effort concerns the analysis of jet stability referred to in this work as the jet break-up length and more formally the coherence length of that jet. Jets issuing from an orifice break up due to two different effects: the Rayleigh–Taylor instability, or RT instability (occurring any time a dense, heavy fluid is accelerated into a light fluid), and Plateau-Rayleigh instability (occurring due to surface tension, which acts to break up a cylindrical jet). This work takes forward work by Grant and Middleman (1966) but bases its definition of length around their underlying principles.

From this, the coherence length (C_L) of a jet is defined as 'the length of the fluid jet from the point of exit from the nozzle, to a point at which the disturbances (ξ) within the fluid jet reach the same radius (r_j) as the initial nozzle opening, shown schematically in Figure 6-1 .

This is a theoretical basis of jet break up, but many relations come from supporting experiments. McCarthy and Molloy (1974) undertook an experimental evaluation of the jet break up length. Their relationships form in the ways shown in Figure 6-2, giving relationships between the jet break up length C_L and jet velocity v_j .

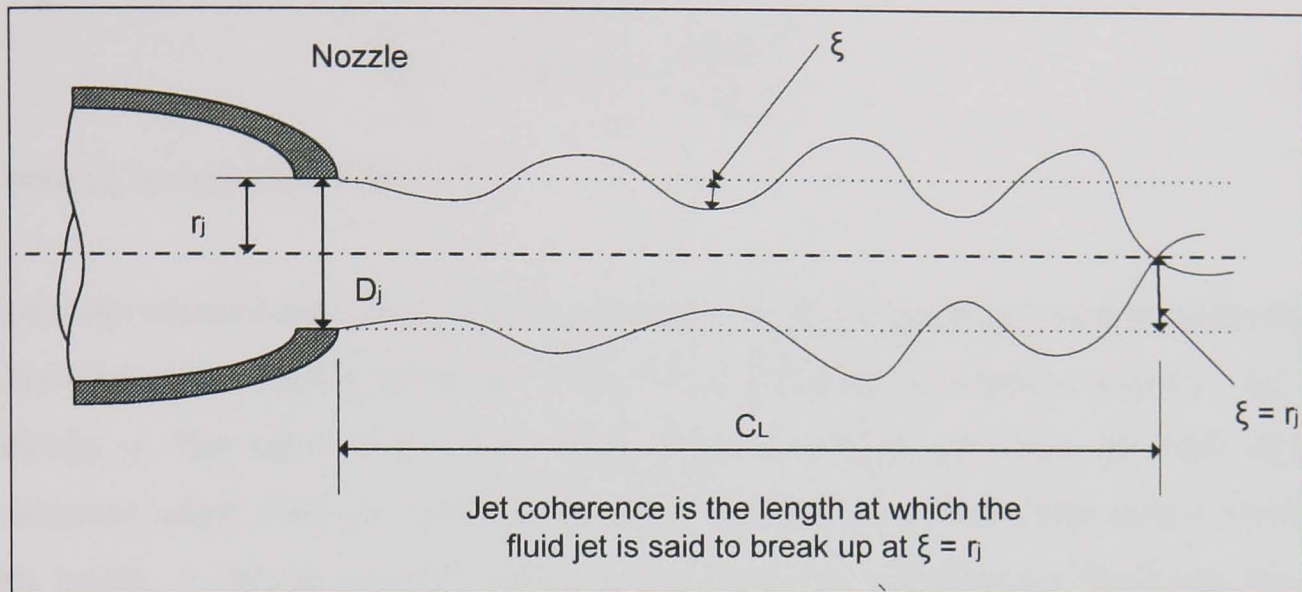


Figure 6-1 Schematic for the definition of coherence length (adapted from Cui 1995)

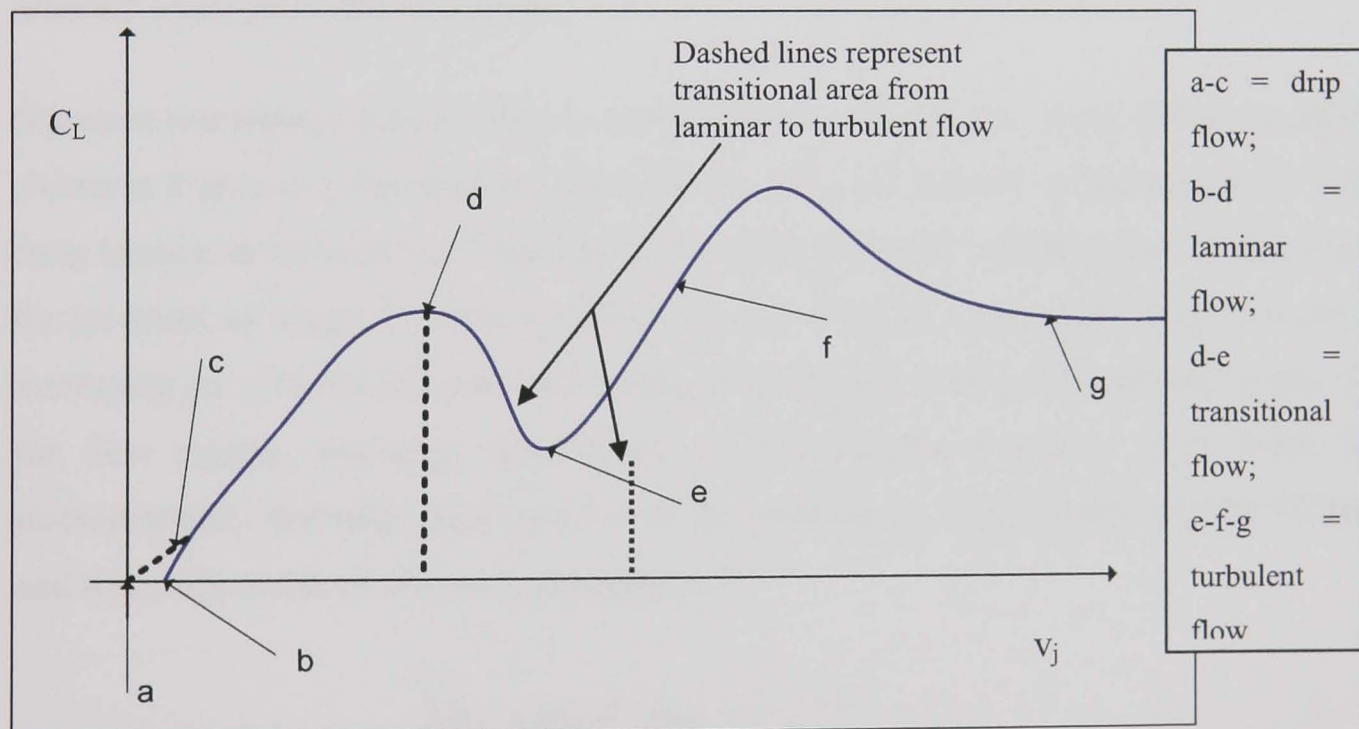


Figure 6-2 General shape of a liquid jet break up curve (adapted from Cui 1995)

In Figure 6-2 point *c* is the point at which the stream changes to a jet flow from that of an ordinary drip flow. Work by Weber (1931) and Grant & Middleman (1966), describes the region from point *c* to point *d*. Their conclusions drawn from experimental effort, place the coherence length as a function of both fluid jet surface tension and aerodynamic forces affecting the surface of the jet. These forces acting upon the fluid jet stream lead to both transverse and symmetric disturbances. Through a process of

experimental work and dimensional analysis, further work to be analysed in this chapter, Grant and Middleman (1966) formed an empirical relationship for the jet coherence length relating to the established constants the Weber number (We) and Reynolds number (Re) in Equation [6.1].

$$\frac{C_L}{D_n} = 19.5 \left(We^{0.5} + \frac{3We}{Re} \right)^{0.85} \quad [6.1]$$

where D_n is the nozzle diameter.

From this equation and Figure 6-2 a peak value for the jet break up length is established. This peak point occurs when the value of V_D (Critical velocity) is equal to the jet velocity v_j . This value of V_D varies from nozzle to nozzle, and forms the basis of this coherence length work on establishing nozzle parameters to investigate their effects on this length. A typical example drawn from Grant and Middleman (1966) sets the jet break up length at 65 mm for a straight-pipe nozzle, with a diameter of 1mm, supplied with a 2.5 m/s jet of distilled water.

Intensive research on the jet coherence length focuses on specific areas within the graph shown in Figure 6-2. The area between d and e , however, known as the transitional area from laminar to turbulent jet flow, has only a small amount of investigation. In this area, the jet break up length C_L reduces as the velocity of the jet v_j increases. Beyond point e increasing jet velocity increases the jet break up length. This is the turbulent region of the flow regime. McCarthy and Molloy (1974) describe this area of jet break up mathematically deriving relations between the jet break up length in this area the Weber and Reynolds numbers shown in equation [6.2].

$$\frac{C_L}{D_n} = 1.7 We^{0.5} (Re \times 10^{-4})^{-0.625} \quad [6.2]$$

Although Newtonian jet stability – that is, the stability of a jet of a Newtonian fluid whose stress versus rate of strain curve is linear and passes through the origin – has been the subject of numerous experimental and theoretical studies, no authors have yet accurately predicted the break up of turbulent jet streams. Theories available in the literature are only applicable to low-speed laminar jets in stagnant air. In practice, the ambient medium, turbulence in the nozzle and the extent of development of the velocity profile all have effects on the stability of a jet and require further investigation.

6.2.1 The turbulent jet

Figure 6-3 shows a typical break up curve covering both laminar and turbulent flow. A point of interest in this graph presented in the work by Grant and Middleman (1966) is the apparent increase of jet stability length with an increase in jet velocity in the turbulent region. Grant and Middleman describe this as a misleading conclusion, as their studies focus on the time to jet break up and state that comparisons must be made with the jet break up time C_L/V . Their conclusions are unhelpful in that they indicate a decreasing break up time with an increasing velocity (the slope of the curve is monotonically decreasing with v); however, this work is concerned with the distance of jet break up and from Figure 6-3, C_L (shown as L in Figure 6-3) does increase with V .

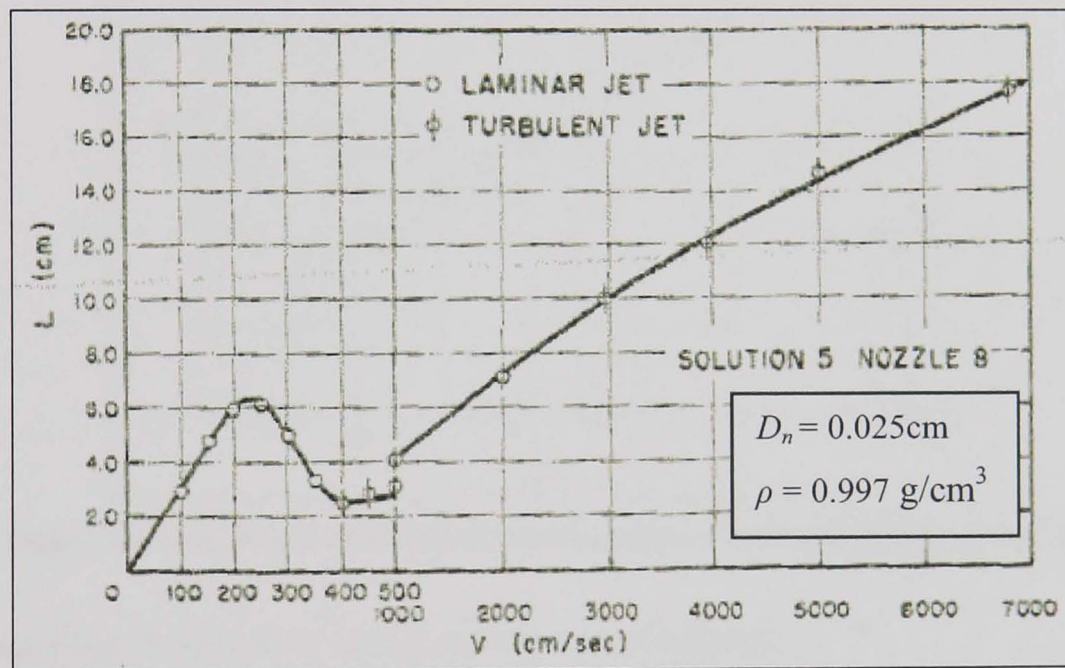


Figure 6-3 Effect of transition to turbulence on break up curve (Grant and Middleman 1966)

Figure 6-4 shows the turbulent break up data from Grant and Middleman (1966) plotted in dimensionless form. They use the square root of the Weber number as the independent variable due to its proportionality to the velocity. From their experimental work Equation [6.3] is drawn.

$$\frac{C_L}{D_n} = 8.51(We^{0.5})^{0.64} \quad [6.3]$$

Equation [6.3] correlates the data with a root-mean-square error of 9.4 per cent. The data presented is, however, only viable for $We^{0.5} > 200$ as their experimental data shows at values lower than this, the concept of jet break up with time loses meaning due to the curve shown in Figure 6-3. Grant and Middleman (1966) go on to present

photographic evidence of jet break up with a water jet entering an atmosphere of air. Their work concludes that at increased velocities beyond the transitional region of the jet, the jet coherence length begins to increase once again. Previous work by McCarthy and Molloy (1974), Lee (1974) and Bogy (1979) forms the basis for jet break up concerning only a circular pipe and flow exiting into a given atmosphere. None of the work takes into account the nozzle geometry and the effect of nozzle factors on the break up length. It is critical that these effects are investigated to aid improved nozzle design.

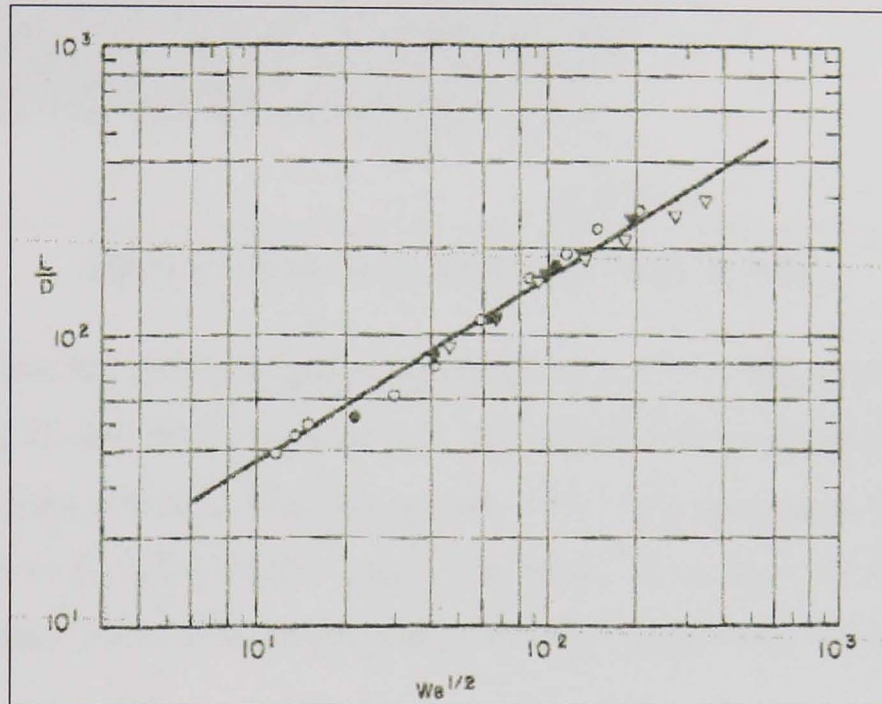


Figure 6-4 Correlation of turbulent breakup data (Grant and Middleman 1966)

Taking equation [6.3] further and including a nozzle factor:

$$\frac{C_L}{D_n} = 8.51 (We^{0.5})^{0.64} \cdot (N_f) \quad [6.4]$$

Where N_f is the combination of all effects relating to the nozzle. Many sources of literature investigate losses within the kind of factors involved with nozzles; however, all investigated pressure losses, or more specifically, energy losses within the flow. This work aims to describe the effect these factors have on the coherence length of the jet.

The factors highlighted as important are:

- nozzle surface finish \rightarrow leading to material roughness (Roughness average - R_a);
- difference between entry diameter and exit diameter (Contraction ratio - C_R);
- nozzle exit edge sharpness;
- nozzle internal body shape.

These factors contribute to the jet instability and better understanding of their relative effects leads to an insight into correct nozzle design for coherent jet nozzles. This work analyses some of these factors both analytically with CFD, and experimentally, to compare those results.

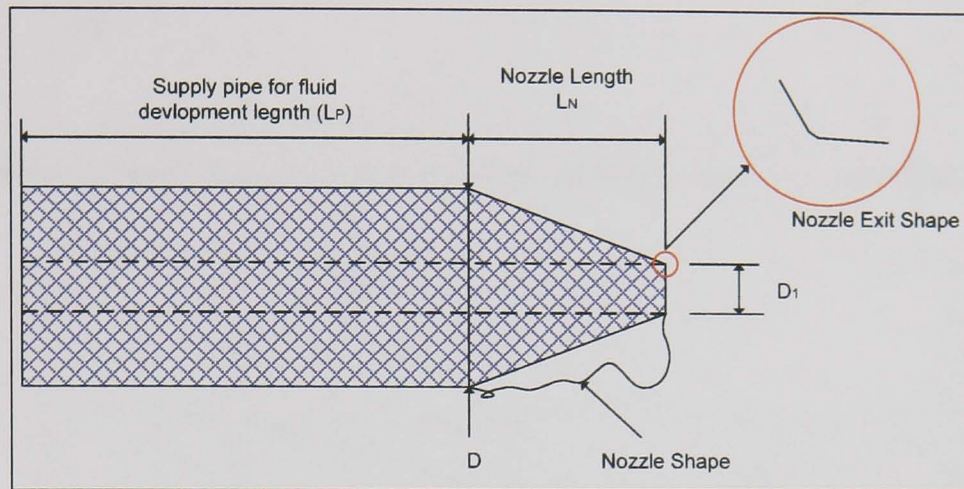


Figure 6-5 Nozzle factors effecting jet break up length

Figure 6-5 shows the variables under investigation in this work, schematically. These are highlighted as the critical four factors and whilst one is under investigation, the others must be kept constant. This also applies to the fluid and supply properties so that only the factor to be analysed is varied. The effect of the flow variables is seen by implementing these into the Weber/Reynolds number respectively into equation [6.4].

6.2.2 Effect of internal nozzle body shape on jet coherency

The first factor under investigation is the internal shape of the body of the nozzle. For comparison, three differing shapes are analysed along with the results for a straight pipe analysis using equation [6.4]. Figure 6-6, Figure 6-7 and Figure 6-8 show the shapes under investigation both experimentally and with the CFD package CFX 10. Working drawings for all the nozzles are shown in Appendix A.

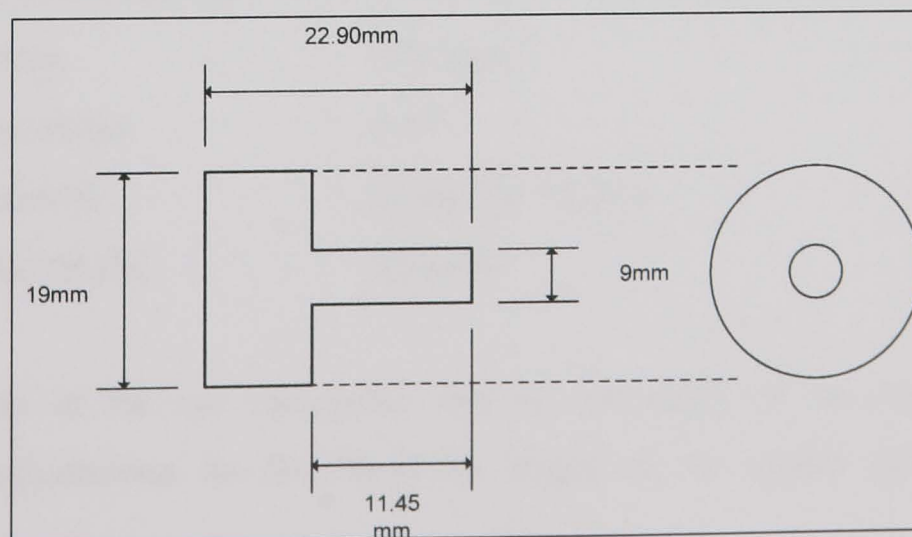


Figure 6-6 Orifice nozzle design (internal area of fluid shown)

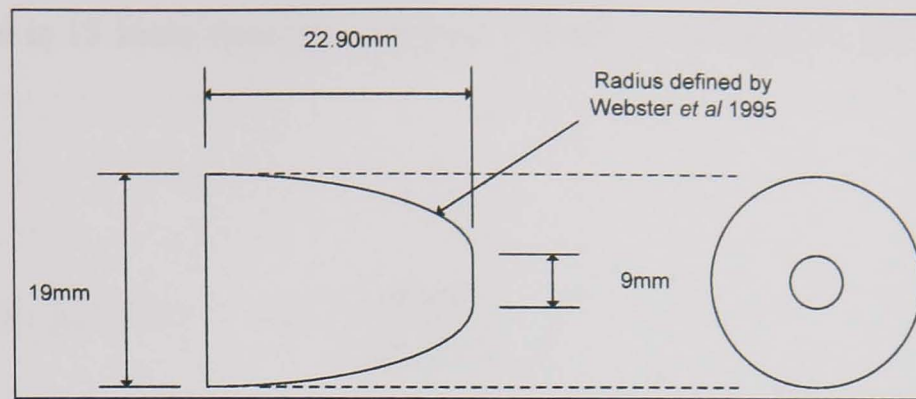


Figure 6-7 Nozzle design based on Webster (1995a) (internal area of fluid shown)

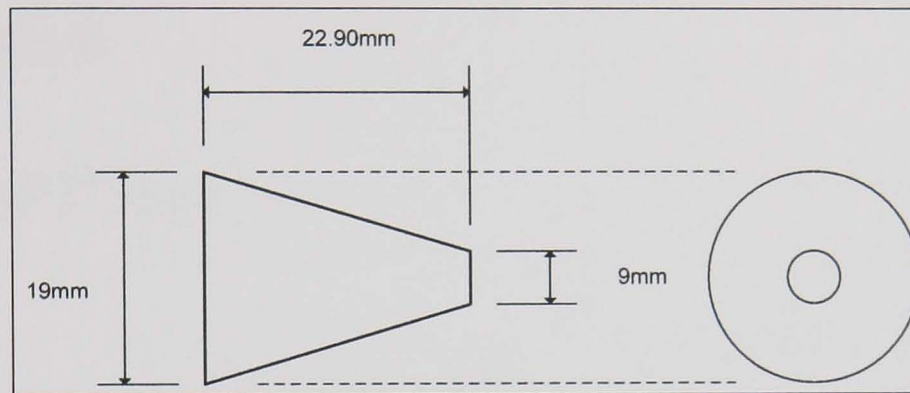


Figure 6-8 Straight sided nozzle design (internal area of fluid shown)

The constants to make certain only the shape effect is investigated are:

- Fluid type: Water with 5 per cent Hysol X
- Kinematic Viscosity: $0.995 \times 10^{-6} \text{ m}^2 \text{ s}^{-1}$
- Mass flow rate: 15 l/min
- Supply pipe diameter: 19 mm
- Nozzle outlet diameter: 9mm
- Fluid Temperature: 25°C
- Surface Tension of water with 5 per cent additives: 72 mN/m (Pallas and Harrison 1990)
- Fluid Density: 998 kgm^{-3}
- Contraction Ratio: 0.47
- Nozzle Material: Brass ($Ra = 2\mu\text{m}$)
- Nozzle Exit Profile: Straight

For calibration of the test equipment and for estimation of the coherence length, preliminary calculations on the break up length of the supply piping alone was undertaken.

If the flowrate is 15 l/min through a circular diameter of 9mm then the fluid velocity is given by:

$$v = \frac{\dot{Q}}{A} \quad [6.5]$$

$$\therefore \text{If } A = \pi r^2 \Rightarrow v = \frac{0.00025}{\pi \times 0.0045^2}$$

$$\therefore v = 3.929 \text{ m/s}$$

From equation [6.4]:

$$\frac{C_L}{D_n} = 8.51 (\text{We}^{0.5})^{0.64} \cdot (N_f)$$

$$\text{If } \text{We} = \frac{\rho v^2 l}{\sigma} \quad [6.6]$$

where

$$\text{Then } \frac{C_L}{D_n} = 8.51 \left(\left(\frac{\rho v^2 l}{\sigma} \right)^{0.5} \right)^{0.64} \cdot (N_f)$$

$$\therefore \frac{C_L}{0.009} = 8.51 \left(\left(\frac{998 \times 3.929^2 \times 0.009}{72 \times 10^{-3}} \right)^{0.5} \right)^{0.64} \cdot (N_f)$$

\therefore Assuming that $N_f = 1$ for a standard pipe

$$\therefore C_L \approx 95.7 \times 0.009 = 0.86 \text{ m}$$

The assumption that $N_f = 1$ for a standard pipe comes from a requirement for the comparison between two nozzles. This factor is dependant on all those factors listed previously, but as a value on its own, is used to compare two nozzles using the model and simulation presented herein.

This figure gives an approximation of the coherence length for a pipe of diameter 9mm with water and 5 per cent Hysol X at 25°C with the stated parameters. This value is much higher than the figures presented in the work by Grant and Middleman (1966). Using the equation for confirmation, with a very small diameter tube, the results fall on the best-fit line described by equation [6.4]. The disparity in the results comes from the pipe diameter and flow rates. To achieve the high velocities used in their work, Grant and Middleman use very fine tubes. This work uses larger openings and therefore applying the high velocities, with much higher pressures, moves the graph line up by a distance. Varying the diameter and velocity however, yields results lying within a range and following the same trend as the results in Figure 6-4. Experimental work to produce a similar curve applying different flowrates and consequently different velocities, allowed for the reproduction of a similar trend to that proposed. For a direct comparison of the curve shape, Figure 6-9 represents the fluid velocity against the coherence length for the same 9mm diameter circular pipe.

Figure 6-9 shows an increase of coherence length as the fluid velocity or flowrate is increased. This follows the predictions of Grant and Middleman (1966). To test this further, presented in the next chapter are experimental investigations of coherence length of a 9mm pipe. Further analytical work for the proof of these equations uses ANSYS CFX with a two-phase flow environment (water dispersing into air). Commonly known as ‘multiphase’ physics, this forms the basis for comparison between experimental investigations, analytical theory, and simulations.

The work by Grant and Middleman (1966) on jet break up presents the beginning of a systematic evaluation of the role played by external effect factors in the destabilisation of a liquid jet. They look systematically into both laminar and turbulent jets, but there still exists no analysis of factors occurring in and around the nozzle. Merzkirch (1987) and Oertel (1989) have divided flow visualisation methods into optical methods, methods with additives and methods with energy supply. The light sheet method uses so-called tracer particles to split the light in the flow. Other visual inspection methods using cameras exist, but little is known about the fluids behaviour inside the actual body of the fluid external to the nozzle orifice. The next section of this work attempts CFD simulations of nozzle geometries, both new and old, to investigate fluid behaviour in jet break up.

Very limited information is available regarding the surface structure of coherent turbulent liquid jets. Some experimental data relating to amplitudes and frequencies of surface disturbances are given by Chen and Davis (1964) and are discussed qualitatively. Appel and Swenson (1968) provide some experimental data on jet surface roughness but this is of limited scope. One interesting element of their work was the finding that of the nozzle with a decreasing aspect ratio, the amplitude and wavelength of the surface roughness of the jet decreased.

An important point to note in this work is this → This is presumably due to the low scale of turbulence generated in such short nozzles, but provides support for the established practice of making the exit nozzle as short as possible.

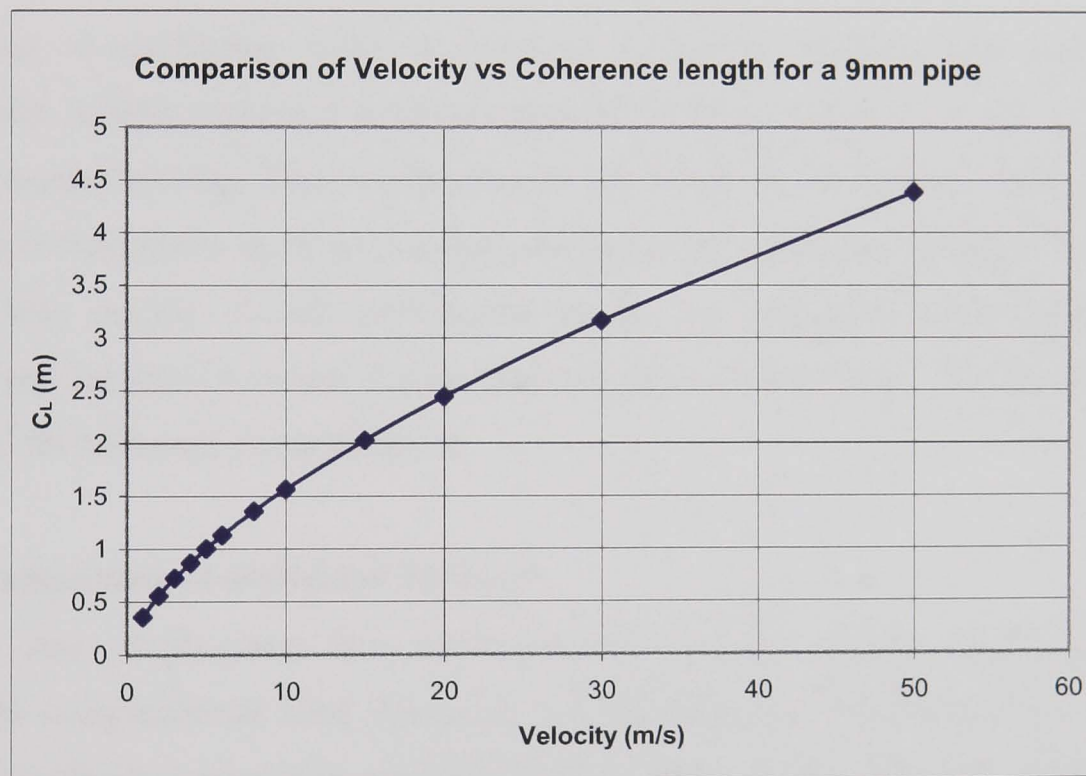


Figure 6-9 Fluid velocity versus coherence length using the Grant and Middleman equations

6.3 Computational modelling of multiphase fluid flows

The tendency in recent years is the appearance, wide distribution and ultimately the use of commercial computational fluid dynamics software tools permitting complex numerical computation of fluid flows. The site www.cfd-online.com, devoted to computational fluid dynamics, lists many of the readily obtainable commercial CFD codes available on the market. The number of publications in the leading international journals on fluid dynamics with results of successful application of commercial CFD tools for prediction of local and integral parameters of flows in hydraulic machines and other technical devices steadily grows (Ruprecht 2002). The popularity of these software tools increases with the advancing computational power available in today's environment.

Modelling of multiphase flows is however, inherently difficult. Full and complete multiphase models require a large computational effort, more so if greater than two phases require solving. This work presents the study of multiphase flows within the grinding environment, more specifically looking at the coherence length of a jet exiting a particular nozzle. A full explanation of all the procedures and theory behind multiphase simulations would detract from the flow of this thesis, for this reason, it is included for reference in Appendix D.

6.4 Comparison of available CFD tools

Initially, only single-phase flow models existed in early versions of the commercial codes for computational fluid dynamics. This progressed with the addition of particle tracking methods. Lagrangian simulation of two-phase flows dominates the multiphase field. It is the default setting for most codes. In subsequent product releases, an Eulerian description of dense multiphase flows is included. In addition to this, many codes contain simplified equation systems for simulation of special case two-phase flows.

6.4.1 PHOENICS

PHOENICS restricts Eulerian multi-fluid models to two phases (CHAM 1991). For turbulent flows, PHOENICS solves equations that are time-averaged without mass weighting. A diffusion term is included in the phase continuity equations because of this. The special function 'Inter-Phase Slip Algorithm' (IPSA) is used in solving the two fluid equations. One limiting factor in the code is the Interphase transfer model. One

example of this is the drag force terms included. Users must add formulae themselves, a practice difficult unless specifically working in the field of CFD.

PHOENICS bases the Reynolds number on the fluid viscosity of the continuous phase rather than on the viscosity of the mixture. No empirical correlations for the mixture viscosity are included in the algebraic slip model. It is calculated from the phase viscosities instead. In practice, an empirical model for the mixture viscosity is necessary. This is an underlying flaw to the code in reality. The simplifications made in analysing the drag force and the mixture viscosity need correcting if the model is to be implemented in practice. The model requires further user editing if the turbulence of the mixture is necessary. Some of the computation and implementation by the user is possible; however, this is difficult for those not working specifically in CFD.

6.4.2 *FLUENT*

FLUENT contains both the Lagrangian and the Eulerian description of multiphase flow. Additionally, a special simplified two-phase model is available for stratified and free-surface flows. One point of note with FLUENT is that a single turbulence field is shared by all phases. With this, the same simple drag laws are implemented. Several limitations restrict the applicability of some of the contained models along with the multiphase model. Multi-component diffusion is not allowed. Mesh deformation for multiphase calculations is not permitted (FLUENT 2003).

In regards turbulence, use of the Reynolds stress is unacceptable. All turbulent quantities are based on the primary phase using the k-e or RNG (renormalisation group) k-e model. The effective viscosity of the secondary phase is obtained from the primary phase turbulent viscosity. No effects of turbulence generation in the secondary phases exist. Turbulence of the primary phase is directly affected by the presence of secondary phases (Manninen and Taivassalo 1996).

6.4.3 *CFX 10*

In the Eulerian multiphase model of CFX 10, the phases can be any combinations of incompressible and weakly compressible phases and laminar or turbulent phases. For each of the turbulent phases, the same turbulence model (k-e, SST, Reynolds etc) is used. The phases can consist of a number of species which undergo mass transfer by

diffusion within each phase and which can be transferred across the phase boundaries (Manninen and Taivassalo 1996). Correlations for the flow of a single particle in infinite fluid, including the correlation of Ihme et al (1972) applicable for all sub-critical Reynolds numbers and special models for the Stokes, Allen and Newton regimes, are available for calculation of the drag force in CFX 10.

There are however, several limitations to the use of CFX 10 for multiphase models. No heat transfer through radiation is described in multiphase flows and conduction in solids is not allowed. One further limitation is that the model assumes a fixed grid and therefore no model for the interaction between two dispersed phases is implemented in the code. These can be written in separate subroutines, available within the code. They were deemed unnecessary for this work. No mixture model is available in the code. It can however, be implemented in the form of a scalar transport equation written for the volume fractions (Manninen and Taivassalo 1996). Not all of the limitations within this model apply to the coherence length of a jet however. The criteria identified as most important to the work was the availability of the free surface model and turbulent interactions (ANSYS 10.0, 2005). In addition to the Lagrangian and Eulerian multiphase models, CFX contains a simplified, homogeneous flow model for two-phase flows for free-surface flows and drag-dominated multiphase flows. This model is the reasoning behind the choice of CFX for this work.

CFD itself is a swiftly developing subject. When describing the turbulent effects, there have been many arguments on using different approaches such as the Reynolds Averaging, Large-eddy simulations or the Navier-Stokes equations. The multiphase model that follows relies heavily on predictive models already in the literature that define the underlying equations behind the simulations. Although the actual results may change depending on the experimental models used, the model for comparison of the coherence length with that of experimental work represents the best estimate of the fluid flow behaviour with the available models and computational power of the literature and laboratory respectively.

6.5 Three dimensional exit flow analysis setup

6.5.1 Geometry creation

The first step in geometry creation uses the revolve command function creating half of the section profile and revolving it around the x-axis marked with a red arrow (Figure 6-10). This creates the body of the nozzle for flow analysis.

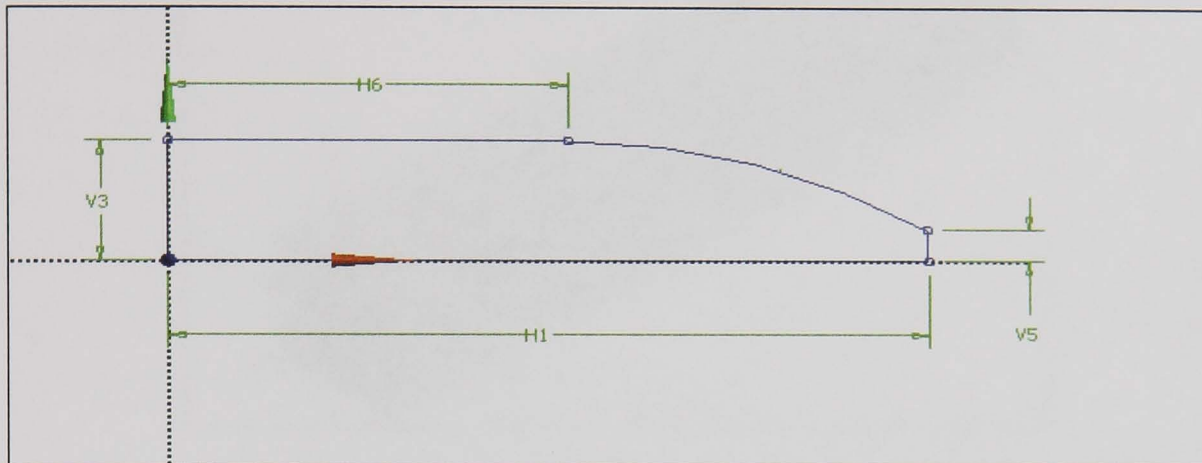


Figure 6-10 Geometry for the Rouse based nozzle body

Where:

- $H1 = 80\text{mm} - H6 = 64\text{mm}$
- $V3 = 9.5\text{mm} - V5 = 4\text{mm}$
-

After the revolve, the section becomes a three-dimensional solid representing the flow region. Note that the actual region of flow is created and not the pipe geometry (Figure 6-11). To move from a created pipe to the flow region using existing geometry the fill command is used. A thin surface between the two (defined in the physics setup) separates the internal liquid region, the nozzle, and the external air region.

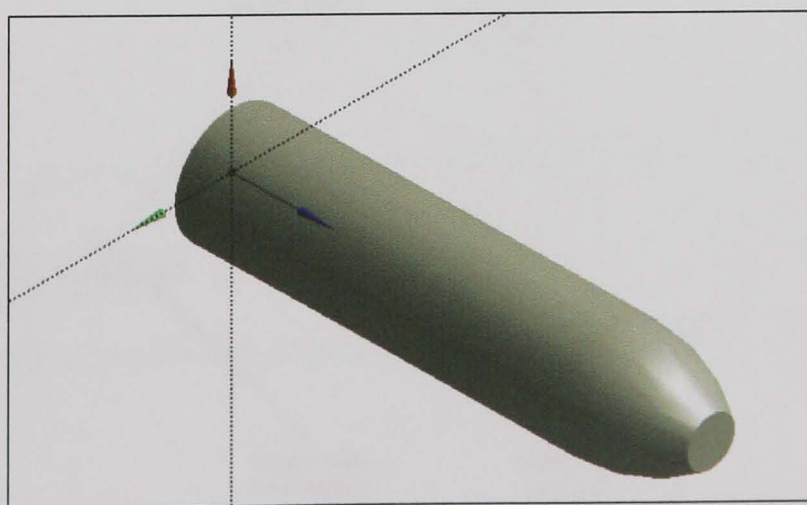


Figure 6-11 Three dimensional geometry of the nozzle flow region

The next step was to create an enclosure around this using the box option with the enclosure specified or by freezing the nozzle, creating a solid around it of the desired dimensions, and then creating an enclosure with a user-specified body. The second of these two options was used in this work and is shown in Figure 6-12.

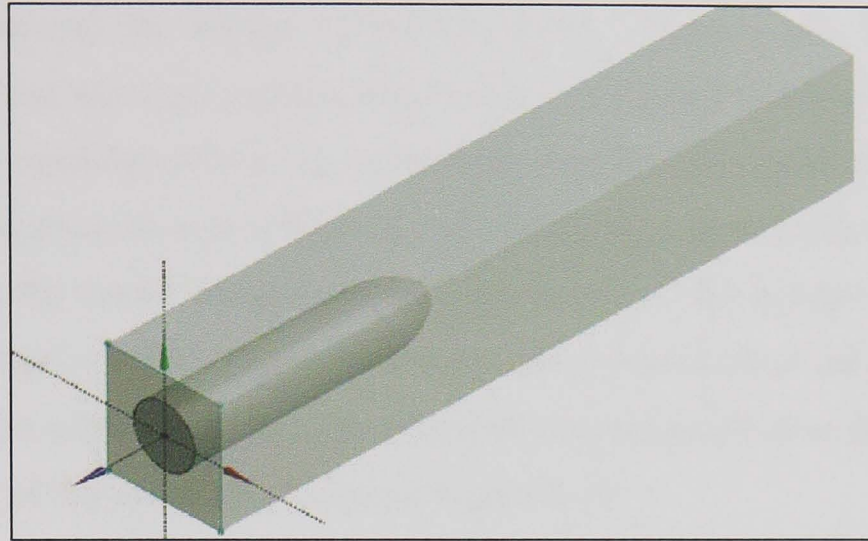


Figure 6-12 Nozzle with the user specified enclosure

This operation forms two parts. Creating a single part using the ‘form new part’ function generates one single domain with two parts visible for mesh manipulation. The next step in this process took the geometry created into ICEM CFD for two-dimensional region creating and then meshing.

6.5.2 Meshing

The first step of the process was to create the two-dimensional regions using the select parts feature of ICEM. Figure 6-13 shows parts for the inlets, outlets, and thin nozzle walls.

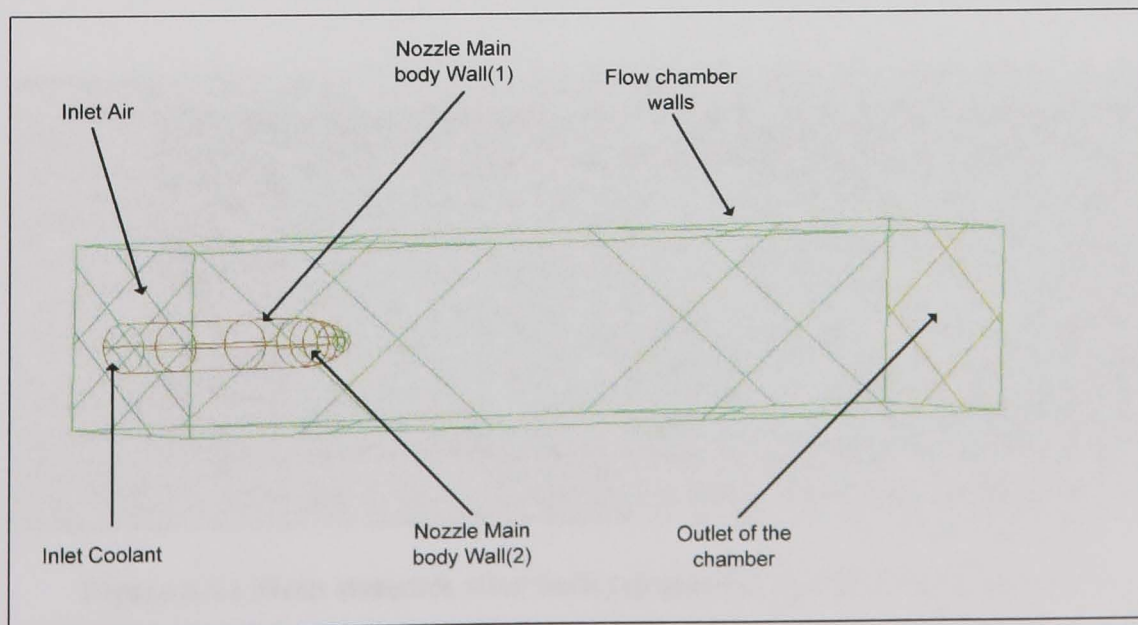


Figure 6-13 2D regions from ICEM

ICEM CFD provided the basis for the meshing. A tetrahedral mesh and prismatic mesh form the volume mesh with details as Table 6-1. Figure 6-14 shows the quality for this mesh after both tetrahedral and prismatic meshing using ICEM and five smoothing operations (this for the nozzle region). The volume mesh illustrated in Table 6-1 does not take into account the outside enclosure however. To mesh this, a series of point controls were used moving from the nozzle exit in a straight but expanding line away from the nozzle opening towards the outlet. This style of mesh made it possible to keep the computation down to a minimum but still investigate those areas of interest at the fluids exit from the nozzle into the surrounding enclosure. The global coarse mesh used the default settings in ICEM. Figure 6-15 shows the overall look of the completed mesh. Smoothing of the mesh took place after this final volume meshing of the entire domain, with the results of the smoothing shown in Figure 6-16.

Tetrahedral Meshing				
<i>Local Element Factor</i>	<i>Local Element Seed Size</i>	<i>Triangular tolerance</i>	<i>Smoothing Iterations</i>	<i>Minimum quality</i>
0.6	8	0.001	5	0.4
Prismatic Meshing				
<i>Height Ratio</i>	<i>Number of Layers</i>	<i>Vol. Smoothing</i>	<i>1st Lay Smooth</i>	<i>Surface Smooth</i>
1.2	4	2	2	1

Table 6-1 Mesh criteria for the Rouse based nozzle

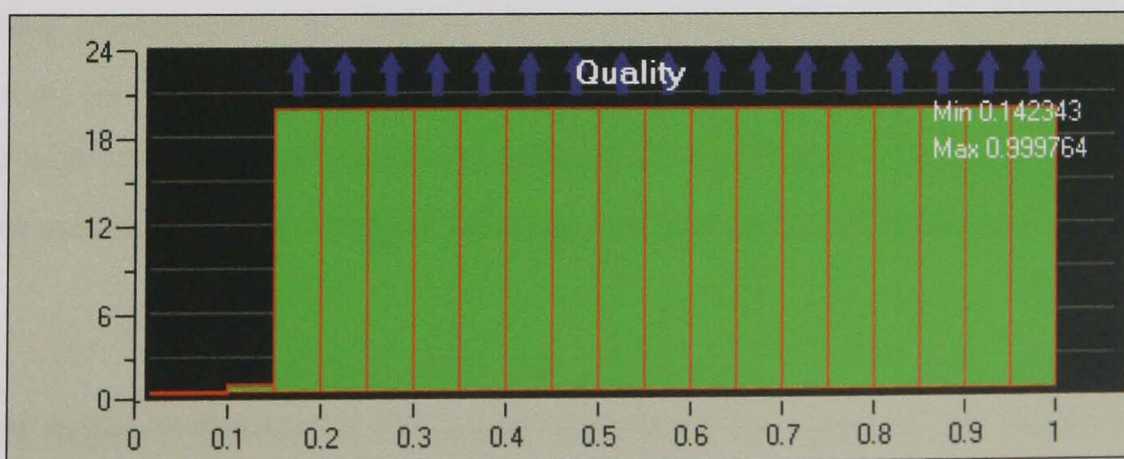


Figure 6-14 Mesh statistics after both tetrahedral and prismatic meshing

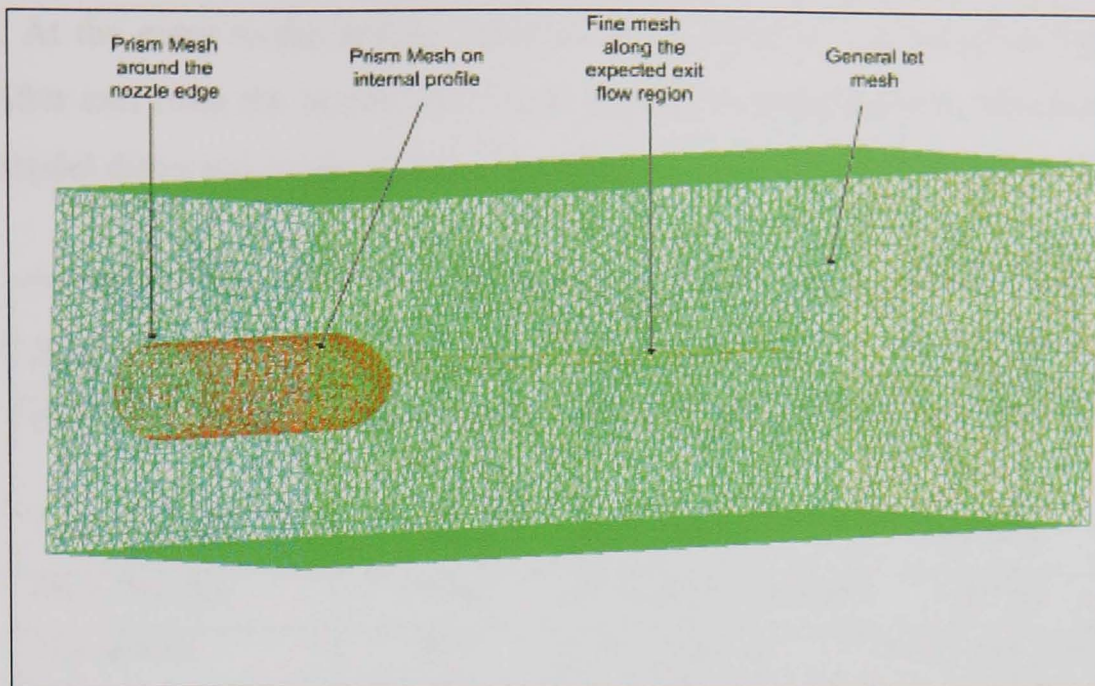


Figure 6-15 Completed volume mesh from ICEM

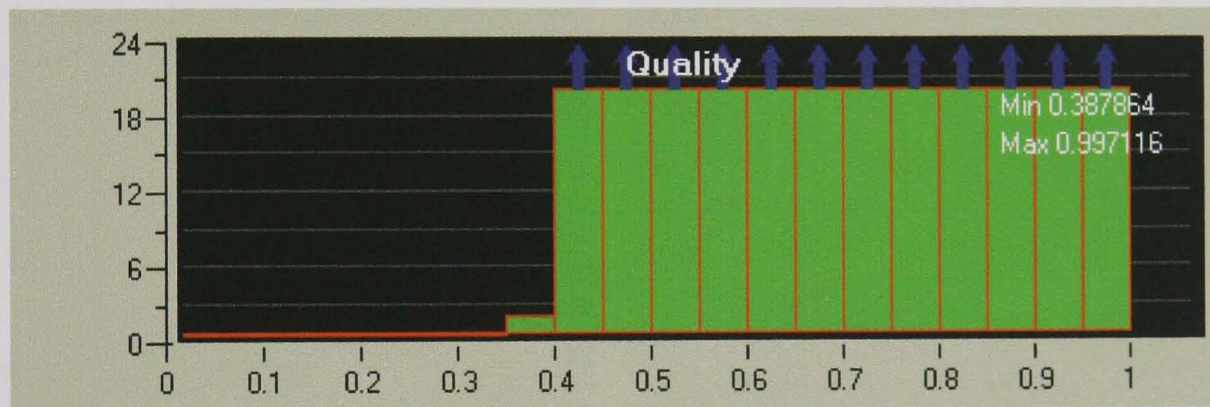


Figure 6-16 Quality of the mesh after 5 smoothing iterations

6.5.3 Pre-processing

Pre-processing for this simulation required the specific definition of the physics behind the process as well as the solver criteria used. Table 6-2 shows a summary of the pre-processing requirements for this simulation. These are similar to previous internal conditions, but now incorporate two-phase flow using both air and water. Specific settings with reasoning are presented in Figure 6-17 to Figure 6-20. The solver criterion specifies running until the solution converges so no number of maximum iterations was set.

The first major difference in the setup came from the necessity to model a domain containing a pair of fluids. Air and water was inserted at the large entry to the chamber with a volume fraction of one for air and zero for water. This means that only air is

inserted. At the entry to the nozzle, reversal of the volume fractions had the opposite effect. After exit from the nozzle, the fluids interact at their surfaces based on the free surface model discussed in the previous section.

Pre-Processing			
Fluid Type	Water/ Air	Inlet Speed	15 m/s
Simulation Type	Steady state Free Surface	Outlet Pressure	Rel: 0 Pa
Reference Pressure	1 [atm]	Wall Criteria	No Slip
Heat Transfer	None	Advection Scheme	Upwind
Turbulence	SST	Convergence	Auto Timescale
Solver	CFX 10	Time Scale	Conservative

Table 6-2 Initial Pre-Process settings

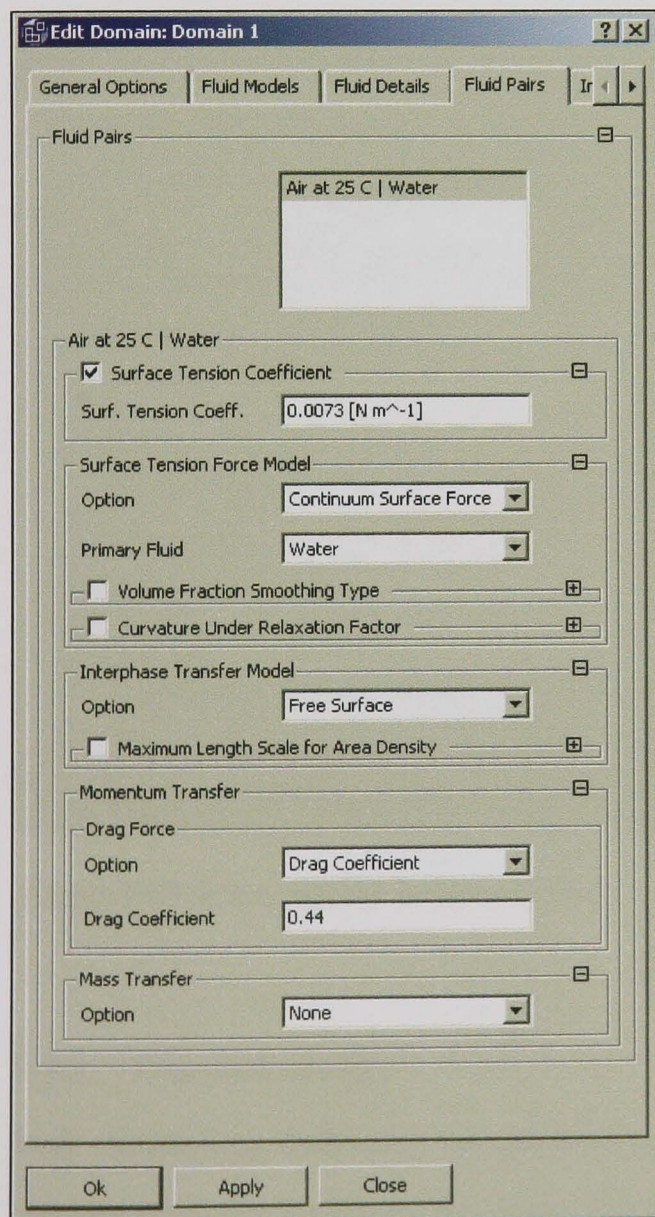


Figure 6-17 Physics for the fluid pairs

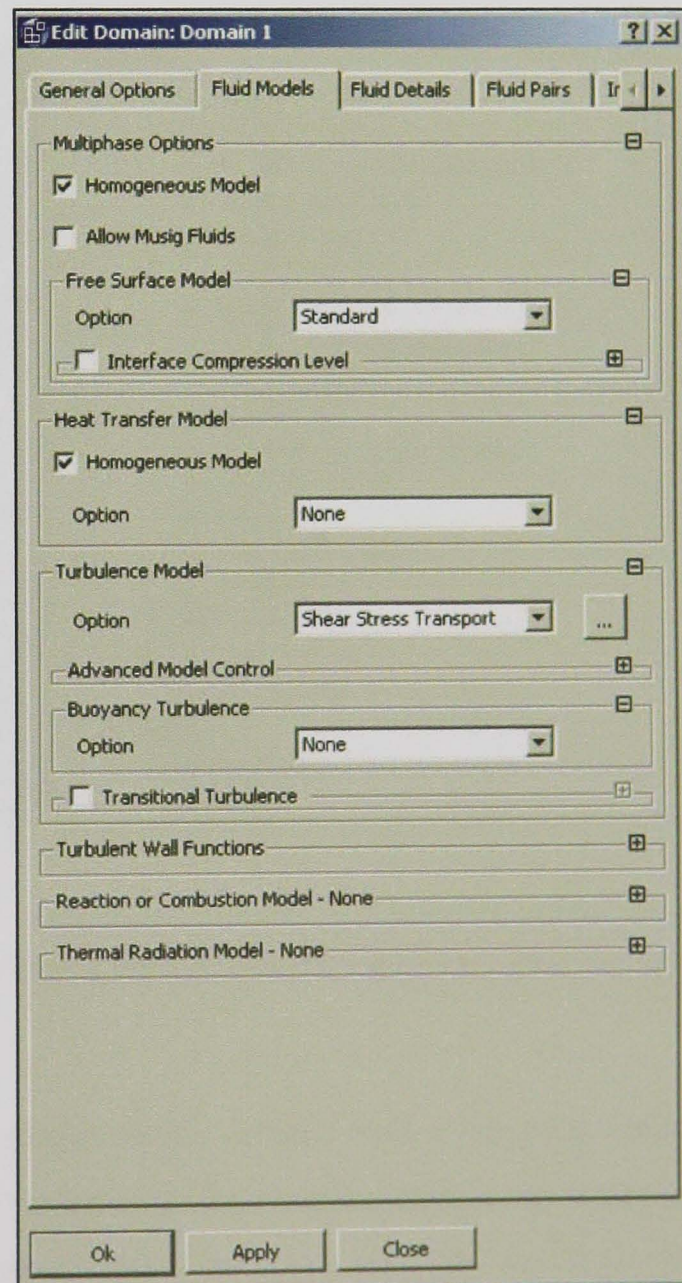


Figure 6-18 Fluid models for use in the simulation

The SST model proposed by Menter (1994), which is a combination of the $k-\omega$ model near the wall and the $k-\epsilon$ model away from the wall, was used for the turbulence modelling. This technique uses both models in areas where they perform best. The reason for using this model was that the mesh was well resolved, resulting in y^+ values that were lower than 20. CFX-5.7.1 uses an automatic wall function, which blends smoothly between a low Reynolds formulation and a standard log-wall function. This gives a more accurate representation of the friction at the wall in the areas where y^+ is smaller than 20. Figure 6-20 shows the entire physics tree for the first free surface flow model. The boundary conditions shown in Figure 6-20 such as the inlets and outlets are detailed in Table 6-3. Due to the simulation build, the 'create thin surface partner' function was used to enable the solver to make a correct distinction of walls at the nozzle boundary, but with no wall at the exit, allowing flow to emerge from the orifice.

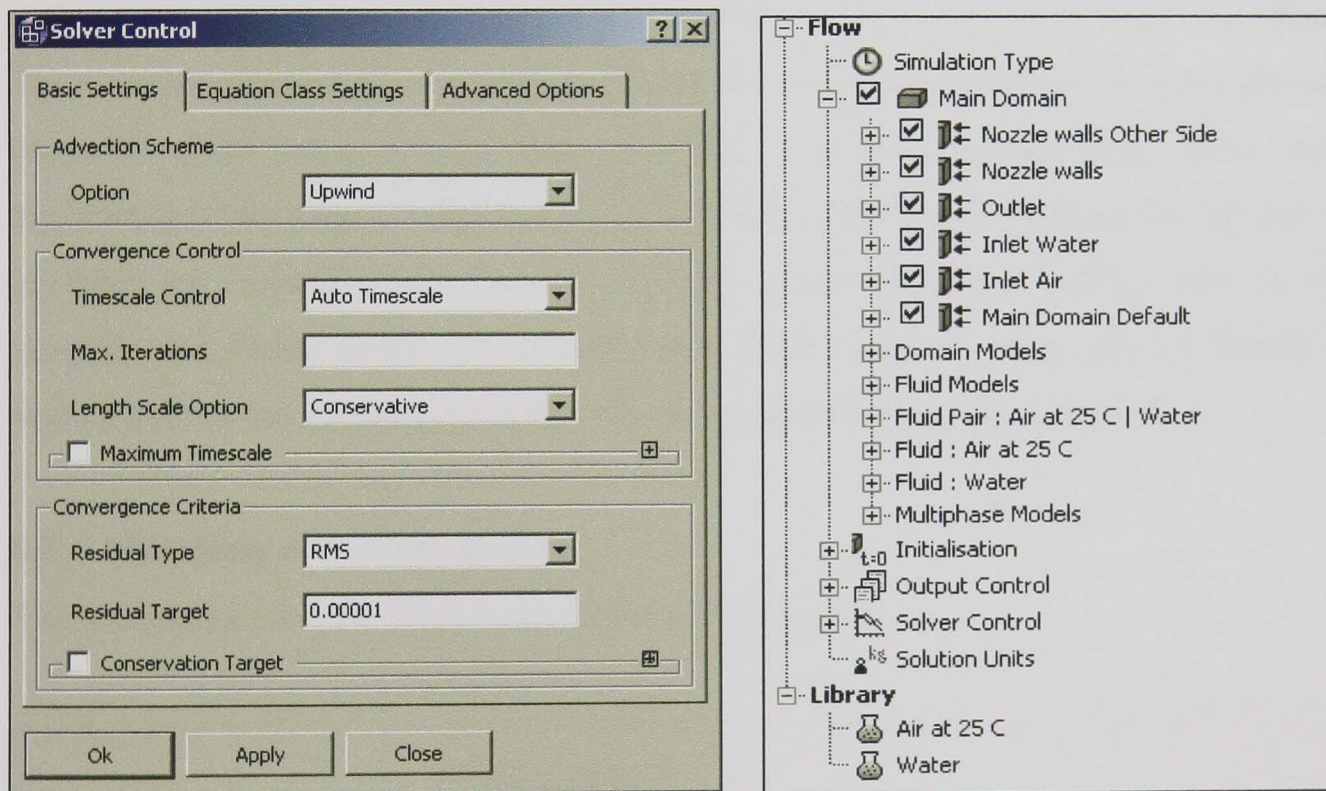


Figure 6-19 Solver criteria for the solution

Figure 6-20 Completed simulation tree from CFX-Pre

6.5.4 Post-processing

Post processing followed the patterns as stated earlier in this work. The plots show images with the z -axis as the main fluid direction and the x and y -axis as the traverse cross-sections of the flow. The graphs illustrated detail the values and axis in which the results are plotted on.

Boundary Conditions			
Boundary Name	Type	Values	Additional
Inlet Air	Inlet	0m/s	Air 1/ Water 0
Inlet Water	Inlet	5/ms	Air 0/ Water 1
Outlet	Opening	Rel. 0 Pa	Both air and fluid may leave the domain
Nozzle Walls	Wall	No slip	No slip solid boundary
Nozzle walls o/s	Wall	Thin surface	Thin surface partner for 'Nozzle Walls'

Table 6-3 Boundary conditions for Rouse based nozzle with free surface flow

6.6 Three dimensional nozzle-exit-flow analyses

This section of work uses ANSYS CFX to model the internal and external flow profiles for a range of nozzles and fluid situations with differing conditions. It includes analyses of the nozzle proposed by Webster et al (1995a) with other nozzles tested for comparison. The simulation is then tested against experimentation to check its validity. The simulation attempts to predict the behaviour of a jet exhausting from a nozzle into a quiescent fluid (air). As the flow emerges into this external fluid, shear layers originating at the orifice of the nozzle are created. These layers separate the fast moving jet from the external fluid, and at a certain critical Reynolds number they become unstable and break down due to turbulence. The length at which the jet breaks up, known here as the coherence length, was the point of interest for this work.

6.7 Modelling of multiphase flow

The simulation process follows the theme in Figure 6-21.

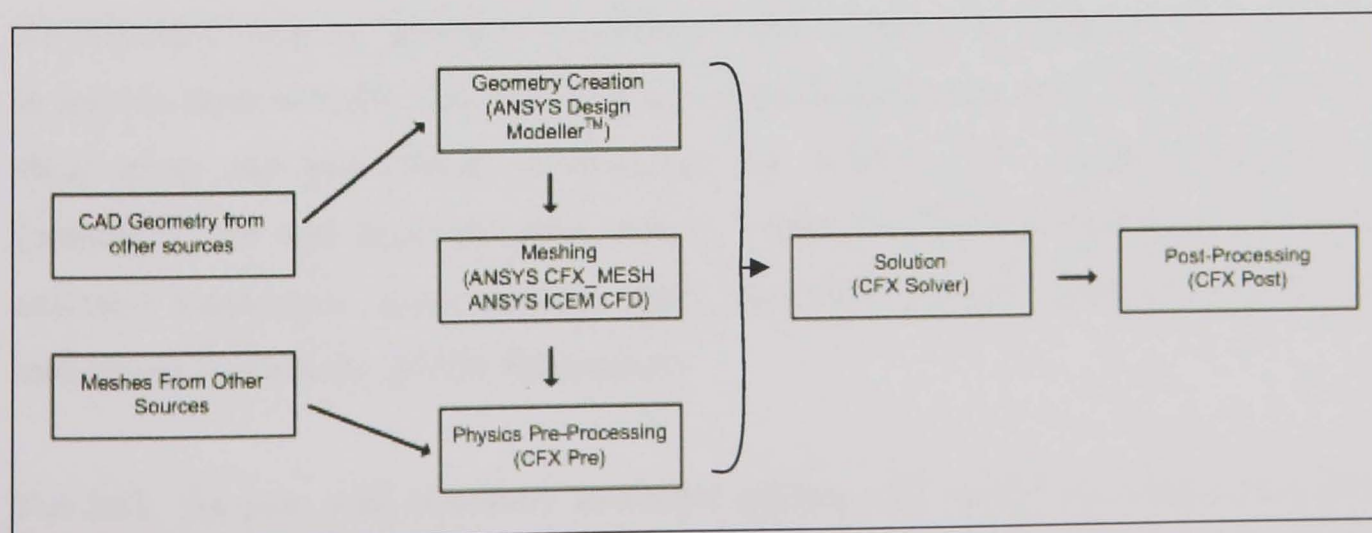


Figure 6-21 Flow chart for simulation setup

6.8 Turbulence models

The standard k - ε model is used in the prediction of most turbulent flow calculations because of its robustness, economy, and reasonable accuracy for a wide range of flows. However, the model performs poorly when faced with non-equilibrium boundary layers. It tends to predict the onset of separation too late as well as to under-predict the amount of separation (ANSYS 10.0, 2005). Separation influences the overall performance of many devices, such as diffusers, turbine blades and aerodynamic bodies. Separation also has a strong influence on other effects, such as wall heat transfer and multi-phase phenomena (important to the later work on jet break-up presented in this work). Predicting reduced separation usually results in an optimistic prediction of machine performance. In some applications, this can have dangerous consequences, a notable example being the prediction of wing stall on airplanes.

6.8.1 Shear stress transport model

To solve this problem, new models have been developed. One of the most effective is the shear stress transport (SST) model of Menter (1993). The model works by solving a turbulence/frequency-based model (k - ω) at the wall and k - ε in the bulk flow. A blending function ensures a smooth transition between the two models. The SST model performance has been studied in a large number of cases. In a NASA technical memorandum (Bardina et al 1997), SST was rated the most accurate model for aerodynamic applications. This work is contained in ANSYS CFX now with robust near wall predictions for turbulent flows.

6.8.2 ANSYS CFX software's near-wall treatment

An important issue in turbulence modelling is the numerical treatment of the equations in regions close to walls. The near-wall formulation determines the accuracy of the wall shear stress and heat transfer predictions. The ANSYS CFX product introduced a formulation for wall function-based models, called scalable wall functions. This only available formulation allows users to apply arbitrarily fine grids without violating the underlying logarithmic profile assumptions.

For SST, the new wall boundary treatment exploits the simple and robust near-wall formulation of the k - ω model and switches automatically from a low-Reynolds number

formulation to a wall-function treatment based on grid density. The user can then make optimal use of the advanced performance of the turbulence model for any given grid.

Figure 6-22 and Figure 6-23 show streamlines for a plane diffuser flow for both models. The SST model predicts the separation zone in close agreement with data, whereas the $k-\varepsilon$ model fails to capture the physics of this flow entirely.

The bounding box was formed of openings (Figure 6-24) instead of walls to allow entrainment of the air into the water and to allow the water to pass through the end of the chamber without recirculation. This was a breakthrough for the model - results are presented herein. The box was extended and a mesh convergence study carried out for the velocity at the output until a steady result was reached. Replication of the mesh allowed for simulation of each of the different nozzles to achieve the required results.

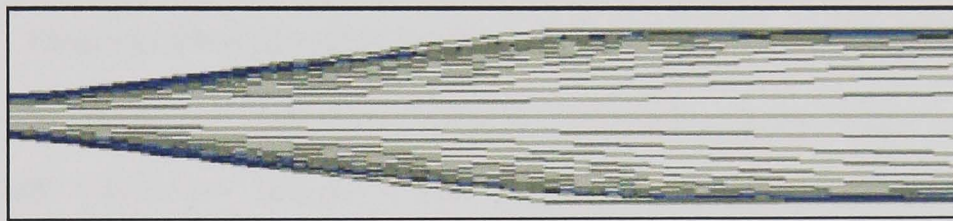


Figure 6-22 $k-\varepsilon$ model prediction of diffuser flows (ANSYS User Guide 2005)

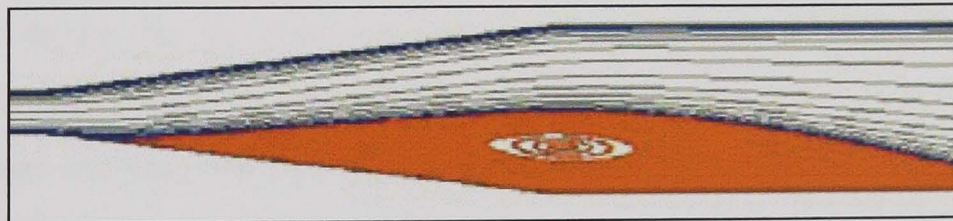


Figure 6-23 SST model prediction of diffuser flows (ANSYS User Guide 2005)

6.9 Results

Experimentation showed that the slant nozzle performed reasonably well in comparison with the Rouse based nozzle. It also outperformed the remaining nozzle types tested. Therefore, this nozzle is examined first. This section contains the results for several nozzle types. The results presented are representations of an advanced working simulation and the flow patterns are concerned primarily with the jet coherence length of the nozzles. Points of interest include the region after the exit to the nozzle and any

losses within the nozzles. The model is very close to the physical system and is unbounded by the flow chamber within which the multiphase flow develops.

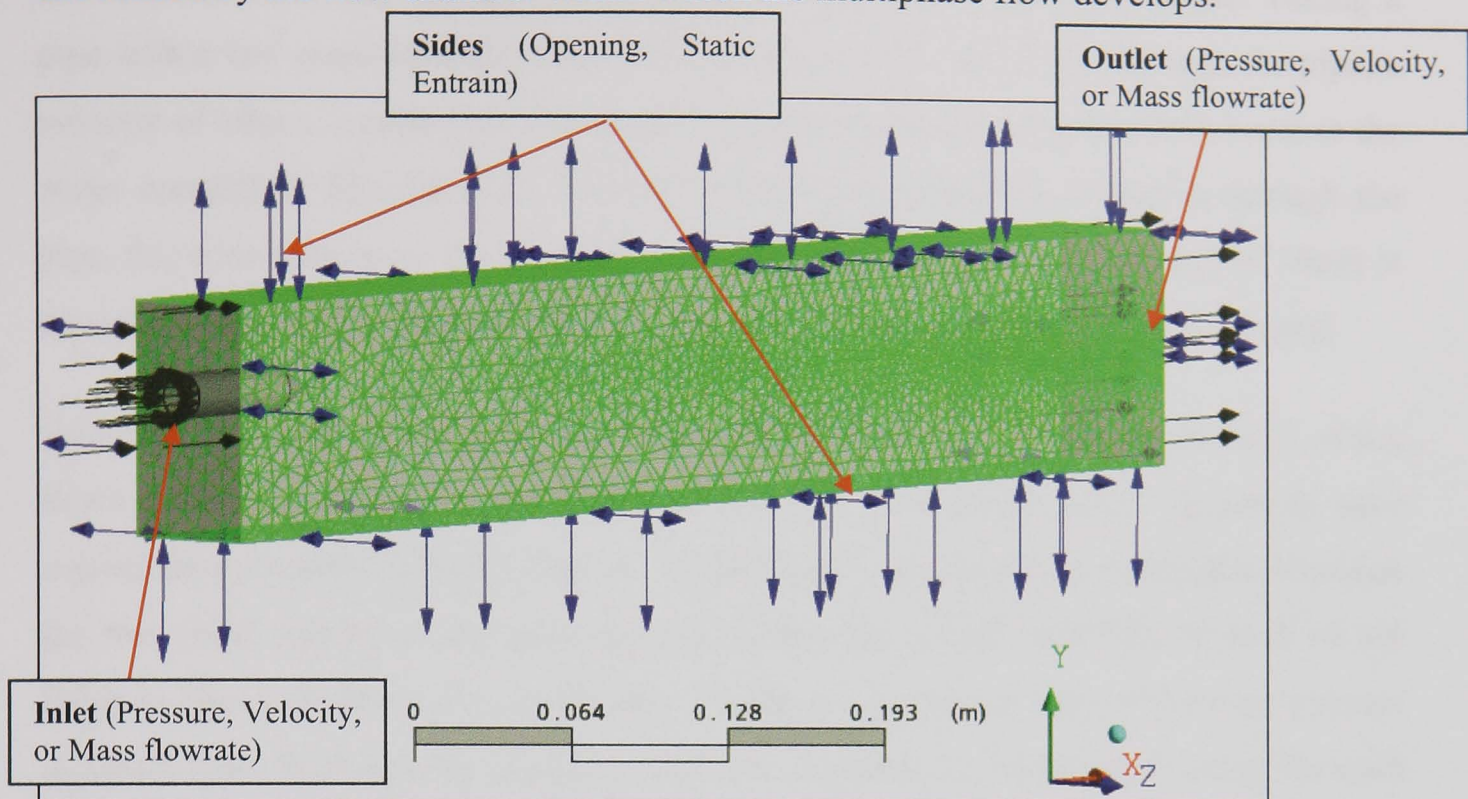


Figure 6-24 Model with adaptive meshing and boundary conditions

To analyse the range of coherence length, differing inputs were analysed. For comparison and validation through experimentation, the results presented are for the 2.5mm \varnothing opening slant nozzle with an inlet flowrate of 10 l/min, in the first instance, and 20 l/min giving jet velocities of ≈ 3 m/s and 6 m/s respectively.

Figure 6-25 shows the jet emerging from the nozzle and flowing into a chamber containing air. The free surface model employed allows the water to interact with the air at the boundary between the two. The velocity exhibits the expected behaviour in that the jet becomes wider due to overall spreading of the fluid however, the peak velocity decreases. It shows the vector plot with the general flow to right of the chamber with a drop in the y-direction due to the slow fluid speed and gravitational effects employed within the model. This drop in flow was observed within experimentation, as expected with gravity, and visually the model correlates with those experimental results examined.

On closer examination of the results, although the jet width and spreading appears to be comparable to experimentation, the peak velocity area of the flow appears to break up earlier than the experimental value. To highlight this clearly, Figure 6-26 shows the velocity vector plot for this nozzle - only the high volume fraction of water is plotted.

This is known as the ‘superficial velocity’. The difference between superficial velocity and what is intuitively thought of as velocity is explained best by example. Taking a pipe with a 1m^2 cross-sectional area; if water were to flow at $10\text{m}^3/\text{s}$ through the pipe, a velocity of $10\text{m}/\text{s}$ is expected. The superficial velocity would also be $10\text{m}/\text{s}$ because the water completely fills the pipe. Similarly, if flow were applied at $10\text{m}^3/\text{s}$ through the pipe, this time with air as the medium, a velocity (and a superficial velocity) of $10\text{m}/\text{s}$ is expected. This is why single-phase flow has only the one output velocity as a visual.

However, the same situation but now with a mixture of $5\text{m}^3/\text{s}$ of water and $5\text{m}^3/\text{s}$ of air, flowing through the pipe, creates a multiphase flow. Both phases, taken separately, have superficial velocities of $5\text{m}/\text{s}$ ($=5\text{m}^3/\text{s} / 1\text{m}^2$). If there was no slip or interaction between the two (both moved at the same velocity), then the actual velocities of both of the fluids is $10\text{m}/\text{s}$. Without slip, each phase would occupy 50 per cent of the pipe’s cross-sectional area. With slip the situation becomes complex, as the actual velocity for each phase differs. Within CFX, one output of the simulation is the quantity termed ‘superficial velocity’, defined as ‘Fluid Volume Fraction’ (the ration of the two fluid media) multiplied by ‘Fluid Velocity’. The components of this vector variable are also available as scalar variables (e.g. Fluid Superficial Velocity X).

Figure 6-26 shows the superficial velocity of water for the slant nozzle. From this plot, it is observed that the main body of flow follows the flow pattern seen in the vector plot (Figure 6-25); however, the area at peak velocity is relatively small. This area appears to be only 80-100mm in length. The expected value of this is much larger. Further investigations into the reasons behind this apparent sudden break up involved analysing the free surface interface between the two phases. Figure 6-27 shows the superficial velocity of the air within the field. As expected, the air appears not to influence the flow within the nozzle or within the area of coherence of the jet. However, the air entrained seems to begin immediately to affect the central core of the flow upon a small distance from the nozzle orifice. This is unexpected, as the air interaction should only affect the free surface interface. With unstructured meshes and those with limited numbers of elements, this is a common occurrence. Within this model, to overcome this problem, two additional levels of mesh refinement were performed in the solver process. The areas of mesh refinement are seen within Figure 6-28.

After the mesh refinement, several plots were created to investigate the areas within a certain velocity boundary. The velocity of water in the vertical plane (y-direction) is shown in Figure 6-29 where the majority of the flow environment is at the same velocity. This velocity is approximately zero, as expected, and confirms that only a small amount of water is escaping from the edges of the jet, adjacent to the nozzle exit.

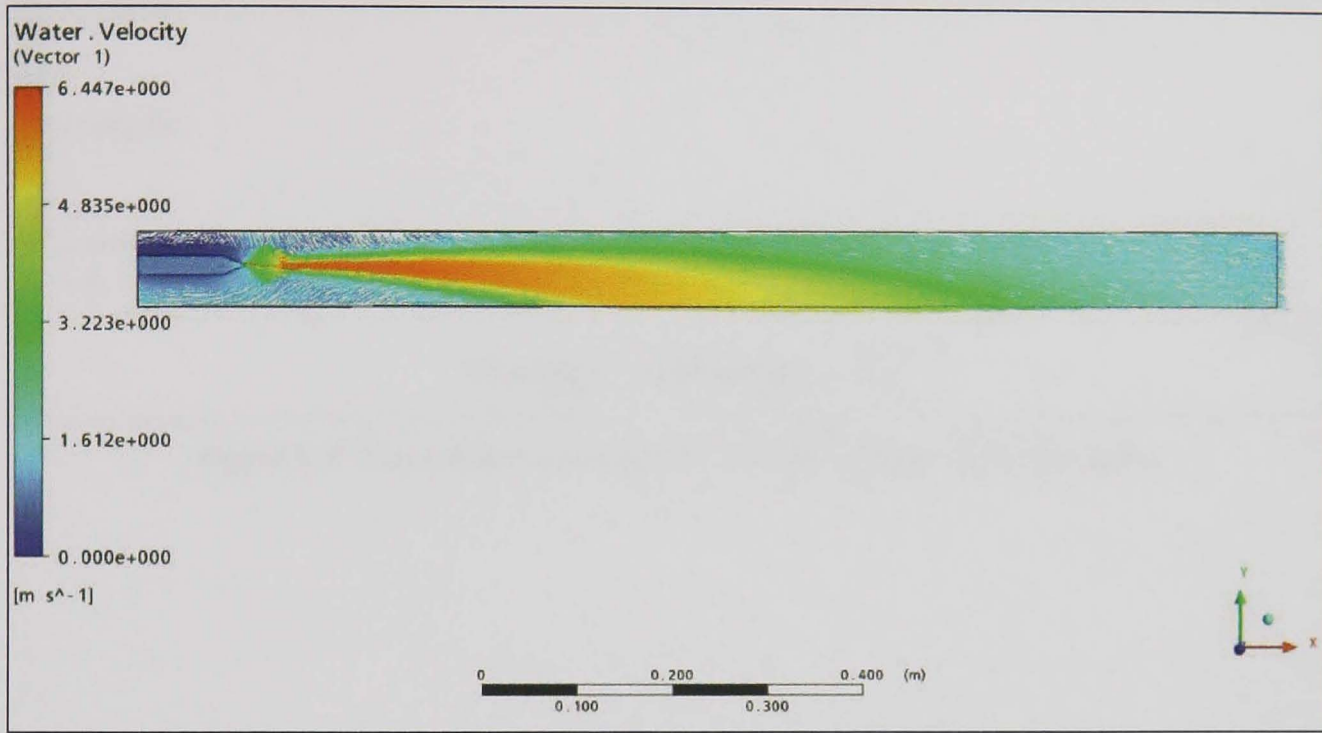


Figure 6-25 Vector plot for the slant nozzle at 10 l/min

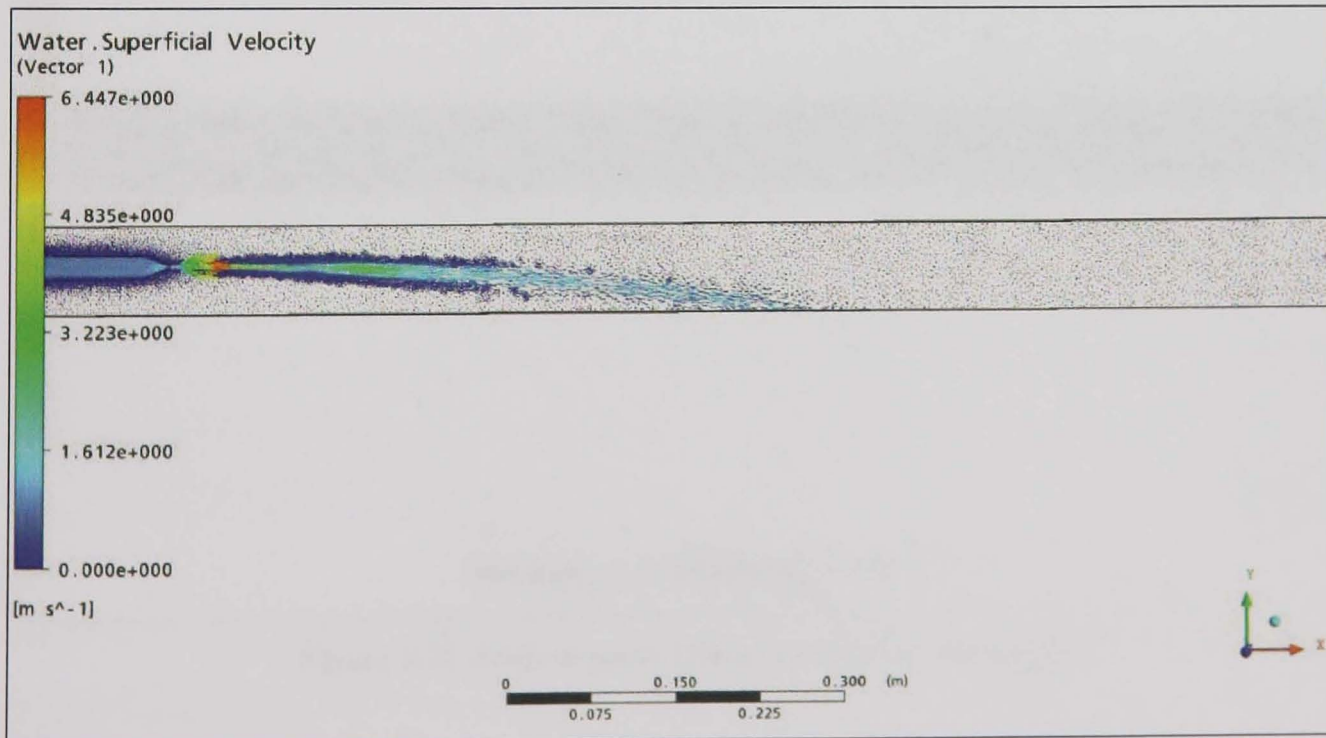


Figure 6-26 Superficial vector plot for the slant nozzle at 10 l/min (water)

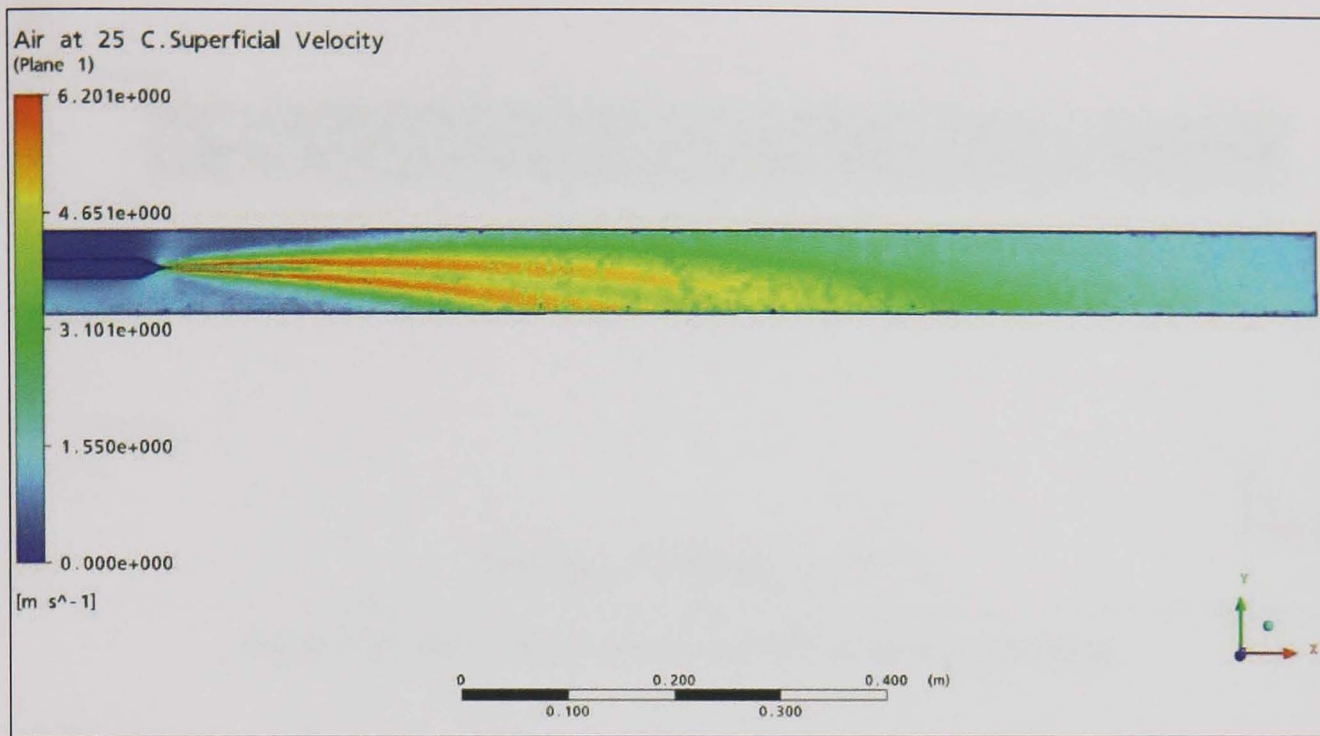


Figure 6-27 Superficial vector plot for the slant nozzle at 10 l/min (air)

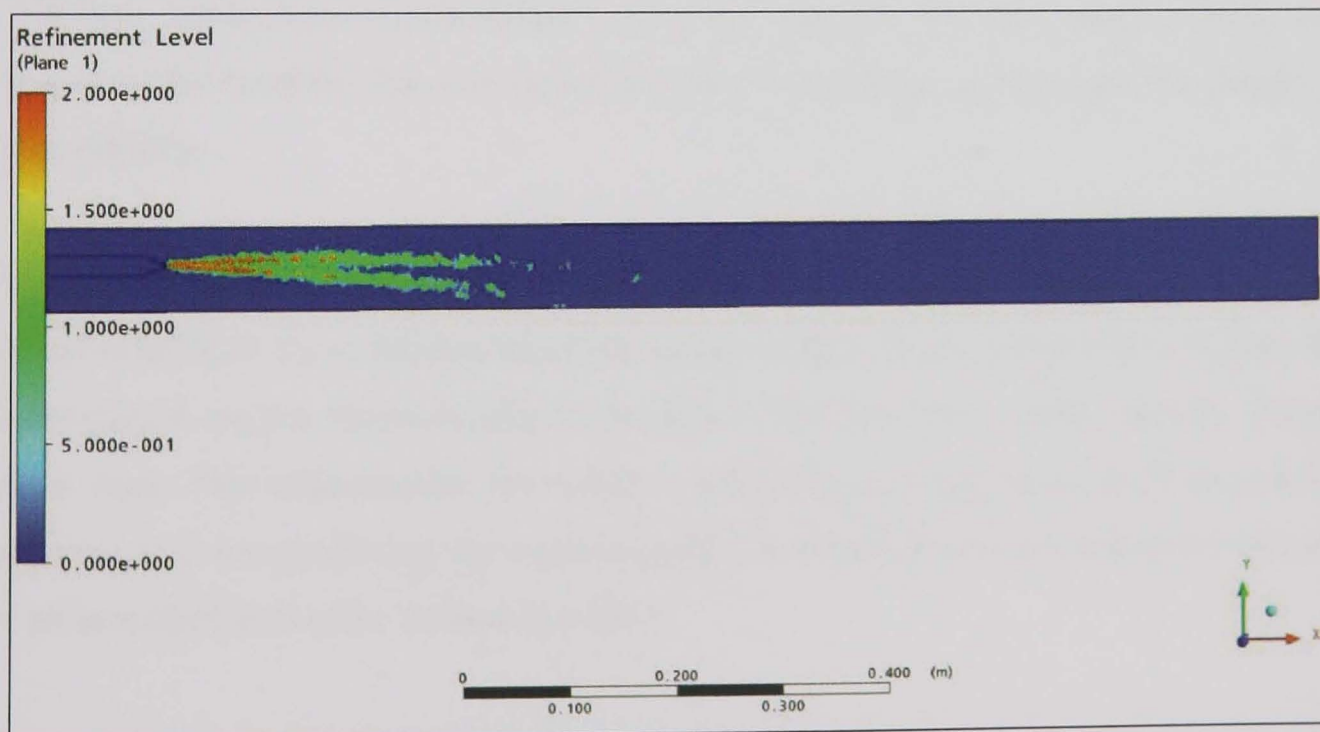


Figure 6-28 Areas of mesh refinement in the slant nozzle

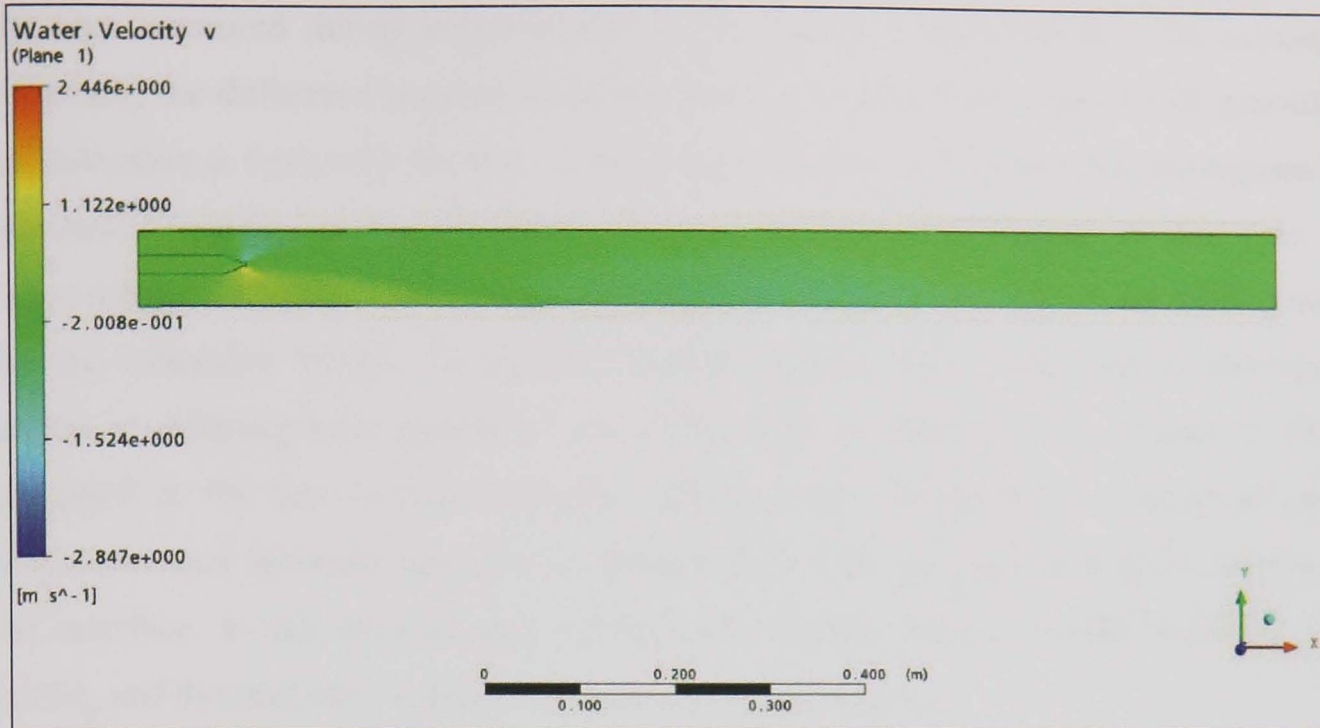


Figure 6-29 Water velocity in the vertical direction (y direction)

For visualisation of jet coherence, and to investigate the lengths at which the fluid stream reaches with a given speed, an 'Isosurface' plot was created. An Isosurface is a surface upon which a particular variable has a constant value, called the 'level'. For instance, an Isosurface of pressure would be a surface consisting of all the points in the geometry where the pressure took a value of a selected value e.g. three bar. In ANSYS CFX-Post, Isosurfaces can be defined using any variable. For this work, velocity was chosen as the variable; this was varied between 4 and 6m/s to highlight the change in peak velocity.

Figure 6-30 shows an Isosurface, of the 2.5mm slant nozzle at 10 l/min, at 4m/s. The region extends to about 800mm from the nozzle orifice. This corresponds well with the experimental results; however, this is the area of the flow not at peak velocity (5m/s), but at 4m/s. This indicates that the model is predicting the path of the fluid accurately; however, it is not predicting the experimentally determined velocity due to the amount of air entrained at the free surface boundary.

Figure 6-31 shows an Isosurface of the same nozzle at 5m/s. This region looks similar to that of the flow at 4m/s however; the region is reduced in both length and width. This stage of the modelling does however reveal a useful tool for accurate positioning of grinding fluid nozzles. The results of this observation and possibilities for future advancement of this technique are contained within chapter 10. This is approximately

the area measured during experimentation but with a small reduction. To compare accurately the difference between experimentation and simulation, Figure 6-32 provides an Isosurface at 6m/s with the true ‘peak velocity’ region as it contains all the regions at maximum velocity within the flow, i.e. flow at 6m/s. The length of this area is approximately 200mm. This shows once more the under-prediction of the CFX model for the coherence length. To test this further, analysis was performed on the same nozzle at differing inlet speeds to see if this had an effect on the amount of flow entrained at the free surface boundary. Results were obtained for a range of inlet conditions, and the modelling was performed both with and without surface tension at the interface. It was deemed that omitting the surface tension would invalidate the model, and this had only a small affect on the overall results.

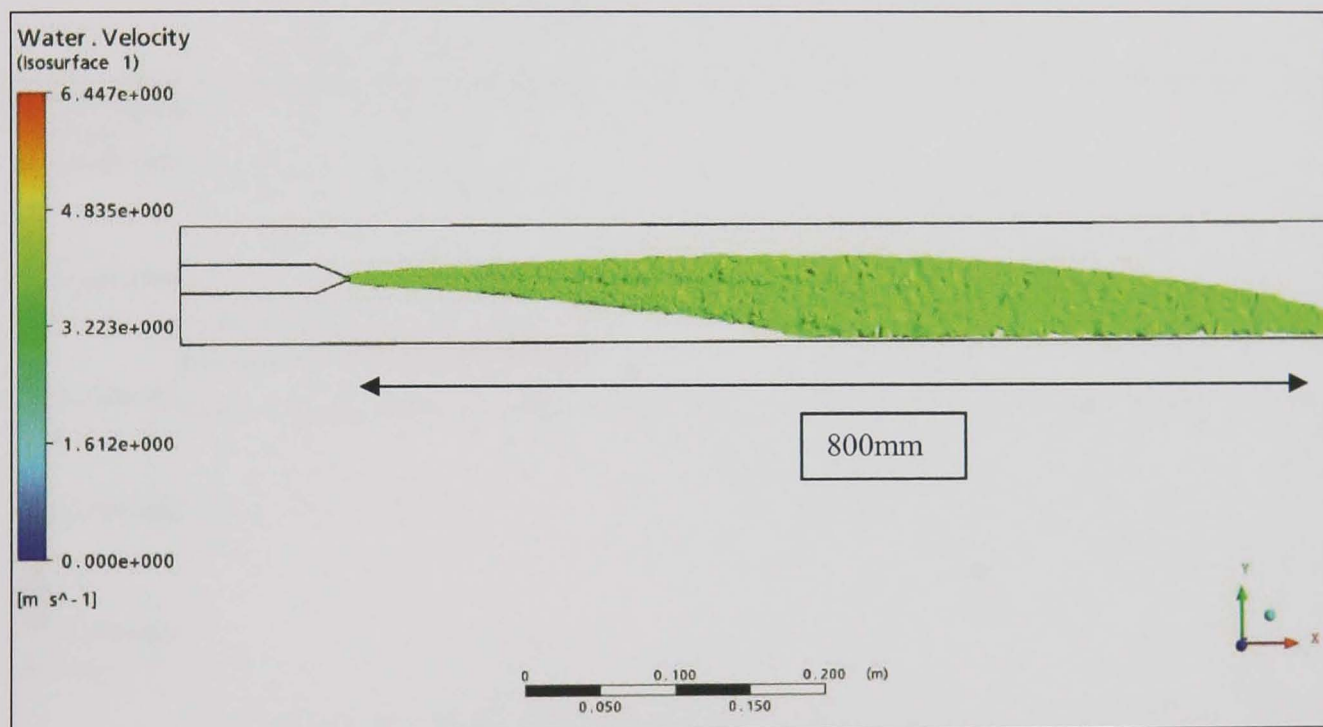


Figure 6-30 Isosurface for velocity at 4m/s

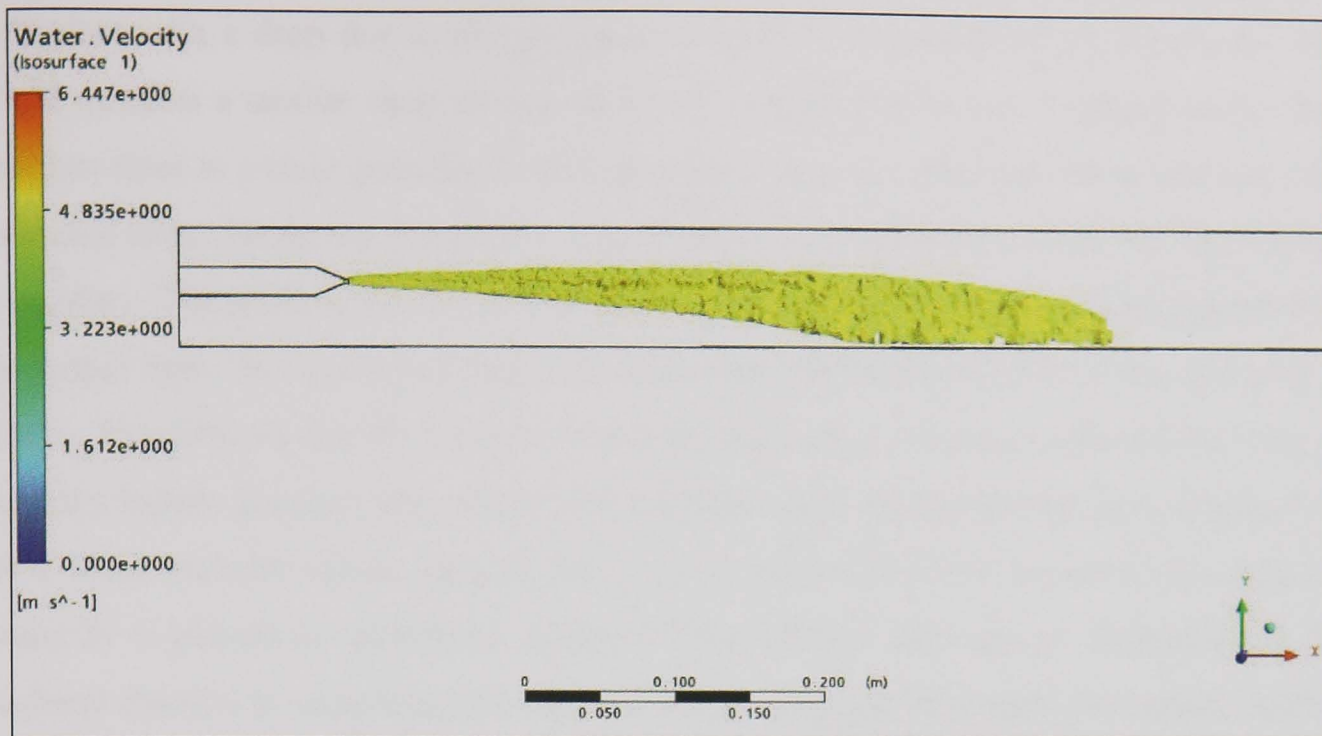


Figure 6-31 Isosurface for velocity at 5m/s

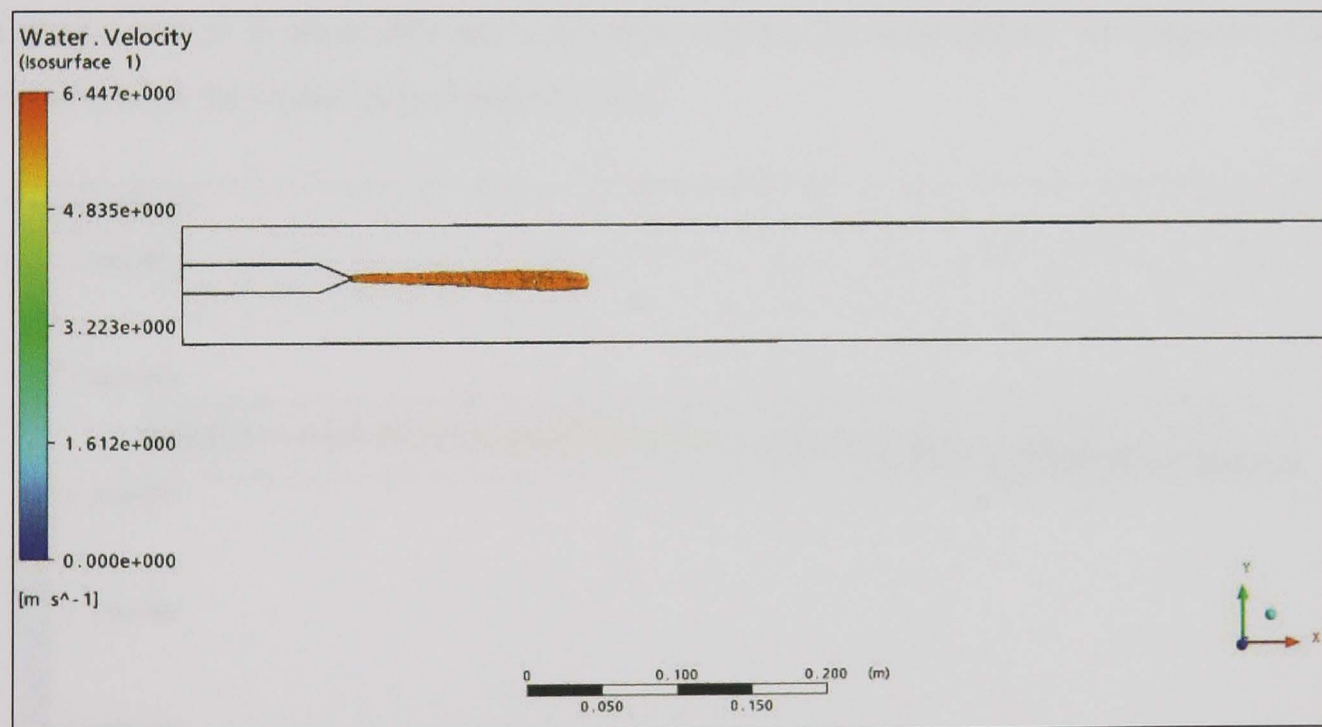


Figure 6-32 Isosurface for velocity at 6m/s

To test the response of the model to increased velocity from increased inlet flowrate, simulations of twice the initial flowrate are presented. These images show the increased length of the jet with relation to the increased inlet velocity of the fluid.

Figure 6-33 and Figure 6-34 show the jet of fluid at an increased flowrate of 20 l/min, emerging from the nozzle and flowing into a chamber containing air. The free surface model employed allows the water to interact with the air at the boundary between the two. Figure 6-33 shows a velocity vector plot with the general flow to right of the

chamber with a drop due to the gravitational effects employed within the model. The fluid exhibits a similar drop to that observed in experimentation. Looking at the flow pattern there is a clear path the fluid takes with a decrease in overall flow velocity with distance from the nozzle due to the effects (such as drag) of the air at the free surface boundary. The point at which the fluid leaves the simulation domain within Figure 6-33 is further from the nozzle exit than that of the flow within the results for the nozzle at 10 l/min. This follows that the increased flowrate leads to an increase in the distance the jet reaches before gravitational effects pull the fluid from the prediction path. Figure 6-34 is a water velocity-vector plot for the slant nozzle at 20 l/min, however this time the velocity is plotted as superficial velocity. This refers to the velocity multiplied by the volume fraction at sample points. From this plot, it is seen that there is a central core of fluid, however the entrainment of the air is, too large and reduces the speed of this central core of fluid in a shorter time than that observed within experimentation. From Figure 6-34, it is clear that the main body of the jet does follow the observed flow pattern from the vector plot (Figure 6-33).

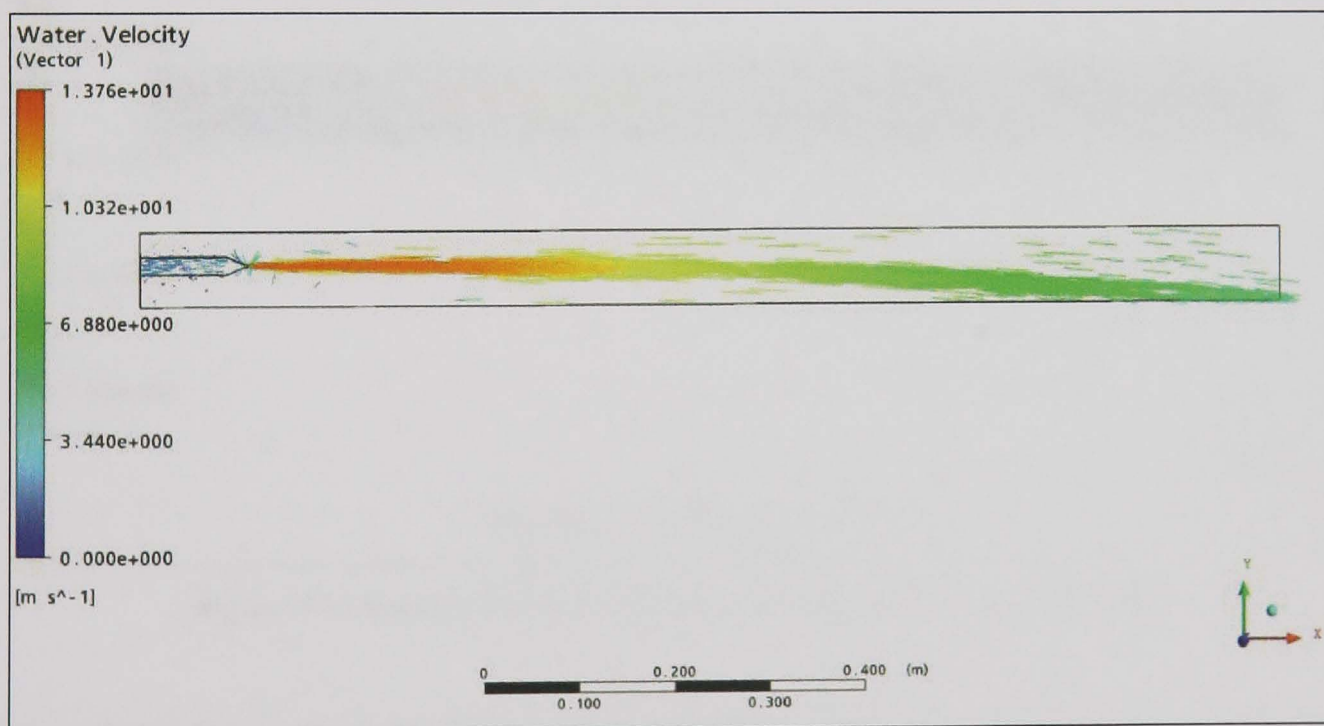


Figure 6-33 Vector plot for the slant nozzle at 20 l/min

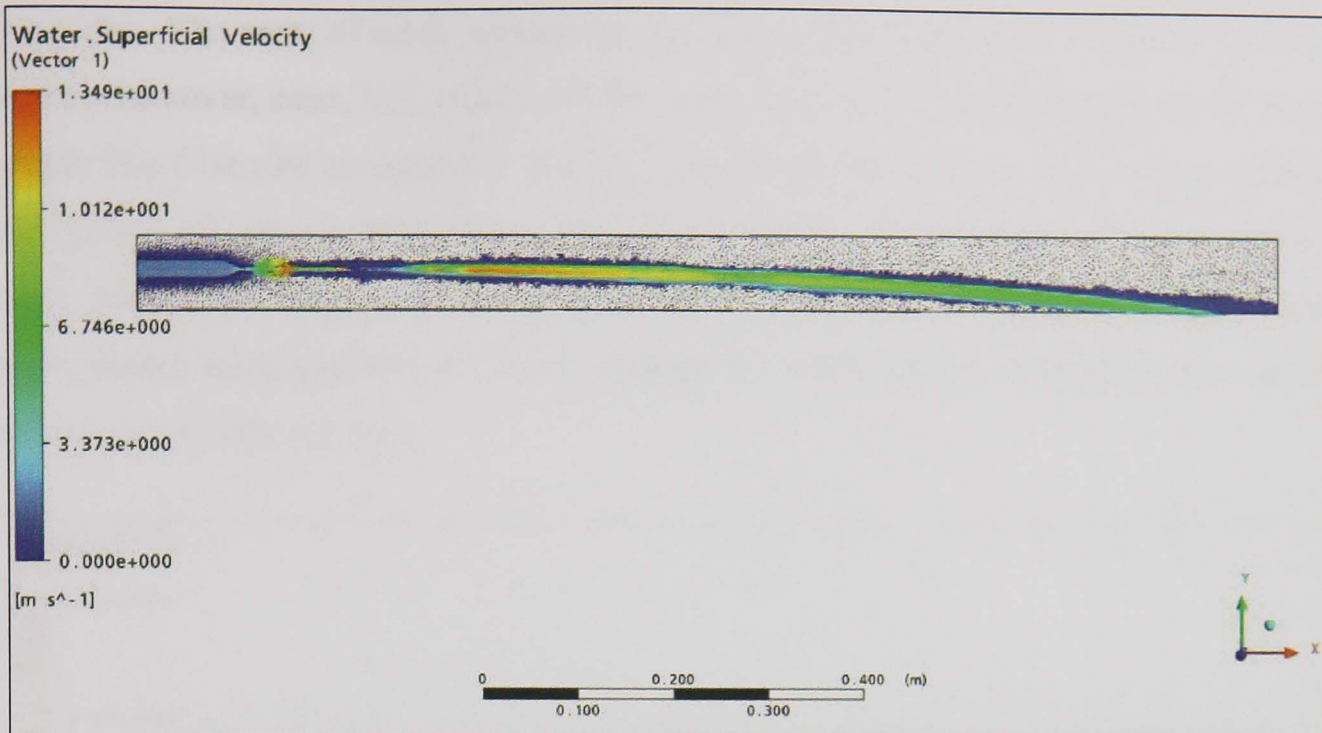


Figure 6-34 Superficial velocity vector plot for the slant nozzle at 20 l/min (water)

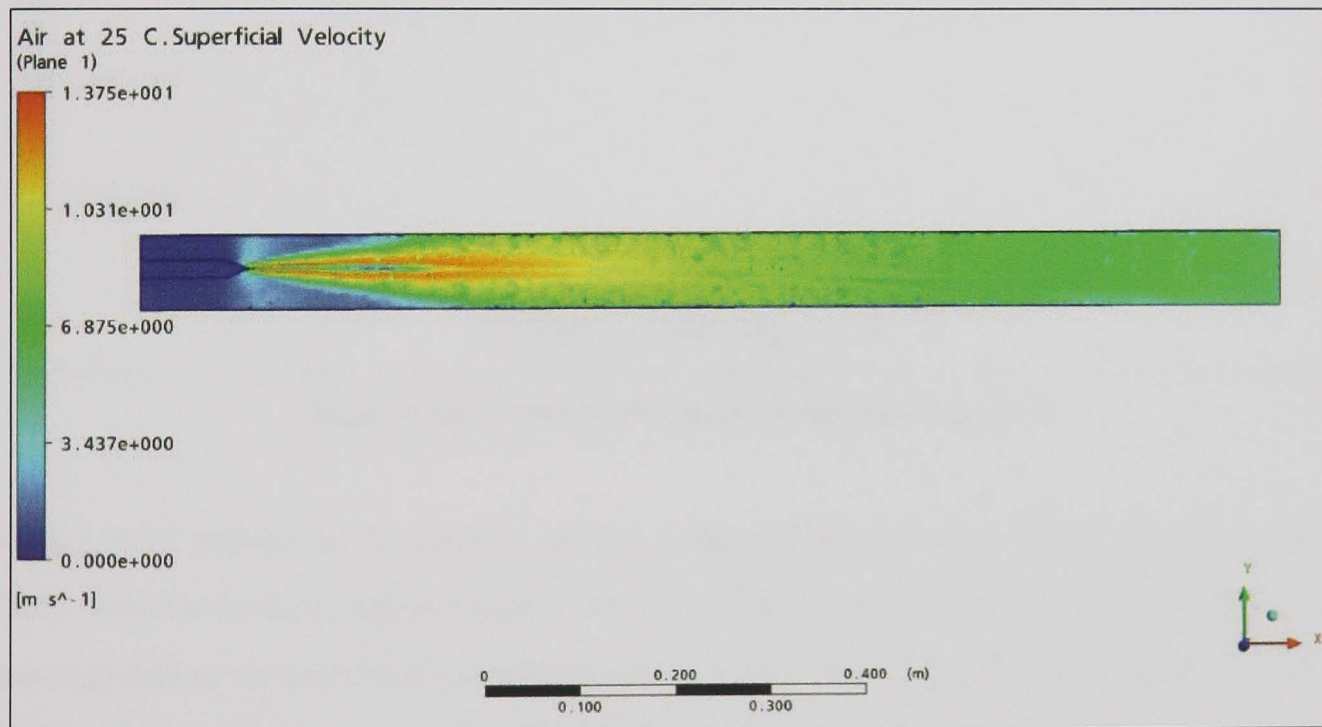


Figure 6-35 Superficial vector plot for the slant nozzle at 20 l/min (air)

Figure 6-35 shows the superficial velocity of the air within the field. Analysing this, the air appears not to influence the flow within the nozzle or within the area of coherence of the jet, as expected. From Figure 6-35 it is apparent from the two red areas either side of the jet that the air is close to the central core velocity. Bearing in mind that this is the superficial velocity, and therefore multiplied by the volume fraction, the model predicts in this region, that there is a large amount of air. This is expected as from the previous example, as the air interaction affects the free surface interface. Within this model, to try to overcome this problem, two additional levels of mesh refinement were performed

in process. The areas of mesh refinement are seen within Figure 6-36. A lot of this air is present however, near, but outside of the interface that has been dragged up to the jet speed. The first plot investigated was the velocity of water in the Y-direction. Looking at Figure 6-37, the majority of the flow environment is at the same velocity. There is some small side leakage at the exit of the nozzle, but the majority of the model environment analysing the exit flow, appears the same colour, indicating this zero Y-component of velocity area.

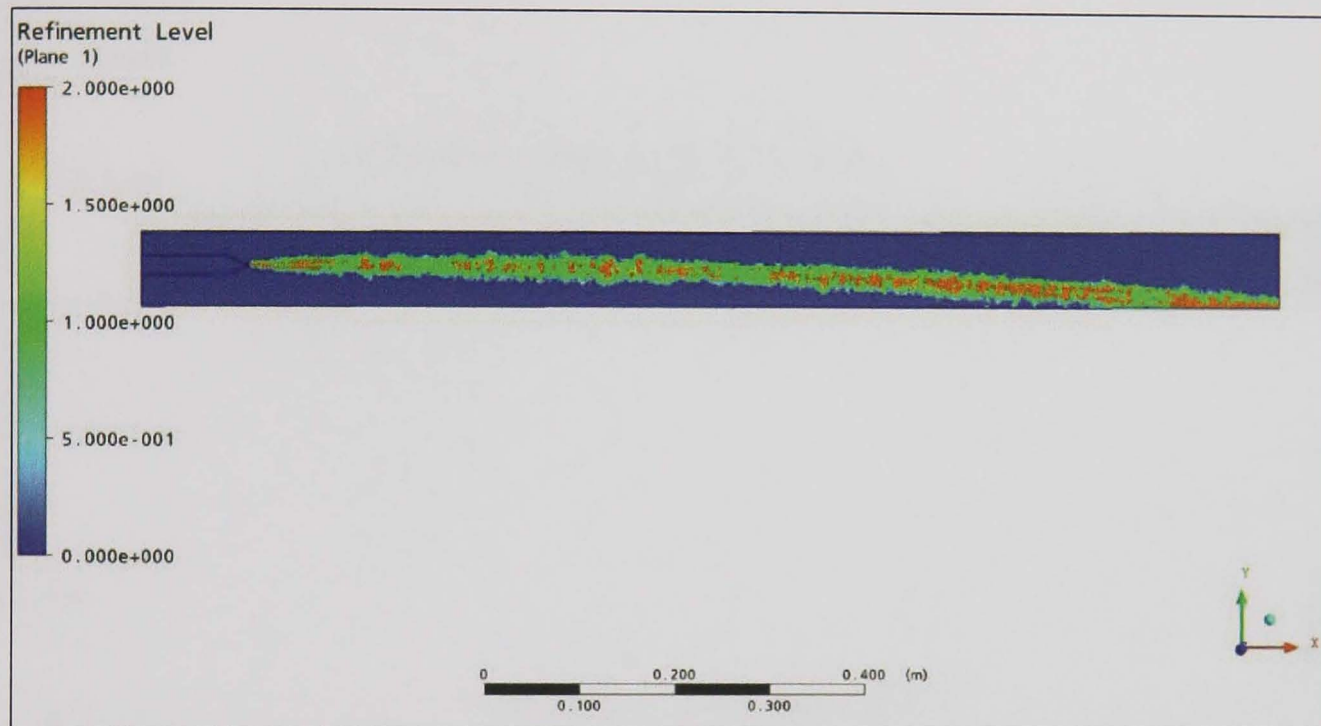


Figure 6-36 Areas of refinement for the slant nozzle jet

Figure 6-38 shows an isosurface, of the 2.5mm diameter slant nozzle at 20 l/min, at 7m/s. The isosurface region extends to about 700mm from the nozzle orifice and this corresponds to those results examined within experimentation; however, this is the area where the jet is not at peak velocity, but only at 7m/s. The actual peak velocity emerging from the jet should lie within the target of approximately 13m/s. This indicates that the model is predicting the path of the fluid accurately; however, it is not predicting the correct velocity due to the amount of air entrained at the free surface boundary. This does however highlight a significant pattern for nozzle design using CFX, as the region shows where positioning of any wheel/workpiece contact, may lay. A point of note within this is also the additional amount of spreading that the air entrainment causes within the jet. It is clear from Figure 6-38 that the jet rapidly expands upon exit of the nozzle orifice indicating significant jet width increase. This is confirmed with the amount of peak velocity break up.

Figure 6-39 shows the 10m/s Isosurface, of the 2.5mm Ø slant nozzle at 20 l/min. This area looks similar to that of the flow at 7m/s however; the region is reduced in both length and width. The region shown is approximately 420mm in length. Comparing this to the experimental results contained within Chapter 8, the model predicts that the area is less than the true region by approximately 100mm; the actual length of the peak velocity from experimentation being 520mm.

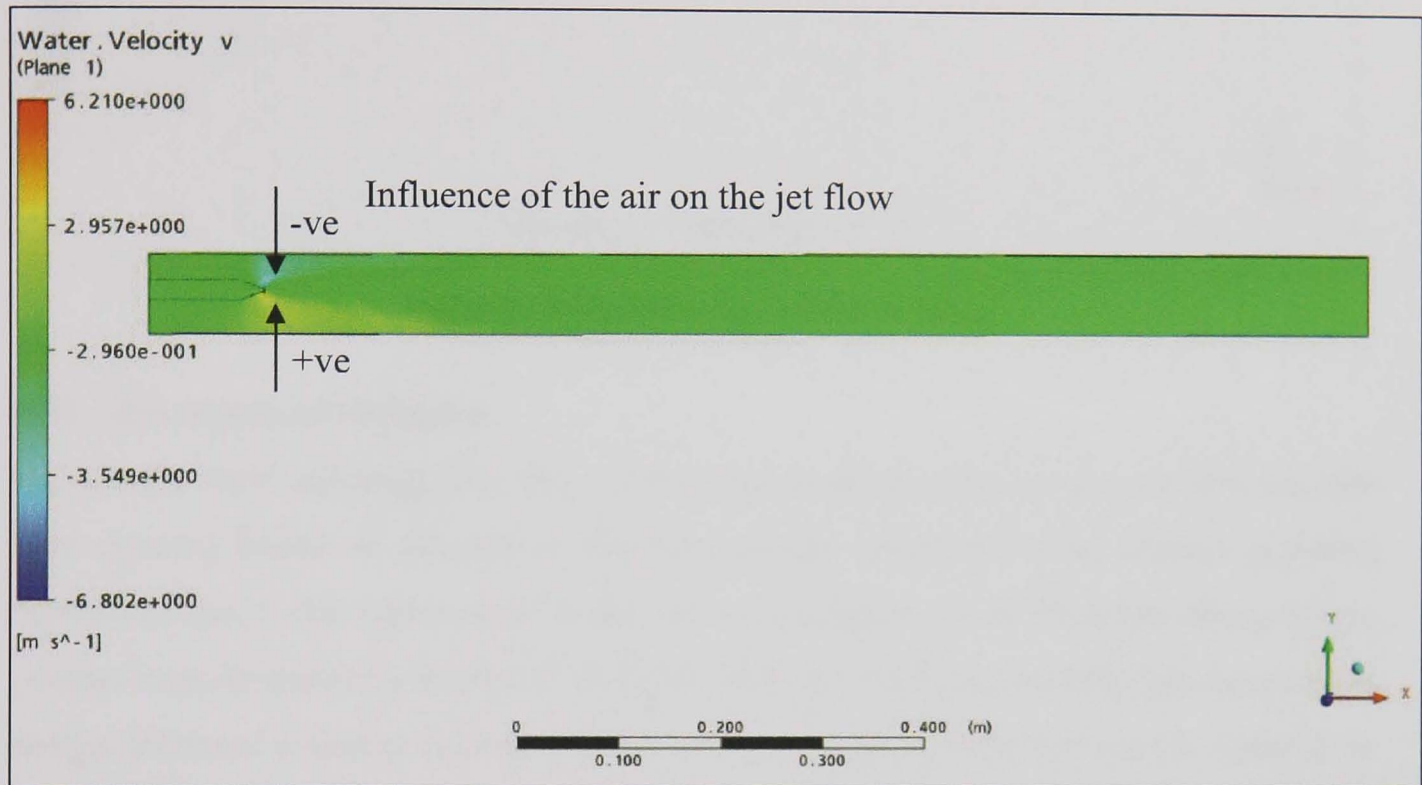


Figure 6-37 Water velocity in the vertical direction (y direction) for the slant nozzle at 20 l/min

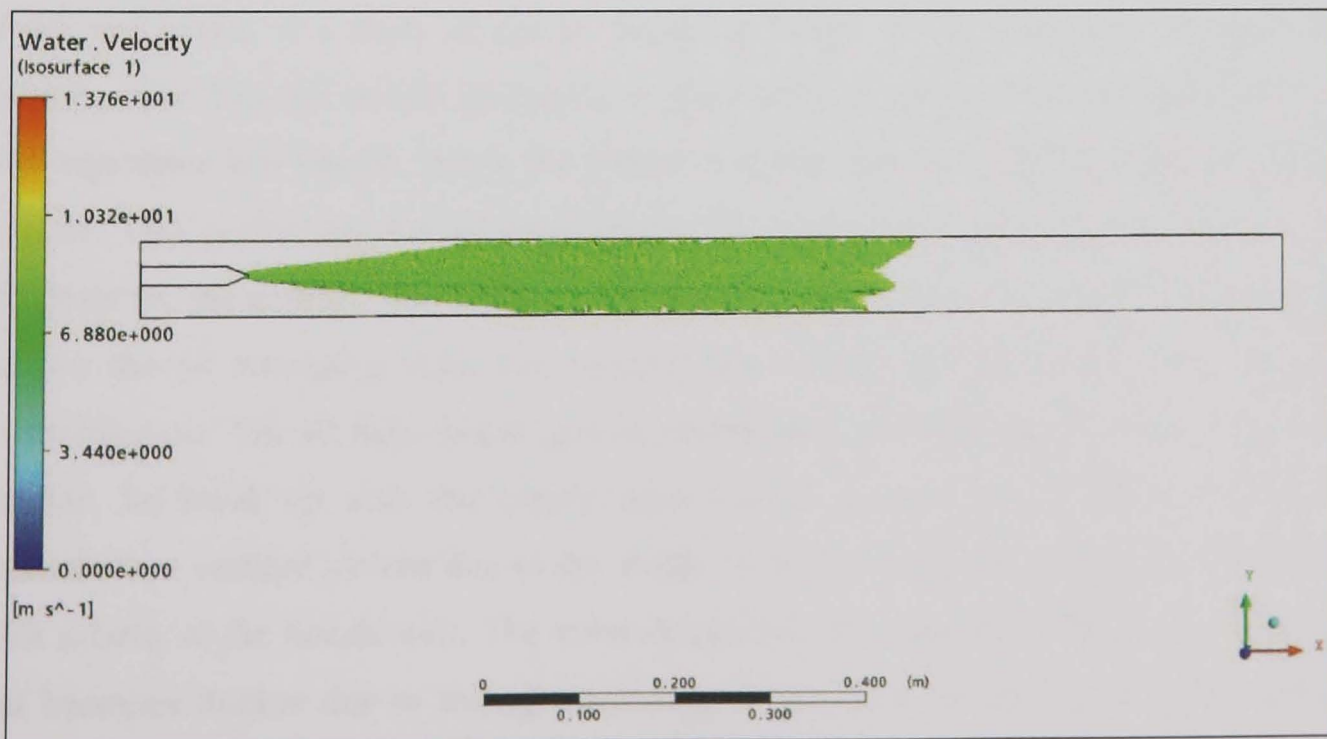


Figure 6-38 Isosurface for velocity at 7m/s

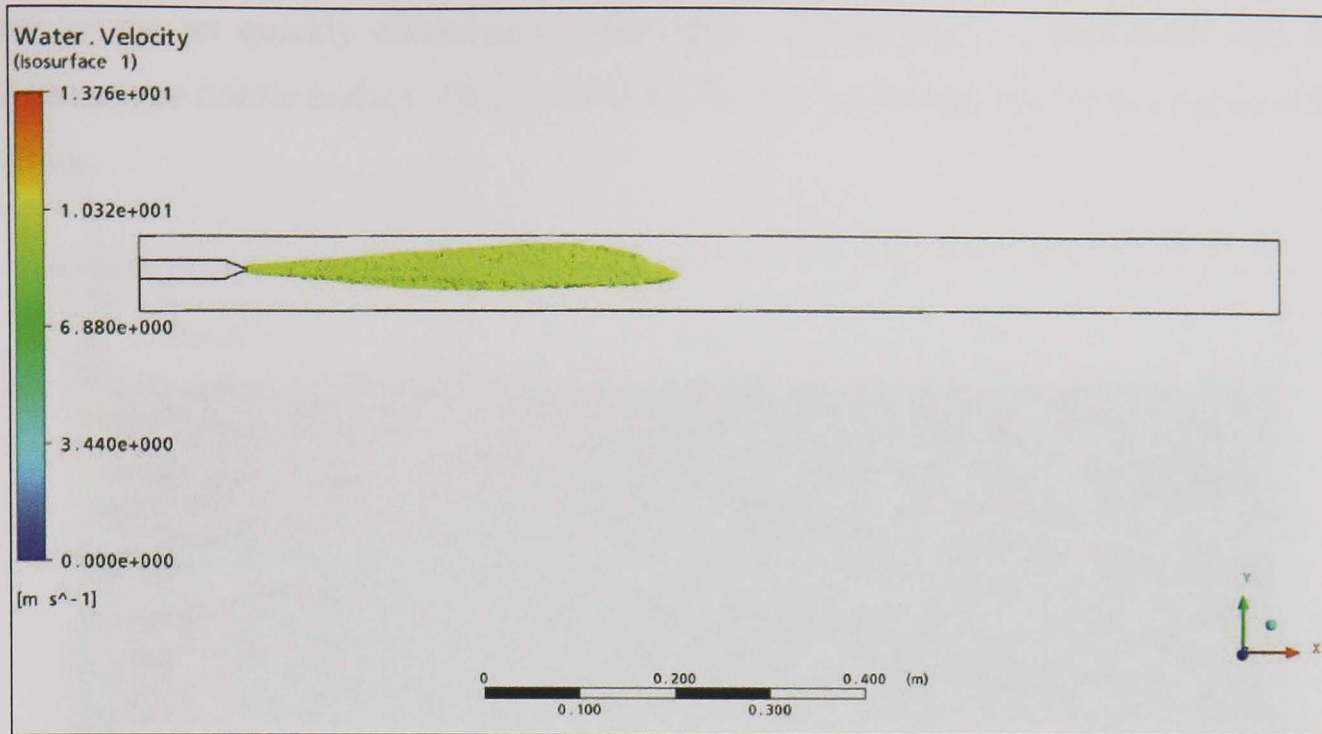


Figure 6-39 Isosurface for velocity at 10m/s

6.10 Slot nozzle investigation

Previously, most investigations into coherent jet nozzles relied on the use of a circular type opening based on the Rouse fire hose design. However, most surface grinding operations use a slot type nozzle to deliver a rectangular jet of fluid into the grinding contact zone. In previous studies (Cui 1995, Webster 1995), the rectangular coherent jet design followed a similar internal profile to the circular coherent jet nozzle. Testing on the nozzle investigated the jet width of the fluid stream with the basic mechanical and visual techniques described in Cui (1995).

Presented herein is a study of the jet break up length of the adjustable coherent slot nozzle. Note that the nozzle illustrated in the results is not the external appearance of the adjustable slot nozzle, but is the internal volume that the fluid occupies inside the nozzle. This is the case for all simulations. The slot nozzle opening was set to 1.6 x 25.5mm for the testing. This is the nozzle exit size used in experimentation. Figure 6-40 shows the jet emerging from the variable slot nozzle and flowing into a chamber containing air. The jet falls due to gravity and spreads in width rapidly from the nozzle orifice. Jet break up with this nozzle type follows the expected path in that the jet spreads in a vertical pattern due to the width of the fluid stream, created by the lateral slot nozzle, at the nozzle exit. The velocity exhibits the expected behaviour in that the jet becomes thicker due to overall spreading of the fluid however, the peak velocity decreases. The peak velocity decrease is rapid with this nozzle. This indicates the useful

part of the jet quickly diminishes indicating a less coherent jet than those with the circular type nozzle bodies. The jet break up for this nozzle appears in the region of 40-50mm.

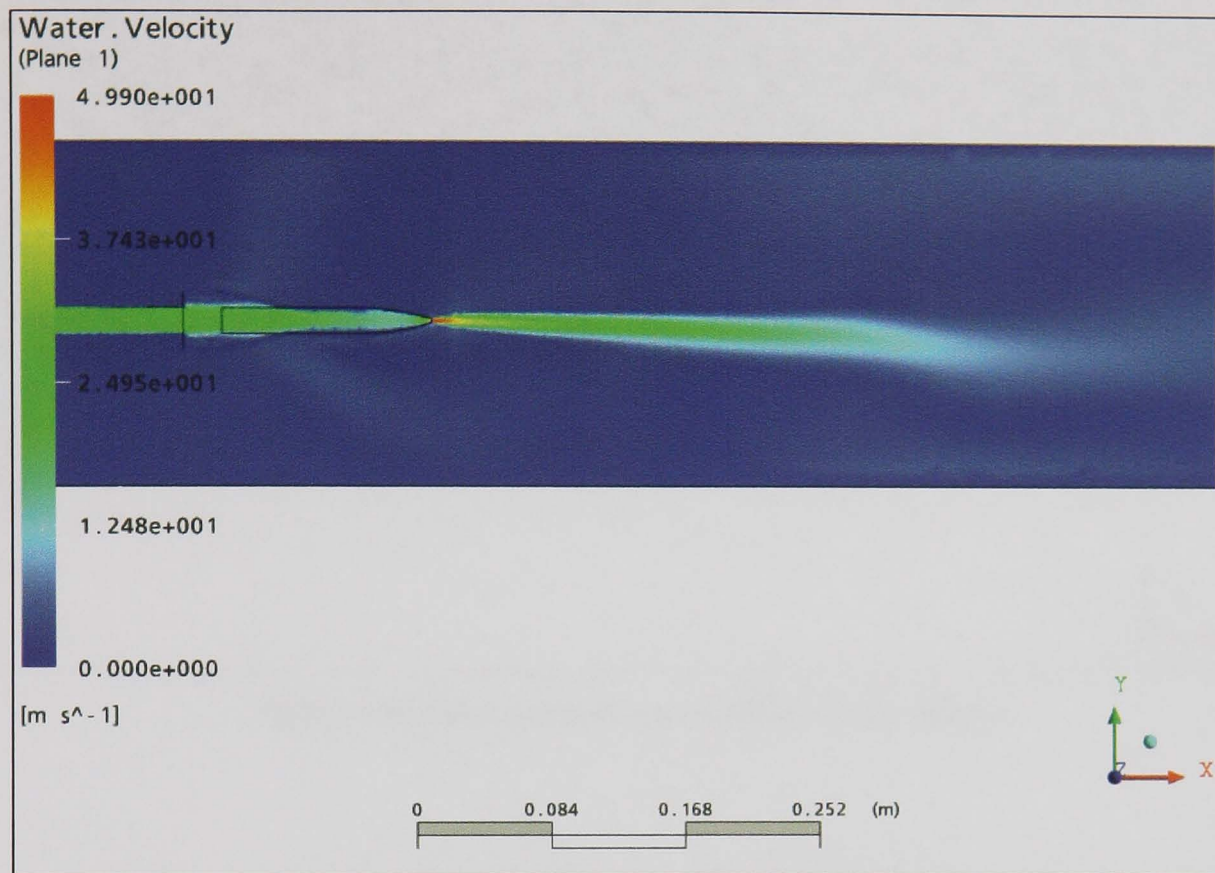


Figure 6-40 Water Velocity on a central slice plane

Figure 6-41 shows the total pressure for the flow simulation. This highlights how the experimental values were obtained. Common theory is that the fluid pressure at the exit of the nozzle drops to zero (relative) at exit of the nozzle. Figure 6-41 shows however that the fluid exerts pressure on itself in the jet as it flows through the air. This pressure is the valued measured with the Pitot tubing in the experimentation used then to convert to velocity. Figure 6-42 shows the velocity profile for water at the exit of the variable slot nozzle. With this nozzle, the velocity profile follows the expected turbulent profile. The fluid velocity in the peak areas differs from one point to the next indicating unstable flow in this region. Figure 6-43 shows the velocity profile of the fluid stream at a range of distances from the nozzle exit. The general trend is a lowering of the overall velocity with a loss of the central peak velocity area. The peak velocity relaxation with the slot nozzle occurs sooner than that of the circular jet nozzles. The total jet width however appears to remain consistent to a point further than this. This agrees with previous research by Cui (1995) but highlights the error in his work - the jet may stay thick, however its useful high velocity part, which penetrates the air barrier, is limited.

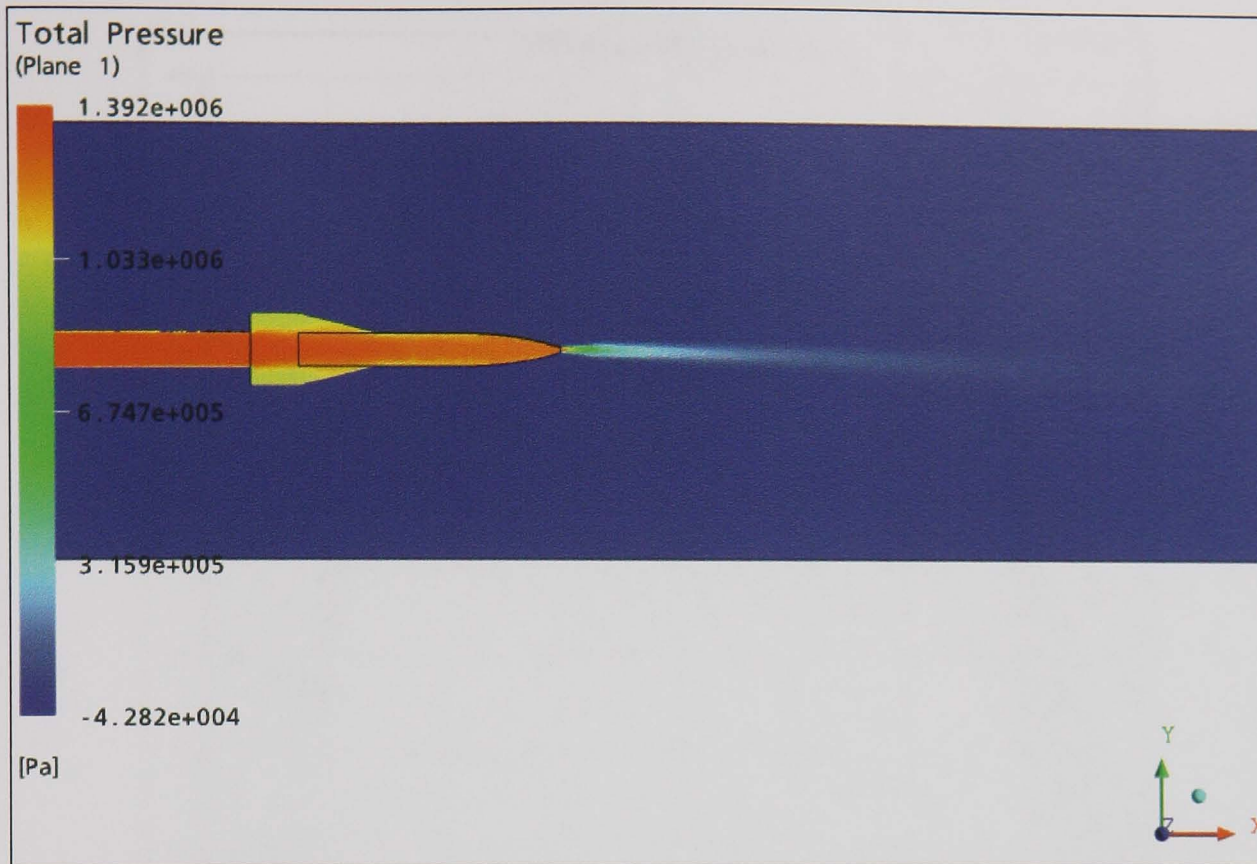


Figure 6-41 Total pressure on a centralised slice plane

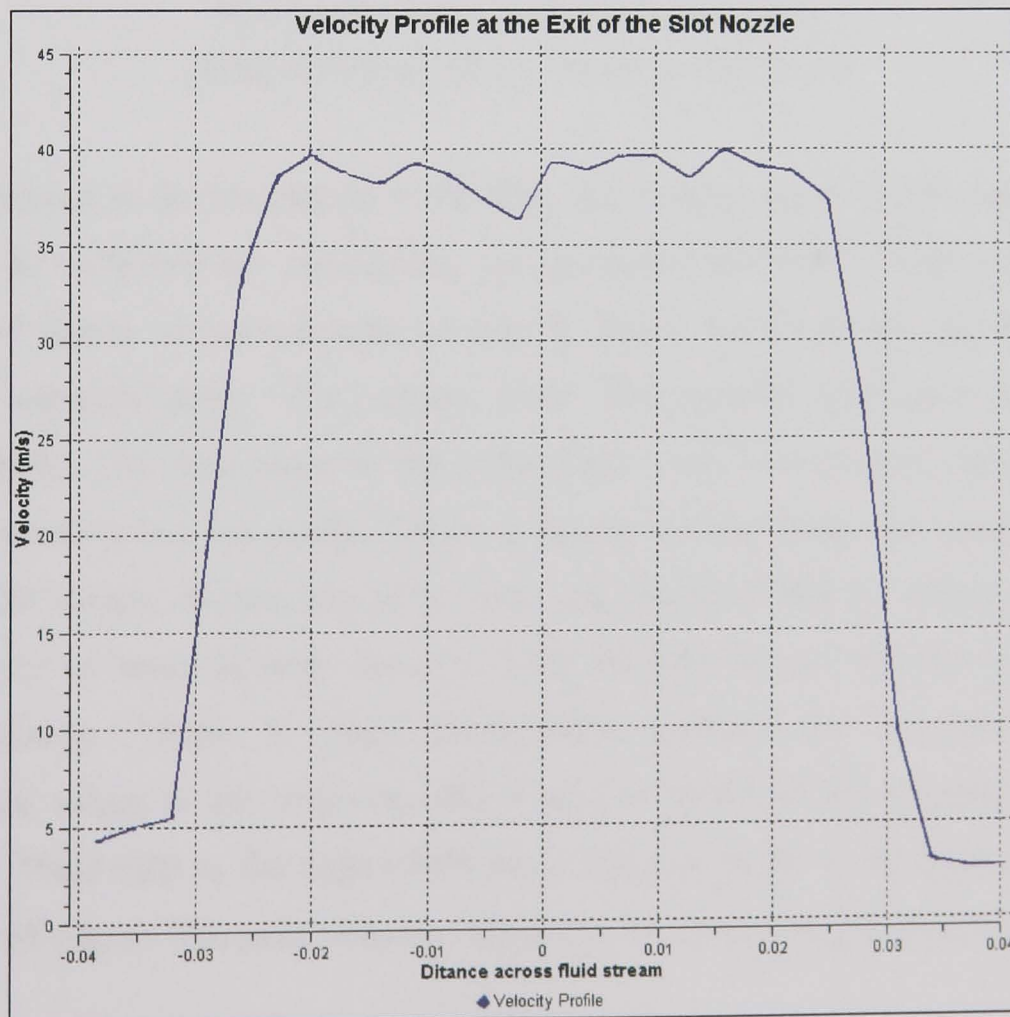


Figure 6-42 Velocity profile at the nozzle exit

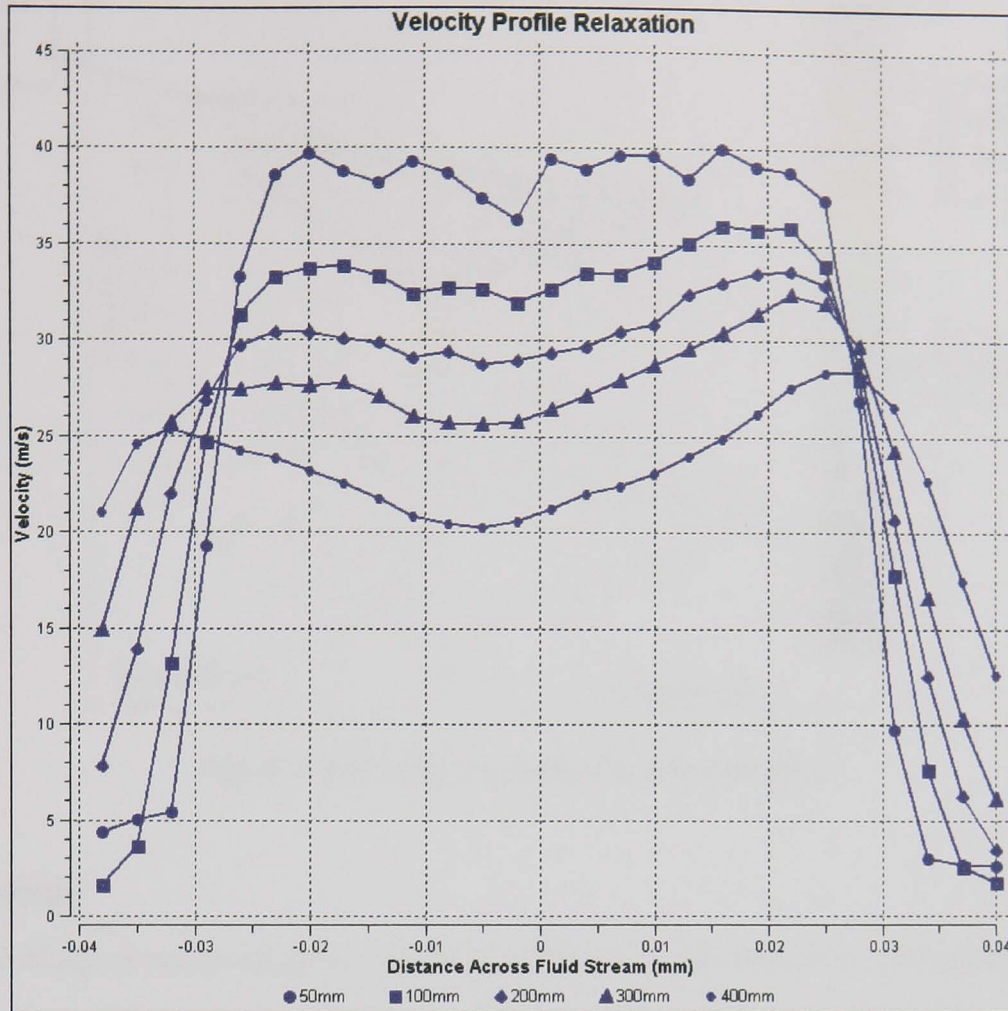


Figure 6-43 Velocity profile relaxation for C_L
(Points left on for clarity – values are simulated)

As a comparison to the simulation work done here, experimental techniques (described in chapter 8) validated the simulations and produced the table shown in Figure 9-1. Figure 6-44 below is one example of this. It shows the result for the above nozzle measured experimentally. The results show this profile relaxation as measured experimentally. The flow rates in the experiment were lower hence the reduction in actual jet velocity but the results follow a similar pattern from the simulation to the experimental values. At first, the jet is wide and maintains this for a short period until the jet begins to lose its peak velocity. After 200mm, the jet narrows and lowers its overall velocity. There is some discrepancy between the simulation and the experimental values at this point but this is said to be due to the bounding box in the simulation. Fluid next to the edge of the jet is making the jet width appear larger than the measured values. The peak velocity, however, does follow the predicted path.

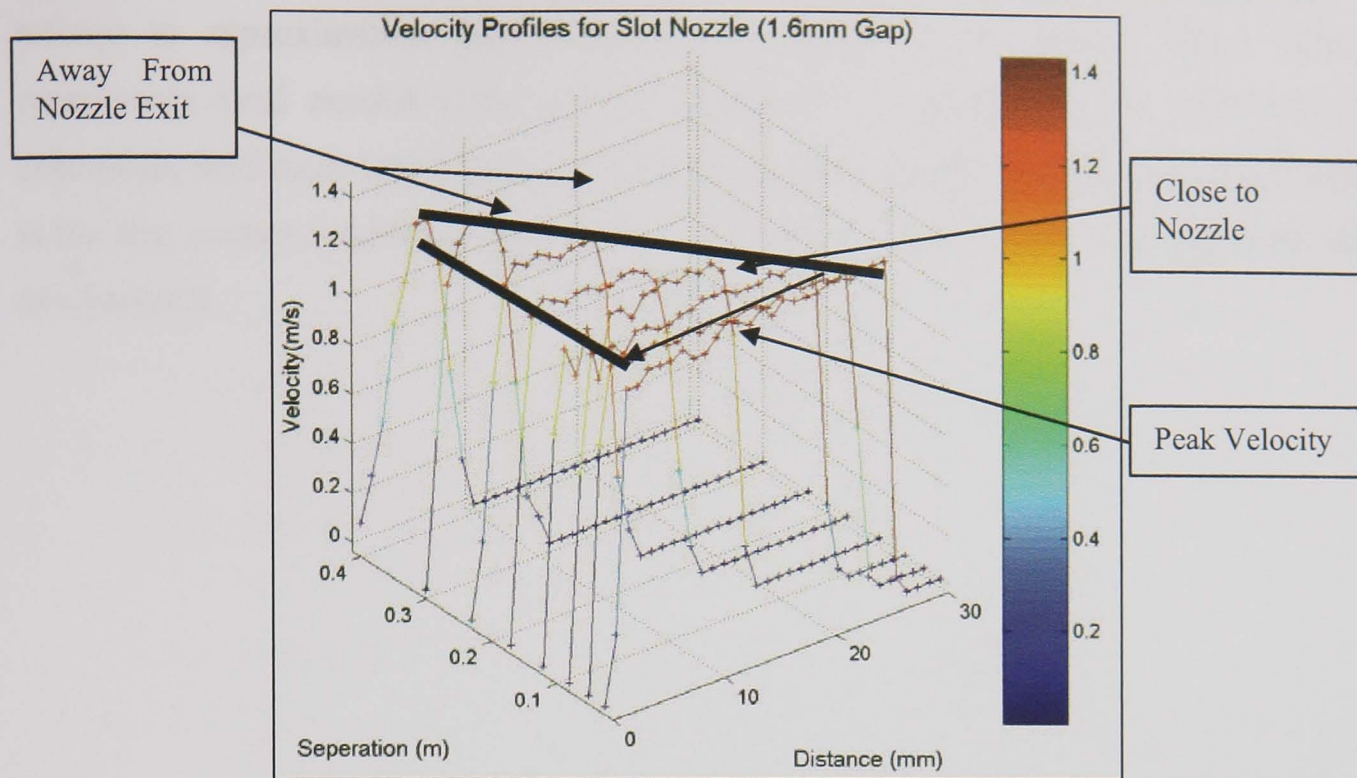


Figure 6-44 Velocity profiles for the slot nozzle

6.11 Summary

The factors studied were determined by the initial scope of the investigation and of the trials possible on the test rig designed and manufactured. Emphasis changed as progression moved from analysing boundary conditions, through multiphase work, and finally onto the free surface boundary. The observations presented in this thesis cover a range of coherency lengths for the nozzles specified in the scope of the work. When analysing one of the more stable nozzles (the Rouse nozzle), there is a difference between the level of coherence in experimentation and in the simulation, $C_L = 520\text{mm}$, $C_L = 400\text{mm}$ respectively. This gave confidence in the simulation as a comparative tool with a given error estimation.

It is difficult to state why the model under-predicts the coherence length leading from the large amount of air entrainment at the nozzle orifice without examining the inner workings of the free surface model employed within CFX10. An initial work looked into this and found complexities within the scale of the element sizes required. A further study was conducted to investigate the behaviour of certain variables at the interface. The results of this are that even with what would be said to be a reasonable mesh for this type of simulation (3-6 million elements with the smallest element at approximately 0.4mm), close examination of contour plots with mesh highlighting turned on, showed large gradients in several variables across single tetrahedral mesh elements. These were

refined to approximately $5\mu\text{m}$ using point controls in the orifice, which helped enormously (and needed close to four gigabytes of memory just to run) with jet coherence. Still more refinement would be required to predict the behaviour accurately at the free surface boundary. Some of this has been conducted and is shown at the end of Chapter 8.

Chapter 7 Construction and Design

This chapter discusses the experimental program of work completed that consists of the following major components:

- Experimental methods and techniques employed;
- The experimental equipment used and design of the test rig;
- The specific test procedure for each test;
- Results and discussion of each test.

7.1 Nozzle design and construction

In total, ten nozzles were used, having dimensions shown in Appendix A. The Nozzle referred to in this work as a Rouse fire-hose nozzle is a scaled down versions based on the work by Rouse et al (1952) and later by Cui (1995). The second main type of nozzle is the rectangular jet nozzle.

Several nozzles have been designed, manufactured and tested during the experimental work:

1. Round conventional nozzles;
2. Round coherent jet nozzles (supplied by J. Webster);
3. Lechler adjustable round nozzles (supplied by Lechler);
4. An adjustable rectangular slot nozzle (supplied by J. Webster);
5. ‘Squashed’ pipe copper and brass nozzle (visual studies only);
6. A selection of conventional nozzles based on the work by Gviniashvili (2003).

The main body of the experimental work focused on the round coherent jet nozzles and the adjustable slot nozzle. The Lechler nozzle, widely used by the project sponsors, was analysed for a comparison with research-based designs.

Figure 3-7 from chapter 3 shows the design of a round nozzle based on the work by Rouse et al (1952) and supplied to the laboratory by J. Webster. The coherent jet nozzles were supplied with a nozzle exit diameter of 1mm. By trimming the nozzle backwards, the profile remains constant and nozzle exit diameters of up to 12mm are possible. Two exit diameters were tested and analysed for this work, one of 2.5mm diameter, and one of 9mm. This gave, with varying flowrates, a range of nozzle exit

velocities, to establish the effect of nozzle exit velocity on the coherence length of the jet. The effect of the vena contracta reduces this nozzle exit diameter making the actual exit jet proportionally smaller than the actual nozzle geometry. This reduction is small in comparison to the overall diameter of the jet, however its importance was not neglected, and the reduction was seen in the simulations and checked for accurate comparisons between experimental and predicted results. An example of this reduction is shown in Table 7-1 with experimental data from Rouse et al (1952).

$\frac{D_n}{D}$	0.297	0.335	0.391	0.446	0.501	0.557
$\frac{D_j}{D_n}$	0.8961	0.8955	0.8951	0.8967	0.8982	0.8976
C_d	0.805	0.806	0.807	0.811	0.817	0.825

Table 7-1 Relationship between (D_n), (D_j) and (C_d) for Rouse based nozzles

where: D = inlet diameter, D_n = nozzle exit diameter, jet diameter = D_j and discharge coefficient = C_d .

Work from Rouse et al (1952) and Cui (1995) suggests the nozzle interior shape is critical to the performance of a coherent jet, stating that a concave inner wall produces increased jet coherent lengths over traditional nozzles with a convex inner wall (as does a straight inner wall, but not to the same extent – a target of this work being to measure this extent). This was shown in chapter 4 investigating the interior design of nozzles, confirming that convex inner walls or sharp inner wall transitions lead to flow separation and subsequently, down stream jet break up. Figure 7-1 shows a typical conventional slot nozzle used in most surface grinding operations with high-speed coolant application. An improvement to this is a nozzle that possesses a concave inner wall based on Rouse et al (1952) with smooth transition from the supply pipe to the nozzle exit. This shape prevents boundary layer growth and subsequently produces an improved coherent jet (Cui 1995). Figure 7-2 shows the suggested improved slot nozzle design.

It was suggested that the size of the slot and subsequently the aspect ratio of the nozzle may have an effect on the coherence length of the jet at a range of jet widths. Test inspecting the variation on the coherence length with respect to the aspect ratio are

investigated in this work. For this reason, an adjustable rectangular slot nozzle was required. The nozzle exit is set to 25.4mm wide with a range of slot heights between 0 and 7.94mm. A detailed drawing of this nozzle with its aperture set to 1.6mm (a figure chosen for relative speed comparison with the smaller coherent jet nozzles) is provided in Appendix A.

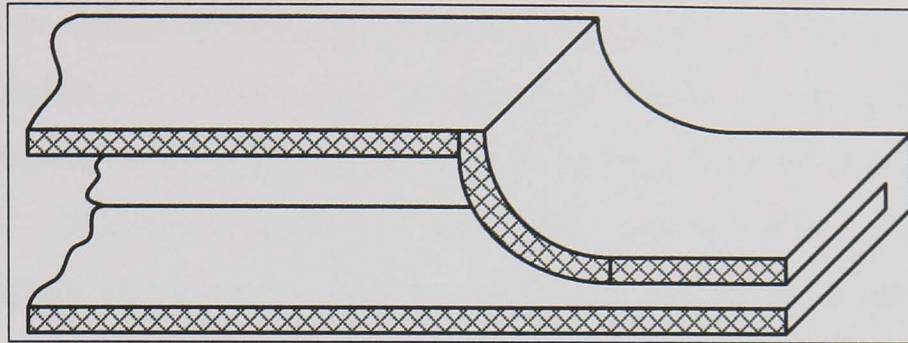


Figure 7-1 Sketch of a conventional high-speed slotted jet nozzle

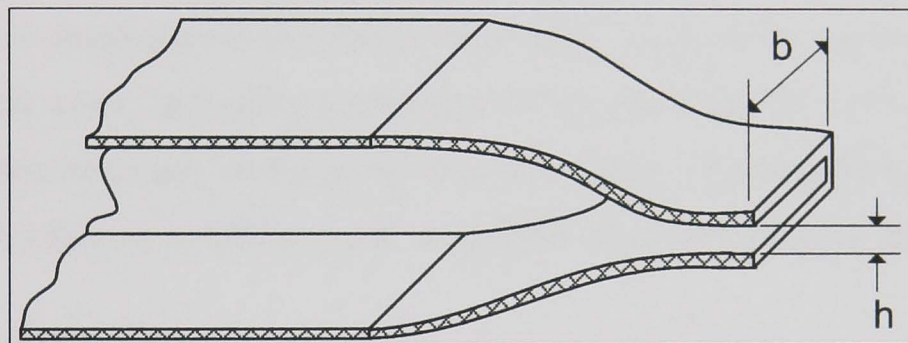


Figure 7-2 Sketch of the new rectangular nozzle proposed in Cui (1995) p.38

A transitional passage adapter was considered in Cui (1995) in order to connect the supply piping with a circular cross-sectional area to the rectangular slot nozzle. This was provided with the nozzle, further specifications and notes on this are available in Cui (1995). One important conclusion by Cui (1995) is $\frac{b}{h} > 6$. This, Cui found, gave the best results for measured coherence of the fluid jet. A limiting factor when describing the requirement for this however is the actual wheel width and the available supply conditions. Taking the value of b/h to much higher values results in a waste of coolant or a restriction in the slot height meaning coolant would not be able to pass through and would block easily. A honeycomb 20mm thick was placed between the adapter and the nozzle, acting on a flow conditioner. It is noted that this is an important consideration when investigating the coherence length of jets. For this reason, work on the effect of the flow conditioner on the coherence length of a 9mm diameter Rouse based circular coherent jet nozzle is given.

7.2 Nozzle exit shape

Webster et al (1995a) predicted that the nozzle exit edge shape (Figure 6-5) would have a significant effect on the coherence length of a turbulent fluid jet. This edge criterion is based on the exit of the nozzle orifice at the nozzle inner wall contour. A sharp exit is said to be favourable (Cui 1995) because it will not generate secondary flow. One common error in nozzle manufacture is the rounding of this nozzle exit. This rounding creates a small radius or convex shape on the nozzle orifice allowing separation of the flow at exit from the nozzle. This, as previously stated with reference to Figure 7-1, is undesirable. To measure the effect of the nozzle exit experimentally, involves the design of multiple nozzles from different materials, and to accurately machine tiny changes at the orifice exit. This would not be practicable and indeed would be prohibitive in view of the time required to conduct the extensive experimental tests and so a method for prediction of the effect was sought. After analysing the capabilities of simulation with small geometrical changes, it was decided that CFX would yield a satisfactory approximation of the actual physical effect. This is highlighted as an area for further investigation in further work to confirm these initial results and findings.

7.3 Flow Conditioners

The coherence length is subject to the effects of velocity profile, swirl and turbulence structure approaching the nozzle exit (McCarthy 1974). Many piping configurations and fittings generate disturbances with unknown characteristics. In reality, multiple piping configurations are assembled in series generating complex flow patterns. The problem is how to minimise the difference between real and fully developed flow conditions.

A method to avoid the influence of the swirl and turbulence fluid on the coherence length is to install a flow conditioner in combination with straight lengths of pipe to isolate the orifice from upstream piping disturbances. Fully developed flow is referred to in terms of swirl-free, axisymmetric time average velocity profiles in accordance with the power law of the wall prediction (Blake et al 1993). This means simply that no profile change would be observed past this point. However, fully developed turbulent flow requires equilibrium of the forces to maintain the random cyclic motions of turbulent flow. Fully developed pipe flow is only achievable after considerable effort in a research lab. For this work, it is impractical (and indeed unnecessary from an industrial point of view) to have pure fully developed flow.

The purpose of the flow conditioner is to lower the permanent pressure loss and eliminate swirl. When the swirl angle is less-than or equal to two, measured using pilot tube devices, swirl is regarded as substantially eliminated (Blake et al n.d.). Flow conditioners may be grouped into three general classes based on their ability to correct the mean velocity profile, bulk, swirl, and turbulence structure. The first class of conditioners is designed primarily to counteract swirl by splitting up the flow into a number of parallel conduits. This class of conditioners includes uniform tube bundles. The most prominent example of this is the Mitsubishi flow conditioner, Figure 7-3, which has a series of uniform parallel holes distributed in a concentric circular pattern through a disk. This type of conditioner does not attempt to produce a uniform velocity profile immediately downstream of the flow conditioner.

The second class of conditioners is designed to generate an axisymmetric velocity profile distribution by subjecting the flow to a single or a series of perforated grids or plates. Use of the blockage factor or porosity of the flow conditioner redistributes the profile. This type of flow conditioner (Figure 7-4) has little effect on reducing the swirling effect. Aichouni et al (1996) conducted an investigation into the effects of entrance flow distortions on the performance of a venturi flowmeter. The flow distortions, when a grid conditioner was inserted, led to deterioration in the discharge coefficient of up to 70 per cent, reducing to about 1 per cent at the higher Reynolds numbers (Aichouni et al 1996).

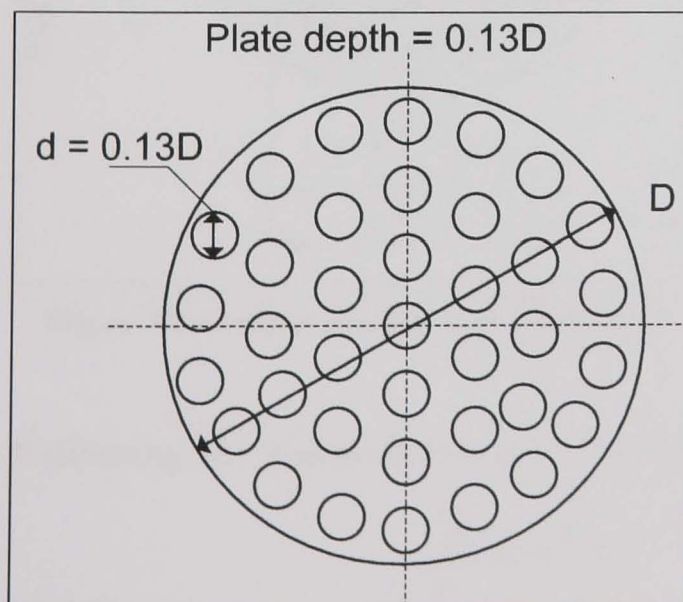


Figure 7-3 Mitsubishi flow conditioner

(See Appendix A)

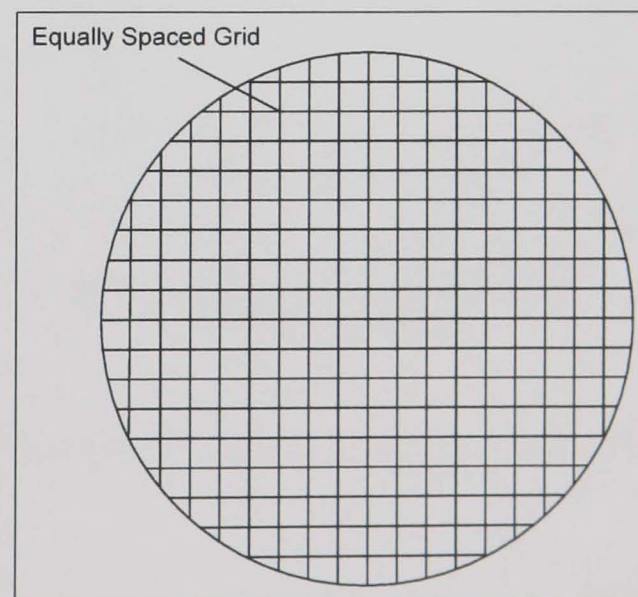


Figure 7-4 Grid based flow conditioner (Grid size varies dependant on research)

The third class of conditioners is designed to generate a fully developed velocity profile distribution through porosity of the conditioner and the generation of a turbulence structure. Varying the radial porosity distribution generates the turbulence structure. The uniform velocity flow meter used in this work is based on the conditioner design in Cui (1995, p31). Figure 7-5 shows this new conditioner and generates a velocity profile similar to Figure 7-6. Working drawings for the three flow conditioners tested is found in Appendix A. After the flow conditioner, the jet is continually bound until the constraints of the nozzle walls are removed, i.e. at the nozzle exit. At this point, the process of velocity profile relaxation occurs through a mechanism in the transverse layers of the fluid by means of momentum transfer. Therefore, as well as the surface tension forces thought of as conventional destabilisation (loss of stability of the jet throw air drag on the surface), the jet experiences internal motion associated with this profile relaxation. Limited experimental data available at the time, combined with the research in Cui (1995), indicates that a uniform velocity profile in the nozzle exit jet enhances the coherence length with destabilisation occurring only at high jet speeds.

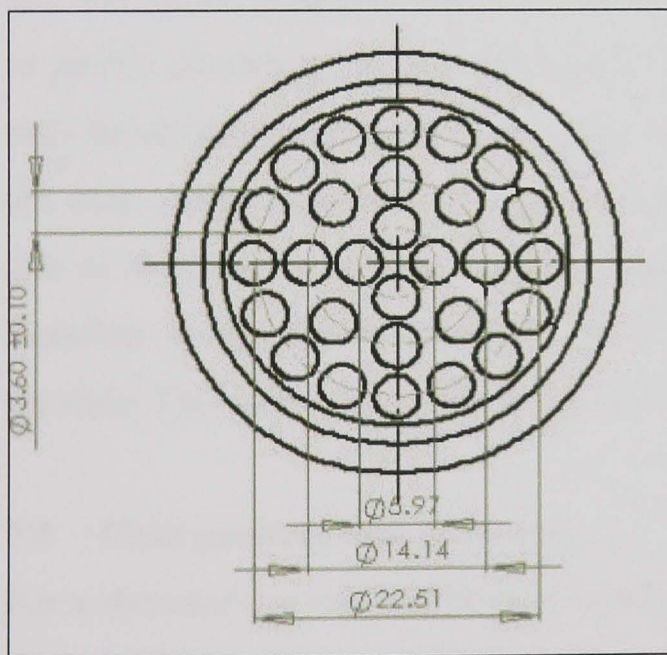


Figure 7-5 Uniform velocity flow conditioner

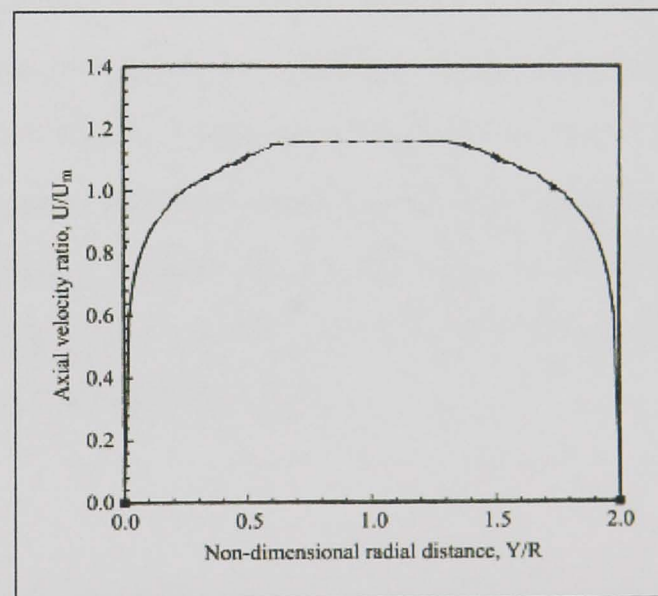


Figure 7-6 Velocity profile after the flow conditioner (Cui 1995)

Examining the energy defect ratio (McCarthy 1974) to investigate the jet coherence

gives

$$\varepsilon = \frac{\int_0^A \{V_2(r)\}^3 dA}{V^3 A} \quad [7.1]$$

where $V_2(r)$ is the local fluid velocity and V the average fluid velocity over area A then:

- for plug flow in a pipe (ideal flow, perfect fluid) $\varepsilon = 1$;
- for fully developed turbulent flow in a pipe $\varepsilon = 1.1$ to 1.2 ;
- for fully developed laminar flow in a pipe $\varepsilon = 2.0$.

ε is also considered as the ratio of kinetic energy of a flow system to the kinetic energy under plug flow conditions. Research from McCarthy (1974) indicates a rate of $\varepsilon = 2.0$ for straight laminar jets. When the jet emerges from the nozzle orifice into the ambient atmosphere, the parabolic profile relaxes to a flat profile at the same average velocity. Hence, there must be energy redistribution within the jet and the forces resulting from this redistribution play a significant role in the ultimate disintegration of the jet (McCarthy 1974). Brun and Lienhard (1968) developed a relation for velocity profile relaxation as a function of downstream distance:

$$\frac{L_R}{d} = 0.025 \text{ Re} . \quad [7.2]$$

where L_R is the length of relaxation, and d is pipe diameter.

Jets with initial parabolic velocity profiles (highest ε) are the most unstable (with regard to profile relaxation), while jets in plug flow (lowest ε) are the most stable. Jets with fully developed turbulent profiles on the exit from the nozzle orifice when $\varepsilon = 1.1$ to 1.2 are only weakly susceptible to profile relaxation. For this reason, the disturbances are due to the actual turbulent internal disturbances within the jet (McCarthy 1974). It, therefore, is reasonable to assume that the entry flow should be as close to laminar as possible. This necessitates use of the flow conditioners discussed.

7.4 Fluid pressure measurements

For a dynamic system, steady-state conditions are defined as no change in the system flow conditions such as flow rate and supply pressure. It is important to keep the system as steady as possible so that the flow readings taken are all within a minor percentage error of each other. Figure 7-7 illustrates a dynamic supply system with fluid flowing through the supply pipe. A static pressure tap is located in the duct wall at point A. The Pitot tube inserted into the flow, measures the total pressure at point B in the system. The total pressure measured at this point is the stagnation pressure. The stagnation pressure is the value obtained when a flowing fluid is decelerated to zero velocity in an isentropic (frictionless) process. This process converts all of the energy from the

flowing fluid into a pressure that can be measured. The stagnation or total pressure is the static pressure plus the dynamic pressure. Measurement of the dynamic pressures allows determination of the fluid velocities and flow rates in the system (Heeley 2005). Static pressure is independent of the fluid movement or flow; it acts equally in all directions. The importance of this is when using pressure sensors. Some measure gauge pressure and some absolute pressure (gauge pressure plus atmospheric pressure). To calculate the local velocity of the fluid, it is important to differentiate between the two. There is a third sensor measuring 'differential pressure' - the difference in pressure between two points.

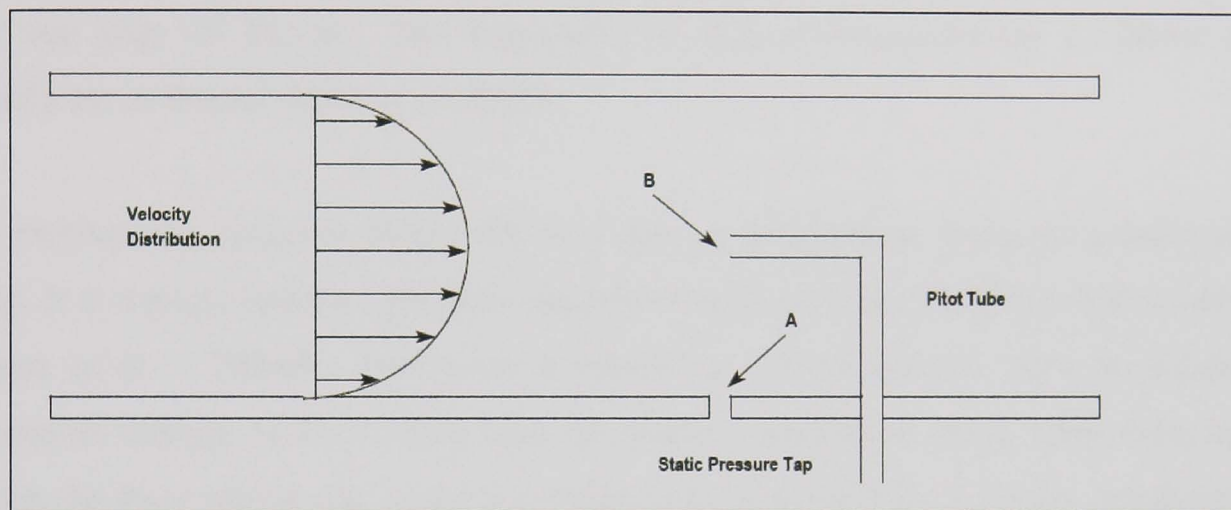


Figure 7-7 Pressure measurements in a dynamic fluid system

Use of a Pitot tube/pressure measurement system allowed for the measurement of pressure losses within the pre-nozzle delivery arrangement. This is an important factor when considering the overall system design for the coolant supply into the grinding zone. Research into the losses in pre-nozzle delivery arrangements was undertaken within the laboratory by Rene (2005). The important concept grasped from this work was the reduction of losses in pre-nozzle delivery systems measured with a Pitot tubing system. Simulation and correlation with the experimental data led to values within 0.5 per cent of the total measured pressure. This gave confidence in the use of ANSYS CFX software in the simulation of flows. This, however, was based on two-dimensional fluid simulations with single-phase fluids.

The objective of defining the fluid velocity profile through the pressure measurement in this work was to investigate the behaviour of the jet after exit of the nozzle. Measuring the pressure then converting to velocity, allowed for velocity measurement of the entire exit jet. Previous studies of jet coherency (Cui 1995, Webster et al 1995, McCarthy 1974) used visual techniques to analyse the properties of the exit jet. The work of Cui

took this further investigating the jet width using a mechanical device. In order to investigate this jet width, Cui used a traversing measurement device able to move in the flow direction of the emerging jet. Attached to this was a rigid bar with two sharp measuring points. Jet width was measured by placing one point at the top surface the other at the bottom surface of the jet. Two vertical readings from the scale were recorded and used as the measure of jet thickness. Although this may be a mechanical measurement method, it is limited in that the user must place the points at the edges of the jet and thus it is a visual measurement. Herein lays an opportunity for error, in that the placement relies on sight from the user, and hence cannot guarantee the point to be the true edge of the jet. The magnitude of this inherent/potential is shown to be significant in Baines-Jones *et al* (2009).

To measure the pressure within the exit flow, a gauge-style pressure transducer was used. It is a piezo resistive pressure transducer with a range of 0-30psi and a full-scale output of 0 – 100mV. This gave a sensitivity of 6.67mV/psi at a recommended excitation voltage of 10 V. This type of pressure transducer has a small inlet hole in which the Pitot tubing sits, making it suitable for the exit-flow velocity measurements. It also has its own static pressure tap to give total pressure measurements (as illustrated in Figure 7-8). It is a Honeywell piezo-resistive pressure transducer, Part number: 24PCDFA1G.

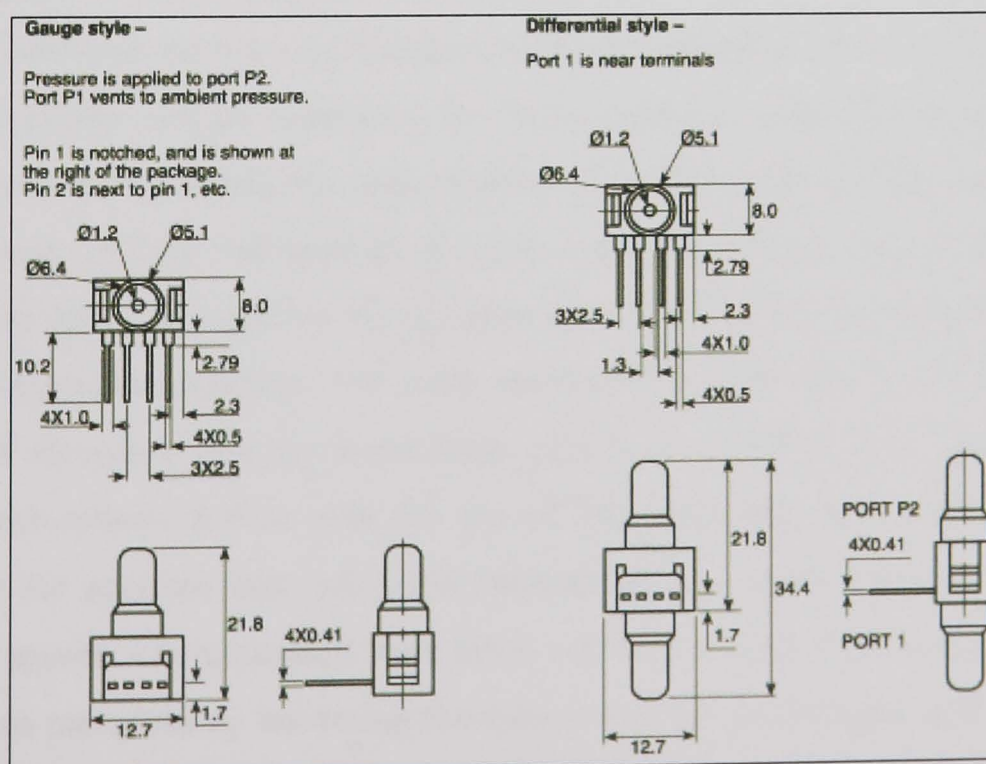


Figure 7-8 Pressure transducer with unamplified output

7.4.1 *Measurement technique*

One pressure transducer was used for this test. The pressure was recorded for a period of 20 seconds at each measurement point, then the Pitot tube was moved to the next point across the fluid stream. This measurement was repeated three times at each step to capture the mean pressure using averaging. The main body of the testing used a modified Jakobson surface grinding machine tool. Aside from the grinding machine tool, additional test rigs were manufactured for inclusion on the grinder to transform this into the nozzle performance and inspection chamber. One additional piece of equipment designed and manufactured was the coolant delivery system to supply the flow to the nozzle arrangement.

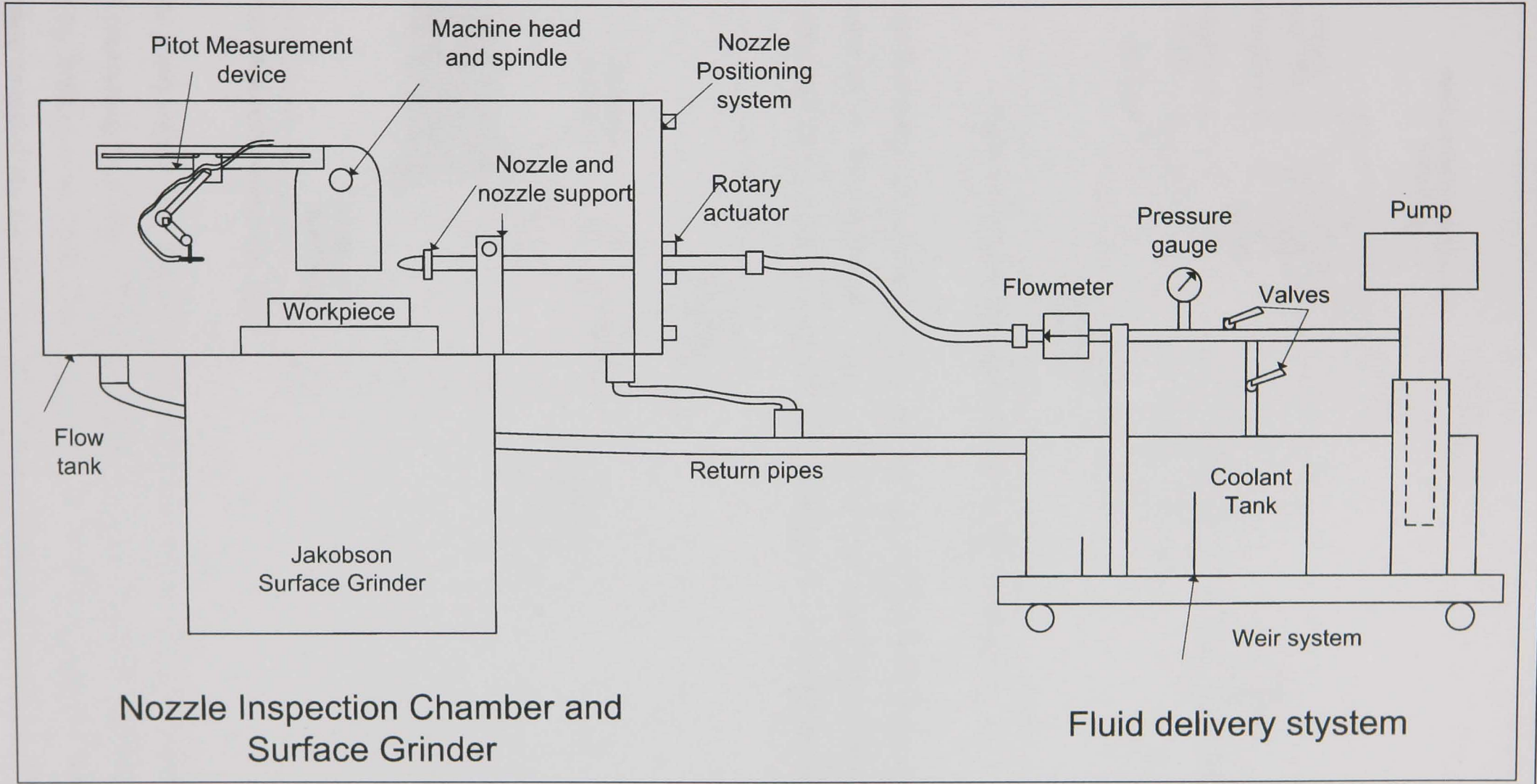
7.5 **Nozzle inspection test rig**

The nozzle inspection rig (Figure 7-9) was built around the Jakobson surface grinder using the machine's in-built lateral traverse mechanism in the X and Y directions. The grinder was adapted to include an inspection chamber, a positioning system, and the Pitot tube arrangement. The inspection chamber consists of a frame mounted to the bed of the surface grinder, removable Perspex panels to act as an observation medium but still allow access for nozzle and machine tool set-up and a detachable back panel allowing the spindle and wheel to move in the X and Y directions for part setting.

7.6 **Pitot system to determine jet coherency**

A Pitot measurement device was designed and implemented (Figure 7-10) to investigate the velocity profile and jet coherency for flows exiting a range of coolant nozzles. In addition, the system allowed for measurement of the flow characteristics after it passed through a range of flow conditioners. A transverse measurement system, previously for traversing the grinding wheel on the machine tool, feeds into a linear scale mounted on top of the inspection chamber. The scale measures the Pitot tube's movement in both the X and Y directions and has a resolution of 0.1mm. The Pitot tube was fixed to the traverse measurement device with the use of two rigid bars with adjustable locking connections for accurate and repeatable positioning. For repeatability of the position, each set of results was calculated three times and then averaged. The coherence length of the jet was measured by traversing the tube across the fluid stream area with overlap on either side. The actual jet width is measured by taking the first point at which the velocity profile curve starts to increase as a direct result of fluid entering the Pitot tube.

Figure 7-9 Modification of the Jacobson surface grinder for experimental nozzle tests



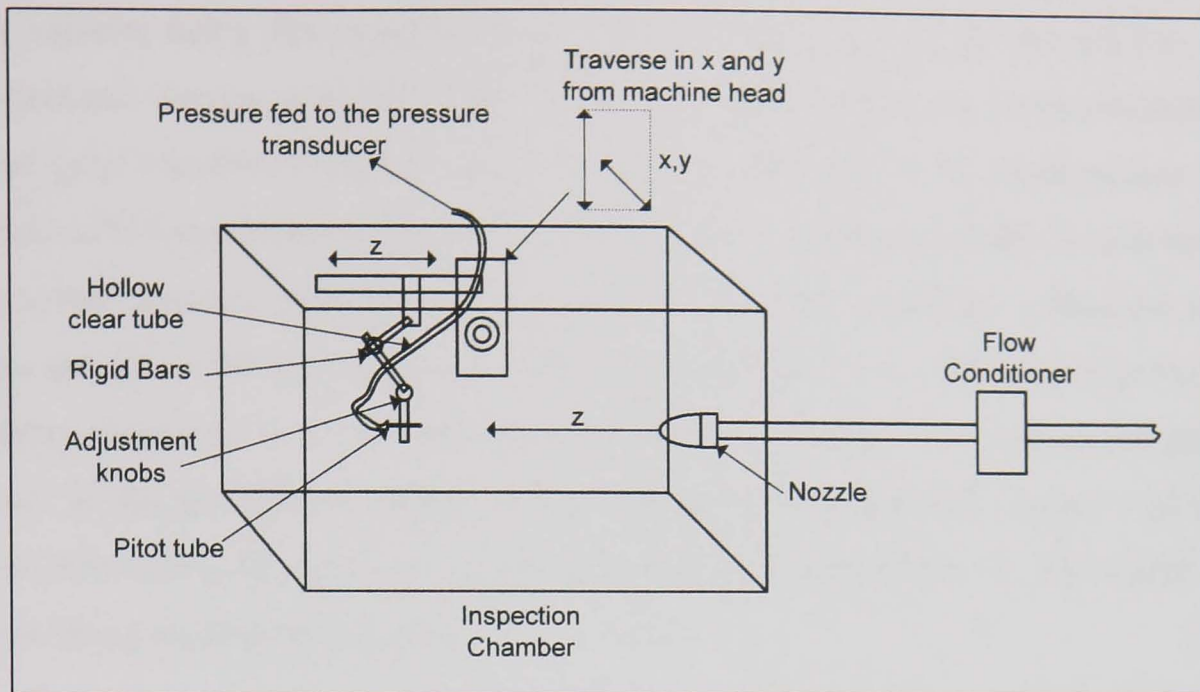


Figure 7-10 Sketch of the jet coherency measurement system

The new method proposed herein, removes operator error from visual inspection for this width measurement. Two readings x_1 and x_2 from the traversing measurement system were recorded and the jet width was calculated as in Figure 7-11 and Equation [7.3].

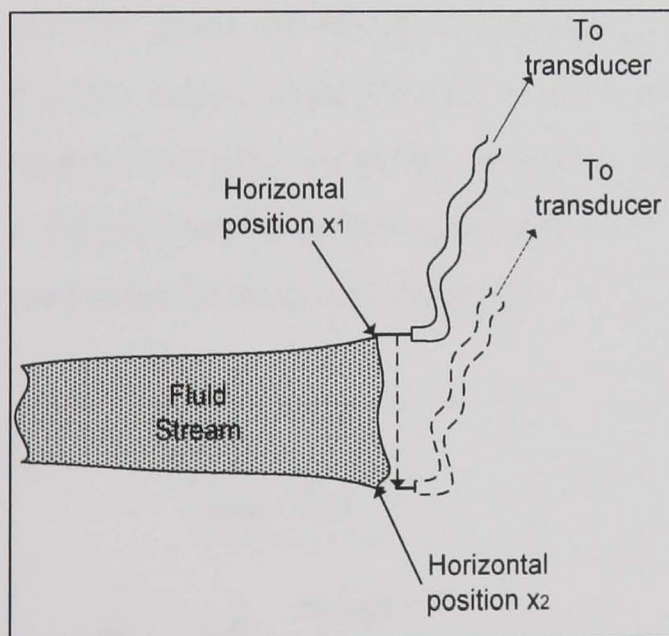


Figure 7-11 Measurement of the jet width

where:

$$H = x_2 - x_1 \quad [7.3]$$

Cui (1995, p.49) states, "this method can be considered as an effective and economical means of measuring jet width." The work compares the measurement method with that proposed by Bulloni et al (1988) and Chao et al (1990). The assumption that this is a good method comes from the fact that the rigid bar should not interfere with the flow upstream, if the flow is supercritical, due to the sharp edges of the measurement system. Supercritical flow occurs when the flow velocity is larger than the wave velocity – the

wave velocity being that velocity of the ripples travelling from the intersection of the measurement device with the fluid itself. Cui (1995) however, underestimates the human error introduced when setting the points to the edge of the fluid stream. Using the Pitot tube measurement system described in this work, the jet width was determined from actual pressure readings and was able to detect any 'shaking' within the jet that makes the jet width appear larger than it actually is. This is of vital importance in grinding situations. It is accepted that the fluid jet should cover the entire grinding contact. If the jet appears thicker visually, some of the grinding contact will not be cooled effectively. In parts of complex geometry, this could lead to large areas of the surface being inadequately cooled.

Since the traverse system can move in the z and y directions, the only other axis that remained was the x -axis. The x -axis movement was achieved by varying the distance of the Pitot tube from the nozzle outlet using a sliding system measured mechanically. This meant that the effective jet width could be measured at any distance from the nozzle exit ($x = 0\text{m}$) up to a physically allowed maximum of $x = 1.4\text{m}$. It is accepted that the closer the nozzle is to the grinding contact zone, the better the fluid delivery. For this reason, most attention was focused on the close range spectrum at values for x approaching zero. To build a complete picture of the jet however, the measurements for x ranged from zero right up to 850 mm from the nozzle orifice. Figure 7-12 shows the measurement setup and technique.

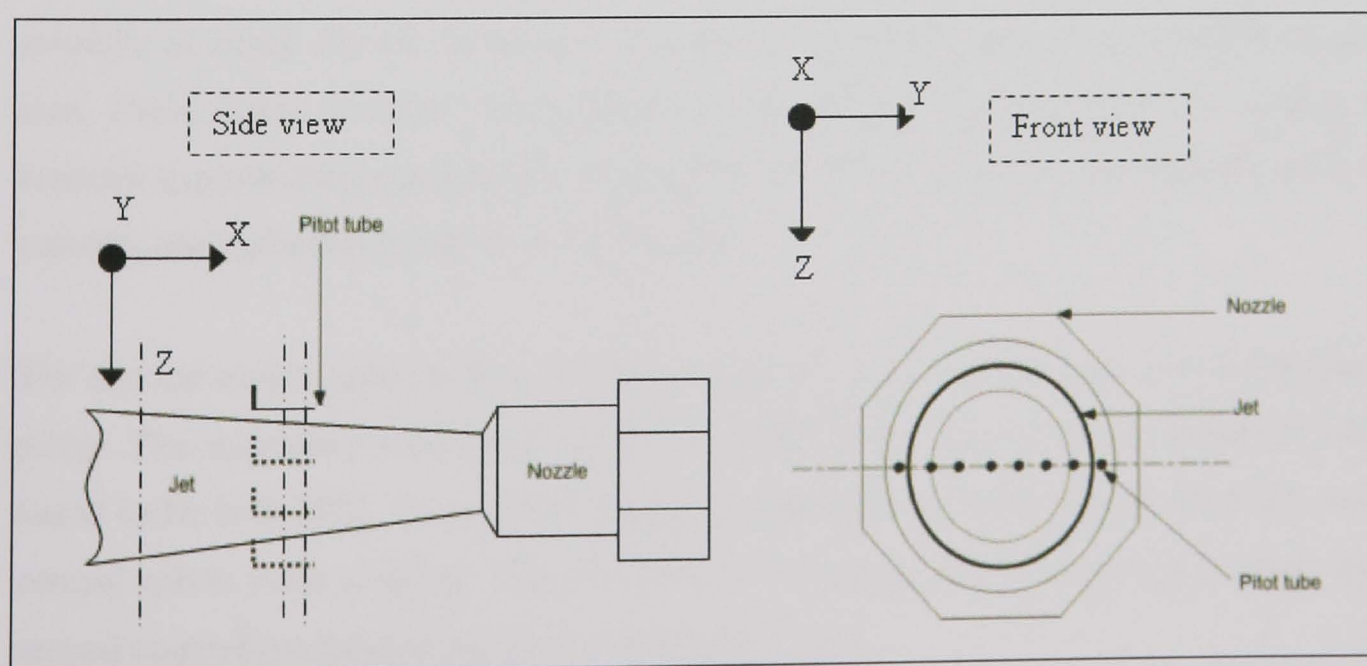


Figure 7-12 Pitot tube motion through the fluid stream

7.7 Fluid delivery system

The fluid delivery system was built separately to the flow inspection chamber on a moving platform with several pieces of flow measurement equipment. A rotameter-type OMEGA FTB792-L turbine flowmeter was situated inline after the pump and before the nozzle system. The flowmeter was factory calibrated before being supplied to the laboratory. A calibration test with water and then with the emulsion with 5 per cent Hysol X confirmed the factory calibration to be correct and accurate to within 0.1 l/min. The flow meter was supplied with an analogue output to trace the changes in flowrate due to fluctuations from the pump. Just before the flowmeter, a pressure gauge was fitted. The pressure gauge was also from OMEGA and was a DPG1000B-500G 0-500PSI. An analogue output was fed into the data acquisition system to eliminate (through adjustments from the input signal) any errors due to fluctuations in the supply flow.

The pipe system used for coherency testing comprised of three main sections. The first section, connecting the pump to a filter, the pressure gauge, the control valves and the flowmeter, consisted of 0.5-inch BSP connectors for each device, connected to a straight-shaft pipe with an internal diameter of 19mm. The second section connecting the fluid delivery system to the nozzle system was made from a section of 19mm diameter hydraulic braided pipe. The final section is a straight aluminium pipe of 19mm diameter that connects this hydraulic pipe, through the flow conditioner and onto the nozzle itself. Although losses occur at each section, these were kept to a minimum by avoiding as many elbows, bends and restrictions as possible before the straight supply area. These losses could not be neglected if they were varying however, so to keep a constant experimental method, the position of the delivery system was kept fixed in a constant configuration for all the nozzle tests.

The coolant supply used in the experimentation was delivered directly from an existing pump. The maximum delivery pressure with the 19mm open pipe was measured and found to be 0.45 MPa. To control the supplied pressure and flowrate of the fluid, two control valves were installed. The first permits fluid to pass into the nozzle system, the second controlling the direct return to the coolant tank.

The temperature of the coolant was measured in this experiment. Many industrial coolant systems come with refrigeration units to cool the coolant back to its suggested supply temperature. With the pump running constantly all day, the fluid may range from 20°C right up to 43°C. With the water-based emulsion, a temperature increase of 10°C would alter the corresponding Reynolds number of the fluid (due to the lowering of the fluid viscosity) by approximately 25 per cent. Therefore, to keep the temperature constant, a thermometer was suspended in the coolant tank, and experiments were undertaken, only when the fluid was between 23°C and 25°C.

7.8 Nozzle positioning system

Most grinding machine tools present in industry are CNC controlled. They typically include an apparatus for automatically positioning the wheel with respect to a workpiece or in relation to axes on the machine tool. On larger scale production, parts are loaded automatically into the centres (in cylindrical grinding for example). Once in place, the spindle is activated and the wheel is positioned to contact the workpiece in order to create the 'no gap' situation - there will be no space between the wheel and the workpiece other than the available pores in the wheel. During grinding of the workpiece, the wheel-workpiece contact is sprayed with a coolant from a nozzle or group of nozzles to reduce the heat created by friction generated between the tool and the workpiece. Consequently, the coolant nozzle must be adjusted with respect to a particular wheel-workpiece combination, to provide adequate cooling and lubrication.

Typically, coolant is presented to the grinding contact through a nozzle connected to a flexible hose. The nozzle and hose are manually positioned each time the process is changed, the hose being configured to maintain the nozzle position substantially when released. Such coolant supply systems, however, can be difficult to position accurately with respect to the grinding contact. Additionally, the operator must manually position the nozzle, which can be dangerous to the operator, particularly if the wheel is in motion while positioning the nozzle. The flexible hose can also be displaced from its position during machining requiring repositioning by the operator.

It would therefore be desirable to provide a coolant nozzle positioning system and method that aids positioning of the nozzle with respect to the grinding contact. The system would ideally maintain its setup position during the entire machining operation.

With nozzle position critical to the cooling process (Ebbrell 2003), techniques to position the nozzle accurately were investigated. Two situations were investigated in this work, to understand and improve nozzle positioning in the grinding environment. The first was a case study carried out at Holroyd Machine Tools & Rotors. Results for this case study are presented in Appendix C. The second is the positioning system used within this work.

A system feeding back from a linear scale and rotary actuator into a display was created (Figure 7-13). This system allowed for accurate positioning of the nozzle in the y and x-axis as well as the nozzle angle with reference to an angle of zero representing tangential fluid supply. It is suggested that nozzle angle has a significant effect on the useful flowrate supplied to the grinding contact (Webster 1995c).

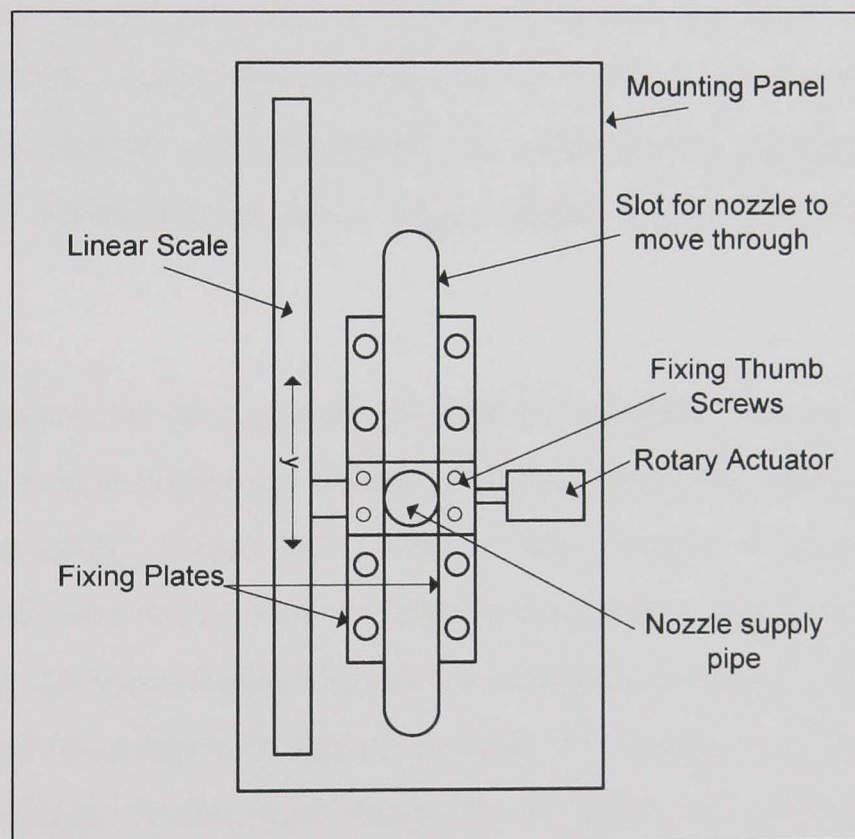


Figure 7-13 Nozzle positioning system

Previous work demonstrated the importance of nozzle position and shape (Webster 1995c). Delivery of fluid approximately tangential to the grinding wheel is a common approach (Akiyama et al 1984). Other investigations report optimal nozzle direction at an angle to the wheel periphery (Trmal & Kaliszner 1976, Campbell 1995). Ebbrell et al (2003) found that delivery of fluid via a tangential jet led to increased side leakage. Raising the nozzle slightly (12mm) reduced side leakage to a negligible quantity. However, Furutani (2002) suggests greater misting with an angled jet. It is clear that

both angle and position need to be under control to overcome these problems. Webster et al (1995a) reported lower grinding temperatures with a coherent jet as opposed to a dispersed jet. However, at the high velocities needed to penetrate the air boundary layer it is more difficult to achieve a coherent jet with water-based coolants at low flowrates.

For some applications a shoe nozzle designed to follow contours and curvature of the wheel, has the potential to result in improved delivery. For CBN wheels, where wheel wear is negligible, Klocke et al (2000) reported significant improvements to workpiece quality using a shoe nozzle. However, as Webster et al (2002) pointed out, shoe nozzles are not useful when wheel wear is significant. In consequence, jet nozzles tend to prevail. A systematic study was required to provide experimental confirmation of useful flow-rates achievable for a range of configurations and improved designs. This requirement leads to the next area of this work, useful flow collection. As stated in Jackson et al (2006), useful flowrate depends on flowrate delivered from the nozzle. However, this is not the sole dependency as other factors increase or decrease this value, such as: wheel bulk porosity, wheel speed, nozzle position, and nozzle jet velocity.

This work measured the flow passing through the grinding contact with emphasis on nozzle position, nozzle design and supply conditions. Previous studies in the laboratory investigated capturing useful flow with a side scraper mechanism. A similar configuration was used in this work to collect fluid during a 'spark out' operation. Spark out occurs when the wheel barely touches the workpiece. There is no in-feed, the wheel stays rotating at a fixed depth for a given number of revolutions to achieve good surface roundness and finish. In this work however, the spark out operation allowed for a minimal gap between the wheel and workpiece.

7.9 Fluid collection

Design of the fluid collector made it possible to capture fluid passing through the grinding contact. This fluid then passed through a pipe system to a container for collection. The fluid collector used side scrapers to hug the wheel so that after the grinding contact, no fluid escaped through side spray. The fluid collector (Figure 7-14) consists of two side scrapers, a workpiece for the touch grind, a collection chamber, an exit pipe system and a top plate surface scraper to capture fluid entrained with the wheel

on exit from the grinding contact. The range of parts for the fluid collector is contained within Figure 7-14.

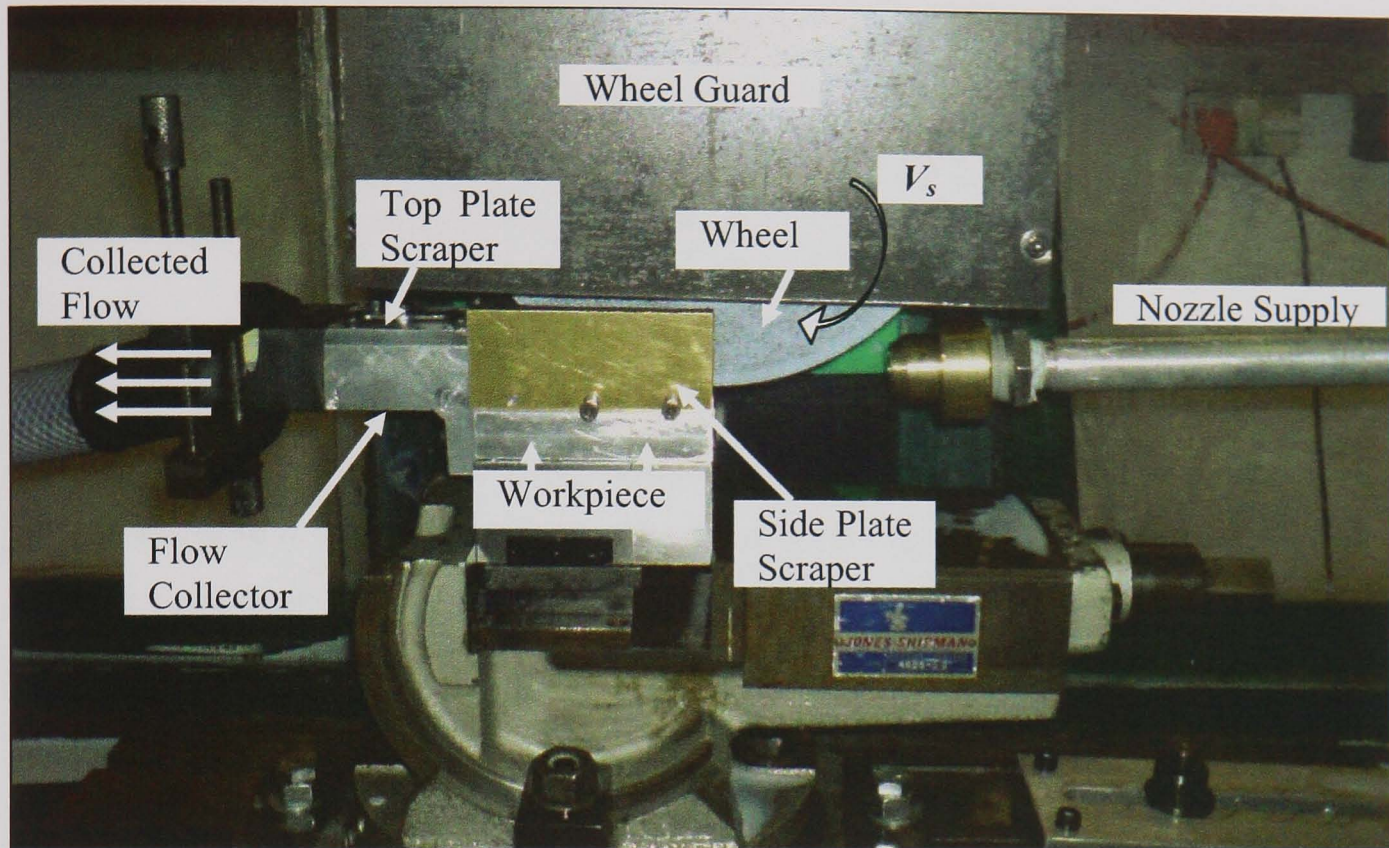


Figure 7-14 Fluid collection method

The work used several nozzles and positions to analyse the nozzle effectiveness and coolant supply to the grinding contact region. Previous works shows that collectable flow could be up to 40 per cent of the applied flow (Engineer 1992).

Chapter 8 Experimental Procedure and Results

This experimental procedure is a detailed, systematic list of the experiments that were conducted to achieve the objectives set out within this work. Within each set of tests, only one variable was changed to allow for comparison with the system constants. Presented, are results for each of the experiments with a discussion of the main findings. All the results are based on measured values.

Additional experimental results are given in Appendix E. The importance of these results lies in the overall trends of coherence length to a variety of flow conditions and test parameters. Hence, selections of results are brought forward into this chapter, with references made to individual figures illustrated. In particular, each graph has only one variable parameter, with the remaining parameters fixed. This permitted close comparison between the simulation and experimental findings. This chapter also contains experimental validation of the multiphase simulations with comparison graphs of both methods.

8.1 Flow conditioner tests

Experimental work on flow conditioners was designed to test their effect on nozzle exit flows. The nozzle based on the design by Rouse et al (1952) was selected. Previous studies (Webster et al 1995a, Cui 1995) claim this to be the most coherent design available. Design and testing of several flow conditioners allowed for investigation of their influence. The flow conditioner tests took place using the flow inspection chamber and fluid delivery mechanisms described previously. The test aimed at measuring fluid velocity-profiles at several points, starting from the nozzle exit, within the jet stream. Plots of the jet break-up length were created using the profiles created. To build the velocity profile at several points within the fluid stream, the traversing Pitot tube system was used. This required the calibration of the pressure transducer to reference fluid velocities to the output of the sensor (mV). Calibration of the pressure transducer involved setting the flow to a given velocity. To achieve this, a given flowrate was constant during this calibration but was varied during the experimentation. This varied to test the range of the pressure transducer. Given the flowrate and the nozzle exit size, the fluid velocity was obtained using the expression: $\dot{Q} = v \times A$.

If the flowrate is 15 l/min through a circular diameter of 2.5mm then the fluid velocity

is given by
$$v = \frac{4 \times \text{flowrate}}{\pi \times (\text{pipe } \phi)^2} \quad \therefore v = 50.9\text{m/s}$$

For each different flow rate, a reading from the sensor was recorded. This is shown graphically in Figure 8-1, with a ‘best-fit’ straight line and the equation for the line. This allowed for calibration of the sensor at any given flowrate. The maximum flowrate possible through the 2.5mm nozzle was 6 l/min. This gave a maximum achievable fluid exit velocity of approximately 20m/s, which is reasonable for the initial testing. For any given nozzle aperture, the jet velocity right at the nozzle exit is Q . Therefore, for calibration, the pitot tube was placed directly at the nozzle exit. To achieve the higher velocities that were required for the actual nozzle testing within the grinding environment, a separate fluid system was required. This is explained in the section on fluid collection experimentation. The equation of the best-fit line gave the correlation between the sensor readings and the fluid velocity. This was used to calculate the velocities within the exit flow. The pressure gauge supplied from OMEGA and the turbine flowmeter were calibrated. The two closely matched the manufacturers stated accuracies to within 0.5 per cent removing the need for any further calibration. To build up the flow patterns, readings were taken at several distances from the nozzle exit namely: 50, 100, 200, 300, 400, 500, 650 and 850mm. It was assumed that this would cover a large range of the jet and give a suitable range for analysis.

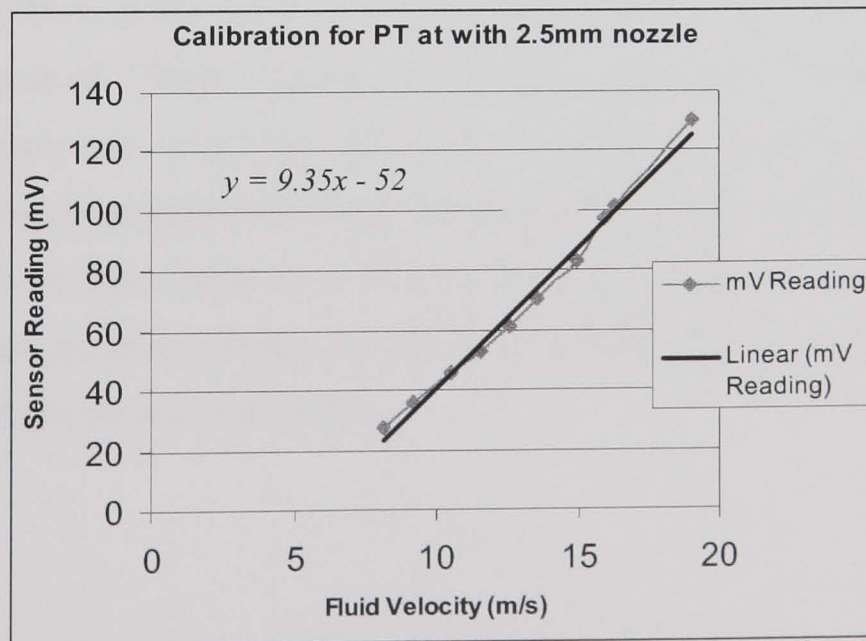


Figure 8-1 Calibration of the pressure transducer

To achieve a zeroing of the measurements at one side of the jet, the Pitot tube was traversed into the flow until a reading was picked up from the pressure sensor. The positioning device was zeroed; then the Pitot tube was traversed throughout the flow.

The pressure transducer used for the 9mm and 2.5mm nozzle tests as well as that for the variable slot nozzle differed from that for flow conditioner tests. For this reason, further calibration was needed. Even though the sensor was the same type as that previously used, for confidence in the results new calibration was used (Figure 8-2).

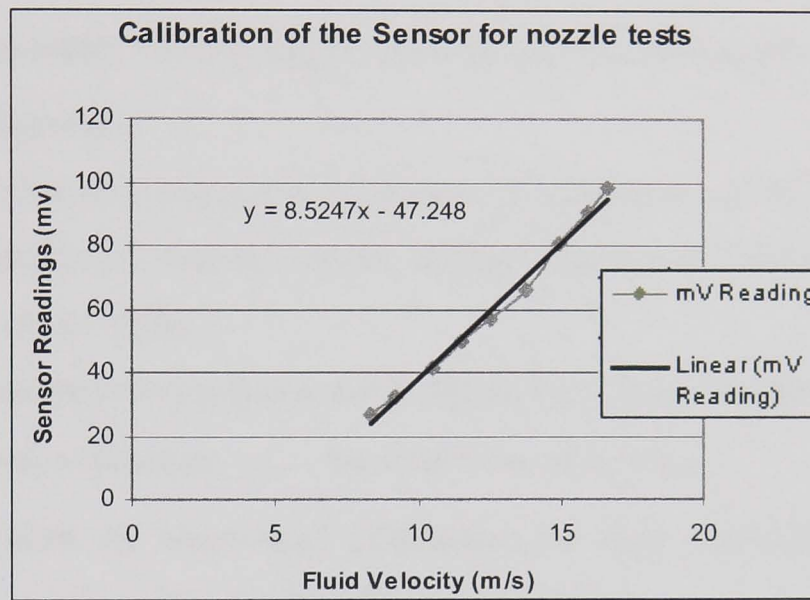


Figure 8-2 Pressure sensor calibration for the nozzle coherence length tests

8.1.1 Flow conditioner design

Testing of the effects of the use of flow conditioners on the exit-jet-width used a round Rouse type nozzle of 2.5mm diameter orifice. The pre-delivery arrangement remained constant for each test with only the flow conditioner varied. The traverse-Pitot measurement system permitted the determination of jet width. Initially the jet width of the system with no flow conditioner was tested. Then, in turn, a range of conditioners were inserted and examined. Figure 8-3 shows the number given to each conditioner for comparison within this results section.

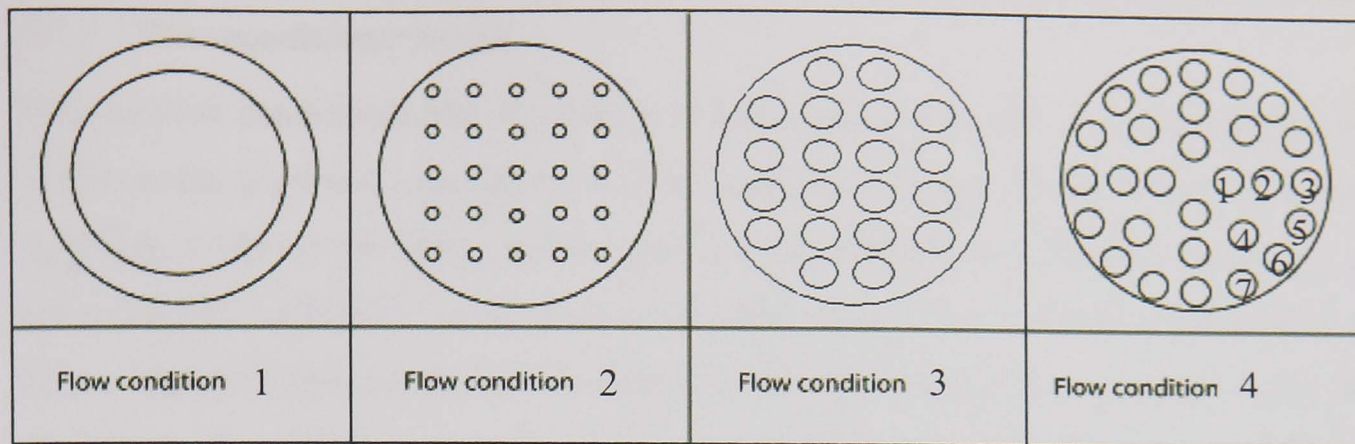


Figure 8-3 Types of flow conditioners used for jet width testing

1. Flow conditioner 1 was a simple ring with an internal diameter d_i of 25.25mm (no conditioning).
2. Flow conditioner 2 had a grid of holes with a diameter, d_h , of 2mm.
3. Flow conditioner 3 was an upgrade of flow conditioner 2, where each hole has a diameter, d_h , of 4mm.
4. Flow conditioner 4 was designed by following a linearised theory from Elder (1959), with a diameter, d_h , for each hole, of 3.6mm.

Cui (1995) describes the theoretical calculation for flow conditioner 4 with results shown in Table 8-1 where D is the diameter of the wholes.

Hole number	1	2	3	4	5	6	7
θ (deg)	0	0	0	45	22.5	67.5	45
PCD (mm)	0.109D	0.258D	0.414D	0.258D	0.414D	0.414D	0.414D

Table 8-1 Distribution of each hole on the disk

The minimum disk depth is 0.134D. The diameter of each hole is $d = 0.134D$. The engineering drawing of flow conditioner four is presented in Appendix A.

Two types of plots are depicted for initial comparison of the coherence length of a jet when influenced by one of the conditioners in Figure 8-3. Figure 8-4 shows the velocity profiles at each of the eight measurement planes downstream of the nozzle orifice. Connecting these with a surface plot using MATLAB provides a picture of the surface structure of the fluid stream as shown (Figure 8-5). Figure 8-4 and Figure 8-5 show these plots for the fluid stream with no conditioner insert (conditioner 1 above). The plots for the other flow conditioners are given in Appendix E.

8.1.2 Flow conditioner results

With no flow conditioner, the jet width increases rapidly from the exit of the nozzle; the peak velocity is curved and reduces with an increasing distance from the nozzle orifice. Appendix E shows the plots for the stream with conditioner 2 inserted. With this in place, the flow exhibits a small amount of improvement. The velocities at the sides of the jet appear improved due to a lowering in the velocities at the extremes of the jet. Observing the angles connecting the plots however, reveals that this conditioner provides poor straightening due to the coherence angle. The coherence angle is the angle at which the jet diverges. It is the angle between the two bottom lines in Figure 8-4. As the case without a flow conditioner, this angle causes the jet to break up earlier than predicted.

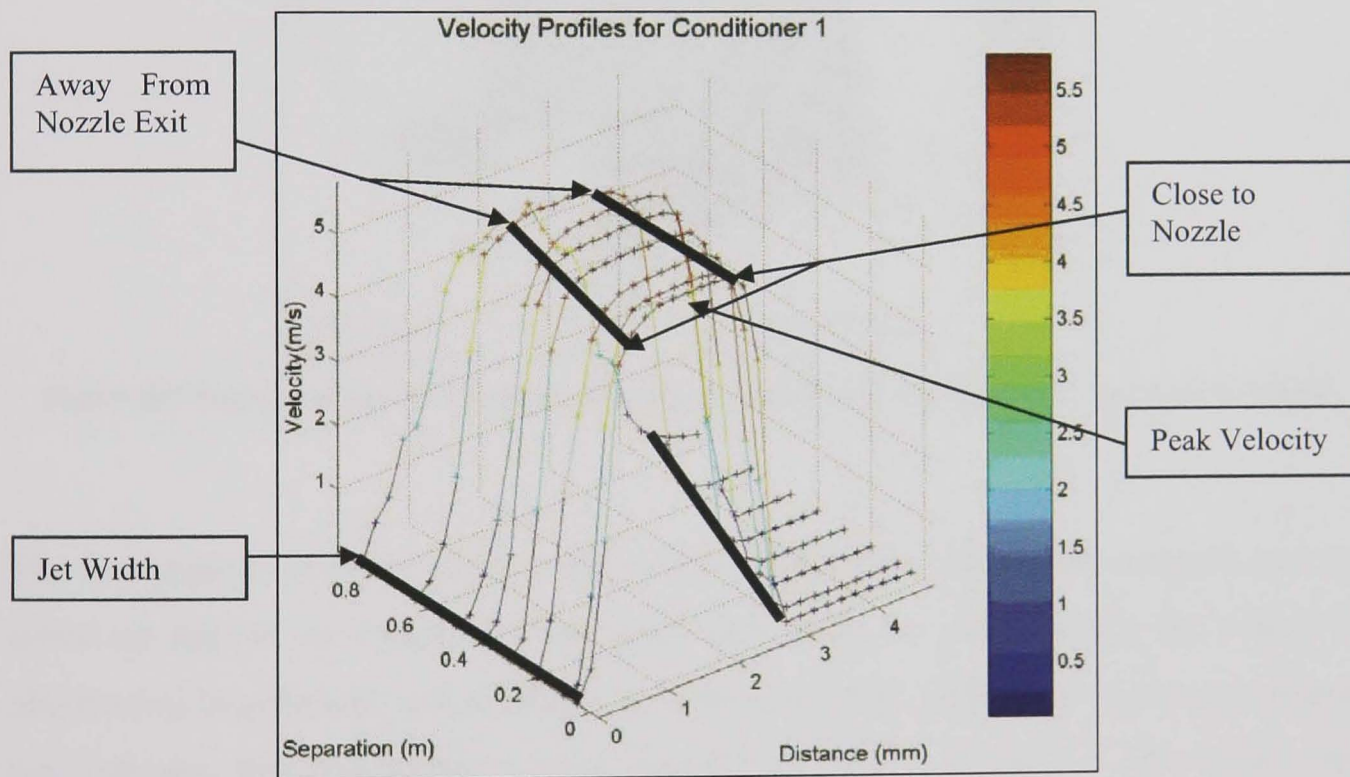


Figure 8-4 Velocity profiles for the stream with no conditioning (conditioner 1- measured values)

With conditioner 3 inserted, the jet width reduces at the far end of the jet stream. The jet maintains a higher peak velocity profile until approximately 400mm from the nozzle orifice. This indicates that the conditioner is achieving the uniform velocity profile required at entry to the nozzle. With conditioner 4 inserted, the jet width is approximately the same as that with conditioner 3 inserted. The notable difference is the region of peak velocity. This is maintained for 100mm more at a 'usable' width

confirming the prediction of the viability of flow conditioning. Figure 8-6 highlights this point further. Although the overall jet width is increasing, the peak velocity profile in the centre of the jet appears constant up to 500mm where the profile begins to narrow. This is ideal for the grinding situation as the nozzle with this conditioner may be placed up to this distance away when encountering awkward positioning, and still achieve adequate cooling in the grinding contact.

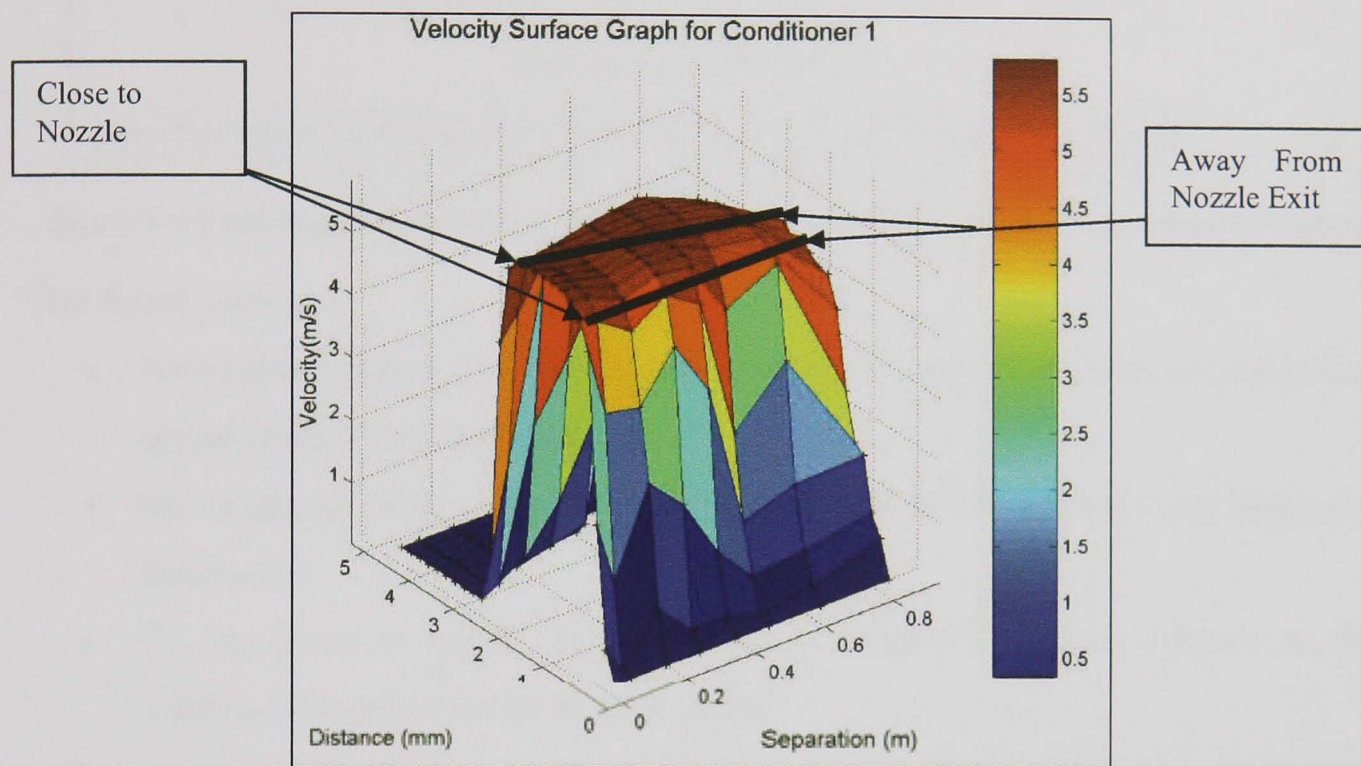


Figure 8-5 Surface image for the stream with no conditioning (conditioner 1- measured values)

The two regions to either side of the central dashed line, the coherent region and the break up region, in Figure 8-6 represent the zones in which firstly the stream is observed to be coherent, and secondly, at which the stream appears to 'break up'. Figure 8-6 indicates that positioning a flow conditioner before entrance to the nozzle can improve poor nozzle entry conditions and remove secondary flows from the delivery systems. With flow conditioners in place, the flow stream looks uniform at the distances relevant to grinding operations. The velocity profiles show increasing jet break up constant throughout confirming the inertial forces and drag on the surface of the jet, yet the core velocity of the fluid stream remains constant for industrially adequate lengths.

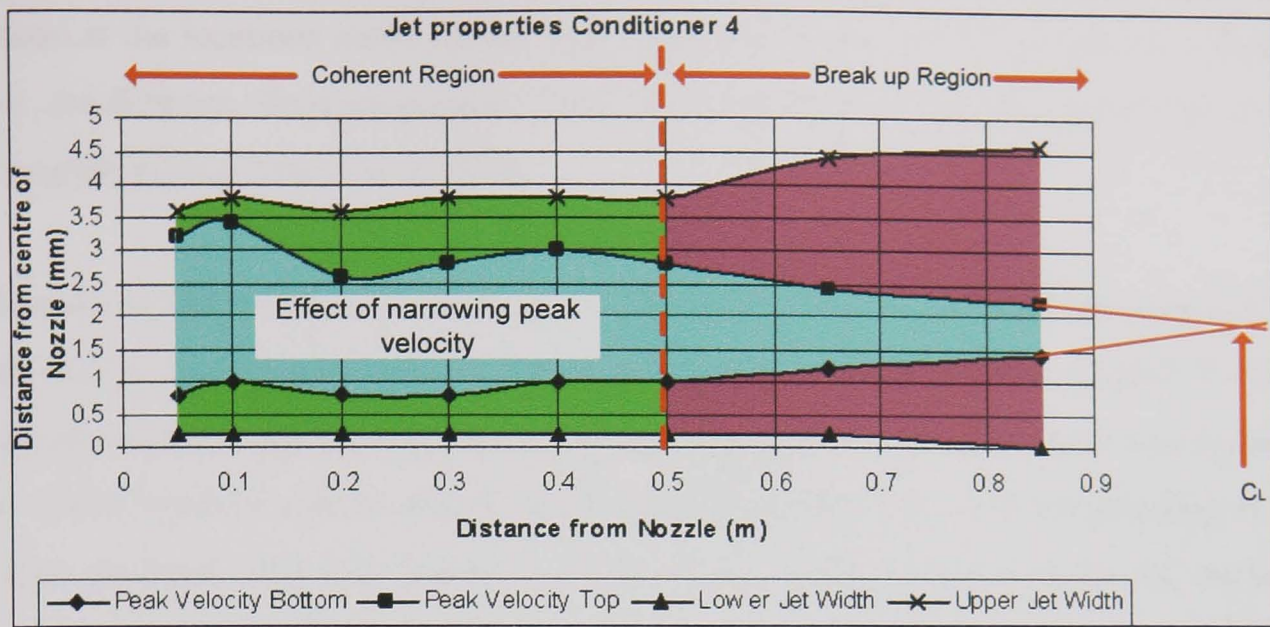


Figure 8-6 Coherence length and jet width for nozzle 5 with flow conditioner 4- measured values

This figure shows:

- the coherent region, that is, the area in which the central velocity core remains at approximately the same volume;
- the break-up region, that is, the area in which the central core begins to deteriorate;
- C_L , the point at which the central peak velocity disappears (known as the coherence length or jet break up length);
- And the peak velocity described by the velocity of the central core of the fluid upon exit from the nozzle chamber.

From investigations in this work, given a velocity profile as such, when traversing vertically through the flow, flow from the lower part of the jet falls earlier due to gravity as only surface tension is acting to accelerate it towards the jet core. The top of the jet is always falling into the faster jet core aiding momentum transfer. This gives the appearance that the upper surface is more disturbed. For this reason, measurements were taken across the flow in the exact same horizontal plane to reduce the ambiguity of the results when taking gravity into consideration.

8.2 Nozzle coherence length tests

For the nozzle tests, focus was on calculating the nozzle ' N_f ' factors affecting the jet coherence length as described in Chapter 6. Investigations used the same system for measurement as the flow conditioner tests. Several nozzles were investigated with focus on coherent jet nozzles, the variable slot nozzle, and nozzles with a slop and orifice interior for comparison. Each nozzle was tested using the traversing measurement

system at the locations noted above. The same sensor was used for all the tests. In each case, the flowrate, fluid temperature, fluid exit velocity, material type, surface finish and the supply piping remained constant.

Once the profile of the jet was built up, the aim of the experimentation was use this information to compare with the simulation model described within Chapter 5. If the experimentation confirms the model findings with only a small amount of relative error, the model could be used to predict exit flows and therefore be used as a grinding nozzle design package. This was the goal of the work, as this would remove the need for expensive testing and confirmation in industrial environments where time is money. One further nozzle examined was the Lechler solid jet nozzle (Appendix A). Lechler nozzles are used within one of the industrial partner's grinding areas and were tested for industrial comparison shown within the case study in Appendix C. The Lechler nozzle is an adjustable round jet nozzle that is relatively easy to position. Testing this nozzle's effectiveness allowed for confidence to be confirmed (or not) for the industrial environment.

Previous work by Cui (1995) had investigated the jet width, H , but did not closely examine the fluid's internal behaviour. The key outcomes of this work were the importance of a fluids internal structure when attempting to cool the grinding contact from a distance. Cui (1995), however, did not investigate the fluids central core. The results from this work highlight an important factor of internal coherent jet behaviour.

8.2.1 Nozzle coherence length determination

Cui (1995) predicted that nozzle coherence length and its usefulness in the grinding environment is based on the width of the actual jet. Much of this work focused on the splitting of the jet and examined the actual jet width. The analysis of the experimental results showed the narrowing of peak velocity, which has never been identified before. It is seen from Figure 8-7 that the useful output of the testing is this 'peak' velocity. Assuming that the preferable practice is to match the wheel speed ($v_j = v_s$) at the point of entry to the grinding contact, the fluid must be at this peak velocity. Therefore, the areas of the jet not at this peak velocity underperform.

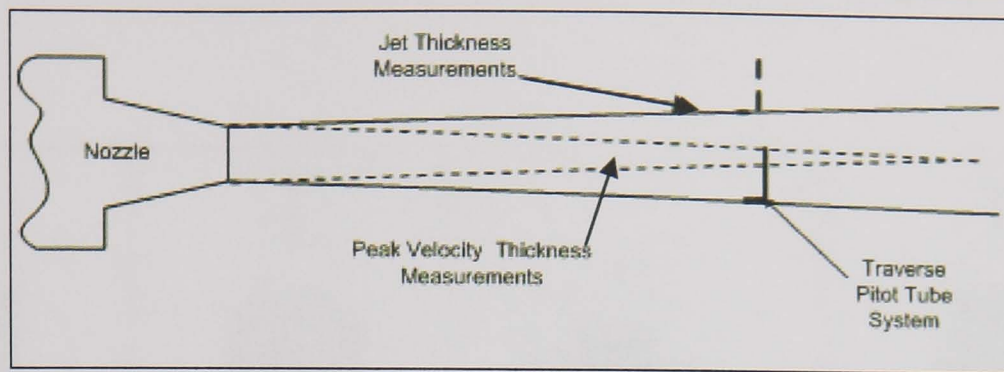


Figure 8-7 Jet width vs. peak velocity width measurements

The graphs shown are a direct comparison of the velocity at a plane across the fluid stream. Each of the curves represent one measurement plane downstream of the nozzle orifice. Eight different nozzles were investigated. The working drawings for each nozzle are contained in Appendix A. Table 8-2 shows a schematic sketch for each of the eight nozzles examined. In addition to the eight circular jet nozzles examined in Table 8-2, a variable slot nozzle was investigated. Results for this follow the work on the circular jet nozzles. No flow conditioner was used during the nozzle tests as even though promising results had been seen with the flow conditioners, these effects needed negating in order to make a fair comparison between the different nozzle types.

Figure 8-8 shows the velocity profiles at each of the eight measurement planes downstream of the nozzle orifice. Plots for all nozzles are given within Appendix E. From inspection of the right hand side of Figure 8-8, a clear trend of the jet width increasing with distance is apparent. The velocity profiles relax and become increasingly centred showing the peak velocity depreciation. The surface plot (Figure 8-9) shows this decreasing trend visualising the effect of jet breakup downstream of the nozzle orifice. With this nozzle, jet breakup appears at some distance (850mm from Figure 8-10) after the nozzle orifice. Theory predicts this breakup length (with all the variables described in Chapter 5) to be approximately 86cm from the nozzle orifice with a turbulent jet. From a three-dimensional plot, a two-dimensional plot' illustrated in Figure 8-10, shows the main areas of interest i.e. the jet width and the peak velocity, as well as an estimation of the actual coherence, or jet break-up length.

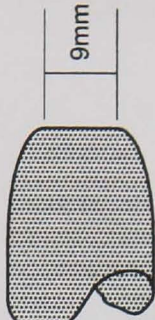
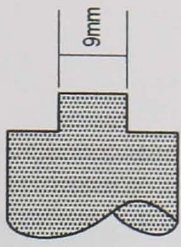
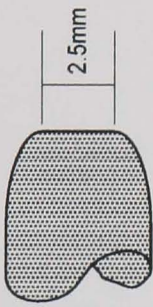
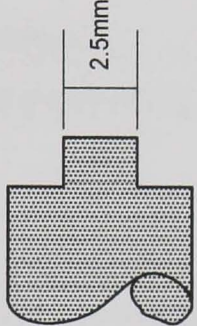
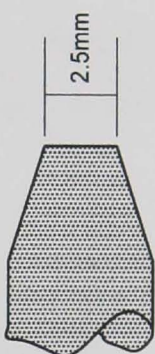
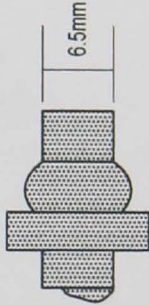
			
<i>Nozzle 1 – Straight pipe</i>	<i>Nozzle 2 –Rouse nozzle</i>	<i>Nozzle 3- step or orifice nozzle</i>	<i>Nozzle 4 – slant nozzle</i>
			
<i>Nozzle 5 – Rouse nozzle</i>	<i>Nozzle 6 – step or orifice nozzle</i>	<i>Nozzle 7 – slant nozzle</i>	<i>Nozzle 8 – Lechler solid jet nozzle</i>

Table 8-2 Eight nozzles investigated in the experimentation

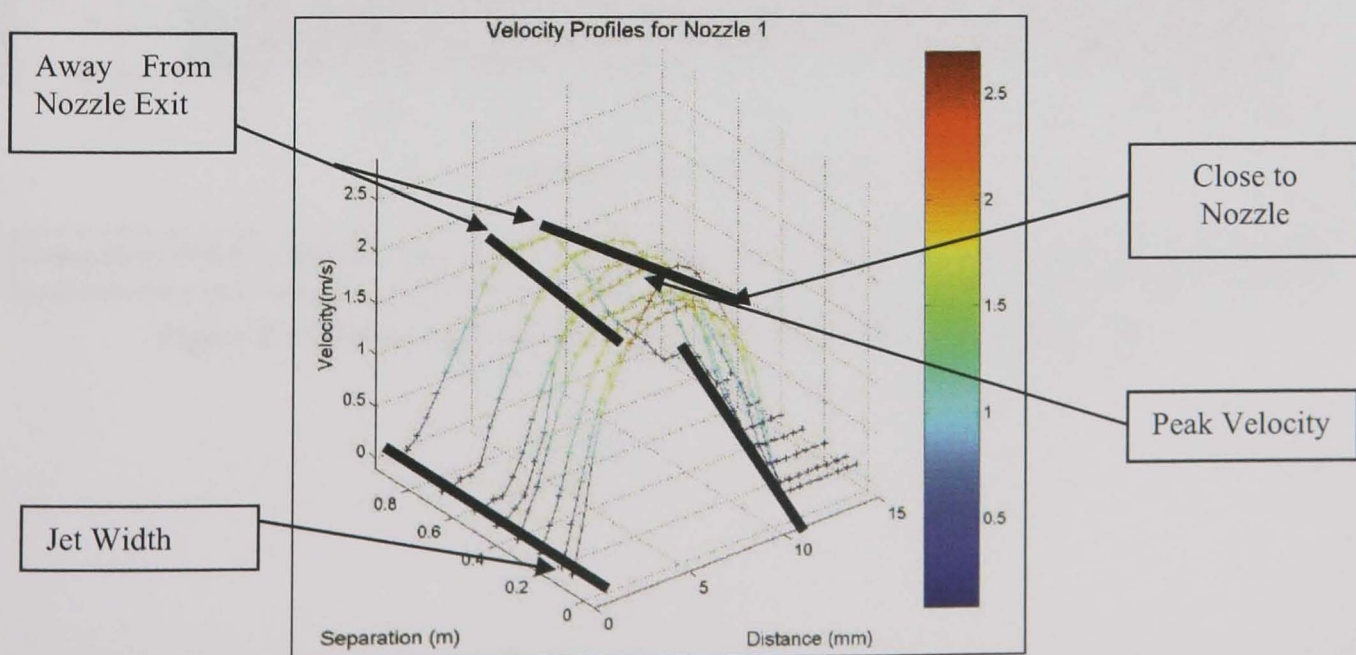


Figure 8-8 Velocity profiles for nozzle 1 - measured values

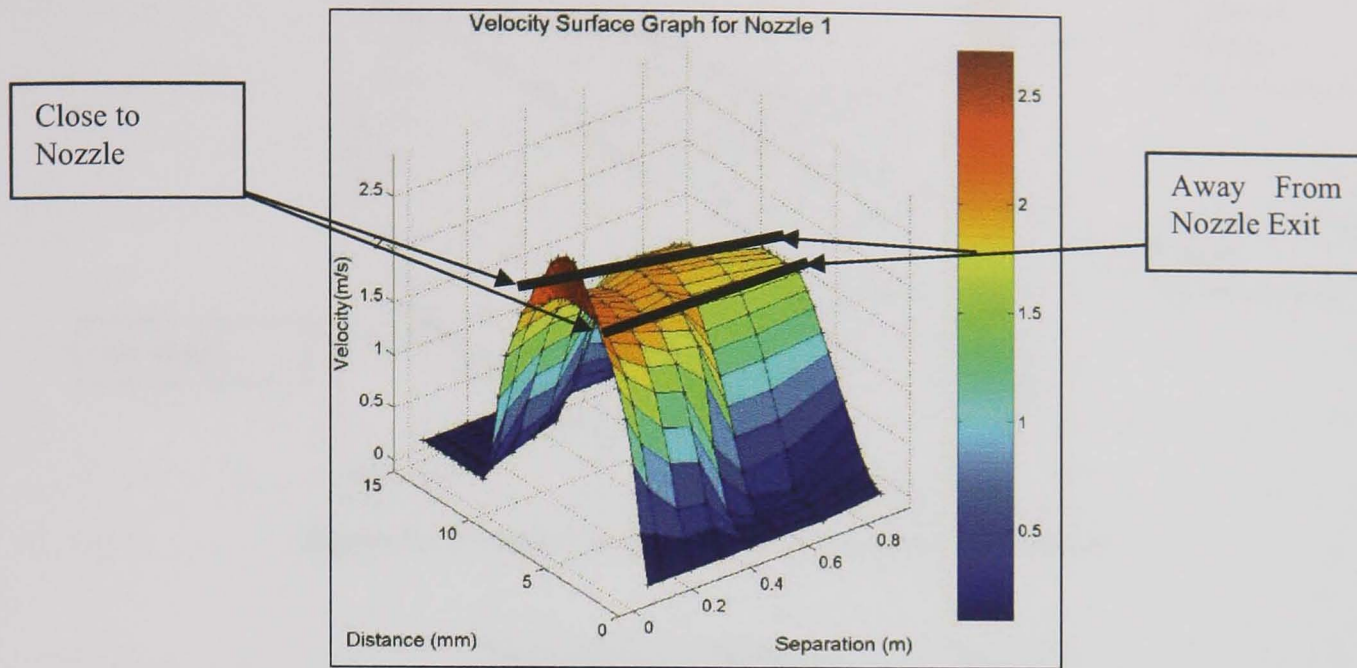


Figure 8-9 Velocity surface graph for nozzle 1- measured values

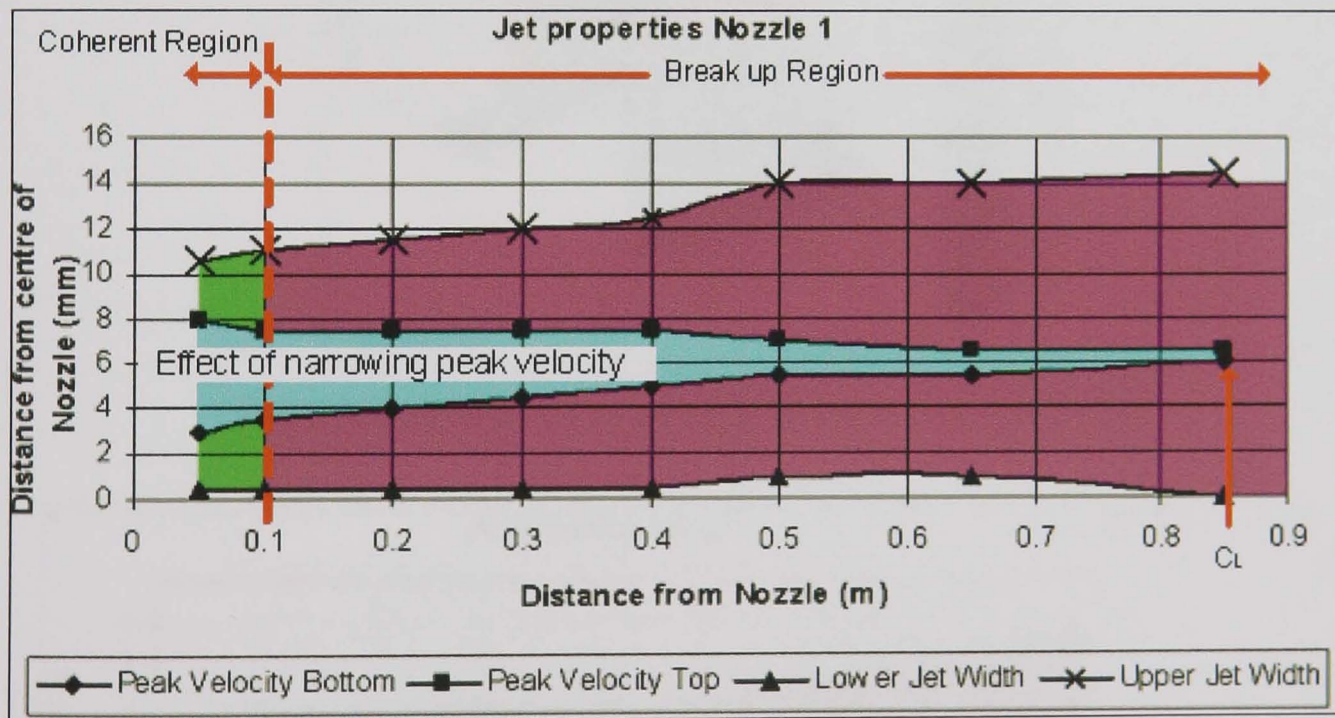


Figure 8-10 Coherence length and jet width for nozzle 1- measured values

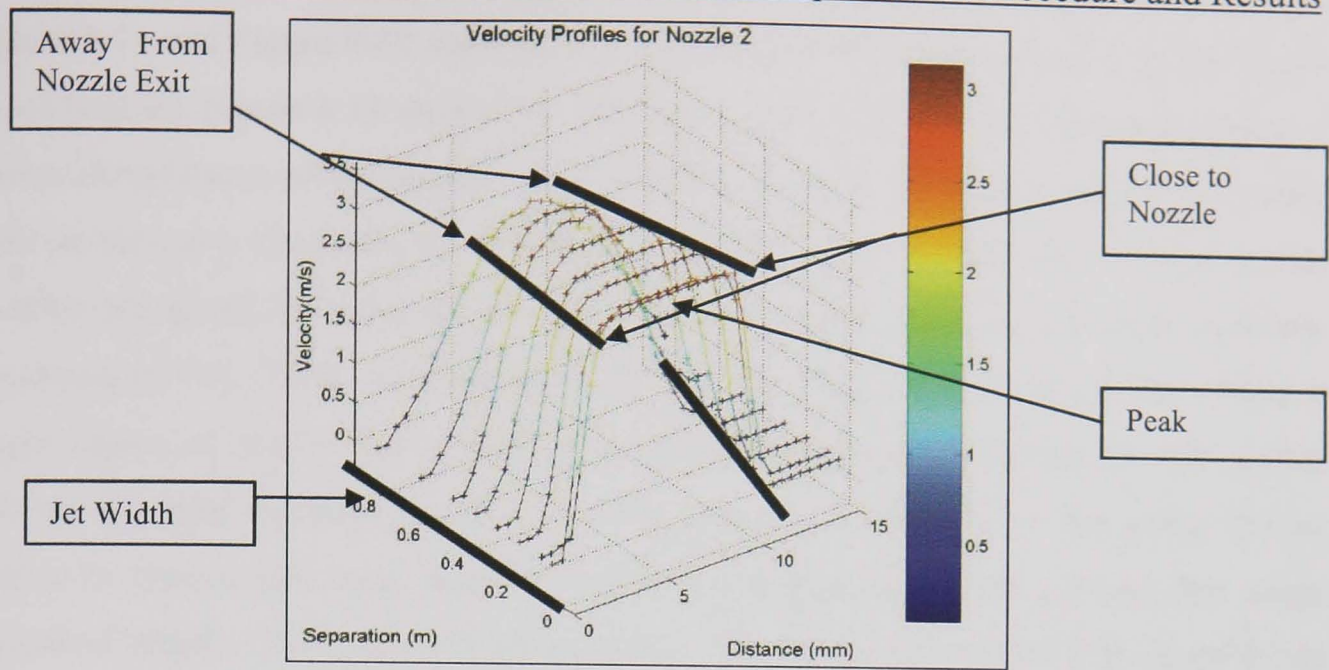


Figure 8-11 Velocity profiles for nozzle 2- measured values

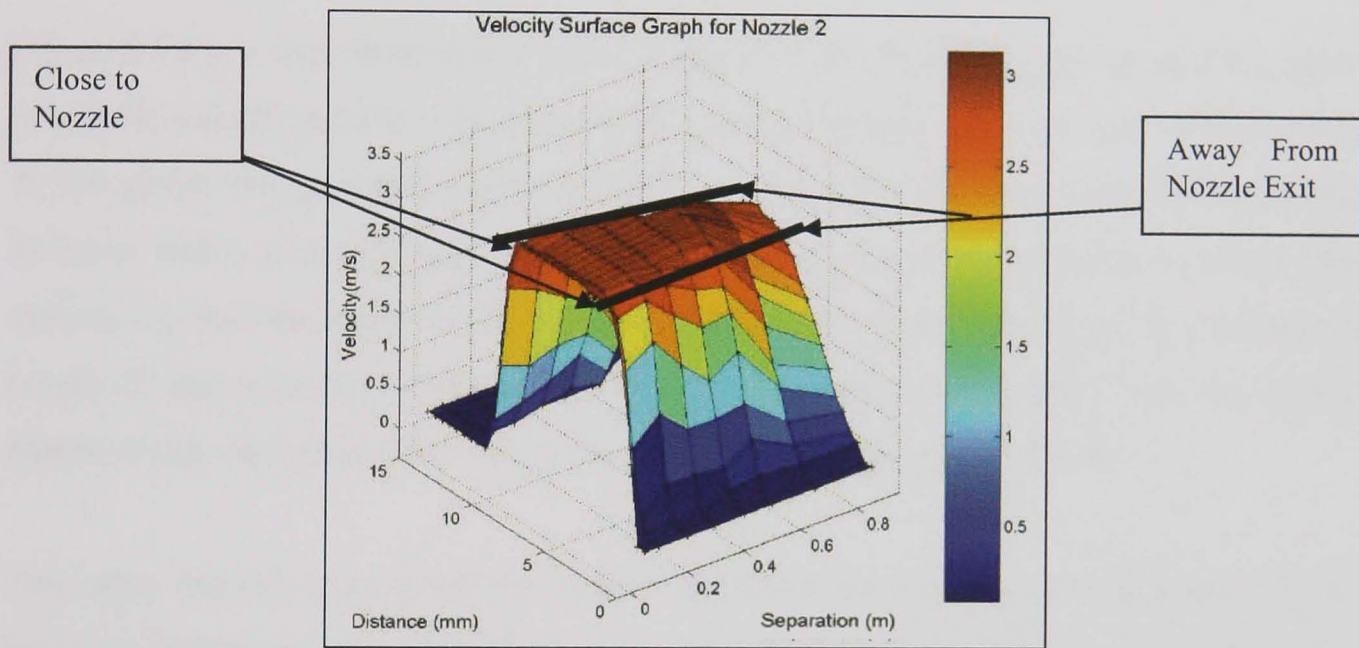


Figure 8-12 Velocity surface graph for nozzle 2- measured values

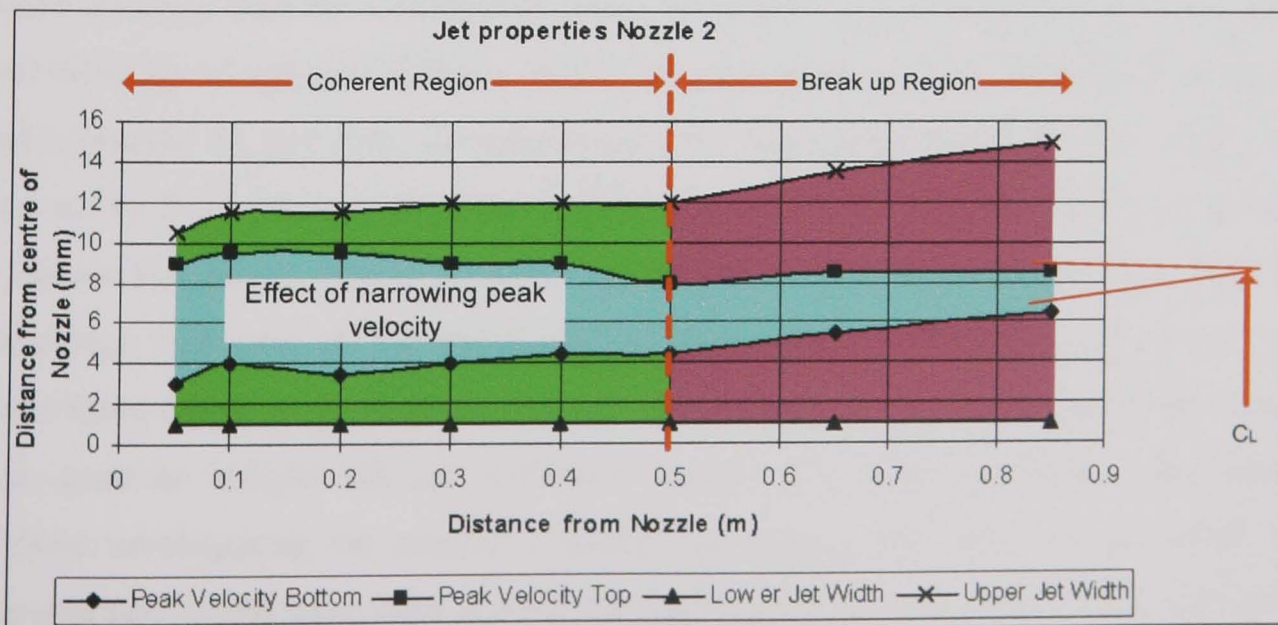


Figure 8-13 Coherence length and jet width for nozzle 2- measured values

Figure 8-11 and Figure 8-12 show plots for the fluid stream with nozzle 2 (9mm Rouse based nozzle). Figure 8-11 shows the velocity profiles at each of the eight measurement planes downstream of the nozzle orifice demonstrating jet coherence. The fluid stream with surface plot illustrates the velocity profile as shown in Figure 8-12. Plots for all nozzles are given in Appendix E. This nozzle is cited as being the most coherent according to Cui (1995) and Webster (1995a). The fluid profiles for nozzle 2 have a larger region of peak velocity than those for the straight pipe (nozzle 1). The profile follows the inlet turbulent profile for a distance up to 500mm. At this point, the jet begins to lose central core velocity, but the core does not break up over the entire measured length. The surface graph confirms this as uniform velocity is observed up until this point.

Figure 8-13 is a two-dimensional representation of the fluid jet break up and the inner-core peak velocity profile. The jet appears to hold its shape until the said 500mm mark. At this point, the jet width begins to increase. Observing the inner core, this maintains its initial width with only slight loss up to this point. After this, it begins to narrow but extends beyond the measurement zone. Extending the lines forward gives a coherence length of approximately 1300mm. This is a 50 per cent improvement over the straight length of pipe and shows the value of the Rouse type coherent jet nozzle.

Two other nozzles were tested for shape comparison for inclusion into the theory for jet break-up length; the slant and the stepped, 9mm round nozzles. The slant nozzle (nozzle 4) exhibits a similar profile break up to the Rouse based nozzle (nozzle 2). The break up length is longer than the measurement area but projecting the lines from the result gives a jet break up of around 1100mm. This is an improvement on the straight 9mm pipe of approximately 33 per cent. In comparison, the stepped nozzle begins to break up as soon as the fluid emerges from the orifice. Results for the stepped nozzle in Appendix E, shows this point, with a jet break up length of approximately 650mm. This is a percentage reduction on the standard coherence length in the region of 24 per cent. These tests, based on the 9mm nozzle exit and compared with the original 9mm straight pipe, gave an insight into the coherence length of a range of nozzle body shapes. Without investigating the internal structure and simply measuring the jet width, this phenomenon would have been missed and had been missed by Petrov et al (1991) Cui (1995), Webster et al (1995a) and Webster et al (1995b).

Analysing the contraction ratio allowed for addition of this effect into the theoretical model. The same three nozzles (slope, step and Rouse-based) were tested; however, the exit diameter was changed to 2.5mm (Table 8-2). The nozzles performed in much a similar way to their counterparts with the 9mm exit gap. The nozzle flowrate was set to 4.5 l/min. The fluid velocity measured inside the nozzle (using the Pitot tube) was approximately 15 m/s. At this increased fluid velocity, the coherence length of the jet reduced. This was the case with all three nozzles, with only the Rouse based nozzle reaching close to the end of the measurement zone. As the jets have less internal diameter and less fluid, the inertial forces inside begin to break up the jet sooner than the jet break up of the larger diameter jets. The peak velocity for nozzle 5 from Appendix E shows the break up point at 850mm. This is close to that predicted by the theory for a standard 9mm pipe at high velocities. This implies that if a jet at high velocity is required up to lengths within this range, the Rouse based nozzle could satisfy this requirement.

A combination of these nozzles, through further development, would allow for cooling of large surface areas in both surface and cylindrical grinding. The real application area for this nozzle type (Rouse based) lies with complex profile grinding where fluid nozzle positioning is difficult, and cooling right in the corner of the profile is required.

Appendix E shows the jet width and peak velocity degradation for nozzle 6. The poor internal geometry of this nozzle (the sudden contraction inside the step) has a significant effect on the peak velocity. Although the jet width looks similar to that for nozzle 5, the peak velocity width decreases over a short distance and no peak velocity remains at a point of 500mm. Cui (1995, p.67) states that “for grinding applications, only a short distance (less than 12 inches or 0.3m) from a nozzle exit to the grinding zone is of interest”. Cui goes on to state that the jet break up length due to the stability is therefore of little interest in his work on the cooling performance of the nozzle. This however is a serious oversight due to this value of the peak velocity width. With the system of jet width measurement the nozzle looks suitable up to a distance of approximately 500mm. However, when investigating the peak velocity width, the nozzle performs satisfactorily only to a point of 200mm. Therefore, if the position lies within the range of 200mm to Cui’s limit of 300mm, the cooling performance will be affected. The areas of the jet not at this peak velocity will be deflected due to the air barrier flowing around the wheel

and therefore will not penetrate into the grinding contact. This will not only affect cooling but due to the lack of sufficient lubrication, the surface finish of the part will reduce in quality (Baines-Jones et al 2008).

Appendix E shows the jet width and peak velocity depreciation for nozzle 7. The internal geometry of this nozzle features a sloped profile to contract the fluid flow uniformly to the point of exit. The jet width looks similar with that for nozzle 6 but shows greater break up at distances above 500mm. The peak velocity width decreases over a short distance as with nozzle 6 and no peak velocity remains at a point of 550mm. This is slightly longer than the nozzle with the sudden contraction. The peak velocity width with this nozzle holds for only a short space up to a point of 220-250mm. Although this is longer than the previous nozzle, the pattern is loose and does not follow a straight path making positioning of this nozzle difficult.

Appendix E contains a representation of the jet profile for nozzle 8. This nozzle had an orifice of 5.85mm in diameter (It is shown as 6.5mm in Table 8-2, however, this is the external profile -the nozzle has a wall thickness). It is an adjustable round solid jet nozzle produced by Lechler. The jet maintains its initial width for only 200mm. After this point, the jet begins to break rapidly and the width increases over the whole length of the measurement area. However, the peak velocity, although it is decreasing over the entire measurement length, contains coherent sections. Up to 400mm, the jet width remains constant, providing adequate coverage to this point. After this, the peak velocity reduces to a small section and maintains this for the next 250mm. This nozzle has a good coverage; it can be positioned at varying angles due to its ball joint. At this point, it is worth noting that the effect of internal angle on coherence length, for this type of nozzle, is one that needs investigation because the angle modifies the internal shape of the nozzle and therefore modifies the internal flow of the nozzle, hence affecting the exit profile. This is proposed for further work.

The Rouse based nozzles provide improved performance, but for work closer to the grinding contact, nozzles based around the Lechler nozzle (Figure 8-14) would adequately cover the grinding contact. The advantage of this nozzle is that the contraction from the larger diameter to the smaller diameter runs with a reverse round profile, and at the point of contraction, contains a small figure eight flow conditioner (Figure 8-15). This, Lechler claim, helps to reduce the effect on break up at this point

within the nozzle, producing a uniform jet at the nozzle orifice. This is to be tested in further work with Lechler nozzles in order to clarify this claim.

Figure 8-16 gives a summary of the peak velocity break up length of each of the nozzles. This chart illustrates the point at which the peak velocity width reduces to zero. The table provides a visual method of comparing each of the nozzles side by side, both with experimentation at this point, and for comparison with simulation later in this chapter.

Parameters used were: Fluid type: Water with 5 per cent Hysol X; Kinematic Viscosity: $0.995 \times 10^{-6} \text{ m}^2 \text{ s}^{-1}$; Mass flow rate: 15 l/min; Supply pipe diameter: 19 mm; Fluid Temperature: 25°C.



Figure 8-14 Lechler solid jet nozzle



Figure 8-15 "figure-8" flow conditioner

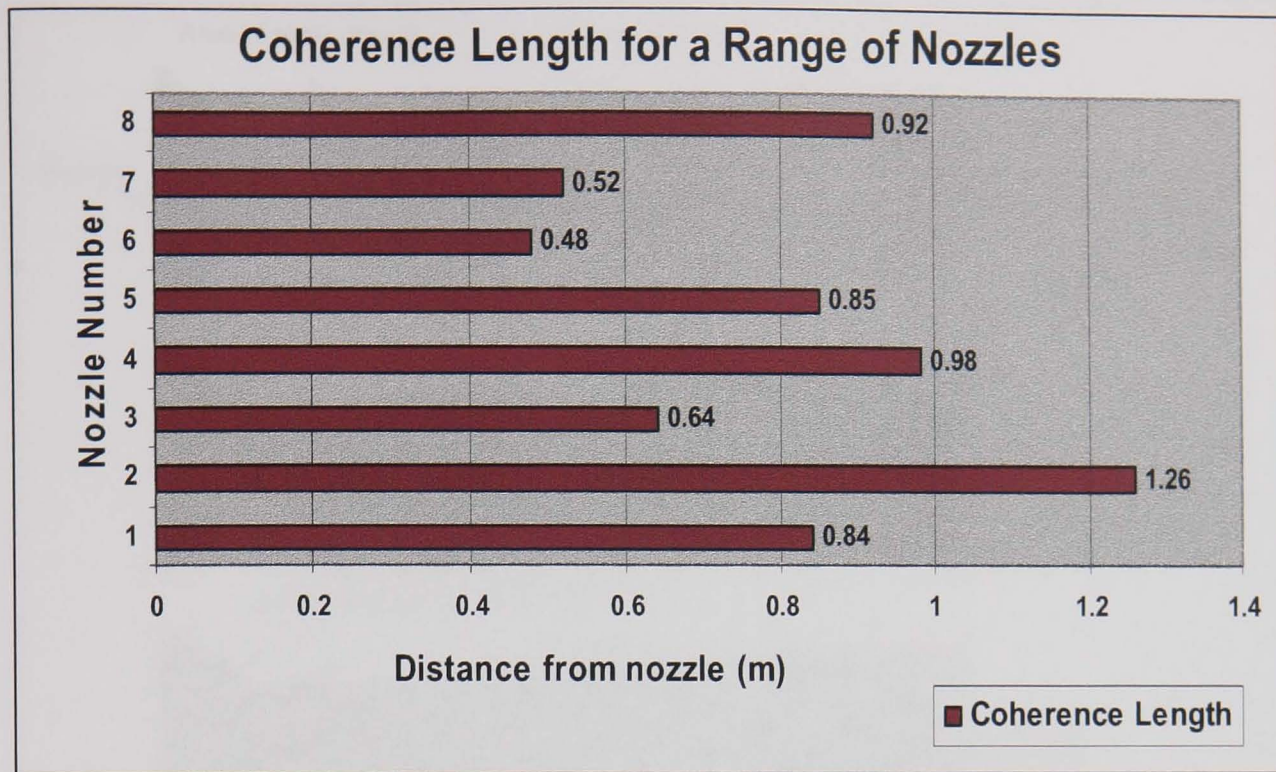


Figure 8-16 Coherence length of each of the nozzles examined experimentally

With process improvements leading to larger wheel/workpiece contacts, whether that be length or width, it is increasingly important that the entire contact be cooled and lubricated. This highlights the significant finding in this work in that the peak velocity of the coolant must be maintained across the entire grinding contact to satisfy the criteria of matching wheelspeed to jet speed. An example of the importance of this prediction, using the models and experimental results within this work, is shown in Figure 8-17. In case (a), the nozzle is positioned too far from the contact zone and approximately only 50 per cent of the area is covered at a sufficient velocity to satisfy the aforementioned wheel/jet speed criteria. In case (b), although sufficient coverage is achieved, this does not optimise (given the matching speed criteria) the distance at which the nozzle could be placed for positioning difficulties. Case (c) represents the optimal (based on coverage) position. Once a manufacturer knows the design constraints of the operation, it would be possible to choose the correct nozzle based upon the distance from which it would have to cover the entire grinding contact. The distances discussed in Figure 8-16 are large in relation to many fluid applications. However, this comparison is made as coherent nozzles allow for targeted cooling from a distance causing less interference with machine tooling. This is also for a relatively large nozzle outlet and hence high coolant use. With much smaller conventional nozzles, the distances are much shorter.

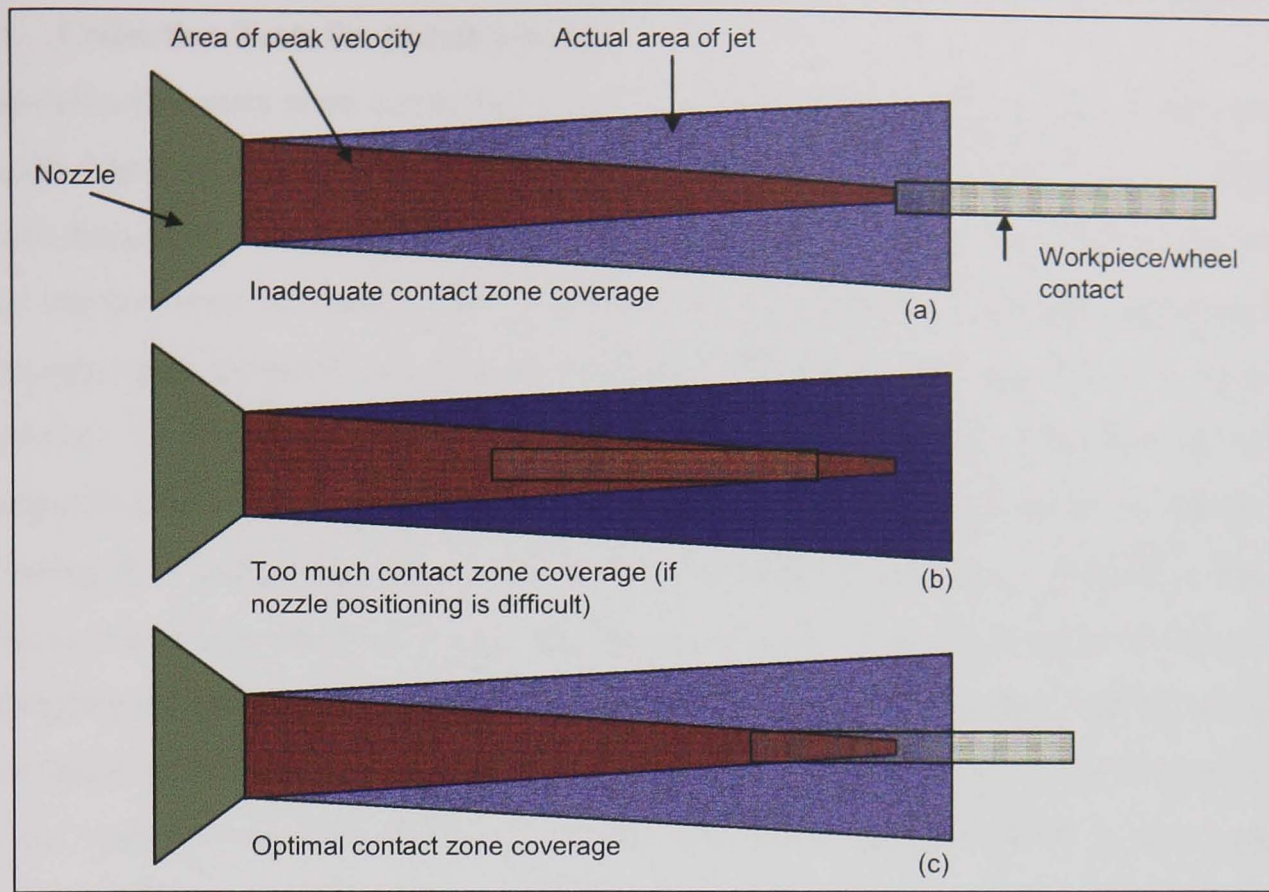


Figure 8-17 Example of coverage using different nozzle to wheel/workpiece contact zone distances

8.3 Collection Tests for nozzle position

The collection tests were conducted using a surface grind operation with an Aluminium Oxide wheel (universal 73a 461 j7v lnaa). The wheel was plunged into a workpiece made from mild steel (BS EN 10025). No actual depth of cut was applied as the wheel was touched onto the surface of the workpiece until spark out occurred. This ensured a minimum gap between wheel and workpiece. The flow was applied at a range of flowrates to test this effect on the amount of fluid collected. For tests on nozzle comparison however, every variable remained constant except the one investigated. The grinding fluid used in the tests was the semi-synthetic grinding fluid 'Hysol X'; this was diluted to a concentration of 5 per cent Hysol X in water. The coolant jet velocity varied depending on the supplied flowrate and the nozzle aperture. The wheel speed was set to a peripheral velocity to match the jet velocity as previous investigations determine this as the way to maximise fluid penetration into the grinding contact. Later work by Jackson (2008) suggests a value of between 0.6 and 0.8 for jet/wheel velocity ratio to be sure that the effects of the air barrier were eliminated. Jackson (2008) gave the performance indicators based on this 'useful flow'. Capturing of the useful flow involved physically isolating the fluid that passes through the grinding contact zone. This required using side scrapers, a workpiece the same width as the wheel and a post-contact zone scraper.

The side scrapers consisted of foam glued to bras spring mounted plates. This allowed the side scrapers to sit closely to the wheel and workpiece creating a physical barrier for the fluid along the sides of the wheel. The scraper to the rear of the workpiece was fixed rigidly to maintain contact with the wheel periphery. Aluminium was used for this scraper as this is considered an easy-to-grind material and would provide minimal resistance to the wheel. Care was taken not to grind too much of this away however as the aluminium is soft and can clog the pores of the grinding wheel.

Care was taken not to grind too much of this away however as the aluminium is soft and can clog the pores of the grinding wheel. The coolant system used was the Arboga Darenth, type 2210/3057. It has a maximum supply of 3.5 MPa at a flowrate of 100 l/min. The Darenth has both a cartridge type and a centrifuge type filtering mechanism. For the nozzle test, very little material was removed and therefore filtration effects were neglected. Experiments were performed under the spark-out condition. For each

experiment, machining the workpiece with two 5 μ m cuts with full coolant at a wheel speed of 2000rpm, gave a constant flat surface for the touch on operation. If the pass failed to provide the required surface (i.e. the constant flat surface), the step was repeated until a suitable surface was achieved.

From the previous results on jet coherence length, it was deemed that the Rouse based coolant nozzle would give the best results for nozzle position due to its coherent nature. This work investigates the positioning effects at greater distances from the grinding contact. It is concerned with coherent jets for situations in which the grinding fluid nozzles cannot be positioning within millimetres of the contact region. Experiments therefore, were conducted with the 2.5mm diameter Rouse-based coherent jet nozzle. The aim of the experiment was to achieve maximum fluid efficiency through nozzle placement with the remaining variables fixed. The fixed variables were:

- Fluid Type → Castrol Hysol X at 10 per cent concentration
- Wheel Periphery Speed → 30 m/s
- Wheel Type → Aluminium Oxide 200mm \emptyset
- Inlet Pipe Diameter → 19mm
- Flow Conditioning → Conditioner 4
- Gap size → Minimum (<0.1mm) (between the wheel and the workpiece)
- Nozzle Flowrate → 9 l/min
- Nozzle → Rouse 2.5mm \emptyset
- Jet Velocity → 30.1 m/s

The Rouse based nozzle was positioned horizontally to the workpiece/wheel contact at an angle of 0° to the horizontal and at a height of 0mm relative to the workpiece surface (at the centre of the jet). The nozzle distance x (Figure 8-18) was varied to investigate this effect on useful flow. The useful flow was measured for 20 seconds, three times for each position, and then averaged to give the mean useful flow. This was then converted to a percentage of the supplied flow to define how much of the supplied flow is carried through the grinding contact in the pores of the wheel at the different positions. This collected flow and nozzle position are plotted together and shown in Figure 8-19.

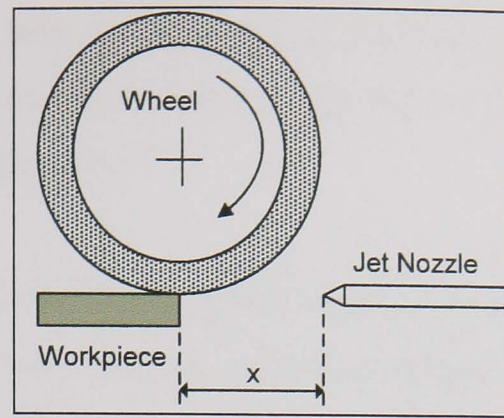


Figure 8-18 Nozzle distance experimental arrangement

At lower flowrates, a linear increase in useful flowrate with nozzle flowrate is observed. However, at higher supply rates, it is observed that the rate of increase in useful flowrate tends to decline. The rate of increase reduces because of the limitation of the volume of fluid that can be transported within the spaces near the surface of the wheel. From the results with coherent jet nozzles however, Figure 8-19 shows that positioning the nozzle closer to the grinding contact leased to increased percentage of collected flow.

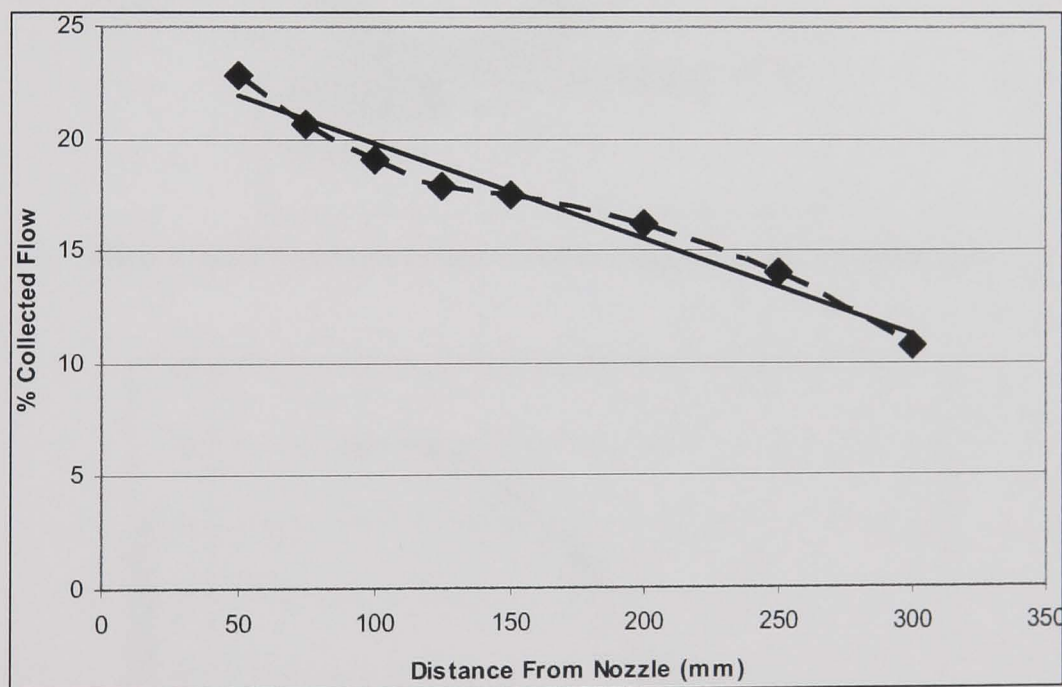


Figure 8-19 Effect of nozzle distance from the grinding contact on collected fluid

As the nozzle is moved further from the contact, the amount of fluid passing through the grinding contact reduces linearly. This result verifies that positioning of the nozzle, as close to the grinding contact is preferable. This agrees with conventional practice directing fluid as close as possible to the minimum gap between the grinding wheel and the workpiece. Traditionally, this is achieved by positioning the nozzle parallel to the

workpiece surface and as near to tangential as possible to the wheel periphery. This positioning is said to work due to the wheel dragging the fluid into the gap and reducing the effect of the air boundary layer.

To determine influence of nozzle position on the percentage of collected fluid, different aiming positions on the wheels surface were investigated. Figure 8-20 shows the first two positions highlighted with the repositioning of the nozzle drawn with dashed lines. The nozzle was first set at a (0,0) position indicating directly at the contact point. It was then moved back by 5mm in x and kept 5mm from the wheel edge each time. Results for this test are illustrated in Figure 8-21. Measurements closer than this were not possible due to the size of the nozzle when both the wheel and workpiece were in position.

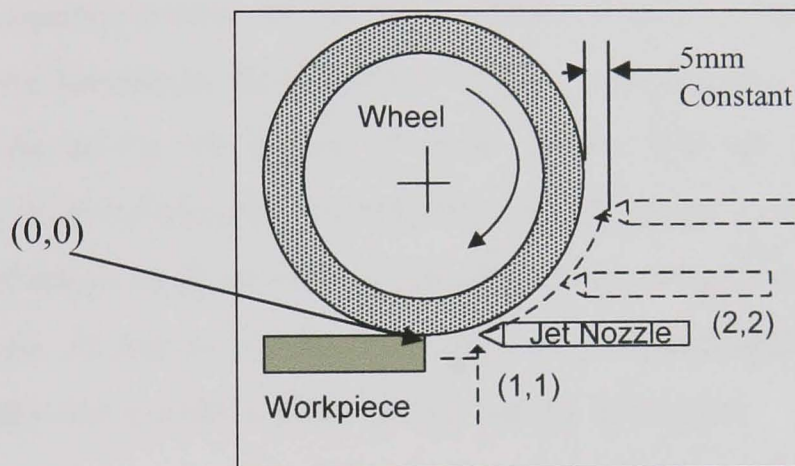


Figure 8-20 Nozzle movement distance experimental arrangement

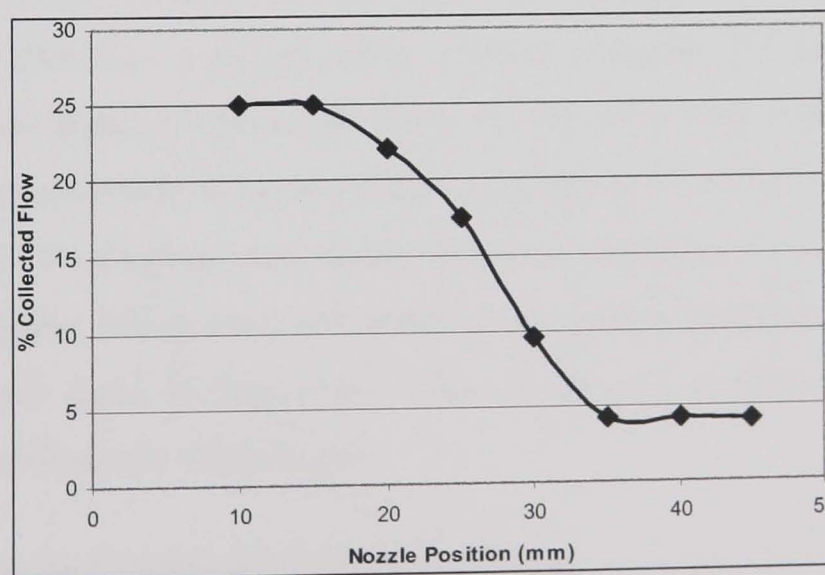


Figure 8-21 Effect of differing nozzle position on collected flow

Figure 8-21 shows the results for the nozzle positions investigated. This method, of moving both up and back, delivers cutting fluid to the wheel surface at a point above the

area of reversed flow. With the nozzle in this position, grinding fluid is directed at the grinding wheel and is carried to the grinding contact with the boundary layer. The grinding wheel can carry the fluid to the grinding contact, as long as the fluid contains sufficient energy and lies in a plane at which the air barrier is unable to reform. The effect of reversed flow at the grinding contact aids the entrance and entrainment of the fluid, as the fluid rides over the high-pressure stagnation points and is driven through the minimum gap between the wheel and the workpiece. Above the region of high pressure, fluid enters the grinding contact and side leakage is reduced as flow runs to the negative pressure on the exit side of the minimum gap. This work is confirmed in work by Ebbrell (2000).

The first interesting result is the marginal reduction with the nozzle lifted in the first two positions. Approximately 25 per cent of the fluid is collected at both these points, indicating no loss due to the distance the nozzle is retreating. This is said in Ebbrell et al (2000) to be as the air barrier at these points does not have the time to reform, permitting fluid entrainment towards the grinding contact area. After this point, there is a linear reduction of fluid passing through the grinding contact, until 35mm from the contact zone. At this point, the collected flow is approximately constant indicating no further losses due to side leakage and air barrier deflection.

Similar trials were conducted for the other nozzles examined within this work. The less coherent nozzles produced much similar results to those presented, but with reduction in overall collected flow due to the spreading of the jet at greater distances. A full analysis of positioning was deemed beyond the scope of this work. This however, either could be calculated experimentally or analysed using a progression of the validated simulation within this work. To progress this, work should be scheduled for a full Taguchi-type design of experiment taking into consideration the areas highlighted in Figure 6-5, on each of the nozzle types in Figure 8-2. This would give a good comparison of the overall nozzle performance of each type.

8.4 Verification and Validation of the Simulations

Measurements on coolant nozzle flows are time consuming to perform and not possible for all situations. Therefore, three-dimensional computational fluid dynamics models have to be used. However, they have to be validated with experimental data. The codes validated within these experiments can be used for the calculation of various properties

in real fluid situations, if the physical models are validated and the test experiments are properly scaled the same fluid mechanics phenomena are addressed. Accurate transient three-dimensional CFD calculations are very demanding on computing power. To overcome this, simplified models for the description of e.g. turbulence, which is very important for the break up of the jet, are used. This section of work attempts to address and define these errors and to validate, practically, the CFD model. Errors and uncertainty are unavoidable aspects of CFD modelling. It is therefore necessary to develop rigorous methods to quantify the confidence levels of the results. Terminology, due to American Institute of Aeronautics and Astronautics (1998), and Oberkampf and Trucano (2002), has now been widely accepted. With this in mind, the methods of verification and validation are discussed.

8.4.1 Verification

Ignoring errors such as computing errors and user errors leaves three areas of error: roundoff error, iterative convergence error and discretisation error.

- *Roundoff error* is assessed by comparing CFD results obtained through a method of analysing the computer's accuracy. A study of this is possible in CFX using single or double precision with 7 or 16 significant figures respectively.
- *Iterative convergence error* is investigated using target variables. In this work the value for velocity at the nozzle exit is known using theoretical fluid mechanics, and is compared to the CFD result to quantify the iterative convergence error.
- *Discretisation error* relates to the errors associated with the level of mesh refinement. A mesh refinement study is used to quantify this error and to reduce it to a minimum to give confidence in the CFD results. The discretisation error is assessed in three ways:
 - The convergence is monotonic (reducing levels of refinement giving reducing value variation for a target variable).
 - The numerical model is in its asymptotic range (The truncation error is dominated by the leading term of the Taylor series expansion).
 - The use of the Taylor series expansions is justified through a sufficiently smooth flow field.

Analysing error estimation by Roache (1997), consider a simple flow problem under steady conditions, the error E_Q in the target quantity Q (e.g. velocity) is a function of the reference size h of the control volumes inside the mesh:

$$E_Q(h) = Q_{exact} - Q \approx Kh^p \quad [8.1]$$

where K is a constant and p is the order of the numerical scheme

Considering a model with one level of mesh refinement, i.e. mesh refinement ratio $r = h_2 / h_1$ and solutions Q_1 and Q_2 , the estimation of the discretisation error is written as:

$$E_{Q,1} = \frac{Q_2 - Q_1}{1 - r^p} \quad [8.2]$$

$$E_{Q,2} = r^p \left(\frac{Q_2 - Q_1}{1 - r^p} \right) \quad [8.3]$$

where $E_{Q,1}$ is the error in the coarse mesh solution and

$E_{Q,2}$ is the error in the fine mesh solution

Roache (1997) also noted that estimates of equations [8.2] and [8.3] are only approximations and do not bound the actual discretisation error. To allow for this within CFD simulations he proposed a grid convergence indicator (GCI) to quantify this error:

$$GCI_Q = F_s E_Q \quad [8.4]$$

where F_s is the safety factor with a conservative value of 3 suggested for most CFD applications.

As truncation errors do not, in all cases, decay in a formal order, Roache (1997) proposed equation [8.4] to find the order \tilde{p} of the truncation decay rate for constant mesh refinement of the order $r = h_2 / h_1 = h_3 / h_2$.

$$\tilde{p} = \ln \left(\frac{Q_3 - Q_2}{Q_2 - Q_1} \right) / \ln(r) \quad [8.5]$$

where $Q_2 - Q_1$ is the difference between the medium and coarse mesh solutions

and $Q_3 - Q_2$ is the difference between the fine and medium mesh solutions.

For high quality CFD simulations such as the one proposed in this work using two or more levels of mesh refinement, Roache (1997) recommends evaluating equations [8.2] and [8.3] with the value of \tilde{p} from equation [8.5] and a safety factor $F_s = 1.25$ in equation [8.4].

A mesh convergence study using Roache's error theories allowed for quantification of the discretisation error within the new results. This was performed analysing solution variables at several places within the domain calculated analytically. The model was refined until only small change (in the region of 1 per cent) were observed in the variables at these selected locations. Figure 8-22 shows the mesh convergence study for the slant-based nozzle for six refinement levels. The point analysed was the nozzle exit pressure in the centre of the nozzle orifice and the maximum pressure in the system.

This result gave the mesh from which the simulation and further decisions on the model were based upon; the mesh at level four was used for all simulation of nozzles. To further increase the accuracy of the model at the points of most variation, and therefore areas needing high accuracy (i.e. at the edge of the jet steam exiting the nozzle orifice), adaptive mesh refinement of the model was selected. Mesh adaption in ANSYS CFX is the process by which the mesh is selectively refined in areas that are affected by the adaption criteria specified. This means that as the solution is calculated, the mesh can automatically be made finer in locations where solution variables change rapidly, in order to resolve the features of the flow in these regions. Each mesh element is given an adaption level. Each time the element is split into smaller elements, the new elements are assigned an adaption level one greater than the element it was generated from. The maximum number of adaption levels is controlled to prevent over-refinement. Figure 8-23 shows this adaptive meshing with two further levels of mesh refinement. This was applied to all simulations modelled. The green areas in Figure 8-23 represent those volumes refined in the first level of mesh refinement. After this, the results are then reprocessed with a second level of refinement (the red elements in Figure 8-23). The gradient in volume fraction of water or 'coolant' was applied as the control for the mesh adaption.

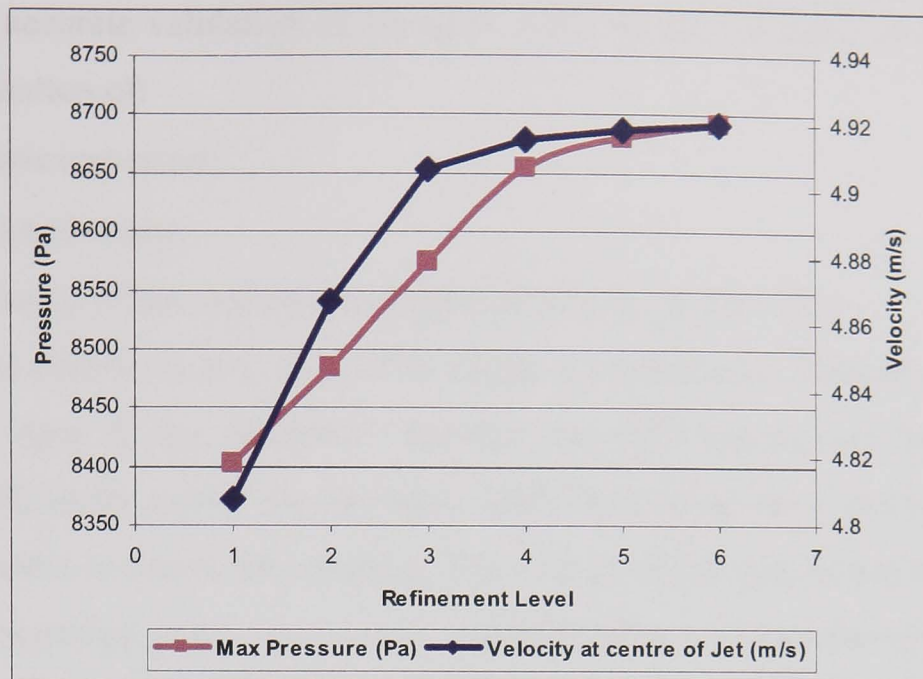


Figure 8-22 Mesh Refinement study for the improved model

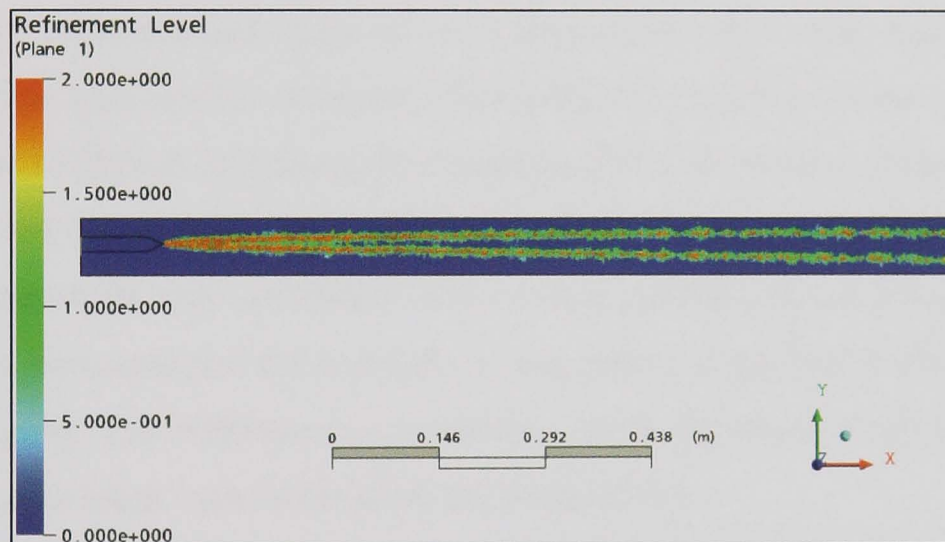


Figure 8-23 Adaptive mesh refinement in the slant nozzle with 2.5mm diameter orifice

8.4.2 Validation

Validation of CFD results involves quantification of both the input uncertainty and the uncertainty of the actual physical model. Input uncertainty is estimated using an uncertainty or sensitivity analysis. This tests a CFD model under several runs with varying values of input data taken from probability distributions based on not only their mean value, but also their expected variations around this mean value. Observing variations in target quantities may produce boundaries for the expected variation, and thus, are an effective way of analysing input uncertainty. This type of validation is justified when analysing several variations and to test its rigour at the extremes. To do this however, some benchmark to test against is required. Oberkampf and Trucano (2002) stated, “Quantitative assessment of the physical modelling uncertainty requires comparison of CFD results with high-quality experimental results.” From their work, it

is noted that accurate validation of the CFD model is only possible in the presence of accurate estimation of:

- all numerical errors;
- input uncertainty;
- uncertainty of the experimental data used in the comparison.

Therefore, the definitive test of a CFD model is comparison between its output and experimental data. If the difference between the CFD model and the experimental results is sufficiently small, for example, when measuring the velocity at the nozzle orifice, the model is said to be validated. The way in which this should be carried out is still under discussion today and various methods such as Coleman and Stern (1997), Oberkampf and Trucano (2002) and Wang and Lehmann (2008) are still in early stages of argument and investigation. Many sources of experimental results are available for common flow problems and some not so common. For this work however, accurate experimentation with control variables allowed for this validation of the simulation. The results of this validation comparing the experimental work and the model are shown in Figure 8-24 and Figure 8-25. The verification involved mapping the peak velocity from both experimentation and simulation. The velocity profiles at set distances from the nozzle orifice were analysed for each nozzle and plotted using MATLAB to produce the validation results. The difference in appearance of the diagrams is due to the different number of points taken in the simulation and experiment.

Looking at Figure 8-24 and Figure 8-25 it is clear that there is a difference between the sizes of the area at peak velocity. With the scale in Figure 8-24, the width of this peak velocity at the first measurement point (50mm from the nozzle orifice) is approximately 5mm. This shows that the nozzle coherence is consistent at this point, and that the coherence length of the nozzle is performing well. When comparing this with the results for simulation (Figure 8-25) however, the area at peak velocity here lies within a width of 4mm. This confirms that the CFX model is slightly under-predicting the coherence length due to the increased fluid entrainment at areas less than 50mm from the nozzle orifice (as explained in Chapter 6). What the two figures do show is that the peak velocity breakup follows a similar type of distribution or break up pattern. This confirms that the model is predicting the actual path of the fluid correctly yet due to the over entrainment, the actual velocity of fluid in the path is lower than that for experimentation. The difference in the two figures comes from those areas not in the

path of peak velocity break-up. On further analysis of the edge areas of the fluid stream, the experimental readings contain exact data from the sensor; the model however, has large gradients where the air and coolant volume fraction changes rapidly. This could be reduced by making the grid extremely fine at those areas of high volume fraction gradient, however, this would require exceedingly large amounts of computational resources and time.

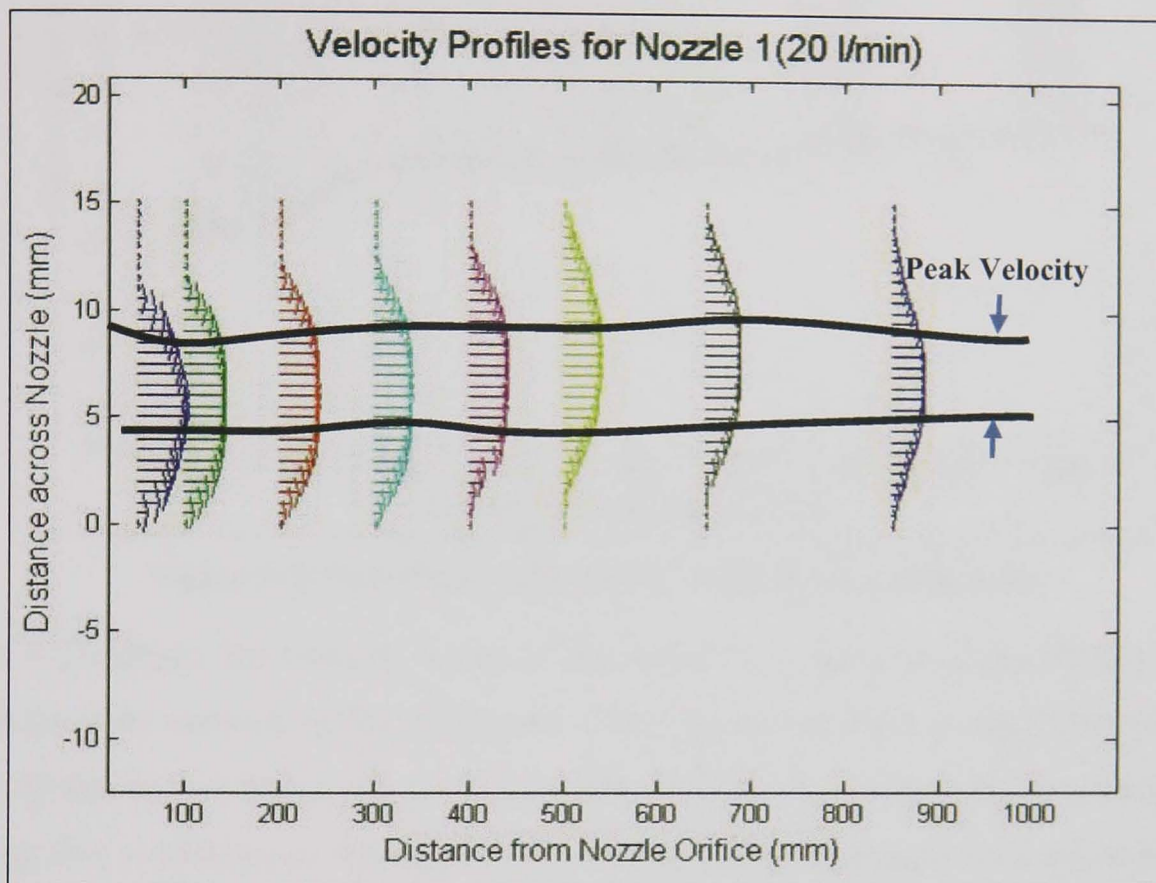


Figure 8-24 Experimental results for Rouse nozzle 9mm @ 20 l/min

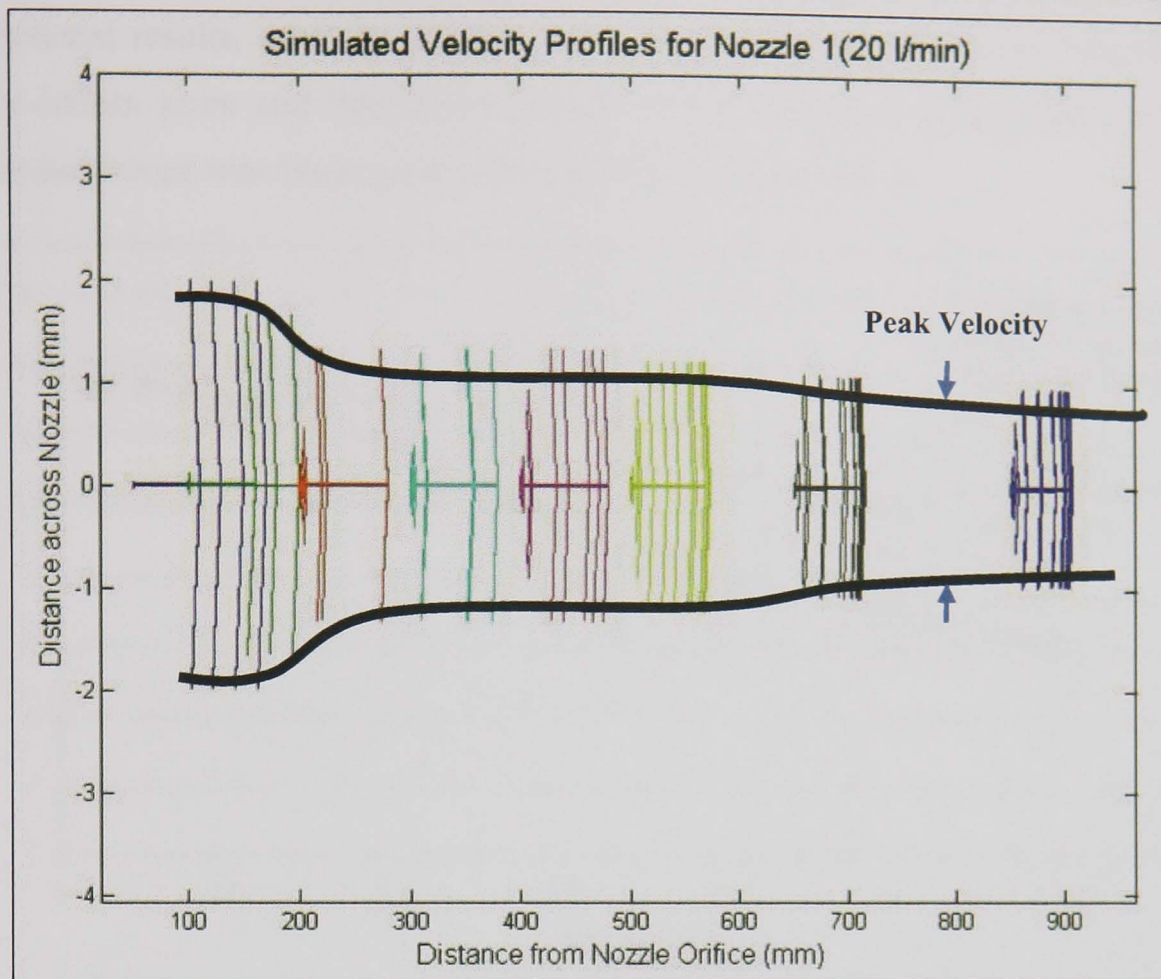


Figure 8-25 Simulation results for Rouse nozzle 9mm @ 20 l/min

Figure 8-26 shows the velocity decay of the water jet at the exit of the 2.5mm \varnothing slant nozzle for a jet velocity of approximately 14m/s produced from an inlet flowrate of 20 l/min. At the exit of the nozzle, the decay rate, both for experiment and simulation, was slow up to $x = 300$ mm at which point the two solutions diverge. In the simulation, the jet decay increased rapidly further downstream. Initially this decay was due to momentum diffusion within and close to the free surface of the jet resulting from the expansion in the water jet and entrainment of the surrounding air. Further downstream the decay due to entrainment into the jet from its surroundings begins to slow at around the 620mm point.

Within the experiment, the jet decayed slower than the simulation after the 300mm point up until this point at 620mm, considered the coherence length of the jet. All velocities have been normalised with the centreline velocity at the exit of the nozzle to compare the numerical results with experimental values. At the nozzle orifice, the velocity for the two results was identical. This shows the model predicts the correct exit velocity due to the reduction in cross-sectional area within the slant nozzle. The predicted decay rate for the water jet matched reasonably with the experimental results up to a point. Although the predicted jet decay rate slightly deviated from the

experimental results, after the 300mm point, the trend was similar i.e. decayed faster after a certain point and then begin to slow at the very end of the fluid jet stream. Similar behaviour was observed for several of the nozzles tested.

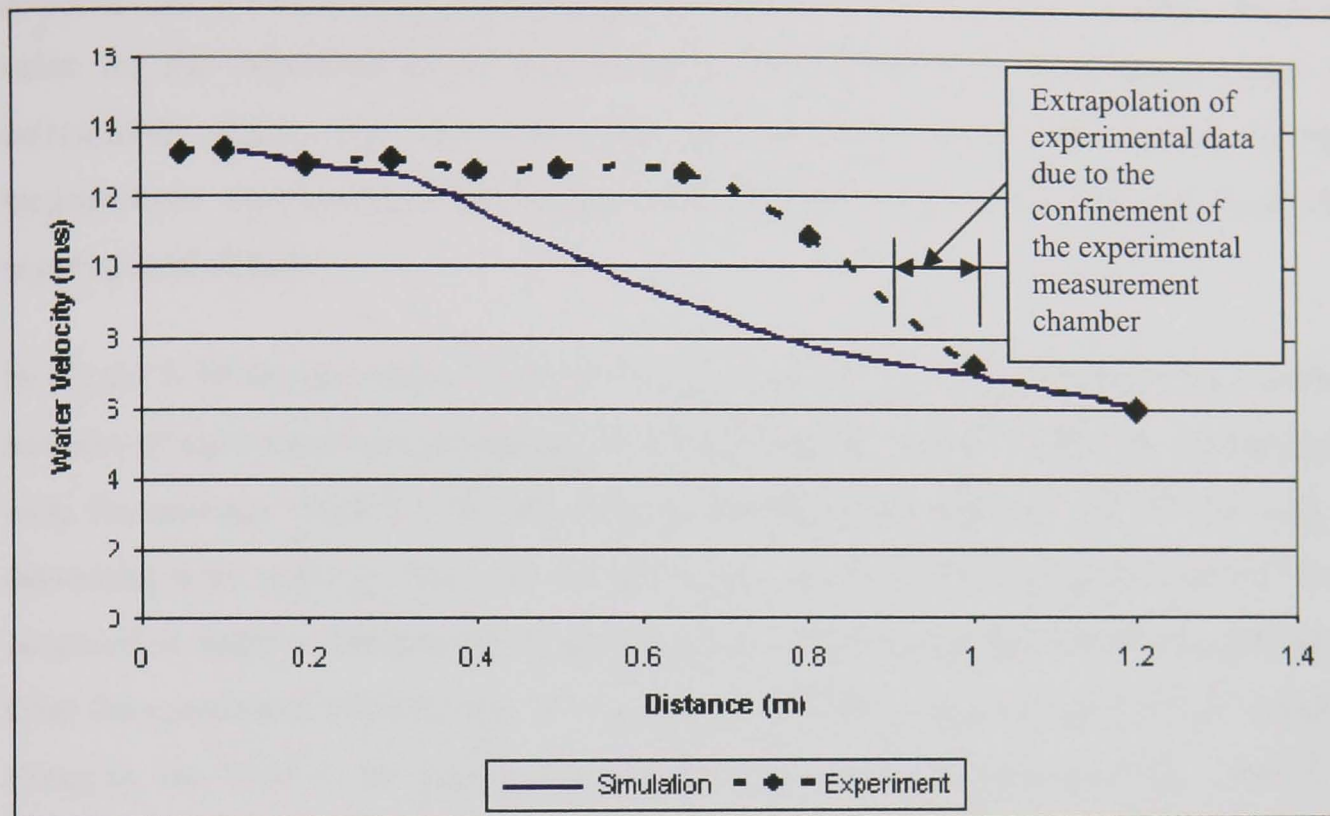


Figure 8-26 Comparison of centre line velocities (2.5 Slant @ 20 l/min)

Transverse velocity profiles for the 2.5mm \varnothing slant nozzle in the y-z plane through the centre of the jet for $x = 0, 100, 450$ and 650mm are shown in Figure 8-27, Figure 8-28, Figure 8-29 and Figure 8-30 respectively and compared with the experimental results. Velocity profiles at the nozzle orifice, Figure 8-27, shows that generally the behaviour of the predicted jet is same as observed in the measured jet. However, there are some deviations between the predicted results and the experimental values. At the nozzle orifice, the peak value of the simulated jet was well matched with the experimental results but the boundaries were narrower on both sides of the jet than the measurements indicated. At 100mm, the predicted values on both sides of the jet matched well, the measured profile had an almost identical peak velocity in the centre of the jet however, the boundary was thinner on both sides side. There is a clear indication of the deviation of the jet towards the sides at this position (indicating jet width increase) although the measured jet deviated more than the predicted jet across the geometric axis. At 450mm, the simulated jet had deviated even more from the geometric axis and the profile had become wider than at 100mm. The experimental jet moved further off from the geometric axis and the peak velocity reduced but not enough to match the simulated jet.

For $x = 650\text{mm}$, Figure 8-30, the predicted jet and the experimental jet showed a similar behaviour in terms of relaxation of the peak velocity. The peak value in the centre line of the geometric axis was under-predicted at 0 and 450mm respectively. At 650mm, the predicted jet deviated (only very slightly) from the geometric axis, whereas the peak value for the experimental jet was along the geometric axis. With the increase of entrainment within the fluid core, the jet deviated towards the bottom of the measurement environment but the deviation was not as slow as expected from the experimental results.

In Figure 8-30 the deviation of the jet was greater and the peak velocity much lower, because of the increased randomness resulting from the mixing of the air environment with the primary fluid jet stream. Similar results were apparent for the jet with a decreased inlet velocity, however the deviations in jet width and peak velocity were observed at shorter distances due to gravitational effects on the fluid jet stream pulling it from the simulation environment. The graphs potentially show that air is being dragged along by the fluid in the simulation. Considering the total momentum by integrating across the profile, simulated results cannot be over twice the amount of the experimental results. Plots of superficial velocity could confirm this as multiplying this result by the volume fraction may bring results closer together. This is considered in further work.

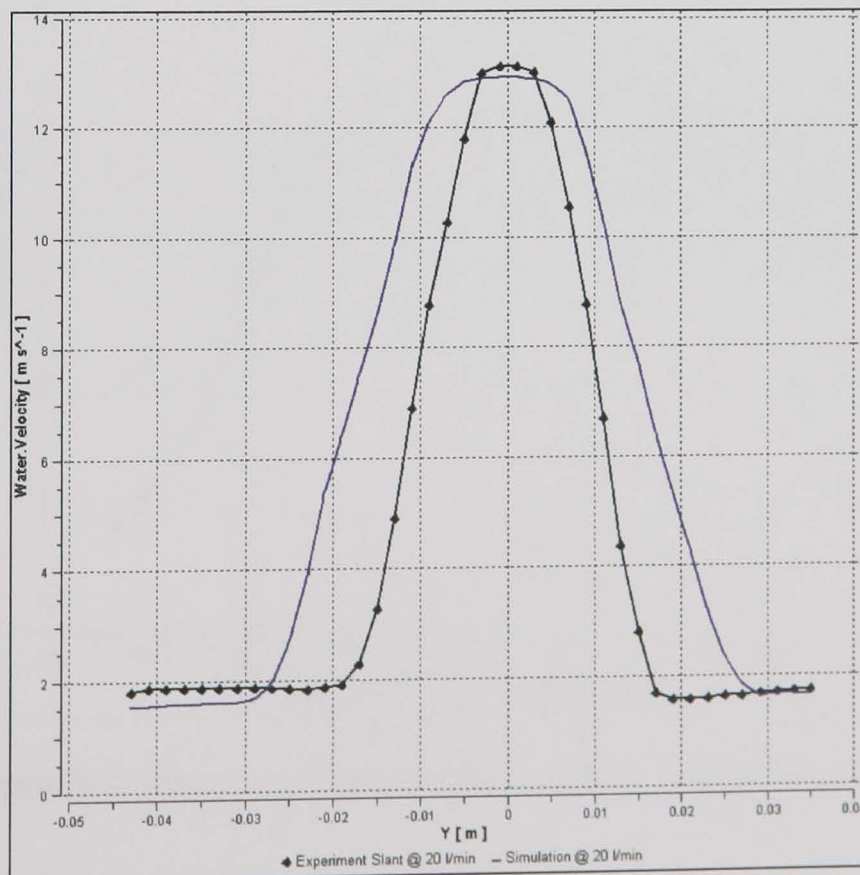


Figure 8-27 Transverse velocity profile at nozzle orifice

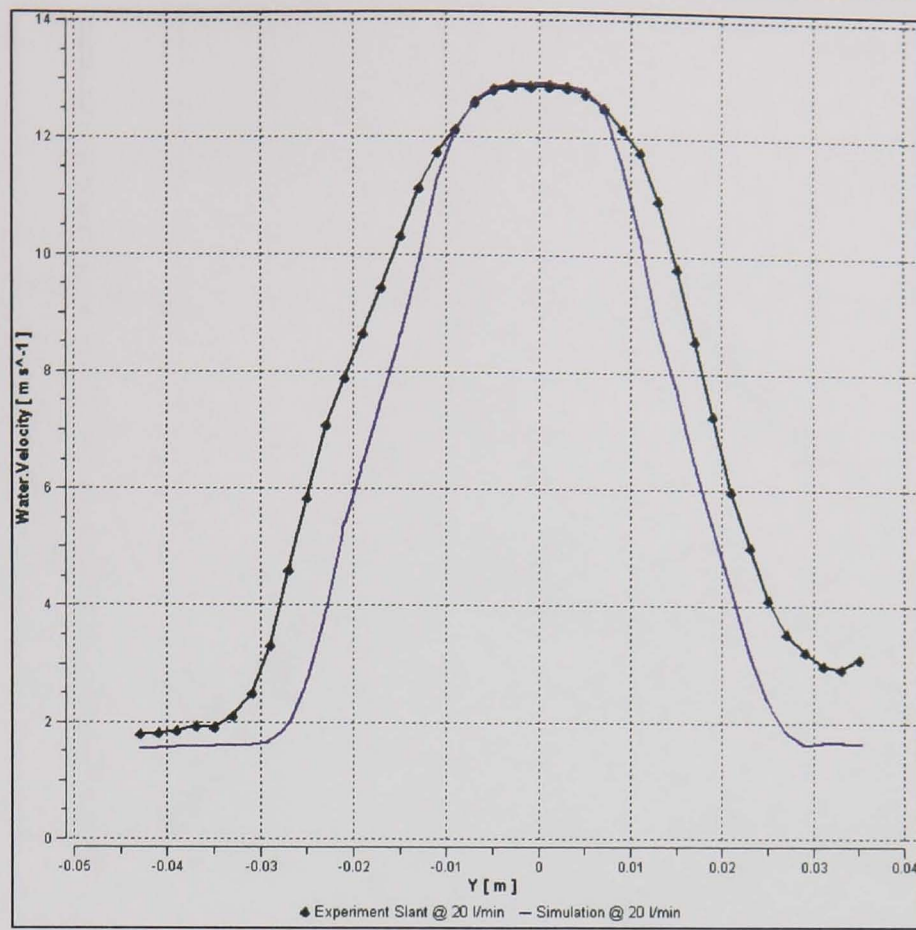


Figure 8-28 Transverse velocity profile at 100mm from nozzle orifice

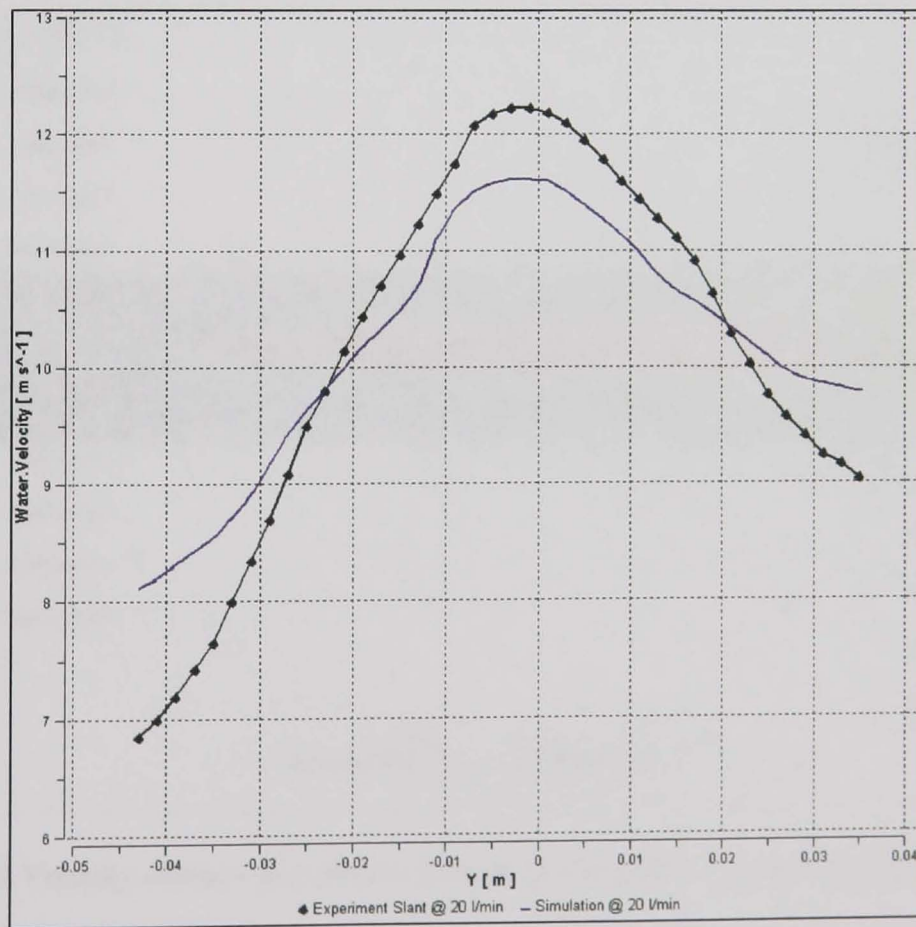


Figure 8-29 Transverse velocity profile at 450mm from nozzle orifice

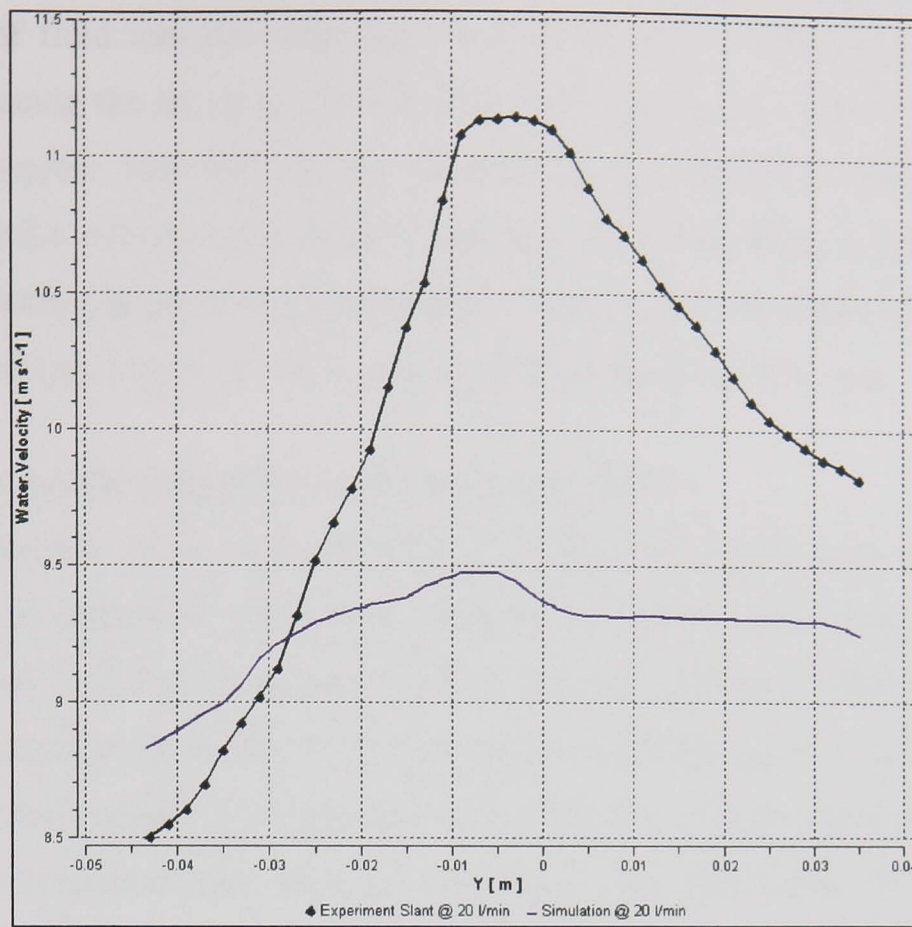


Figure 8-30 Transverse velocity profile at 650mm from nozzle orifice

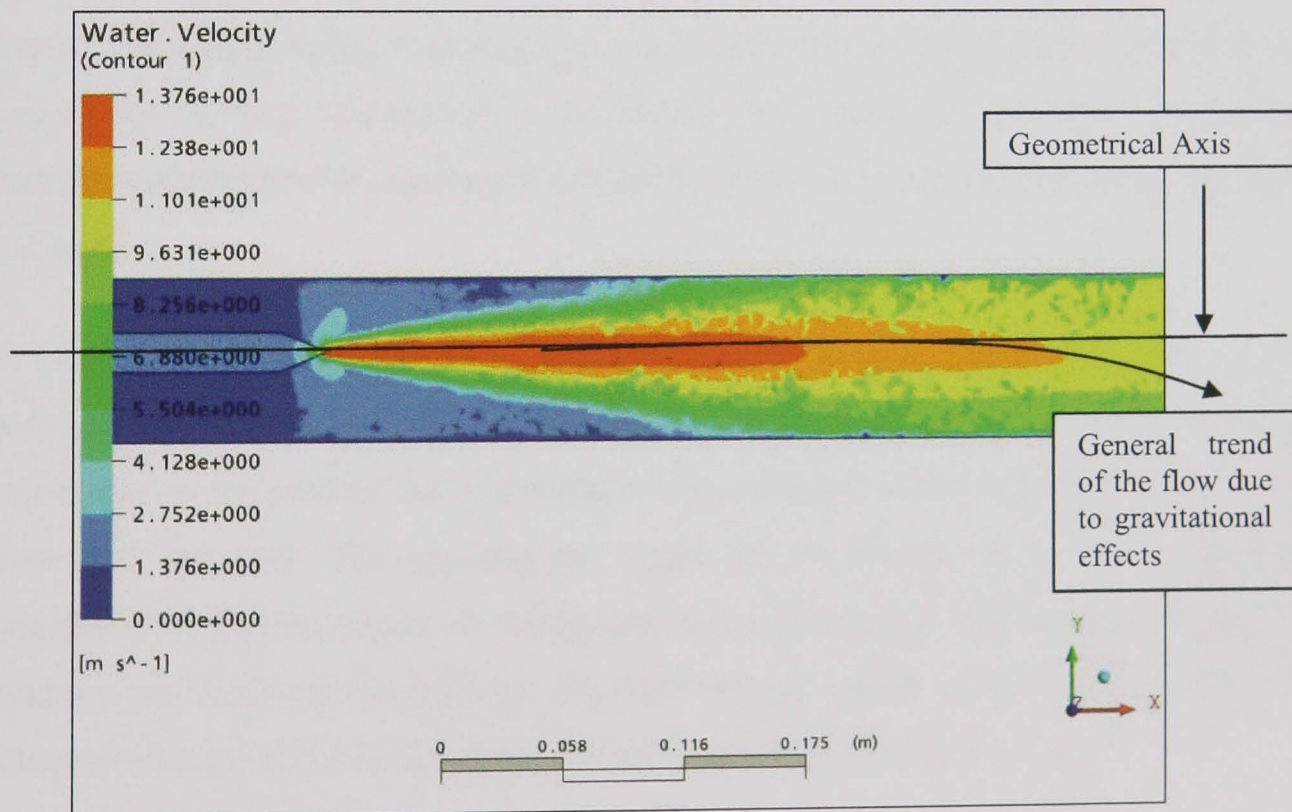


Figure 8-31 Velocity contour plot for the 2.5mm Ø slot nozzle through the centre of the jet

In Figure 8-31 the jet separated completely after 350mm, whereas it is neither completely attached nor separated before this point, consistent with the observations from experimentation. The separation of the jet from the nozzle exit resulted in

entrainment of fluid into the main fluid stream. Because of the sum of gravitational effects influencing the jet, at greater distances from the nozzle orifice, the jet falls off from the geometric axis towards the base of the simulation environment. With the increase of the jet velocity ratio, from increasing the flowrate from 10 l/min to 20 l/min, the jet completely separated at approximately 350mm and the width of separation was increased resulting in more deviation of the jet from the geometric axis.

8.5 Further nozzle comparison and verification work

In the comparison work reported herein, testing was performed to evaluate the applicability of improved simulation methods to nozzle exit flows, directly. The performance of two 9mm diameter nozzles with two different chamber profiles was measured to examine the effect of nozzle contour on performance in terms of coherence or nozzle break-up length. Both nozzles were designed with the same inlet profile, exit diameter, and expansion ratio. Because the supply pipe and nozzle are one continuous structure, each piece of hardware is simply identified by the nozzle shape, i.e. Rouse or orifice, from here on. The Rouse nozzle had a gradual contraction for 22mm (See Appendix A, Figure A-9). This nozzle was originally tested in this section with fewer elements. The orifice nozzle was designed via the Rowe et al (2004) code (Appendix A, Figure A-7). A two dimensional simulation was used to generate theoretical performance predictions to compare the characteristic nozzle efficiencies presented later in this work.

Both nozzles tested were fabricated via the same techniques using plain brass with smooth internal turning and milling. The supply chamber profiles were identical from the inlet pipe to the start of the contraction. The contours of the nozzles are shown in Figures A-7 and A-9. The convergence angle of the Rouse nozzle has a gradual contraction with a given radius, as stated, and the orifice nozzle has an exact 90-degree contraction just before the exit plane. The outer section of the nozzle had no effect on nozzle performance and was therefore, left up to standard fabrication design.

The same fluid types and models were used in all testing. The simulation was designed with a meshing strategy to produce a core of finer elements (becoming even finer still with mesh adaption) that followed the areas of jet break up at the free surface (i.e. at the sides of the fluid stream). In the chamber, air is allowed to pass through freely. By changing the inlet speeds, the coherence length varied - this factor permitted a direct

comparison between the slant and the orifice nozzle. An inlet speed of 16 m/s was selected as the baseline for this work since that was nominal design operating point for this nozzle type (for a conventional grinding trial). Tests at 25, 50, 75, 125 and 150 per cent speed were also run to investigate the sensitivity to changes. These results showed varying coherence lengths (as expected).

8.6 Results

For direct comparison of the effect of velocity break-up, a method was required to analyse the effect of velocity decay, not just from the centreline, but also from the centre of the jet (a velocity streamline through the core velocity of the jet). Figure 8-32 shows the two lines used for comparison. The vertical lines shown in Figure 8-32 represent the planes on which results were taken to plot graphs of the jet velocities across the fluid-stream at varying locations increasing from the nozzle orifices.

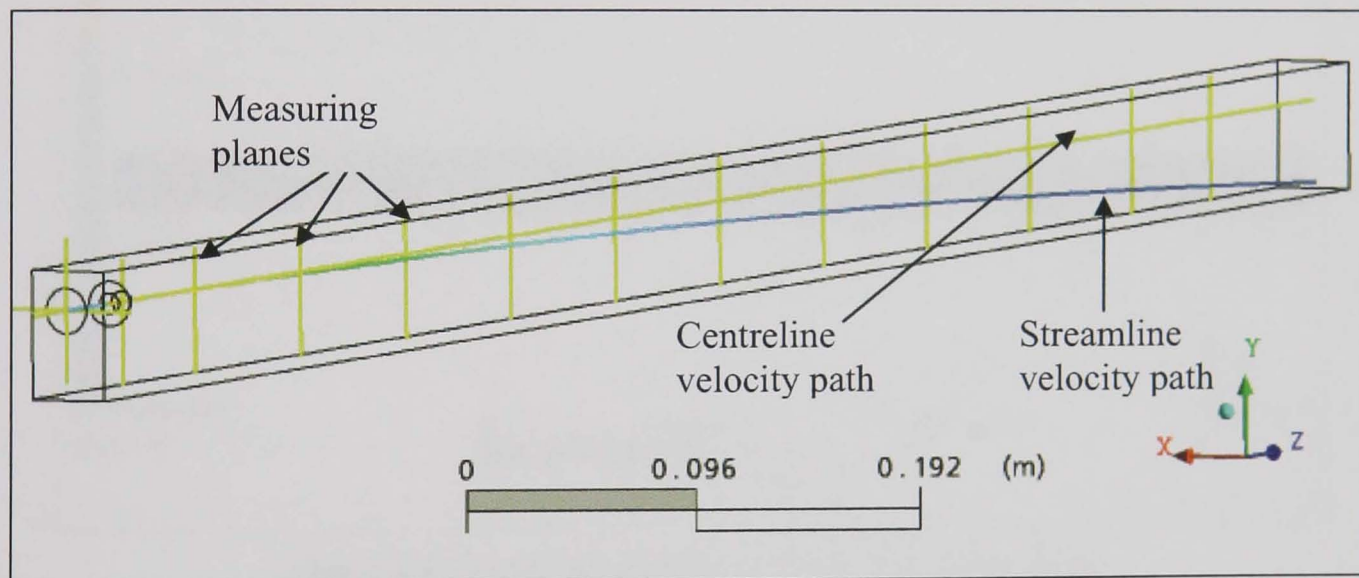


Figure 8-32 Illustration of the paths for centreline and streamline velocity predictions

The simulation domain was 0.3m x 0.5m x 1.2m with the nozzle towards the top of one of the 0.3m x 0.5m faces (the centre shown with the cross in Figure 8-32). Openings (as in Figure 6-24) were placed above, below, and to the sides of the jet, and at the start and end of the measurement chamber. These had a relatively large area to reduce bounding of the jet and consequently disturb the jet as little as possible. The simulation result for the orifice nozzle is shown in Figure 8-33.

Figure 8-33 shows the water velocity mapped on a slice plane through the centre of the domain for the orifice nozzle using the scale shown. When analysing the central core

velocity of this plot, it is clear that as soon as the jet exits the orifice, the fluid velocity decreases rapidly and the jet loses its coherence. This indicates a poor performing nozzle as the fluid is not holding together but is breaking up. The main core velocity appears to break up between 0.2m and 0.3m from the nozzle orifice. To observe this phenomenon clearly, and to aid comparison, Figure 8-34 shows a plot of these velocities at varying distances (Z in Figure 8-34) from the nozzle orifice. Both lines follow an identical path on exit from the nozzle showing that the central core velocity is not only dropping from the centreline, but is also losing magnitude within itself. This means that the jet ensuing from the nozzle is breaking up and mixing with the air. This, in turn, creates more drag on the jet itself leading to a further reduction in jet velocity. This, once again, indicates a poor performing nozzle (in relation to coherence length).

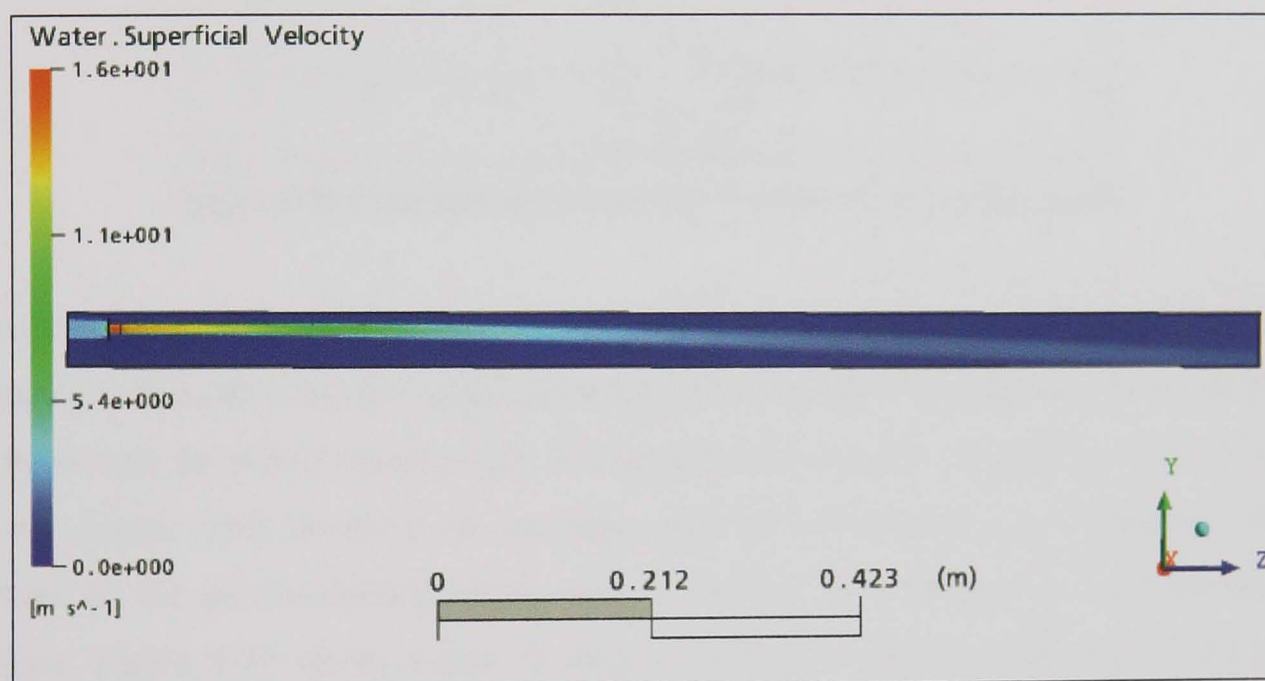


Figure 8-33 Water Superficial velocity for the orifice nozzle

Figure 8-35 shows the water velocity mapped on a slice plane through the centre of the domain for the Rouse based nozzle using the scale shown. Unlike the plot shown in Figure 8-34, when analysing the central core velocity of this plot, it is clear that the fluid maintains a central core velocity (i.e. it maintains its coherence) all the way towards the end of the measurement chamber. This indicates a good performing nozzle as the fluid is holding together (the fluid has much less disturbance before the fluid exits from the nozzle) and is not breaking up - the orifice nozzle did. The main core velocity exits the measurement chamber at 0.7m - 0.8m from the nozzle orifice and even at this point, it has maintained its initial exit velocity.

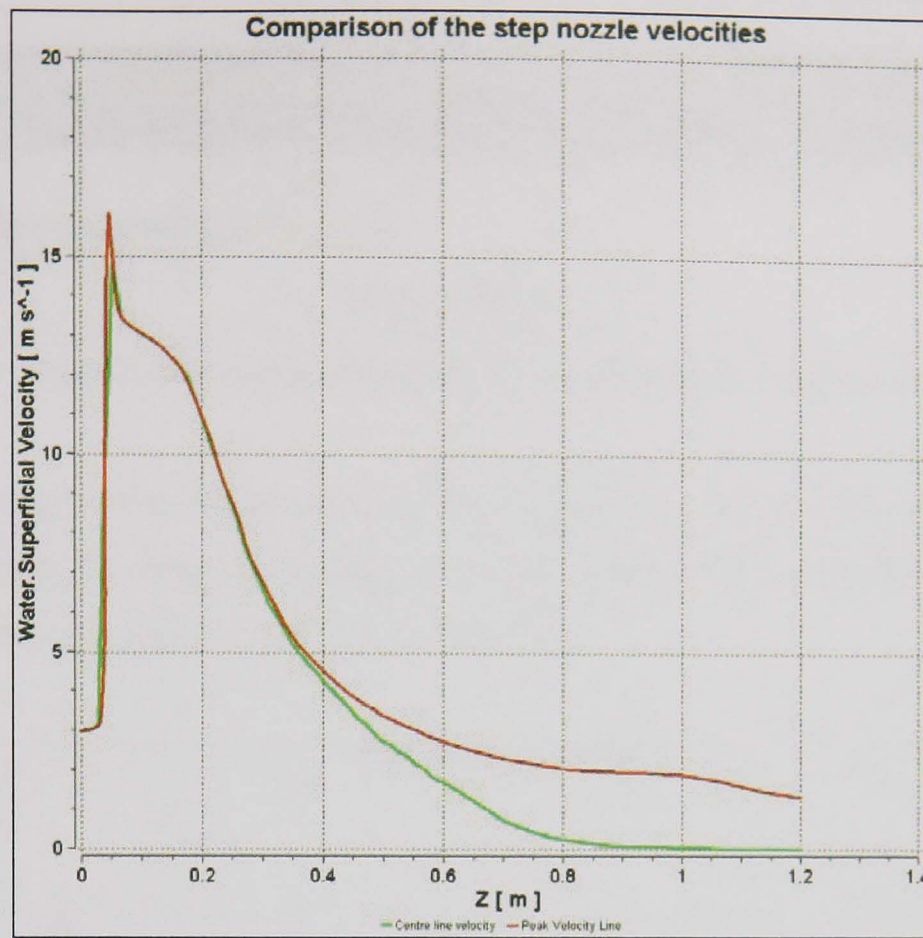


Figure 8-34 Centreline and streamline velocities for the orifice nozzle

The straight (yellow) line in Figure 8-35 shows the centreline of the nozzle. The fluid dips away from this line due to gravitational affects. Figure 8-36 shows a close up of the fluid exiting the Rouse based nozzle. It highlights the smooth, gradual increase of speed in the nozzle until the point of discharge, then the maintenance of coherence length shown by the solid-coloured central core of the jet For comparison with the orifice nozzle, Figure 8-37 shows a plot of these velocities at varying distances (Z in Figure 8-37) from the nozzle orifice.

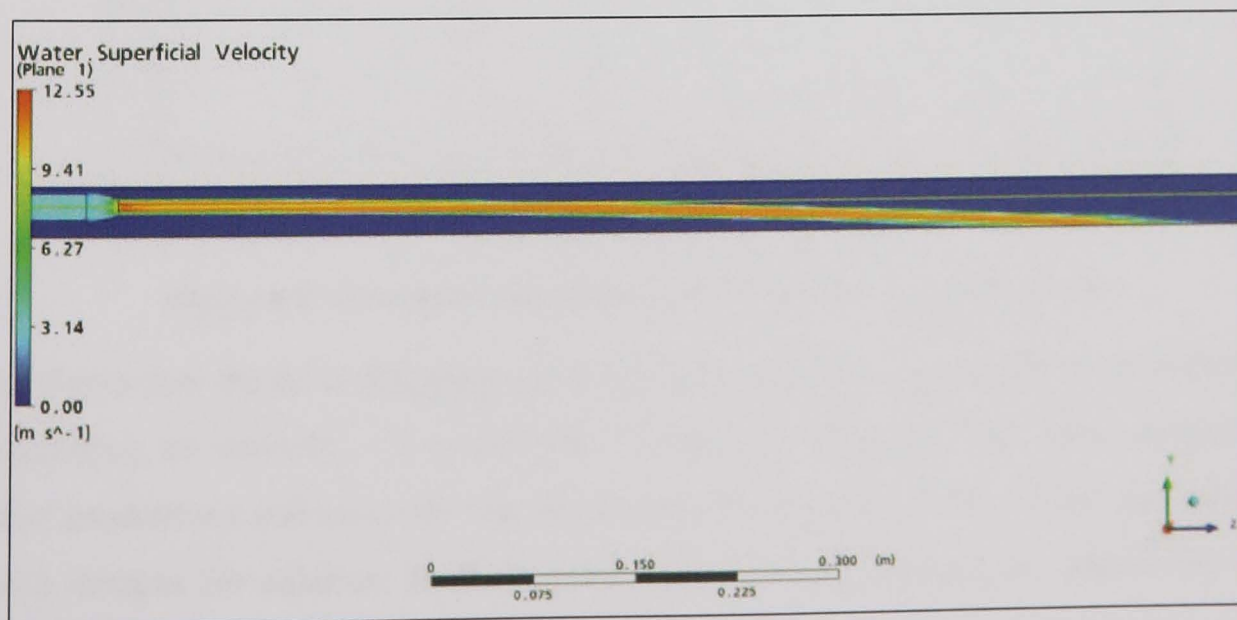


Figure 8-35 Water Superficial velocity for the Rouse based nozzle

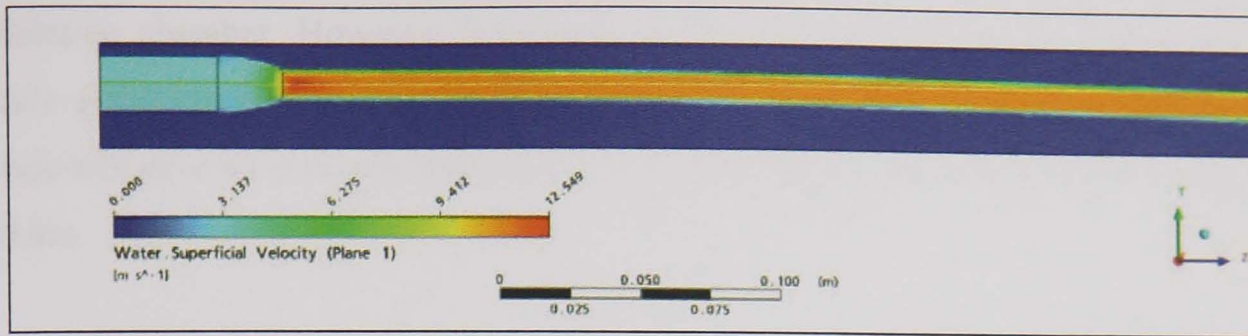


Figure 8-36 Close up of the central core of the Rouse based nozzle

In stark contrast to the orifice nozzle plot, Figure 8-34, the plot for the Rouse based nozzle (Figure 8-37) shows a sudden drop in centreline velocity, combined with a level velocity for the streamline (central core of the jet).

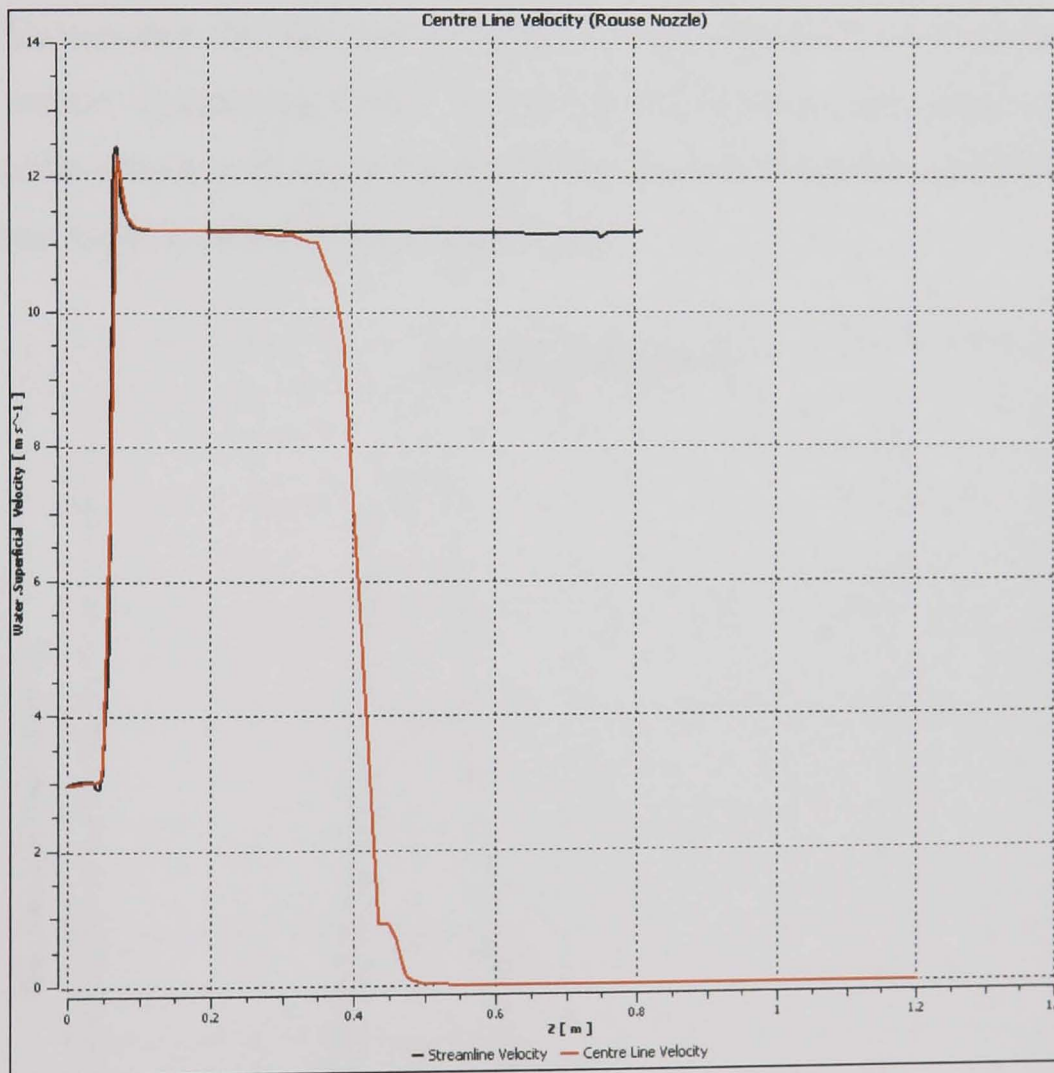


Figure 8-37 Centreline and streamline velocities for the orifice nozzle

This shows that the jet is dropping due to gravity, however, the central core of the jet is maintaining its velocity – it is therefore, termed a “coherent jet”. This supports the earlier predictions and literature that the Rouse based nozzle is one of the most efficient nozzle designs for coherent fluid delivery. The maximum distance at which this could be measured was 0.8m from the nozzle exit. This is due to the constraints of the

simulation chamber. However, it is unlikely that component geometry would require nozzle positioning at greater distances than 0.8m. From this, it can be said that the nozzle will give an even coverage (at its peak velocity) over its entire width, at least up to 0.8m.

The graphical results in Figure 8-38 and Figure 8-39 were obtained by reading the speed of the jet at the appropriate points. For comparisons, a result was taken for every 0.1 metre up to 1.2 metres. Figure 8-38 is the velocity decay plot for the step nozzle. The fluid exits the nozzle with a velocity of around 14 m/s. It rapidly decreases to around 2.5m/s at 400-500mm from the nozzle orifice. After this point, the velocity decrease is gradual and the fluid velocity tapers off to around 1.8m/s at 1100mm from the nozzle orifice. This indicates that the fluid is rapidly mixing with air in the chamber, upon exit from the nozzle. The finding shows that the jet is losing its core, peak velocity. The result matches closely with experimentation that showed the orifice nozzle dropping its peak velocity around 400-600mm (Figure 8-10).

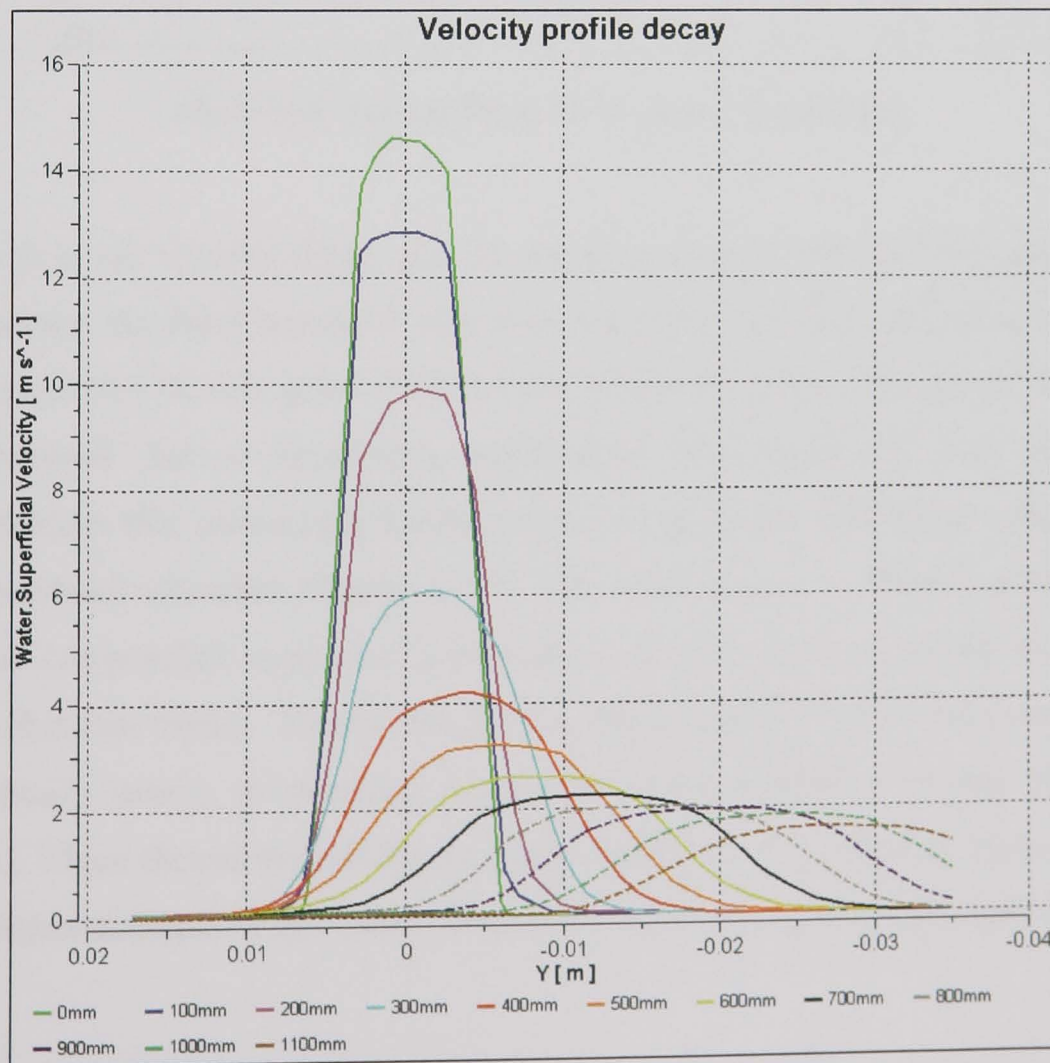


Figure 8-38 Velocity decay for the orifice nozzle

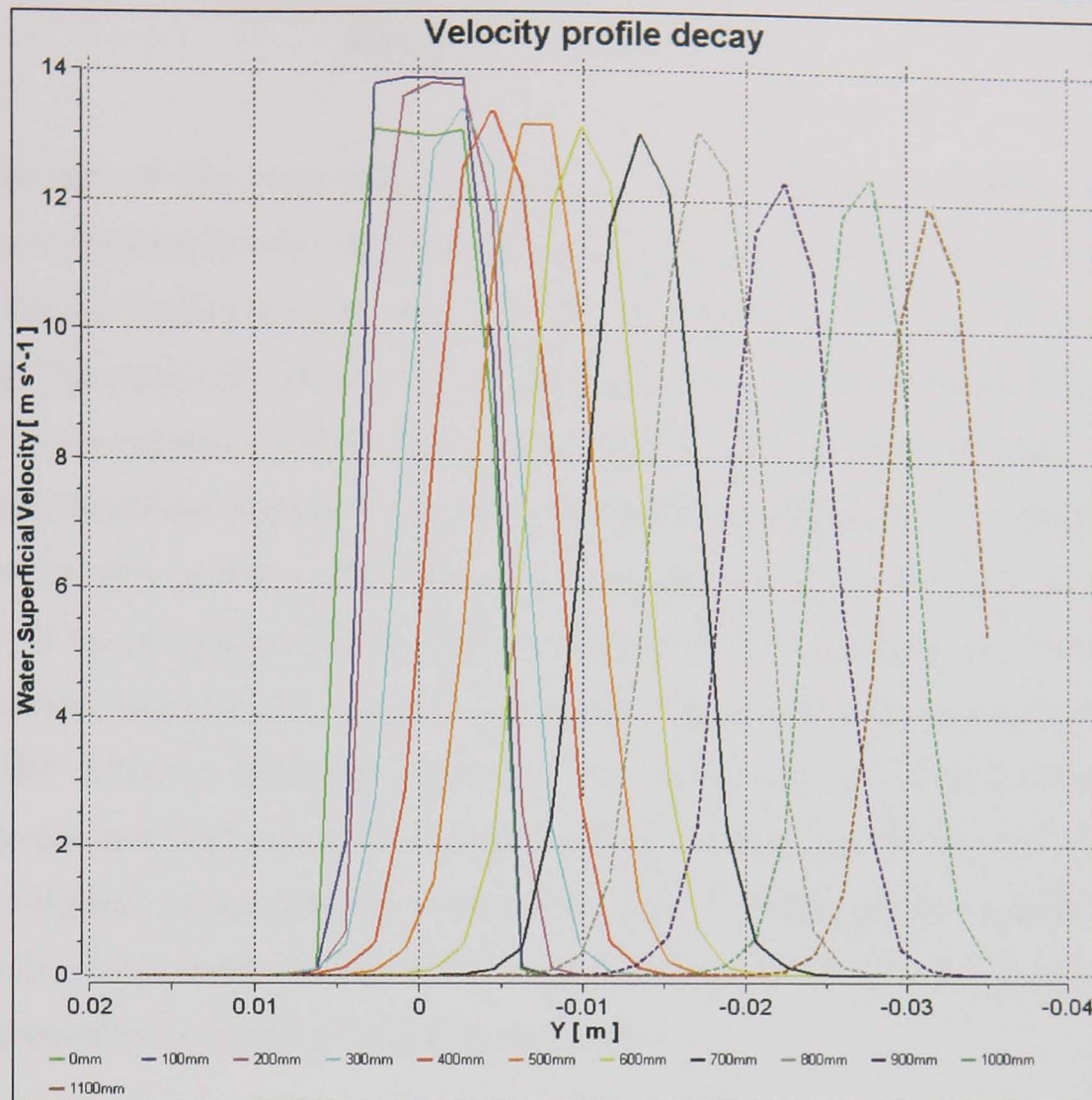


Figure 8-39 Velocity decay for the Rouse based nozzle

Figure 8-39 is the velocity decay plot for the Rouse based nozzle. Once again, as with the step nozzle, the fluid leaves the nozzle orifice with a velocity of close to 14 m/s. The fluid jet maintains its exit speed (within 10% of the exit velocity) right up until the last point measured due to simulation constraints. This result matches closely with experimentation that showed the Rouse based nozzle dropping its peak velocity outside the measurement chamber (Figure 8-13). This indicates a “coherent” nozzle. It also shows that it is possible to predict jet behaviour using the methodologies for simulation shown within this thesis. To test this further, the chamber would need extending both experimentally (costly in monetary terms) and using simulation (costly in computer resources). These should be possible for future work and could confirm up to what point the simulation maintained this close comparison with the experimental values.

Chapter 9 Discussion

The main aim of this work was to conduct a full investigation in order to deliver a solution to fluid application in grinding, therefore, the work concentrated on analysing nozzle design aspects for the achievement of better fluid delivery in conventional grinding. The main question that arose from this work was; “Can fluid simulations, with reliable experimental validation, be used to solve realistic grinding problems and how does fluid simulation compare with other experimental techniques?” In reference to the first part of this question, this chapter summarises the main findings to show the promise of the system to predict coolant nozzle position. As regards the second part of the question, it is beyond the scope of this thesis to give a full and unbiased comparison of all the different modelling methods; the work here has concentrated on the development and application of a single method, namely the development of a CFD model, validated experimentally. As has been shown throughout the results, the code used in this work needs further enhancement; this would be possible with a body of work concentrated on purely modelling techniques.

9.1 Development of the simulation

Work in Chapters 5 and 6 shows that the simulation results have real physical interpretations of the coherence length and hence peak velocity distribution for the nozzle under examination. This means that, for example, inserting a nozzle geometry directly into the model tree (and then coping with additional mesh tuning), would give the relevant peak velocity distribution directly from modelling. However, the basic premise that it is more appropriate to solve a simulation on a PC than run expensive trials and produce many samples, is still valid. From an end-user point of view, an interpretation of the physics of the process is less important since the requirement is to enter a problem definition and obtain the results with little or no interaction. One method of using these results in a controlled way would be using a User Guidance Manual (UGM) that operators could input data into and then, through networks of intelligence, selective criteria can be displayed to the end-user. The development of a UGM ran concurrently with this work and it is hoped that a workable tool for industrial use would be possible with user input. More on this is included in the further work section.

A criticism often directed at simulation modelling methods is that they obtain a solution based on theoretical predictions alone. For other set-up methods, the user has to perform some manipulation of standard equations or has to have some working knowledge of the expected behaviour of the system in order to define the problem and hence set the application system to suit the parameters of the grinding situation. From this, it is suggested that the user has a better understanding of the underlying mechanisms at work, however much of coolant application in practice is done merely from trial and error, this being costly. It is true, to a certain extent, and it is possible, for example, to achieve the desired cooling of the contact with no appreciation of how the fluid interactions combine to produce this cooling. However, such an understanding of the basic processes needed to achieve the correct cooling may not be necessary. In reality, it may be an advantage to need to know nothing about how the actual cooling system operates and what standard approaches are required. For example, to obtain sufficient cooling in a standard surface grinding operation, the model automatically takes care of the positioning of the nozzles and what type of nozzle to implement (with reference to further work applied in the UGM). To achieve the same fluid application rules by other means, it may be necessary to assume some previous knowledge with the machine operators and hence, increases the overall cost of setting up a system due to increased skilled labour costs.

One of the features of the simulation method is that output (velocity, pressure distribution etc) information is available at all points in the mesh (measurement environment) throughout the entire simulation time. Most of this information will never be used directly by a machine operator but it is necessary to obtain the solution throughout the entire mesh even for a single output point. The conventional method in grinding is to follow the knowledge of machine operators and to create new systems from this. With information available for the entire domain, it is possible to predict fluid flow not only in the grinding contact, but also around the wheel and other machine places. This could influence all features of the fluid application design, from basic pipe positions, to sensitive equipment placement. Some success has been shown for predicting the trajectory of fluid flow, and therefore of predicting fluid flow into the grinding contact. There may be other methods of reducing the quantity of lubricant necessary, as more accurate positioning requiring less pressure and flowrate, becomes available; however, this entails further investigation on a complete grinding simulation.

9.1.1 *Limitations of the simulation*

It is important to inspect the solution output from a simulation before applying any post-processing operations. If the data contains any significant differences between experimental results (such as a higher expected output velocity) then suitable adaption and redefining is required. However, if adaption is applied unnecessarily, it will reduce the accuracy of the results as the grid quality has significant influence on the solution accuracy. A high quality mesh is considered a mesh that does not suffer from large increases in cell sizes (high aspect ratio cells), local mesh clustering (localised areas of small cells within the domain) and low orthogonal cells (geometrical shape of the initial cells). The latter cannot be controlled during the adaptation process since it is entirely dependent on the initial mesh and hence necessitates the development of an accurate mesh base to begin with. Large aspect ratios after mesh adaptation mainly occur at the connection between the Cartesian mesh and the areas of high interest around the free surface boundary.

A disadvantage of large aspect ratios is a local non-smooth solution. This non-smoothness can become so large that extra mesh refinement is generated, further increasing the aspect ratio. Local mesh clustering causes non-smooth solutions as well as unnecessary small cells, i.e. both the numerical accuracy and computational efficiency decrease with increased local mesh clustering. Local cell clustering depends on the mesh refinement strategy and hence requires a good initial setup to facilitate improved accuracy of the results around the areas of interest.

A problem was identified with the under-prediction of the coherence length due to increased entrainment of air at the free surface boundary. This offered difficulty for the work presented here since predictions of effects on the coherence length had to be based on initial calculations from the simulation and hence could only be part validated experimentally. When an improved mesh was used at the free surface boundary, the error between the simulation and the experimental results was reduced; however, there remained errors in the region of 10 per cent in the velocity profile at set distances from the nozzle orifice. This mainly affected the velocity of the jet in the central core region and hence had an effect on the peak velocity distribution. Change in the overall coherence length however, was found to be of the same order for both the simulation and experimental methods.

Considerable effort was spent in trying to ensure correct break up and interaction between the two phases at the free surface interface but it appears that effort in this area requires remodelling of the situation using code expansion and exploration. There is an inevitable loss of velocity when momentum information is passed from the region of high water concentration to the region of high air concentration and this is significant even in the models where velocities are relatively low. The adaption technique was used to increase the mesh resolution in regions where these significant changes occurred and to move imperfect numerical boundaries away from the region of interest. This limited errors within the overall length to approximately 10 per cent; however, the field of break up was intensely difficult to improve in this way.

Further testing of the simulation (highlighted towards the end of chapter 8) shows that the model can, and does perform well for a selection of nozzles, however, doubt remains due to the limited nozzles tested and at limited operating speeds and conditions. It would be necessary to test the models ability to cope with differing fluid types, nozzle geometries, inlet speeds, nozzle surface finish, and the other influencing factors highlighted in Chapters 3 and 5. Predictions for the Rouse and orifice (step) nozzle closely match the experimental results however, and this gives good confidence in the simulation's progress.

9.1.2 Experimental methods

One of the first problems tackled using the Pitot tube method was that of measuring the coherence length of a fluid jet stream under constant supply. This allowed for analysis of the effect of nozzle body shape on this length. The values obtained agree to within 10% of the analytical values and results have been presented that confirm this. The results were shown to be repeatable and differences between the predicted length and that measured were within ten per cent of the overall length (Figure 9-1). Table 8-2 shows the different nozzle types. Based on these tests, it is suggested that conclusions may be readily drawn from the work and are presented within the next chapter.

Figure 9-1 does however contain a limitation of the simulation. The results presented are based on the prediction of coherence length with the central core velocity at a value lower than that measured experimentally. These would match more closely given the computational power. The results shown contain predictions assuming that the central

core (peak velocity) of the fluid is that at which the majority of the core remains until the break up length. Some of the values contained within Figure 9-1 are predicted values as the measurement chamber was not great enough to capture right to the end. These are predicted using the analytical work in Chapter 6 and the simulation / modelling work.

Results have been presented to show the effect of a change in nozzle section on the coherence length of a jet. Inspection of the velocity profiles shows that a sudden change in section causes distortion of the exiting stream as well as introducing large eddies within the fluid stream causing it to break up sooner than a standard pipe.

1		Rouse 2.5
2		Rouse 9
3		Step 2.5
4		Step 9
5		Slant 2.5
6		Slant 9
7		Straight pipe
8		Lechler

Table 9-1 Different nozzle types examined

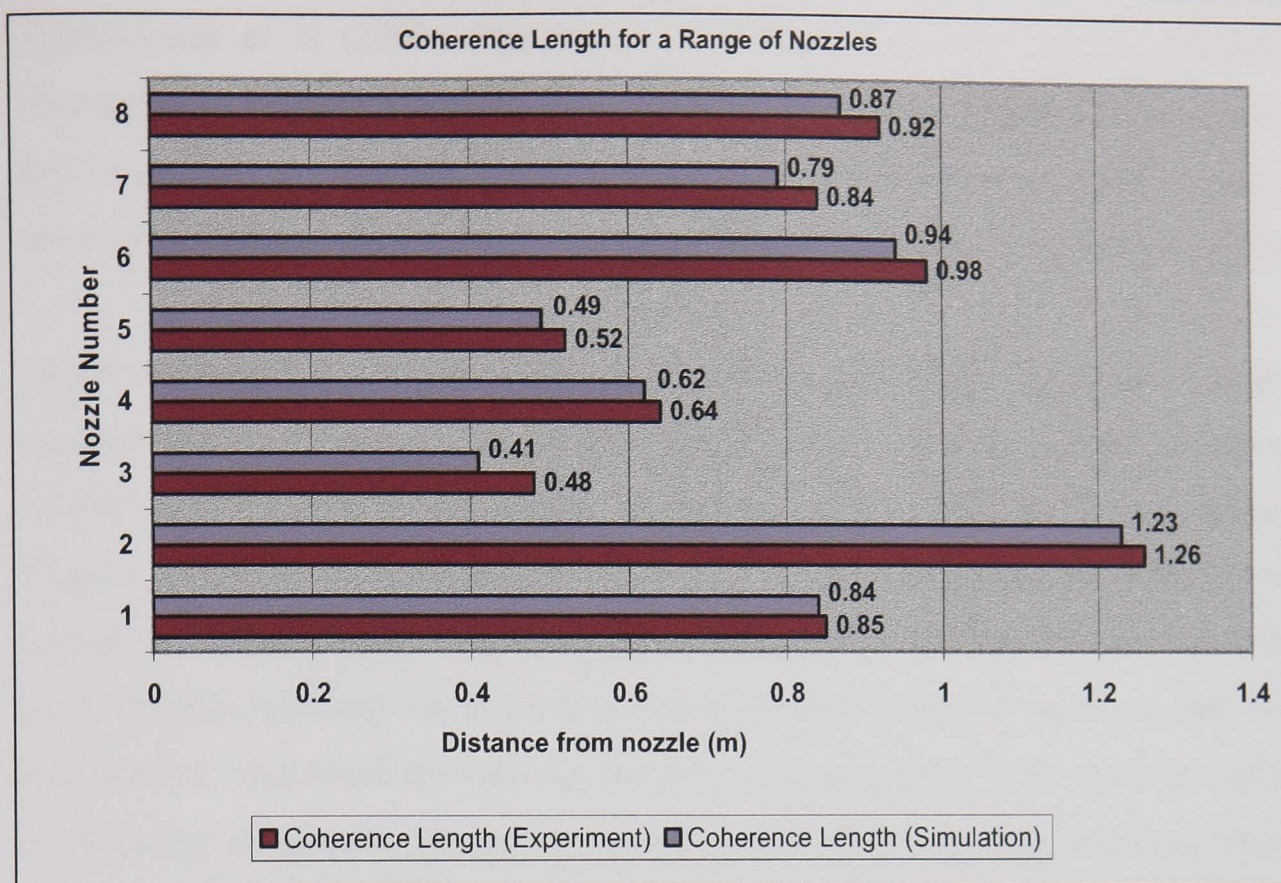


Figure 9-1 Experimental and predicted values of coherence length

For a nozzle geometry where the cavity has curved sidewalls (Rouse based nozzles), the jet expands along the geometric axis of the measurement area even when the velocity was increased by narrowing the nozzle aperture but keeping the flowrate constant. By replacing the curved walls in the nozzle with uniformly converging walls (slant-based nozzles), the centreline velocity decay within the jet stream was increased, reducing the peak velocity area leading to a decrease in coherence length. The jet deflected strongly towards the long face of the cavity for all velocity ratios (inlet to outlet velocity). The degree of deflection of the jet increased with velocity ratio. For nozzles with a straight contraction (orifice type nozzles), the jet dispersed at around half the downstream distance with reference to Rouse based nozzles and became very unstable in a short period. This confirms existing theory of losses within sudden contractions and the formation of vena contracta leading to reduced jet stability.

The velocity profiles from experiment have been compared with simulation and there is good agreement with those profiles at the exit, however further from the nozzle exit, the profiles from simulation have lower peak velocities and wider distributions due to increased entrainment of the air. Simulations have also been performed to assess the effect of small changes in the nozzle orifice and, as expected, greater variations are experienced with less sharp exits from the nozzle orifice. These results are presented in

Baines-Jones et al (2009). Numerical modelling is an ideal tool to perform such investigations because it is possible to vary a single parameter with all other parameters kept constant. It also precludes the need for production of many nozzles and environments, and direct testing is possible without the need for complex machinery.

Coherence length is a useful measure in a fluid application system as it allows for accurate prediction of stream behaviour, and hence correct nozzle positioning. A method has been developed which enables the nozzle loss factor N_f (discussed in Chapter 6) to be obtained from the experimental data over the whole range of operational conditions. It is only possible at present to calculate this as a relative factor as N_f contains multiple variables that would require extensive work on each of these individually. This involves mapping the fluid stream and, for each jet to be analysed, it is necessary to process the data produced from a large number of measurements for accurate observation of the break up length and hence this N_f factor. Values of the nozzle factor obtained by this method for a range of nozzles (presented in Table 9-2) are in good agreement with analytical results. Further work is required however to analyse the individual factors within this grouped factor and to investigate for a range of nozzle types and supply conditions.

The reference for Table 9-2 is that a 9mm straight pipe with the given flowrates would produce an N_f of 1. This methodology assumes that the standard (9mm \emptyset) pipe is "1" for N_f , regardless of how the geometry and other factors discussed actually affect this flow. Further work is required to analyse the exact influence of the nozzle factors on this value to obtain actual values for peak velocity break-up. Values for Table 9-2 are calculated by comparing the values obtained through simulation and experimentally, from Table 9-1, with those for a standard 9mm round pipe - equation [6.4]

Nozzle Type	Rouse (9mm \emptyset)	Slant (9mm \emptyset)	Orifice (9mm \emptyset)	Slot (1.6mm gap)
Factor (N_f)	1.5	1.17	0.76	≈ 0.21
Nozzle Type	Rouse (2.5mm \emptyset)	Slant (2.5mm \emptyset)	Orifice (2.5mm \emptyset)	Lechler (7.5mm \emptyset)
Factor (N_f)	1.01	0.61	0.57	1.1

**Table 9-2 Nozzle loss factors for coherence length
(based on the performance of a standard 9mm circular pipe)**

9.2 Summary

In summary, some concerns are apparent with the simulation technique. The free surface modelling cannot be considered as the unique indicator of the coherence length for a given nozzle due to the significant entrainment of the air present for some nozzle types. However, the most recent simulations (run on a x64 bit platform with more computing resources than first available, allowing more elements to be analysed in a faster time), towards the end of Chapter 8, closely match the experimental values obtained for the nozzles. This gives good confidence that with further studies and some tweaking, the simulation tool could be used as a cheap and cost-effective way of analysing nozzle performance and identifying suitable nozzles for a given grinding operation.

Identified from the experimentation is that changes within the nozzle have significant effects on the overall length of the jet stream and the peak velocity distribution within this stream. A critical evaluation of the potential factors affecting the integrity of the jet is necessary and is achievable with an advanced model, and using the experimental techniques described within this work. Within the limits of this work, smooth transitional regions within nozzles and sharp nozzle orifices may be considered as important properties when selecting a coolant nozzle for grinding processes where the nozzle cannot be positioned directly in (or as close as possible to) the wheel/workpiece contact. The satisfactory results achieved by using the Rouse based nozzle may allow less coolant to be used to achieve desired results and optimise the grinding process.

To achieve sufficient supply of coolant into the wheel/workpiece contact, it is necessary to optimise the supply conditions including all factors affecting the nozzle, supply pump, plumbing system and positioning of the grinding fluid nozzle. This work has demonstrated combinations of these factors required to achieve a specific peak velocity distribution that allows the user to predict the path of a fluid jet and therefore optimally position the nozzle with respect to the wheel/workpiece contact.

Chapter 10 Conclusions and Recommendations for Future Work

10.1 Conclusions

With stricter requirements of environmental legislation and cost implications associated with the use of coolants within the grinding process, it is of utmost importance that manufacturers optimise their particular process so that little of the fluid supplied is wasted. At present, most use large quantities of grinding coolant aimed roughly at the grinding contact in order to achieve the desired cooling, lubrication and chip removal. This work aimed to analyse existing cooling methods for grinding and improve strategies for coolant delivery based on coolant nozzle position and performance. With increased levels of technology, use of higher speeds and improved material removal rates, supplying coolant accurately to the grinding contact becomes a necessity.

The major study of this work on jet coherence has implications in all grinding applications, in that accurate coverage of the wheel/workpiece contact, to satisfy the criterion of matching wheel speed to jet speed for high speed grinding, is achievable using coherent nozzles at greater distances from the grinding contact. This means that manufacturers may position nozzles further from the contact allowing increased clearance within the machine tool for the dressing operation, wheel heads, gauging, and automatic part loaders.

Simulations for grinding fluid nozzles were undertaken and partly validated through experimentation to provide a physical understanding of the mechanisms of coolant behaviour on both the exterior and interior of grinding fluid nozzles.

Nozzle improvement was proved possible using the internal nozzle simulations to analyse areas of high recirculation and stagnation. This means that a better understanding of nozzle flow will allow for achievement of the desired cooling and lubrication, whilst maintaining good coverage of the grinding contact. This was backed up by an experimental comparative study of nozzles. This utilised an experimental arrangement that has been established for fluid tests.

Jet instability is what causes a jet to break up and is influenced by the surface tension (σ), viscosity (η), and density (ρ) of the fluid. Newtonian jet instability, using a function

of the Weber number (equation [6.4]), was applied to determine, quantitatively, distances at which peak velocity break up occurred. This length was deemed the coherence length. A simulation to predict coherence length by taking into account both coolant properties and the environment into which the jet exited was developed. This model allowed specific ' N_f ' factors to be introduced to combine the effect of nozzle shape change on this coherence length.

The simulation prediction was in good agreement with experimental measurements in terms of jet width increase, and overall jet coherence. The simulation was most effective at higher jet speeds and using the more coherent jet nozzle shapes.

From the studies on coherence length, nozzle profiles based on the Rouse fire hose design allowed for better coherence at greater distances from the contact zone. Taking this further however, a model to predict the 'peak velocity breakup' or coherence length for several nozzles, makes possible, accurate positioning of grinding fluid nozzles.

A study on nozzle positioning proved that with coherent nozzles, firing the jet directly into the 'nip' or wheel/workpiece contact, improves the amount of flow passing through this contact. It is noted also, that firing the jet in this way improves on the useful flow rather than firing the jet at tangential positions above the line of the workpiece surface. This study was conducted with the air barrier present around the wheel and therefore this air entrainment influences this result. This raises the question again of correct nozzle position and is an area for further investigation.

10.2 Recommendations for future work

With grinding such a considerably costly machining process, when introducing developments into an industrial environment, the economic cost and benefits must be addressed. Optimisation of the grinding process using a particular type of fluid application system encompassing: the fluid, nozzle type, positioning method and supply conditions, for economic purposes and having respect for environmental concerns, is essential for good grinding practice.

With this in mind, the following areas are suggested for further investigations:

- To design a new nozzle(s) so that flat coolant can be evenly distributed across the grinding wheel/workpiece contact.
- Experimentation investigating temperature rise during grinding using thermocouple techniques whilst using the coherent jet nozzles, is suggested for further examination.
- Further work into traditional ‘bent copper pipe’ nozzles as well as click and fit nozzles is required to assess whether these are suitable and repeatable for use within the grinding process.
- Develop numerical models encompassing the effect of other factors discussed in Chapter 6, as well as a possible alteration of the free-surface boundary properties due to increased air entrainment, and validate these against the results of experimentation.
- It is suggested that a detailed two-dimensional analysis should be carried out; valid for the core region of the slot nozzle and the round nozzles. This would reduce the computational costs but give some idea of the correct flow pattern.
- Investigations into fluid delivery whilst using CBN wheels at speeds in excess of 80m/s are proposed.
- It is recommended that studies be planned to develop secondary nozzles (based on the principles laid out in this work) for use in fluid-delivery system optimisation.
- A method that combines two non-intrusive imaging techniques, particle-tracking velocimetry (PTV) and laser-induced fluorescence (LIF) could be used to make simultaneous measurements of velocity and concentration in a neutrally buoyant turbulent round jet.

References

- Abtec, 2008. Available at <http://abtecindustries.com/productdetail.asp?product=76>. [Accessed 22nd Jan 2010].
- Adeniji-Fashola, A., Chen, C.P., 1990. Modeling of confined turbulent fluid-particle flows using Eulerian and Lagrangian schemes. *Int. J. Heat Mass Transfer*, 33, p.691-701.
- Ahmadi, G., Ma, D., 1990. A thermodynamical formulation for dispersed multiphase turbulent flows. I. Basic Theory, *Int. journal Multiphase flows*. 16(2), p. 323-340.
- American Institute of Aeronautics and Astronautics, 1998. Guide for the verification and validation of computational fluid dynamics simulations. AIAA Guide G-077.
- Aichouni, M., Laws, E.M., Ouazzane, A.K., 1996. Experimental study of the effects of up stream flow condition upon venturi flowmeter performance. *6th International Symposium on Flow Modelling and Turbulence Measurement*, Tallahassee, FL.
- Akagawa, A., 1997. Development of cutting fluids which are environment and human friendly, *Int. J. of the Japan Society for Precision Engineering*, 31 (4), p.253-256.
- Akiyama, T., Shibata, J., Yonetsu, S., 1984. Behaviour of grinding fluid in the gap of the contact area between a grinding wheel and workpiece. *Proc. of the fifth Int. Conf. On Prod. Eng.*, Tokyo.
- ANSYS CFX-5.7.1, 2003. References and tutorials. User manual. Contained within the software.
- ANSYS Solutions | 2006 Volume 7, Issue 5 2006 Available at: http://www.ansysolutions.com/final_volume7_issue5.pdf [Accessed 22nd March 2007].
- ANSYS 10.0., 2005. Complete User's Manual Set. KS00000315. 1st 20 part 1. [Accessed 18-Aug-05].
- Appel, D.W., Swenson, F.R. 1968. Tappi, (51), p.132.
- Bader, S., 2004. Abrasive, belt grinders, belt grinder, grinding, belt grinding, belt polishing, belt Centreless, Finishing, Belt finishing, Polishing, Abrasive belt grinding, Airfoil grinding, Airfoil polishing, Abrasive belt center. [Online]. November 1998 [Accessed June 2004]. Available from: <http://www.stephenbader.com/>.
- Badger, J.A., Torrance, A., 2000. Burn awareness. *Cutting Tool Engineering*, 52 (12).
- Baines-Jones V.A., Morgan M.N., Batako A.D., Brown E., 2009. The role of Computational Fluid Dynamics for coolant delivery in industrial grinding of steels and cast iron. 9th International Conference and Exhibition on Laser metrology, machine tool, CMM and robotic performance LAMDAMAP 2009. 30th June - 2nd July 2009.
- Baines-Jones V.A., Morgan M.N., Batako A.D., Brown E., 2008. Modelling and simulation of grinding fluid nozzles. The 6th International Conference on Manufacturing Research (ICMR08) Brunel University, UK, 9-11th September 2008.
- Baldocchi, D., 2005. Lecture 18, Wind and Turbulence, Part 1, Surface Boundary Layer: Theory and Principles, *Ecosystem Science Division, Department of Environmental Science, Policy and Management*, University of California, CA: USA.

- Bardina, J.E., Huang, P.G., Coakley, T.J., 1997. Turbulence Modeling, Validation, Testing and Development. NASA Technical Memorandum, 110446. AIAA Paper 1997 p-2121.
- Barth, T.J., Jespersen, D.C., 1989. The design and application of upwind schemes on unstructured meshes. AIAA Paper, 89(03) p.66.
- Barth, T.J., 1992. Aspects of unstructured grids and finite-volume solvers for the Euler and Navier-Stokes equations, *AGARD Report*, 787, p.61-661.
- Batako, A.D.L., Koppal, S., 2007. Process monitoring in high efficiency deep grinding-HEDG. IOP. [Online] *Journal of Physics: Conference Series* 76 (2007) 012061 Available using: doi:10.1088/1742-6596/76/1/012061. [Accessed 18-Dec-07].
- Bathe, K.J., 1996. *Finite Element Procedures*. Prentice-Hall Inc, New Jersey.
- Benedict, R.P., 1984. *Fundamentals of temperature, pressure, and flow measurements*. John Wiley & Sons.
- Bijl, H., van Zuijlen, A.H., van Mameren, P., 2005. Validation of adaptive unstructured hexahedral mesh computations of flow around a wind turbine airfoil. *International Journal for Numerical Methods Fluids*, 48 (9), p.929-45.
- Blake, K.A., Kinghorn, F.C., Stevenson, R., 1993. The design of flow straightener/nozzle packages for acceptance testing of air compressors and exhausters. NEL Report No. 673.
- Blenkowski, K., 1993. Coolants and lubricants: part 1—the truth. *Manufacturing Engineering*, p.90–96.
- Bogy, D.B., 1979. Drop formation in a circular liquid jet. *Ann. Rev. Fluid Mech.* 11, p. 207.
- Braaten, M., Shyy, W., 1986. A study of recirculating flow computation using boundary-fitted co-ordinates: consistency aspects and mesh skewness. *Num. Heat Transfer*, 9, p.559-74.
- Brackbill, J. U., Kothe, D. B., Zemach, C., 1992. A continuum method for modeling surface tension. *J. Comput. Phys.*, 100, p.335.
- Brinksmeier, E., Minke, E., 1993. High-performance surface grinding - the influence of coolant on the abrasive process. *Annals of the CIRP*, 42(1), p.367-370.
- Brinksmeier, E., Eckebrecht, J., 1994. Possibilities for the disposal of grinding swarf. *CIRP Annals, Manufacturing Technology*, 43 (2), p.593–597.
- Brinksmeier, E., Heinzl, C., Wittman, M., 1999. Friction, cooling and lubrication in grinding. *Annals of the CIRP*, 48 (2), p.581–598.
- Bullen, P.R., Cheeseman, D.J., Hussain, L.A., Ruffell, A.F., 1987. The determination of pipe contraction pressure loss coefficients for incompressible turbulent flow. *Int. J. of heat and fluid flow*, 8(2), p.111-118.
- Bulloni, M., Desilvestri, S., Liu, Y., Magni, V., 1988. High resolution measurement of jet stream thickness by optical ranging. *Optics Communications*, 66, p.133-143.
- Campbell, J.D., 1997. Tools to measure and improve coolant application effectiveness.

In the Proceedings of the *Second International Machining and Grinding Conference*, Dearborn, Michigan, 8–11 September 1997.

Campbell, J.D., 1995. Optimised coolant application. In the *1st Int. Machining and Grinding Conf.*, Michigan, USA, 12–14 Sept. Society of Manufacturing Engineers.

CFX, 2003 CFX-5.71, 2004. User Documentation, ANSYS-CFX.

Chakrabarty, S.K., 1990. Vertex-based finite-volume solution of the two-dimensional Navier-Stokes equations. *AIAA J.*, 28 (10), p.1829-31.

CHAM., 1991. *The Phoenix reference manual*. London, UK. Concentration, Heat and Momentum Ltd.

Chand, K.K., 2005. Component-based hybrid mesh generation. *Int. J. Num. Meth. Engineering*, 62 (6), p.747-33.

Chang, J.I, J.J. Lin, J.S. Huang and Y.M. Chang. Recycling oil from grinding swarf. *Resources, Conservation and Recycling*, Volume 49, Issue 2, December 2006, Pages 191-201

Chao, Y.C., Han, J.M., Jeng, M.S., 1990. A quantitative laser sheet image processing method for the study of the coherent structure of a circular jet flow. *Exp. In Fluids*, 9, p.323-332.

Chen F.T, Davis J.P, 1964. *Proc, ASCE, Hyd. Div.*, 90, p.175.

Chen, X., Rowe, W.B., McCormack, D.F., 2000. Analysis of the transitional temperature for tensile residual stress in grinding. *Journal of Materials Processing Technology*, 107 (1–3) p.216–221.

Cho, M.J., Chung, M.K., 1994. New treatment of nonorthogonal terms in the pressure correction equation. *Num. Heat Transfer, Part B*, 26, p.133-45.

Churchill, S.W., 2002. Reinterpretation of the Turbulent Prandtl Number. *Ind. Eng. Chem. Res.*, 41 (25), p.6393 - 6401.

Cinetic Landis Ltd, 2007. Picture available from <http://www.feehery-grind.com/Landis.jpg>., Accessed 19th Feb 2007.

Clift, R., Grace, J.R., Weber, M.E., 1978. *Bubbles drops and particles*. Academic Press.

Coirier, W.J., 1994, An adaptively-refined, cartesian, cell-based scheme for the Euler and Navier-Stokes equations, NASA TM-106754.

Coleman, H.W., Stern, F., 1997. Uncertainties and CFD code validation. *J.Fluids Eng.*, Trans ASME, 199, p.795-803.

Crumpton, P.I., Giles, M.B., 1995. Aircraft computations using multigrid and unstructured parallel library. *AIAA*, 95, p.210

Cui, C., 1995. *Experimental investigation of thermofluids in the grinding zone*. PhD dissertation, University of Connecticut.

Cui, C., Webster, J.A., 1994. Experimental investigation of coolant jet design for Creep Feed grinding of gas turbine airfoils. *IGTI*, ASME, Cogen Turbo Power, p.91–96.

Dahmen, N., Schon, J., Schmieder, H., Ebert, K., 1997. Supercritical fluid extraction of

- grinding and metal cutting waste contaminated with oils. *ACS S. Series*, 670, p.270–279.
- Demirdzic, I., 1982. *A finite volume method for the computation of fluid flow in complex geometries*. PhD thesis, University of London, London, UK.
- Dervieux, A., 1985. Steady Euler simulations using unstructured meshes. *VKI Lect. Ser.*, (04).
- Desa, O., Bahadur, S., 1999. Material removal and subsurface damage studies in dry and lubricated single-point scratch tests on alumina and silicon nitride. *Wear*, 225–229 (II) p.1264–1275.
- Drew, D., Lahey, R.T.Jr, 1979. Application of general constitutive principles to the derivation of multidimensional two-phase flow equations. *Int. J. of Multiphase Flow*, 5, p.243-264.
- Durlofsky, L.J., 1993. A triangle based mixed finite-element-finite volume technique for modelling two phase flow through porous media. *J. Comp. Physics*, 105, p.252-66.
- Ebbrell, S., Woolley, N.H., Tridimas, Y.D., Allanson, D.R., Rowe, W.B., 2000. Effects of cutting fluid application methods on the grinding process. *International Journal of Machine Tools and Manufacture*, 40 (2), p.209–223.
- Eda, H., Kishi, K., Ueno, H., Nomura, K., 1985. Effective method of using the jet infusion in grinding. *Bull. Japan SOC. Prec. Eng.*, 19 (1), p.49-51.
- Elder, J.W., 1959. Steady flow through Non-uniform Gauzes of Arbitrary Shape. *J. Fluid Mech.*, 5, p.355-368.
- Elghobashi, S.E., & Abou-Arab, T.W., 1983. A two-equation turbulence model for two-phase flows. *Phys. Fluids*, 26 (4), p.931-938.
- Engineer, F., Guo, C., Malkin, S. 1992. Experimental measurement of fluid flow through the grinding zone. *ASME Journal of Engineering for Industry* 114: pp.61-66.
- ESDU, 05024, 2005. Flow through Sudden Contractions of Duct Area: Pressure Losses and Flow Characteristics.
- ESDU, TN 06023, 2007. CFD Validation Studies for Pressure Loss and Flow Characteristics in Sudden Contractions. ISBN: 1:86246:600:9.
- FLUENT, 2007. A brief history of computational fluid dynamics (CFD). Fluent Inc.10 Lebanon, NH 03766U.S.A November 1998 Available from: <http://www.fluent.com/about/cfdhistory.htm>. [Cited on Feb 7th 2007]
- FLUENT, 2003. FLUENT 6.1, 2003. User's Guide, FLUENT Inc.
- Furutani, K., Ohguro, N., Trong Hieu, N., & Nakamura, T., 2002. In process measurement topography change of grinding wheel by using hydrodynamic pressure. *Int. J. Machine Tools & Manufacture*, 42, p.1447-1453.
- Ge, P.Q., Li, J.F., Lu, C.H., Liu, Z.C., 2003. Performance evaluation and action mechanism analysis of extreme pressure additives used for oil-based cutting fluids. *Key Engineering Materials*, 250, p.281–286.
- Ge, P.Q., Wang, L., Luan, Z.Y., Liu, Z.C. 2004. Study on service performance evaluation of grinding coolants. *Key Engineering Materials*, 258 (259) p.221–224.

- GG199. 1999. *Optimising the use of metalworking fluids*. Available from. <http://www.envirowise.gov.uk/uk/Our-Services/Publications/GG199-Optimising-the-Use-of-Metalworking-Fluids.html>. [Cited 3rd Jan 2006].
- Gidaspow, D., 1994. *Multiphase flow and fluidization: continuum and kinetic theory descriptions*. PhD Thesis, Academic Press, Boston, US.
- Glenn, T.F., VanAntwerpen, F., 1988. Opportunities and market trends in metalworking fluids. *Lubrication Engineering*, 54 (8), p.31-34.
- Gou, C., Malkin, S., 1994. Analytical and experimental investigation of burnout in creep-feed grinding. *CIRP Annals*, 43, p.283–286.
- Grant, R.P., & Middleman, S., 1966. Newtonian jet stability. *Journal for the American Institute of Chemical Engineers*, (A.I.Ch.E), 12 (4), p.669-678.
- Guo, C., Malkin, S. 1992. Analysis of fluid flow through the grinding zone. *Journal of Engineering for Industry*, 114, p.427–434.
- Gviniashvili, V., Rowe, W.B., Morgan, M.N., 2003. Flowrate model through the grinding zone based on the specific fluid spindle power. Submitted to the *Int. J. of Machine Tools and Manufacture*.
- Gviniashvili, V.K., Woolley, N.H., Rowe, W.B., 2004. Useful coolant flowrate in grinding. *Int. Journal of Machine Tools and Manufacture*, 44 (6), p.629–636.
- H.S.E., 2002. *Working safely with metalworking fluids* HSE Press Release E198:02 [online] - 15 October 2002. Accessed 15th November 2006. <http://www.hse.gov.uk/press/2002/e02198.htm>
- H.S.E., 2003. *Warnings for grinding coolants*, *Metalworking Production*, 147 (5) p. 44.
- Hallo, L., le Ribault, C., Buffat, M., 1997. An implicit mixed finite-volume-finite-element method for solving 3D turbulent compressible flows. *International Journal for Numerical Methods Fluids*, 25, p.1241-61.
- Haselbacher, A., Blasek, J., 2000. On the accurate and efficient discretisation of the Navier-Stokes equations on mixed grids. *AIAA J.*, 38, p.2094-102.
- Heeley, D., 2005. *Understanding pressure and pressure measurement*. Application note, Freescale Semiconductor Phoenix, Arizona AN1573 Rev 1, 05/2005.
- Hoff, M.L., 2002. Cutting fluids: necessary nuisance to productivity tool. *Society of Manufacturing Engineers*, MR (MR02-302), p. 1–6.
- Howes, T.D., Tönshoff, H.K., Heuer, W., 1991. Environmental aspects of grinding fluids. *Annals of CIRP*, 40 (2), p.523-630.
- Hoyt, J.W., Taylor, J.J., 1974. Turbulent structure in a water jet discharging in air. *J. Fluid Mech.*, 63, p.635-640.
- Huebner, K.H.H., Dewhirst, D. L., Smith, D. E., Byrom, T. G., 2001. *Finite Element Method*. J. Wiley & Sons, New York.
- Hwang, G.J., 1989. *Modelling two-phase flows of fluid and solid mixture*, PhD dissertation, Ann Arbor, MI: Clarkson University, p.163.
- Idelsohn, S.R., & Onate, E., 1994. Finite volumes and finite elements: two “good

- friends". *Int. J. for Numerical Methods. Eng.*, 37, p.3323–3341.
- Inasaki, I., 1998. *Fluid film in the grinding arc of contact*. Contribution on January-27th CIRP Meeting, Paris, 27.-31. Jan.
- Irani, R., Bauer, R.J., Warkentin, A., 2005. A review of cutting fluid application in the grinding process. *Int. J. of Machine Tools & Manufacture*, 45 (15), p.1696–1705.
- Ishii, M., 1975. *Thermo-Fluid Dynamic Theory of Two-Phase Flow*. Collection de la Direction des Etudes et Recherches d'Electricite de France, Eyrolles, Paris.
- Ishii, M & Mishima, K. 1984. Flow regime transition criteria for upward two-phase flow in vertical tubes. *Int. J. Heat Mass Transfer*, 27 (5), p.723–737.
- Jackson, A., 2008. *Fluid delivery in grinding*. PhD thesis, Liverpool John Moores University, UK.
- Jackson, A., Batako, A.D., Morgan, M.N., 2005. Fluid delivery in grinding – a review of the term useful flow. Submitted to GARS-2005, LJMU, UK, 22 June.
- Jackson, A., Morgan, M.N., Rowe, W.B., 2006. Fluid application in grinding. *Mission of Tribology Research*, 15, 6th December, IMechE, London.
- Jameson, A., Baker, T.J., Weatherill, N.P., 1986. Calculation of inviscid transonic flow over a complete aircraft. *AIAA*, 86, p.103
- Kannapan, S., & Malkin, S., 1972. Effects of grain size and operating parameters on the mechanics of grinding. Transactions of the ASME. *Journal of Engineering for Industry*, p.833-842.
- Kawaguti, M., 1953. Numerical solution of the ns equations for the flow around a circular cylinder at Reynolds number 40. *Journal of Phy. Soc. Japan*, 8, p747-757.
- Khudobin, L.V., Vetkasov, N.I., Korshunov, D.A., 2003. Efficiency of internal grinding with composite grinding wheels. *Vestnik mašinstroeniâ ISSN 00424633*, 7, p.44-47.
- Klocke, F., Eisenblätter, G., 1997. Dry cutting. *Annals of CIRP*, 46 (2), p.519-26.
- Klocke, F., Baus, T., Beck, A., 2000. Coolant induced forces in CBN high speed grinding with shoe nozzles. *CIRP Annals, Manufacturing Technology*, 49 (1), p.241–244.
- Koobus, B., Farhat, C., 2004. A variational multiscale method for the large eddy simulation of compressible turbulent flows on unstructured meshes – application to vortex shedding. *Comp. Meth. Appl. Mech. Eng.*, 193, p.1367-83.
- Kovacevic, R., Mohan, R., 1995. Effect of High Speed Grinding Fluid on Surface Grinding Performance, In: *Technical Papers of the 1st International Machining and Grinding Conference*, p.917-931, Dearborn, Michigan, Sept. 12-14.
- Launder, B.E., Spalding, D.B., 1972. Mathematical models of turbulence. London: Academic Press Inc. Paper, 169pp. *2.50 Journal of Sound and Vibration*, 25 (4), p.651.
- Lechler GmbH, n.d. • Ulmer Straße 128 • 72555 Metzingen (Germany)
- Lehnhauser, T., Schafer, M., 2002. Improved linear interpolation practice for finite-volume schemes on complex grids. *Int. J. for Num. Meth. Fluids*, 38 p.625-45.

- Lehnhauser, T., Schafer, M., 2003. Efficient discretisation of pressure-correction equations on non-orthogonal grids. *Int. J. for Num. Meth. Fluids*, 42, p.211-31.
- Leib, S.J., Goldstein, M.E., 1986. Convective and absolute instability of a viscous liquid jet. *Phys Fluids*, 29, p.952-954.
- Lee, H.C., 1974. Drop formation in a liquid jet. *IBM J Res. Dev.* 18, p.364.
- Lin, S.P., and Lian, Z.W., 1990. Mechanism of the breakup of liquid jets. *AIAA Journal*, (28), p.120-126.
- Lyra, P.R.M., Morgan, K., Peraire, J., Peiro, J., 1994. TVD algorithms for the solution of the compressible Euler equations on unstructured meshes. *International Journal for Numerical Methods. Fluids*, 19 p.827-47.
- Malkin, S., Cook, N.H., 1971. The wear of grinding wheels: Part 2 — fracture wear. *ASME Journal of Engineering for Industry*. November, p.1129–1133
- Malkin, S., 2008. *The Way Things Can Work: Theory and Applications of Machining with Abrasives*. Industrial Press, Inc.; 2 edition (April 15, 2008). ISBN-10: 0831132477
- Manninen, M., Taivassalo, V., 1996. *On the mixture model for multiphase flow*. ISBN 951-38-4946-5, ISSN 1235-0621 Julkaisija – Utgivare – Publisher
- Mavriplis, D.J., 1995. Three-dimensional multigrid Reynolds-averaged Navier-Stokes solver unstructured meshes. *AIAA J.*, 33, p.445-53.
- McCarthy, M.J., Molloy, N.A., 1974. Review of stability of liquid jets and the influence of nozzle design, *Chem.Eng. J.* p.7-10
- Menter, F.R., 1993. Zonal two-equation $k-\omega$ turbulence models for aerodynamic flows. *AIAA Paper 93-2906*.
- Menter, F.R., 1994. Two-equation eddy-viscosity turbulence models for engineering applications. *AIAA Journal*, 32 (8), p.269–289.
- Merzkirch, W., 1987, *Flow Visualization*, Second Edition, Orlando, Florida: Academic Press.
- Meteger, J.L., 1986. *Superabrasive Grinding*. Butterworth, Oxford, UK.
- Minke, E., 1999. Contribution to the role of coolants on grinding process and work results. Technical Paper-Society of Manufacturing Engineers MR (MR99-227) p.1–18.
- Monici, R.D. et al., 2005. Analysis of the different forms of application and types of cutting fluid used in plunge cylindrical grinding using conventional and superabrasive CBN grinding wheels. *International Journal of Machine tools and Manufacture* (46) 2, p.122-131
- Morgan, M.N., (2008) [Discussion on creep feed grinding] (Personal communication. 15th March 2008).
- Mostafa, A.A., Mongia, H.C., 1988. On the interactions of particles and turbulent fluid flow. *Int. J. Heat Mass Transfer*, 31(10), p.2063-2075.
- Motta, M.F., Machado, A.R., 1995. Cutting fluids: types, functions, selection, application methods and maintenance. *Metals and Machines Magazines* Sept. p.44 -56.

- Moulinec, C., Wesseling, P., 2000. Collocated schemes for the incompressible Navier-Stokes equations on non-smooth grids for two-dimensional problems. *Int. J. Num. Meth. Fluids*, 32, p.349-64.
- Oberkampf, W.L., Trucano, T.G., 2002. Verification and Validation in Computational Fluid Dynamics. *Prog.Aerosp.Sci.*, 33, p.209-272.
- Oertel, H., Oertel, H.jr., 1989. *Optische Strömungsmeßtechnik*, G.Braun, Karlsruhe.
- Okuyama, S., Nakmura, Y., Kawamura, S., 1993. Cooling action of grinding fluid in shallow grinding. *Int. J. Mach. Tools Man.*, 33(1), p.13-23.
- Ott, H.W., Storr, M., 2001. *Grinding Fluids of the Future*. Oel-Held GmbH 2001, D-70188 Stuttgart, Germany.
- Ouazzane, A.K., Benhadj, R., 2002. Flow conditioners design and their effects in reducing flow metering errors. *Sensor Review*, 22 (3), p. 223-231, ISSN 0260-2288.
- Owczarek, J.A., Rockwell, D.O., 1972. An Experimental Study of Flows in Planer Nozzles. *Journal of Basic Engineering*, 94 (3), p.682-688.
- Pallas, N.R., & Harrison, Y., 1990. An automated drop shape apparatus and the surface tension of pure water. *Colloids and Surfaces*, 43, p.169-194.
- Patankar., S.V., 1980. *Numerical Heat Transfer and Fluid Flow*. Taylor & Francis Inc (1 Jan 1980) ISBN-13: 978-0891165224.
- Peric, M., 1990. Analysis of pressure-velocity coupling on nonorthogonal grids. *Num. Heat Transfer, Part B*, 17, p.63-82.
- Perry, R.H., & Chilton, C.H., eds. 1973. *Chemical Engineers' Handbook*. 5th Edition. New York, New York: McGraw-Hill. TIC: 242591.
- Petrov, T.S., Sabotinov, N.V., 1991. Simplified dye jet nozzle construction and interferometric method for jet thickness measurement. *Meas. Sci. Technol.*, 2, p.1074-1077.
- Powell, J, W., 1979. *The application of grinding fluid in creep feed grinding*. PhD Thesis, University of Bristol.
- Prakash, C., Patankar, S.V., 1985. A control volume-based finite-element method for solving the Navier-Stokes equations using equal-order velocity-pressure interpolation. *Numerical Heat Transfer*, 8, p.259-80.
- Radhakrishnan, V., Fazlur Rahman, J., 1977. Preliminary investigation on the condition of the grinding wheel surface by airflow measurements. *Annals of the CIRP*, 25 (1), p.147-150.
- Rene J., 2005. *An investigation of losses in pre-nozzle fluid delivery arrangements in grinding*. Diploma Thesis, Liverpool John Moores University, Liverpool, UK.
- Reyes, M., Rincon, J., Damia, J., 2001. Simulation of turbulent flow in irregular geometries using a control-volume finite-element method. *Numerical Heat Transfer, B*, 39, p.79-89.
- Roace, P., 1997. Quantification of uncertainty in Computational Fluid Dynamics. *Ann.Rev.Fluid Mech.*, 29, p.123-160.

- Roace, P., 1998. *Verification and Validation of Computational Fluid Dynamics Simulations*. Hermosa, Albuquerque, NM.
- Rouse, H., Asle, M., Howe, J.W., Metzler, D.E., 1952. Experimental investigation of fire monitors and nozzles. *117th ASCE Transactions*.
- Rowe, W. B., 2000. Thermal analysis of high efficiency deep grinding, *Int. Journal of machine tool and manufacture*, 41, p.1-19.
- Rowe, W.B., McCormack, D.F., Jin T., 2001. Controlling the surface integrity of ground components. *Abrasives* (Dec/Jan); p.24–30.
- Rowe, W.B., Jin, T., 2001. Temperatures in high efficiency deep grinding (HEDG). *CIRP Annals—Manufacturing Technology*, 50 (1), p.205–208.
- Rowe, W.B., Morgan, M.N., Batako, A.D.L, Jin, T., 2003. Energy and temperature analysis in grinding. Keynote Paper, *6th Int. LAMDAMAP Conf. and Exhibition on Laser Metrology*, Laser Metrology and Machine Performance VI, p.3-23.
- Rowe, W.B, Marinescu, I.D., Dimitrov, B., Inasaki, I., 2004. *Tribology of abrasive machining processes*. William Andrews, NY. ISBN. 0-8155-1490-5.
- Rowe, W.B., (2008) [Discussion on performance of cooling in the contact] (Personal communication, 15th February 2008)
- Runge, P.R.F., Duarte, G.N., 1990. Lubricants in the Industries—Production, Maintenance and Control Triboconcept. Technical Editions, p.71–99.
- Ruprecht, A., 2002. Unsteady flow simulation in hydraulic machinery. *Task Quarterly*, 6 (1), p.187-208.
- Schumack, M.R., Chung, J.B., Schultz, W.W., Kannatey-Asibu, E., 1991. Analyses of fluid flow under a grinding wheel. *Transactions of the ASME*, 113, p.190–197.
- Sinota, O., Chevrierb, P., and Padillaa, P., 2005. Experimental simulation of the efficiency of high speed grinding wheel cleaning. *International Journal of Machine Tools and Manufacture* [Online] Volume 46, Issue 2, February 2006, Pages 170-175. Elsevier. At: doi:10.1016/j.ijmachtools.2005.04.016 [accessed 10 September 2007].
- Silva, E.J. da, et al., 2002. The inlet engine valves grinding using different types of cutting fluids and grinding wheels. *Mat. Res.*, 5 (2), p.187-194. ISSN 1516-1439.
- Sluhan, C.A., 1994. Selecting the right cutting and grinding fluids. *Tooling and Production*, 60 (2), p.7.
- Sorensen, K.A., Hassan, O., Morgan, K., Weatherill, N.P., 1999. An agglomeration unstructured hybrid mesh method for 2d turbulent compressible flows. *ISCFD*, Bremen.
- Spirax, 2007. *The Steam and Condensate Loop*. ISBN 978-0-9550691-4-7
- Spur, G., Brucher, T., 1995. Optimization of cutting fluid system for grinding of advanced ceramics. In: *Proceedings of the 1st International Machining and Grinding Conference*, p.933-947, Dearborn, Michigan.
- Taylor, G.A., Bailey, C., Cross, M., 2003. A vertex-based finite volume method applied to non-linear material problems in computational solid mechanics. *International Journal for Numerical Methods in Engineering*, 56, p.507-29.

- Trent, E.M., Wright, P.K., 2000. *Metal Cutting*. 4th ed., Butterworth-H, Oxford, UK.
- Trmal, G. Kaliszer, H., 1976. Delivery of cutting fluids in grinding. In: *Proceedings of the Inst. Mech. E.*, 23. p.52–57.
- Tu, J.Y., Fletcher, C.A.J., 1994. An improved model for particulate turbulence modulation in confined two-phase flows. *Int. Commun. Heat Mass Transfer*. 21 (6), p.775-88.
- Vansevenant, I.E., 1987. *A subsurface integrity model in grinding*, Dr.-Ing. Diss.. Katholieke Universiteit te Leuven.
- Versteeg, H.K., Malalasekera, W., 1995. *An introduction to computational fluid dynamics, the finite volume method*. Longman, Scientific & Technical, Essex, UK.
- Wang, Z., Lehmann, A., 2008. *Recent Advances in Modeling and Simulation Tools for Communication Networks and Services*. Springer US DOI 10.1007/978-0-387-73908-3 ISBN 978-0-387-73907-6 (Print) 978-0-387-73908-3 (Online) DOI 10.1007/978-0-387-73908-3_11 pp. 227-240.
- Webster J.A., Cui C., 1995a. Flow rate and jet velocity determination for design of a grinding cooling system. Technical Papers Supplement of the *First International Machining and Grinding Conference*, Dearborn, Michigan, 12–14 September.
- Webster, J.A., Cui C., Mindek, R.B.Jr., 1995b. Grinding fluid application system design. *CIRP Annals*, 44 (1), p.333–338.
- Webster, J.A., 1995c. Selection of Coolant Type and Application Technique in Grinding. *Supergrind 1995 – Grinding and Polishing with Superabrasives*. Connecticut, USA, November 2-3, p.205 – 220.
- Webster, J.A., 1999. Optimizing coolant application systems for high productivity grinding. *Abrasives* October/November, p.34–41.
- Webster, J.A., Brinksmeier, E., Heinzl, C., Wittman, M., Thoens, K. 2002. Assessment of grinding fluid effectiveness in continuous-dress creep feed grinding. *CIRP Annals*, 48 (2), p.581–598.
- Webster, J.A., 2002. Grinding fluid effectiveness in CDCF grinding. *Grinding and Abrasives*, June/July, p.24–26.
- Webzell, S., 2007. *Time to come clean*. [Online] From Metalworking Production, 08 March 2007, available at <http://www.mwponline.com/>. (Accessed 13th March 2007)
- Weiss, J.M., Maruszewski, J.P., Smith, W.A., 1999. Implicit solution of preconditioned Navier-Stokes equations using algebraic multigrid, *AIAA J.*, 37 (1), p.29-36.
- Wu, H., Lin, B., Tridimas, Y.D., Morgan, M.N., 2007. Analysis of fluid flow in grinding using the Laser Doppler Anemometry (LDA) technique. *Advances in Abrasives Technology X*, ISAAT 2007, p.1-8.
- Yokogawa, M., Yokogawa, K., 1993. Improving grinding performance of CBN wheels by dual-fluid supply method. *International Journal of the Japan Society for Precision Engineering*, 27 (1).

Yoon, S.C., Krueger, M., 1999. Optimizing grinding performance by the use of sol-gel alumina abrasive wheels and a new type of aqueous metalworking fluid. *Machining Science and Technology*, 3 (2), p.287-294.

Zhen-Chang, L., Satoshi, A., Masahiro, N. 1995. Influence of grinding oil viscosity on grinding heat and burn damage in creep-feed grinding. *Lubrication Engineering*, 51(8), p.647-651.

Zhu, M., Shimizu, Y., Nishimoto, N., 2004. Calculation of curved open channel flow using physical curvilinear non-orthogonal co-ordinates. *Int. J. for Num. Methods Fluids*, 44, p.55-70.

Zienkiewicz, O.C., Morgan, K. 1983. *Finite Element and Approximation*. Wiley, New York, NY.

APPENDIX : NOT COPIED

ON INSTRUCTION FROM

UNIVERSITY

Appendix B Photographs

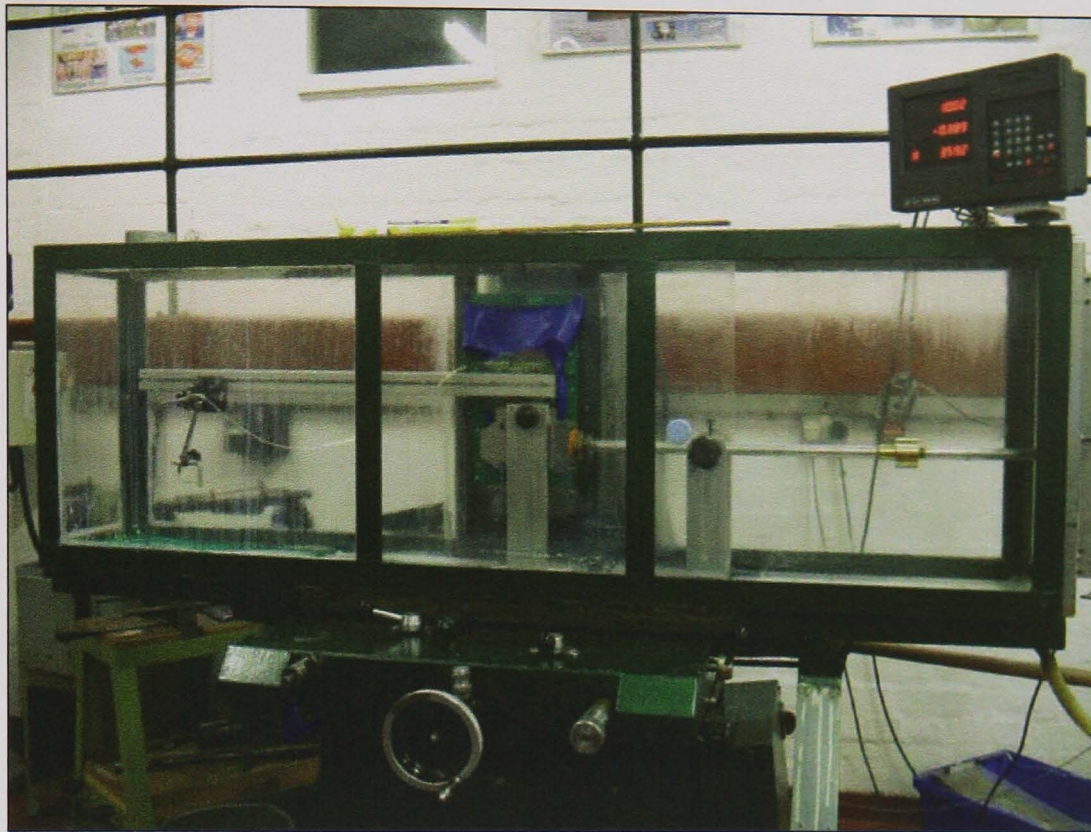


Figure B-1 Inspection tank fitted to the Jakobson surface grinder



Figure B-2 Fluid delivery and data acquisition system

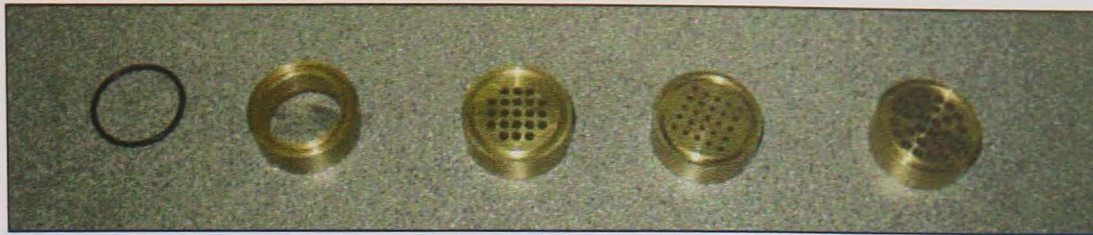


Figure B-3 The four methods of flow conditioning

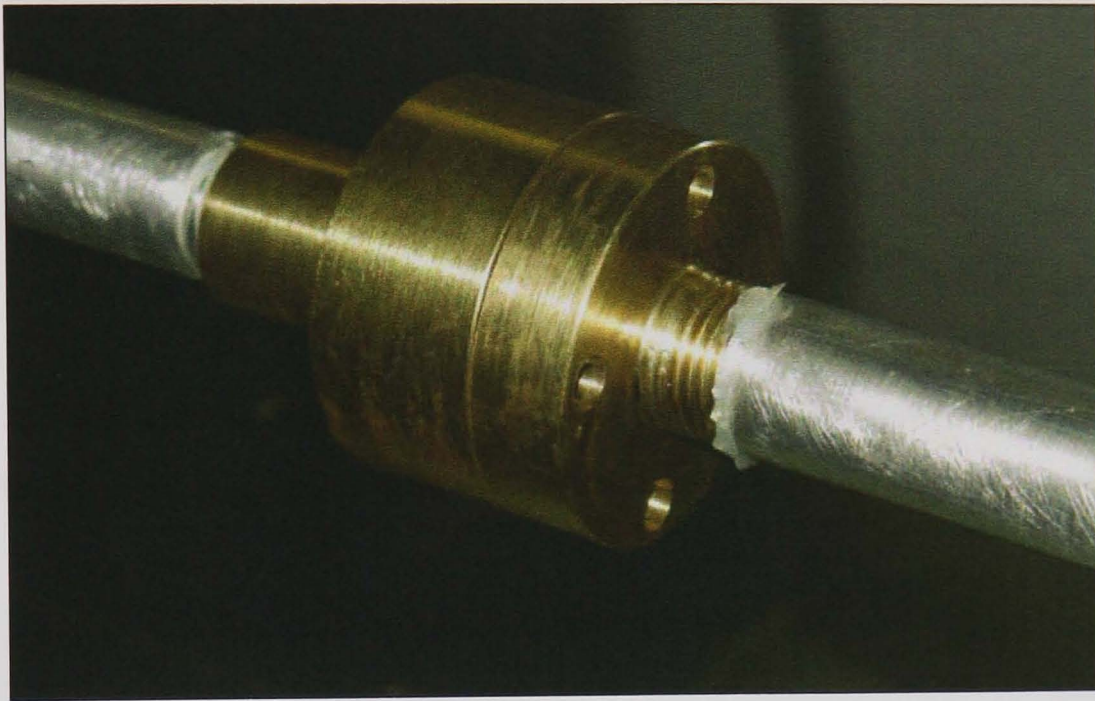


Figure B-4 Flow conditioner holding device



Figure B-5 Inside of the flow conditioner holder showing the o-ring and internal bore

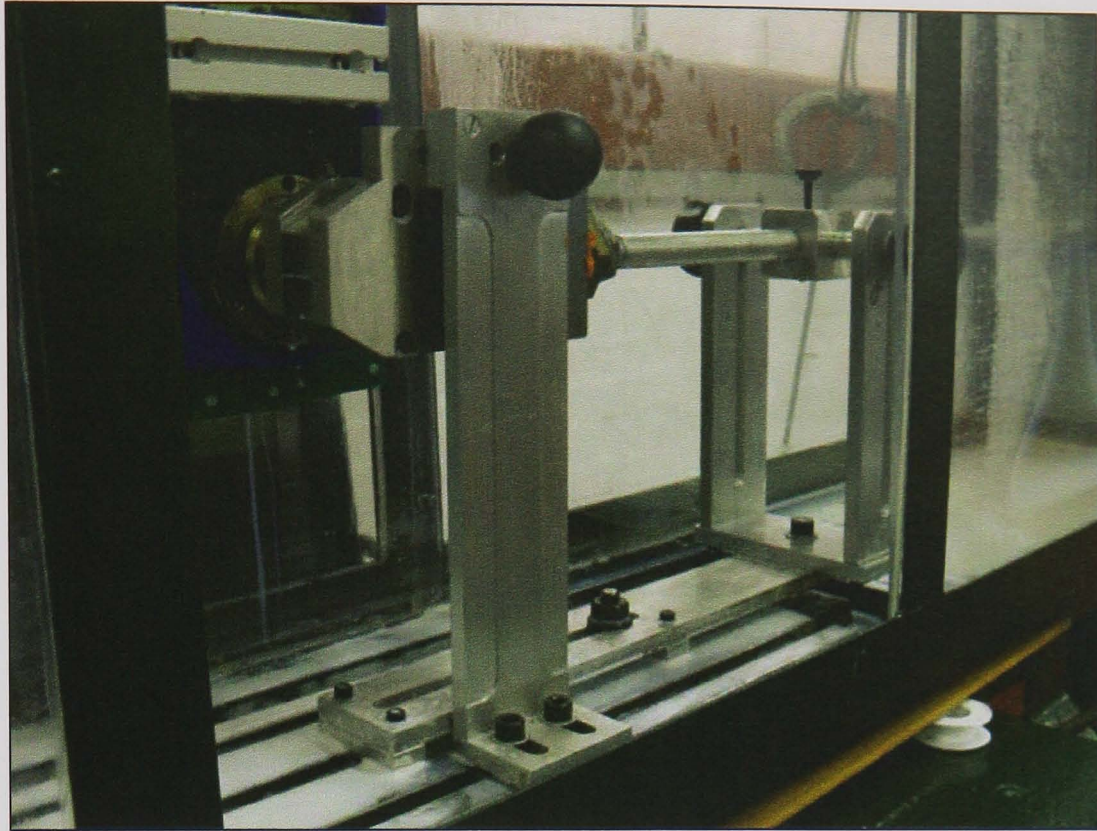


Figure B-6 Variable slot nozzle clamped to the bed with the angle adjust mechanism

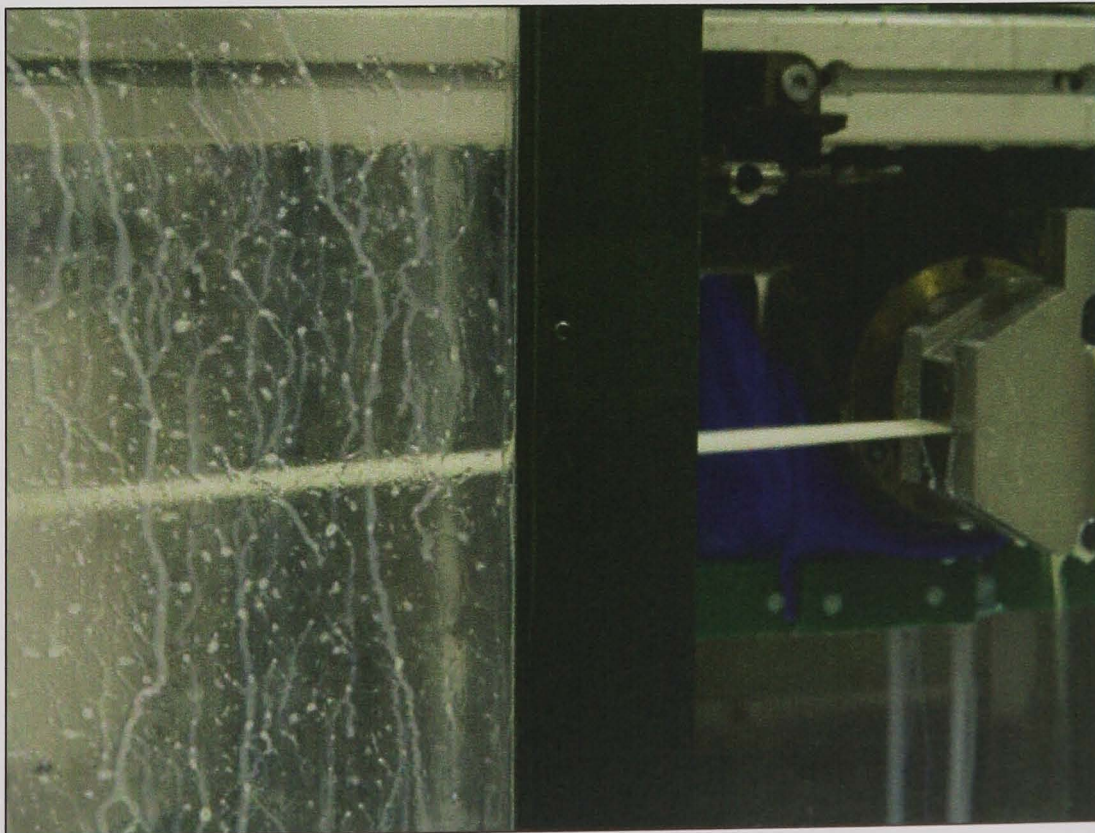


Figure B-7 Variable slot nozzle in action (gap 1.6mm, coolant is Castrol HysolX 10%)

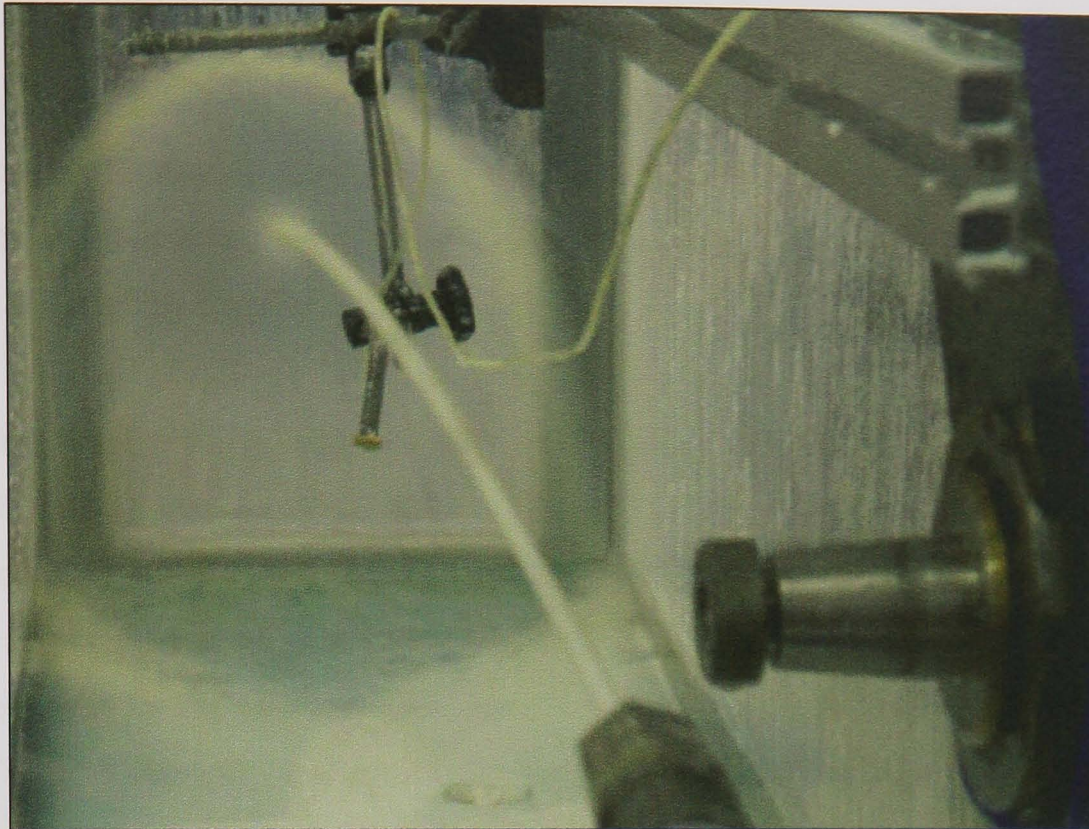


Figure B-8 A 9mm jet nozzle at 25 l/min showing the Pitot tube measurement system

Appendix C Positioning Case Study

Holroyd is a relatively small manufacturing outfit (compared with the larger manufacturers supplying broad-based machine tools) based in Rochdale, England. Its main area of focus is in the highly specialised area of screw machining technology. It is possibly the leading supplier in the world.

Machining and grinding high-precision worm gears is still an important part of the business serving customers in both civil and military aerospace, screw compressor rotors and even smaller niche markets such as racing cars. Holroyd has also established itself as a specialist in super abrasive machining of difficult materials. The focus of this case study was on the screw compressor side of the business based in Holroyd's rotor shop. A typical example of a pair of rotors manufactured by Holroyd machines is shown in Figure C-1.

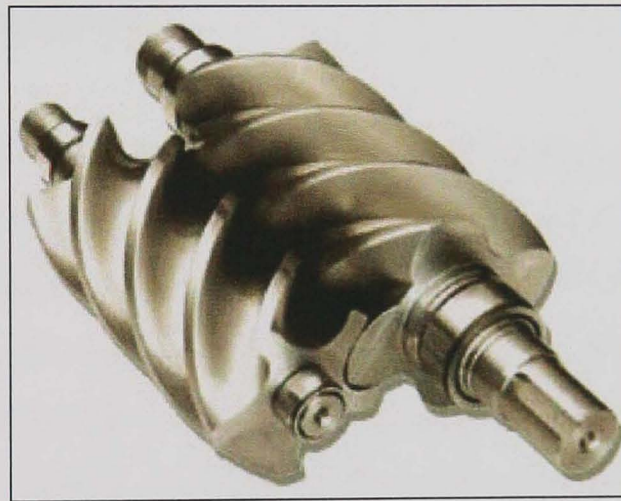


Figure C-1 Typical male and female screw compressors

The case study began with a tour of the three machines finishing screw compressors. Conventionally, the Lechler nozzles used (shown in Figure C-2) were positioned by loosening of the nut very slightly and tapping the head of the nozzle with a small hammer. This, as could be seen in the factory, led to deterioration of the nozzle over time and improper positioning of the coolant nozzles. It is very important that the nozzles are positioned accurately as the contact between the profiled grinding wheel and the flute of the rotor can be up to 0.75m from the nozzle orifice. Removal of material from a workpiece at high feed rates requires a significant quantity of coolant that must be delivered precisely and in sufficient quantities at, and across the entire profile of, the

interface between the grinding wheel and the workpiece. The coolant nozzles at Holroyd are positioned, at present, manually by an operator based on experience and an estimate of an orientation and position that will deliver the coolant stream directly at the wheel/workpiece interface. The significant volume and pressure of the stream of coolant during a grinding operation, for example, floods the grinding compartment and obscures any view of the exact position of the coolant stream's impact and at the grinding contact. Often, if the coolant stream has not been precisely delivered to the machining interface, the machined workpiece will have flaws due to excessive heat build-up or material removal, and must be reworked or scrapped (Webster et al 1995a).

Therefore, further improvements are needed to ensure that an adequate stream of coolant is delivered precisely and in sufficient quantities between the grinding wheel and the workpiece. It is also important that the jet coming out of the nozzle is coherent. This was one of the aims of the work in this thesis. In this case study, however, only the positioning aspect is highlighted.

Figure C-2 below shows the plate used on the head for the rotor grinder with several Lechler solid-jet nozzles mounted. On one of them is the positioning device. The positioning device consists of a very simple piece of metal turned down to fit over the end of the Lechler nozzles with a snug fit. The device is knurled on the end to give the operator something with which to grip the positioning device and ultimately hold whilst positioning the nozzle. Inside this adapter fits a 9mm bore laser pointer. These are commercially available for aligning weapons. They have a high-accuracy laser. The total cost of the unit including manufacture is around £150. This is a fraction of the cost of the parts scrapped at Holroyd due to incorrect set up of the coolant nozzles.

To predict the path of the fluid and therefore position the nozzle without the coolant on, the positioning device is fitted to the nozzle, the machine is then dry-cycled with only 0.5mm stand-off and the operator can switch between each nozzle, observing the point of contact and tweaking until the laser point hits the required grinding contact point. This has the advantage of a) removing the need to have coolant flowing with the door interlocks bypassed b) the stopping and starting of the pumps to look and then tweak the nozzle each time c) removing any operator error of judgement from a distance d) hitting of the nozzle causing damage. Figure C-3 is an overview of this system. Figure C-4

shows the laser in action with the beam pointed at the grinding contact. All adjustment is done without the risk of operator contamination, as the oil coolant is not flowing.

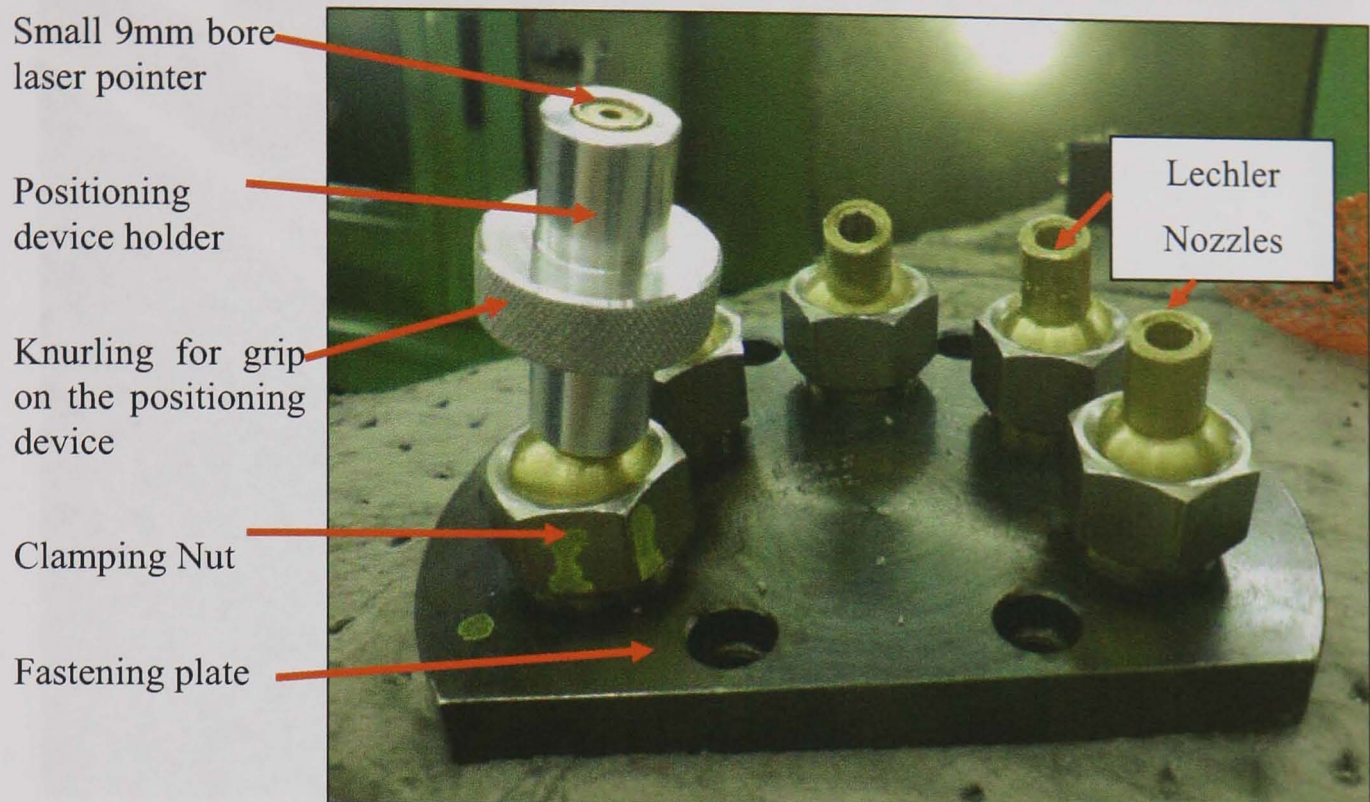


Figure C-2 the nozzle system for the rotor-grinder with positioning device

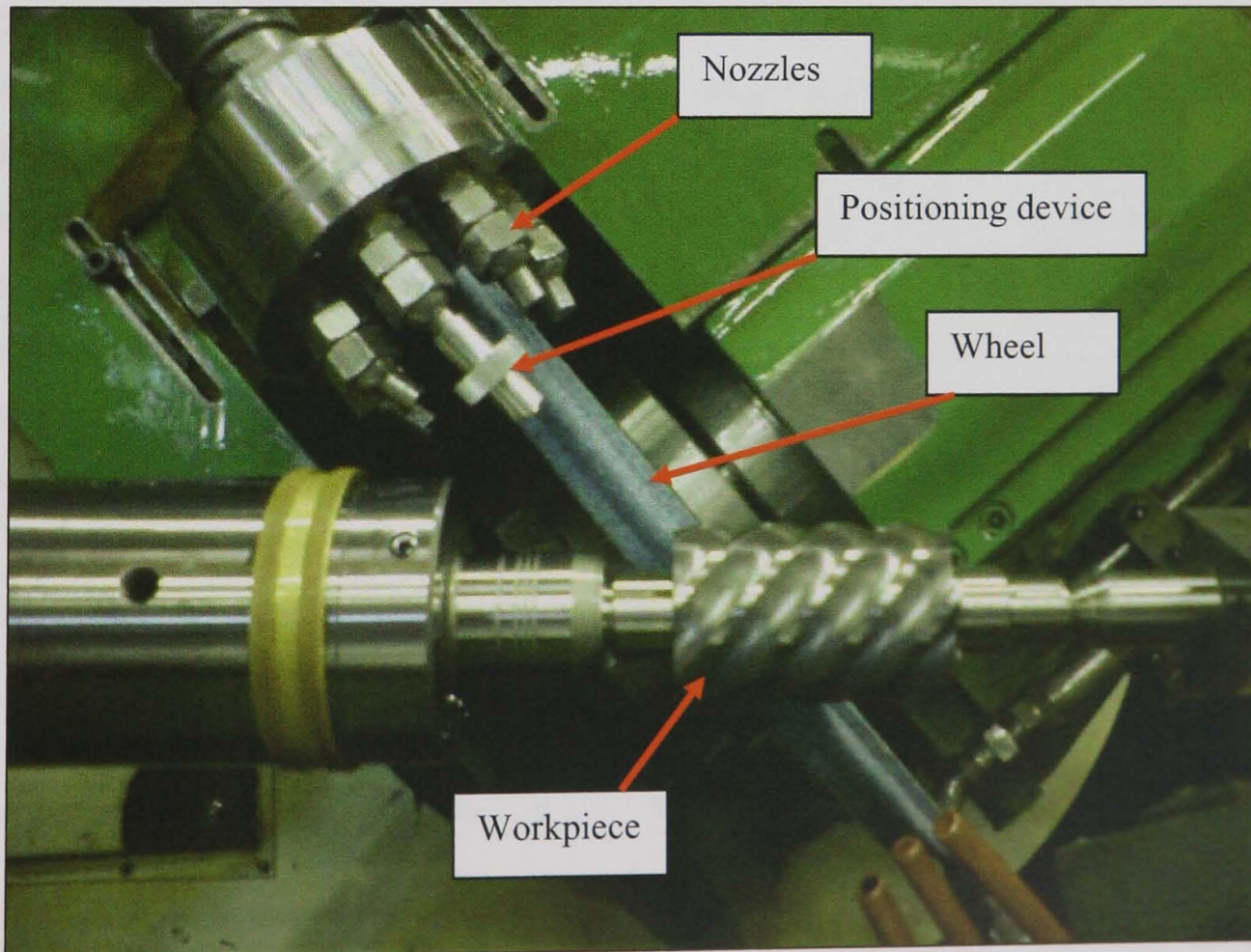


Figure C-3 the machine setup with the nozzles and positioning device in place

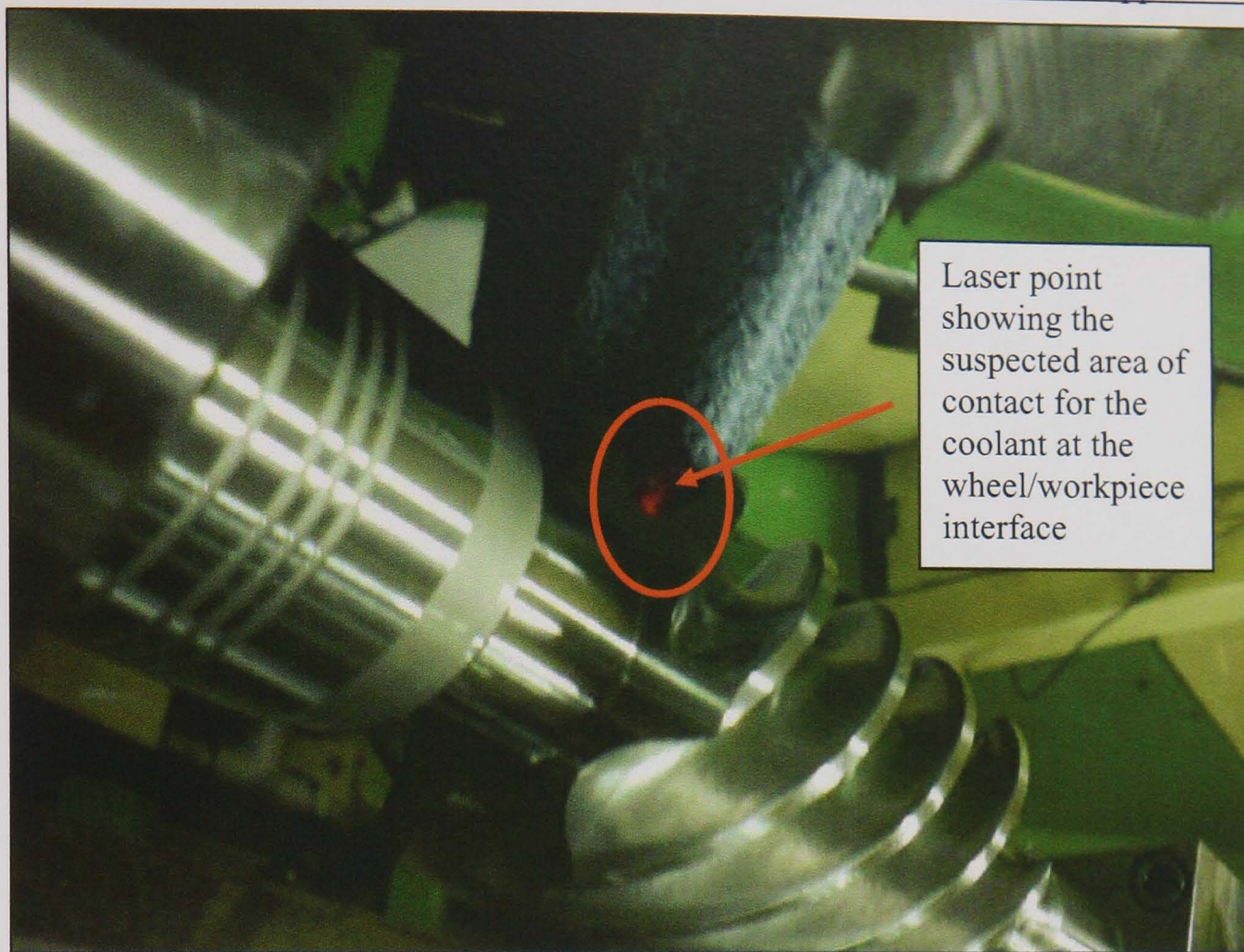


Figure C-4 the positioning of the nozzle with beam showing

Results

The positioning device proved a success with the operators at Holroyd because they could use it without being contaminated by oil. They also commented on the ease of use of the pointing device and its ability to point the nozzle directly at the grinding contact. For comparison, two batches of 10 rotors were ground – one set with the operator setting up the nozzles in the conventional way to the best of his ability, and the second set with the same operator using the nozzle-positioning laser. The screws were checked on a Leitz CMM machine. The complete set of results are shown in Figure C-5 to Figure C-14. A brief summary of the success of the trials is as follows:

- Form accuracy improved by 5 μ m;
- Min and Max deviation improved by total of 6 μ m;
- Maximum 12% improvement on pitch;
- Maximum 23% improvement on lead errors;
- Reduction in setup time of 70%.

Overall the test at Holroyd proved the suitability and need for a correct nozzle-positioning device. Further work would be required to assess long-term potential.

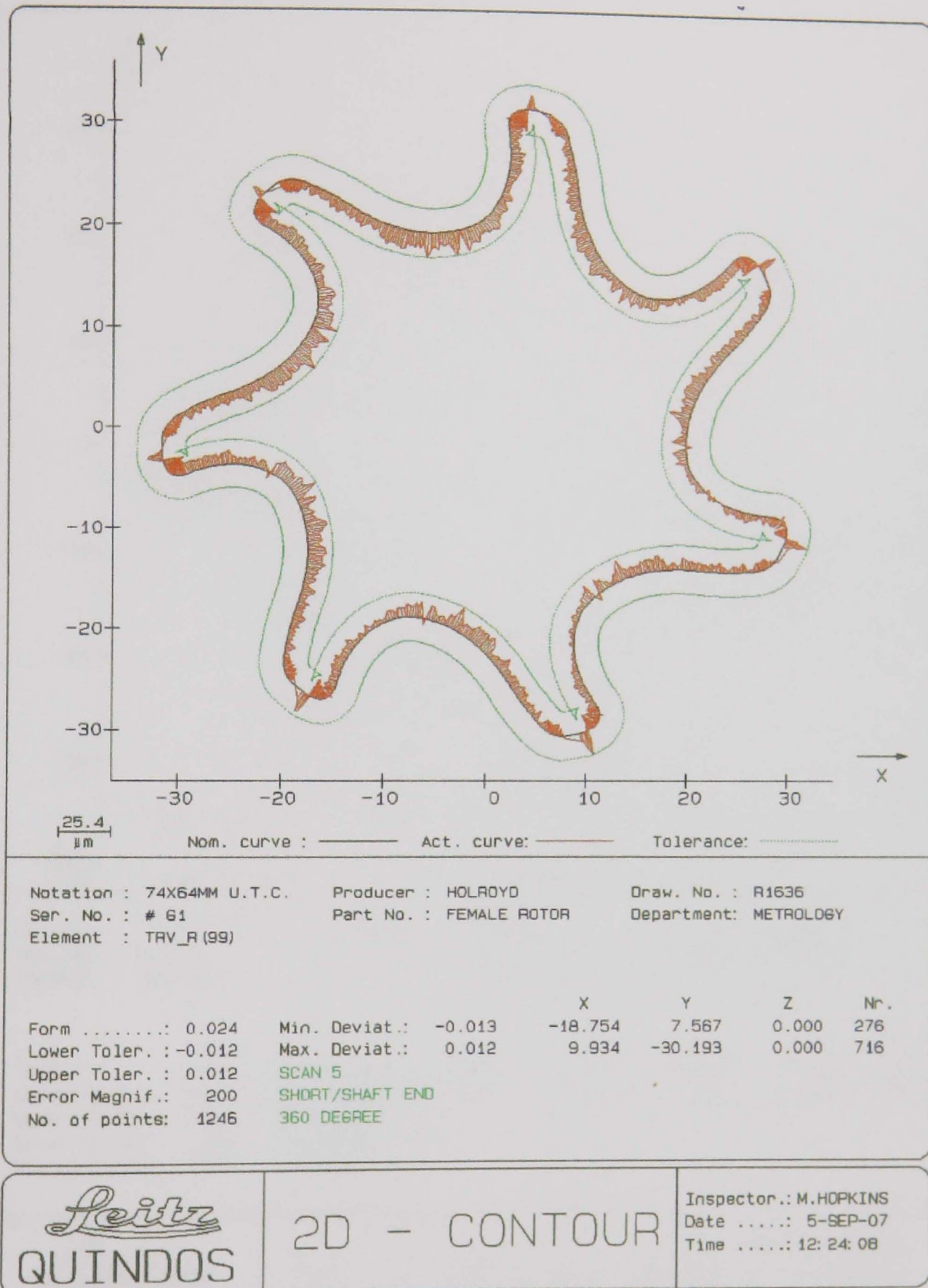


Figure C-5 manually operated adjustment – 2D contour of short/shaft end

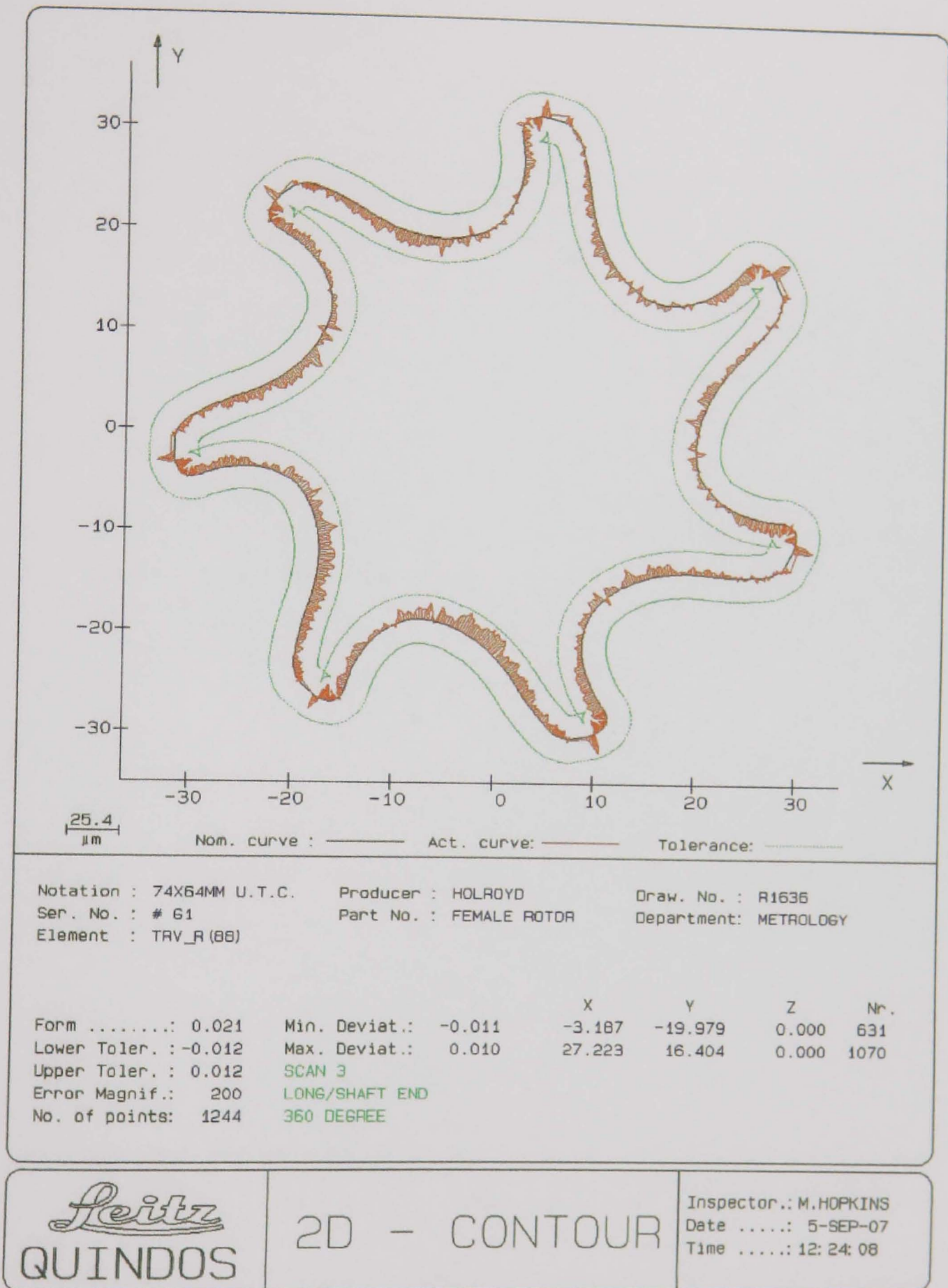


Figure C-6 manually operated adjustment – 2D contour of long/shaft end

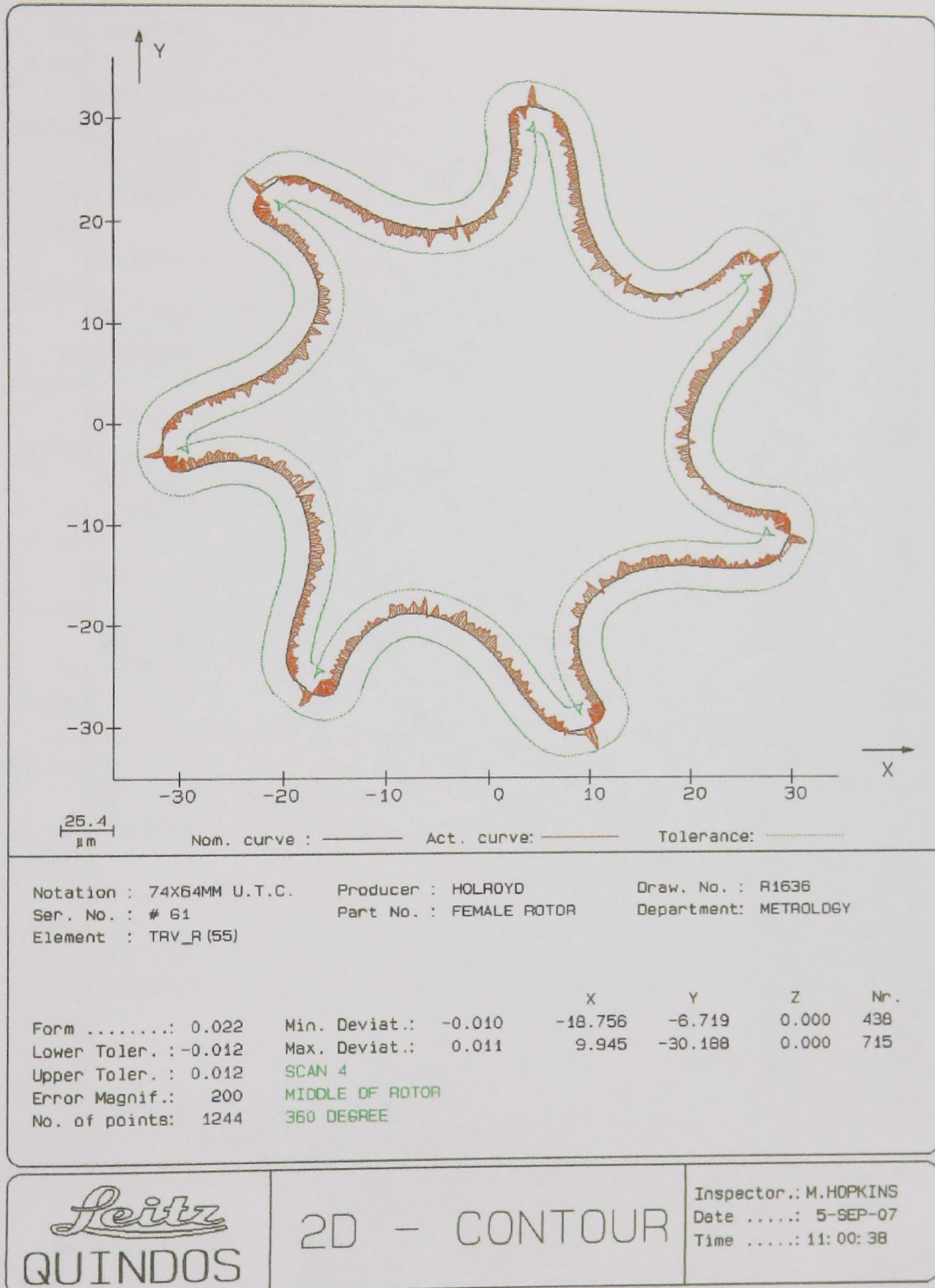


Figure C-7 manually operated adjustment – 2D contour of middle of rotor

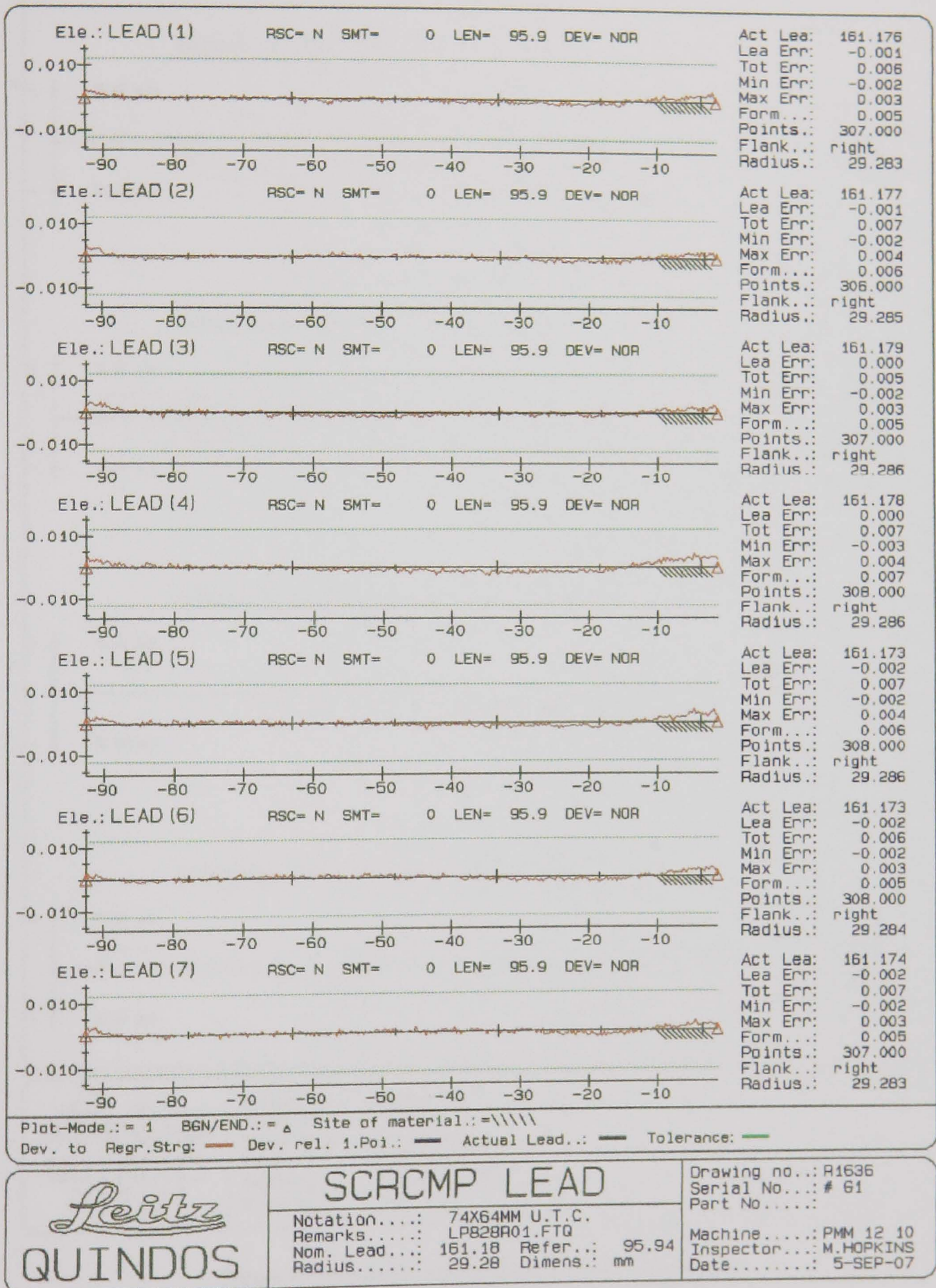


Figure C-8 manually operated adjustment - Lead error traces

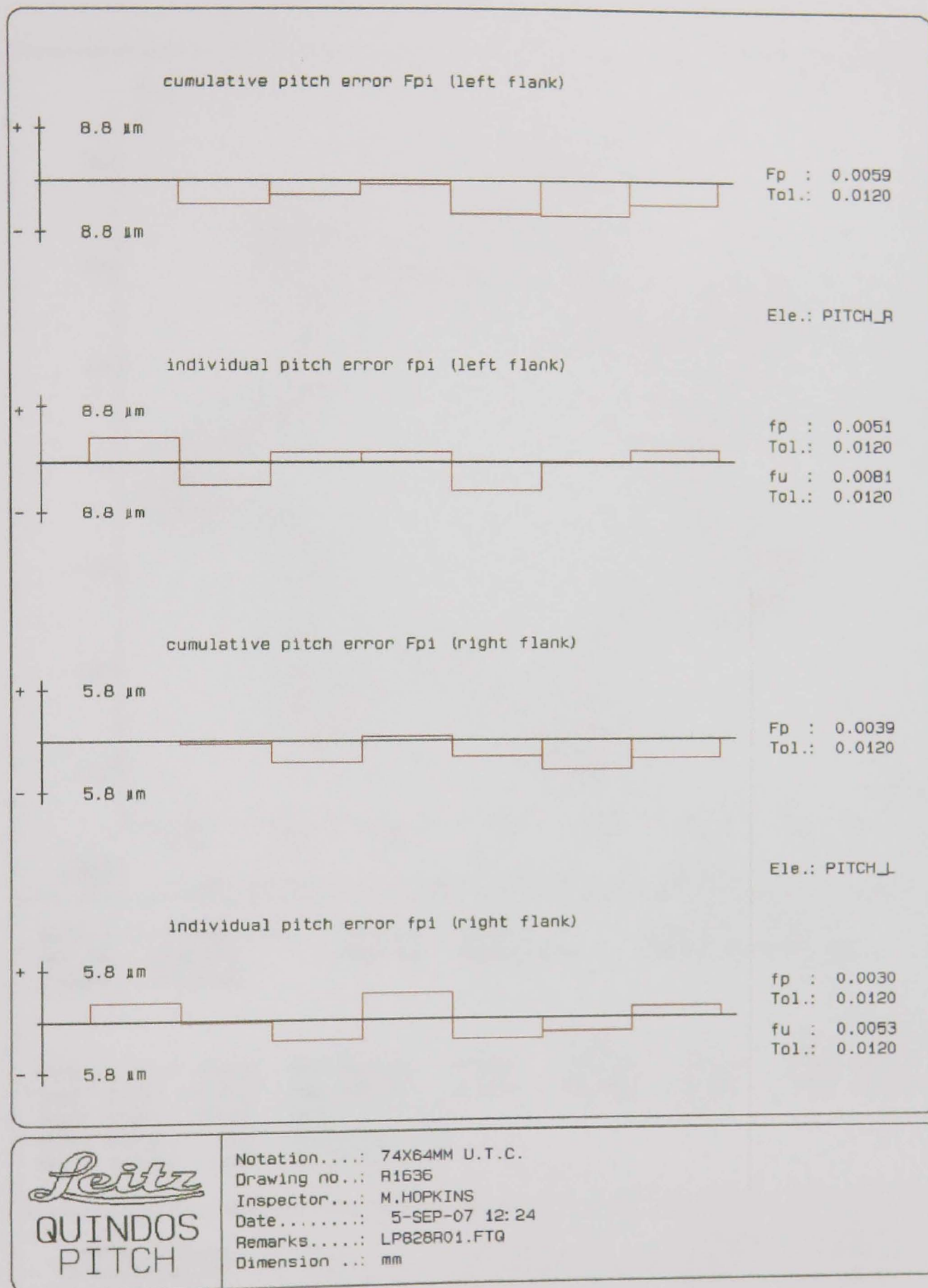


Figure C-9 manually operated adjustment – Pitch plots

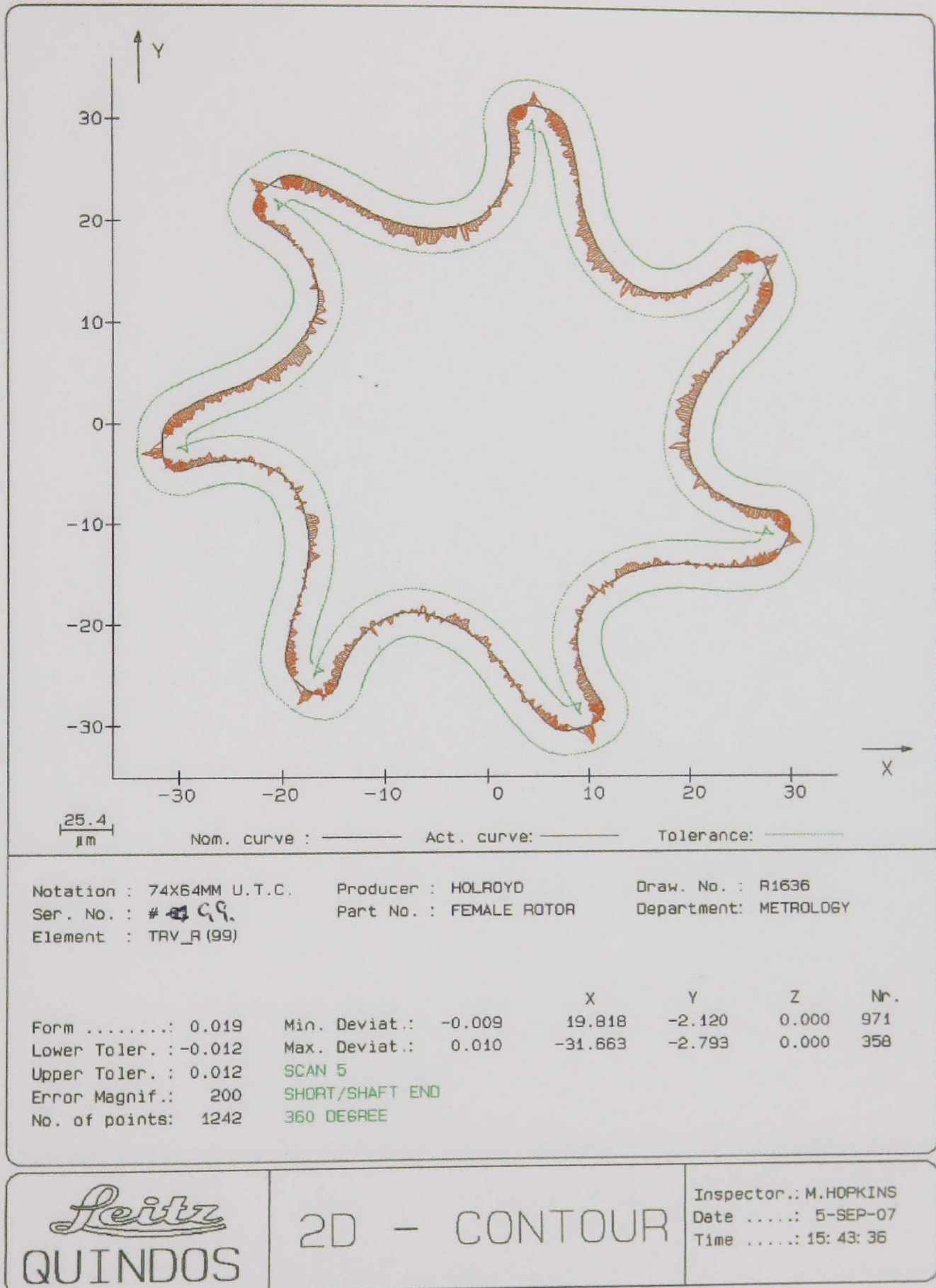


Figure C-10 laser guided adjustment – 2D contour of short/shaft end

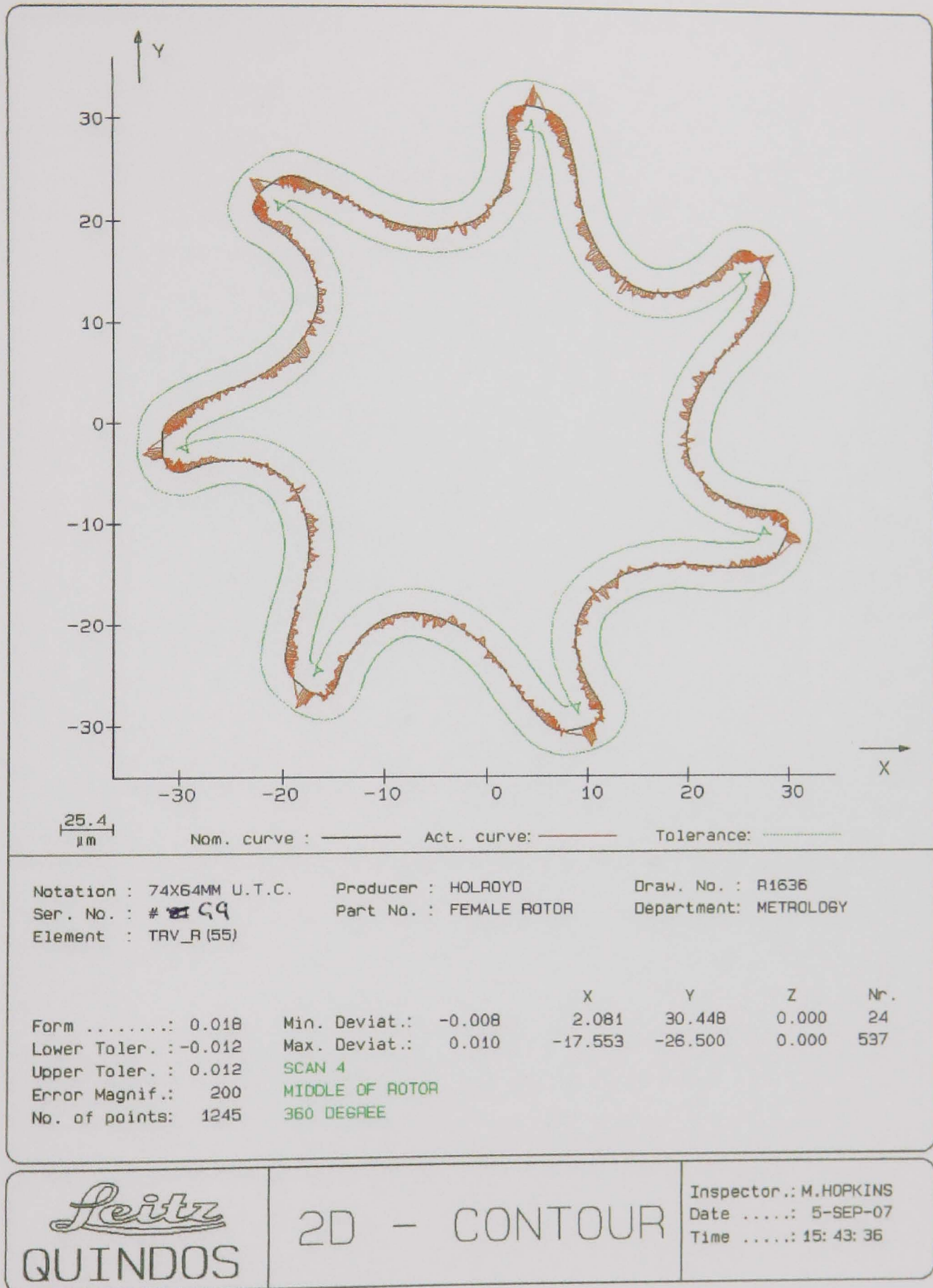


Figure C-11 laser guided adjustment – 2D contour of middle of rotor

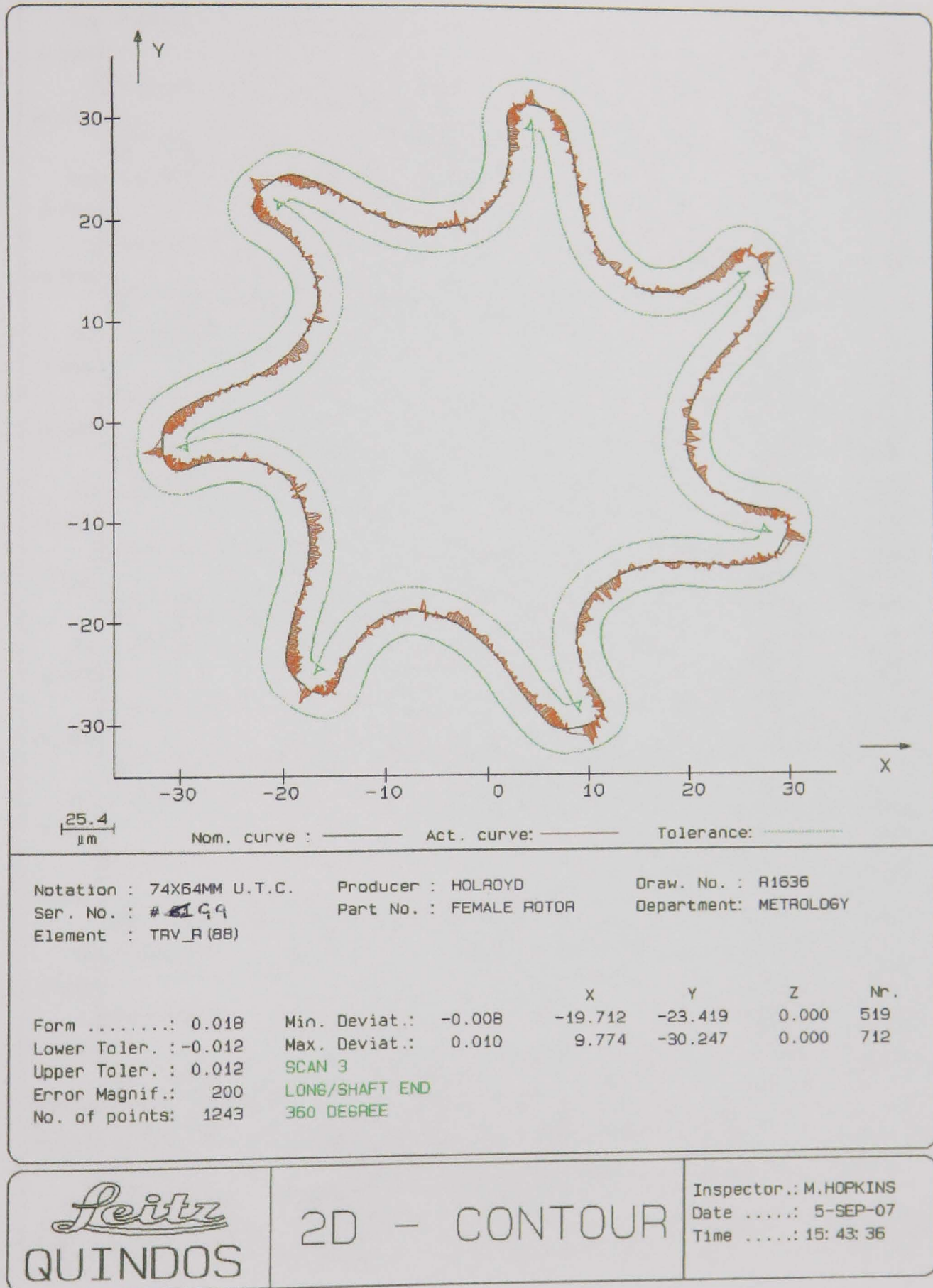


Figure C-12 laser guided adjustment – 2D contour of long/shaft end

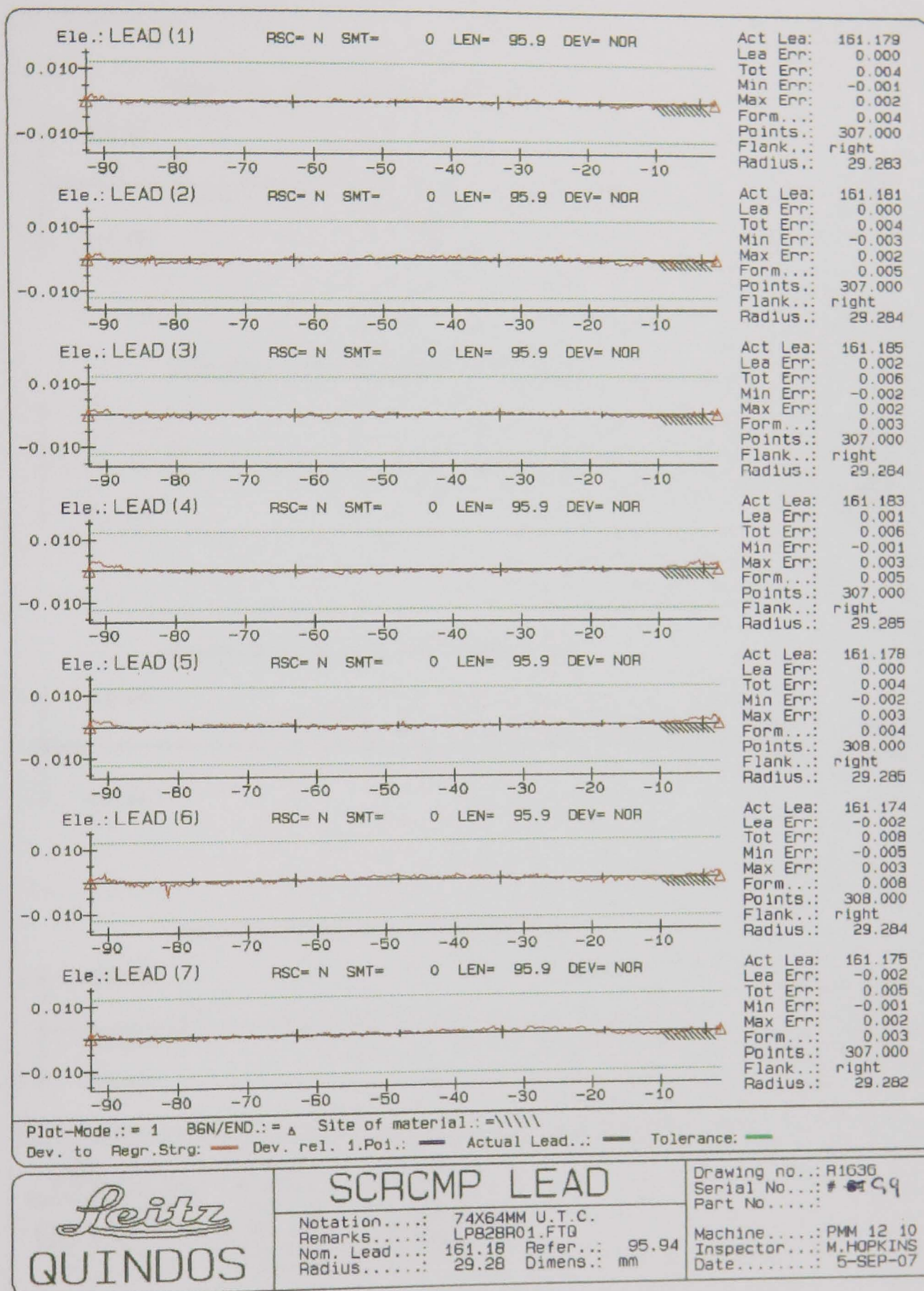


Figure C-13 laser guided adjustment –Lead error traces

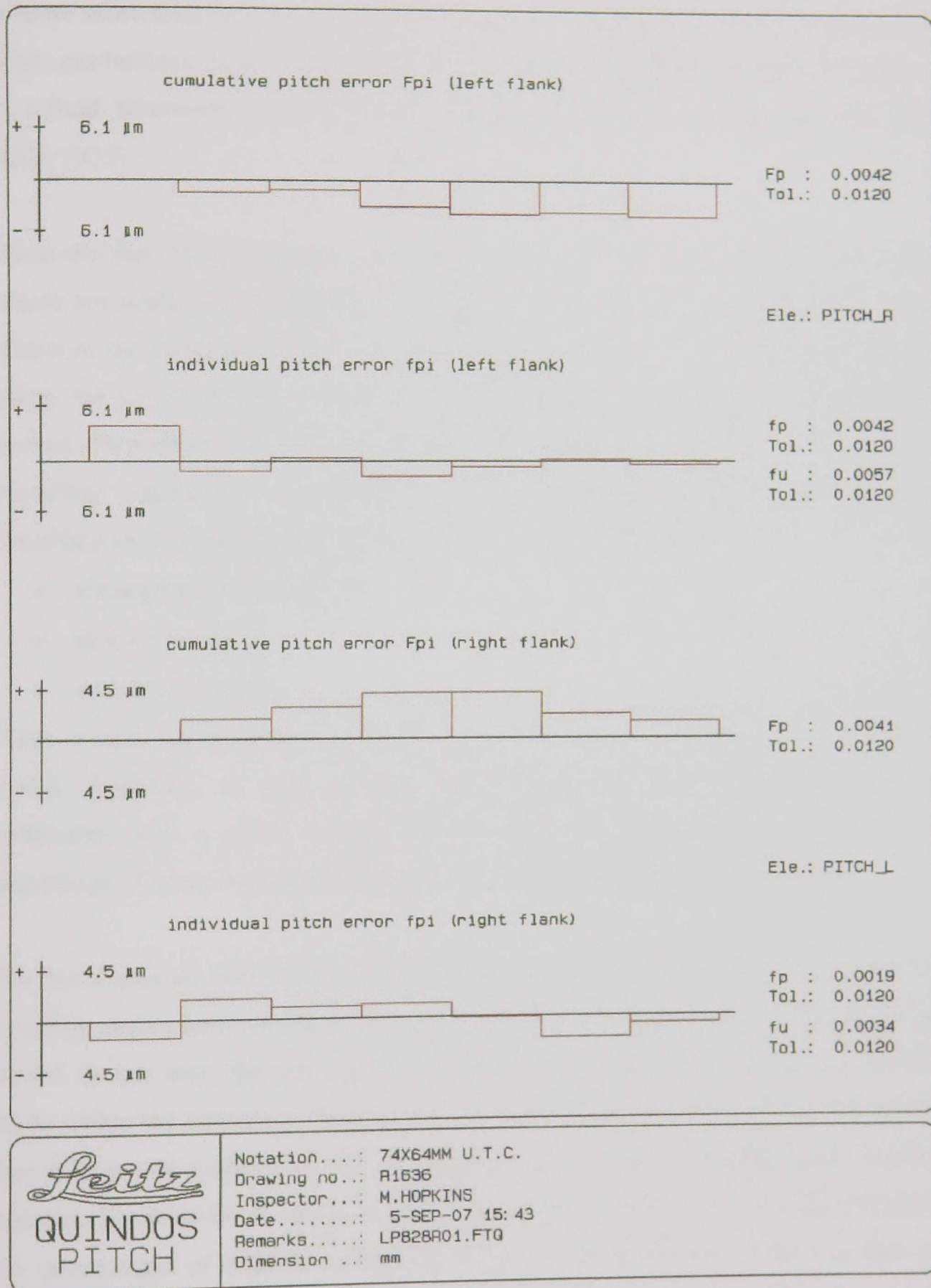


Figure C-14 laser guided adjustment – Pitch plots

Appendix D Multiphase systems theory

A multiphase system is defined as a mixture of the phases of solid, liquid and gas of one or more substances (including immiscible liquids). Familiar examples are water droplets in air, gas bubbles rising in a liquid and solid particles such as dust particles transported by a fluid. Multiphase flows are often classified according to the nature of the system (Ishii, 1975).

When the flow phenomenon is dominated by one phase and the amounts of the other phases are small, multiphase flow is in practice described as single-phase flow and all effects of the secondary phases are neglected. This work focuses on multiphase flows where the secondary phase cannot be ignored due to its importance for the method studied. Depending on the strength of the coupling between the phases, different modelling approaches are possible for the solution to multiphase problems. Classification of these approaches falls into one of three categories:

- homogeneous flow models
- mixture models
- multiphase models

There is also the possibility of combining these models to make a new multiphase model. Typically, in most models, each phase is treated as an interpenetrating continuum with a given volume fraction parameter. The volume fraction is the percentage of space occupied by that fluid or solid within a region of the flow.

The homogeneous flow model is applicable in drag-dominated flows in which strong coupling occurs between the phases and their velocities equalise over a relatively small period. In this way, the velocity of each phase is assumed to be similar and therefore taken within the continuity equations as being the same. A single momentum equation then solves the velocity of the mixture. For each phase, an individual continuity equation is solved for to obtain its volume fraction. This figure is vital in determining the percentages of mixture within the flow and the effect that it has on that said continuous flow. The usual method involves user input of initial conditions to start with followed by a calculation using the fundamental equations to estimate the volume fraction at any given point.

The main difficulties associated with all multiphase models lies within the discontinuities associated to them as well as the interactions between the two phases (Ishii & Mishima 1984). When developing a multiphase model, the formulation of the constitutive equations is the greatest difficulty (Drew & Lahey 1979). As a result, the constitutive equations applied still include significant uncertainties. Experimental validation is therefore a valuable and essential part of the simulation process. Although the full multiphase equations are theoretically more advanced, the uncertainties in the closure relations make them less reliable than the simpler models. This is another justification of using the simpler homogeneous flow models if possible.

In section F.3.7, a short discussion of the multiphase flow models of three commercial computer codes (PHOENICS, FLUENT and CFX 5) is given. Although the main interest of this work is in the use of ANSYS CFX, the multiphase models of the other commercial codes are also described. The model used within this work is implemented only using ANSYS CFX 5.71 and 10.

D.1.1 Multiphase Equations

To understand the relationship happening at the interactions between the two phases present within this work, equations for multiphase flow are presented. The analysis is restricted to the mechanics of the multiphase system not considering any thermodynamic relations.

When deriving the equations for multiphase flow, two different definitions of the average velocity are commonly used. If the local instant velocity of phase α is denoted by $U_{I\alpha}$, the average velocity can be defined as $u_\alpha = \overline{U_{I\alpha}}$, where the over bar indicates an average inside some averaging domain (volume, time-step, a set of experiments, a group of particles for instance). The alternative definition of the average velocity is based on weighting the velocity with the local density $\rho_{I\alpha}$

$$U_\alpha = \frac{\overline{\rho_{I\alpha} U_{I\alpha}}}{\rho_\alpha} = \frac{\overline{\rho_{I\alpha} U_{I\alpha}}}{\rho_\alpha} \quad [D.1]$$

where ρ_α is the average material density.

This mass-weighted averaging known as Favre averaging, yields a simple form for the continuity equation (Ishii, 1975). Throughout this work, U_α denotes the Favre-averaged velocity. The Favre-averaged balance equations have been presented by several authors (e.g., Ishii 1975, Ishii & Mishima 1984, Ahmadi & Ma 1990, Hwang 1989, Gidaspow 1994). Following the notations of Ishii (1975) and writing the continuity and momentum equations for each phase α as follows gives:

Conservation of mass for phase α :

$$\frac{\partial}{\partial t}(r_\alpha \rho_\alpha) + \nabla \cdot (r_\alpha \rho_\alpha U_\alpha) = \sum_{\beta=1}^N (\dot{m}_{\alpha\beta} - \dot{m}_{\beta\alpha}) \quad [\text{D.2}]$$

where r = volume fraction

β = the second phase

ρ = density

U = velocity

N = total number of phases, and the mass transfer rate between phases is represented by \dot{m} .

This right hand side of the equation represents the mass generation rate at the interface.

The sum of the volume fractions is unity:

$$\sum_{\alpha} r_{\alpha} = 1 \quad [\text{D.3}]$$

Following the notations of Ishii (1975) and writing the continuity and momentum equations for each phase (α and β) as follows:

Conservation of momentum for phase α :

$$\begin{aligned} \frac{\partial}{\partial t}(r_\alpha \rho_\alpha U_\alpha) + \nabla \cdot (r_\alpha \rho_\alpha U_\alpha \otimes U_\alpha) - \nabla \cdot (r_\alpha \mu_\alpha (\nabla U_\alpha + (\nabla U_\alpha)^T)) \\ = -r_\alpha \nabla p + r_\alpha \rho_\alpha g + M \end{aligned} \quad [\text{D.4}]$$

where μ = viscosity in equation [D.4] and represents the viscous stress tensor for the continuity equation

p = pressure

T = temperature of the phase

M = sum of interfacial forces (drag, lift, virtual mass, turbulent dispersion, wall lubrication forces and momentum transfer associated with mass transfer)

$$M = F_D + F_L + F_M + F_T + F_W + \sum_{\beta=1}^N (\dot{m}_{\alpha\beta} U_{\beta} - \dot{m}_{\beta\alpha} U_{\alpha}) \quad [\text{D.5}]$$

Conservation of energy for phase α is

$$\begin{aligned} \frac{\partial}{\partial t} (r_{\alpha} \rho_{\alpha} h_{\alpha}) + \nabla \cdot (r_{\alpha} \rho_{\alpha} U_{\alpha} h_{\alpha}) - \nabla \cdot (r_{\alpha} k_{\alpha} \nabla T_{\alpha}) = \\ \sum_{\beta=1}^N c_{\alpha\beta}^{(h)} (T_{\beta} - T_{\alpha}) + \sum_{\beta=1}^N (\dot{m}_{\alpha\beta} h_{\beta} - \dot{m}_{\beta\alpha} h_{\alpha}) \end{aligned} \quad [\text{D.6}]$$

where h = enthalpy

k = thermal conductivity

c = Interfacial heat transfer as

$$c_{\alpha\beta}^{(h)} = h_{\alpha\beta} A_{\alpha\beta} \quad [\text{D.7}]$$

A point of interest in equation [D.6] is that the temperature differences drive the heat transfer.

The mass fractions used for the approximation of mass transfer between the phases is

$$\begin{aligned} \frac{\partial}{\partial t} (r_{\alpha} \rho_{\alpha} Y_{A\alpha}) + \nabla \cdot (r_{\alpha} \rho_{\alpha} U_{\alpha} Y_{A\alpha}) - \nabla \cdot (r_{\alpha} \rho_{\alpha} D_{A\alpha} \nabla Y_{A\alpha}) = \\ \sum_{\beta=1}^N c_{\alpha\beta}^{(A)} (C_{A\beta} - C_{A\alpha}) + \sum_{\beta=1}^N (\dot{m}_{\alpha\beta} Y_{A\beta} - \dot{m}_{\beta\alpha} Y_{A\alpha}) \end{aligned} \quad [\text{D.8}]$$

(cf. Ishii 1975 p.72)

This equation defines the multi-component, multiphase flow describing the interactions between each phase within each element of processing. A point of interest in equation [D.8] is that interphase transfer is driven by concentrations.

From this, the solver implements the multiphase momentum equation

$$\frac{\partial}{\partial t}(r_\alpha \rho_\alpha U_\alpha) + \nabla \cdot (r_\alpha \rho_\alpha U_\alpha \otimes U_\alpha) = -r_\alpha \nabla p + \nabla \cdot (r_\alpha \mu_\alpha (\nabla U_\alpha + (\nabla U_\alpha)^T)) \quad [\text{D.9}]$$

$$+ r_\alpha \rho_\alpha g + M_\alpha + S_\alpha$$

where M includes drag, lift, virtual mass and turbulent dispersion forces and momentum transfer associated with mass transfer so that the momentum carried between phases either by drag or through mass exchange is

$$M_\alpha = \sum_{\beta=1}^N c_{\alpha\beta}^{(d)} (U_\beta - U_\alpha) + \sum_{\beta=1}^N (\dot{m}_{\alpha\beta} U_\beta - \dot{m}_{\beta\alpha} U_\alpha) + \dots \quad [\text{D.10}]$$

D.1.2 Calculation of drag force for use within the model

The empirical relationship used to determine the inter-phase drag coefficient is

$$c_{\alpha\beta}^{(d)} \quad [\text{D.11}]$$

(cf. Ishii 1975 p.78)

The actual drag force, D , is calculated using

$$\underline{D} = \frac{1}{2} C_D \rho_f A_p |\underline{U}_r| \underline{U}_r \quad [\text{D.12}]$$

where subscript p = particle phase

f = continuous fluid phase.

where the actual change in velocity is

$$\underline{U}_r = \underline{U}_f - \underline{U}_p \quad [\text{D.13}]$$

and the area of the particle is represented by

$$A_p = \frac{\pi d_p^2}{4} \quad [\text{D.14}]$$

The drag coefficient C_D in [D.12] depends on various factors. At small particle Reynolds numbers, Stokes's law gives the total drag coefficient

$$C_{D,St} = \frac{24}{Re_p} \quad [D.15]$$

The drag coefficient, C_D , required for implementation into the model, is a function of the particle Reynolds number in that

$$Re_p = \frac{\rho_f |\underline{U}_r| d_p}{\mu_f} \quad [D.16]$$

When the particle Reynolds number increases however, Stokes's law underestimates the drag. The standard drag curve in Figure D-1 shows the dependence of the drag on Re_p .

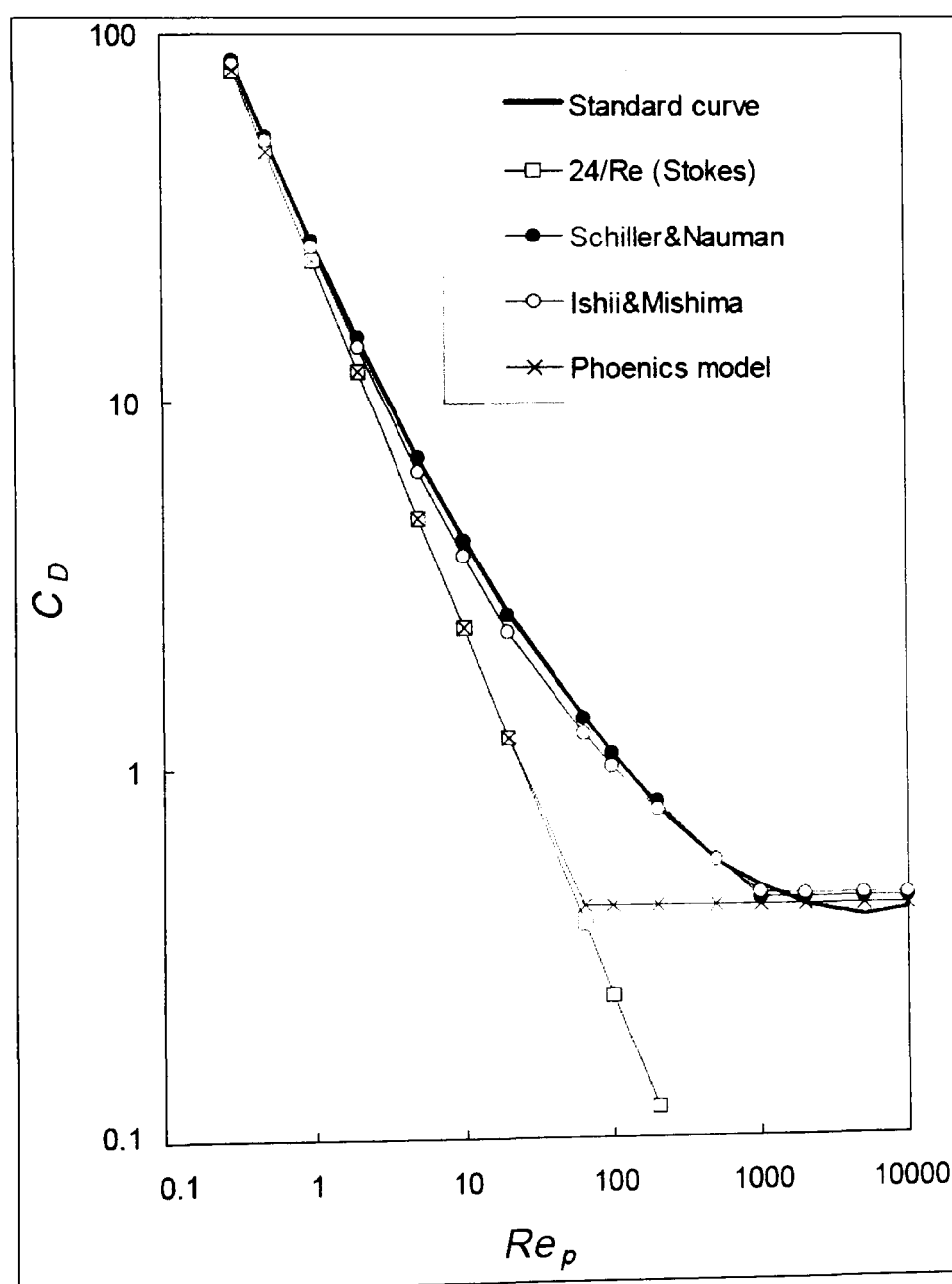


Figure D-1 Standard drag curve (Clift et al 1978) and various simplified correlations in the low Reynolds number region

Schiller & Nauman formulation is a frequently used expression for the drag coefficient (Clift et al 1978).

$$0 \leq \text{Re}_p \leq (10^3) \quad C_D = \frac{24}{\text{Re}_p} (1 + 0.15 \text{Re}_p^{0.687}) \quad [\text{D.17}]$$

This expression gives basis also for the drag coefficient proposed by Newton namely

$$0(10^3) \leq \text{Re}_p \leq (10^5) \quad C_D = 0.44 \quad [\text{D.18}]$$

A combination of the Schiller & Nauman model with that from Newton gives

$$(0 \leq \text{Re}_p \leq (10^3) - 0.15 \text{Re}_p^{0.687}), 0.44) \quad [\text{D.19}]$$

Figure D-2 shows the effect of an increasing Reynolds particle number on the drag coefficient for the solution. Classification of the regions in the form of a summary is:

- Stokes' regime ($0 < \text{Re}_p < 0.2$)
 - Very slow laminar flow
- Transitional regime ($0 < \text{Re}_p < (10^3)$)
 - Drag due to viscous and inertia forces, hence also called Viscous regime
- Newton regime ($(10^3) < \text{Re}_p < (10^5)$)
 - Drag due almost entirely to inertial forces, hence independent of particle Reynolds number
- Super-Critical regime ($\text{Re}_p > (10^5)$)
 - Transition from laminar to turbulent boundary layer, separation occurs further back within the flow, causing drag reduction

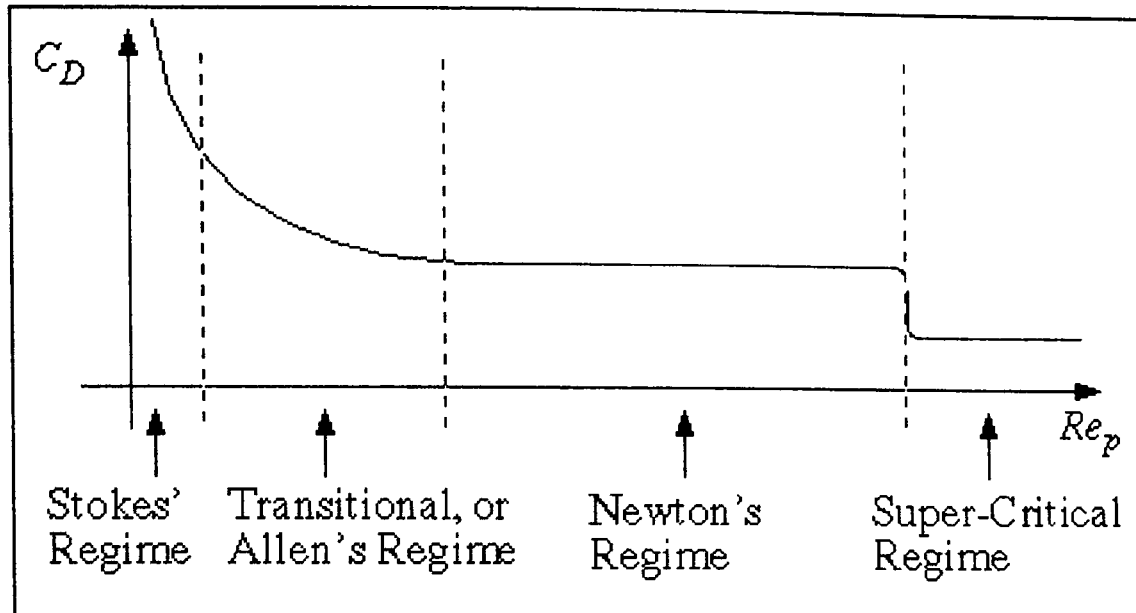


Figure D-2 Graphical representation of the change in the drag coefficient with an increasing Re_p

If the volume of a single particle is

$$V_p = \frac{\pi d_p^3}{6} \quad [\text{D.20}]$$

with the surface area of a single particle noted as

$$S_p = \pi d_p^2 \quad [\text{D.21}]$$

and the number of particles per unit volume given by

$$n_p^m = \frac{\text{volume fraction in the cell}}{\text{volume of the particle}} = \frac{r_p}{V_p} = \frac{6r_p}{\pi d_p^3} \quad [\text{D.22}]$$

Then the interfacial area density (m^2/m^3), a fundamental quantity for inter-phase transfer, is given by

$$A_{\alpha\beta} = S_p n_p^m = \frac{6r_p}{d_p} \quad [\text{D.23}]$$

The total drag force therefore becomes

$$\underline{D} = n_p \underline{D} = \frac{3}{4} C_D \frac{r_p \rho_f}{d_p} |\underline{U}_r| \underline{U}_r \quad [\text{D.24}]$$

Relating C_D back to $c_{\alpha\beta}^{(d)}$ and comparing the total drag force to the right hand side of the momentum equation

$$\underline{D} = n_p \underline{D} = \frac{3}{4} C_D \frac{r_p \rho_f}{d_p} |\underline{U}_r| \underline{U}_r = c_{\alpha\beta}^{(d)} \underline{U}_r \quad [\text{D.25}]$$

Expressing this in terms of interfacial area density $A_{\alpha\beta}$

$$c_{\alpha\beta}^{(d)} = \frac{3}{4} C_D \frac{r_p \rho_f}{d_p} |\underline{U}_r| = \frac{1}{8} C_D A_{\alpha\beta} \rho_f |\underline{U}_r| \quad [\text{D.26}]$$

The above equations allow advanced users of CFD software to add their own interfacial transfer models. Ishii & Mishima (1984) describe some commonly used models for implementation into CFD code. The modelling work by researchers looking into the mixture models requires implementation of the following equations:

$$\text{Drag Force} \quad \underline{D}_{\alpha\beta} = C_D \rho_{\alpha\beta} A_{\alpha\beta} |\underline{U}_r| \underline{U}_r \quad [\text{D.27}]$$

$$\text{Density of the phase} \quad \rho_{\alpha\beta} = r_\alpha \rho_\alpha + r_\beta \rho_\beta \quad [\text{D.28}]$$

$$\text{Area of the phase} \quad A_{\alpha\beta} = \frac{r_\alpha r_\beta}{d_{\alpha\beta}} \quad [\text{D.29}]$$

C_D and $d_{\alpha\beta}$ are specified by the user from the graphical user interface (GUI) and are set in code conversion language (CCL) using

FLUID PAIR: → Interfacial Area Density

An example of this is the particle model & mixture model (CFX Help, 2006)

$$\frac{3}{4} C_D \frac{r_p \rho_f}{d_p} |\underline{U}_r| \underline{U}_r = C'_D (r_p \rho_p + r_f \rho_f) A_{\alpha\beta} |\underline{U}_r| \underline{U}_r \quad [\text{D.30}]$$

$$C_D = C'_D \quad [\text{D.31}]$$

$$A_{\alpha\beta} = \frac{3r_p \rho_f}{4d_p (r_p \rho_p + r_f \rho_f)} \quad [\text{D.32}]$$

In more sophisticated models, $d_{\alpha\beta}$ or $A_{\alpha\beta}$ may be a function of the flow regime, and C_D may be a function of some Reynolds number. An example of this is the mixture Reynolds number (CFX Help, 2006)

$$\text{Re} = \frac{\rho_{\alpha\beta} |\underline{U}_\beta - \underline{U}_\alpha| d_{\alpha\beta}}{\mu_{\alpha\beta}} \quad [\text{D.33}]$$

with

$$\mu_{\alpha\beta} = r_\alpha \mu_\alpha + r_\beta \mu_\beta \quad [\text{D.34}]$$

D.1.3 Multiphase Turbulence

An active field of current research and development is that of multiphase turbulence. There exists many different modelling approaches with none of these currently set as the ‘industrial standard’. The turbulence within a multiphase model raises complex issues regarding the interaction of the averaging processes for multiphase and turbulent flows. CFX-5 (the software used in this work) implements simplest reasonable models.

Different turbulence models can be used for each phase, if using inhomogeneous Eulerian multiphase models. For the continuous-phase, a model where any single-phase turbulence model is allowed for example the k-e, SST, and Reynolds stress model. For the dispersed-phase a model using laminar, the dispersed phase zero-equation or one in

which the model relates dispersed phase turbulence to continuous phase turbulence, is allowed.

D.1.3.1 Dispersed phase zero equation model

This model assumes dispersed phase turbulence proportional to continuous phase turbulence (CFX Help, 2006).

$$v_{td} = \frac{v_{tc}}{\sigma} \Rightarrow \mu_{td} = \frac{\rho_d}{\rho_c} \frac{\mu_{tc}}{\sigma} \quad [\text{D.35}]$$

where σ = Eddy Viscosity Turbulent Prandtl Number. This is defined experimentally and given a value based on the Reynolds number and the turbulent shear in the flow. For a full definition, consult Churchill (2002).

If the particle relaxation time, t , is short compared to turbulence dissipation timescales, σ may be set as one. This is the default value in CFX-5 and is most frequently used. If however, t is long compared to turbulence dissipation timescales, values for σ less than one are implemented. There are several models available in the literature (Elghobashi & Abou-Arab 1983, Mostafa & Mongia 1988, Adeniji-Fashola & Chen 1990, Tu & Fletcher 1994), however these models are case specific and require experimental data so in this work the default model is implemented. Models valid for all possible multiphase situations do not exist due to the complexity of multiphase flows. In several cases, the availability of data is lacking and therefore model database expansion is difficult. Prediction of new or hypothetical situations is therefore difficult (Ishii & Mishima 1984).

With respect to CFD codes, frequently, limited computer resources restrict the possibilities of using fine computational meshes and full equation systems. Simplified forms of the interphase forces are often applied. Commercial CFD code use these simplified interphase turbulence models, for general description of the fluid behaviour. For accurate results to be drawn, intensive computational power and years of modelling on each specific case would be required.

Within CFD codes, the default zero-equation model is based on correlations for single-phase pipe flows. It must be used with caution for multiphase flow but there is the possibility for the user to supply their own prescription for eddy viscosity (either constant or an expression). The Dispersed Phase Zero Equation model is the recommended algebraic model for a dispersed phase. It is only available if the continuous phase is non-laminar (CFX Help, 2006).

D.1.3.2 Homogeneous Turbulence Models

Homogeneous turbulence models use the same turbulence model for each phase. Within this, any single-phase turbulence model is allowed such as the k- ϵ , SST, and Reynolds stress models. The solver solves for single bulk turbulence fields, averaged over all of the phases hence it ignores complex turbulence interactions. This technique is implemented in this work, as it is recommended for separated two-phase flow (e.g. liquid-liquid, gas-liquid).

Another possibility within this area is the use of a homogeneous turbulence model in inhomogeneous flow. When using the inhomogeneous model (particle and mixture models), the possibility of selecting homogeneous turbulence exists. This produces a single turbulence field common to all phases. It uses independent turbulence models in both phases that can be non-physical and numerically unstable (no coupling between the fields). CFX Help (2006) recommends this for

- free surface flows using inhomogeneous model
- separated flows
- stratified flows
- any situation where the flows tend to separate out

D.1.3.3 Turbulence enhancement

Large particles can increase continuous-phase turbulence, due to wake effects behind the particles within the flow (Figure D-3). A model by Sato (2005) for particle-induced turbulence for bubbly flow addresses this and is given by the following equation

$$\mu_{tc} = \mu_{ts} + \mu_{tp}; \quad \mu_{tp} = C_{\mu p} \rho_c r_d d_p |\underline{U}_d - \underline{U}_c| \quad [D.36]$$

Where μ_{ic} = usual shear-induced eddy viscosity

μ_{ip} = additional particle-induced eddy viscosity

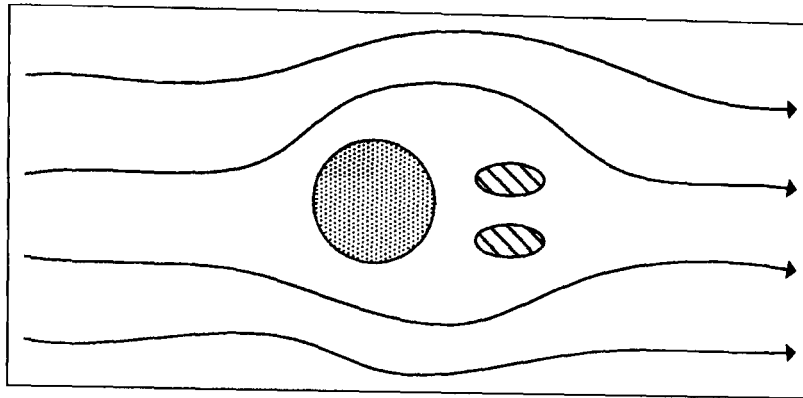


Figure D-3 Turbulence enhancement within a two-phase flow

D.1.4 Homogeneous multiphase model

In the region of infinite interphase drag, a single velocity field result can solve for an homogeneous field from the bulk momentum equation. This is particularly useful for free surface flow where the phases are separated by a distinct macroscopic interface. The volume fractions are zero or one except near the interface where the multiphase models are solved using the continuity equations for the particular location volume fraction. Figure D-4 shows a typical homogeneous multiphase flow regime. For this work, phase α represents the gas, with phase β the liquid.

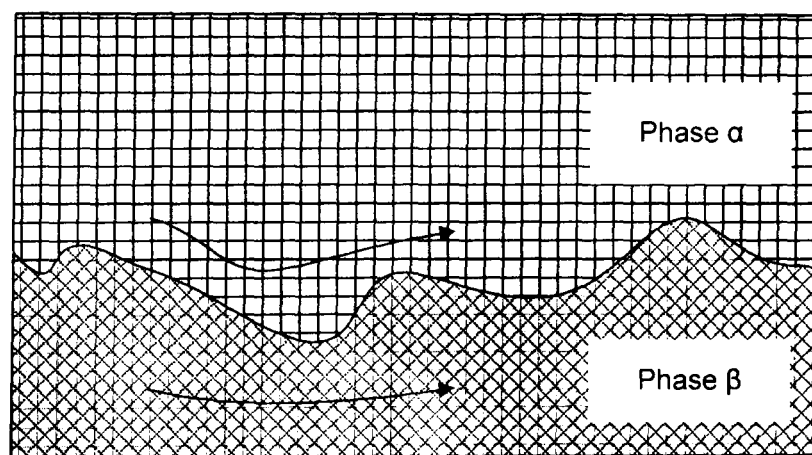


Figure D-4 Homogeneous multiphase flow interactions

In the free surface flow model, air and water are separated by a distinct free surface interface. There is only one velocity at each point in space given from the bulk velocity

$$U_{\alpha}^i = U_{\beta}^i = \sum_{\alpha} r_{\alpha} U_{\alpha}^i = U^i \quad [\text{D.37}]$$

For free surface flows of this type, it is sufficient to solve for this bulk velocity field. The model is also valid when interphase drag is very large and body forces are absent. Referring back to the continuity equations for multiphase flows [D.2] to [D.10] based on the notations by Ishii (1975)

The phasic momentum equation is

$$\frac{\partial(r_{\alpha}\rho_{\alpha}U_{\alpha}^i)}{\partial t} + \frac{\partial(r_{\alpha}\rho_{\alpha}U_{\alpha}^jU_{\alpha}^i)}{\partial x^j} = -r_{\alpha}\frac{\partial p}{\partial x^i} + r_{\alpha}\rho_{\alpha}g^i + \frac{\partial(r_{\alpha}\tau_{ji})}{\partial x^j} + M_{\alpha} \quad [\text{D.38}]$$

Taking further for the sum over the phases

$$\frac{\partial(\rho U^i)}{\partial t} + \frac{\partial(\rho U^j U^i)}{\partial x^j} = -\frac{\partial p}{\partial x^i} + \rho g^i + \frac{\partial \tau^{ji}}{\partial x^j} \quad [\text{D.39}]$$

Where

$$\rho = \sum_{\alpha} r_{\alpha}\rho_{\alpha} \quad , \quad \tau^{ji} = \sum_{\alpha} r_{\alpha}\tau_{\alpha}^{ji}$$

Essentially this is a single-phase momentum equation with mixture density and viscosity. For phasic continuity

$$\frac{\partial(r_{\alpha}\rho_{\alpha})}{\partial t} + \frac{\partial(r_{\alpha}\rho_{\alpha}U_{\alpha}^j)}{\partial x^j} = 0 \quad [\text{D.40}]$$

If the model is homogeneous and therefore the velocity is of the entire fluid and not that of one phase,

$$\frac{\partial(r_{\alpha}\rho_{\alpha})}{\partial t} + \frac{\partial(r_{\alpha}\rho_{\alpha}U^j)}{\partial x^j} = 0 \quad [\text{D.41}]$$

Neglecting compressibility as the equation is symmetric for all phases. Therefore solving for (N-1) volume fractions and treating the other as ballast, the volume continuity is

$$\frac{\partial U^j}{\partial x^j} = 0 \quad [D.42]$$

Within these equations, incompressibility is assumed for clarity only and is not a fundamental limitation.

Bulk equations are solved for other homogeneous field variables such as turbulence. Energy is a special case as the temperature is homogeneous, therefore enthalpy is a principal variable, i.e. it is not shared among the fluids of the multiphase. The solution to this involves solving two phasic equations with a large interphase heat transfer term, to force the temperatures to be the same.

In multiphase flow (MPF) models of this type, the model is most frequently set as homogeneous. The solution uses a compressive discretisation advection scheme for the main with the use of transient terms at the interface, typically smeared over 2-3 elements of the grid. For the pressure-velocity coupling (Rhie-Chow) special treatment of buoyancy force, the flow well must behave well at the interface.

D.1.5 Surface Tension

Surface tension (σ) is defined as the force along a line of unit length where the force is parallel to the surface but perpendicular to the line. An attractive force at the free surface interface applies the surface tension in free surface flow (Figure D-5).

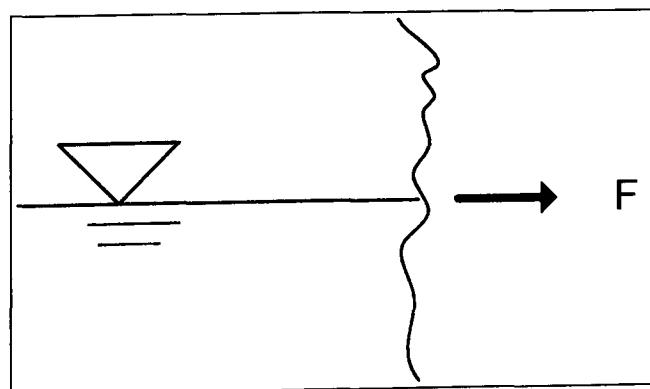


Figure D-5 Surface tension force on a surface

In its simplest form

$$\sigma = \frac{F}{L}$$

[D.43]

The normal component of the surface tension acts to smooth regions of high curvature and induces a pressure rise within a droplet denoted as

$$\Delta p = \sigma \kappa \quad [D.44]$$

The tangential component moves fluid along the interface towards a region of high σ , often called the Marangoni effect. This effect also takes into account the fact that σ decreases with temperature. The forces acting on the fluid lead to the two dimensionless numbers namely the Weber number[D.45] , and the Marangoni number[D.46].

$$\text{We} = \frac{\rho U^2 L}{\sigma} = \frac{\text{Inertial force}}{\text{Surface tension force}} \quad [D.45]$$

$$\text{Ma} = -\frac{\partial \sigma}{\partial T} \frac{\Delta T L}{\mu \alpha} \quad [D.46]$$

The work of Brackbill, Kothe and Zemach (1992) allowed for modelling of the surface tension in free surface flows. Conceptually, surface force at the interface is

$$\vec{f}_s = -\sigma \kappa \hat{n} + \nabla_s \sigma \quad [D.47]$$

However, with this equation it is awkward to deal with interface topology. Reformulating equation [D.47] as a continuum force (Brackbill, Kothe, Zemach, 1992) gives

$$\begin{aligned} \vec{F}_s &= \vec{f}_s \delta_s \\ \delta_s &= |\nabla r| \\ \kappa &= \nabla \cdot \hat{n} \\ \hat{n} &= -\nabla r / |\nabla r| \end{aligned} \quad [D.48]$$

with the wall contact angle specifying the direction of normal at the wall.

Appendix E Additional Figures

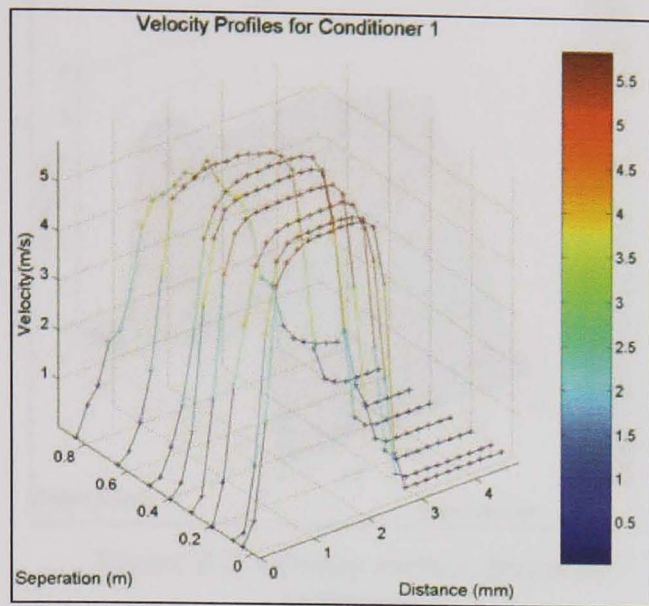


Figure E-1 Velocity profiles for Conditioner 1

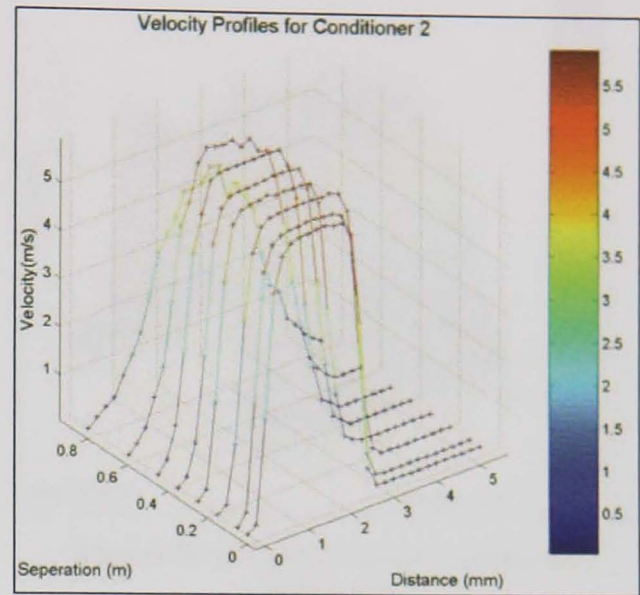


Figure E-2 Velocity profiles for conditioner 2

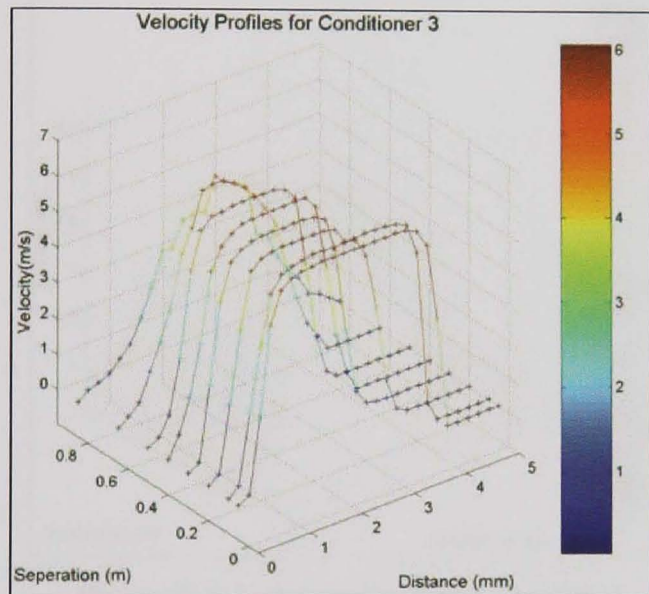


Figure E-3 Velocity profiles for conditioner 3

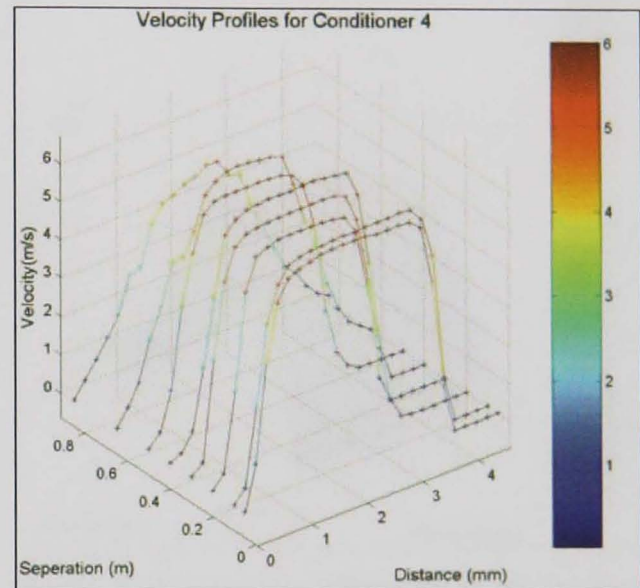


Figure E-4 Velocity profiles for conditioner 4

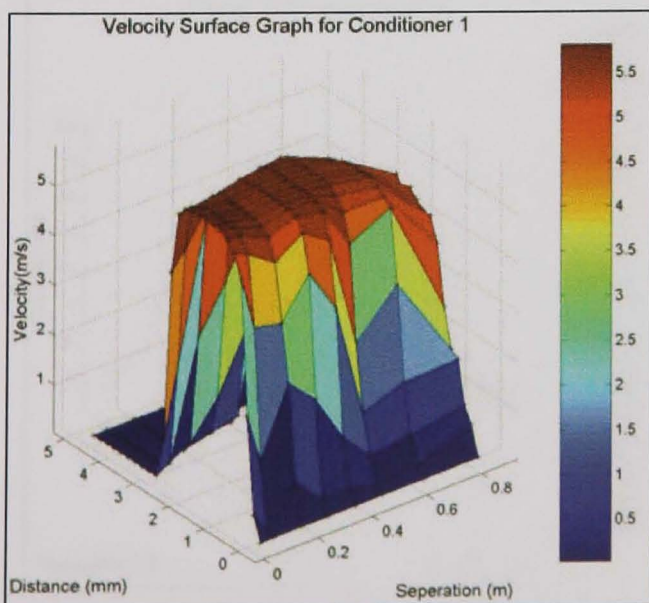


Figure E-5 Surface graph for conditioner 1

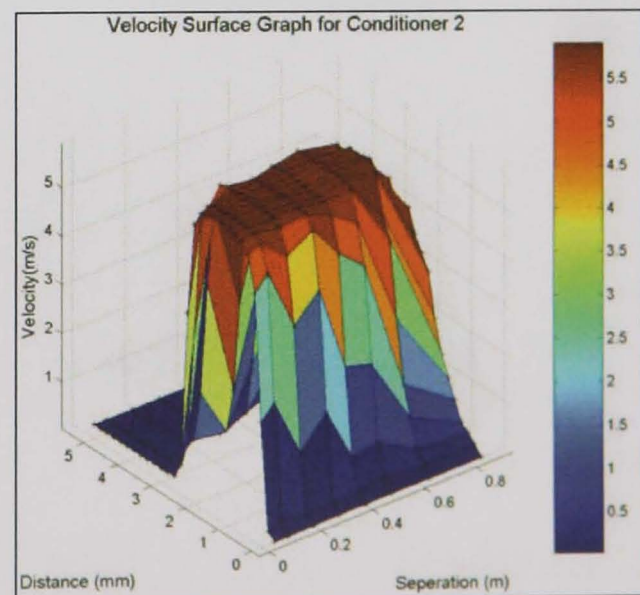


Figure E-6 Surface graph for conditioner 2

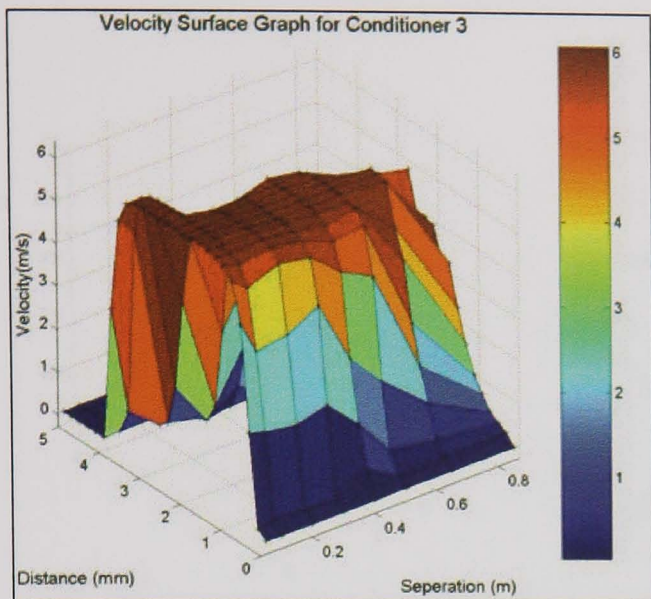


Figure E-7 Velocity surface graph for conditioner 3

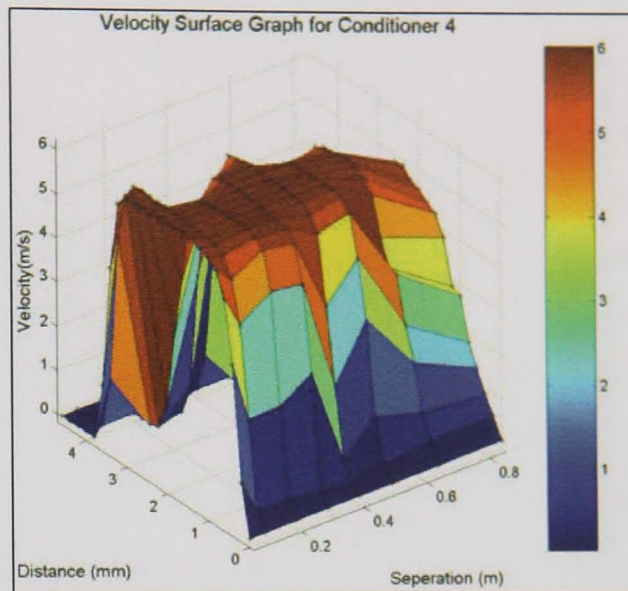


Figure E-8 Velocity surface graph for conditioner 4

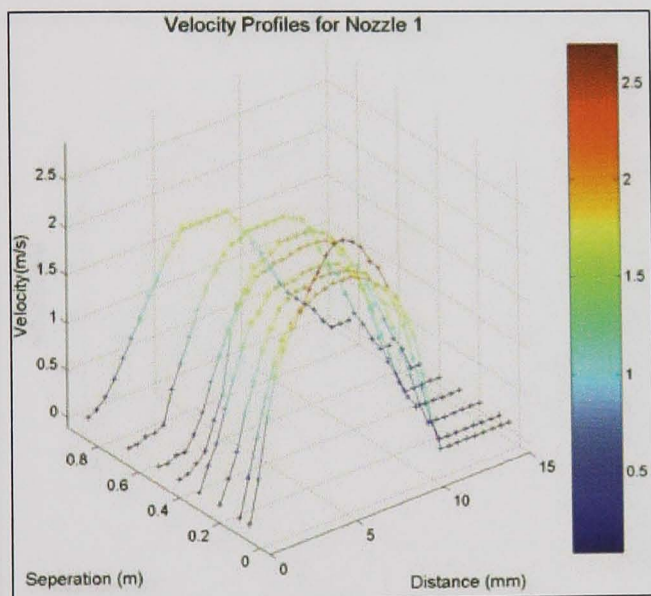


Figure E-9 Velocity profiles for nozzle 1

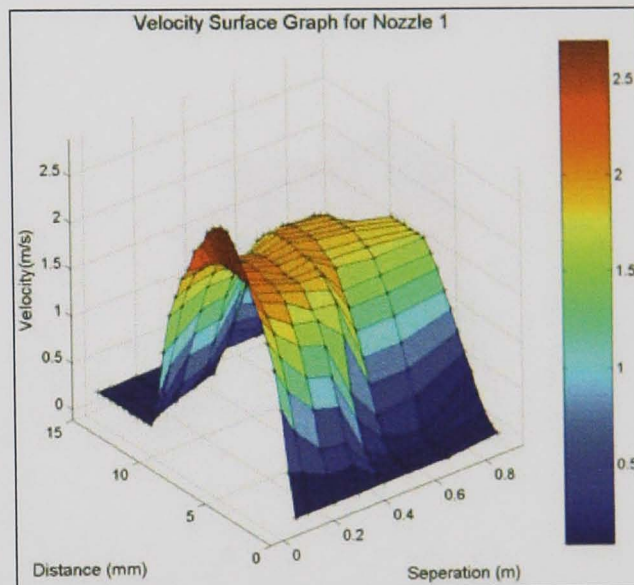


Figure E-10 Velocity surface graph for nozzle 1

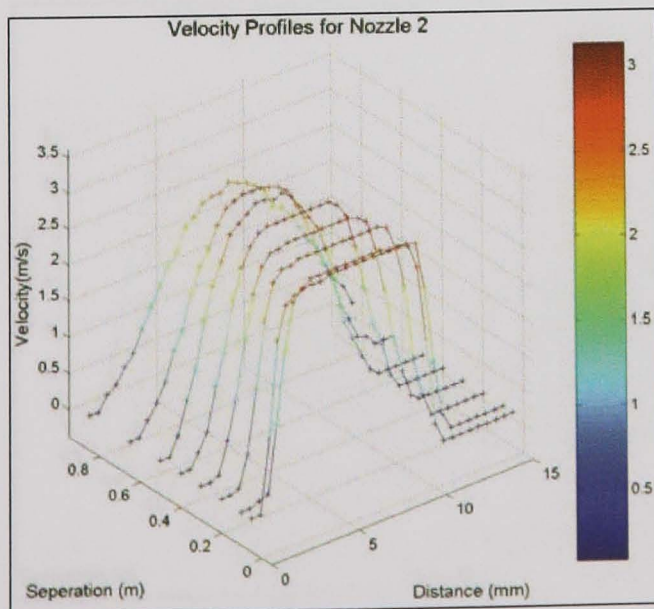


Figure E-11 Velocity profiles for nozzle 2

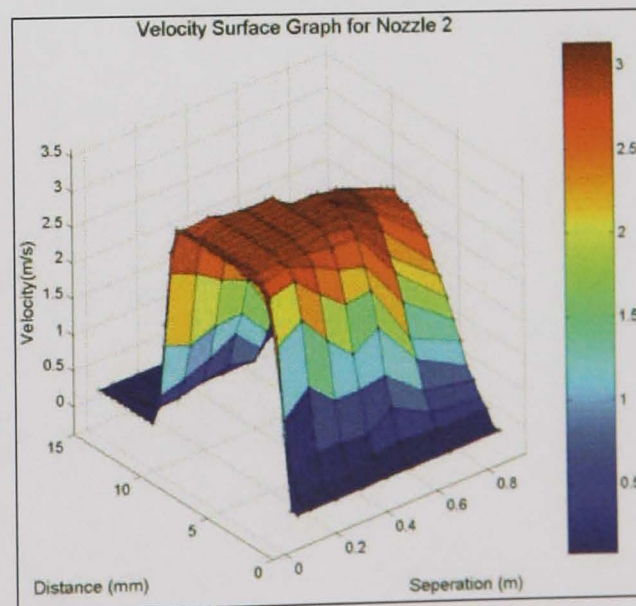


Figure E-12 Velocity surface graph for nozzle 2

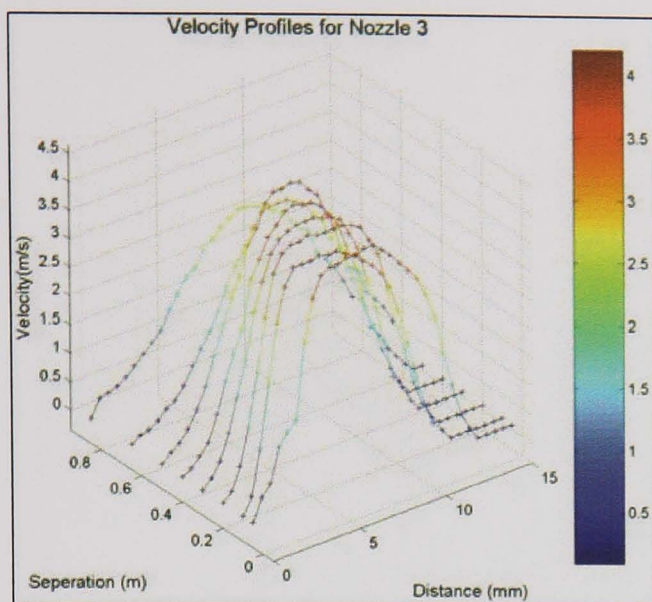


Figure E-13 Velocity profiles for nozzle 3

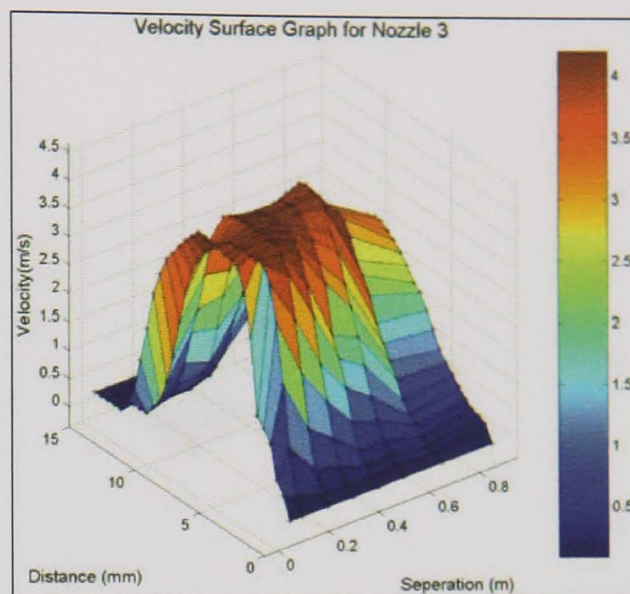


Figure E-14 Velocity surface graph for nozzle 3

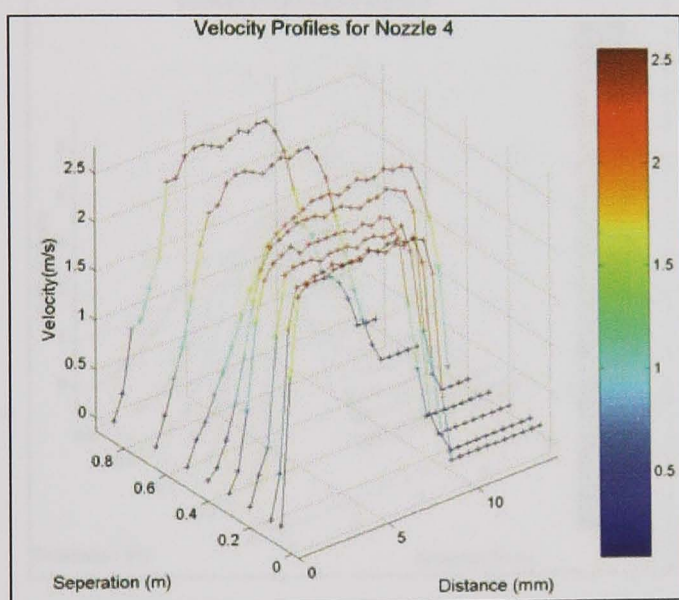


Figure E-15 Velocity profiles for nozzle 4

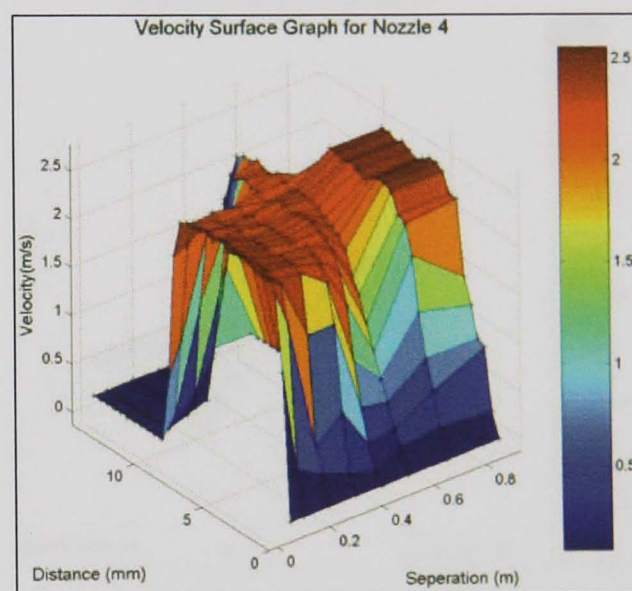


Figure E-16 Velocity surface graph for nozzle 4

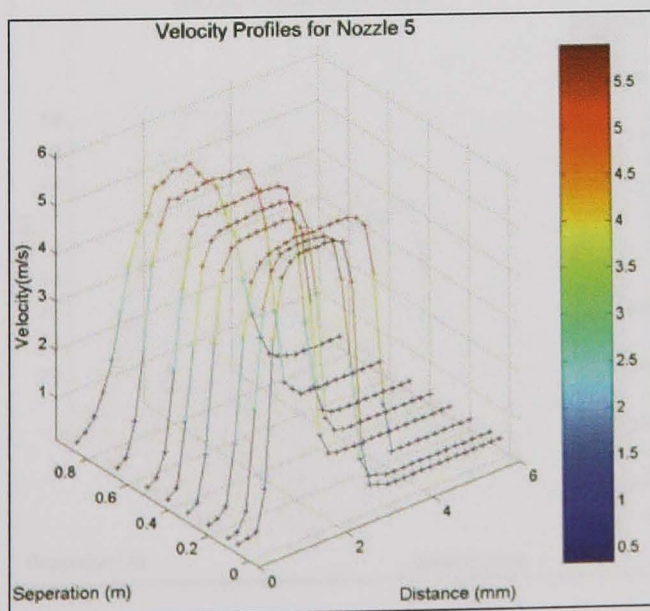


Figure E-17 Velocity profiles for nozzle 5

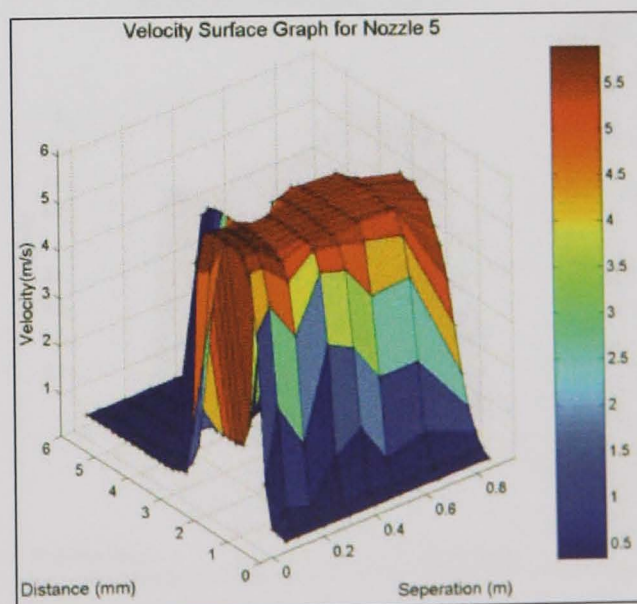


Figure E-18 Velocity surface graph for nozzle 5

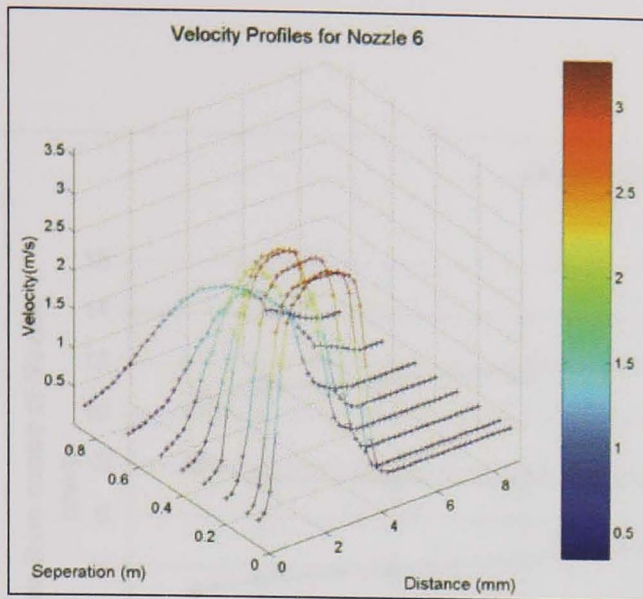


Figure E-19 Velocity profiles for nozzle 6

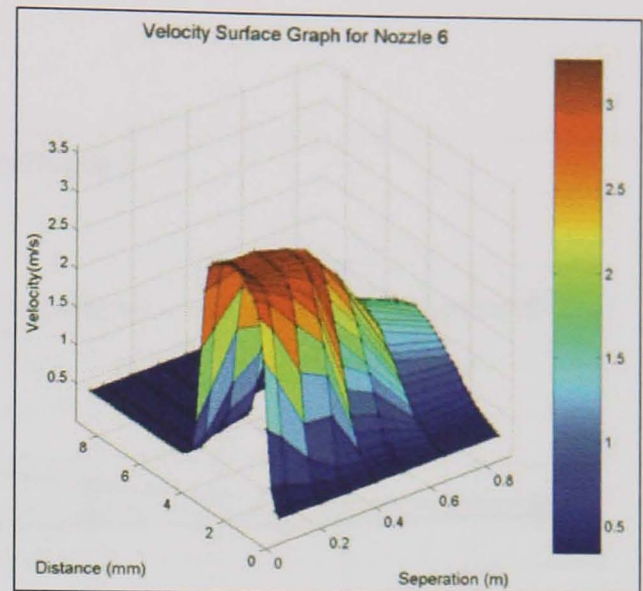


Figure E-20 Velocity surface graph for nozzle 6

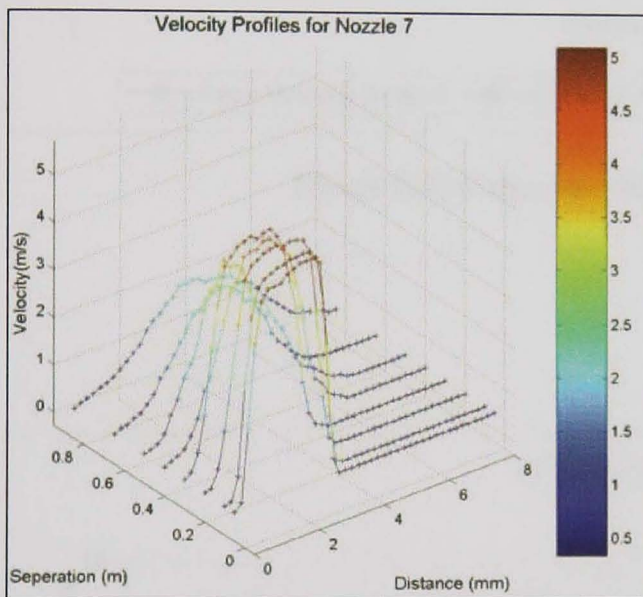


Figure E-21 Velocity profiles for nozzle 7

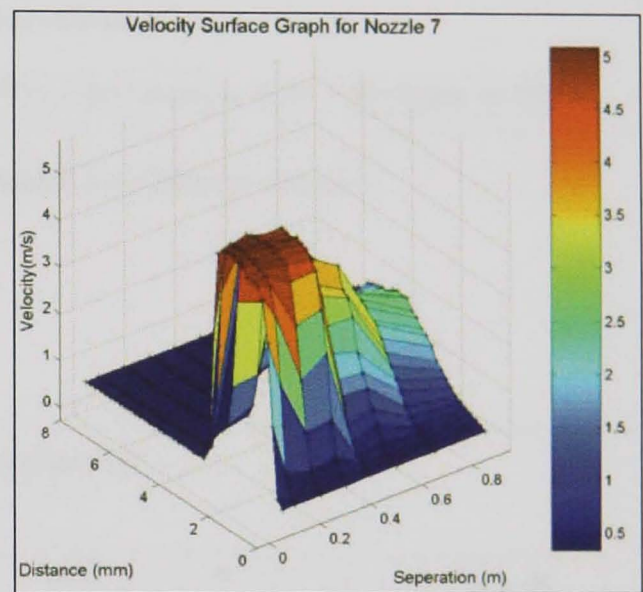


Figure E-22 Velocity surface graph for nozzle 7

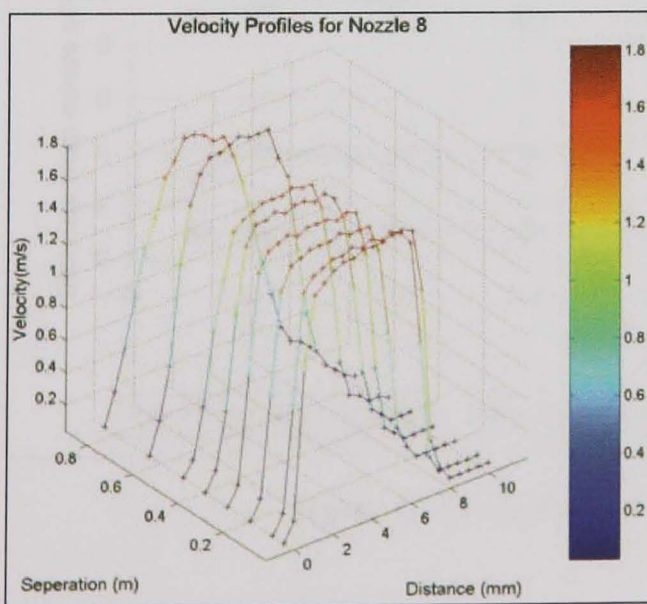


Figure E-23 Velocity profiles for nozzle 8

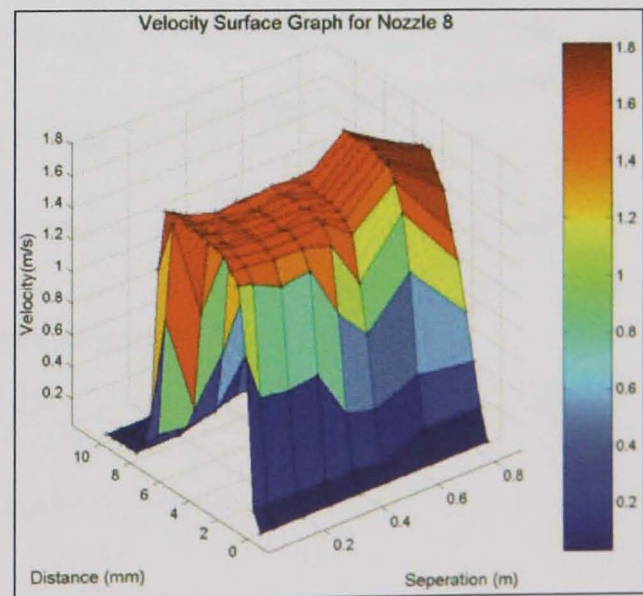


Figure E-24 Velocity surface graph for nozzle 8

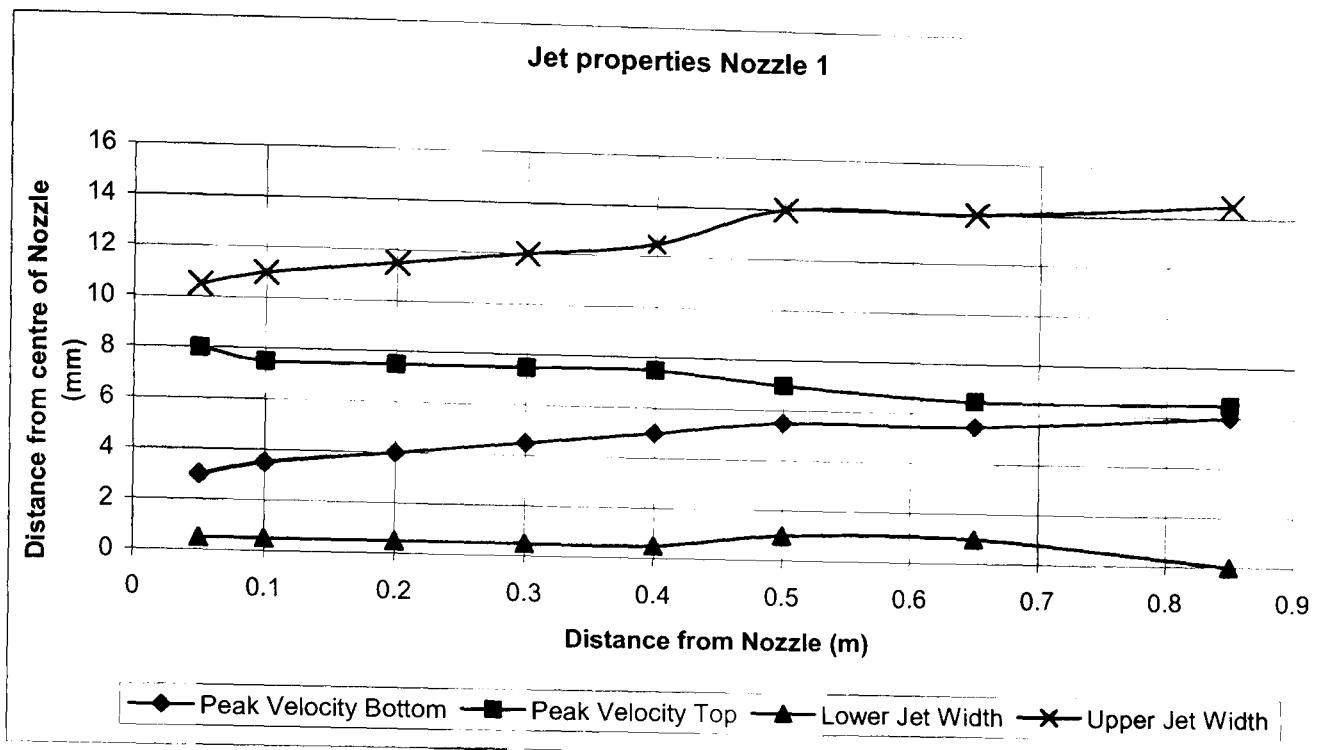


Figure E-25 Coherence length and Jet width for nozzle 1

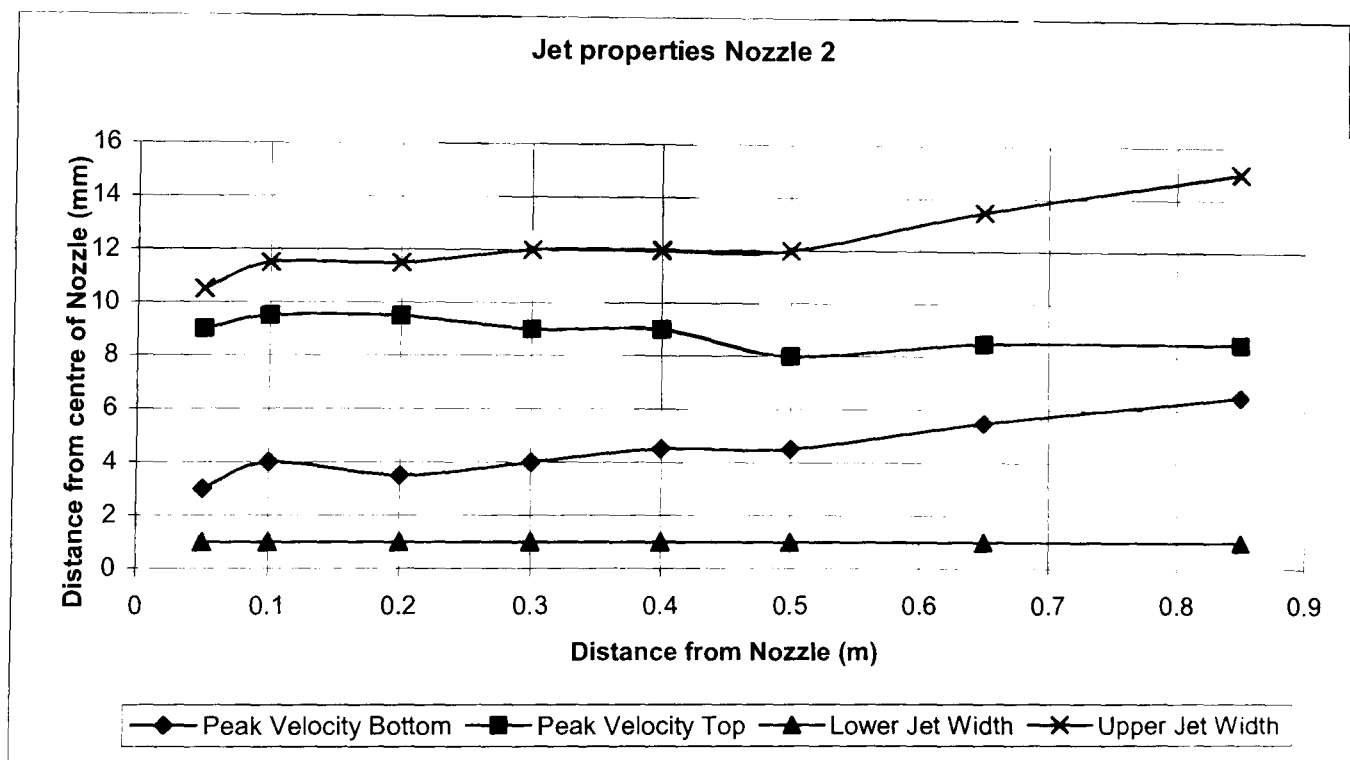


Figure E-26 Coherence length and Jet width for nozzle 2

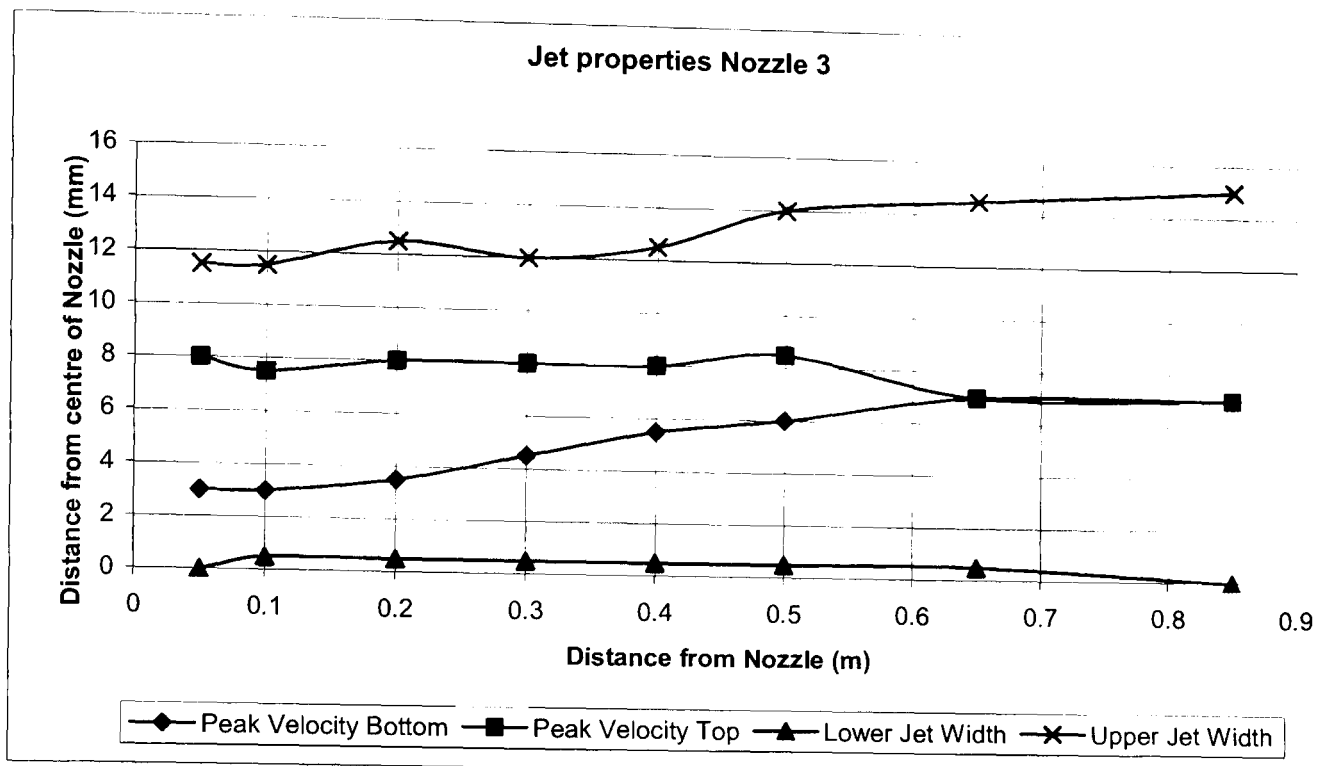


Figure E-27 Coherence length and Jet width for nozzle 3

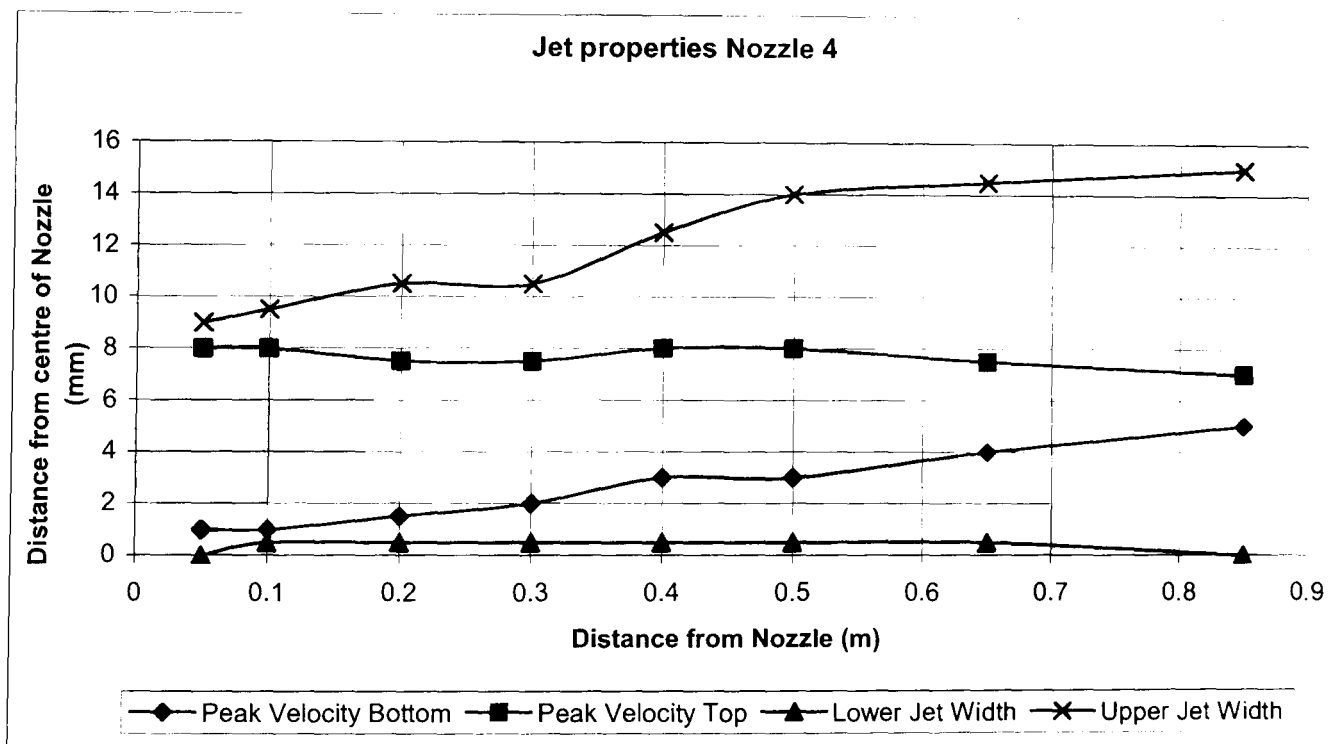


Figure E-28 Coherence length and Jet width for nozzle 4

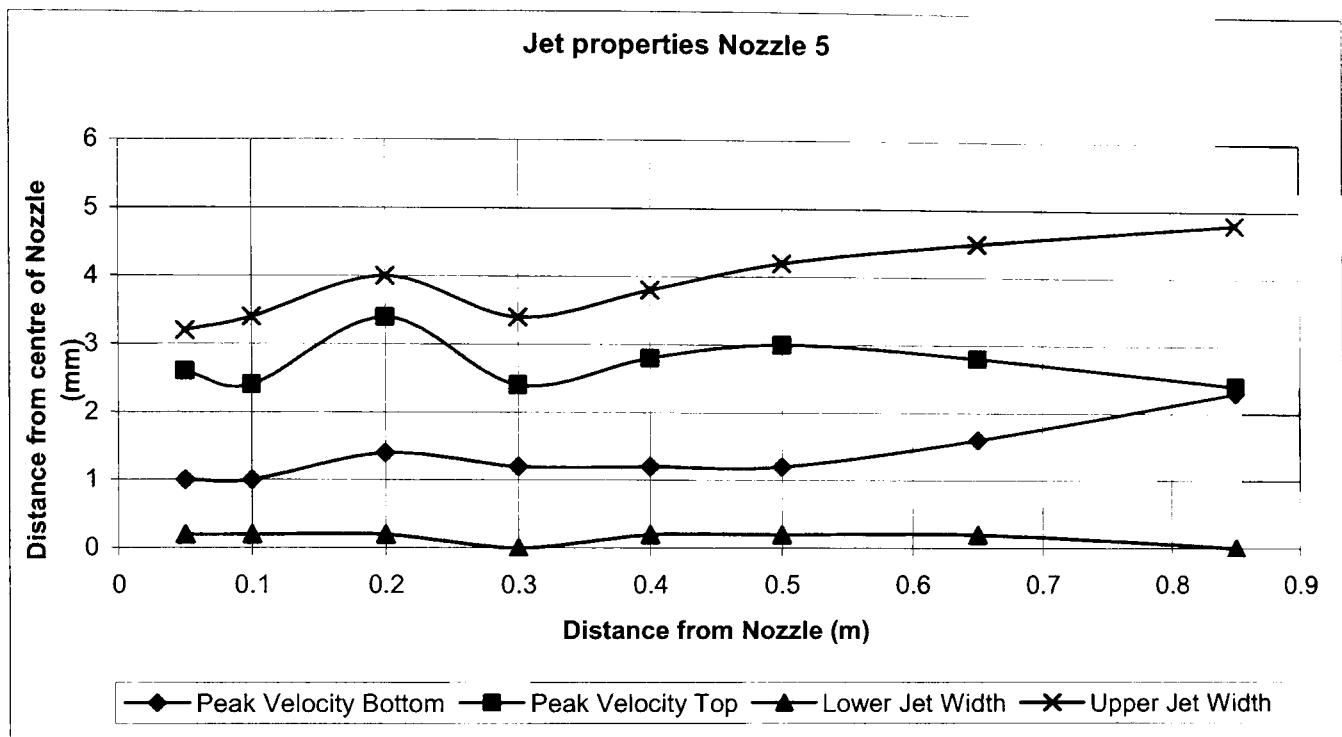


Figure E-29 Coherence length and Jet width for nozzle 5

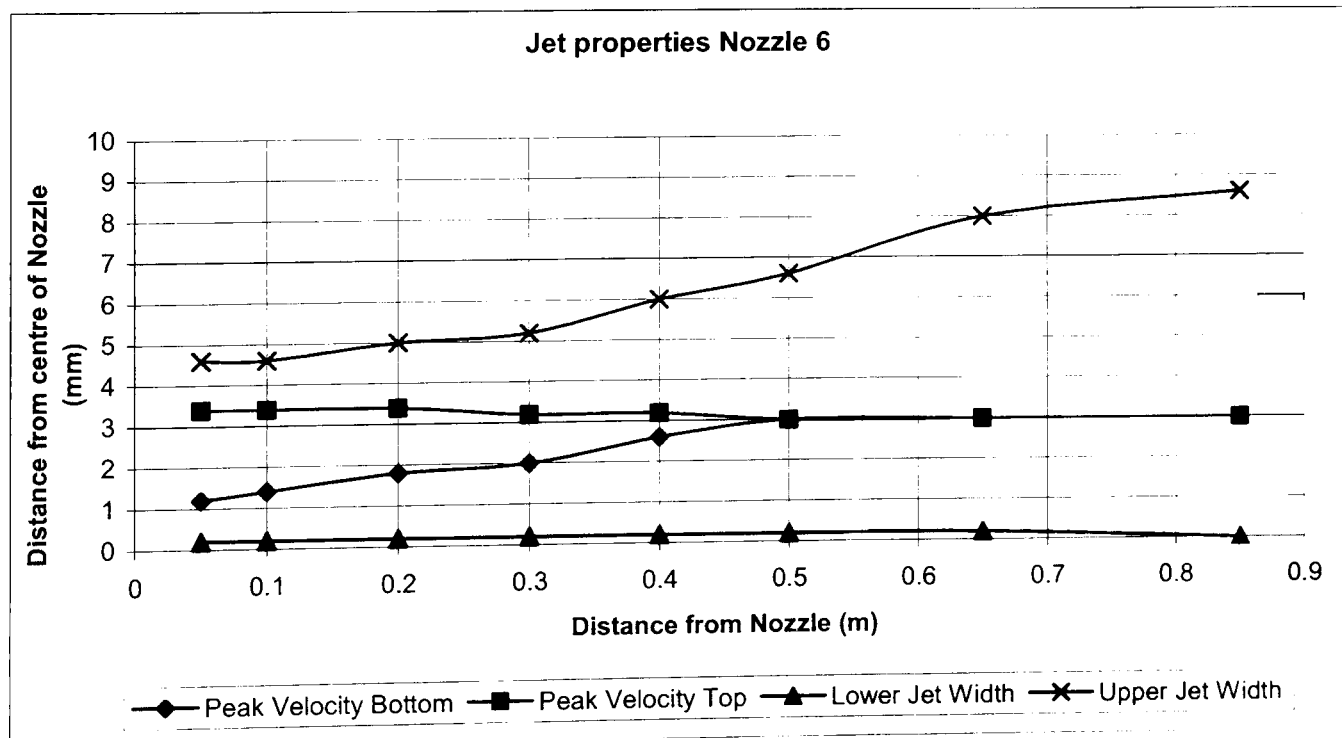


Figure E-30 Coherence length and Jet width for nozzle 6

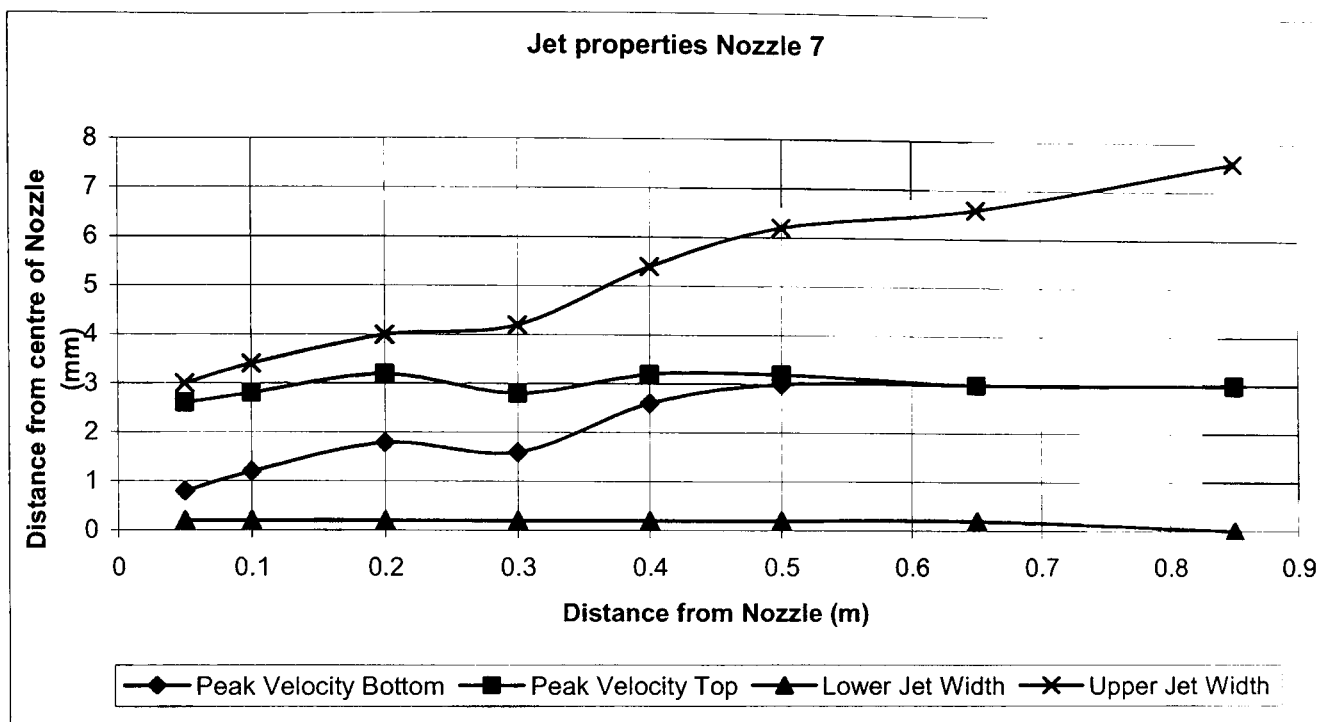


Figure E-31 Coherence length and Jet width for nozzle 7

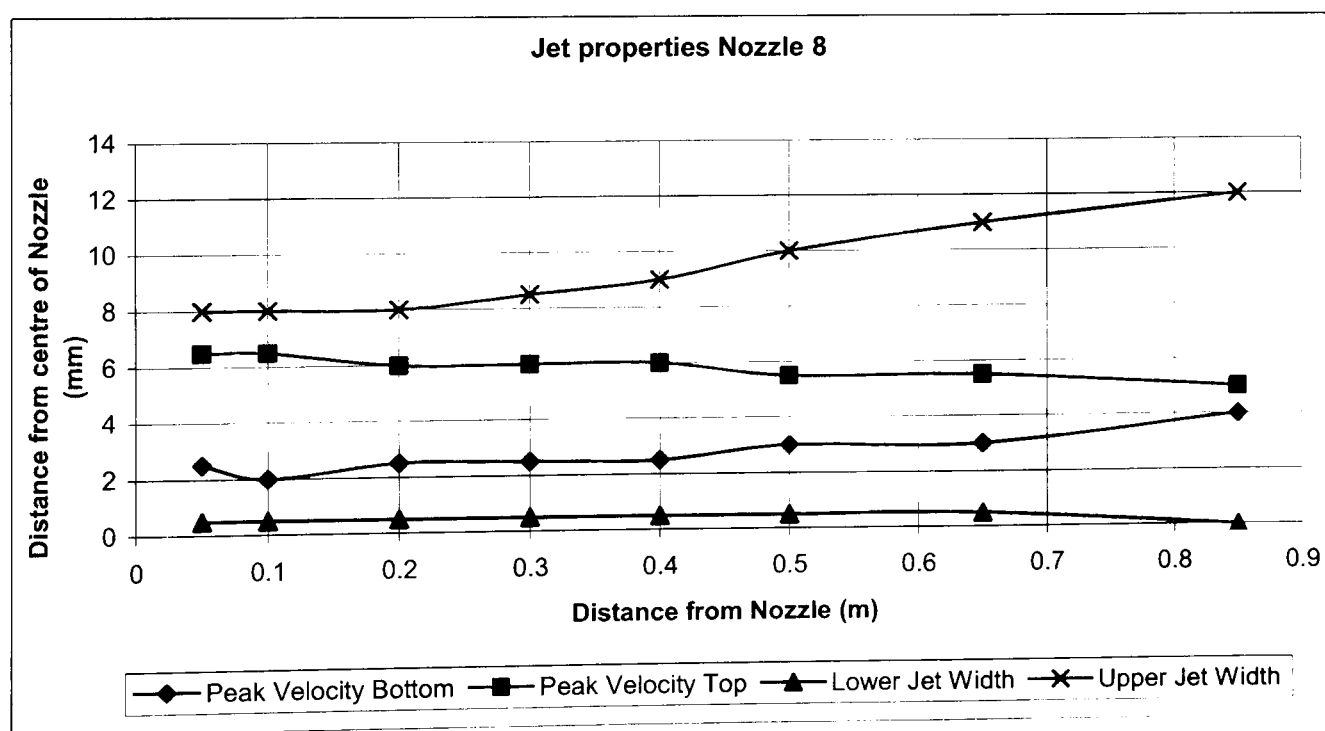


Figure E-32 Coherence length and Jet width for nozzle 8

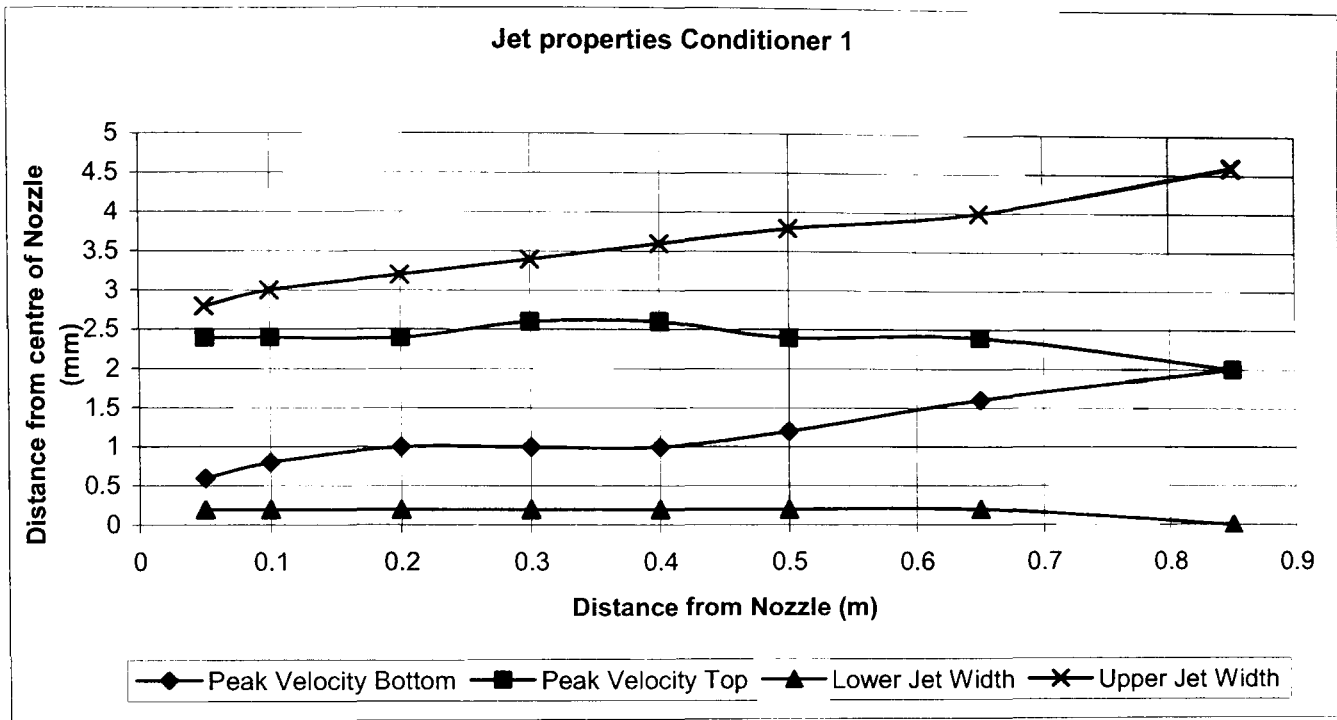


Figure E-33 Coherence length and Jet width for nozzle 5 with conditioner 1

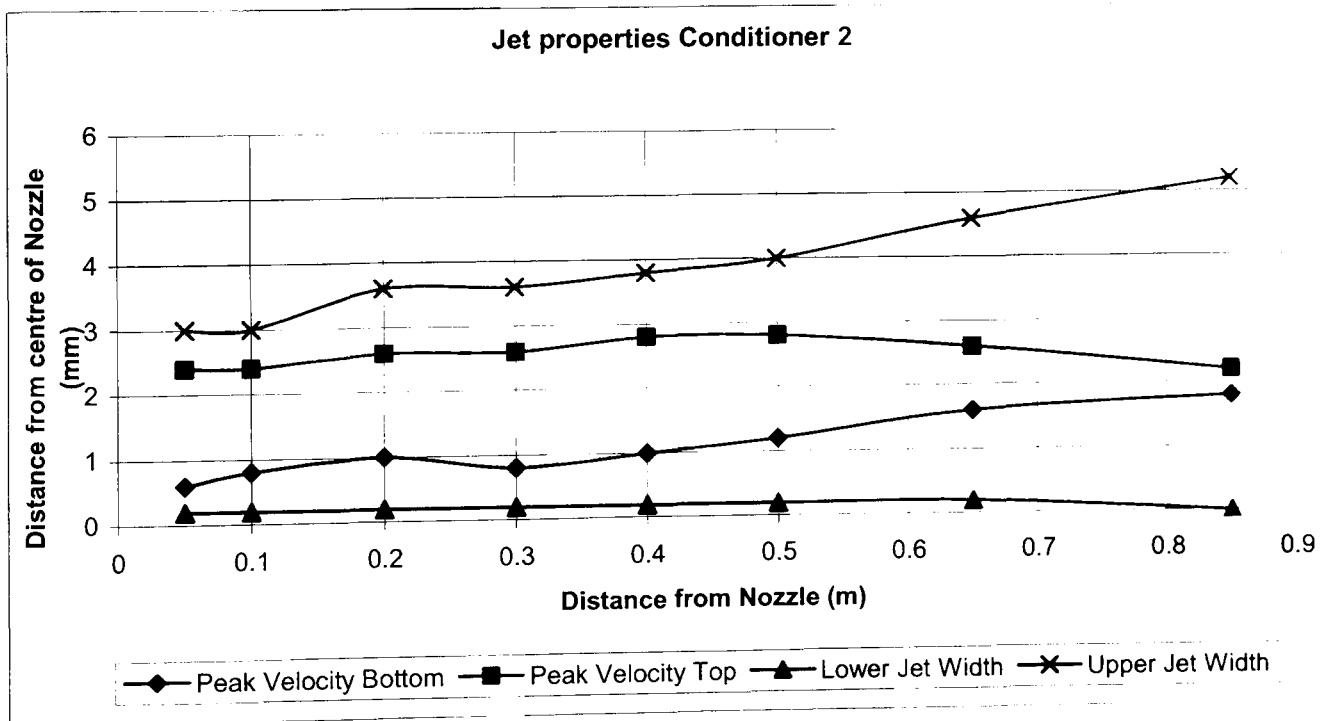


Figure E-34 Coherence length and Jet width for nozzle 5 with conditioner 2

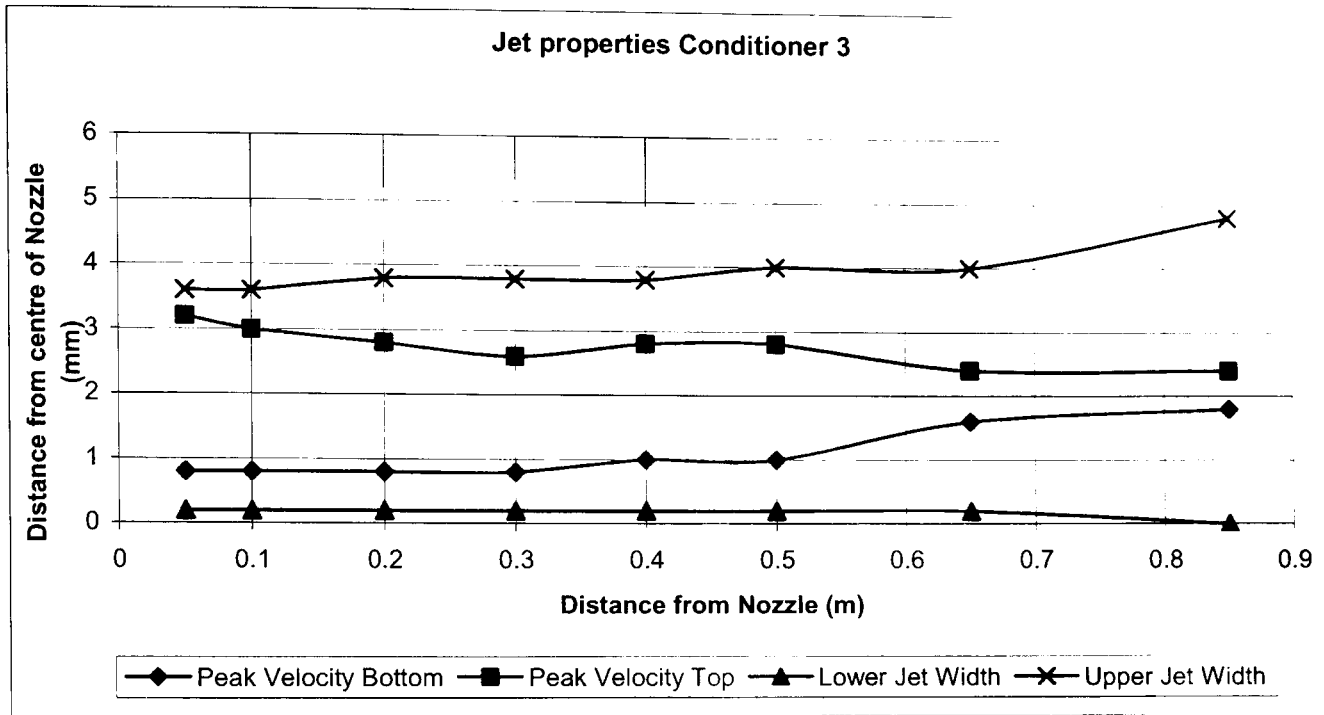


Figure E-35 Coherence length and Jet width for nozzle 5 with conditioner 3

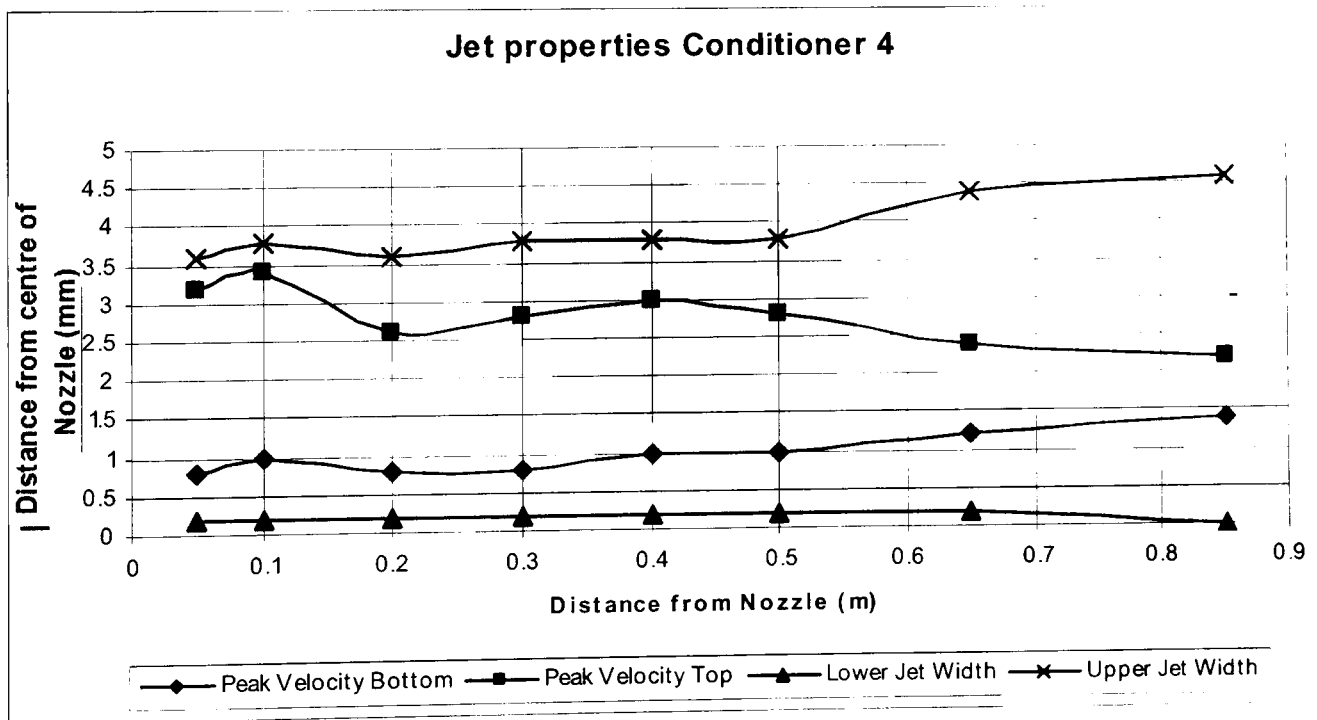


Figure E-36 Coherence length and Jet width for nozzle 5 with conditioner 4

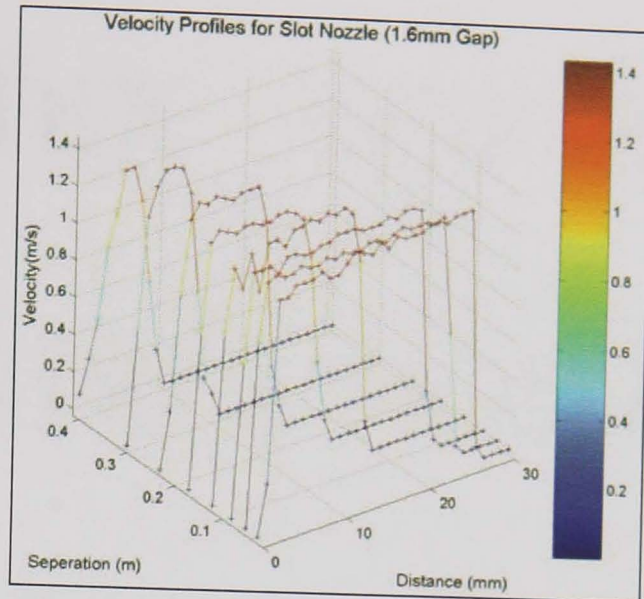


Figure E-37 Velocity profiles for the variable slot nozzle (gap 1.6mm)

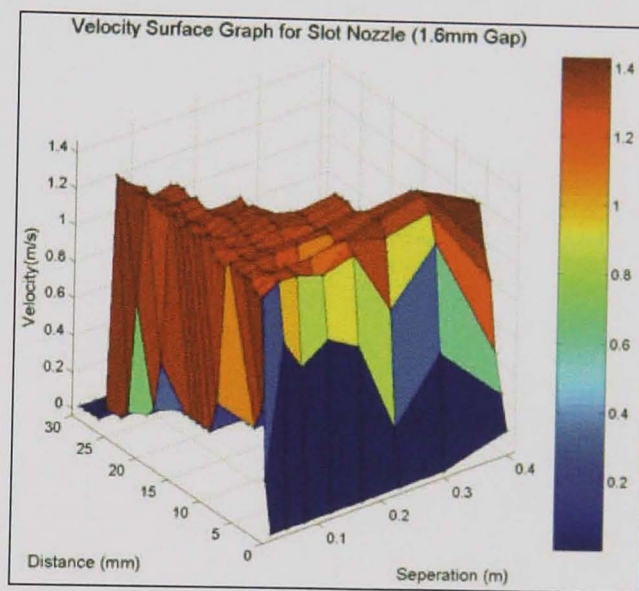


Figure E-38 Surface velocity graph for the variable slot nozzle (gap 1.6mm)

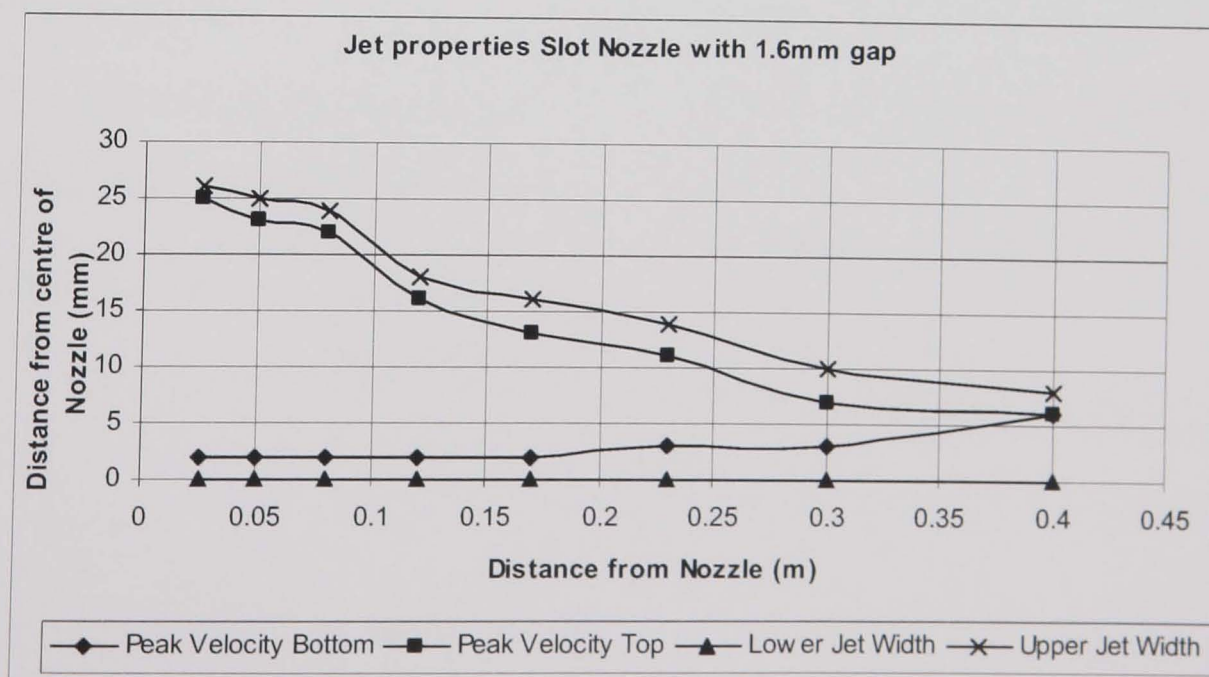


Figure E-39 Coherence length and jet width for the variable slot nozzle (Gap 1.6mm)

APPENDIX NOT COPIED

ON INSTRUCTION FROM

UNIVERSITY

Appendix G Publications

Baines-Jones V.A., Morgan M.N., Batako A.D., Brown E., 2009. The role of Computational Fluid Dynamics for coolant delivery in industrial grinding of steels and cast iron. 9th International Conference and Exhibition on Laser metrology, machine tool, CMM and robotic performance LAMDAMAP 2009. 30th June - 2nd July 2009.

Baines-Jones V.A., Morgan M.N., Batako A.D., Brown E., 2008. Modelling and simulation of grinding fluid nozzles. The 6th International Conference on Manufacturing Research (ICMR08) Brunel University, UK, 9-11th September 2008.

M N Morgan, A R Jackson, V Baines-Jones, A Batako, H Wu, W B Rowe, "Fluid delivery in grinding" *Annals of the CIRP*, 2008, 57/1 363-366. DOI: 10.1016/j.cirp.2008.03.090.

M N Morgan, V Baines-Jones, "On the coherent length of fluid nozzles in grinding" 2008, Invited paper: Special Topic Volume- Progress in Abrasive and Grinding Technology, *Key Engineering Materials*, doi:10.4028/www.scientific.net/KEM.404.61.

Baines-Jones V.A., Morgan M.N., Batako A.D., Allanson D.R., 2007. Computational Fluid Dynamics Analysis of Grinding Fluid Nozzles. The 3rd GERI annual research synopsis (GARS) Liverpool John Moores University, UK, 27th June 2007.

Baines-Jones V.A., 2007. Grinding Coolant Application in Grinding, and Associated Problems in an Industrial Environment. GERI weekly seminar, Liverpool John Moores University, UK, 2nd March 2007.

Baines-Jones V.A., Jackson, A., 2006. Post Graduate Training - UKGRAD. GERI weekly seminar, Liverpool John Moores University, UK, 28th April 2006.

Baines-Jones V.A., Morgan M.N., Batako A.D., Allanson D.R., 2005. Grinding fluid delivery system design - nozzle optimisation. The 1st GERI annual research synopsis (GARS) Liverpool John Moores University, UK, 22nd June 2005.

Baines-Jones V.A., 2005. An investigation into system design for optimal useful fluid flow in grinding. GERI weekly seminar, Liverpool John Moores University, UK, 7th December 2005.